Transactions of the ASME, Journal of Heat Transfer (ISSN 0022-1481) is published monthly by The American Society of Mechanical Engineers, Three Park Avenue, New York, NY 10016. Periodicals postage paid at New York, NY and additional mailing offices. POSTMASTER: Send address changes to Transactions of the ASME, Journal of Heat Transfer, c/o THE AMERICAN SOCIETY OF MECHANICAL ENGINEERS, 22 Law Drive, Box 2300, Fairfield, NJ 07007-2300. **CHANGES OF ADDRESS** must be received at Society headquarters seven weeks before they are to be effective. Please send old label and new address. **STATEMENT from By-Laws.** The Society shall not be responsible for statements or opinions advanced in papers or ... printed in its publications (B7.1, Para. 3).

Journal of Heat Transfer

Published Monthly by ASME

VOLUME 127 • NUMBER 8 • AUGUST 2005

EDITORIAL

HEAT TRANSFER PHOTOGALLERY

PHOTOGALLERY

(Contents continued on inside back cover)

This journal is printed on acid-free paper, which exceeds the ANSI Z39.48-1992 specification for permanence of paper and library materials. ♾™
♻ 85% recycled content, including 10% post-consumer fibers.

(Contents continued)

Journal of Heat Transfer Volume 127, Number 8 AUGUST 2005

RESEARCH PAPERS

TECHNICAL BRIEFS

(Contents continued on facing page)

(**Contents continued**)

ANNOUNCEMENT

Call for Photographs: Photogallery—Heat Transfer Visualization

The ASME Journal of Heat Transfer is abstracted and indexed in the following:

Applied Science and Technology Index, Chemical Abstracts, Chemical Engineering and Biotechnology Abstracts (Electronic equivalent of Process and Chemical Engineering), Civil Engineering Abstracts, Compendex (The electronic equivalent of Engineering Index), Corrosion Abstracts, Current Contents, E & P Health, Safety, and Environment, Ei EncompassLit, Engineered Materials Abstracts, Engineering Index, Enviroline (The electronic equivalent of Environment Abstracts), Environment Abstracts, Environmental Engineering Abstracts, Environmental Science and Pollution Management, Fluidex, Fuel and Energy Abstracts, Index to Scientific Reviews, INSPEC, International Building Services Abstracts, Mechanical & Transportation Engineering Abstracts, Mechanical Engineering Abstracts, METADEX (The electronic equivalent of Metals Abstracts and Alloys Index), Petroleum Abstracts, Process and Chemical Engineering, Referativnyi Zhurnal, Science Citation Index, SciSearch (The electronic equivalent of Science Citation Index), Theoretical Chemical Engineering

Journal of Heat Transfer

Editorial

It is a privilege and an honor for me to succeed my friend, Professor Vijay Dhir, a distinguished and well-known scholar, as the new Editor of ASME's *Journal of Heat Transfer*. Over the past five years as Editor, Vijay has made many substantial improvements in the Journal, including increasing the frequency from bi-monthly to monthly and bringing out special issues on important areas of heat transfer. I am also honored to follow in the footsteps of the previous Editors of the Journal. It is an awe-inspiring list of leaders in the field of heat transfer and includes Professors E. M. Sparrow, K. T. Yang, G. M. Faeth, R. Viskanta, J. R. Howell, and V. K. Dhir. All these Editors have made the Journal what it is today and we all owe them much gratitude for their contributions. I have personally gained a lot from them, particularly from Ray Viskanta and Jack Howell, with whom I served as Associate Editor. I hope to continue the high standards and traditions set by them.

The *Journal of Heat Transfer* has grown substantially in recent years, both in terms of the number of papers published and the impact on the field. It has become one of the preeminent avenues for the dissemination of research results in heat transfer and serves as a dominant source of archival information for academia, industry, national labs and other organizations. However, the scope and impact of the field of heat transfer has also changed and grown over the past two decades. Since heat transfer is concerned with the transport of thermal energy, the field is intimately coupled with a wide variety of problems and systems. These include problems arising in diverse areas such as energy, environment, transportation, space, electronics, manufacturing, refrigeration and air-conditioning, biological systems, security and, of course, heat transfer equipment. Thus, heat transfer must be considered in its broader concept of thermal sciences and engineering. The Journal welcomes papers in all such areas in which thermal energy transport is a major consideration. Obviously, specialized journals have been developed to present concerns and solutions in different areas, such as polymer processing, crystal growth, combustion, engines, gas turbines, electronic packaging and solar energy. However, basic and long-range concerns with heat transfer are common to many of these areas and similar solution strategies may be adopted. The *Journal of Heat Transfer* could be the natural venue for publishing the relevant analysis, experimentation and results.

My main goal is to maintain the high quality and standards that the Journal is known for, while striving to expand its reach and impact. It is important to ensure that the papers are reviewed and published in a timely manner. The use of electronic submission and review has been a major help in this direction. Electronic submissions have also become critical due to the strong international base of authors, readers, reviewers and Associate Editors. I expect the international contributions to grow in the future, as research in thermal sciences and related areas continues to grow around the world. The participation of industry has increased somewhat in recent years, but clearly much more effort is needed to publish high quality, archival material that would be of practical and engineering interest to non-academic researchers and engineers. Similarly, publication of relevant papers by industrial researchers through review articles or contributed papers will strengthen the coupling between academic research and industrial needs.

I realize that serving as the Editor of a prestigious journal such as the *Journal of Heat Transfer* is quite challenging. But the Journal has been fortunate in having had the support of many dedicated Associate Editors, who have spent enormous time and effort getting the papers reviewed by appropriate referees in time. The large number of reviewers used by the Journal has been instrumental in achieving the goals of timeliness and quality. The publishing department at ASME is staffed with very experienced, capable, dedicated and sincere people. I look forward to interacting with them, as I seek their help, guidance and support. The Heat Transfer Division has been a major partner in the growth and development of the Journal. I look forward to interacting with the Executive Committee of the Division as we go forward.

Best wishes to all the authors, reviewers, Associate Editors, past Editors, ASME publishing staff and all others who have interest in the *Journal of Heat Transfer*.

Yogesh Jaluria
Editor

Journal of Heat Transfer

Heat Transfer Photogallery

The Ninth "Heat Transfer Photogallery" was sponsored by the K-22 Heat Transfer Visualization Committee for the 2004 International Mechanical Engineering Congress and Exhibition (IMECE) held in Anaheim in California, on November 13–19, 2004. The peer-reviewed evaluation process for the presented entries identified the thirteen entries for publication in the *ASME Journal of Heat Transfer*.

The purpose of publishing these entries is to draw attention to the innovative features of optical diagnostic techniques and aesthetic qualities of thermal processes. To focus on visualization images and schematics, the text is kept to a minimum and further details should be found directly from the authors. My wish is that the journal readers enjoy viewing these collections, acquire knowledge of the state-of-the-art features, and promote their participation in the 2005-IMECE Photogallery session presentation (http://www.asmeconferences.org/congress05). The Call for Photos for the 2005-IMECE is also announced in this issue of *ASME Journal of Heat Transfer*.

The photogallery entries are listed based on their technical topics as briefly summarized:

Natural Convection Phenomena

- Multi-Scale Natural Convection Problem (A. K. da Silva and A. Bejan, Duke University)
- Temperature-Velocity Measurements for Transient Natural Convection (I. Nakane, A. Narumi, and K. Fukuda, Kanagawa Institute of Technology, Japan)
- Dual-Wave Holographic Interferometry for Solidification and Mass Convection (N. Tsushima, Tokyo A&T, A. Narumi and I. Nakane, Kanagawa Institute of Technology, T. Kashiwagi and A. Akisawa, Tokyo A&T)

Boiling

- Bubble Formation and Surrounding Flow From a Heated Wire (H. Wang, Tsinghua University, China, and X. Peng, D. M. Christopher, and S. V. Garimella, Purdue University)
- Single, Twin and Multiple Bubble Agglomeration for Nucleate Boiling in Microchannels (D. Liu, P.-S. Lee, and S. V. Garimella, Purdue University)
- Bubble Formation Under Variable Gravity (C. Herman, E. Iacona, Z. Liu, and S. Chang, Johns Hopkins University)

Forced Heat and Mass Convection

- Simultaneous Measurements of Flow/Concentration by PIV/LIF (E. H. Jeong, S. Y. Yoon, and K. C. Kim, Pusan National University, Korea)
- Temperature Gradient Measurements for Electrophoretic Convection Flow in a Microfluidic Device (D. Huber and J. G. Santiago, Stanford University)
- CFD Visualization Results for Continuous Caster of Steel Slab (B. Zhao, B. G. Thomas, S. P. Vanka, UIUC., and R. J. O'Malley, Nucor Steel)

Nano-Scale Transport and Phenomena

- Optical Resonance in Microcavity (250 nm) (Z. Guo and H. Quan, Rutgers University, and S. Pau, Lucent Technology/Bell Laboratory)
- Joule Expansion Coefficient Measurements for Thin Metallic Film (100 nm) (S. P. Gurrum, Y. K. Joshi, W. P. King, and K. Ramakrishna, Georgia Institute of Technology)
- Thermal Conductivity of Nanoparticles (11 nm $\sim$150 nm) in Suspension (C. H. Chon and K. D. Kihm, University of Tennessee)

Combustion

- Non-Piloted Ignition on a PMMA Surface (S. L. Manzello, H. Gotoda, and T. Kashiwagi, NIST)

It has been my pleasure to present entries submitted from a number of outstanding research groups across the nation.

Kenneth D. Kihm
Department of Mechanical, Aerospace
and Biomedical Engineering,
University of Tennessee,
Knoxville, TN 37996-2210

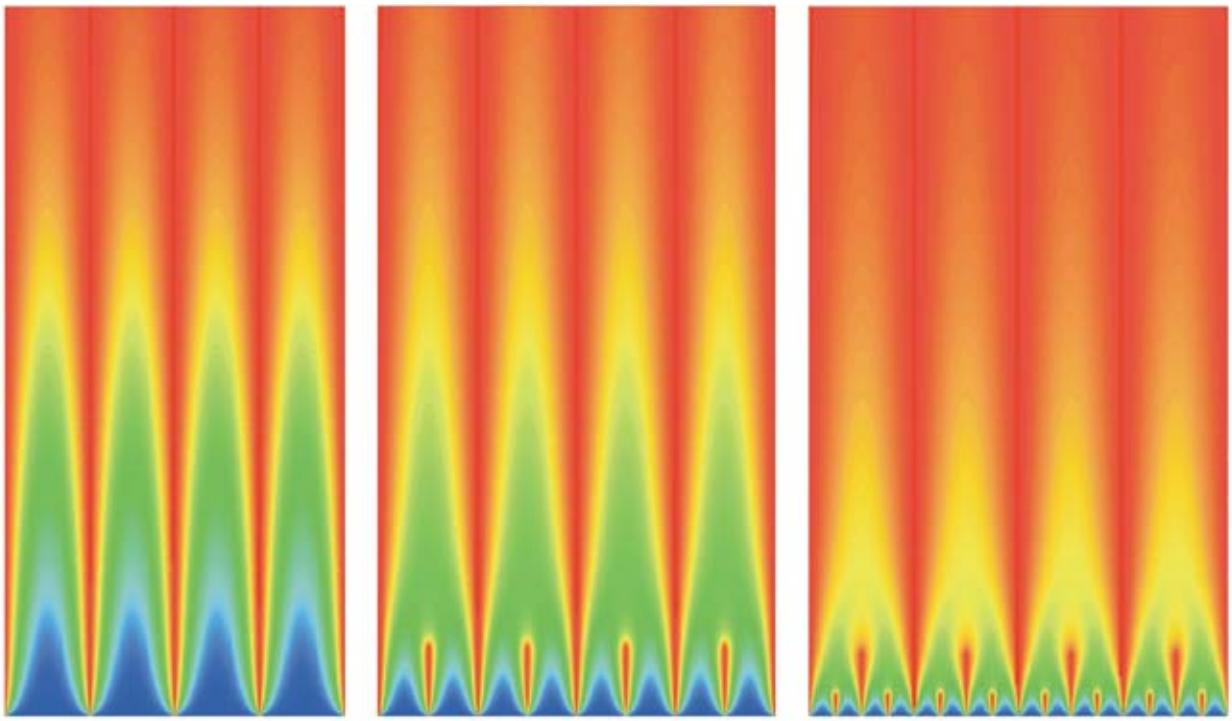

One length scale | Two length scales | Three length scales

Constructal multi-scale package of vertical channels with natural convection and maximal heat transfer density.

CONSTRUCTAL DESIGN: THE GENERATION OF MULTI-SCALE HEAT AND FLUID FLOW STRUCTURES

Alexandre K. da Silva* and Adrian Bejan

Duke University, Department of Mechanical Engineering and Materials Science,
Box 90300, Durham, NC 27708-0300

This is a new constructal design concept for generating multi-scale structures in natural convection with the objective of maximizing the heat transfer density, or the heat transfer rate per unit of volume[§]. The flow volume is filled with vertical equidistant heated blades of decreasing lengths. The spacings between the blades are optimized for maximal heat transfer density. Smaller blades are installed in the center plane between two adjacent longer blades, in the entrance region where the boundary layers are thin and the fluid is unheated. New generations of smaller blades are added stepwise to the multi-scale structure. Constructal theory is applied to each new generation of blades.

The above figures show the dimensionless numerical temperature distribution inside a flow volume composed of four main channels, for optimized structures with one, two and three length scales, at $Ra = 10^6$ and $Pr = 0.7$. The temperature ranges between two main colors, red ($\tilde{T} = 1$) and blue ($\tilde{T} = 0$). As the number of length scales increases, the color red is distributed more uniformly, illustrating the progress towards maximal heat transfer rate density, i.e. the constructal principle of "optimal distribution of imperfection". The average heat transfer density increases by 12% from the simplest structure (one length scale) to two length scales, and by 6% from two

* Corresponding Author: (akd3@duke.edu) Tel.: +1 (919) 660-5299 Fax: +1 (919) 660-8963

§ Alexandre K. da Silva and Adrian Bejan, Constructal multi-scale structure for maximal heat transfer density in natural convection, *International Journal of Heat and Fluid Flow*, v. 26, n. 1, p. 34-44, 2005.

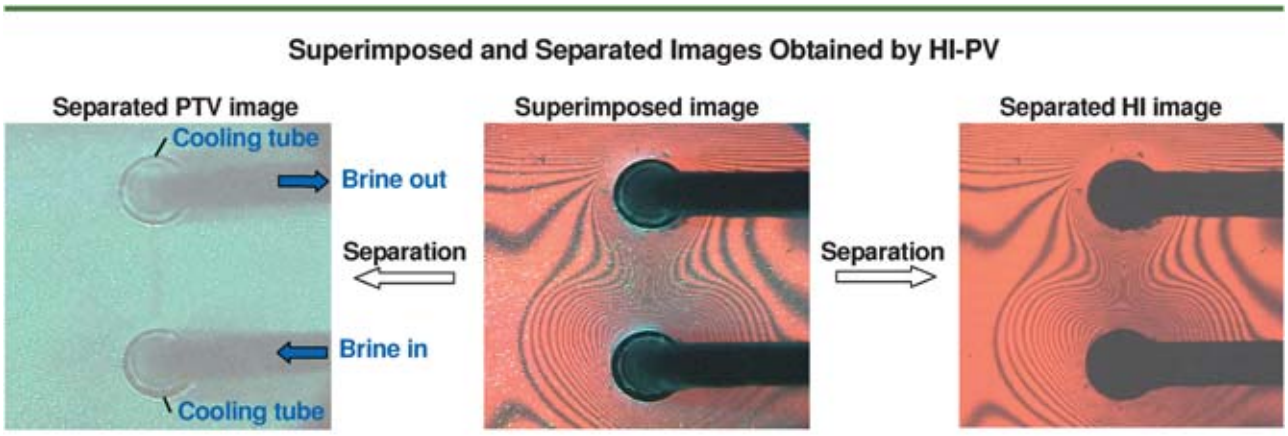

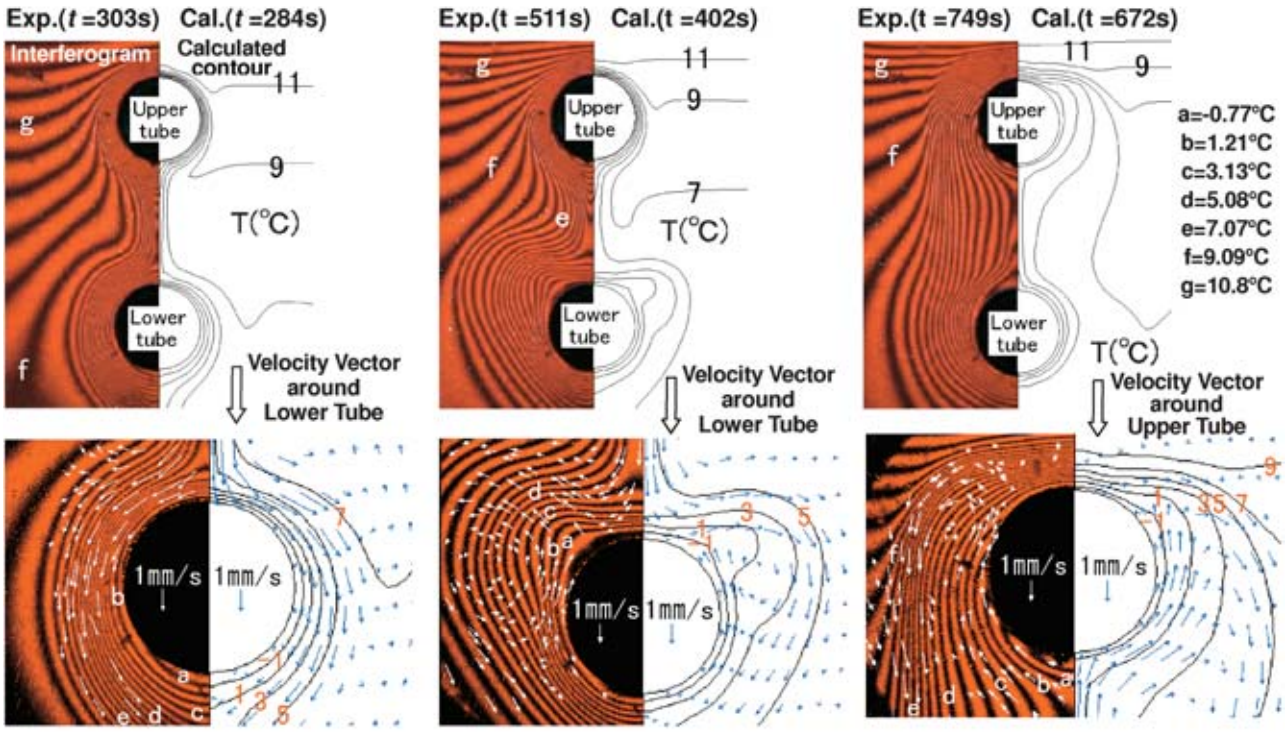

Simultaneous Visualization of Velocity and Temperature Fields of Transient Natural Convection

Ichiro NAKANE and Akira NARUMI, Department of Mechanical Engineering, Kanagawa Institute of Technology
Kentaro FUKUDA, Graduate Student, Kanagawa Institute of Technology

A new visualization technique to measure transient 2-D profiles of velocity and temperature was developed. Particle tracking velocimetry (PTV) and real time holographic interferometry (HI) are combined into the new technique, and it will be called as HI-PV. HI-PV's accuracy depends on the clarity of separation of PTV and HI images. We propose two different techniques to separate PTV and HI images: (1) separate two images using a digital image processing after recording the superimposed image with a digital video camera and (2) record the two images separately by two digital video cameras attached with blue or red color filter.

HI-PV was applied to the transient natural convection of water around two cooling tubes. Water: initial temperature = 13°C was cooled by two tandem cooling tubes: surface temperature = -4.3°C, and natural convection with density inversion occurs. A numerical calculation was also made and its results were favorably compared to the corresponding visualized results by HI-PV. HI-PV is proven to be a very useful technique to measure simultaneously transient 2-D profiles of velocity and temperature.

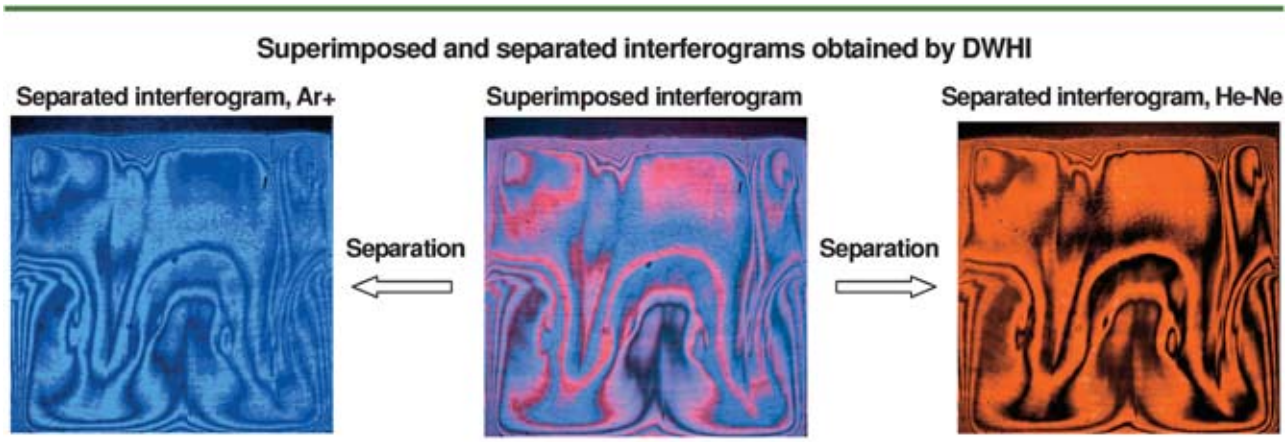

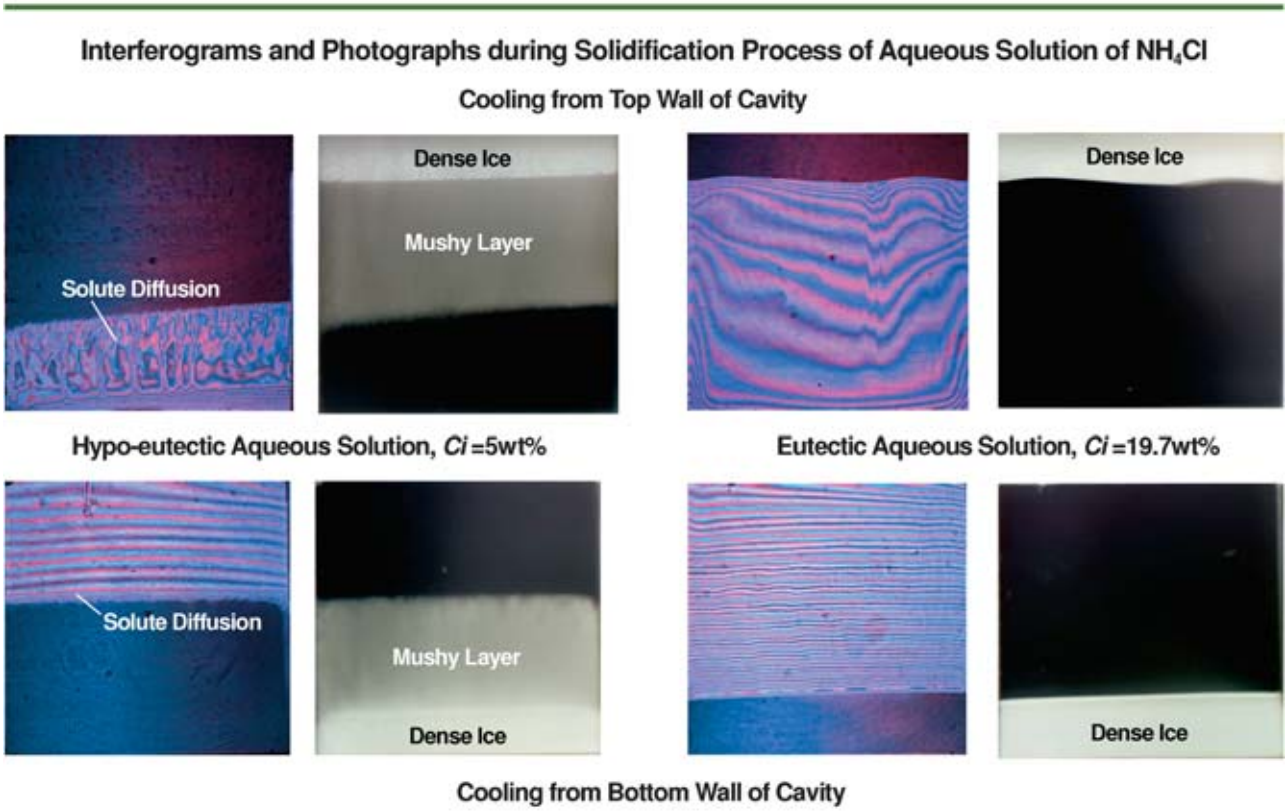

Visualization of Transient Solidification Process of Aqueous Solution by Dual Wavelength Holographic Interferometry

Noboru TSUSHIMA, Division of Mechanical System Engineering, Faculty of Engineering, Tokyo A & T
Akira NARUMI and Ichiro NAKANE, Department of Mechanical Engineering, Faculty of Engineering, Kanagawa Institute of Technology
Takao KASHIWAGI and Atsushi AKISAWA, Division of Mechanical System Engineering, Faculty of Engineering, Tokyo A & T

The solidification process of an aqueous solution of NH_4Cl in a 2-D square cavity was visualized and measured using dual wavelength holographic interferometry (DWHI). The aqueous solution of NH_4Cl was cooled from the top or bottom wall of the cavity, and the initial concentration of NH_4Cl, Ci, was varied. The visualized results represent the followings:
(1) The ice-liquid mushy layer grows on the dense ice during the solidification process of Ci =5wt%, but in the case of Ci =19.7wt%, the mushy layer isn't observed and solid/liquid interface is sharp like pure substances.
(2) When the aqueous solution is cooled from the bottom wall, both temperature and concentration gradients stabilize the stratified configuration of the density field. However, in the case of cooling from the top wall, natural convection is caused by density differences and the solute diffusion is more conspicuous by this convection.

Velocities measured with PIV in bubble-top jets (water, T_{wire}= 378 K, T_{bulk}= 320 K)

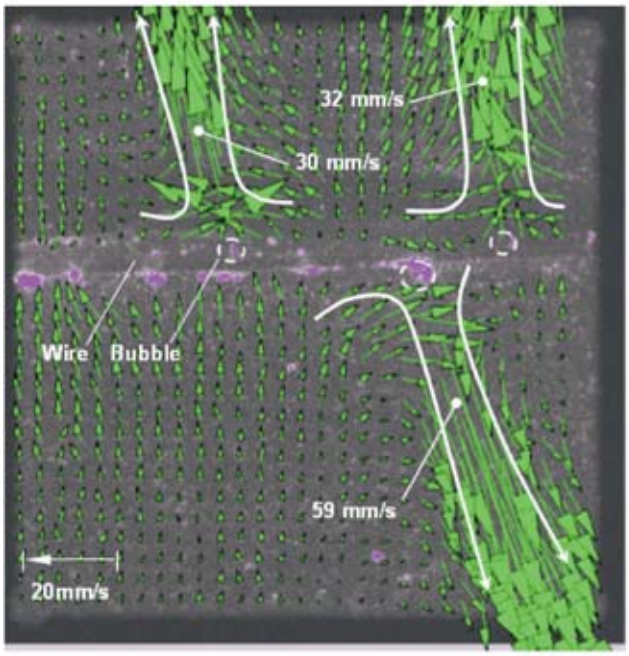

Two stages of the bubble-top jet formation process: Incipience (a)-(c), and Growth (d)-(f) (water, T_{wire}= 376 K, T_{bulk}= 330 K)

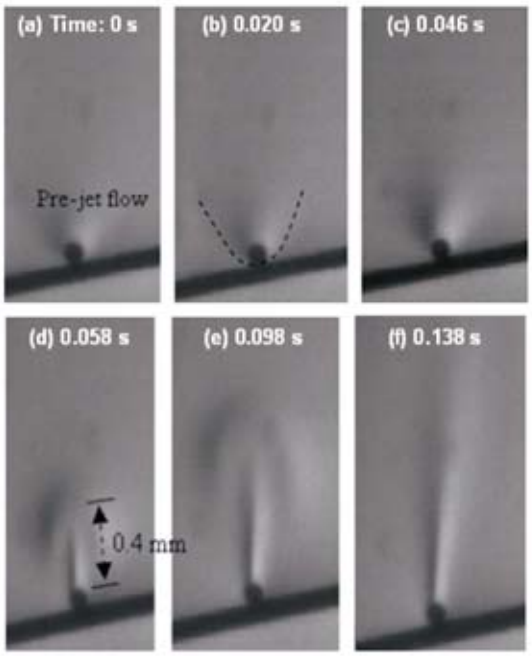

Bubble-top jet flow

- Hot liquid is pumped by Marangoni flow from around the bubble and the heater wire up into the bulk liquid.
- Maximum velocity above the bubble is some distance above the bubble top.
- Pumping effect enhances the single-phase heat transfer, and creates strong interactions among neighboring bubbles.

Simulation of butterfly-like structure of multi-jet flow: Velocity contours [m/s] (water, T_{wire}= 385 K, T_{bulk}= 335 K)

Experimentally visualized butterfly-like structure of multi-jet flow (water, T_{wire}= 376 K, T_{bulk}= 330 K)

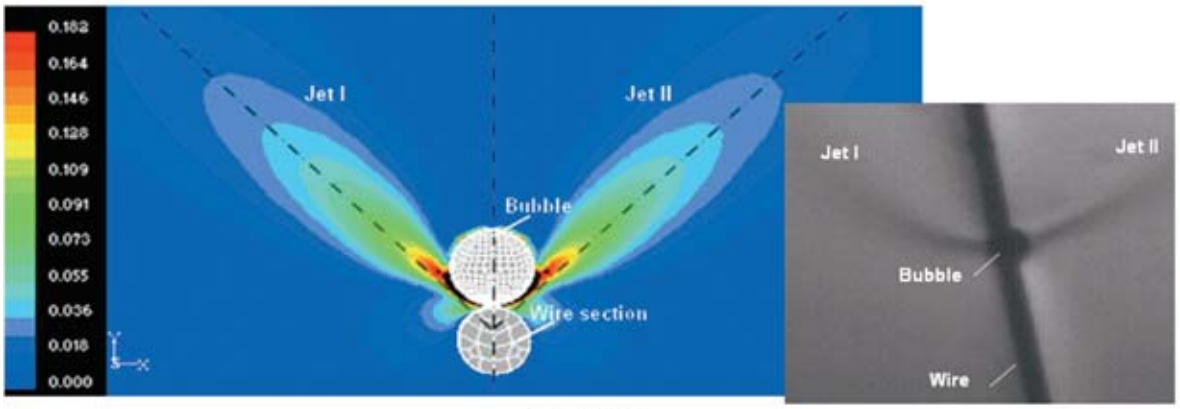

Multi-jet flow

- Multi-jet flow with symmetric butterfly-like structure was predicted in simulation and confirmed in experiment.
- Multi-jet flows tend to form with larger bubbles; phase-change heat transfer plays an important role in controlling the jet structure.

Jet Flows Around Microbubbles In Subcooled Boiling

Hao Wang[a], Xiaofeng Peng[b], David M. Christopher[b] and Suresh V. Garimella[a]
[a]School of Mechanical Engineering, Purdue University, West Lafayette, Indiana, USA
[b]Laboratory of Phase-change and Interfacial Transport, Tsinghua University, Beijing, China

Strong jet flows were observed emanating from micro bubbles on a 100 μm diameter wire during subcooled nucleate boiling. The flow velocities were visualized with high-speed photography and quantified with a PIV analysis. The bubble-top jet flows were characterized by a single jet at the bubble top. Both experiments and simulations indicated that the bubble-top jet flows are induced by Marangoni effects due to temperature gradients near the wire, rather than due to condensation at the bubble top. The evaporation and condensation does, however, control the jet flow intensity. Multiple jets from a single bubble were sometimes observed on bubbles that were generally larger than the heater wire. The jets were driven by the Marangoni flow at cool regions on the bubble sides resulting from upward flow of subcooled liquid.

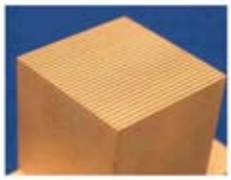

Microchannel heat sink

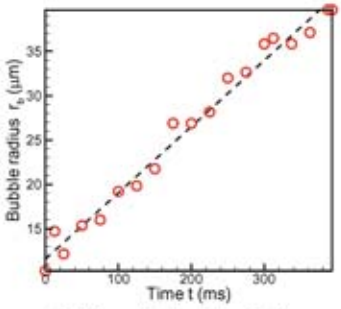

Bubble evolution during boiling

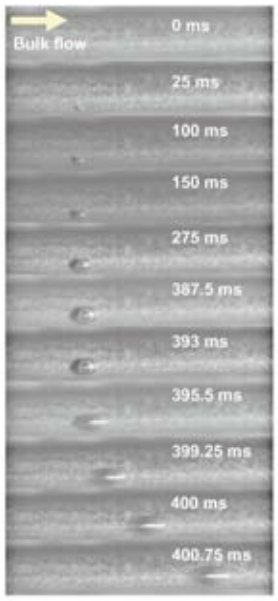

Single bubble nucleates, grows and departs from the bottom wall (4000 fps).

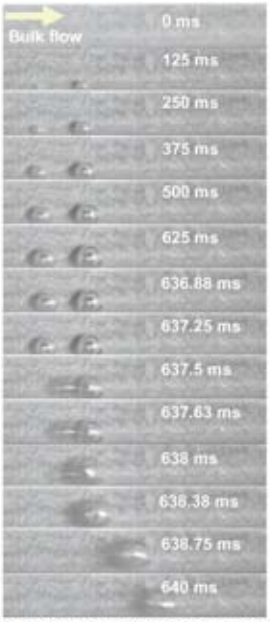

Twin bubbles agglomerate after growth and travel down the channel (8000 fps).

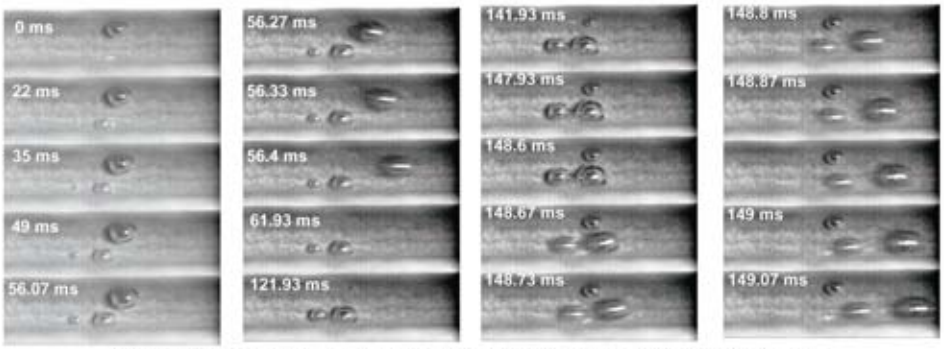

Multiple bubbles grow and depart from the bottom wall without agglomeration (15,000 fps).

Nucleate Boiling in Microchannels

Dong Liu, Poh-Seng Lee and Suresh V. Garimella
Purdue University, West Lafayette, Indiana 47907-2088

An understanding of bubble motion and evolution during nucleate boiling is necessary for the analysis of convective heat transfer rates in microchannels. High-speed photography is used in this study to reveal the complex bubble dynamics during nucleate boiling in copper microchannels of hydraulic diameter 384 μm (275 μm wide and 636 μm high) and 25.4 mm length. De-ionized water flows through the microchannels at a velocity of 0.68 m/s (Re = 735) and an inlet temperature of 86.5°C. The exit pressure is maintained at 1.05 bar. A constant heat flux of 16 W/cm^2 is applied at the bottom of the microchannel heat sink. A high-speed digital video camera is used to observe the boiling process at 4,000, 8,000 and 15,000 frames per second.

The images shown looking down into the microchannels reveal the transient processes of nucleation, growth, subsequent departure and interaction of bubbles from nucleation sites on the bottom wall of the channel. The measured bubble radius indicates a linear evolution with time. These results are useful in proposing predictive models for boiling heat transfer in microchannel heat sinks.

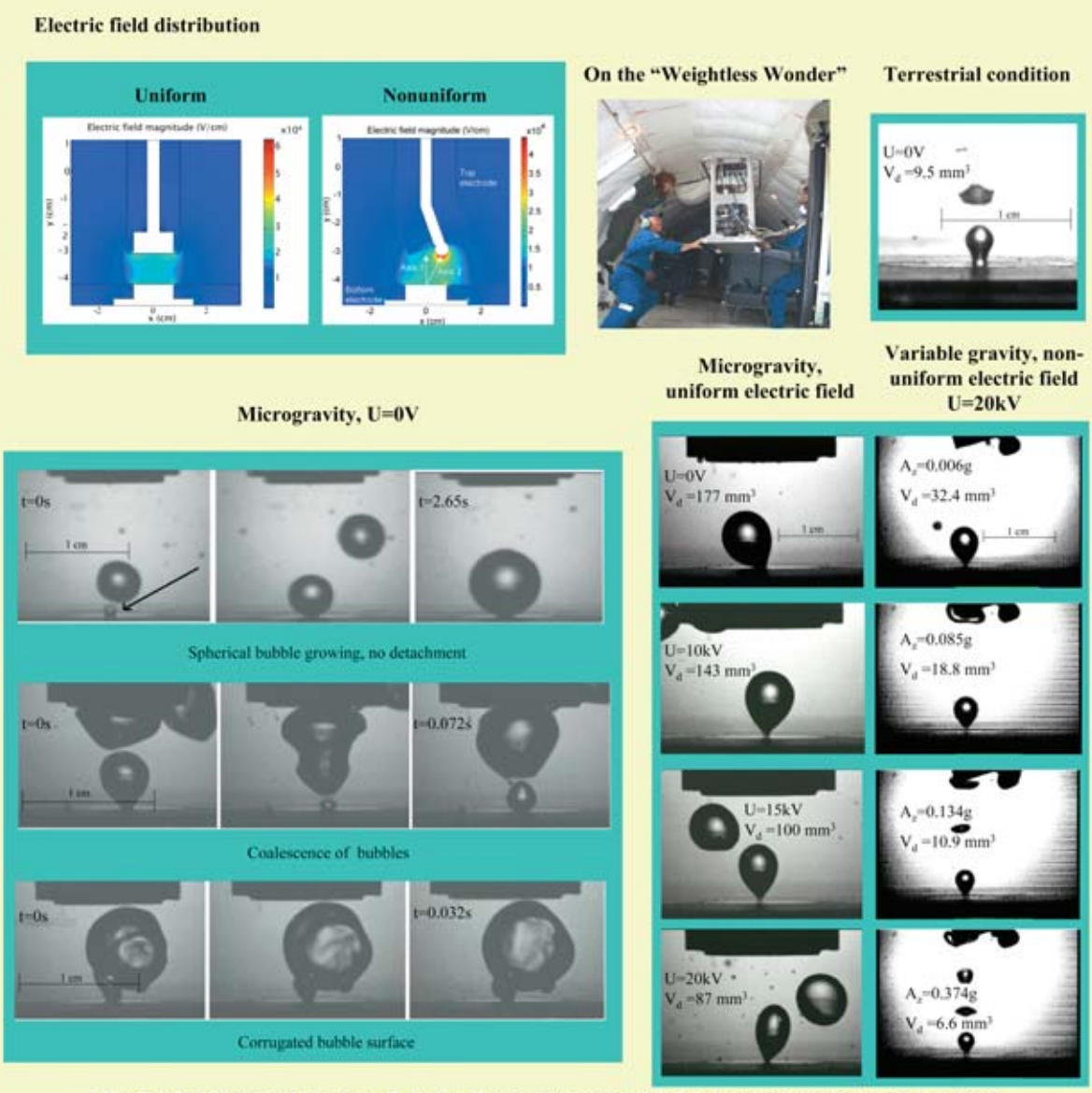

Bubble formation and detachment in variable gravity environment under the influence of electric fields

C. Herman*, E. Iacona†, Z. Liu, S. Chang

Department of Mechanical Engineering, The Johns Hopkins University, Baltimore, MD 21218, U.S.A., *

†Current address: Laboratoire EM2C-Ecole Centrale Paris, Grande Voie des Vignes, 92295 Chatenay Malabry France

The formation and detachment of air bubbles injected into a stagnant, isothermal liquid through an orifice in a plane surface were studied at various reduced gravity levels under the influence of electric fields. Reduced gravity experiments were carried out in NASA's reduced gravity aircraft, the KC-135. The objective of this study is to investigate and explore the possibility of substituting the buoyancy force with the electric field force by applying external electric fields in two phase flow and boiling. Two top electrode geometries were used: flat and off-axis spherical, to generate a uniform and non-uniform electric field, respectively. The bubble life cycle was first experimentally visualized, and then the characteristic dimensions of the bubble and its volume at the moment of detachment were measured using digital image processing. It is shown that both the level of gravity and the magnitude of the electric field significantly affect the bubble formation and detachment. Under microgravity with uniform electric fields, an increasing electric potential from U=0 to 20 kV decreases the detachment volume V_d by 51%. In a nonuniform electric field with U=20 kV, the detachment volume decreases by 80% as the gravity increased from 0.006g to 0.374g. The volume flow rates in variable gravity and terrestrial conditions are 2.57×10^{-7} m³/s and 3.33×10^{-7} m³/s, respectively.

Acknowledgments:

This research was supported by a NASA research grant. The experiments in the KC-135 aircraft were carried out by Cila Herman, Gorkem Suner, Steven Marra, and Ed Scheinerman. The support by the KC-135 crew and NASA Glenn Research Center was invaluable for the successful completion of the experiments.

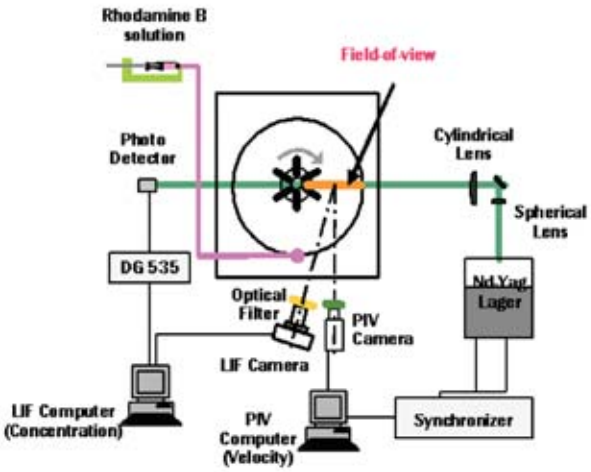

Fig. 1 Experimental Setup for PIV/LIF simultaneous measurement

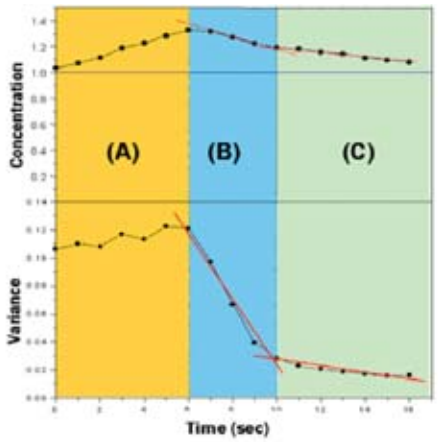

Fig. 2 Different three mixing periods
(A) : Continuous infusing period, (B) : Rapid turbulent mixing period, (C) : Slow molecular mixing period

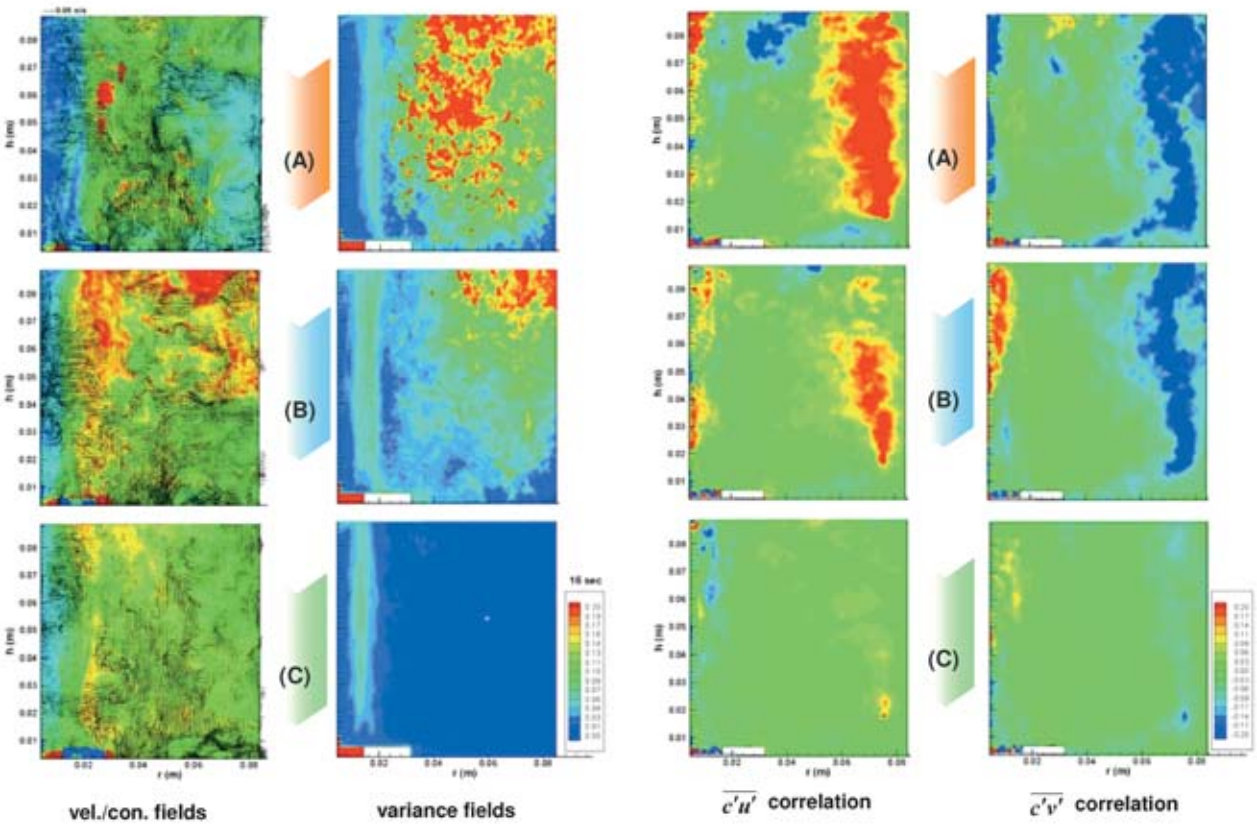

Fig. 3 The temporal and spatial mixing characteristics in a stirred mixing tank

VISUALIZATION OF TURBULENT MASS TRANSFER IN A STIRRED MIXER

Eun Ho Jeong, Sang Youl Yoon and Kyung Chun Kim
Microfluidics and Bio-Fluids Laboratory, Pusan National Univ., Korea

Simultaneous measurements of turbulent velocity and concentration fields in a stirred mixer tank have been carried out by using a combined PIV/LIF technique. Instantaneous velocity fields are measured by a 1K×1K CCD camera while the concentration fields are determined by measuring the fluorescence intensity of Rhodamine B tracer excited by the second pulse of Nd:Yag laser light (Fig. 1). It is shown that the general features of the mixing patterns are highly dependent on the local flow characteristics during the rapid decay of the mean concentration. However, the small scale mixing is found to be independent of the local turbulent velocity fluctuations

The correlation fields between concentration fluctuation and velocity fluctuation represents the active mixing region.

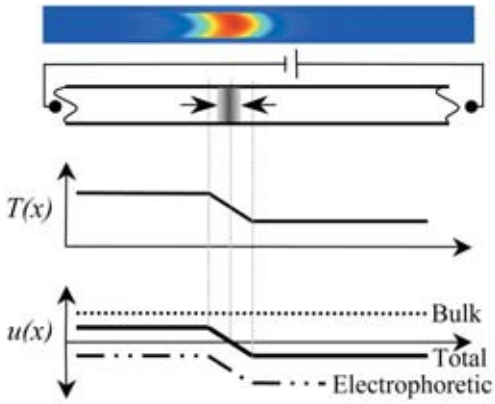

(a) Focusing schematic

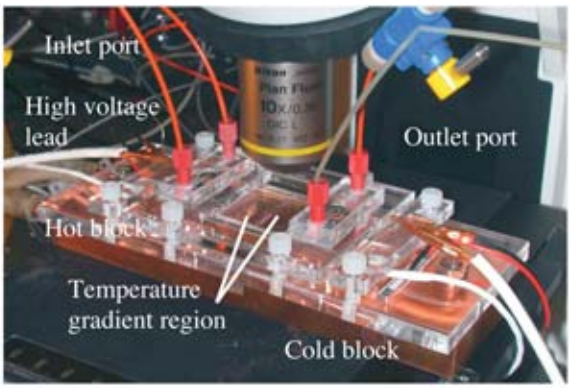

(b) Experimental setup

(c) Raw image of temperature-dependent rhodamine B fluorescence intensity at $\lambda = 580$ nm

(d) Contour plot of processed temperature field showing 2.5°C isotherms

(e) Focusing of bodipy sample in thermal gradient shown in (d) with E = 40 V/mm and $\lambda = 530$ nm

Temperature Gradient Focusing in a Microfluidic Device

David Huber and Juan G. Santiago
Mechanical Engineering Department, Stanford University

Thermal gradient focusing leverages a temperature gradient imposed along the axial direction of a microchannel to effect a gradient in electrophoretic mass flux. When a bulk flow is imposed in the opposite direction, charged analytes separate and focus at points where their net bulk velocities (advective plus electrophoretic) sum to zero (a). The experimental setup (b) consists of epifluorescence optics (collecting at two wavelengths), thermoelectric-regulated temperature blocks at each end of the microchannel, a high voltage power supply, and a custom pressure controller. Embedded RTDs provide reference temperatures for system calibration.

Scalar fluorescence images are presented from a 20x200 μm rectangular borosilicate capillary with an applied electric field of 40 V/mm. Image (c) shows the fluorescence intensity of 100 μM rhodamine B, a dye whose quantum efficiency is a strong function of temperature. Rhodamine B intensities are converted to temperatures (d) by normalizing for non-uniform illumination using an isothermal reference image, then applying an experimentally determined intensity vs. temperature calibration curve. Image (e) shows 500-fold electrophoretic focusing of bodipy dye.

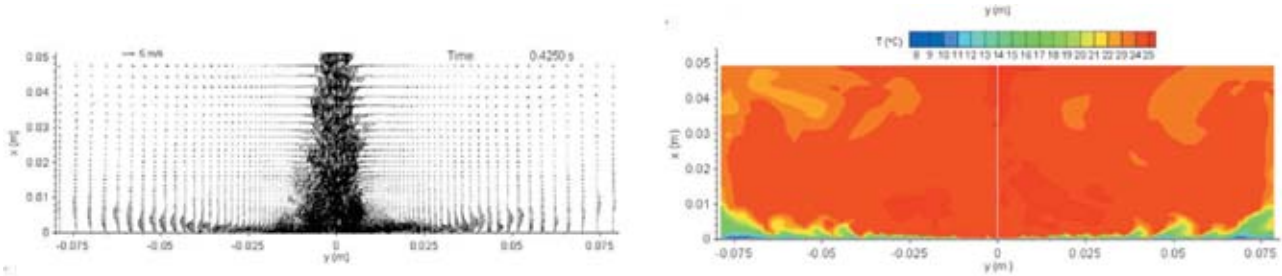

Fig.1 Instantaneous Flow and Temperature Fields for an Impinging Circular Jet

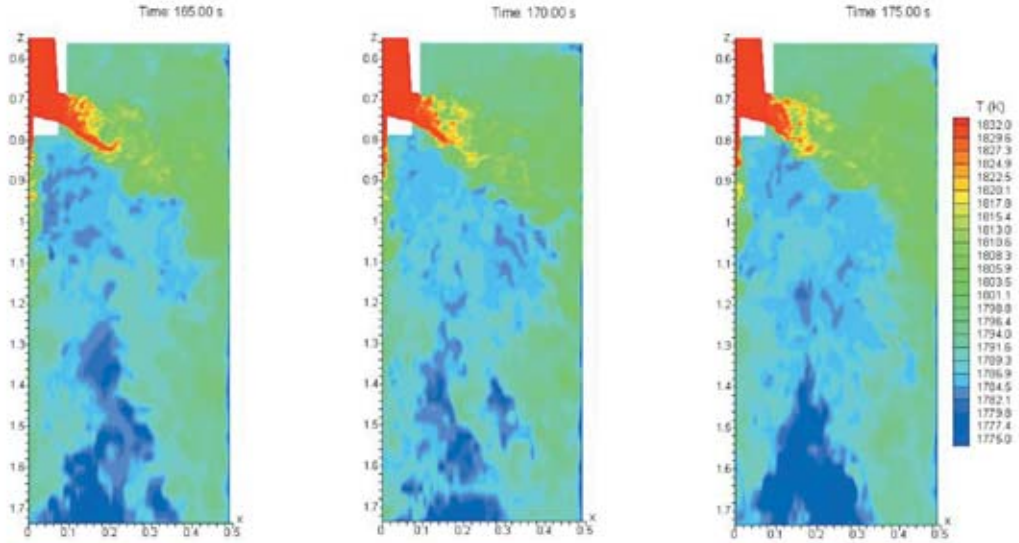

Fig. 2 Instantaneous Temperature Fields in the Mold region of a Continuous Caster of Steel

Transient Flow and Temperature Transport in Continuous Casting of Steel Slabs

B. Zhao[1], B.G. Thomas[1], S. P. Vanka[1] and R. J. O'Malley[2]

[1] Department of Mechanical and Industrial Engineering, University of Illinois at Urbana-Champaign,

[2] Nucor Steel, PO Box 2249, Decatur, AL 35609

The above pictures show the flow and temperature fields in an impinging circular jet and temperature fields in a continuous caster of steel slabs. These pictures were obtained from Large Eddy Simulations using very fine grids, and show instantaneous snap shots. These calculations used approx. 800,000 control volumes for the impinging jet and 1.6 million volumes for the caster simulations. The instantaneous flow structures and temperature contours show the complex turbulence structures that exist in the caster. These temperature fields are important to the understanding of the production of defects in steel casting, and in predicting heat transfer rates to the solidifying region. A classic double-roll flow pattern is confirmed for this 132×984mm slab caster at 1m/min casting speed. The results show that temperature in the top of the molten pool is about 30% of the superheat temperature difference. About 12 percent of the superheat is extracted from the narrow face, where the peak heat flux averages almost 750 kW/m^2 and instantaneous peaks exceed 1500 kW/m^2. Two thirds of the superheat is removed in the mold. The jets exiting the nozzle ports are shown to fluctuate, producing temperature fluctuations in the upper liquid pool of ±4 °C and peak heat flux variations of ±350 kW/m^2.

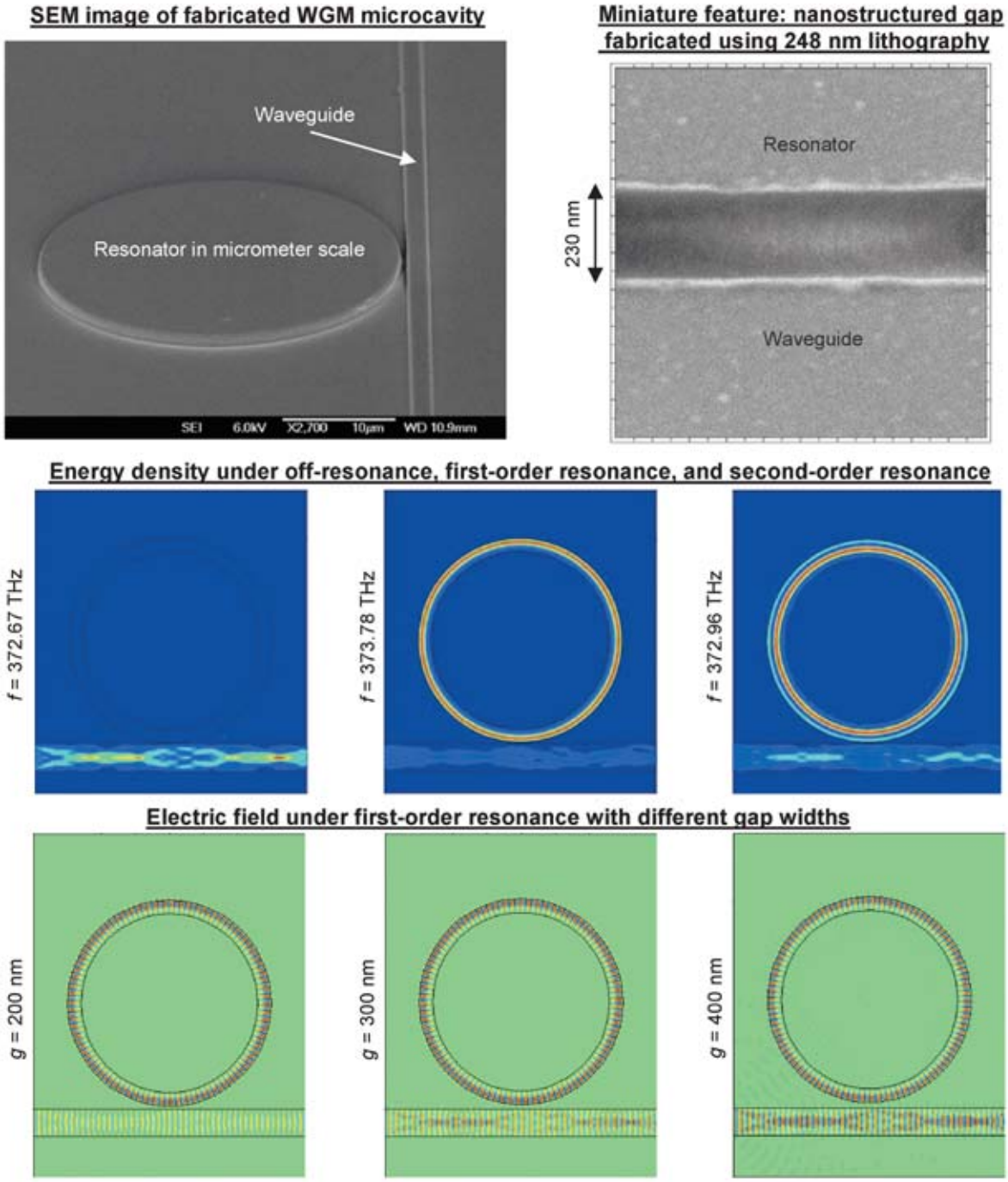

Optical Resonance in Fabricated Whispering-Gallery Mode Microcavity

Zhixiong Guo and Haiyong Quan
Rutgers University – New Brunswick/Piscataway, NJ

Stanley Pau
Lucent Technologies/Bell Labs., Murray Hill, NJ

Whispering-gallery mode (WGM) optical resonance has attracted increasing attention due to its high potential for realization of microlasers, miniature biosensors, narrow filters, etc. An array of WGM miniature sensors has been fabricated using 248 nm optical lithography and conventional silicon IC processing. Photon tunneling was found between the waveguide and resonator. Under the first-order resonance, an extremely brilliant ring exists close to the peripheral surface of the resonator due to high energy storage. Two rings (with a brighter internal ring) are found under the second-order resonance. With the gap distance separating the waveguide and resonator decreases, the EM field in the waveguide becomes weaker and more energy is stored in the resonator. Since no WGM phenomenon occurs in the case of zero gap distance, an optimal gap may exist in the design of WGM microcavities.

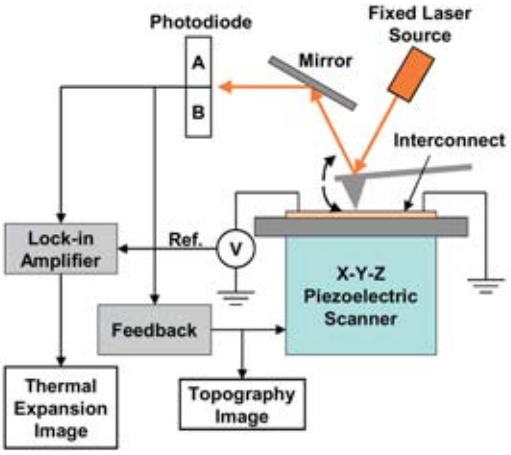

Figure 1: Scanning Joule Expansion Microscopy (SJEM) setup. The interconnect is periodically heated to induce a vertical thermal expansion that causes the cantilever to oscillate at the same frequency. The lock-in amplifier measures the amplitude of this particular frequency. The heating frequency is made much higher than the feedback bandwidth to the piezoelectric scanner, which thus can detect only the topography.

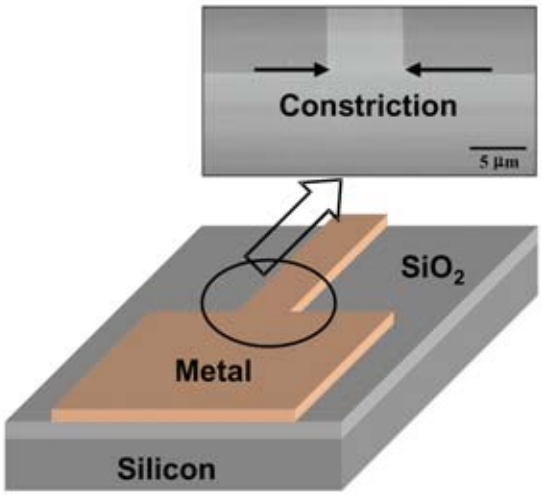

Figure 2: Schematic of constriction in a gold thin film. The metal thickness is ~ 40 nm, which is roughly the mean free path of electrons. A thin layer of parylene (~ 100 nm) is coated on the whole sample to increase the expansion amplitude.

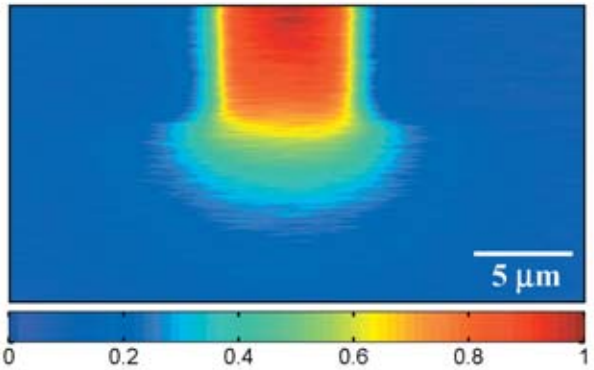

Figure 3: Thermal expansion image of the constriction at 20 kHz heating frequency. The units are arbitrary and the color bar is scaled from 0 to 1.

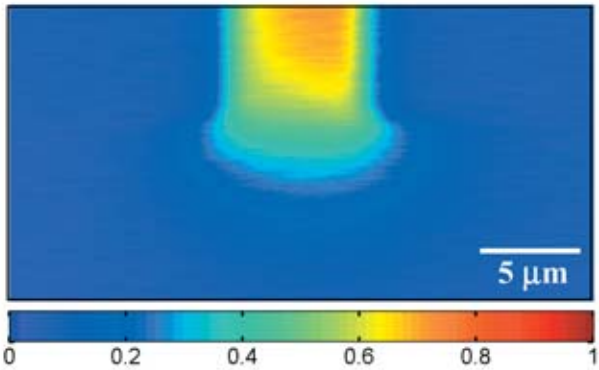

Figure 4: Thermal expansion image of the constriction at 100 kHz heating frequency. Voltage amplitude and color map are same as for the case in Fig. 3.

SCANNING JOULE EXPANSION MICROSCOPY OF A CONSTRICTION IN THIN METALLIC FILM

Siva P. Gurrum, Yogendra K. Joshi, and William P. King
G. W. Woodruff School of Mechanical Engineering
Georgia Institute of Technology, Atlanta, GA 30332

Koneru Ramakrishna
CMOS Platform Device Development,
Technology Solutions Organization,
Freescale Semiconductor, Inc., Austin, TX 78721

Temperature rise in on-chip interconnects is expected to steadily increase with each generation of microprocessors. Continuous scaling has led to feature sizes in the 100 nm range. Existing and future interconnect architectures include *vias* connecting metal lines in different levels. These vias typically cause current crowding and can significantly affect temperature rise. It is thus highly important to characterize thermal phenomena in nanoscale complex structures.

Figure 1 schematically shows the setup for Scanning Joule Expansion Microscopy (SJEM) developed by Varesi and Majumdar (1998). It involves measuring the expansion amplitude of the interconnect surface due to temperature oscillations caused by a periodic voltage input. The topography of the constriction studied in this work is shown in Fig. 2. A thin (100 nm) parylene layer was coated on top of the whole structure. Expansion images obtained using a closed-loop Atomic Force Microscope (AFM) are shown in Fig. 3 and Fig. 4 for 20 kHz and 100 kHz heating frequencies respectively. The technique captures current crowding and heat generation in films as thin as 40 nm, which is roughly the mean free path of electrons. Due to high signal-to-noise ratio, this technique allows quantitative measurement of the lateral penetration depth of the periodic heating signal, from which thermal diffusivity of films deposited on the metal film can be extracted.

J. Varesi and A. Majumdar, "Scanning Joule expansion microscopy at nanometer scales," *Applied Physics Letters*, vol. 72, pp. 37-39, 1998.

TEM Images (x50000) of Nanoparticles

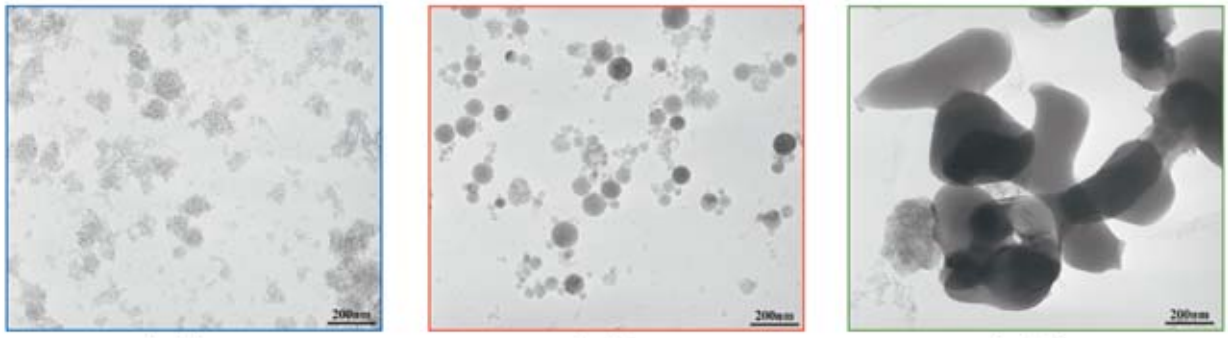

d = 11nm *d* = 47nm *d* = 150nm

Optical Microscopic Images (x630) of Nanoparticle Brownian Motions in Water

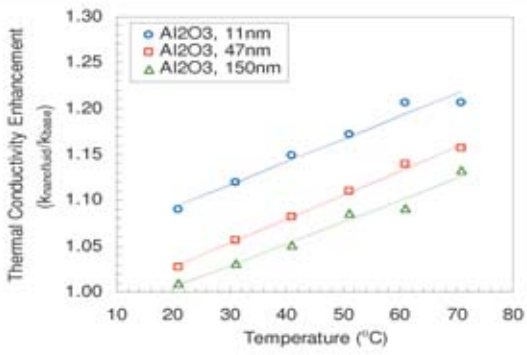

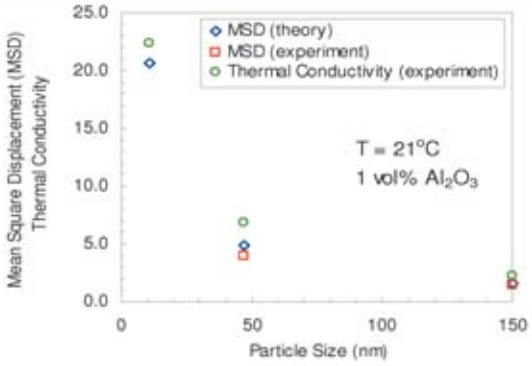

Thermal Conductivity Enhancement of Nanofluids by Brownian Motion

C. H. Chon and K. D. Kihm
Micro and Nano Scale Fluidics and Energy Transport Laboratory [www.engr.utk.edu/~minsfet]
University of Tennessee, Knoxville, Tennessee

Thermal conductivity has increased dramatically in a nanofluid, which included small portion of nano-sized metal particles. A key mechanism of enhanced thermal conductivity is Brownian motion called micro-convection, millions of times interaction between nanoparticles and base fluid molecules. And the smaller nanoparticles increase their surfaces and the number of interaction and it leads the more enhanced thermal conductivity of a nanofluid. Furthermore higher temperature of a base fluid leads more active Brownian motion of nanoparticles. With the experimental measurement of thermal conductivity and optical visualization of particle motions, the relationship between Brownian motion and enhanced thermal conductivity based on different sized nanoparticles and temperature changes was observed.

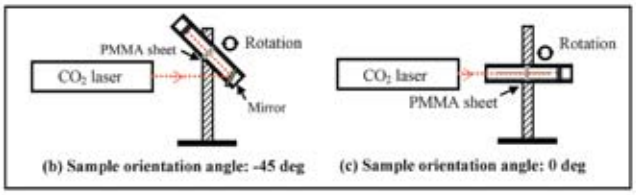

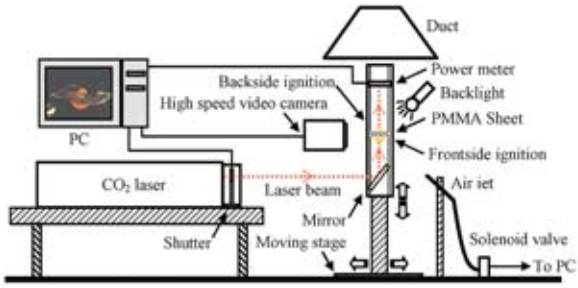

Experimental apparatus

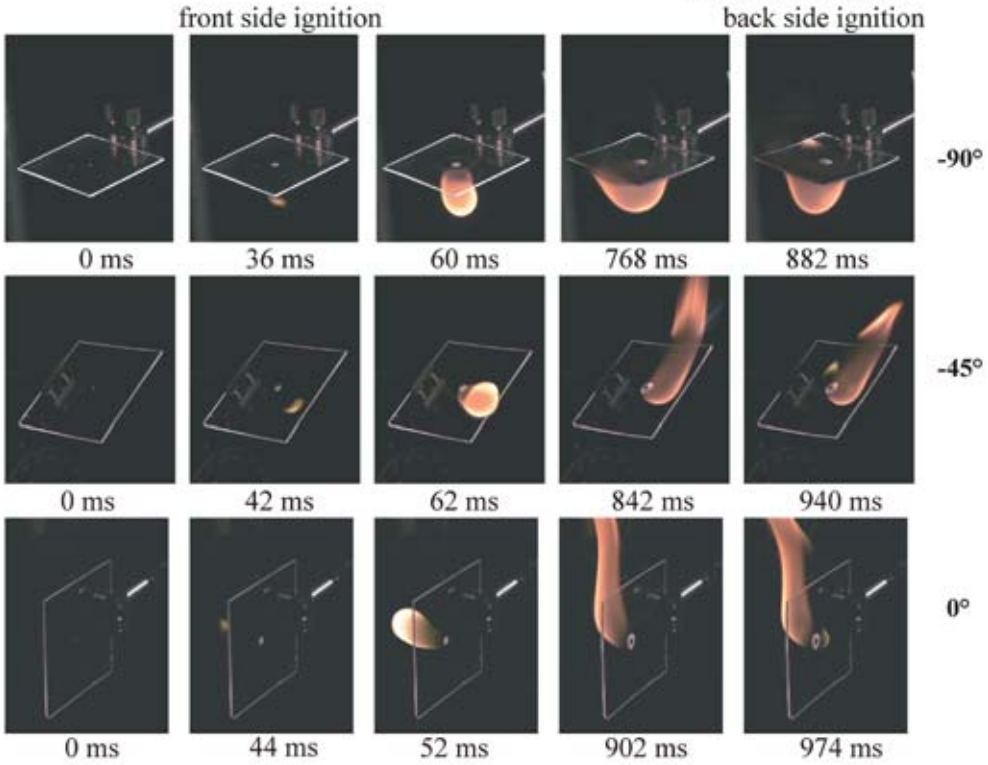

Non-Piloted Ignition Visualization on a Thin Poly(methylmethacrylate) (PMMA) Surface

Samuel L. Manzello, Hiroshi Gotoda, and Takashi Kashiwagi
Building and Fire Research Laboratory (BFRL), NIST, Gaithersburg, MD USA

Understanding the variation in flame ignition delay time and flame spread on solid materials is necessary to prevent fire hazards. In enclosed room fires, the surface of solid materials is always subjected to radiation from hot combustion products in various directions (e.g., ceiling, wall, and floor). The goal of the present study is to reveal the effect of radiation direction on flame ignition and spread using PMMA as the solid material. The thickness of the PMMA surface was 0.5 mm and ignition was obtained using a CO_2 laser. The phenomena of non-piloted ignition over the irradiated PMMA surface and subsequent ignition over the backside surface was imaged using a Digital High Speed Camera at 500 frames per second with shutter speed set to 50 ms. The camera was fitted with a 60 mm micro lens to obtain the required spatial resolution to capture images of the ignition and flame spread process. Three different orientations of the PMMA sample are shown. The incident laser flux was kept constant and the laser beam diameter was ≈ 4000 μm. In each case, back side ignition was observed after hole formation in the PMMA.

Response of Wall Hot-Film Gages With Longitudinal Diffusion and Heat Conduction to the Substrate

F. Sedat Tardu
e-mail: sedat.tardu@hmg.inpg.fr

C. Thanh Pham

Laboratoire des Ecoulements Géophysiques et Industriels, INPG, UJF, CNRS, B.P. 53X 38041, Grenoble Cédex, France

The effects of heat transfer into a substrate and axial diffusion are analyzed through numerical simulations in order to elucidate the frequency response of wall hot-film gages. The ratio of the conductivities of the substrate and fluid plays an important role in steady flows when it is larger than 5 and the Péclet number is smaller than 50. The equivalent film length increases considerably with the conductivity ratio, and it decreases when a thin film of low conductivity is sandwiched between the hot-film gage and the substrate, showing a net improvement of the heat transfer conditions. The frequency response in unsteady flows is highly attenuated in the presence of heat transfer into the substrate. The cutoff frequency is strongly dependent on the conductivity ratio. Improved response is obtained with the two-layer substrate configuration. It is further shown that axial diffusion considerably affects the frequency response when the shear and/or the streamwise length of the film are small. [DOI: 10.1115/1.1928907]

Keywords: Hot-Film Gauge, Axial Diffusion, Conduction to the Substrate, Frequency Response, Full 2D Simulations

1 Introduction

The wall shear stress is a fundamental quantity in near-wall turbulent flows. It provides a rapid diagnostic of the flow and is essential in drag reduction problems, which are of great industrial importance. The suboptimal or optimal control of drag requires, however, a highly dense distribution of the actuators and wall shear stress sensors [1]. The streamwise and spanwise spacing of these MEMS (micro-electromechanical systems) have to be as small as the viscous sublayer thickness to obtain a drag reduction of about 20%. That means that the largest dimension of the shear stress sensors used for control purposes has to be smaller than about 100 μm even at moderate Reynolds numbers. This miniaturization poses problems, because some effects that are neglected under conventional situations have to be thoroughly taken into account in the physical mechanisms governing the sensor under these circumstances.

The direct measurements of wall shear stress turbulent fluctuations are still not feasible [2]. The classical indirect measurements are based either on heat (thermo-anemometry) or mass (electrochemical-anemometry) transfer techniques. The latter presents some advantages caused by an absence of the parasitical effects of the substrate, but it can only be used in some liquid flows. Thus development of measurement techniques of shear stress through hot-film gages is an ongoing challenge, especially with regard to the MEMS sensors design [3].

Complete analytical solutions of the full problem governing heat transfer over the wall hot-film (WHF) do not exist for the following reasons.

i. The indirect heat transfer from the hot film to the substrate by conduction, and the subsequent transfer from the substrate to the fluid and its interaction with the convective direct heat transfer are not explicitly known.
ii. The coupling of the effect of the longitudinal diffusion through the trailing and leading edge singularities with the unsteady response of the thermal boundary layer increases the complexity of the problem. Longitudinal diffusion plays an important role when the streamwise length of the film and/or the shear is small. The boundary layer approximation in the convective heat transfer equation is not valid under these circumstances. This effect may be more severe for MEMS micro-sensors and severely decrease the frequency response.

There are many studies available in the literature on the thermal boundary layer characteristics induced by a hot-film gauge (HFG) flush mounted at the wall. Several theoretical, numerical, and experimental studies have been reported in the past since the classical Lévêque solution of the thermal boundary layer problem over a finite strip maintained at a constant temperature. The validity of the boundary layer approximation is questioned in the numerical analysis conducted by Ling [4], and later in the theoretical approach of Springer and Pedley [5] and Springer [6]. These authors have shown that axial diffusion may be predominant at small Péclet numbers, i.e., either when the streamwise length of the film or the shear stress is small. The perturbation analysis conducted by Ackerberg et al. [7] has clearly indicated that the Lévêque solution is valid only for Péclet numbers larger than roughly 100. Their theoretical analysis is in good agreement with measurements obtained by electrochemical probes.

Lighthill [8] was first to investigate the unsteady response of a thermal boundary layer over a plate maintained at constant temperature. He showed that the thermal inertia decreases the unsteady response in the high-frequency regime. Bellhouse and Schultz [9] analyzed the influence of the fluctuating wall shear stress on the frequency response of a hot film by using Lighthill's technique with a 1D model. They showed the importance of the substrate conductivity on the frequency response. Brison et al. [10] studied the same problem in a 2D configuration. They used a quasi-steady forced convection law and ignored axial diffusion. The conjugated heat transfer problem was examined by Cole and Beck [11] and Moen and Schneider [12] without the effect of axial diffusion.

The present investigation studies the combined effects of axial diffusion through the trailing and leading edges of the HFG and conduction to the substrate on the frequency response of the wall

Contributed by the Heat Transfer Division for publication in the JOURNAL OF HEAT TRANSFER. Manuscript received: December 3, 2003. Final manuscript received: March 4, 2005. Review conducted by: Stefan Thynell.

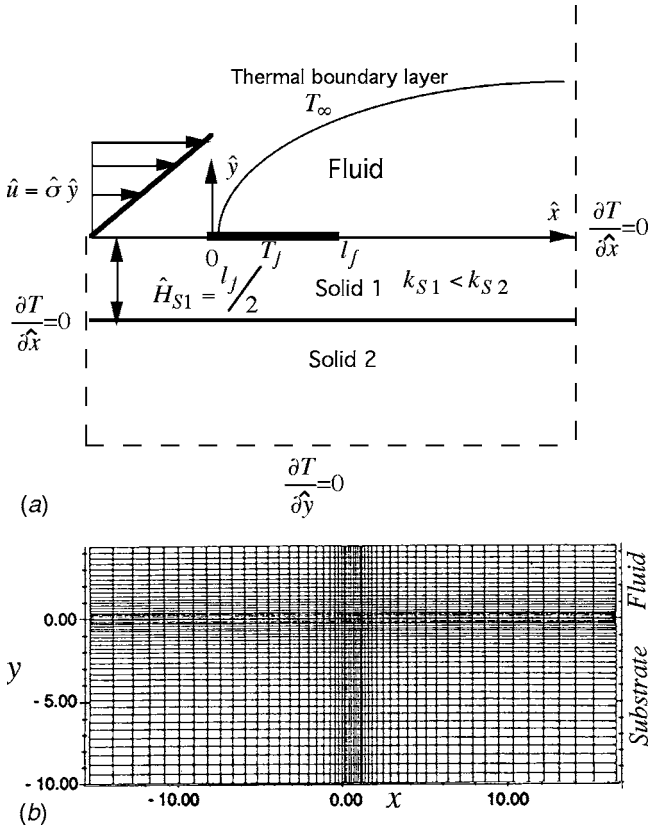

Fig. 1 (*a*) Model with a two-layer substrate and the corresponding boundary conditions. (*b*) Typical computational domain and mesh distribution.

shear stress sensors. The full 2D formulation of the conjugate heat transfer problem is presented here, and the results are analyzed both in the steady and unsteady regimes.

2 Formulation of the Problem and the Numerical Method

The dimensionless equations in the fluid F, in the solid S, and at the fluid-solid (substrate) $F-S$ interface are respectively

$$F: \quad \frac{\partial \theta}{\partial t} + u\frac{\partial \theta}{\partial x} = \frac{\partial^2 \theta}{\partial x^2} + \frac{\partial^2 \theta}{\partial y^2} \tag{1a}$$

$$S: \quad \frac{\alpha_F}{\alpha_S}\frac{\partial \theta}{\partial t} = \frac{\partial^2 \theta}{\partial x^2} + \frac{\partial^2 \theta}{\partial y^2} \tag{1b}$$

$$F-S: \quad \frac{k_F}{k_S}\frac{\partial \theta_F}{\partial y} = \frac{\partial \theta_S}{\partial y} \tag{1c}$$

The boundary conditions are $\partial\theta/\partial x \to 0$, and $\partial\theta/\partial y \to 0$, as $x, y \to \infty$, in the substrate and $\partial\theta/\partial x \to 0$ for $x \to \pm\infty$, and $\theta \to 0$ when $y \to \infty$ in the fluid. The velocity distribution in the forced convection heat transfer equation is either $u(y)=\sigma y$ or $u(y,t)=\sigma y(1 + a \sin \omega^* t)$ depending on whether a steady or unsteady problem is studied. The velocity is linear since the thermal boundary layer is thin, exactly as in the classical Lévêque's problem. The shear parameter is given by $\sigma = \mathrm{Pr}(l_f u_\tau/\nu)^2 = \mathrm{PrRe}_f^2$.

The sizes of the computational domain are $70l_f$ in the x direction, as well as $6l_f$ in the fluid and $20l_f$ in the substrate in the y direction. It was carefully checked that these dimensions are large enough to guarantee the validity of the boundary conditions. Figure 1(*a*) shows schematically the computational domain and the boundary conditions for a two-layer substrate.

The heat transfer law generally used for wall shear stress measurements (the Nusselt number $\mathrm{Nu} \propto \sigma^{1/3}$) is based on the simplest solution which assumes $\partial\theta/\partial t = \partial^2\theta/\partial x^2 = 0$ in the fluid (quasi-steadiness and no longitudinal diffusion) and $k_S = 0$. More complete solutions have been considered in the past, for instance with $\partial\theta/\partial t \neq 0$ [13–15] or with $k_S \neq 0$ (in the 1D case by Bellhouse and Schultz [9] and the 2D case by Brison et al. [10]). The full simulation introduces the additional parameter of the diffusivity ratio α_F/α_S, which points to the importance of *how fast* the heat is transferred to the fluid after conduction through the solid in addition to *how much* heat is transferred this way as compared to the direct transfer on the film.

Upstream weighted differencing [16] and ADI (alternated direction implicit), combined with stretched coordinates [17], near the trailing and leading edges of the WHF, as well as near the wall have been used. The ADI is chosen because it is unconditionally stable and quite efficient in problems involving heat and mass transfer. The upstream weighted differencing scheme is essentially a control-volume approach. The temperatures on the control mesh are determined with unknown interpolation coefficients, which are given later as data for the computation. These coefficients depend on the problem studied and the mesh sizes of the computational space. The resulting equation is stable if all the coefficients are positive. The time step is chosen uniform over the whole range of the computational space. One of the advantages of this strategy is that the same code may be run for different cases, as for example the boundary layer approximation ($\partial^2\theta/\partial x^2 = 0$), by simply setting the corresponding coefficients equal to zero. The numerical scheme is of second order in time and space.

The analysis of heat transfer near the singularities at the wall and trailing and leading edges requires a dense grid distribution. Stretching coordinates are used to avoid the numerical problems caused by a nonuniform grid distribution. The stretching function in the streamwise x coordinate is $x(\xi) = \sin^2(\pi/2\xi)$ for $0 \leqslant x, \xi \leqslant 1$. The stretching is symmetrical with respect to the center of the hot film. The smallest grid size near the singularities is $\Delta x = \sin^2[\pi/(4K)^2]$, where K is the number of grid points on the film. One has $\Delta x \ll 1/K^2$ for a moderate K. The same stretching approach is used upstream and downstream of the film, and it is matched with the coordinate system on the film. A typical computational domain is shown in Fig. 1(*b*). The number of computational nodes varied between 70×50 (in streamwise and wall normal directions, respectively) to typically 120×150.

The stretching method used in the fluid and substrate following the wall normal direction is of the form $y = \eta^2$. Thus for the model shown in Fig. 1(*a*), the coordinate transformations are

$$F: \quad 0 \leqslant y \leqslant H_F, \quad 0 \leqslant \eta \leqslant c_F H_F; \quad y(\eta) = \eta^2/(c_F^2 H_F)$$

$$S1 \text{ (solid 1)}: \; -H_{S1} \leqslant y \leqslant 0, \quad -c_{S1}H_{S1} \leqslant \eta \leqslant 0;$$

$$y(\eta) = -\eta^2/(c_{S1}^2 H_{S1})$$

$$S2 \text{ (solid 2)}: \; -(H_{S1} + H_{S2}) \leqslant y \leqslant -H_{S1},$$

$$-(c_{S1}H_{S1} + -c_{S2}H_{S2}) \leqslant \eta \leqslant -c_{S1}H_{S1};$$

$$y(\eta) = -(\eta + c_{S1}^2 H_{S1})^2/(c_{S2}^2 H_{S2}) - H_{S1}$$

The coefficients c_F, c_{S1}, and c_{S2} can be modified to adapt the stretching to different zones. The maximum resolution occurs at the interfaces where the derivative $dy/d\eta = 0$. The upstream weighting difference and ADI problems are formulated in the (ξ, η) domain and the resulting system was resolved by the classical Thomas algorithm.

Several computations were performed to check the performance of the numerical method. We first consider a steady flow on a perfectly isolated substrate. Figure 2 shows the local flux $q_w^* = -(\partial\theta/\partial y)_{y=0}\sigma^{-1/3}$ over the film for two values of the shear pa-

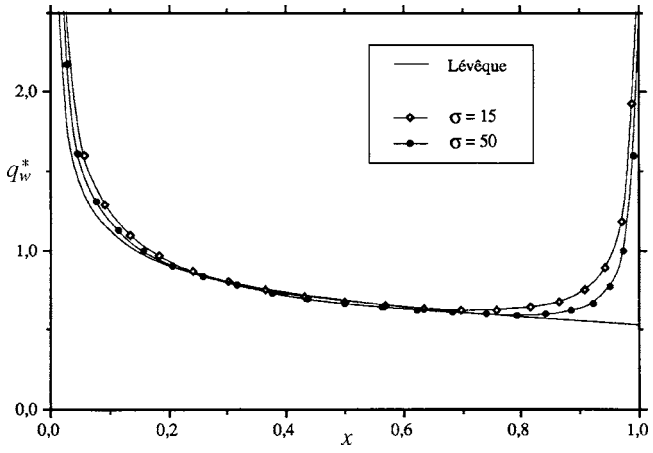

Fig. 2 Local heat flux over the film compared with the boundary layer approximation (Lévêque solution)

rameter. The effect of the trailing edge singularity increases with decreasing Péclet number. The computed global heat flux is compared with Ling [4] and Springer [6] in Fig. 3. There is an excellent agreement with the asymptotic analysis of Springer [6], and the difference between the computations and his theoretical approach is less than 1%.

3 Results

3.1 Two-Layer Configuration; Homogeneous Substrate. The global heat transfer rates per unit span Q for the coupled glass/water (conductivity ratio $k_S/k_F=1.27$) and glass/air ($k_S/k_F=25.3$) cases are shown in Tables 1(*a*) and 1(*b*) as a function of the Péclet number $\sigma=\mathrm{Pr}l_f^{+2}$. The notations are illustrated in Fig. 4. In the steady regime, the heat transfer from the film to the substrate Q_{fS} must be balanced by heat loss from the semi-infinite substrate to the fluid. Thus, $Q_{fS}=Q_{SF}^-+Q_{SF}^+$. This balance is, by the way, a good check for computational accuracy. The fluid is heated by the upstream heat transfer rate Q_{SF}^- before it reaches the film. This decreases both the direct transfer rate from the film Q_{fF} and the downstream transfer rate Q_{SF}^+. The latter extends the heating of the fluid further downstream and smoothes the effect of the axial diffusion at the trailing edge singularity. The conductivity ratio k_S/k_F is the only relevant parameter describing the substrate's direct and indirect influences. The direct transfer is reduced because of the wake effect due to Q_{SF}^- and the indirect transfer

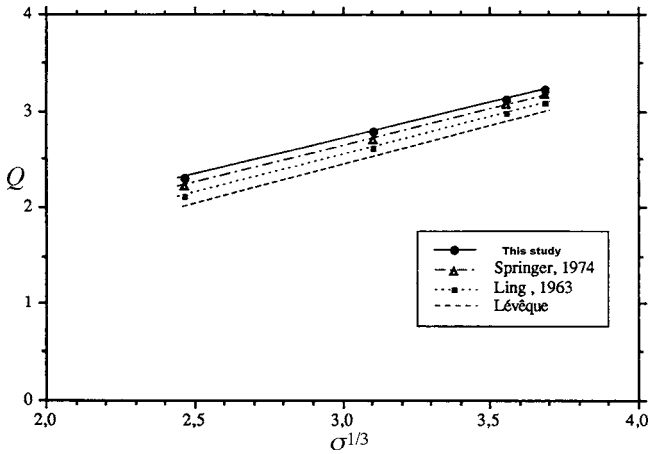

Fig. 3 Global heat flux with the longitudinal diffusion term and comparison with past studies

Table 1 Global heat transfer rates versus the shear parameter. For the notations see Fig. 4. (*a*) Water/glass. (*b*) Air/glass.

σ	Q	Q_{fF}	Q_{fS}	Q_{SF}^-	Q_{SF}^+	$Q_{Lévêque}$
3	9,74	0,63	9,11	5,37	3,74	1,16
15	12,79	1,05	11,74	7,37	4,37	1,99
23	13,70	1,23	12,47	7,89	4,57	2,30
30	14,00	1,34	12,66	8,05	4,60	2,51
38	14,26	1,43	12,82	8,18	4,65	2,71
45	14,39	1,50	12,89	8,23	4,66	2,87

together with the ratio Q_{fS}/Q_{fF} increase with k_S/k_F.

The heat flux to the substrate Q_{fS} is smaller than the direct transfer Q_{fF} for small conductivity ratios as expected (Fig. 5(*a*)). On the contrary, the ratio Q_{fS}/Q_{fF} is as large as 10 for the combination air-glass with $k_S/k_F=25.3$ as seen in Fig. 5(*b*). For both cases the ratio Q_{fS}/Q_{fF} decreases with increasing Péclet number, because the transfer to the substrate Q_{fS} depends only slightly upon σ, while the transfer from the film to the fluid Q_{fF} increases much more rapidly with the Péclet number by forced convection.

For the combination water/glass, the direct transfer from the film to the fluid is approximately equal to the Lévêque solution,

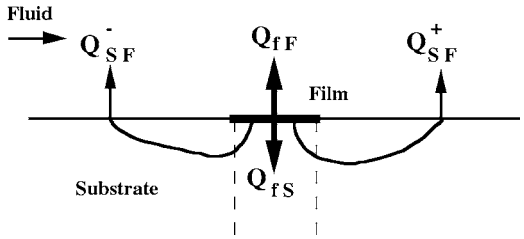

Fig. 4 Sketch of heat transfer definitions over the hot film gage

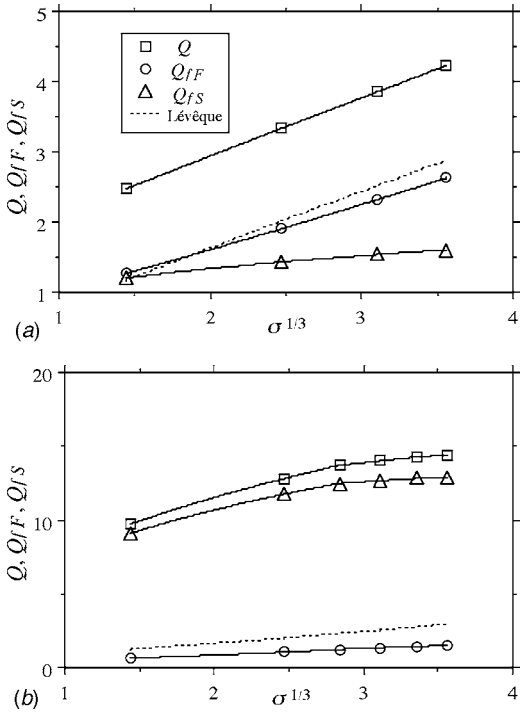

Fig. 5 Direct transfer to the fluid and transfer to the substrate compared with the Lévêque solution. (*a*) Water/glass. (*b*) Air/glass. Legend on (*a*).

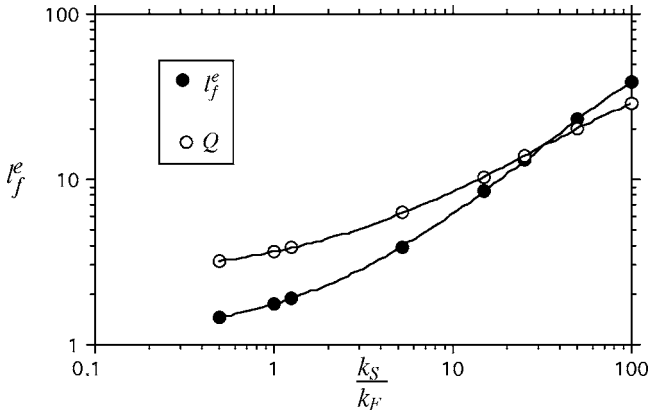

Fig. 6 Effective length of the hot film gage versus the conductivity ratio for $\sigma=30$

i.e., $Q_{fF} \approx Q_{Lévêque} = 0.81\sigma^{1/3}$ (Fig. 5(*a*)). For large σ values, Q_{fF} is smaller than $Q_{Lévêque}$, but the difference never exceeds 10%.

3.2 Effect of the Conductivity Ratio. The effect of heat transfer via the substrate may be characterized by an "equivalent length" l_f^e defined by $Q = Q_{fF} + Q_{fS} = 0.81\sigma^{1/3}(l_f^e)^{2/3}$. Hence, l_f^e is the dimensionless length of a hypothetical film on a perfectly nonconducting substrate, obeying the Lévêque law giving the same total heat transfer as the real film. The impact of the ratio k_S/k_F on the heat transfer process is further analyzed for a fixed Péclet number $\sigma=30$. Figure 6 shows that the effective length and the global transfer Q increase considerably with the conductivity ratio. A regression analysis shows that

$$Q = 2.44\left(\frac{k_S}{k_F}\right)^{0.54} \text{ and } l_f^e = 0.96\left(\frac{k_S}{k_F}\right)^{0.81}$$

in the range $5 < k_S/k_F < 100$. Hence, the effective length is 1.5 times more sensitive to the conductivity ratio than Q. The global flux depends strongly upon the conductivity ratio and varies approximately as the square root of k_s/k_F. These results show that the hot-film gauge can be applies to the mixtures such as helium-air, because the variations of heat transfer rates depend on the conductivity of the fluid, which is a function of the composition of the binary mixture. The increase of the global heat transfer rate is obviously due to the importance of heat conduction to the substrate Q_{fS} at high conductivity ratios (Fig. 7(*a*)). The upstream heat transfer rate q_{SF}^- is always larger than Q_{SF}^+ and the difference $Q_{SF}^- - Q_{SF}^+$ increase with k_s/k_F (Fig. 7(*b*)). Consequently, the direct transfer is weakend by the wake effect caused by upstream transfer Q_{SF}^-. The ideal Lévêque solution is never exactly reached even at low conductivity ratios such as $k_S/k_F \approx 1$.

3.3 Two-Layer Substrate. Computations were also carried out for a two-layer substrate configuration, in which a thin isolating mylar film of thickness $0.5l_f$ is sandwiched between the hot wall film and the substrate. Such a configuration exists commercially (DANTEC glue-on probe 55R47). The transfer depends on both k_{S1}/k_F (mylar-fluid) and k_{S2}/k_F (substrate-fluid). Two cases were studied, namely

(i) $k_{S1}/k_F=1$, $k_{S2}/k_F=5.2$ (helium-mylar-glass),
(ii) $k_{S1}/k_F=4.9$, and $k_{S2}/k_F=25.3$ (air-mylar-glass)

A low indirect transfer Q_{fS} is expected in the first case, since the ratio k_{S1}/k_F is relatively small. Case (i) is indeed somewhat similar to the water-glass combination ($k_S/k_F=1.3$). The equivalent film lengths are indeed approximately equal in these cases (Fig. 8). The indirect transfer is, however, 10% larger in case (i), compared to water-glass because of larger k_{S2}/k_F and this explains the slight differences observed in Fig. 8.

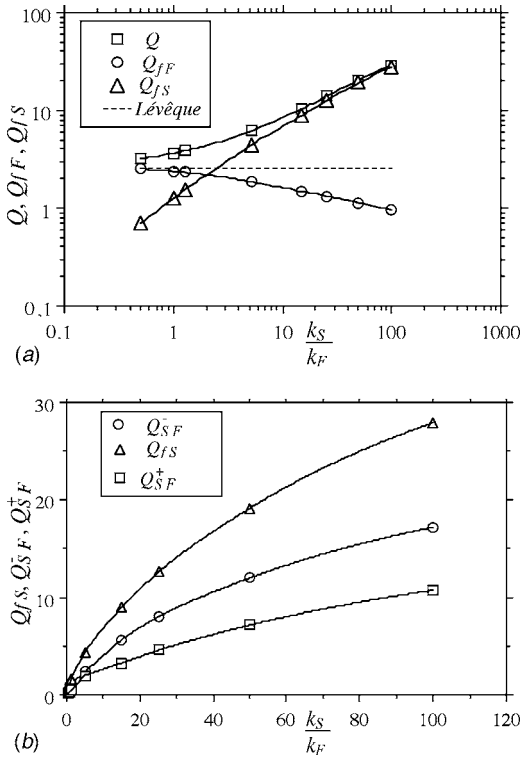

Fig. 7 Global heat transfer rates versus the conductivity ratio. (*a*) Transfer to the fluid and to the substrate. (*b*) Transfer rates from the substrate to the fluid upstream and downstream of the hot film.

The case of air-mylar-glass is more interesting because it shows how the isolating thin film may improve the global performance of the hot film gauge. Thus, the effective length and the transfer to the substrate decrease by a factor of 2, and the direct transfer Q_{fF} is 30% larger compared with the mono-layer glass substrate. Moreover, the relationship $Q=f(\sigma^{1/3})$ tends rapidly to a Lévêque's type law $Q=A\sigma^{1/3}+B$ when the Péclet number is high enough, more rapidly with the isolating film than without. This is summarized in Fig. 9. The explanation of the decrease of the equivalent length with increasing velocity (or shear) and increasing values of the ratio k_F/k_S lies in the increased capacity of the fluid to carry away the heat conducted through the solid or, in other words, in the capacity of the fluid to cool the solid substrate heated above ambient temperature in the vicinity of the film.

The temperature at the wall decreases rapidly in a zone of radius l_f in the case of a double-layer substrate (Fig. 10). Figure 11

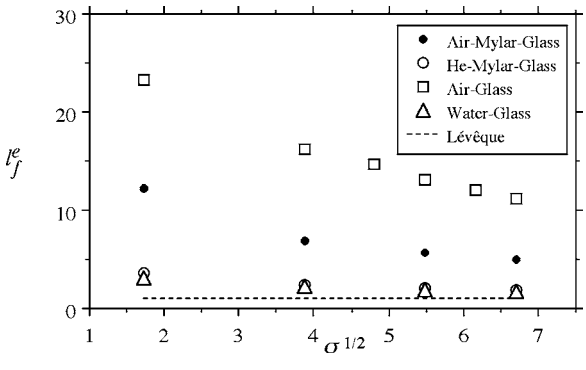

Fig. 8 The effective length of the hot film with a double-layer substrate

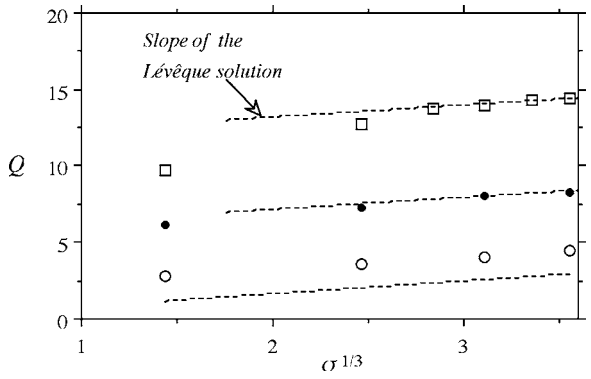

Fig. 9 Global heat flux for different substrate configurations and comparison with the Lévêque solution. For legend see Fig. 8.

shows that the local flux is also more important compared with the air-glass case. The heat flux at the trailing edge is two times larger when the substrate has a multi-layer structure.

3.4 Frequency Response. The frequency response of the hot film gauge is determined by imposing a sinusoidal shear parameter $\sigma=\overline{\sigma}(1+a\sin\omega t)$. The periodical variations of the direct and indirect transfer rates as a function of the imposed frequency ω^* are determined for different configurations. The unsteady computations were started from the time-mean steady field and were carried out until the difference in temperature at any point was less than 0.01% between two successive imposed periods. The dimensionless parameters governing the problem are $\overline{\sigma}$, a, ω^*, k_S/k_F, α_S/α_F, k_{S1}/k_{S2}, and α_{S1}/α_{S2} with the last two parameters

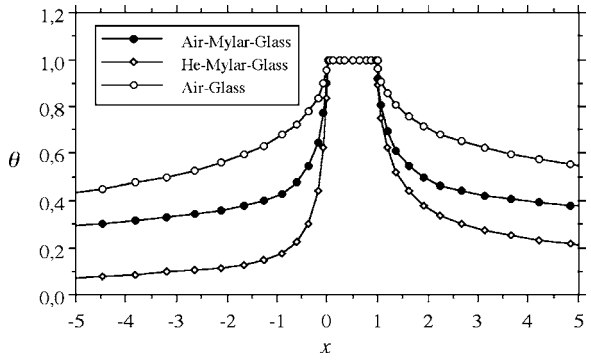

Fig. 10 Wall temperature distribution for several fluid/sunstrate combinations

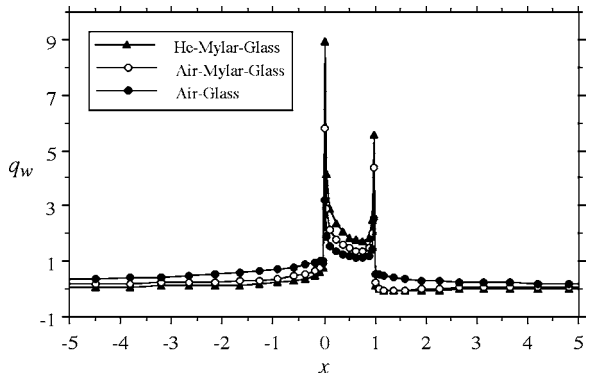

Fig. 11 Effect of the fluid/substrate configuration on the local flux for $\overline{\sigma}=30$

only entering into the consideration in the double-layer substrate configuration. To limit the number of cases considered, results for $\overline{\sigma}=30$ and $a=0.5$ are presented. The imposed frequency ω^* ranged from 10^{-6} to 10. Typical dimensions of commercial films are $l_f=0.2$ mm, so that $\sigma=30$ in air corresponds to $u_\tau=0.5$ m/s, i.e., to a boundary layer with a free stream velocity of $\hat{u}_\infty=12$ m/s.

The code was tested by investigating the exact 1D time-dependent three-layer case of Bellhouse and Schultz [9] (*F-S-F*, with solid thickness l_f and with the same flow on both sides of the solid slab). Figure 12 shows the relative amplitude of the heat transfer versus frequency for the case of air and water flow over glass. The reference amplitude is that of the quasi-steady case. The oscillations of the total heat transfer rate are damped with increasing frequency because the part transferred through the solid is filtered. This part is proportionally larger in air than in water flow and is increased by the effect of longitudinal diffusion in the fluid and in the solid (which is, of course, inherently neglected in the 1D solution of Bellhouse and Schultz). Figure 12 shows also that the attenuation of the frequency response of the full simulation, which takes axial diffusion into account, starts at a frequency which is about ten times lower than in the 1D exact solution.

The anemometer measures the total heat transfer from the film to the fluid and to the solid $Q=Q_{fF}+Q_{fS}$. In the unsteady regime, there cannot be an instantaneous balance between Q_{fS} and $(Q_{SF}^-+Q_{SF}^+)$ as in the steady regime because the heat flux variations imposed at the solid surface by the velocity changes are filtered to variable degrees by the substrate, depending upon the distance to the film and the frequency.

The attenuation of the hot-film response is seen in Figs. 13 and 14 for the air-glass configuration. The cyclic variations of the relative transfer rates scaled with their time-mean values such as $Q_{fF}/\overline{Q_{fF}}$ (Fig. 13), $Q_{fS}/\overline{Q_{fS}}$, and the relative total flux $Q/\overline{Q}$ (Fig. 14) are shown versus time divided by the imposed period $P=2\pi/\omega^*$ for respectively a low ($\omega^*=10^{-3}$) and high frequency ($\omega^*=3$). One has $\omega^*=\sigma\omega^+$, where ω^+ is the frequency scaled with the shear and the viscosity, i.e., with the inner variables of a near wall turbulent flow. Thus, $\omega^*=3$ is quite high and corresponds to $\omega^+=0.1$, which is the frequency where the energy spectrum of the velocity is maximum near the viscous layer. This is also approximately 1/15 of the Kolmogoroff frequency near the wall under these flow conditions. The low frequency $\omega^*=10^{-3}$ is nearly in the quasi-steady regime, wherein the transfer rates are in time equilibrium with the shear modulation. The real quasi-steady regime is difficult to reach, since the distance to which the heat diffuses during the period of oscillation is $\delta^2\approx\alpha_S T$, i.e., $\delta^2\approx(2\pi/\omega^*)\times(\alpha_S/\alpha_F)l_f^2$. The transfer through the substrate can only respond without time lag to velocity variations if $\delta\ll l_f^e$, i.e., if $\omega^*\ll 2\pi(l_f/l_f^e)^2(\alpha_S/\alpha_F)$. Since for air-glass combination $\alpha_S/\alpha_F=0.017$ and $l_f^e=13l_f$, for $\sigma=30$, this requires $\omega^*\ll 6\times10^{-4}$, a very small frequency indeed. Clearly, the air-glass combination is unfavorable for two reasons: first, because of the larger transfer through the substrate due to the large value of the conductivity ratio k_S/k_F, and, second, because $\alpha_S/\alpha_F\ll 1$, which results in considerable filtering of the variations of upstream and downstream transfers via the substrate. Similar computations indicate that the quasi-steady regime is reached for $\omega^*\ll 4.7$ (water/glass) and $\omega^*\ll 9\times10^{-4}$ (He/mylar/glass or air/mylar/glass).

The frequency response of the direct transfer $Q_{fF}/\overline{Q_{fF}}$ is not significantly sensitive to the diffusivity and conductivity ratios. This can be seen in Fig. 13, which compares the cyclic modulation of the ideal Lévêque solution, the quasi-steady and high-frequency response of the hot film in air on a glass substrate. Figure 15 compares the direct transfer response of the air/glass with water/glass configurations for which it is recalled that the conductivity ratios vary by a factor 20. $Q_{fF}/\overline{Q_{fF}}$ is less modulated in air/glass but the difference is only a few percent. The modula-

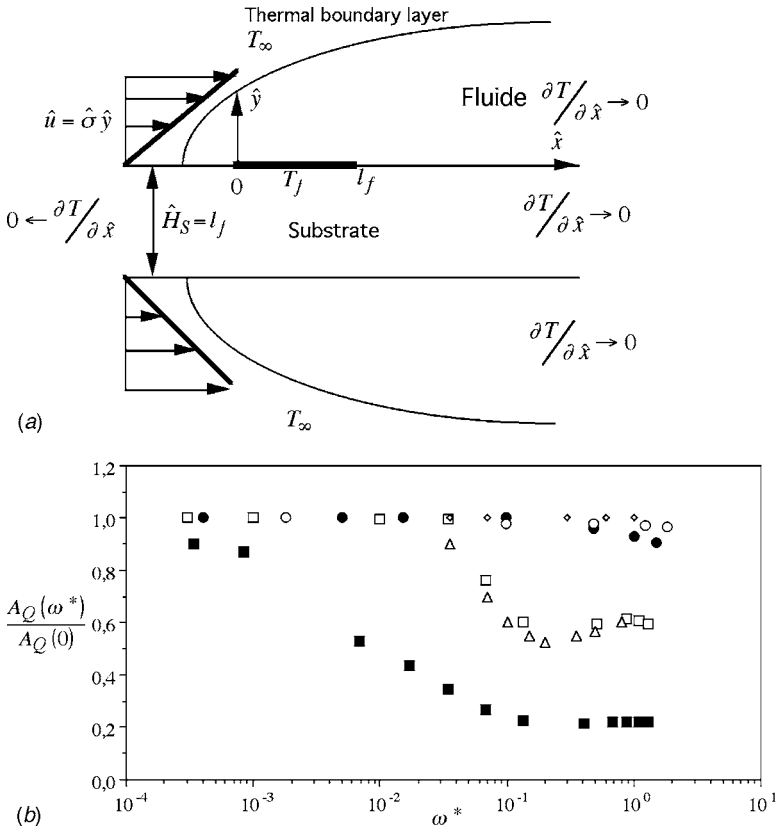

Fig. 12 (*a*) Problem investigated by Bellhouse and Schultz (1968). (*b*) Comparison with the present numerical results. ■: Air with axial diffusion. □: Air without axial diffusion. ●: Water with axial diffusion. ○: Water without axial diffusion. △: Bellhouse and Schultz air. ◇: Bellhouse and Schultz water.

tion of the indirect transfer $Q_{fS}/\overline{Q}_{fS}$ is entirely frozen in the high-frequency regime as seen in Fig. 14, by comparing $Q_{fS}/\overline{Q}_{fS}$ in the quasi-steady $\omega^*=1.7\times10^{-4}$ and the high-frequency $\omega^*=3$ regimes. It can be easily shown that the amplitude of the global heat transfer A_Q is the sum $A_{Q_{fS}}+A_{Q_{fF}}$ if the phase shifts can be neglected, which is approximately the case here. Since in the high-frequency regime $A_{Q_{fS}}\approx 0$, the amplitude of the global transfer decreases drastically by some 60% in the high-frequency regime. For low conductivity ratios as for water/glass configuration, the decrease of the amplitude $A_{Q_{fS}}$ is only 12%, and the global transfer responds acceptably well in the high-frequency regime (Fig. 16).

Some values of the frequency response of the wall hot film are plotted in Fig. 17 for $\overline{\sigma}=30$. The amplitude of the global flux A_Q is scaled with the amplitude in the quasi-steady regime $A_Q(\omega^*=0)$ that was determined here at $\omega^*=10^{-6}$. The limiting value of the attenuation is $1/5$ when the mean flow parameter $\sigma=30$ in the air-glass case. This value is in reasonable agreement with the reduced turbulent intensity of the wall shear stress measured by some authors in air flows [18]. It is seen that the amplitude is already reduced by a factor of $1/2$ when $\omega^*=3\times10^{-4}$, while the thin insulating mylar film improves somewhat the response com-

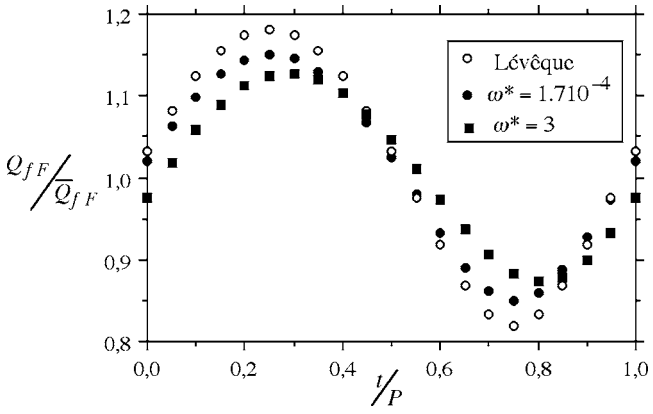

Fig. 13 Direct flux from the film to the fluid for air/glass case

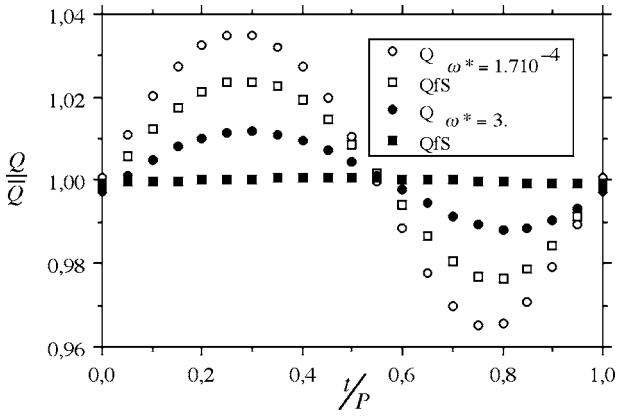

Fig. 14 Total flux and indirect flux from the film to the substrate for the air/glass configuration

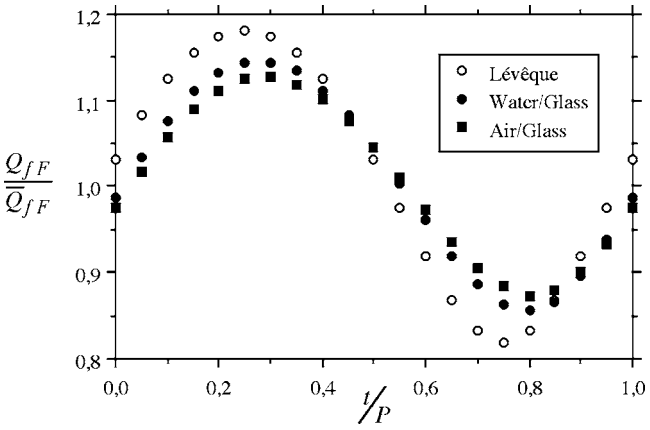

Fig. 15 Cyclic modulation of the direct flux for different configurations compared with the ideal Lévêque solution

pared with the air/glass case, but this improvement is far from being totally satisfactory. The thermal boundary layer itself has a finite frequency response owing to the finite transit time over the film l_f/u_τ. But this frequency limit ($\omega^* \approx 1$) is much higher than the limit imposed by the transfer via the substrate.

To show how severe the filtering effect of the substrate may be in the air/glass case, consider a turbulent boundary layer with $\hat{u}_\infty = 12$ m/s and $\mathrm{Re}_\delta = 5 \times 10^4$. The Kolmogoroff frequency is roughly 5 kHz in this case. The dimensionless frequency $\omega^* = 0.1$ at which the attenuation is 1/5 is only 10 Hz, i.e., nearly three orders of magnitude smaller than the Kolmogoroff frequency.

The comparison the water/glass with the He/mylar/glass reveals the predominance of the conductivity ratio in the dynamic response rather than the diffusivity ratio. The ratio of conductivities are respectively $k_{Mylar}/k_{He} = 1$, $k_{Glass}/k_{He} = 5.2$, and $k_{Glass}/k_{Water} = 1.3$. The diffusivities vary considerably from a factor 4000 to 1000 with $\alpha_{Glass}/\alpha_{Water} = 4190\alpha_{Mylar}/\alpha_{He}$ and $\alpha_{Glass}/\alpha_{Water} = 1157\alpha_{Glass}/\alpha_{He}$. The distribution $A_Q(\omega^*)/A_Q(0)$ for the He-mylar-glass is below the water/glass configuration because k_{Glass}/k_{He} is higher than k_{Glass}/k_{Water}, but the large variations of the diffusivities do clearly not play a significant role in the heat transfer process.

The frequency response for the water/glass combination is reasonably acceptable. The attenuation is only 20% at $\omega^* = 10$. The ratio $A_Q(\omega^*)/A_Q(0)$ is roughly 0.65 at the Kolmogoroff frequency $\omega_K^* = 2\pi f_K^* = 60$ in a turbulent fully developed water channel flow with a Reynolds number based on the half-channel height of 10^4. Thus wall shear stress measurements in a fully developed turbulent water channel flow by a hot film on glass can be reliably performed, except maybe at the smallest turbulent scales. Recall that the satisfactory frequency response of the case water/glass does not mean that there is no parasitic heat conduction to the substrate. On the contrary, the ratio Q_{fS}/Q_{fF} varies between 1 and 3/5 as seen in Fig. 5(*a*). Yet, this ratio reaches values as large as 10 in the case air/glass (Fig. 5(*b*)). The heat loss ratios of roughly $Q_{fS}/Q_{fF} \approx 1$ do not affect considerably the frequency response at least up to $\omega^* = 1$.

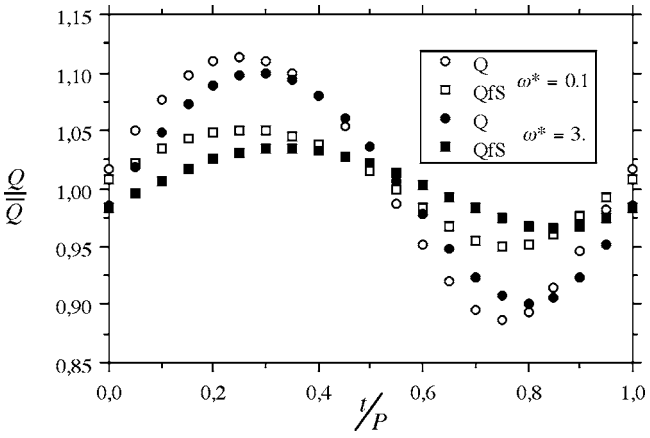

Fig. 16 Modulation of the total and indirect fluxes for the water/glass configuration

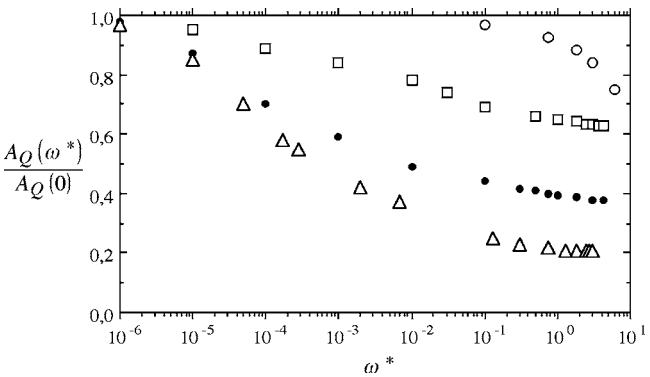

Fig. 17 Frequency response of the hot-film gage in different fluid/substrate configurations. ○: Water-glass. □: Helium-mylar-glass. ●: Air-mylar-glass. △: Air-glass.

4 Conclusion

A numerical investigation of heat transfer of wall-mounted hot film gages shows that heat transferred to the fluid via the substrate has important effects. For high values of the conductivity ratios k_S/k_F, the transfer from the film to the substrate may be considerably larger than the direct transfer to the fluid. For the air/glass combination, the transfer to the fluid through the substrate is about 10 times larger than the direct transfer from the film. Because of the hot wake, the downstream transfer from the substrate to the fluid is roughly half of the upstream value.

The importance of conduction into the substrate increases with decreasing velocity. A thin layer of material with low conductivity inserted between the film and substrate attenuates this effect.

The frequency response of the total heat transfer from the film, as measured by an anemometer set, is dominated by the filtering effect of the transient heat transfer via the substrate when $k_F \ll k_S$ and $\alpha_F \gg \alpha_S$. For the air/glass combination, the response is attenuated as soon as $\omega^* > 10^{-6}$. This limit is much lower than the cutoff frequency of the thermal layer.

There is a limit of the spanwise length l_{fz} of the hot film probes to avoid spanwise averaging of the turbulence producing structures in the near wall region. According to Blackwelder and Haritonidis [19], this requires $l_{fz}^+ = l_{fz}(u_\tau/\nu) < 20$. The streamwise sensing length of some commercial wall hot-film gages is, $l_f = \frac{1}{8} l_{fz}$ to prevent both the spanwise conduction effects and to ensure two-dimensionality. Therefore, the previous condition gives $l_f^+ < 2.5$. The corresponding Péclet number concerning the measurements of the wall shear stress and wall shear stress intensity in water is $\sigma = \mathrm{Pr} l_f^{+2} < 44$. Clearly the axial diffusion through the leading and trailing edges singularities has to be taken into account under these circumstances. Note that the estimations given above constitute an upper limit. More careful measurements require at least $l_{fz}^+ < 10$ and $\sigma < 10$. Neglecting the axial diffusion term in the energy equation when the Péclet number is small may generate serious errors in predicting the frequency response of the hot film. These points have to be taken into account in MEMS sensor designs.

Acknowledgment

We are thankful to Professor Stefan Thynell for his continuous help in the editing process of this paper.

Nomenclature

A_q = amplitude of the quantity q
a_q = $A_q/\overline{q}$, relative amplitude of the quantity q
a = relative amplitude of the shear parameter
$h(\hat{x})$ = local heat transfer coefficient
H = $\int_0^l h(\hat{x})d\hat{x}$, global heat transfer coefficient
K = number of grid points over the hot film
k = conductivity
l_f = streamwise length of the hot film
l_f^e = $(Q/Q_{Lévêque})^{3/2}$, dimensionless equivalent hot-film length
Nu = H/k_F, Nusselt number
P = $2\pi/\omega^*$, dimensionless period of the imposed velocity oscillations
Pr = ν/α, Prandtl number
Q_{fF} = dimensionless direct total heat flux from the film to the fluid
Q_{fS} = dimensionless heat flux from the film to the substrate
$Q_{Lévêque}$ = $0.81\sigma^{1/3}$, dimensionless direct heat flux over the film of the Lévêque solution.
Q_{SF}^- = dimensionless heat flux from the substrate to the fluid upstream of the hot film
Q_{SF}^+ = dimensionless heat flux from the substrate to the fluid downstream of the hot film
Q = $Q_{fF}+Q_{fS}=\int_{Film} q_w dx$, dimensionless hot-film global heat transfer rate per unit span
$\overline{q}$ = time mean of the quantity q
q^+ = quantity q nondimensionalized with the shear velocity u_τ and viscosity ν
q_w = $-(\partial\theta/\partial y)_{y=0}$, local heat flux
q_w^* = $-(\partial\theta/\partial y)_{y=0}\sigma^{-1/3}$, dimensionless local heat flux scaled with the shear parameter
Re_δ = $\hat{u}_\infty\delta/\nu$, turbulent boundary layer Reynolds number
Re_f = $l_f u_\tau/\nu$, hot film Reynolds number
T = temperature
$\hat{t}$ = dimensional time
t = $(\hat{t}/l_f^2)\alpha_F$, dimensionless time
$\hat{u}$ = dimensional velocity
u = $\hat{u}/u_\tau$, dimensionless velocity
u_τ = $\sqrt{\tau/\rho_F}$, shear velocity
$\hat{x}$ = dimensional streamwise distance
x = $\hat{x}/l_f$, dimensionless streamwise coordinate
$\hat{y}$ = dimensional wall normal distance
y = $\hat{y}/l_f$, dimensionless wall normal coordinate

Greek symbols

α = diffusivity
δ = boundary layer thickness
η = wall normal stretched coordinate
ν = kinematic viscosity
ρ = density
σ = $\mathrm{Pr}(l_f u_\tau/\nu)^2$, shear parameter
$\overline{\sigma}$ = time-mean shear parameter
θ = $(T-T_\infty)/(T_f-T_\infty)$, dimensionless temperature
τ = wall shear stress
$\hat{\omega}$ = dimensional angular frequency of the imposed oscillations
= dimensionless angular frequency
ω^+ = $\hat{\omega}(\nu/u_\tau^2)$, imposed frequency in wall units.
ξ = streamwise stretched coordinate

Abbreviations

F = fluid
S = substrate
WHF = wall hot film

Subscripts

F = fluid
S = substrate
f = hot film
∞ = bulk

References

[1] Tardu, S., 2001, "Active Control of Near Wall Turbulence by Local Unsteady Blowing," J. Fluid Mech., **43**, pp. 217–253.
[2] Tardu, S., and Michelutti, L., 2004, "Microsystèmes Utilisés dans les Grands Écoulements," *Microfluidique*, S. Colin, ed., Hermès, Paris, pp. 349–389.
[3] Meunier, D., Tardu, S., Tsamados, D., and Bousssey, J., 2003, "Realization and Simulation of Wall Shear Stress Integrated Sensors," Microelectron. J., **34**, pp. 1129–1136.
[4] Ling, S. C., 1963, "Heat Transfer from a Small Isothermal Spanwise Strip on an Insulated Boundary," ASME J. Heat Transfer, **85**, pp. 203–235.
[5] Springer, S. G., and Pedley, T. J., 1973, "The Solution of Heat Transfer Problems by the Wiener-Hopf Technique. Leading Edge of a Hot-film," Proc. R. Soc. London, Ser. A, **333**, pp. 347–362.
[6] Springer, S. G., 1974, "The Solution of Heat Transfer Problems by the Wiener-Hopf Technique. Trailing Edge of a Hot-film," Proc. R. Soc. London, Ser. A, **337**, pp. 395–412.
[7] Ackerberg, R. C., Patel, R. D., and Gupta, S. K., 1978, "The Heat/mass Transfer to a Finite Strip at Small Péclet Numbers," J. Fluid Mech., **86**, pp. 49–65.
[8] Lighthill, M. J., 1954, "The Response of Laminar Skin Friction and Heat Transfer to Fluctuations in Stream Velocity," Proc. R. Soc. London, **224**, pp. 1–23.
[9] Bellhouse, B. J., and Schultz, D. L., 1968, "The Measurement of Fluctuating Skin Friction in Air with Heated Thin-film Gauges," J. Fluid Mech., **32**(2), pp. 675–680.
[10] Brison, J. F., Charnay, G., and Comte-Bellot, G., 1979, "Calcul des Transferts Thermiques Entre Film Chaud et Substrat Pour un Modèle à deux Dimensions," Int. J. Heat Mass Transfer, **22**, pp. 111–119.
[11] Cole, K. D., and Beck, J. V., 1988, "Conjugated Heat Transfer from a Hot-film Probe for Transient Air Flow," ASME J. Heat Transfer, **110**, pp. 290–296.
[12] Moen, M. J., and Schneider, S. P., 1993, "The Effect of Sensor Size and Substrate Properties on the Performance of Flush-mounted Hot-film Sensors," Thermal Anemometry-1993, Stock, S. A. Sherif, A. J. Smits, J. Davidson, eds., ASME, New York, pp. 249–261.
[13] Pedleys, T. J., 1975, "A Thermal Boundary Layer in a Reversing Flow," J. Fluid Mech. **67**, pp. 209–225.
[14] Fortuna, G., and Hanratty, T. J., 1971, "Frequency Response of the Boundary Layer on Wall Transfer Probes," Int. J. Heat Mass Transfer, **14**, pp. 1499–1507.
[15] Kaiping, P., 1983, "Unsteady Forced Convective Heat Transfer from a Hot Film in Non Reversing and Reversing Shear Flow," Int. J. Heat Mass Transfer, **26**(4), pp. 545–557.
[16] Raithby, G. D., and Torrance, K. E., 1974, "Upstream-weighted Differencing Schemes and Their Application to Elliptic Problems Involving Fluid Flow," Comput. Fluids, **2**, pp. 191–206.
[17] Kalnay de Rivas, E., 1972, "On the Use of Nonuniform Grids in Finite Difference Equations," J. Comput. Phys., **10**, pp. 202–210.
[18] Chambers, F. W., Murphy, H. D., and McEligot, D. M., 1983, "Laterally Converging Flow. Part 2. Temporal Wall Shear Stress," J. Fluid Mech., **127**, pp. 403–428.
[19] Blackwelder, R. F., and Haritonidis, J. H., 1983, "Scaling of the Bursting Frequency in Turbulent Boundary Layers," J. Fluid Mech., **132**, pp. 87–103.

An Experimental Study on the Effect of Gravitational Orientation on Flow Boiling of Water in 1054 $\times$ 197 μm Parallel Minichannels

Satish G. Kandlikar
e-mail: sgkeme@rit.edu

Prabhu Balasubramanian
e-mail: prabhu@mechtech.com

Thermal Analysis and Microfluidics Laboratory,
Mechanical Engineering Department,
Rochester Institute of Technology,
Rochester, New York 14623, USA

Microchannels and minichannels are being considered for high heat flux applications under microgravity environment in space missions. An experimental study is undertaken to determine the effect of gravitational orientation on flow boiling characteristics of water in a set of six parallel minichannels, each 1054 μm *wide by* 197 μm *deep and* 63.5 mm *long with a hydraulic diameter of* 333 μm. *Three orientations—horizontal, vertical downflow, and vertical upflow—are investigated under identical operating conditions of heat and mass fluxes. High-speed images are obtained to reveal the detailed two-phase flow structure and liquid-vapor interactions. The experimental data and high speed flow visualization indicate that compared to the horizontal case, the flow becomes less chaotic for the vertical upflow case, while the reversed flow becomes more pronounced in the vertical downflow case. The resulting increase in the backflow is responsible for channel-to-channel flow maldistribution and heat transfer degradation. From the heat transfer data it is concluded that the performance of the tested channels in a microgravity environment will be similar to the horizontal flow case.* [DOI: 10.1115/1.1928911]

Introduction

Microchannels and minichannels are being considered in systems that need to dissipate large heat fluxes efficiently while keeping the surface temperatures within prescribed limits. The effect of microgravity on the flow boiling heat transfer characteristics is an area of great interest in establishing the viability of microchannels and minichannels in space applications. The effect of gravity under different orientations is also an area of interest for earth-based systems.

Complex interactions have been observed among the liquid and vapor phases and the channel walls during flow boiling in small diameter channels. These interactions have been found to be further dependent on the heat flux [1]. The effect of surface tension forces is also expected to be important [2].

The low mass flow rate during flow boiling combined with the small channel diameter yields the all-liquid flow Reynolds numbers that are in the laminar region. In many cases, the Reynolds number is on the order of 100 or lower. Before developing generalized flow pattern maps, and heat transfer and pressure drop models, it is essential to gain a clear understanding of the two-phase flow characteristics under flow boiling conditions through high-speed imaging along with accurate experimental data for local heat transfer coefficients.

Kandlikar [3] reviewed the forces experienced by the liquid interface during flow boiling in small diameter channels. As the channel dimensions become smaller, the ratio of the surface area to the flow volume increases and the surface tension forces becomes more dominant. Another force that plays a major role is the momentum force caused by the rapid evaporation of liquid at the liquid-vapor interface. The influence of the gravitational force is expected to be small because of the higher surface area to flow volume ratio. Since the interface shape and its motion determines the liquid-vapor flow patterns, it is reasonable to expect a diminishing effect of gravitational forces on the flow boiling phenomena in narrow channels. This feature makes the flow boiling in narrow channels very attractive for space systems as the evaporator performance is expected to remain unaffected by the microgravity environment. The present investigation is aimed toward experimentally evaluating the influence of gravity on the flow boiling phenomena. This is accomplished by changing the orientation of the flow channel. Three orientations are studied, horizontal, vertical upflow, and vertical downflow with flow boiling of water in a set of six parallel minichannels of 1054 $\times$ 197 μm rectangular cross-section.

Literature Review

Early studies on small diameter channels focused on gas-water flows; Fukano et al. [4] used horizontal tubes with inner diameters of 1.0 to 4.9 mm and Wambsganss et al. [5] used a horizontal round tube of inside diameter 2.90 mm. Kasza et al. [6] studied a rectangular channel of 2.5 mm by 6.0 mm and compared the flow pattern transitions with the available flow pattern maps. They confirmed the presence of bubbly, plug, slug, and annular flow patterns, with a stratified region limited to very small flow rates. Triplett et al. [2] used circular microchannels with inner diameters of 1.1 and 1.45 mm. They suggested that due to the dominance of surface tension forces, stratified flow is essentially absent, slug (plug) and churn flow patterns occur over extensive ranges of parameters, and the slip velocity under these flow patterns is small. The flow pattern observations were done in a systematic fashion by Cornwell and Kew [7] with R-113 in 0.9×1.2 mm^2 rectangular minichannels. They identified a flow pattern referred to as the confined bubble region. Here the bubbles nucleate and grow to occupy the entire channel. Large vapor bubbles fill the channel with liquid slugs between the consecutive elongated bubbles. This flow pattern is similar to plug flow. Kandlikar and Balasubramanian [8] compared the flow patterns for single and multiple channels and found that the backflow was significantly reduced for a single channel. A detailed summary of flow pattern visualization in minichannels is given by Kandlikar [9].

Contributed by the Heat Transfer Division for publication in the JOURNAL OF HEAT TRANSFER. Manuscript received: April 19, 2004. Final manuscript received: February 8, 2005. Review conducted by: Chang Oh.

Hetsroni et al. [10] investigated microchannels of 103–129 μm hydraulic diameter with all-water Reynolds numbers in the range of 20–70. They visualized the flow to be annular, with intermittent dryout and rewetting of the channels. Nucleation was not reported during the annular flow. Vapor was observed in the inlet plenum; similar observations were made by Kandlikar et al. [1] for 1 mm parallel channels. The instability resulting from the boiling in parallel channels was observed in microchannels as well.

Kandlikar et al. [1] and Kandlikar [3] report the flow patterns in a 1 mm^2 stainless steel channel heated with oil. They noted significant flow oscillations due to localized boiling. The expanding bubbles at any location experience very large growth rates and cause the liquid fronts to move away on both sides of the bubble in the channel. The resulting flow reversal introduces significant pressure fluctuations in the channels. The reversed flow in the channels causes the vapor to flow back into the inlet manifold, leading to flow maldistribution in the inlet header. This behavior leads to the premature critical heat flux (CHF) condition.

Although high speed cameras were used by earlier investigators to visualize the flow boiling phenomena, the rapidly moving liquid-vapor interface has not been clearly observed by them under high heat flux conditions. Use of low frame rates can mask some of the observed flow patterns. The shortest exposure time used in the present investigation was 1/80,000 s, and the image capture rate varied from 6000 to 15,000 fps.

Objectives of the Present Work

The present work focuses on obtaining very clear images using frame rates of up to 15,000 fps coupled with very short exposure times of down to 1/80,000 s. This enables, for the first time, clear visualization of the interface motion resulting from rapid growth of nucleating bubbles and fast moving vapor plugs during flow boiling in minichannels. Very high-resolution images (1024 $\times$512 pixels) of the fast moving liquid-vapor interface are obtained by adjusting the frame rate, exposure time, and lighting conditions. These clear images are then used in understanding the differences in flow patterns for the three orientations and relating them to the quantitative data on heat transfer and pressure drop performance.

The effect of gravitational orientation on flow boiling in parallel minichannels is studied for the three cases—horizontal flow, vertical downflow, and vertical upflow—under the same heat and mass flux conditions. The effect of orientation on the heat transfer performance and pressure drop characteristics is studied. The effects of flow structure on heat transfer and pressure drop characteristics for the three orientations are investigated. Specifically, the average surface temperature for these three orientations is studied in an effort to reveal the effect of gravitational orientation on the heat transfer phenomena.

Experimental Setup

The experimental setup is designed for testing the flow boiling performance of a rectangular minichannel test section under horizontal, vertical upflow, and vertical downflow orientations. Suitable test fixtures are designed to facilitate changing the test section orientation without interruption during testing under the same heat and mass flux conditions. The experimental setup is shown in Fig. 1. It consists of (1) test section, (2) water supply loop, (3) data acquisition system, and (4) high speed camera system. The data acquisition and high speed camera systems are not shown in Fig. 1.

Figure 2 shows the details of the test section, which is a combination of three layers. The top layer is made of Lexan, an optically clear polycarbonate material with a thermal conductivity of 0.19 W/mK. The second layer is a copper block that contains the parallel minichannels. The copper is an electrolytic tough pitch alloy number C11000. It is comprised of 99.9% copper and 0.04% oxygen (by weight) with a thermal conductivity of 388 W/mK at

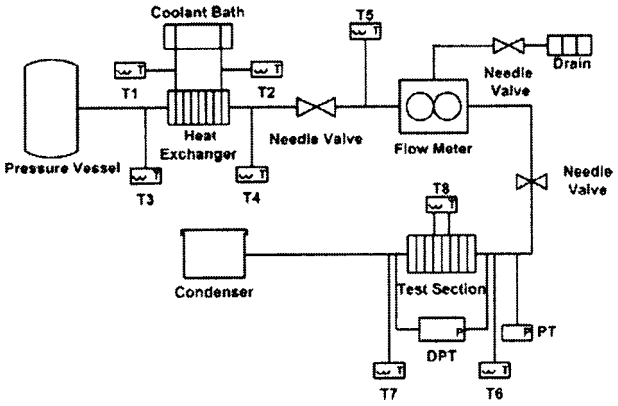

Fig. 1 Test loop

20°C. The third piece is made of Phenolic, a laminate of epoxy and paper with a thermal conductivity of 0.2 W/mK and acts as an insulator on the bottom side of the copper block. A cartridge heater supplied with a constant dc input power is used for heating the test section. These three layers form the test section assembly, which is held together by a set of ten mounting screws.

Thermocouples were placed in two layers in the copper block under the channel walls. Each layer contained six thermocouples placed at equal distance along the length of the flow channel. The layers were 2.97 and 6.14 mm below the channel walls. A one-dimensional heat conduction equation was used to predict the channel wall temperature from the thermocouple measurements. This approach was earlier verified by Steinke and Kandlikar [11].

Six parallel minichannels are machined into the copper substrate. Using a microscopic vision system, the channel depth and width are measured at six locations along the channel length of 63.5 mm. The average channel dimensions are 1054 μm wide by 197 μm deep with a hydraulic diameter of 333 μm. All measured width and depth values fall within ±10 and ±7 μm of the average values, respectively.

The copper test section surface was lapped to provide a leak-free seal with the Lexan cover. The Lexan cover also serves as a header for the supply of water to the minichannels. The inlet and exit plenums are machined in the Lexan cover so as to minimize any preheating of water before it enters the minichannels. The plenums are 3.175 mm in diameter. A differential pressure transducer is connected between the inlet and the exit plenums through the holes drilled in the Lexan cover. The pressure in the exit plenum was observed to be very close to the atmospheric pressure.

Experimental Procedure

The experimental procedure for preparing degassed water and collecting experimental data is outlined in this section. Eight MΩ deionized, and degassed water is used in the experiments. A commercially available pressure cooker equipped with a deadweight

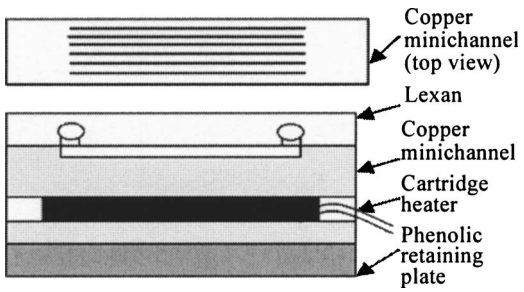

Fig. 2 Cross section of the test section

to attain a pressure of about 1 atm (14.7 psi) is used for preparing degassed water and supplying pressurized water to the test section. The pressure cooker is filled with deionized water and pressurized to about 1 atm (14.7 psi) by supplying heat. Once the chamber attains the set pressure, it is suddenly depressurized by removing the deadweight. This process leads to a very vigorous boiling, forcing the dissolved gases with steam out of the chamber. Repeating the above procedure two more times results in degassed water that remains degassed to a saturation temperature of 121°C. The remaining dissolved air present in the water will not precipitate as long as the temperature of the contacting surface stays below 121°C. The details of the degassing procedure are given by Kandlikar et al. [1] and Steinke and Kandlikar [11].

Once the test section is assembled and well insulated, heat loss experiments are conducted. The heat loss calibration chart is plotted between the supplied power to the empty test section in watts and the difference in temperature between the test section surface and the ambient. For example, $\Delta T_{\text{s-amb}}$ of 50°C and 90°C had corresponding heat losses of 3.26 and 5.86 W, respectively. The heat loss data are used in calculating the actual heat carried away by water during the test.

All experiments were performed with degassed water. The water is drawn from the bottom of the pressure cooker and is passed through a flat plate heat exchanger to provide the desired water inlet temperature to the test section. Subcooled water was provided at the inlet in all experiments. The outlet of the test section is connected to a large vessel opened to atmospheric pressure. A flow meter is used to measure the flow rate. The accuracy of the flow meter is 3% of the full scale, or 0.25 cc/min. A commercial software LabVIEW is used to monitor the thermocouples. Flow is started in the channel and the cartridge heater is powered. The mass flux is held constant while the input power is varied through the desired range. The resulting performance was recorded in terms of water flow rate, inlet and outlet water temperatures, temperatures inside the copper block along the flow length, and the inlet and exit pressures.

The images are acquired using a high speed camera after the system reaches steady state. It was observed that steady state is reached when the surface temperature reaches a constant value without any fluctuations for a time period of 15 min. An AF Micro Nikkor lens is used with the camera to gather detailed images of specific features and events. Most of the images were recorded at frame rates between 4000 and 15,000 fps, with exposure times of down to 1/80,000 s.

The experiments were conducted with the same mass flux and heat flux conditions for each orientation as described in Table 1. These conditions are $G=120$ kg/m^{2}s and $q''=317$ kW/m^2, resulting in an exit quality of 0.382.

Uncertainty

The uncertainty of the experimental data was determined. The pressure transducer has an accuracy of ±0.69 kPa. The temperature reading accuracy is ±0.1°C. The power supply accuracy for voltage and current supply are volts = ±0.05 V, $I=\pm 0.005$ amp. The resulting differential pressure accuracy is DP = ±1.03 kPa. The calculated uncertainty in the heat transfer coefficient is 8.6%.

Data Analysis

The equations used in calculating the local heat transfer coefficient and quality are explained in this section. Although flow fluctuations were observed during experiments, a uniform flow distribution is assumed in each channel. The local heat transfer coefficient and quality are therefore representative of respective time-averaged values. A linear variation in pressure is assumed in the channel to calculate the local saturation pressure and the corresponding saturation temperature. The surface temperature is calculated by assuming one-dimensional heat conduction from the thermocouple layer to the base layer of the minichannels. The heat flux q'' is determined from the power supplied by the cartridge heater. The uniform heat flux assumption at the channel walls was confirmed by Steinke and Kandlikar [11]. The local heat transfer coefficient at a given section along the flow length is then calculated by using Eq. (1):

$$h = \frac{q_{in} - q_{loss}}{A_{HT}(T_s - T_{sat})} \tag{1}$$

where T_s is the local surface temperature calculated by extrapolating the temperature readings from the two thermocouples placed in two layers underneath the channel walls in the copper block at the given location. The local quality is calculated from the following equation:

$$x = \frac{q'' \times 6(2H + W) \times Z_{sat})}{\dot{m} \times h_{fg}} \tag{2}$$

where Z_{sat} is the length from the location where $x=0$ in the channel. Since the top surface is covered with Lexan, heat is supplied only to the three sides of the minichannels.

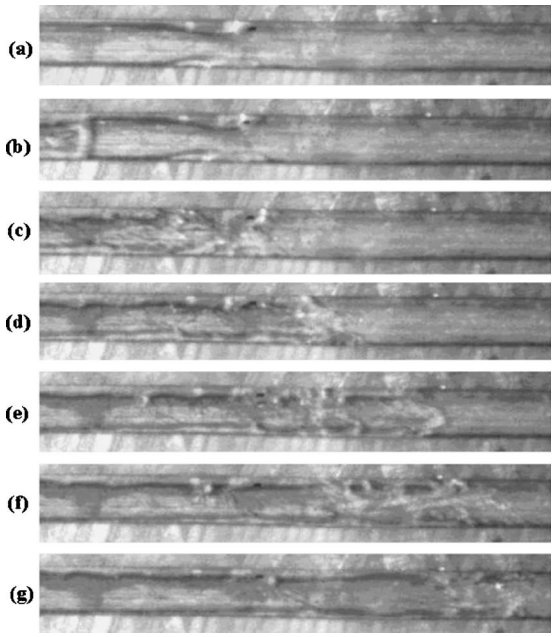

Fig. 3 Churn flow. Successive frames from (*a*) to (*g*) taken at 0.16 ms time interval indicating churn flow in a single channel from a set of six parallel horizontal minichannels. $G=120$ kg/m^{2}s, $q''=317$ kW/m^2, $T_s=110.9$°C, $x=0.361$, flow from left to right. Scale: channel width—1054 μm.

Results

The high speed pictures for the three orientations are presented in this section in Figs. 3–17. The heat and mass fluxes and local quality at the exit end of the images are included in the figure titles. This is followed by the local heat transfer and pressure drop data. In all video images, the channel width is clearly visible and provides the necessary length scale (channel width—1054 μm). This scale is also mentioned in each figure title.

The results for the horizontal flow case are presented first, followed by the vertical downflow and vertical upflow, respectively. Churn flow, which is not widely reported in literature, was observed in the horizontal flow. The events leading to this flow pattern are illustrated in Fig. 3. The bulk flow in the channels is from left to right. Churn flow is defined as the occurrence of intense mixing of the liquid and vapor phases during flow boiling in a channel. As seen from frames (*a*) and (*b*) in Fig. 3, waves in the liquid film surrounding the vapor core sometimes occupy the en-

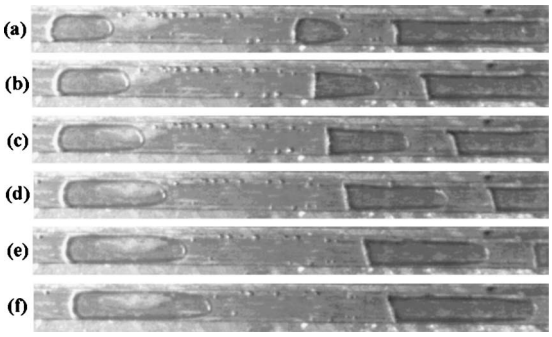

Fig. 4 Plug flow. Successive frames from (*a*) to (*f*) taken at 0.16 ms time interval indicating plug flow in a single channel from a set of six parallel horizontal minichannels. G =120 kg/m^{2}s, q''=317 kW/m^2, T_s=110.9°C, x=0.361, flow from left to right. Scale: channel width—1054 μm.

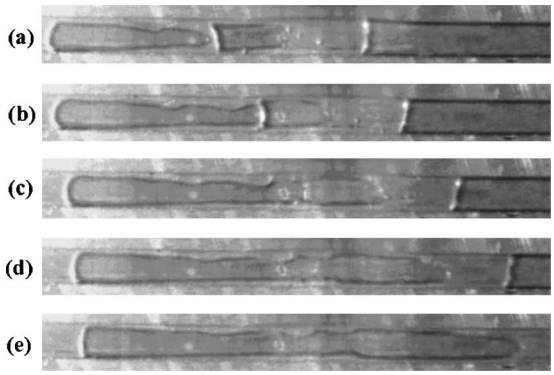

Fig. 6 Wavy flow. Successive frames from (*a*) to (*g*) taken at 0.16 ms time interval indicating wavy flow in a single channel from a set of six parallel horizontal minichannels. G =120 kg/m^{2}s, q''=317 kW/m^2, T_s=110.9°C, x=0.361, flow from left to right. Scale: channel width—1054 μm.

tire channel. Their subsequent breakup, as shown in frames (*c*) to (*g*), leads to localized churn flow and its movement towards the channel exit. From this observation it can be seen that churn flow is caused by intense mixing of the liquid and the vapor phases present in the channel.

Figure 4 illustrates the plug flow. The bubbles nucleate near the edges and grow to fill the entire channel width leading to plug flow. Once the bubbles fill the entire channel, they start to expand by pushing the liquid fronts on both sides. This expansion of the bubble results in a vapor plug. The size of the plug is dependent on the upstream and downstream flow conditions. In certain cases, the plug can grow to fill the entire length of the channel, causing dryout downstream. In the case presented in Fig. 4, the plugs are shown to grow to a certain size as they exit the field of view. Also seen in the Fig. 4 are small nucleating bubbles that float in the liquid slugs present between two successive vapor plugs.

Another interesting feature to note is that the plug, which is present towards the left of the channel in frames (*a*) to (*f*), anchors itself near the nucleation site and grows in size forcing the other plugs to move faster along the direction of the bulk flow.

Figure 5 shows a very interesting instance of vapor plug disappearance, which has not been reported by any of the earlier investigations. Frames (*a*) and (*b*) show two plugs present in the channel; flow is from left to right. The plug on the left side has just nucleated and is growing. The plug towards the right side of the channel has already grown and is expanding in length in both directions (notice the associated reversed flow). Frames (*c*) to (*f*) show the interesting feature of the plug on the left reducing in size and the plug on the right increasing in size. Frame (*f*) shows the plug to the left almost reduced to a thin crescent and about to collapse completely. Frame (*g*) shows no trace of this plug, and the plug on the right is filling up the entire channel. The fluctuating pressure in the channel is seen as the main reason for the collapse of the vapor plug. The growth of a bubble and its development into a plug in the channel is affected by pressure fluctuations caused by channel-to-channel interactions through the inlet header.

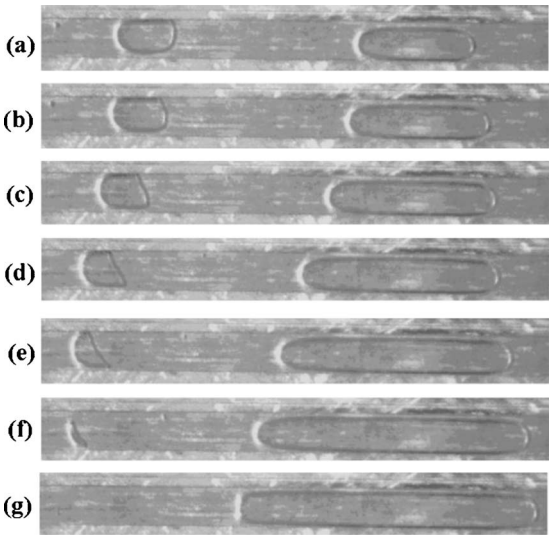

Fig. 5 Vapor plug disappearance due to pressure wave. Successive frames from (*a*) to (*g*) taken at 0.16 ms time interval indicating plug flow in a single channel from a set of six parallel horizontal minichannels. G=120 kg/m^{2}s, q''=317 kW/m^2, T_s =110.9°C, x=0.180, flow from left to right. Scale: channel width—1054 μm.

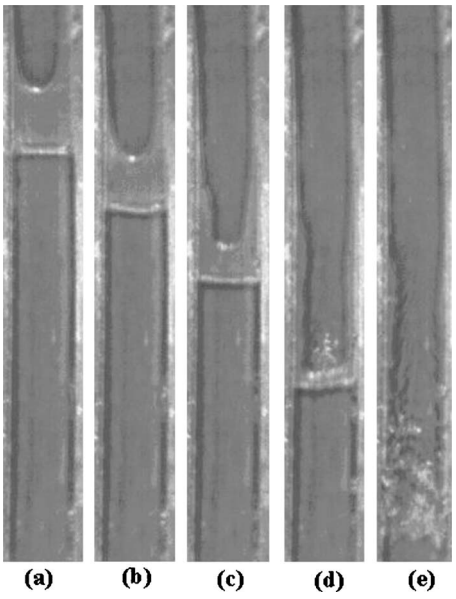

Fig. 7 Breakup of liquid slug. Successive frames from (*a*) to (*e*) taken at 0.16 ms time interval indicating breakup of a liquid slug, with a brief churn flow section in a single channel from a set of six parallel vertical minichannels with downward flow. G=120 kg/m^{2}s, q''=317 kW/m^2, T_s=114.5°C, and x=0.181. Scale: channel width—1054 μm.

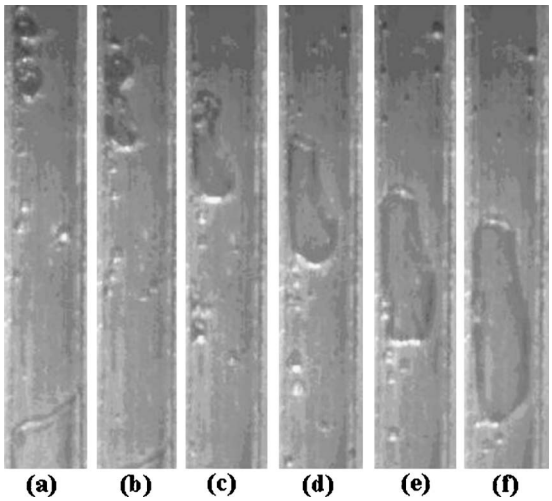

Fig. 8 Bubble merger. Successive frames from (*a*) to (*f*) taken at 0.33 ms time interval indicating bubble merger in a single channel from a set of six parallel vertical minichannels with downward flow. $G=120$ kg/m^{2}s, $q''=317$ kW/m^2, $T_s=114.5°$C, and $x=0.362$. Scale: channel width—1054 μm.

Figure 6 shows the occurrence of wavy flow. Wavy flow is observed when there is a disturbance in the liquid-vapor interface. Frame (*a*) shows the presence of individual vapor plugs. Frame (*b*) shows the collision of two vapor plugs and the resulting wavy interface. This collision is very similar to the observation reported in Fig. 3, but instead of an intense mixing we see a disturbance in the interface between the liquid and vapor phases resulting in a wavy flow. The liquid film near the edges is somewhat thicker in this case compared to that in Fig. 3. Frames (*c*) to (*e*) show the propagation of this disturbance at the interface throughout the channel. The waves are the result of the vapor shear at the liquid-vapor interface, surface tension forces, and the wall shear forces.

Flow patterns are investigated for vertical upflow and vertical downflow cases under the same operating conditions as for the horizontal case presented in Figs. 3–6. Figures 7–15 describe the flow patterns for the vertical downflow case, while Figs. 16 and 17 correspond to the vertical upflow case. Detailed descriptions for each of the flow patterns are given next.

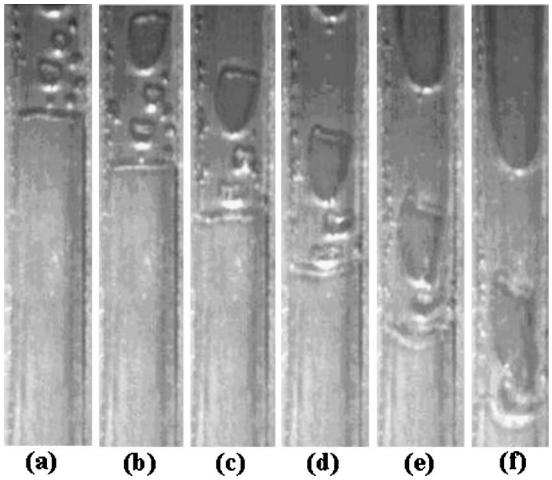

Fig. 9 Bubble and vapor plug merger. Successive frames from (*a*) to (*f*) taken at 0.16 ms time interval indicating bubble, plug merger in a single channel from a set of six parallel vertical minichannels with downflow. $G=120$ kg/m^{2}s, $q''=317$ kW/m^2, $T_s=114.5°$C, and $x=0.362$. Scale: channel width—1054 μm.

Fig. 10 Bubbly flow in liquid slug. Successive frames from (*a*) to (*f*) taken at 0.16 ms time interval indicating bubbly flow in a single channel from a set of six parallel vertical minichannels with downward flow. $G=120$ kg/m^{2}s, $q''=317$ kW/m^2, $T_s=114.5°$C, and $x=0.362$. Scale: channel width—1054 μm.

Figure 7 shows the interaction between the successive vapor plugs under downflow conditions. Here the bulk flow is from top to bottom. Frames (*a*)–(*e*) show the occurrence of churn flow in a vertical channel. Frame (*a*) shows the presence of two vapor plugs in the channel separated by a liquid front. Frame (*b*) shows the upstream vapor plug breaking through the liquid front and reaching the vapor plug downstream. Frame (*c*) shows the change in the shape of the head of the plug as it continues to pierce through the liquid front. Frame (*d*) shows the diminishing thickness of the liquid slug trapped between the two vapor plugs just prior to their

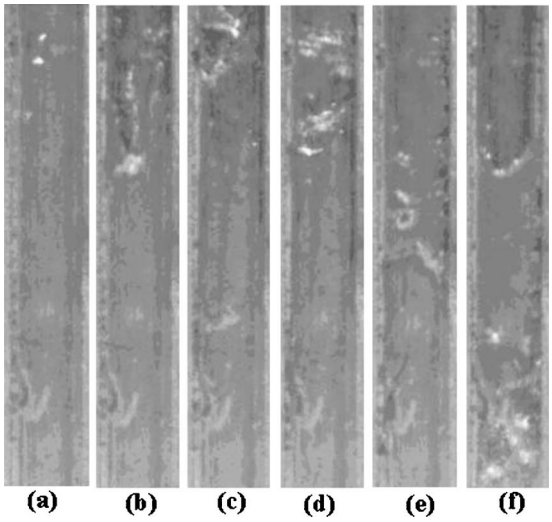

Fig. 11 Churn flow with presence of bubble, slug, and annular flow. Successive frames from (*a*) to (*f*) taken at 0.33 ms time interval indicating churn flow with the presence of bubbly and plug flow in a single channel from a set of six parallel vertical minichannels with downward flow. $G=120$ kg/m^{2}s, $q''=317$ kW/m^2, $T_s=114.5°$C, and $x=0.362$. Scale: channel width—1054 μm.

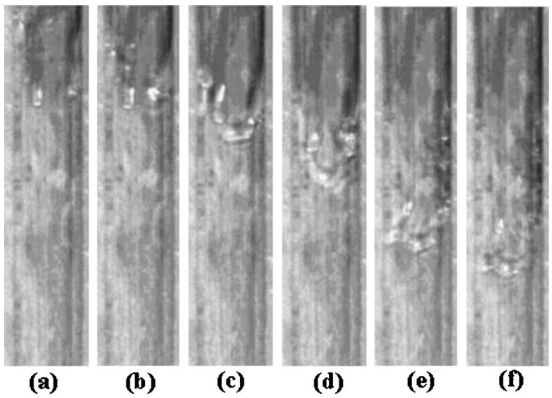

Fig. 12 Dry out and rewetting. Successive frames from (*a*) to (*f*) taken at 0.33 ms time interval indicating dry out and rewetting in a single channel from a set of six parallel vertical minichannels with downward flow. $G=120$ kg/m^{2}s, $q''=317$ kW/m^2, $T_s=114.5°$C, and $x=0.362$. Scale: channel width—1054 μm.

merger. Frame (*e*) shows the breakup of the liquid plug resulting in a momentary churn flow as seen in previous cases described in Fig. 3 for the horizontal flow case.

Figure 8 shows the sequence of bubble merger and development of a vapor plug. Flow is from left to right. In the present work on horizontal flows, bubble merger was not observed. Instead, individual bubbles nucleated and grew into vapor plugs. Frame (*a*) shows a cluster of bubbles nucleating at the left side of the channel wall. Also, we can see some individual bubbles floating upstream in the bulk liquid. Frames (*c*) and (*d*) show the bubble merger and growth into a vapor plug. The interface of the plug has a wavy shape as it is not completely developed and continues to gather neighboring nucleating bubbles. Frame (*d*) also shows the developing plug with tiny bubbles floating upfront. Frame (*e*) shows bubbles nucleating in the thin film around the vapor plug. Frame (*f*) shows the plug almost filling the entire width of the channel.

A high record rate is needed to capture minute details of flow boiling in small hydraulic diameter channels. Frame (*a*) in Fig. 9 shows the channel filled with bubbles at the top and a vapor plug filling up the rest of the channel (flow is vertical downflow). Notice the distinctive shapes of the front (bottom) and the back (top) interfaces of a vapor plug. Frames (*b*) and (*c*) show some of the

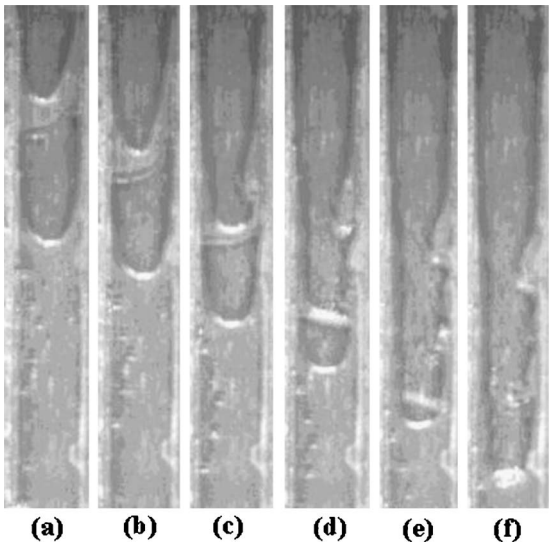

Fig. 13 Plug to annular flow. Successive frames from (*a*) to (*f*) taken at 0.16 ms time interval indicating plug to annular flow in a single channel from a set of six parallel vertical minichannels with downward flow. $G=120$ kg/m^{2}s, $q=317$ kW/m^2, $T_s=114.5°$C, and $x=0.362$. Scale: channel width—1054 μm.

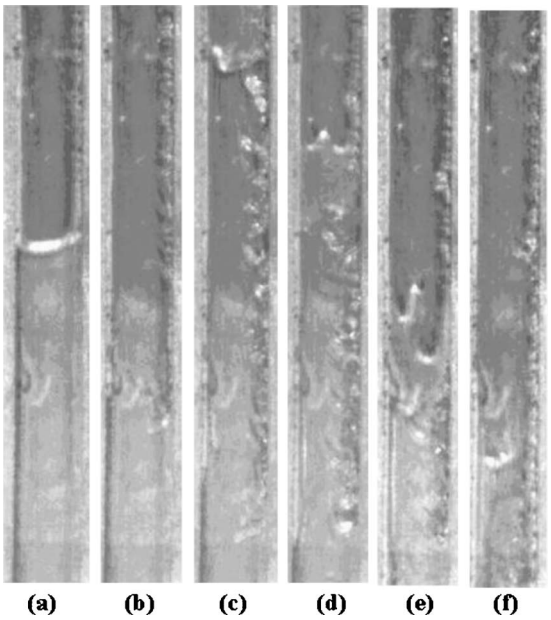

Fig. 14 Wavy annular flow with strong thin film nucleation. Successive frames from (*a*) to (*f*) taken at 0.33 ms time interval indicating wavy flow with strong thin film nucleation in a single channel from a set of six parallel vertical minichannels with downward flow. $G=120$ kg/m^{2}s, $q''=317$ kW/m^2, $T_s=114.5°$C, and $x=0.362$. Scale: channel width—1054 μm.

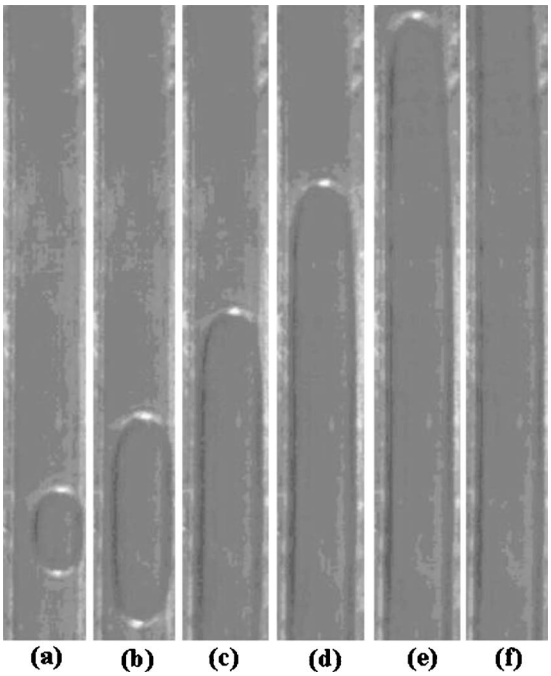

Fig. 15 Backflow or flow reversal extending into the inlet manifold. Successive frames from (*a*) to (*f*) taken at 0.33 ms time interval indicating back flow in a single channel from a set of six parallel vertical minichannels with downflow. $G=120$ kg/m^{2}s, $q''=317$ kW/m^2, $T_s=114.5°$C, and $x=0.181$. Scale: channel width—1054 μm.

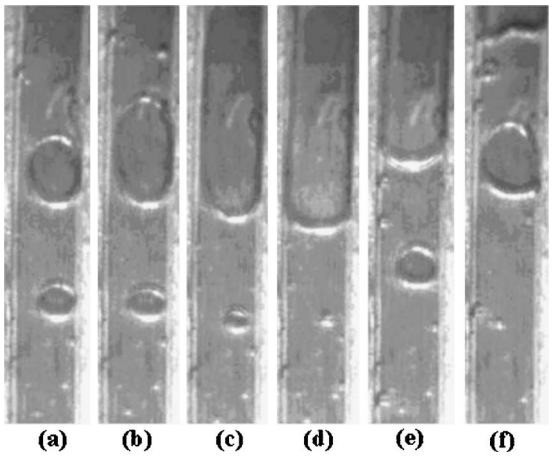

Fig. 16 Bubble growth fluctuation. Successive frames from (*a*) to (*f*) taken at 0.83 ms time interval indicating bubble becoming smaller as a result of back flow of the upstream interface in a single channel from a set of six parallel vertical minichannels with upward flow. $G=120$ kg/m^{2}s, $q''=317$ kW/m^2, $T_s=110.6°$C, and $x=0.179$. Scale: channel width—1054 μm.

bubbles growing into plugs and pushing the liquid front downstream. Frames (*d*) and (*e*) show the developed plug compressing the liquid front with the bubbles floating and becoming squeezed between another plug present up front and the channel walls. Frame (*f*) shows the plug with the bubbles breaking through the slug causing an intense mixing. For the same operating condition different flow patterns are seen at the same location, and from this observation it can be concluded that the flow patterns in minichannels are time dependent.

Figure 10 shows the presence of bubbly flow with bubbles nucleating along the left wall of the channel (flow is vertical downflow). From the observations made over longer time intervals, the bubbles were observed to nucleate at high frequency and then flow along in the bulk liquid. Frames (*a*) and (*b*) show the bubbles nucleating along the left wall. The lower half of the channel is filled with a vapor plug. Frames (*c*)–(*f*) show the nucleating bubbles being pushed downstream by the rapid expansion of another vapor plug present upstream in the channel.

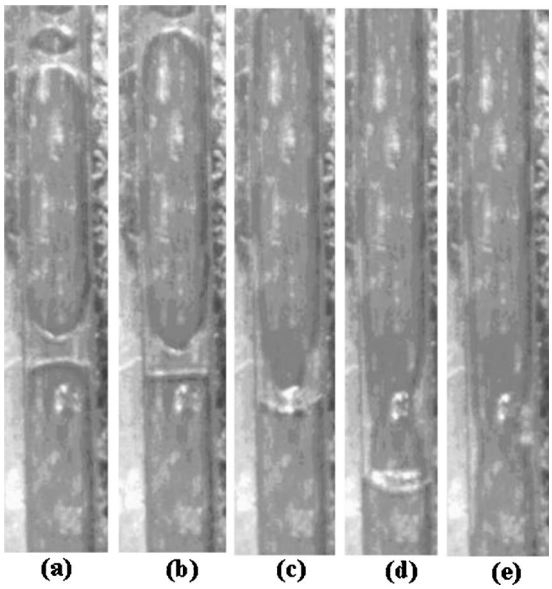

Fig. 17 Merger of vapor plugs during backflow. Successive frames from (*a*) to (*f*) taken at 0.33 ms time interval indicating plug to annular flow in a single channel from a set of six parallel vertical minichannels with upward flow. $G=120$ kg/m^{2}s, $q''=317$ kW/m^2, $T_s=110.6°$C, and $x=0.179$. Scale: channel width—1054 μm.

Figure 11 shows the occurrence of churn flow along with bubbly and plug flow (flow is vertical downflow). Frame (*a*) shows the entire channel filled with liquid. The sequence of events shown in frames (*b*)–(*e*) leads to churn flow as seen at the lower end of frame (*f*). Frame (*e*) shows an array of bubbles nucleating on the right side of the channel wall. Frame (*f*) shows a new upstream plug flowing down the channel.

Figure 12 shows the occurrence of periodic dryout and rewetting of the channel (flow is vertical downflow). The bright light reflected from the bottom of the channel indicates the absence of a liquid film (dryout condition) in front of the approaching liquid in frames (*a*)–(*f*). Frame (*a*) shows the channel completely dried out and frames (*b*)–(*d*) show the liquid front rewetting the channel and subsequently becoming dried out as it flows down the channel. Frame (*f*) again shows the entire channel going into a dryout condition. Note the intense agitation seen at the liquid front in frames (*e*) and (*f*). This figure shows the nature of the dryout leading to the critical heat flux condition in small hydraulic diameter channels.

Plug to annular flow transition is seen in Fig. 13. Frame (*a*) shows two individual vapor plugs present in the channel (flow is vertical downflow). Note the tapering shape of the head of the vapor plug present at the top of the channel. Frame (*c*) shows the change in shape of the head of the vapor plug from a tapering head to a round head. Frames (*d*) and (*e*) show the vapor plug cutting through the liquid front and colliding with another vapor plug present downstream. Also the wavy interface in the slug can be noted from frames (*e*) and (*f*).

Figure 14 shows strong thin film nucleation present during flow boiling in minichannels (flow is vertical downflow). Frame (*a*) shows a vapor plug flowing down the channel. As described before there is a thin film of liquid present on the sides of the vapor plug. As this vapor plug flows down the channel, the nucleating cavities present on the channel walls under the thin water film begin to nucleate. Frames (*e*) and (*f*) show bubbles nucleating in the thin film and interacting with the vapor plug. This thin film nucleation results in a strong interaction with the vapor core.

Figure 15 shows backflow or flow reversal in a minichannel. The inlet manifold (not shown) is located close to the top in the figure. Frame (*a*) shows a single bubble nucleating from the right wall of the channel. Frame (*b*) shows the bubble developing into a plug and expanding on both sides of the channel pushing water present upstream and downstream of the channel. Frames (*c*)–(*e*) show the plug expanding all the way towards the inlet manifold of the channel located at the top. Frame (*f*) shows the plug filling the entire channel and entering the inlet manifold. This results in severe flow maldistribution, which affects the pressure drop and heat transfer characteristics as explained in subsequent sections.

Figures 16 and 17 correspond to the vertical upflow case. The test section orientation is switched so that the inlet plenum is now located at the bottom and the exit plenum is located at the top of the channels. The rest of the experimental setup remains the same. An interesting observation of bubble growth and fluctuations is seen to occur in the present case as shown in frames (*a*)–(*f*) in Fig. 16. Frame (*a*) shows two bubbles nucleating on the same side of the channel. Frames (*b*)–(*d*) show one of the bubbles reducing in size and almost about to collapse as a result of the backflow induced by a rapidly expanding downstream slug. Frame (*e*) shows the bubble again growing back to its original size and developing into a plug.

Figure 17 shows flow in the vertical upflow direction. Frames (*a*) and (*b*) show two vapor plugs present in the channel. The bulk flow is from bottom to top. Frame (*c*) shows the plug present in

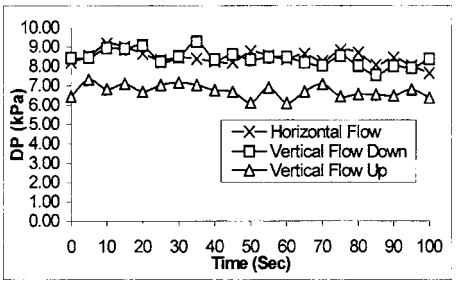

Fig. 18 Time-averaged pressure drop fluctuations after correcting for the gravitation term. $G=120$ kg/m^{2}s, $q''=317$ kW/m^2, and $T_s=110.6°$C.

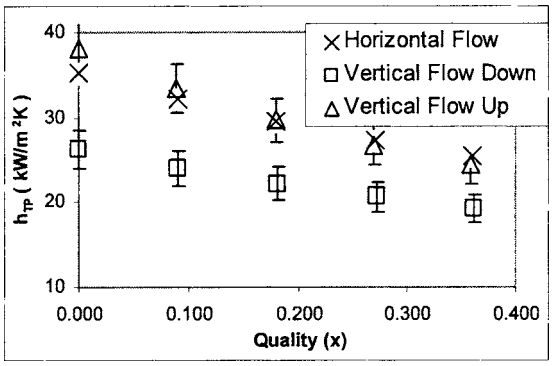

Fig. 19 Quality versus. heat transfer coefficient. $G=120$ kg/m^{2}s, $q''=317$ kW/m^2, and $T_s=110.6°$C.

the downstream section expanding on both sides of the channel and on the verge of merger with the vapor plug present upstream. Frame (*e*) finally shows a single plug filling the entire channel, leading to annular flow.

Other flow patterns observed in the vertical upflow case were quite similar to the horizontal case; however, the interactions between the two phases were less chaotic, and the severity of backflow was also less.

Comparison of Flow Pattterns for Three Orientations

A comparison of the flow patterns and flow characteristics for the three orientations is now discussed. Vertical downflow is characterized by its distinct bullet-shaped vapor plugs. Thin film nucleation is seen very clearly in all cases. Merger of bubbles and vapor plugs coupled with rapid evaporation leads to churn flow in all cases.

Backflow is seen in every case, but the intensity is seen to be much stronger in the vertical downflow case. Rapid evaporation in a vapor plug aided by gravity causes the vapor to flow backward in a more pronounced fashion in the vertical downflow case. The resulting vapor backflow extends all the way into the inlet manifold for the conditions investigated here causing flow maldistribution in the channels. The heat transfer and pressure drop characteristics are affected by this maldistribution. This is confirmed by the results presented in the next section.

Another observation is made regarding the nonequilibrium effects. As a result of backflow, pressure fluctuations are observed in the channel. A detailed study of pressure fluctuations, dominant frequency, and its magnitude is reported in a separate study by Balasubramanian and Kandlikar [12]. In most experiments, the pressure fluctuations were between 1 and 1.5 kPa. The changes in local saturation temperature resulting from these pressure fluctuations play a role in condensation of bubbles as seen in Figs. 5 and 16. The time-dependent nature of flow patterns, presence of thin film nucleation and churn flow, influence of nonequilibrium effects, and nature of gravitational influence along the flow direction are major observations made from the high-speed images obtained in this study.

Heat Transfer and Pressure Drop Characteristics for Three Orientations

The effect of gravitational forces normal to the flow direction is not expected to be significant for hydraulic diameters smaller than the boiling length scale, derived as $=\sqrt{\sigma/g(\rho_L-\rho_V)}$. For water at atmospheric pressure, this length scale is 2.5 mm, which is considerably larger than the flow channel hydraulic diameter of 0.333 mm. However, the orientation of channel length with respect to gravity vector may be important.

In an effort to study this effect, the local heat transfer coefficient is calculated using Eqs. (1) and (2) for the three cases under the same operating conditions. The associated pressure drops are also measured, and the results are discussed in this section. First the pressure drop results are presented.

The instantaneous values of pressure drop obtained from the pressure transducer were averaged over a 5 s time interval (to filter out higher frequency terms) and are plotted in Fig. 18 for the three orientations tested under the same operating conditions. The gravitational pressure drop term has been accounted for by subtracting it for the downflow case and adding it for the upflow case. Average test section quality was used in the calculations of gravitational pressure drop under homogeneous flow assumption. Although this assumption is not supported by the visual observations, the error introduced is believed to be quite small as the same procedure was applied to all three cases in making this comparison. Also, the magnitude of the gravitational pressure drop contribution was quite small (0.5 kPa) compared to the total pressure drop of around 6–9 kPa. It can be seen from Fig. 18 that the pressure drops are very similar for the horizontal and vertical downflow cases, while it is about 25 percent lower in the vertical upflow case.

The variation of the local heat transfer coefficient with quality for the three orientations is plotted in Fig. 19. The associated error bars are also indicated for each data point. It can be seen that the vertical upflow and horizontal flow cases yield very similar results, but the vertical downflow case results in a considerably lower performance (30–40 percent).

The decreasing trend in h with quality seen in Fig. 19 for all three cases is consistent with the earlier observations by Steinke and Kandlikar [13]. This trend indicates the dominance of nucleate boiling. This finding is supported by the high speed images in Figs. 3–17 showing the presence of nucleating bubbles at the walls during bulk liquid flow as well as in the thin liquid film surrounding a vapor plug or during annular flow. Further, the periodic movement of the advancing and receding interfaces over the channel walls is similar to the bubble motion during its ebullition cycle in nucleate pool boiling as described by Kandlikar [3].

Table 1 Summary of experimental results for horizontal flow, vertical upflow, and vertical downflow orientations

Test parameters	Horizontal flow	Vertical upflow	Vertical downflow
G (kg/m^{2}s)	120	120	120
q" (kW/m^2)	317	317	317
Avg. T_s (°C)	110.9	110.6	114.5
ΔP (kPa)	8.50	6.75	8.60
$h_{TP,avg}$ (kW/m^{2}K)	29.8	30.4	22.4

Table 1 gives the summary of values of mass flux and heat flux along with corresponding average values of surface temperatures, pressure drops, and heat transfer coefficients in the two-phase region for all three cases. The average values in this table are determined in the test section using the temperature measurements in the two-phase region only (identified as the region where thermodynamic quality is greater than zero). It can be seen that the vertical upflow case has the lowest average pressure drop and highest average heat transfer coefficient. The lowest value of pressure drop for the vertical upflow case is the result of buoyancy aiding the vapor flow and causing fewer chaotic liquid-vapor interactions as confirmed from the visual observations. The downflow has the highest pressure drop. The opposing buoyancy force is believed to cause more vigorous interactions between the two phases, causing more severe backflow characteristics.

The average heat transfer coefficient for the horizontal and upflow cases are similar. However, the downflow case resulted in a lower heat transfer coefficient. The main difference noted from the high-speed visual observations was that the backflow in the downflow case was more severe, with pronounced reversed flow of vapor into the inlet manifold. The resulting increase in flow maldistribution is the primary cause of the heat transfer degradation for the vertical downflow case.

The reversed flow characteristics in the horizontal flow and vertical upflow cases were observed to be similar. Although the pressure drop for the upflow case was lower, it did not influence the heat transfer coefficient. Thus, the only cause for heat transfer degradation is seen to be due to enhanced flow maldistribution in the vertical downflow case. Extending this to a microgravity environment, the absence of gravity is expected to yield heat transfer and pressure drop results very similar to the horizontal case, since the absence of the gravity vector should not cause any changes in the forces along the flow direction when compared to the horizontal case. Further, the backflow characteristics are also expected to remain unaltered from the horizontal case. This conclusion is important in confirming that the microgravity environment will not alter the flow boiling characteristics of minichannels and microchannels. However, it is strongly recommended that actual experiments under a microgravity environment should be performed before any firm conclusions are drawn. Further, efforts should be made to remove the backflow problem associated during flow boiling in minichannels and microchannels as this condition is not acceptable in safe operation of heat transfer equipment is space application. Experimental work on this aspect is currently being undertaken.

Conclusions

1. High resolution images of flow patterns in minichannels under (a) horizontal flow, (b) vertical upflow, and (c) vertical downflow orientations are reported. Frame rates of 6000–15,000 fps and exposure times of up to 1/80,000 s are used to capture clear images of the rapidly evolving events during flow boiling in small diameter channels. Use of lower frame rates may mask the occurrence of some of the observed flow patterns. Shorter exposure times are needed to provide clear pictures of the liquid-vapor interfaces.
2. It is found that the flow patterns are time dependent. Bubbly flow, thin film nucleation, plug flow, annular flow, and churn flow are observed in all three orientations. Thin film nucleation and rapid evaporation during bubble and vapor plug mergers lead to localized churn flow.
3. The flow patterns for the three orientations are observed to be similar, except for the changes in the shape of the vapor plugs (bullet shaped for vertical downflow) and the flow reversal characteristics.
4. Flow reversal is observed in all three orientations, but the effect is most pronounced in the vertical downflow case. Reversed flow of vapor into the inlet manifold is observed to be quite severe for this case.
5. Vertical upflow has a lower pressure drop when compared to the horizontal flow and the vertical downflow cases. This difference is attributed to the less chaotic two-phase flow observed in the vertical upflow case.
6. The vertical upflow case has a higher average heat transfer coefficient than the vertical downflow case under the same operating conditions in this study. This is mainly due to the backflow of vapor into the inlet manifold, causing increased flow maldistribution in the vertical downflow case. The heat transfer performance for vertical upflow is very similar to the horizontal flow case.
7. The nucleating bubbles are found on the wall during passage of the bulk liquid as well in the thin liquid film surrounding the vapor plug and in the annular film. These visual observations support the conclusions indicating dominance of nucleate boiling as seen from the decreasing trend in h versus x reported in this (Fig. 19) as well as other earlier investigations, e.g., Steinke and Kandlikar [13].
8. The rapidly moving interface of a fast growing bubble and the liquid front near dryout condition are observed to reveal the mechanisms leading to CHF. Further work in this area is recommended.
9. The flow boiling performance of the minichannel under a microgravity environment is expected to be similar to the horizontal case as the absence of the gravity vector, which is normal to the flow direction in the horizontal case, is not expected to alter the backflow characteristics. The backflow characteristics are found to be mainly responsible for the increased flow maldistribution and associated reduction in the heat transfer performance in the vertical downflow case. Actual experiments under microgravity environment are recommended before any firm conclusions can be made even under the current test conditions, and especially over a wider range of operating conditions.

Acknowledgment

All of the work is performed in the Thermal Analysis and Microfluidics Laboratory at RIT. Part of the work was conducted under the NSF Grant No. CTS-0245642.

Nomenclature

A_{HT} = heat transfer surface area, m^2
G = mass flux, kg/m^2s
g = gravitational acceleration, m/s^2
H = height of the minichannel, m
h = heat transfer coefficient, W/m^2K
Z_{sat} = length from location where $x=0$ in the channel
ΔP = pressure drop, Pa
q_{in} = power input to the test section, W
q_{loss} = heat loss from the test section, W
CHF = critical heat flux, W/m^2
q'' = heat flux, W/m^2
T_s = surface temperature, °C
T_{sat} = saturation temperature, °C
W = width of the minichannel, m
x = local quality

Greek letters

ρ_L = liquid density, kg/m^3
ρ_V = vapor density, kg/m^3
σ = surface tension, N/m

References

[1] Kandlikar, S. G., Steinke, M. E., Tian, S., and Campbell, L., 2001, "High-

Speed Photographic Observation of Flow Boiling of Water in Parallel Minichannels," ASME National Heat Transfer Conference, paper no. NHTC01-11262, Los Angeles, CA.
[2] Triplett, K. A., Ghiaasiaan, S. M., Abdel-Khalik, S. I., LeMouel, A., and McCord, B. N., 1999, "Gas-Liquid Two-Phase Flow in Microchannels Part II: Void Fraction and Pressure Drop," Int. J. Multiphase Flow, **25**, pp. 395–410.
[3] Kandlikar, S. G., 2004, "Heat Transfer Mechanisms During Flow Boiling in Microchannels," ASME J. Heat Transfer, **126**(1), pp. 8–16.
[4] Fukano, T., Kariyasaki, A., and Kagawa, M., 1989, "Flow Patterns and Pressure Drop in Isothermal Gas-Liquid Flow in a Horizontal Capillary Tube," ANS Proceedings, 989, ISBN 0-89448-149-5, Vol. 4, pp. 153–161.
[5] Wambsganss, M. W., France, D. M., Jendrzejczyk, J. A., and Tran, T. N., 1993, "Boiling Heat Transfer in a Small Diameter Tube," ASME J. Heat Transfer, **115**(4), pp. 963–972.
[6] Kasza, K. E., Didascalou, T., and Wambsganss, M. W., 1997, "Microscale Flow Visualization of Nucleate Boiling in Small Channels: Mechanisms Influencing Heat Transfer," Proceeding of International Conference on Compact Heat Exchanges for the Process Industries, R. K. Shah, ed., Begell, House, Inc., New York, pp. 343–352.
[7] Cornwell, K., and Kew, P. A., 1992, "Boiling in Small Parallel Channels," *Proceedings of CEC Conference on Energy Efficiency in Process Technology*, Athens, Elsevier Applied Sciences, paper 22, pp. 624–638.
[8] Kandlikar, S. G., and Balasubramanian, P., 2003, "High Speed Photographic Observation of Flow Patterns During Flow boiling in Single Rectangular Minichannel," ASME Heat Transfer Conference, Las Vegas, Nevada, paper no. HT2003-47175.
[9] Kandlikar, S. G., 2002, "Fundamental Issues Related to Flow Boiling in Minichannels and Microchannels," Exp. Therm. Fluid Sci., **26**(2–4), pp. 389–407.
[10] Hetsroni, G., Mosyak, A., and Segal, Z., 2001, "Nonuniform Temperature Distribution in Electronic Devices Cooled by Flow in Parallel Microchannels," IEEE Trans. Compon., Packag. Manuf. Technol., Part A, **24**, pp. 16–23.
[11] Steinke, M. E., and Kandlikar, S. G., 2003, "An Experimental Investigation of Flow Boiling Characteristics of Water in Parallel Microchannels," ASME J. Heat Transfer, **126**(4), pp. 518–526.
[12] Balasubramanian, P., and Kandlikar, S. G., 2004, "Experimental Study of Flow Patterns, Pressure Drop and Flow Instabilities in Parallel Rectangular Minichannels," *Second International Conference on Microchannels and Minichannels*, Rochester, NY, paper no. ICMM2004-2371, pp. 475–482.
[13] Steinke, M. E., and Kandlikar, S. G., 2004, "Control and Effect of Dissolved Air in Water During Flow Boiling in Microchannels," Int. J. Heat Mass Transfer, **47**(8-9), pp. 1925–1935.

Effects of Wall Rotation on Heat Transfer to Annular Turbulent Flow: Outer Wall Rotating

Joon Sang Lee[1]

Xiaofeng Xu[2]

Richard H. Pletcher[3]
Professor
e-mail: pletcher@iastate.edu

Department of Mechanical Engineering, 3024 Black Engr. Building, Iowa State University, Ames, IA 50011

Simulations were conducted for air flowing upward in a vertical annular pipe with a rotating outer wall. Simulations concentrated on the occurrence of laminarization and property variations for high heat flux heat transfer. The compressible filtered Navier-Stokes equations were solved using a second-order accurate finite volume method. Low Mach number preconditioning was used to enable the compressible code to work efficiently at low Mach numbers. A dynamic subgrid-scale stress model accounted for the subgrid-scale turbulence. When the outer wall rotated, a significant reduction of turbulent kinetic energy was realized near the rotating wall and the intensity of bursting appeared to decrease. This modification of the turbulent structures was related to the vortical structure changes near the rotating wall. It has been observed that the wall vortices were pushed in the direction of rotation and their intensity increased near the nonrotating wall. The consequent effect was to enhance the turbulent kinetic energy and increase the Nusselt number there. [DOI: 10.1115/1.1929788]

Keywords: Large Eddy Simulation, Finite Volume Formulation, Compressible Navier-Stokes Equations, Annular Pipe Flow, Wall Rotation

1 Introduction

Annular pipe flow has attracted the attention of many researchers due to its numerous engineering applications including heat exchangers and advanced power reactors for both fission and fusion. The application of heat transfer with wall rotation also appears in many mechanical and chemical engineering areas. These applications commonly employ turbulent flow with significant heat transfer resulting in large property variations. However, many experiments provide poor correlations for convective heat transfer owing to the difficulties of the measurements.

Numerous researchers have found that the wall rotation in pipe flows has a large influence on the suppression of turbulence due to radially growing centrifugal forces. The mean velocity profiles of rotating pipe flows were measured by Murakami and Kikuyama [1], Kikuyama et al. [2], and Nishbori et al. [3] at various Reynolds numbers and rotation rates. These experimental results showed that the flow was laminarized near the rotating wall with increasing rotation rate. Imao and Itoh [4] reported that the turbulent fluctuations were also suppressed as a result of the wall rotation.

Several numerical studies were carried out for rotating pipe flows using a Reynolds shear stress model [5] and using a two-equation model [6]. These numerical calculations predicted the suppression of turbulence as found by experiments. In the 1990s, several papers reported results about rotating turbulent pipe flows based on large eddy simulation (LES) [7] and direct numerical simulation (DNS) [8]. These simulations have predicted turbulent drag reduction with increasing rotational rates. However, heat transfer effects were not considered.

Fewer studies have been reported involving wall rotation in annular passages. The previous studies of annular pipe flow with a rotating wall [9–12] showed that the Nusselt number is dependent on the following variables:

1. Speed of rotation of wall
2. Axial velocity of fluid
3. Gravitational force
4. Surface roughness

Since smooth walls are used throughout this study, the heat transfer rates are functions only of axial velocity (or Reynolds number based on the inlet axial mean velocity), wall rotational speed (or Taylor number), and gravitational force (or Grashof number).

The rotation of the outer wall can induce stabilization of the flow, whereas the enhancement of the turbulence is observed when the inner wall is rotating. This phenomenon is related to Taylor vortices and is well documented in Becker and Kaye [9] and Schlichting [13]. In this paper, attention is only paid to turbulent annular pipe flow with a rotating outer wall.

Hirai et al. [14] employed the k-ε model to observe the laminarization phenomena in an axially rotating annular pipe flow, but failed to correctly predict the mean velocity profile trends for different pipe rotation rates. According to Yang [15], the two-equation k-ε model performs poorly for flows with rotational effects and it is necessary to use a full Reynolds stress model for better predictions.

DNS and LES provide means for obtaining detailed information about turbulent flows. Such simulations can provide information that is difficult to obtain experimentally. The objectives of the present study were to investigate the turbulent structures near the rotating and nonrotating walls and to summarize the results for the heat transfer when an inner wall is heated and an outer wall is rotating and adiabatic. These wall rotation and heat transfer conditions were selected with a view toward applications involving nuclear power reactors and heat exchangers.

[1]Current address: Mechanical Engineering Department, Wayne State University, 5050 Anthony Wayne Drive, Rm. 2100, Detroit, MI 48202

[2]Current address: Department of Mechanical Engineering, The Johns Hopkins University, 223 Latrobe Hall, Baltimore, MD 21218

[3]Corresponding author

Contributed by the Heat Transfer Division for publication in the JOURNAL OF HEAT TRANSFER. Manuscript received September 23, 2003; final manuscript received August 28, 2004. Review conducted by: Surya Pratap Vanka.

2 Governing Equations

For gas flows with property variations (density, viscosity, and thermal conductivity), the compressible Navier-Stokes equations are applicable even if a low-speed case is dealt with.

2.1 Compressible Nondimensional Navier-Stokes Equations. The set of dimensional Navier-Stokes (N-S) equations has been nondimensionalized by dimensional reference quantities. The nondimensional variables are defined as follows:

$$x_i = x_i^*/L_0, \quad u_i = u_i^*/U_0, \quad t = t^*/(L_0/U_0)$$
$$\rho = \rho_i^*/\rho_0, \quad p = p_i^*/\rho_0 U_0^2, \quad \mu = \mu_i^*/\mu_0 \tag{1}$$
$$k = k_i^*/k_0, \quad T = T^*/T_0$$

where the superscript * denotes the dimensional variables and the subscript 0 denotes values at a reference state. L_0, U_0, ρ_0, and T_0 are the hydraulic diameter $[=2(r_2-r_1)]$, initial bulk velocity, density, and temperature, respectively.

After the nondimensionalization process, the governing equations are

Conservation of mass

$$\frac{\partial \rho}{\partial t} + \frac{\partial(\rho u_i)}{\partial x_i} = 0 \tag{2}$$

Conservation of momentum

$$\frac{\partial(\rho u_i)}{\partial t} + \frac{\partial(\rho u_i u_j)}{\partial x_j} = -\frac{\partial p}{\partial x_i} + \frac{\partial \sigma_{ij}}{\partial x_j} - \frac{\mathrm{Ra}}{(2\epsilon \mathrm{PrRe}^2)}\rho \delta_{1i} \tag{3}$$

Conservation of energy

$$\frac{\partial(\rho E)}{\partial t} + \frac{\partial(\rho E u_j)}{\partial x_j} = -\frac{\partial(p u_j)}{\partial x_j} - \frac{\partial q_j}{\partial x_j} + \frac{\partial(\sigma_{ij} u_i)}{\partial x_j} - \frac{\mathrm{Ra}}{(2\varepsilon \mathrm{PrRe}^2)}\rho u_i \delta_{1i} \tag{4}$$

where δ_{1i} is the Kronecker delta, and the specific total energy is $E = e + (u_j u_j)/2$.

The nondimensional heat flux vector is

$$q_j = -\frac{C_p \mu}{\mathrm{PrRe}} \frac{\partial T}{\partial x_j} \tag{5}$$

the dimensionless viscous stress term σ_{ij} is

$$\sigma_{ij} = \mu\left(\frac{\partial u_i}{\partial x_j} + \frac{\partial u_j}{\partial x_i}\right) + \lambda \frac{\partial u_k}{\partial x_k}\delta_{ij} \tag{6}$$

and the Rayleigh number Ra is

$$\mathrm{Ra} = \frac{2\epsilon g \rho_0^2 L_0^3 \mathrm{Pr}}{\mu_0^2} \tag{7}$$

ε is the temperature difference defined by

$$\epsilon = (T_{\mathrm{in}} - T)/T \tag{8}$$

where T_{in} represents the inner wall temperature.

A perfect gas equation of state was used since the intermolecular forces were assumed to be negligible

$$p = \rho R T \tag{9}$$

where R is the nondimensional gas constant. For the property evaluations, the following functions were used:

$$\mu = k = T^a \tag{10}$$

The exponent a has been taken as 0.71.

2.2 Filtering. To separate the large-scale (or resolved) variables, denoted by an over bar, from the small-scale variables, a filtering operation needs to be defined as

$$\overline{f}(x) = \int_D f(x') G(x,x') dx' \tag{11}$$

where G is the filter function, and D is the entire domain.

There are three different forms of the filter function that have been used in CFD applications, the spectral cutoff, Gaussian, and top-hat functions. In this research, the top-hat function was used, and it is defined as

$$G(x) = \begin{cases} 1/\Delta & if\ |x| \leqslant \Delta/2 \\ 0 & \text{otherwise} \end{cases} \tag{12}$$

where Δ is the filter width given by $\Delta = (\Delta_x \Delta_y \Delta_z)^{1/3}$. Δ_x, Δ_y, and Δ_z are the control volume dimensions in the x, y, and z directions.

The filtered equations used in the present study are given in Xu et al. [16] and contain terms representing the subgrid stresses and heat flux terms that require modeling to obtain closure. These subgrid-scale terms were represented using the dynamic model discussed below.

3 LES Methodology and Boundary Conditions

3.1 Dynamic Model. Dynamic modeling of the subgrid-scale stresses was introduced by Germano et al. [17]. Unlike the Smagorinsky model, the model coefficient C_d is computed dynamically as the computation progresses. Before the dynamic model coefficients are introduced, a test filter should be given by

$$\hat{\overline{f}}(x) = \int_D f(x') \hat{G}(x,x') dx' \tag{13}$$

where $\hat{G}$ is the test filter. In this work, the test filter was two times larger than the filter function G. The dynamic model for this research was based on Wang's [18] derivation. By use of Lilly's [19] approach, the unknown parameter C_d can be determined as

$$C_d = \frac{\langle L_{ij} M_{ij} \rangle}{\langle M_{kl} M_{kl} \rangle} \tag{14}$$

where

$$L_{ij} = \widehat{\overline{\rho}\widetilde{u}_i\widetilde{u}_j} - \frac{\widehat{\overline{\rho}\widetilde{u}_i}\,\widehat{\overline{\rho}\widetilde{u}_j}}{\hat{\overline{\rho}}} \tag{15}$$

$$M_{ij} = -2\hat{\overline{\rho}}\hat{\Delta}^2 |\hat{\widetilde{S}}|\left(\hat{\widetilde{S}}_{ij} - \tfrac{1}{3}\hat{\widetilde{S}}_{kk}\delta_{ij}\right) + 2\Delta^2 \overline{\rho}|\widetilde{S}|\left(\widetilde{S}_{ij} - \tfrac{1}{3}\widetilde{S}_{kk}\delta_{ij}\right) \tag{16}$$

and the angular brackets denote spatial averaging along the stream- and spanwise directions of the flow, $|S|$ is the magnitude of strain rate tensor, Δ is the filtered width $[=(\Delta_x \Delta_y \Delta_z)]^{1/3}$, and α is the strain grid ratio $(=\hat{\overline{\Delta}}/\overline{\Delta})$. The superscripts $(\hat{\ }, \overline{\ }, \widetilde{\ })$ denote the nonlinear function of a Favre-filtered quantity, large scale component of filtered quantity, and large scale component of Favre filtered quantity, respectively.

The SGS stress tensor and the turbulent heat flux in the filtered equations need to be modeled following Wang [18] and Moin et al. [20]

$$\tau_{ij} - \tfrac{1}{3}\tau_{kk}\delta_{ij} = -2C_d \overline{\rho}\overline{\Delta}^2 |\widetilde{S}|\left(\widetilde{S}_{ij} - \tfrac{1}{3}\widetilde{S}_{kk}\delta_{ij}\right) \tag{17}$$

$$q_{tj} = -\overline{\rho}\nu_H \frac{\partial \widetilde{T}}{\partial x_j} \tag{18}$$

where the SGS eddy heat diffusivity is

$$\nu_H = -\frac{C_d \overline{\Delta}^2}{\mathrm{Pr}_t}|\widetilde{S}_{ij}| \tag{19}$$

and the turbulent Prandtl number Pr_t is

$$\mathrm{Pr}_t = -c_p C_d \frac{\langle F_j F_j \rangle}{\langle H_k F_k \rangle} \tag{20}$$

where

$$H_j = c_v \left(\widehat{\overline{\rho} \widetilde{u}_j \widetilde{T}} - \frac{\widehat{\overline{\rho u_j \rho T}}}{\hat{\overline{\rho}}} \right) \tag{21}$$

$$F_j = \hat{\overline{\rho}} \hat{\Delta}^2 |\hat{\widetilde{S}}| \frac{\partial \hat{\widetilde{T}}}{\partial x_j} - \Delta^2 \widehat{\left(\overline{\rho} |\widetilde{S}| \frac{\partial \widetilde{T}}{\partial x_j} \right)} \tag{22}$$

4 Boundary Conditions

The governing equations require specification of boundary conditions at the wall, inlet, and exit due to the elliptic nature of the equations. Nonslip wall conditions were imposed at the wall. The outer wall velocity in the circumferential direction was specified. Since fully developed annular pipe flow was considered in this study, periodic and stepwise periodic boundary conditions were used at the inlet and outlet as follows:

$$\begin{aligned} p_p &= p_p(L_x, r) \\ \rho u(0, r) &= \rho u(L_x, r) \\ v(0, r) &= v(L_x, r) \\ w(0, r) &= w(L_x, r) \\ T(0, r) &= T(L_x, r) - \Delta T_x \end{aligned} \tag{23}$$

where p_p is the periodic component of the pressure, and L_x is the length of the channel in the streamwise direction. The pressure gradient parameter β was adjusted at each time step to maintain the desired mass flow rate (Dailey [21]). The nondimensional temperature difference ΔT_x was calculated by

$$\Delta T_x = \frac{(2\pi r_{\mathrm{in}}) q_{w_{\mathrm{in}}} L_x}{\dot{m}} \tag{24}$$

where r_{in} is the nondimensional inner wall radius, L_x is the nondimensional length of the pipe in the streamwise direction, $\dot{m}$ is the nondimensional mass flow rate, and $q_{w_{\mathrm{in}}}$ is the dimensionless inner wall heat flux.

The inner wall of the annular pipe was heated with constant heat flux. The isoflux thermal boundary condition is typically implemented by setting

$$T_{\mathrm{in}} = T_{nw_{\mathrm{in}}} + \frac{\Delta y q_{w_{\mathrm{in}}}}{k} \tag{25}$$

where the subscript *nw* denotes the near-wall value. But using Eq. (25) can generate unrealistic nonzero fluctuations near the solid wall. The alternative method of specifying a linear distribution of wall temperature was used. The parameters for the linear distribution can be determined by running several trials using Eq. (24).

The adiabatic boundary condition ($q_{w_{\mathrm{out}}} = 0$) was applied for the outer wall throughout this study.

5 Finite Volume Approach

A coupled finite volume method was used to solve the filtered compressible Navier-stokes equations based on Cartesian coordinates. This approach has been successfully tested on planar channel flow with Cartesian hexahedral control volumes [21]. The finite volume formulation used here is valid for general, non-Cartesian control volumes.

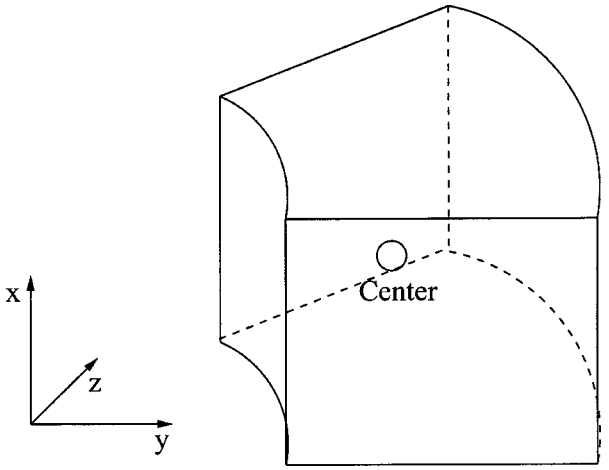

Fig. 1 Sketch of control volumes

The control volume is defined as shown in Fig. 1 and the primitive variables p, u_i, and T are stored at the cell centers. The surface integral was approximated as

$$\oint_S \vec{F} \cdot d\vec{S} = \sum_{\beta=1}^{k} [(F_x n_x + F_y n_y + F_z n_z) S]_\beta \tag{26}$$

where $\vec{F}$ is the flux vector at a point on the surface, $d\vec{S}$ is the surface normal at that point, β denotes the k surfaces of the control volumes, and (n_x, n_y, n_z) are the Cartesian components of the unit outward normal to the surface.

Gradients were calculated using the Gauss divergence theorem

$$\oint_{\Omega'} \nabla \phi d\Omega' = \oint_{\partial\Omega'} \phi d\vec{S}' \tag{27}$$

where ϕ is a scalar, Ω' is the volume of auxiliary control volume, which was obtained by shifting the main control volume a half index in the direction of the surface on which the gradients were calculated.

Time-derivative preconditioning was used to enable the computation of low Mach number flows with property variations. Time integration was performed using the implicit LU-SGS scheme [22] with a dual time-stepping approach, and the solver was second-order accurate in both space and time.

6 Computational Domain

The computational domain for the annular flow is shown in Fig. 2. A $4.5r_2 \times 2r_2 \times 2\pi r_2$ computational domain in the x (streamwise), r (radial), and z (tangential) directions was employed, where r_2 is the outer radius of the annulus. The Prandtl number was assumed to be 0.71.

The rotating ratios, N, of a outer wall velocity to the bulk velocity were 0, 0.7, and 1.3. The isoflux wall boundary condition $q_{\mathrm{wall}_{\mathrm{in}}}$ and the adiabatic wall condition were used for the inner and outer walls, respectively.

7 Results and Discussion

Simulations were conducted for air flowing upward in a vertical annular pipe with a rotating outer wall. Simulations concentrated on the occurrence of laminarization and property variations for high heat flux heat transfer as follows:

1. turbulent flow with no (or small) property variations with and without outer wall rotation.
2. large property variations with and without the outer wall rotation.

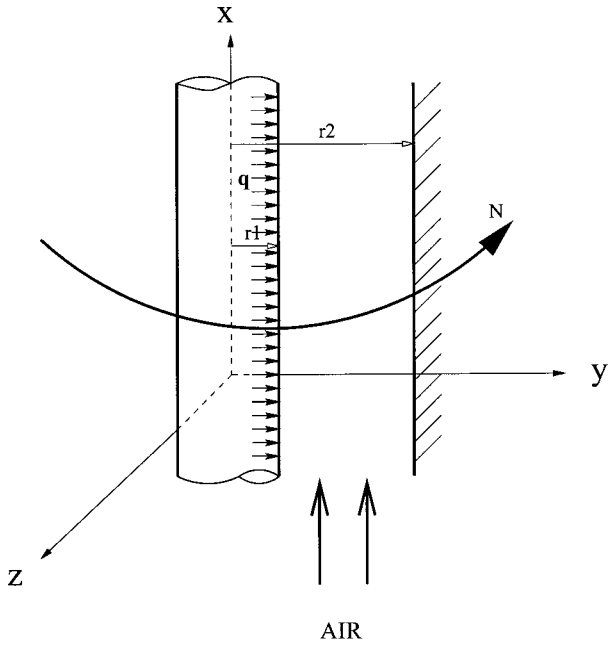

Fig. 2 The configuration for annular pipe flow with outer wall rotation

To obtain the above conditions, inlet Reynolds numbers of 6200, 7100, 8000, and 9700 based on the hydraulic diameter [$=2(r_2-r_1)$] as

$$\mathrm{Re}_{\mathrm{in}} = \frac{\rho_b u_b [2(r_2 - r_1)]}{\mu_b} \tag{28}$$

were used. The parameters r_2 and r_1 represent the outer and inner radii. And nondimensional inner wall heating rates, $q_{w_{\mathrm{in}}}$ ($=q^* w_{\mathrm{in}}/p_{\mathrm{ref}} V_{\mathrm{ref}} T_{\mathrm{ref}} c_p^*$), of 0, 0.20×10^{-3}, and 2×10^{-3} were used. Detailed conditions are tabulated in Table 1. Grid sizes ($48\times48\times80$ and $96\times96\times100$ (for Case 3-1)) were used throughout this study.

The rotation rate and the Grashof number are defined as

$$N = \frac{w_{\mathrm{wall}}}{u_b} \tag{29}$$

where w_{wall} is the tangential velocity of the pipe outer wall, and

$$\mathrm{Gr} = \frac{g\beta(T_{w_{\mathrm{in}}} - T_b)[2(r_2 - r_1)]^3}{\nu^2} \tag{30}$$

where β represents volumetric thermal expansion coefficient, and $T_{w_{\mathrm{in}}}$ and T_b denote the inner wall and bulk temperatures. Note that the buoyancy force parameter ($=\mathrm{Gr}/\mathrm{Re}_{\mathrm{in}}^2$) is significantly less than one, so that buoyancy effects played a minor role relative to rotational effects in this study.

The Nusselt numbers for cases without rotation are plotted against Reynolds number in Fig. 3, where the experimental correlation of turbulent heat transfer proposed by Dalle Donne and Merwald [23]

$$\mathrm{Nu}_b = 0.018\left(\frac{d_{\mathrm{out}}}{d_{\mathrm{in}}}\right)^{0.16} \mathrm{Re}_b^{0.8}\mathrm{Pr}^{0.4} \tag{31}$$

is included.

Table 1 Parameters for cases

CASE	N	q_w	Gr	Gr/Re^2	Re_{in}	r_1/r_2
1	0	0.2×10^{-3}	23031	6.0×10^{-4}	6200	0.5
2	0	0.2×10^{-3}	35382	7.0×10^{-4}	7100	0.5
3	0	0.2×10^{-3}	98320	1.0×10^{-3}	9700	0.5
3-1(Fine Grid)	0	0.2×10^{-3}	98320	1.0×10^{-3}	9700	0.5
4	0	0.0	0	0	8000	0.3
4-1	0	0.0	0	0	12000	0.3
5	0.7	0.0	0	0	8000	0.3
6	1.3	0.0	0	0	8000	0.3
7	0.0	0.0	0	0	8000	0.6
7-1	1.3	0.0	0	0	8000	0.6
8	0	2×10^{-3}	1119962	1.7×10^{-2}	8000	0.3
9	0.7	2×10^{-3}	962416	1.5×10^{-2}	8000	0.3
10	1.3	2×10^{-3}	849438	1.3×10^{-2}	8000	0.3

The temperature correction term for the effects of variable properties was not included due to its small variation.

The Nusselt number is defined as

$$\mathrm{Nu}_b = \frac{2h(r_2 - r_1)}{k_b} \tag{32}$$

where h is the heat transfer coefficient, k_b is the bulk thermal conductivity, r_1 and r_2 are the inner and outer wall radii, respectively.

For Cases 1, 2, and 3 (low heating cases), the deviation from Eq. (31) is seen to be minor (about 10% difference) and the data follow the general trend of the correlation well.

Figure 4 shows streamwise mean velocity profiles for the low heating cases in the global and wall coordinates. The radial distance is rescaled and it ranges from 0 to 2 as shown in the global coordinate. Chung et al. [24] conducted numerical simulations using DNS for annular pipe flow with a radius ratio of 0.5 and the data are included for comparison. Chung et al. [24] used Re

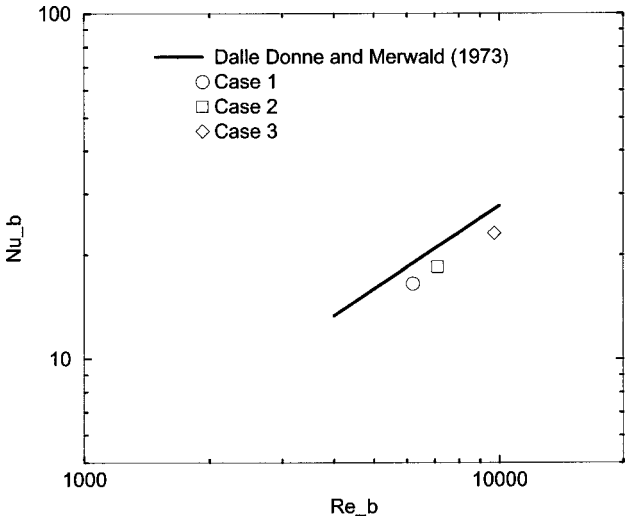

Fig. 3 Variation of Nusselt number along with correlation data

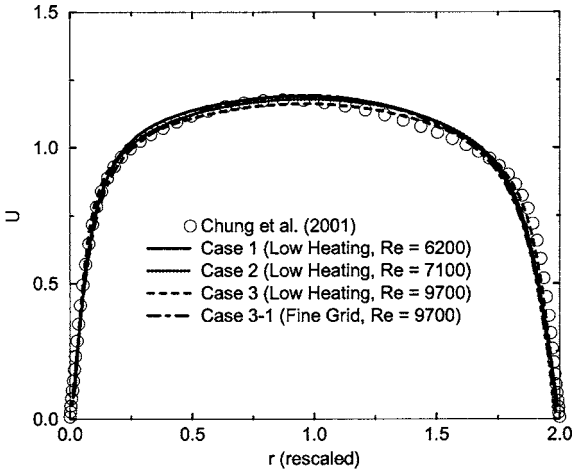

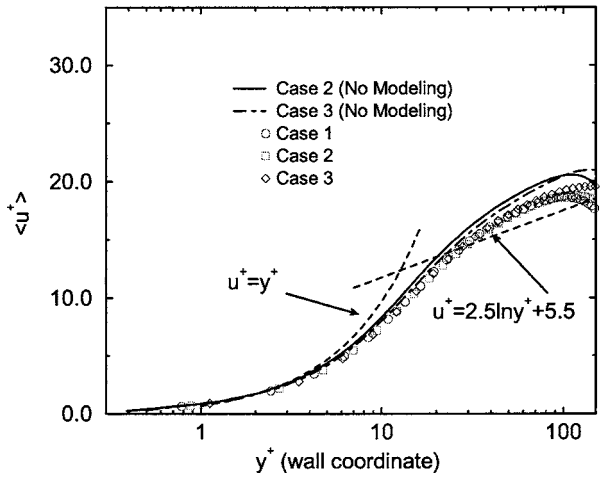

Fig. 4 Mean streamwise velocity for low heating case

=8900 based on the hydraulic diameter. A fine grid case (Case 3-1) is also included to check the grid independence. As Re increases, the profiles become flatter at the center. The current study yields good agreement with the reference data and the disagreement between the results of coarse and fine grids is fairly small.

In the wall coordinate, y^+ (based on average friction velocity) at the first grid point for Cases 1, 2, and 3 near the wall is less than 1.0, indicating that the near wall region is well resolved. As it is also shown in the figure, there is an overshooting of $\langle u^+ \rangle$ within the logarithmic region for the cases without modeling. This may be due to the fact that the coarse grid for the no-modeling cases underpredicted the shear stress.

The rms profiles (*U*rms and *V*rms) in the streamwise and radial directions for the low heating case (Case 3) are presented in Fig. 5, along with the Chung et al. [24] profiles. The present LES results have been nondimensionalized by the average of u_τ over both surfaces. Unlike the *U*rms plot, a significant difference is noticed in the *V*rms profile near the outer wall, although there is some uncertainty about the nondimensionalization of the Chung et al. data. It seems that the differing surface areas of the inner and outer walls promote the asymmetric *V*rms profile (the reduction of the *V*rms values near the outer wall). According to Nouri et al. [25] and Malik [26], the velocity maximum should be located toward the inner wall, causing a large velocity gradient near the inner wall. They also found that the maximum shear stress ($\overline{u'v'}$) appeared near the inner wall, supporting our asymmetric rms profiles. But the reason for the differences between the present results

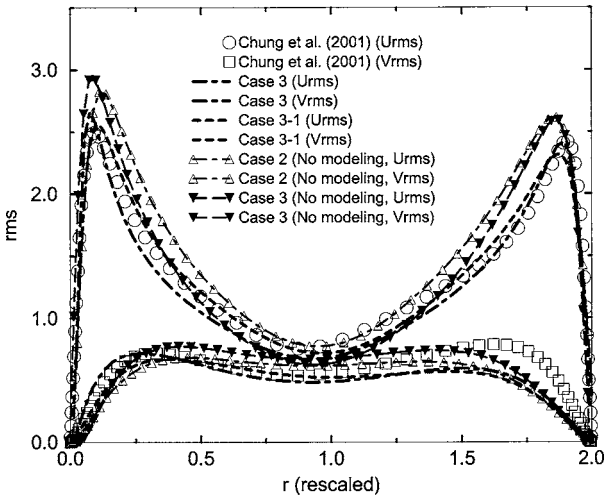

Fig. 5 Turbulent intensities for low heating case in streamwise and radial directions

and those by Chung et al. [24] is not clearly known. As was observed in the wall coordinate velocity profiles, there is an overshooting of rms for the cases without modeling. The LES modeling presents a better match, especially near the wall regions.

The effects of the rotation rate *N* on the axial velocity distribution for fully developed flow conditions are shown in Fig. 6. With increasing rotation rate, the axial velocity profiles gradually approach a laminar-like profile near the rotating wall ($r=1.0$), but the velocity profiles are maintained as turbulent near the nonrotating wall ($r=0.3$). According to the experimental pipe flow results [2], pipe wall rotation deforms the fully developed turbulent profile of the axial velocity into a laminar-like velocity profile.

The influence of the rotation on the second-order turbulence statistics was investigated by plotting the velocity rms and the turbulent kinetic energy profiles as shown in Fig. 7 for Cases 4, 5, and 6. The Turbulent Kinetic Energy (TKE) was normalized by the square of the average friction velocity ($u_{\tau_{\text{avg}}}$) for the inner and outer walls. Close to the rotating wall, the profiles tend to decrease, showing the centrifugal flow effects. However, close to the stationary (inner) wall, the intensity increases.

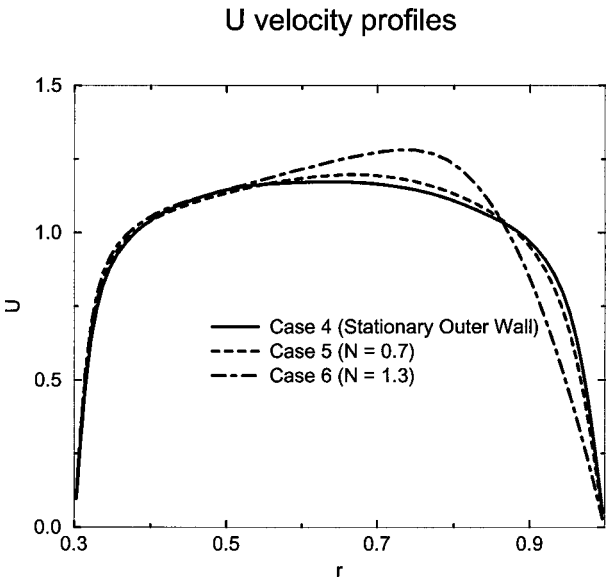

Fig. 6 Streamwise velocity profiles for cases 4, 5, and 6

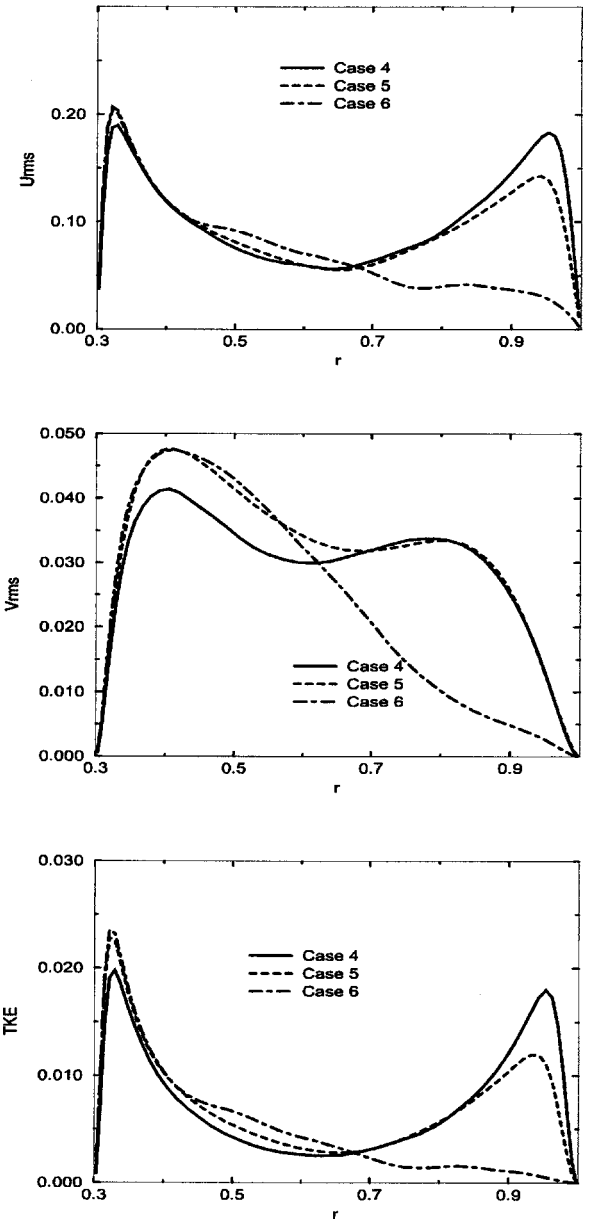

Fig. 7 ***U*rms, *V*rms, and TKE profiles for cases 4, 5, and 6**

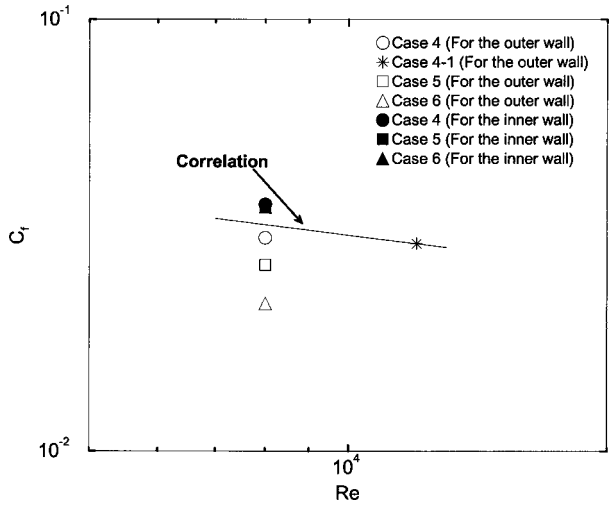

Fig. 8 Effect of Re and rotation rate on friction coefficient

7.1 Wall Friction. The swirl in the region of the wall rotation suppresses the turbulent momentum transfer and decreases the wall friction [14]. In the next two sections, the friction coefficient and the Nusselt number are studied for different rotation rates. First, the friction coefficient C_f for the inner and outer walls is plotted against Re for various values of the rotation rate in Fig. 8. The friction coefficient for a stationary wall predicted by the Blasius resistance formula, $C_f=0.0791\mathrm{Re}^{-0.25}$, is also plotted for comparison. The figure shows that the friction coefficient for the outer wall decreases with increasing rotation rate, whereas the friction coefficient for the inner wall remains almost constant. This phenomenon for the outer wall is caused by the suppression of the turbulent momentum exchange $\rho\overline{u'v'}$ due to the rotation. According to Hirai et al. [14], this reduction of $\overline{u'v'}$ is caused by the production terms, P_1 $(=-\overline{v'^2}\partial U/\partial r)$ and P_2 $(=\overline{u'w'}W/r)$. Particularly, in the case with swirl, P_2 becomes a negative production term, which reduces the magnitude of $\overline{u'v'}$. These production distributions for P_2 are shown in Fig. 9. P_2 is nearly zero in the nonrotation case (Case 4), but in the presence of rotation, P_2 becomes negative.

7.2 The Heat Transfer. The calculated results for Nu are shown in Table 2. It shows that Nu tends to increase with an increase of the rotation rate. This tendency is due to the fact that the turbulence is slightly enhanced near the inner wall, as shown in Fig. 7, as the rotation rate increases. This enhancement of the turbulence helps to increase the heat transfer coefficient near the inner wall. The enhancement of the turbulence level far from the rotating pipe wall was also observed by Orlandi and Fatica [8].

7.3 Computer Visualization. To illustrate the effect of turbulence suppression and the effect of rotation, Reich and Beer [27] used the Richardson number (RI). Figure 10 shows RI contour plots for Cases 9 and 10. RI is defined as

$$\mathrm{RI}=\frac{2(W/r^2)(\partial/\partial r)(Wr)}{(\partial U/\partial r)^2+[r(\partial/\partial r)(W/r)]^2} \tag{33}$$

According to Bradshaw [28], the centrifugal forces suppress (enhance) the turbulent fluctuations if $\mathrm{RI}>0(\mathrm{RI}<0)$. In the center of the annular flow ($r=0.55$ for Cases 9 and 10), the maximum positive value of the RI is found for both cases. Therefore, the turbulence suppression due to the rotation is most pronounced there.

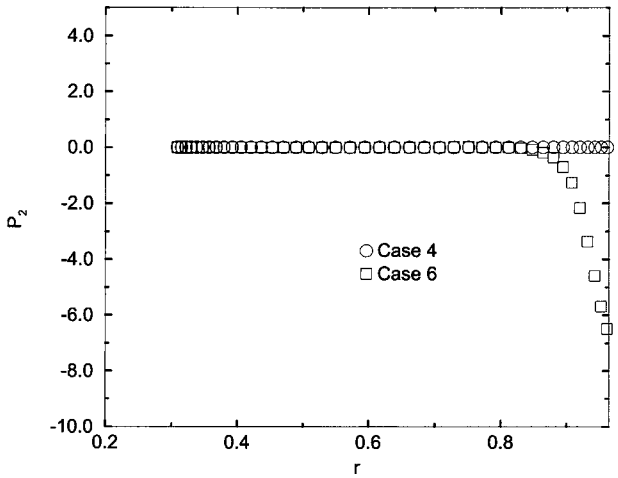

Fig. 9 The radial profiles of the second production term (P_2) in transport equations for $\overline{u'v'}$

Table 2 Comparison of Nu

CASE	rotation rate (N)	Nu	% diff.
8	0	28.19	0
9	0.7	32.90	16.71
10	1.3	34.36	21.89

The value of the maximum RI becomes larger with increasing rotation rate as shown in Fig. 10.

The magnitude of the instantaneous vorticity for different physical time steps is shown in Fig. 11. The physical time step was initiated when the rotational wall boundary condition was applied to the stationary, fully developed annular pipe flow. The transient results may not be exactly correct due to the assumption of spatial periodicity, but these figures provide a qualitative description of how the turbulent structure is altered as wall rotation is initiated. A significant change of the structures can be seen near the rotating wall as the nondimensional physical time increases.

Rotation also influences the heat transfer in the flow. Figure 12 shows the instantaneous temperature plot for Cases 8 and 10. A higher temperature is observed near the inner wall for Case 8, indicating that convection is less efficient compared to Case 10.

The instantaneous streamwise velocity contour plot is shown in Fig. 13. The larger structures are observed near the rotating wall and fine structures appear near the inner wall for Case 6. For Case 4 (no rotation), the turbulent structures can be seen near both walls.

8 Conclusions

Simulations were obtained for air flowing upward in a vertical annular pipe with a rotating outer wall. The wall rotation influenced the turbulent structures and resulted in a suppression of the turbulent motion near the rotating wall, and an enhancement of the turbulent intensity close to the stationary (inner) wall.

The variations in the streamwise velocity distribution due to the influence of rotation were evident near the rotating wall (outer wall). With increasing rotation rate the axial velocity profiles gradually approached a laminar-like profile near the rotating wall, but the velocity profiles were maintained as turbulent near the nonrotating wall and, in fact, steepened somewhat, which may account for the increase in turbulence near the stationary wall. A similar influence of rotation was observed in the distribution of the turbulent intensities. Close to the rotating wall, the rms values tended to decrease, showing the effects of rotation.

The friction coefficient for the rotating wall decreased with in-

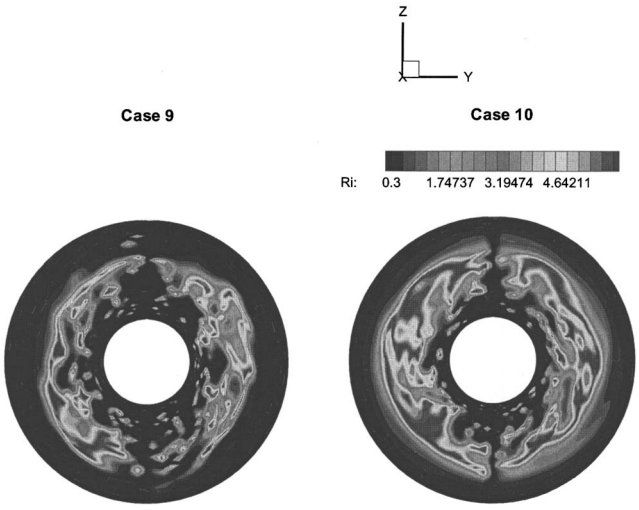

Fig. 10 Richardson number contour plot for radius ratio=0.3

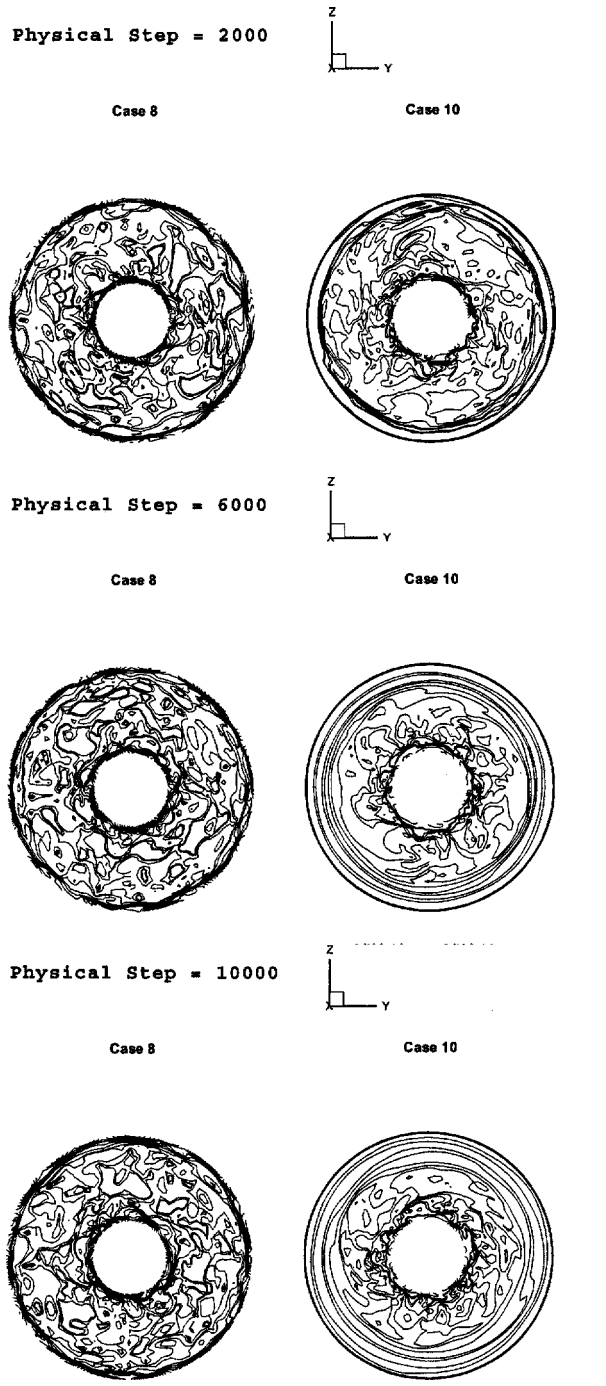

Fig. 11 Vorticity contour plot for nonrotating and rotating cases at 2000, 6000, and 10,000 physical time steps

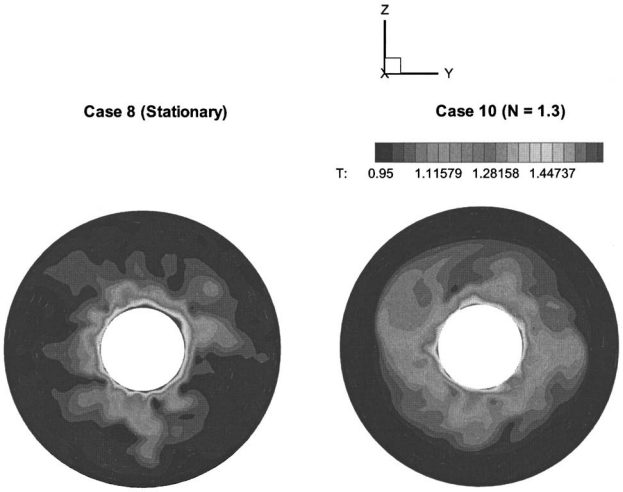

Fig. 12 Instantaneous temperature contour plot for nonrotating and rotating cases

creasing strength of rotation. This phenomenon is believed to be caused by the suppression of the turbulent momentum exchange $\rho\overline{u'v'}$ due to the rotation. In the case with rotation, P_2 $(=\overline{u'w'}W/r)$ became a negative production term, which reduced the magnitude of $\overline{u'v'}$.

The Nusselt number tended to increase with an increase of the rotation rate. This tendency was due to the fact that the turbulence was slightly enhanced near the inner wall, which was heated.

The flow visualization revealed that larger structures were observed near the rotating wall and fine structures appeared near the stationary (inner) wall.

Acknowledgments

The authors are grateful to the National Science Foundation and the Department of Energy under the NERI program for support through Grants No. CTS-9806989 and No. DE-FG03-995F21924, respectively. The Iowa State High Performance Computing Center and University of the Minnesota Supercomputing Institute provided computational resources needed for this research.

Nomenclature

C_d, C_I = dynamic subgrid-scale model coefficients
C_f = friction coefficient $[=2\tau_w/(\rho_b u_b^2)]$
C_p = constant pressure specific heat, coefficient of pressure
C_v = constant volume specific heat
D_h = hydraulic diameter
d_{in} = inner wall diameter
d_{out} = outerwall diameter
G = filter function
Gr = Grashof number
g = gravitational constant
H = total enthalpy $(=h+u_i u_i/2)$
h = heat transfer coefficient, or specific enthalpy
$\vec{i}, \vec{j}, \vec{k}$ = unit vectors for Cartesian coordinate system
k = thermal conductivity
L_0 = reference length $[=2(r_2-r_1)]$
L_x = streamwise length of pipe
Ma = Mach number
m = pseudotime index
N_{stat} = number of time steps for turbulent statistics
Nu = Nusselt number $(=hL_0/k_b)$
n = physical time index
ni, nj, nk = control volume number in streamwise radial, and circumferential directions
$\vec{n}$ = unit normal vector
n_x, n_y, n_z = components of unit normal vector
p_p = periodic component of the pressure
Pr = Prandtl number $(=\mu c_p/k)$
Pr_t = turbulent Prandtl number
p = thermodynamic pressure
Q_j = subgrid-scale turbulent heat flux vector
Q_{tj} = test filtered heat flux vector
q_j = heat flux vector
q_{tj} = Favre filtered heat flux vector
q_w = nondimensional wall heat flux
R = gas constant
U_{rms} = root-mean-square velocity in the x direction $(=\sqrt{\langle U'^2\rangle/N_{\text{stat}}})$
Re = generic Reynolds number
S = magnitude of cell face area vector or skeness factor
$\vec{S}$ = cell face area vector
S_{ij} = strain rate tensor
T = thermodynamic temperature
T_b = bulk temperature
T_{ij} = test filtered stress tensor
t = physical time
$[U]$ = vector of conserved variables
u_τ = friction velocity $(=\sqrt{\tau_w/\rho_w})$
u, v, w = Cartesian velocity components in x, r, θ directions
V_r = reference velocity
x, y, z = Cartesian coordinates

Greek Symbols

β = volumetric thermal expansion coefficient
γ = ratio of specific heats
Δ = grid filter width
$\hat{\Delta}$ = test filter width
δ = Kronecker delta
ϵ = temperature difference $[=(T_{in}-T)/T]$
λ = coefficient of bulk viscosity
μ = molecular dynamic viscosity
μ_t = subgrid-scale turbulent viscosity
ν = molecular kinematic viscosity $(=\mu/\rho)$
ν_t = subgrid-scale turbulent kinematic viscosity
ρ = thermodynamic density
σ_{ij} = shear stress tensor
τ_{ij} = subgrid-scale stress tensor
Ω = cell volume

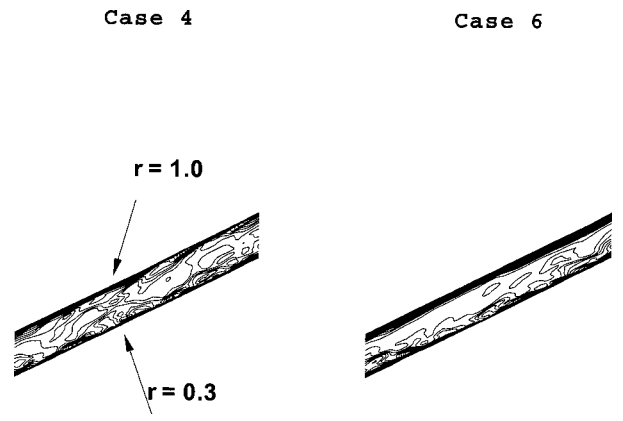

Fig. 13 Instantaneous *U* velocity plot for nonrotating and rotating cases

Subscripts

b = bulk property
i,j,k = indices for Cartesian coordinates
in = property near inner wall
out = property near outer wall
nw = near-wall cell quantity
p = periodic component
r = associated with radial direction of pipe
rms = root-mean-square
w = wall value
x,y,z = associated with Cartesian direction
x,r,θ = associated with cylindrical direction

Superscripts and Other Symbols

$'$ = fluctuation with respect to ensemble average, or unresolved or subgrid-scale components of filtered quantity
$\overline{\ }$ = resolved or large-scale component of filtered quantity
$\tilde{\ }$ = resolved or large-scale component of Favre filtered quantity
$\hat{\ }$ = nonlinear function of Favre filtered quantity
$\langle\rangle$ = ensemble-averaged quantity

Abbreviations

CFD = computational fluid dynamics
DNS = direct numerical simulation
LES = large eddy simulation
rms = root-mean-square
SGS = subgrid scale

References

[1] Murakami, M., and Kikuyama, K., 1980, "Turbulent Flow in Axially Rotating Pipes," ASME J. Fluids Eng., **102**, pp. 97–103.
[2] Kikuyama, K., Murakami, M., and Nishibori, K., 1983, "Development of Three-dimensional Turbulent Boundary Layer in an Axially Rotating Pipe," ASME J. Fluids Eng., **105**, pp. 154–160.
[3] Nishibori, K., Kikuyama, K, and Murakami, M., 1987, "Laminarization of Turbulent Flow in the Inlet Region of an Axially Rotating Pipe," Bull. JSME, **30**, pp. 255–260.
[4] Imao, S., and Itoh, M., 1996, "Turbulent Characteristics of the Flow in an Axially Rotating Pipe," Int. J. Heat Fluid Flow, **17**, pp. 444–451.
[5] Hirai, S., Takagi, T., and Matsumoto, M., 1988, "Predictions of the Laminarization Phenomena in an Axially Rotating Pipe Flow," ASME J. Fluids Eng., **110**, pp. 424–430.
[6] Kawamura, H., and Mishima, T., 1992, "Numerical Prediction of Turbulent Swirling Flow in a Rotating Pipe by a Two-Equation Model of Turbulence," Bull. JSME, **57**, pp. 1251–1256.
[7] Eggels, J., Unger, F., Weiss, M., Westerweel, J., Adrian, R., Friedrick, R., and Nieuwstadt, F., 1994, "Fully Developed Turbulent Pipe Flow: A Comparison Between Direct Numerical Simulation and Experiment," J. Fluid Mech., **268**, pp. 175–209.
[8] Orlandi, P., and Fatica, M., 1997, "Direct Numerical Simulation of Turbulent Flow in a Pipe Rotating About Its Axis," J. Fluid Mech., **343**, pp. 43–72.
[9] Becker, K., and Kaye, J., 1962, "Measurements of Diabatic Flow in an Annulus With an Inner Rotating Cylinder," ASME J. Heat Transfer, **84**, pp. 97–105.
[10] Bjorklund, I. S., and Kays, W. M., 1959, "The Heat Transfer Between Concentric Rotating Cylinders," ASME J. Heat Transfer, **81**, pp. 175–186.
[11] Gazley, C., 1958, "Heat-Transfer Characteristics of Rotational and Axial Flow Between Concentric Cylinders," Trans. ASME, **80**, pp. 79–90.
[12] Lee, J. S., Xu, X., and Pletcher, R. H., 2003, "LES of Compressible Turbulent Annular Pipe Flow with a Rotating Wall," *Proc. ASME IMECE*, Nov. 16–21.
[13] Schlichting, H., 1968, *Boundary Layer Theory*, McGraw-Hill, pp. 553–558.
[14] Hirai, S., Takagi, T., Tananka, K., and Higashiya, T., 1986, "Turbulent Heat Transfer to the Flow in a Concentric Annulus With a Rotating Inner Cylinder," *8th Int. Heat Transfer Conf.*, 3, pp. 895–900.
[15] Yang, Z., 2000, "Large Eddy Simulation of Fully Developed Turbulent Flow in a Rotating Pipe," Int. J. Numer. Methods Fluids, **33**, pp. 681–694.
[16] Xu, X., Lee, J. S., and Pletcher, R. H., 2004, "Large Eddy Simulation of Turbulent Forced Gas Flows in Vertical Pipes with High Heat Transfer Rates," Int. J. Heat Mass Transfer, **47**, pp. 4113–4123.
[17] Germano, M., Piomelli, U., Moin, P., and Cabot, W., 1991, "A Dynamic Subgrid-Scale Eddy Viscosity Model," Phys. Fluids A, **3**, pp. 1760–1765.
[18] Wang, W., 1995, "Coupled Compressible and Incompressible Finite Volume Formulations for the Large Eddy Simulation of Turbulent Flow with and Without Heat Transfer," Ph.D. thesis, Iowa State University, Ames, IA.
[19] Lilly, D. K., 1992, "A Proposed Modification of the Germano Subgrid-Scale Closure Method," Phys. Fluids A, **4**, pp. 633–635.
[20] Moin, P., Squires, K., Cabot, W., and Lee, S., 1991, "A Dynamic Subgrid-scale Model for Compressible Turbulent and Scalar Transport," Phys. Fluids A, **3**, pp. 2746–2757.
[21] Dailey, L. D., 1997, "Large Eddy Simulation of Turbulent Flows With Variable Property Heat Transfer Using a Compressible Finite Volume Formulation," Ph.D. thesis, Iowa State Univ., Ames, IA.
[22] Xu, X., Lee, J. S., and Pletcher, R. H., 2002, "Cartesian Based Finite Volume Formulation for LES of Mixed Convection in a Vertical Turbulent Pipe Flow," *Proc. ASME IMECE*, Nov. 17–22, New Orleans, LA.
[23] Dalle Donne, M., and Merwald, E., 1973, "Heat Transfer Friction Coefficients for Turbulent Flow of Air in Smooth Annuli at High Temperature," Int. J. Heat Mass Transfer, **16**, pp. 787–801.
[24] Chung, S. Y., Rhee, G. H., and Sung, H. J., 2001, "Direct Numerical Simulation of Turbulent Concentric Annular Pipe Flow," *Turbulence and Shear Flow Phenomena, Stockholm*, June 27–29, 1, pp. 377–382.
[25] Nouri, J. M., Umur, H., and Whitelaw, J. H., 1993, "Flow of Newtonian and Non-Newtonian Fluids in Concentric and Eccentric Annuli," J. Fluid Mech., **253**, pp. 617–641.
[26] Malik, M. R., 1978, "Prediction of Laminar and Turbulent Flow Heat Transfer in Annular Passages," Ph.D. thesis, Iowa State University, Ames, IA.
[27] Reich, G., and Beer, H., 1989, "Fluid Flow and Heat Transfer in an Axially Rotating Pipe-1: Effect of Rotation on Turbulent Pipe Flow," Int. J. Heat Mass Transfer, **32**, pp. 551–562.
[28] Bradshaw, P., 1969, "The Analogy Between Streamline Curvature and Buoyancy in Turbulent Shear Flow," J. Fluid Mech., **36**, pp. 177–191.

Effects Of Dimple Depth on Channel Nusselt Numbers and Friction Factors

N. K. Burgess

P. M. Ligrani

Convective Heat Transfer Laboratory,
Department of Mechanical Engineering,
University of Utah,
50 S. Central Campus Drive,
Salt Lake City, UT 84112-9208

Experimental results, measured on dimpled test surfaces placed on one wall of different rectangular channels, are given for a ratio of air inlet stagnation temperature to surface temperature of approximately 0.94, and Reynolds numbers based on channel height from 9940 to 74,800. The data presented include friction factors, local Nusselt numbers, spatially averaged Nusselt numbers, and globally averaged Nusselt numbers. The ratios of dimple depth to dimple print diameter δ/D are 0.1, 0.2, and 0.3 to provide information on the influences of dimple depth. The ratio of channel height to dimple print diameter is 1.00. At all Reynolds numbers considered, local spatially resolved and spatially averaged Nusselt number augmentations increase as dimple depth increases (and all other experimental and geometric parameters are held approximately constant). These are attributed to (i) increases in the strengths and intensity of vortices and associated secondary flows ejected from the dimples, as well as (ii) increases in the magnitudes of three-dimensional turbulence production and turbulence transport. The effects of these phenomena are especially apparent in local Nusselt number ratio distributions measured just inside of the dimples and just downstream of the downstream edges of the dimples. Data are also presented to illustrate the effects of Reynolds number and streamwise development for $\delta/D=0.1$ dimples. Significant local Nusselt number ratio variations are observed at different streamwise locations, whereas variations with the Reynolds number are mostly apparent on flat surfaces just downstream of individual dimples.
[DOI: 10.1115/1.1994880]

Introduction

In recent years, new interest has developed regarding the use of dimples to produce substantial surface heat transfer augmentations, with relatively small pressure drop penalties in internal passages [1–17]. Such dimpled passages are useful for a variety of practical applications, such as internal cooling passages of turbine blades and vanes employed in gas turbine engines, electronics cooling, heat exchangers, microscale passages, biomedical devices, and combustion-chamber liners. Using dimpled surfaces in these situations requires knowledge of the effects of different dimple geometry characteristics; however, at present, the archival literature is deficient in providing such data for many important geometric parameters. The present study is aimed at partially remedying this deficiency by providing a systematic set of data that illustrates the effects of dimple depth on local and spatially averaged surface Nusselt number distributions, as well as on friction factors.

Recent dimple investigations employ flows over flat walls with regular arrays of spherical pits [6], flows in annular passages with a staggered array of concave dimples on the interior cylindrical surface [7], flows in single hemispherical cavities [8,9], flows in diffuser and convergent channels each with a single hemispherical cavity [10], and flows in a narrow channel with spherically shaped dimples placed in relative positions on two opposite surfaces [11]. Heat transfer augmentations as high as 150%, compared to smooth surfaces, are reported, sometimes with appreciable pressure losses [7]. Other recent data show that the enhancement of the overall heat transfer rate is about 2.5 times smooth surface values over a range of Reynolds numbers, and pressure losses are about half the values produced by conventional rib turbulators [12]. A computational simulation of flows over dimpled surfaces in a channel gives flow structures, flow streamlines, temperature distributions, and resulting surface heat transfer distributions for similar geometries and flow conditions [13]. Moon et al. [14] give data that show that improvements in heat transfer intensification and pressure losses remain at approximately constant levels for different Reynolds numbers and channel heights. Mahmood et al. [1] describe the mechanisms responsible for local and spatially averaged heat transfer augmentations on flat channel surfaces with an array of dimples on one wall for one channel height, equal to 50% of the dimple print diameter. Other recent investigations consider flow and heat transfer in single spherical cavities [15]; effects of dimples and protrusions on opposite channel walls [4,5]; the effects of dimple depth on vortex structure and surface heat transfer [16]; the effects of deep dimples on local surface Nusselt number distributions [2]; the combined influences of aspect ratio, temperature ratio, Reynolds number, and flow structure [3]; and the flow structure due to dimple depressions on a channel surface [17].

The present study is unique, and different from existing studies because the effects of dimple depth, with nondimensional δ/D values ranging from 0.1 to 0.3, are investigated. Data are also presented to illustrate the effects of Reynolds number and streamwise development for $\delta/D=0.1$ dimples. The experimental results are given for a ratio of air inlet stagnation temperature to surface temperature of approximately 0.94, a ratio of channel height to dimple print diameter of 1.00, an inlet turbulence intensity level Tu of 0.033, and Reynolds numbers based on channel height from 9940 to 74,800. The data presented include friction factors, local spatially resolved Nusselt numbers, spatially averaged Nusselt numbers, and globally averaged Nusselt numbers.

Experimental Apparatus and Procedures

Channel and Test Surface for Heat Transfer Measurements. A schematic of the facility used for heat transfer measurements is given by Burgess et al. [2] and by Mahmood and Ligrani [3]. The

Contributed by the Heat Transfer Division for publication in the JOURNAL OF HEAT TRANSFER. Manuscript receieved December 1, 2003. Final manuscript received October 6, 2004. Review conducted by: Sumanta Acharya.

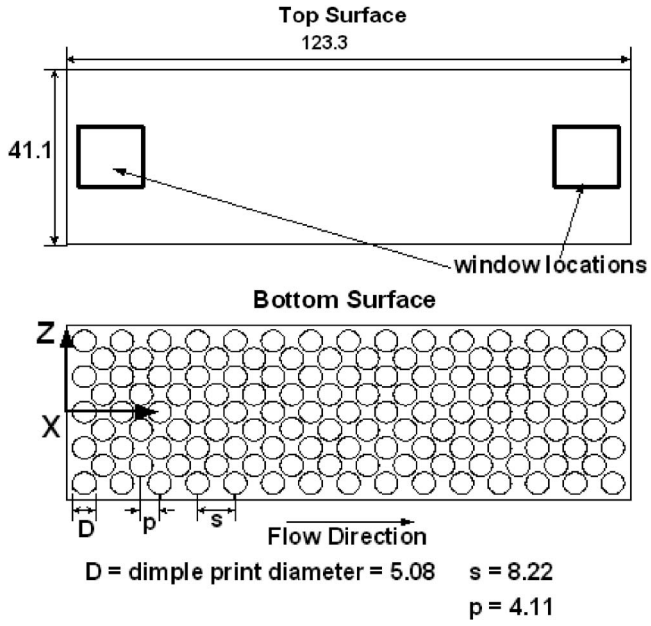

Fig. 1 Schematic diagrams of the top and bottom dimpled test surfaces. All dimensions are given in centimeters.

air used within the facility is circulated in a closed loop. One of three circuits is employed, depending on the Reynolds number requirements in the test section. For Reynolds numbers $Re_H < 10{,}000$, a 102 mm inner diameter pipe is used, which is connected to the intake of an ILG Industries 10P-type centrifugal blower. For Reynolds numbers between 10,000 and 25,000, the 102 mm pipe is connected to the intake of a Dayton 7C554 radial drive blower. For higher Reynolds numbers, a 203 mm inner diameter pipe is employed with a New York Blower Co. 7.5 HP, size 1808 pressure blower. In each case, the air mass flow rate from the test section is measured (upstream of whichever blower is employed) using an ASME standard orifice plate and Validyne M10 digital pressure manometer. The blower then exits into a series of two plenums (0.9 m square and 0.75 m square). A Bonneville cross-flow heat exchanger is located between two of these plenums. As the air exits the heat exchanger, it enters the second plenum, from which the air passes into a rectangular bell-mouth inlet, followed by a honeycomb, two screens, and a two-dimensional nozzle with a contraction ratio of 10. This nozzles leads to a rectangular cross section, 411 mm $\times$ 50.8 mm inlet duct, which is 1219 mm in length. This is equivalent to 13.5 hydraulic diameters (where a hydraulic diameter is 90.4 mm). Boundary layer trips are employed on the top and bottom surfaces of the inlet duct, just upstream of the test section, which follows with the same cross-section dimensions. It exits to a 0.60 m square plenum, which is followed by two pipes, each containing an orifice plate, as previously mentioned.

Figure 1 presents geometric details of the test section, including the bottom dimpled test surface and the top smooth surface. The dimple pattern and spacing are uniform in the X and Z directions. Dimple geometry details are then given in Fig. 2. In the present study, a total of 29 rows of dimples are employed in the streamwise direction, with four or five dimples in each row. The dimples are positioned on the surface in a staggered array. Also identified in Fig. 1 is the test section coordinate system employed for the study. Note that the Y coordinate is normal from the test surface. The longitudinal turbulence intensity level and length scale at the test section inlet are 0.033 and 15.4 mm, repectively.

Local Nusselt Number Measurement. All exterior surfaces of the facility (between the heat exchanger and test section) are insulated with Styrofoam ($k=0.024$ W/mK) or 2–3 layers of 2.54 cm thick Elastomer Products black neoprene foam insulation ($k=0.038$ W/mK) to minimize heat loss. Calibrated copper-constantan thermocouples are located between the three layers of insulation located around the entire test section to determine conduction losses. Between the first layer and the 3.2 mm thick acrylic dimpled test surface is a custom-made Electrofilm etched-foil heater (encapsulated between two thin layers of Kapton) to provide a constant heat flux boundary condition on the bottom dimpled test surface. This heater is designed and constructed so that it follows the convex contour of the test surface behind each dimple. A schematic drawing of this arrangement is given by Mahmood and Ligrani [3]. The bottom dimpled acrylic surface contains 24 copper-constantan thermocouples. Each of these thermocouples is located 0.05 cm just below this surface to provide measurements of local surface temperatures, after correction for thermal contact resistance and temperature drop through the 0.05 cm thickness of acrylic. Acrylic is chosen because of its low thermal conductivity ($k=0.16$ W/mK at 20 °C) to minimize streamwise and spanwise conduction along the test surface, and thus minimize "smearing" of spatially varying temperature gradients along the test surface. The surface of the acrylic is painted flat black to improve its surface emissivity for the infrared imaging. The power to the foil heater is controlled and regulated using a variac power supply. Energy balances performed on the heated test surface then allow determination of local magnitudes of the convective heat flux.

The mixed-mean stagnation temperature of the air entering the test section is measured using five calibrated copper-constantan thermocouples spread across the inlet cross section. To determine this temperature, measured temperatures are corrected for thermocouple wire conduction losses, channel velocity variations, as well as for the differences between stagnation and recovery tempera-

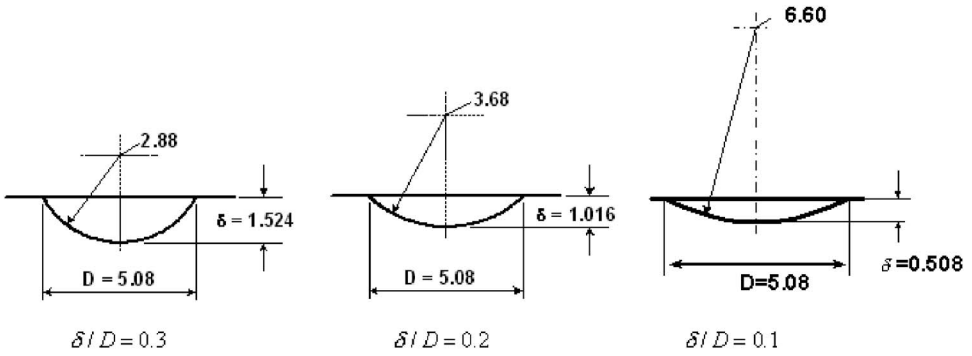

Fig. 2 Schematic diagrams of individual dimple geometry details. All dimensions are given in centimeters.

ture. Magnitudes of the local mixed-mean temperatures at different locations though the test section T_{mx} are then determined using energy balances and the mixed-mean temperature at the inlet of the test section. Because of the way in which it is measured, this inlet temperature is also a stagnation value. The thermal conductivity k used to determine local Nusselt numbers is based on this inlet stagnation temperature. Because mixed-mean temperature variations through the test section are always $<3.0\ ^\circ$C, thermal conductivity magnitudes based on inlet stagnation temperature are only slightly different from values based on local mixed-mean temperature.

Five calibrated copper-constantan thermocouples are also spread over the exit of the test section duct. Mixed-mean temperatures, estimated from measured temperatures, match values determined from energy balances within $\pm 7-10\%$ for all experimental conditions investigated. All measurements are obtained when the test facility is at steady state, achieved when each of the temperatures from the 24 thermocouples (on the bottom dimpled test surface) vary by $<0.1\ ^\circ$C over a 10 min period.

To determine the surface heat flux (used to calculate heat transfer coefficients and local Nusselt numbers), the total convective power level provided by the etched foil heater is divided by the flat projected test surface area corresponding to that foil heater. Spatially resolved temperature distributions along the bottom test surface are also determined using infrared imaging in conjunction with thermocouples, energy balances, digital image processing, and *in situ* calibration procedures. To accomplish this, the infrared radiation emitted by the heated interior surface of the channel is captured using a VideoTherm 340 Infrared Imaging Camera, which operates at infrared wavelengths from 8 to 14 μm. Temperatures measured using the calibrated, copper-constantan thermocouples distributed along the test surface adjacent to the flow are used to perform the *in situ* calibrations simultaneously as the radiation contours from surface temperature variations are recorded.

This is accomplished as the camera views the test surface through a custom-made, zinc-selenide window (which transmits infrared wavelengths between 6 and 17 μm) located on the top wall of the test section. Reflection and radiation from surrounding laboratory sources are minimized using an opaque shield that covers the camera lens and the zinc-selenide window. As shown in Fig. 1, this window can be positioned either at an upstream or downstream location. Note that the downstream location is located just above the 26th to 29th rows of dimples downstream from the leading edge of the test surface. Twelve thermocouple junction locations are present in the infrared field viewed by the camera. The exact spatial and pixel locations of these thermocouple junctions and the coordinates of a 12.7 cm $\times$ 12.7 cm field of view are known from calibration maps obtained prior to measurements. During this procedure, the camera is focused and rigidly mounted and oriented relative to the test surface in the same way as when radiation contours are recorded. Voltages from the thermocouples are acquired using a Hewlett-Packard 44422T data acquisition card installed in a Hewlett-Packard 3497A data acquisition control unit, which is controlled by a Hewlett-Packard A4190A Series computer.

With these data, gray-scale values at pixel locations within digitally-acquired images from the infrared imaging camera are readily converted into local Nusselt number values. Because such calibration data depend strongly on camera adjustment, the same brightness, contrast, and aperture camera settings are used to obtain the experimental data. The *in situ* calibration approach rigorously and accurately accounts for these variations.

Images from the infrared camera are recorded as 8-bit gray scale directly into the memory of a Dell Dimension XPS T800r PC computer using a Scion Image Corporation Frame grabber video card and SCION image v.1.9.2 software. Three sets of 60 frames are recorded at a rate of 1 fps. All of the 180 resulting images are then ensemble averaged to obtain the final gray-scale data image. This final data set is then imported into MATLAB version 6.0.0.88 (Release 12) software to convert each of 256 possible gray-scale values into local Nusselt numbers at each pixel location using calibration data. Each individual image covers a 300 pixel $\times$ 300 pixel area.

Friction Factor Measurement. Wall static pressures are measured along the test section, simultaneously, as the heat transfer measurements are conducted, using 12 static pressure taps located 25.4 mm to 80 mm apart along one of the test section sidewalls. These measurements are made in the test section with the dimples, as well as in a baseline test section with smooth surfaces on all four walls. Friction factors are then determined from streamwise pressure gradient magnitudes. Pressures from the wall pressure taps are measured using Celesco LCVR pressure transducers. Signals from these transducers are processed using Celesco CD10D Carrier-Demodulators. Voltages from the Carrier-Demodulators are acquired using a Hewlett-Packard 44422A data acquisition card installed in a Hewlett-Packard 3497A data acquisition control unit, which is controlled by a Hewlett-Packard A4190A Series computer. With this apparatus, 100 sequential measurements are acquired and measured from each pressure transducer, over a time period of $\sim$20 s.

Uncertainty Estimates. Uncertainty estimates are based on 95% confidence levels and are determined using methods described by Kline and McClintock [21] and Moffat [22]. Uncertainty of temperatures measured with thermocouples is $\pm 0.15\ ^\circ$C. Spatial and temperature resolutions achieved with the infrared imaging are about 0.5 mm and 0.8 °C, respectively. This magnitude of temperature resolution is due to uncertainty in determining the exact locations of thermocouples with respect to pixel values used for the *in situ* calibrations. Local Nusselt number uncertainty is then about $\pm 6.8\%$. Corresponding Nusselt number ratio uncertainty is about ± 0.14, or about $\pm 9.4\%$. Note that uncertainties of local Nusselt numbers consider variations of surface heat flux that may be present because of small changes of the thickness of the acrylic that comprises the dimpled test surface and because of different heat flux variations on the acrylic dimpled surface compared to the distributions produced by the contoured etched-foil heater. Friction factor ratio uncertainty is approximately $\pm 5.0\%$ for f/f_o equal to 1.40. Reynolds number uncertainty is about $\pm 2.0\%$ for Re_H of 12,000.

Experimental Results and Discussion

Baseline Nusselt Numbers. Two different sets of baseline Nusselt numbers are measured for two different purposes. In both cases, constant-property baseline Nusselt numbers are measured in a smooth rectangular test section with smooth walls on all surfaces and no dimples, for a ratio of inlet stagnation temperature to surface temperature of 0.93–0.94 and an inlet turbulence intensity level of 3.3%. The baseline measurements are also time–averaged and made in the downstream portion of the test section at X/D from 21.0 to 24.0, where the channel flow is hydraulically and thermally fully developed. The *first set* is measured in a channel with an aspect ratio of 4 with heating on all four channel surfaces (with constant heat flux boundary condition around the entire test section) to verify the experimental apparatus and procedures employed. The *second set* is measured in a channel with an aspect ratio of 8 (which is the same aspect ratio employed for the present dimple surface measurements) to provide baseline Nusselt numbers Nu_o to normalize values measured on the dimpled surface. In this case, only the bottom channel surface is heated to provide the same type of thermal boundary condition as when the dimples are installed. Except for the absence of the dimples, all geometric characteristics of the channel are then the same as when the dimpled test surface is installed.

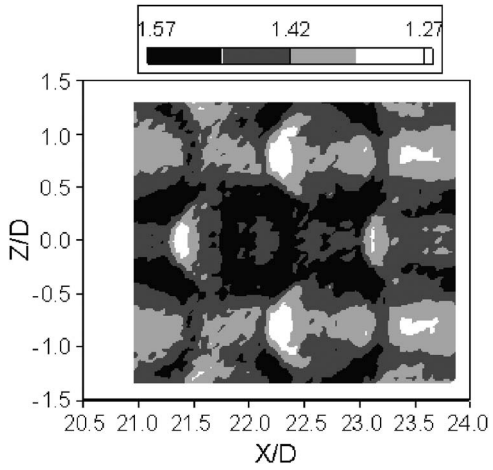

Fig. 3 Local Nusselt number ratio data from a channel with shallow dimples on one channel surface and heating on one channel surface, for $\delta/D=0.1$, $H/D=1$, $Tu=0.033$, and $Re_H=17{,}800$

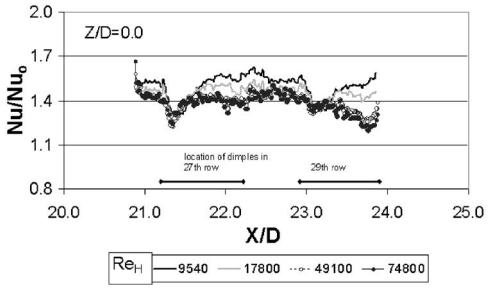

Fig. 4 Local Nusselt number ratios along the test surface spanwise centerline, $Z/D=0.0$, for different Reynolds numbers Re_H from a channel with shallow dimples on one channel surface and heating on one channel surface, for $\delta/D=0.1$, $H/D=1$, and $Tu=0.033$

Baseline Nusselt numbers for the first set of conditions are in agreement with the Dittus-Boelter smooth circular tube correlation [23], which is given by

$$Nu_o = 0.023\, Re_{Dh}^{0.8}\, Pr^{0.4} \quad (1)$$

The agreement between Eq. (1) and the first set of baseline data (obtained with all four walls heated) is described by Burgress et al. [2] for the entire range of Reynolds numbers Re_{Dh} examined and provides a check on the experimental apparatus and procedures. This first set of spatially-averaged Nusselt numbers is determined from measurements made on the top and bottom walls.

Because of the different thermal boundary conditions employed, baseline Nusselt numbers with heating only on one wall are generally lower than the values given by Eq. (1), when compared at the same Reynolds number based on hydraulic diameter [2]. As mentioned, these values are employed to normalize dimpled surface Nusselt numbers.

Effects of Reynolds Number. Local Nusselt number ratios are given in Fig. 3, which are measured with shallow dimples on one channel surface and heating on one channel surface, for $\delta/D=0.1$, $H/D=1$, $Re_H=17{,}800$, $Tu=0.033$, and no augmentation of turbulence intensity levels. Note that the baseline Nusselt numbers, used for normalization of the values presented, are obtained using the same thermal boundary conditions and heating arrangement as when dimples are used on the measurement surfaces. In addition, heat transfer coefficients and heat flux values (used to determine Nusselt numbers) are based on flat projected areas in both cases.

The bulk flow direction in Fig. 3 is from left to right in the direction of increasing X/D. Each $\delta/D=0.1$ dimple is located in the vicinity of each circular Nusselt number distribution. Note that local Nu/Nu_o values are lowest in the upstream halves of the dimples. Each of these is positioned beneath a region of recirculating flow, where advection velocities in the flow located adjacent to the surface are very low. Nusselt number ratios then increase progressively with X/D along the dimpled surface. Values then become highest near the diagonal and downstream edges of the dimples and on the flat surfaces just downstream of these locations. Here, local Nu/Nu_o augmentations are >1.55 and as high as 1.6 because of reattachment of the shear layer that forms across the top of each dimple and because of the multiple vortex pairs that are periodically shed from each dimple. When $\delta/D=0.1$, $Re_H=17{,}800$, and $H/D=1.0$, one relatively large vortex pair is shed from the central part of each dimple and two smaller vortex pairs are shed from the spanwise edges of each dimple [1,3,17]. These edge-formed vortex pairs then strengthen as they advect downstream next to the edges of other dimples. This occurs because of the staggered arrangement of the dimples on the test surface, which causes each "edge" vortex pair to be located first on the right edge of a dimple, then on the left edge of another dimple, and so on. The result is interconnected regions of high local Nusselt number ratios, located diagonally between adjacent dimples, as shown in Fig. 3.

Figure 4 shows local Nusselt number ratios along the test surface spanwise centerline, $Z/D=0.0$, for different Reynolds numbers Re_H from a channel with shallow dimples on one channel surface, and heating on one channel surface, for $\delta/D=0.1$, $H/D=1$, and $Tu=033$. Figure 5 shows local Nusselt number ratios along a line of constant $X/D=23.18$ for different Reynolds numbers Re_H for the same channel geometry and experimental conditions. Both of these figures show that Nusselt number ratios, measured at different Reynolds numbers, are similar within the upstream parts of the dimples, where local values are also lowest. Local ratios then generally increase as the Reynolds number decreases at other locations. This is due to stronger secondary flows and vortices produced by the dimples at lower Reynolds numbers, and some suppression of secondary flows and turbulent transport capabilities of these secondary flows and vortices at higher Reynolds numbers. In some cases, local Nusselt number ratio spatially-resolved distributions vary from one dimple to another; however, these variations are always less than the Nusselt number ratio experimental uncertainty. Note that the local ratio distributions for the 29th row of dimples may be slightly altered because of their locations within the last streamwise dimple row along the test section.

The effects of these phenomena are also apparent in Figs. 6 and 7. Figure 6 presents Nusselt number ratios that are spanwise-averaged over one period of dimple surface geometry, for different Reynolds numbers Re_H from a channel with shallow dimples

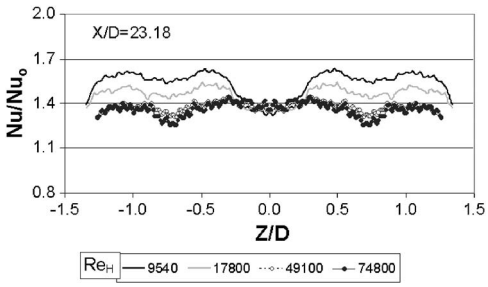

Fig. 5 Local Nusselt number ratios along a line of constant $X/D=23.18$ for different Reynolds numbers Re_H from a channel with shallow dimples on one channel surface, and heating on one channel surface, for $\delta/D=0.1$, $H/D=1$, and $Tu=0.033$

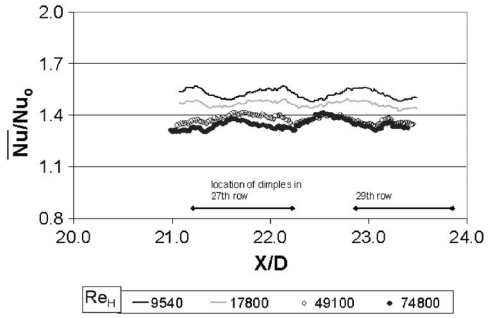

Fig. 6 Nusselt number ratios spanwise-averaged over one period of dimple surface geometry, for different Reynolds numbers Re_H from a channel with shallow dimples on one channel surface and heating on one channel surface, for $\delta/D=0.1$, $H/D=0.1$, and $Tu=0.033$

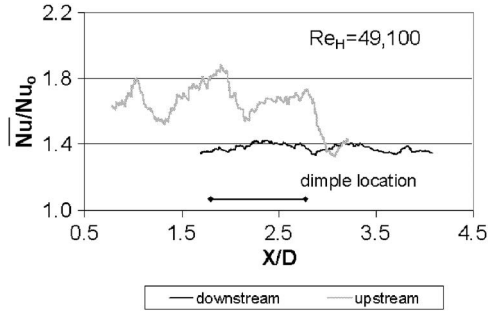

Fig. 9 Nusselt number ratios spanwise averaged over one period of dimple surface geometry, measured at upstream and downstream locations shown in Fig. 1, from a channel with shallow dimples on one channel surface and heating on one channel surface, for $\delta/D=0.1$, $H/D=1$, $Tu=0.033$, and $Re_H=49{,}100$

on one channel surface, and heating on one channel surface, for $\delta/D=0.1$, $H/D=1$, and $Tu=0.033$. Figure 7 gives Nusselt number ratios that are streamwise-averaged over one period of dimple surface geometry, for the same channel geometry and experimental conditions. In both cases, spatially-averaged Nusselt number ratios generally increase as the Reynolds number decreases for most of the locations shown.

Effects of Streamwise Development. Figure 8 presents Nusselt number ratios which are measured along the test surface spanwise centerline, $Z/D=0.0$. Figure 9 then gives Nusselt number ratios that are spanwise-averaged over one period of dimple surface geometry. In both cases, the data are given for the upstream and downstream locations, corresponding to the window locations shown in Fig. 1. To make the comparison, the downstream data are displaced by a distance of 20 X/D. The data are obtained from a channel with shallow dimples on one channel surface and heating on one channel surface, for $\delta/D=0.1$, $H/D=1$, $Tu=0.033$, and $Re_H=49{,}100$. The Nusselt number ratio data measured at the upstream location are generally higher, with larger variations at different X/D streamwise locations compared to the data measured at the downstream locations. This is mostly because of thinner thermal boundary layers at the upstream locations. This smaller thermal boundary layer thickness makes them more susceptible to the effects of the different vortices and secondary flows that are produced by the dimples.

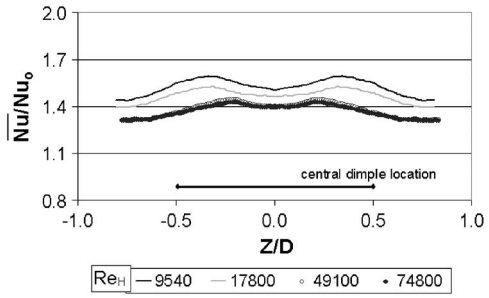

Fig. 7 Nusselt number ratios streamwise averaged over one period of dimple surface geometry for different Reynolds numbers Re_H from a channel with shallow dimples on one channel surface and heating on one channel surface, for $\delta/D=0.1$, $H/D=1$, and $Tu=0.033$

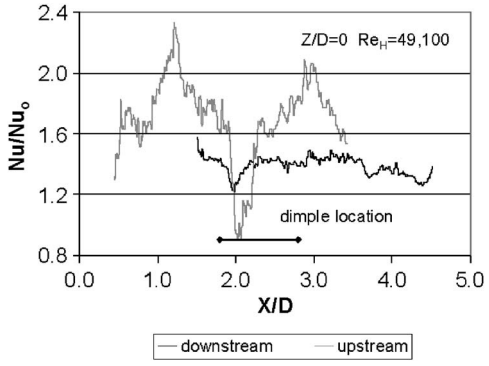

Fig. 8 Nusselt number ratios along the test surface spanwise centerline, $Z/D=0.0$, measured at upstream and downstream locations shown in Fig. 1, from a channel with shallow dimples on one channel surface and heating on one channel surface, for $\delta/D=0.1$, $H/D=1$, $Tu=0.033$, and $Re_H=49{,}100$

Effects of Dimple Depth. Figure 10 presents local dimpled channel Nusselt number ratios as dependent on X/D along the test surface spanwise centerline at $Z/D=0$. Data are given for (i) $\delta/D=0.1$, $H/D=1$, and $Re_H=17{,}800$ from the present study; (ii) $\delta/D=0.2$, $H/D=1$, and $Re_H=20{,}000$ from Mahmood et al. [1]; and (iii) $\delta/D=0.3$, $H/D=1$, and $Re_H=17{,}200$ from Burgess et al. [2]. Note that the X/D values of the Mahmood et al. [1] data are shifted so that they are positioned at the same relative location with respect to the dimples. The X/D ranges of values for dimples located in the 27th and 29th rows are also shown in Fig. 10. The $\delta/D=0.3$ Nusselt number ratio data are generally higher than the $\delta/D=0.2$ data, and the $\delta/D=0.2$ Nusselt number ratio data are generally higher than the $\delta/D=0.1$ data, for almost every X/D location shown in Fig. 10. In addition, Nu/Nu_o variations with X/D for $\delta/D=0.1$ are also smaller than the variations that are

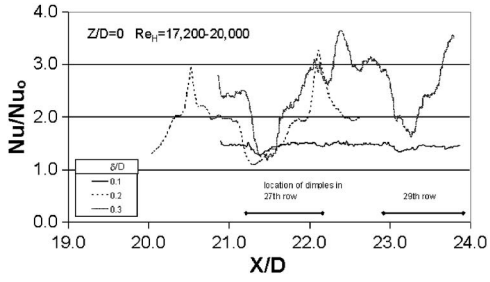

Fig. 10 Local dimpled channel Nusselt number ratios as dependent on X/D along the test surface spanwise centerline at $Z/D=0$. Data are given for (i) $\delta/D=0.1$, $H/D=1$, and $Re_H=17{,}800$ from the present study; (ii); $\delta/D=0.2$, $H/D=1$, and $Re_H=20{,}000$ from Mahmood et al. [1]; and (iii) $\delta/D=0.3$, $H/D=1$, and $Re_H=17{,}200$ from Burgess et al. [2].

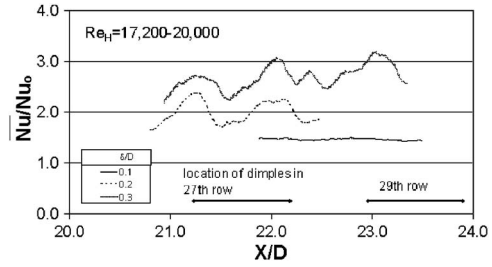

Fig. 11 Nusselt number ratios spanwise-averaged over one period of dimple surface geometry, as dependent on X/D. Data are given for (i) $\delta/D=0.1$, $H/D=1$, and $Re_H=17,800$ from the present study; (ii) $\delta/D=0.2$, $H/D=1$, and $Re_H=20,000$ from Mahmood et al. [1]; and (iii) $\delta/D=0.3$, $H/D=1$, and $Re_H=17,200$ from Burgess et al. [2].

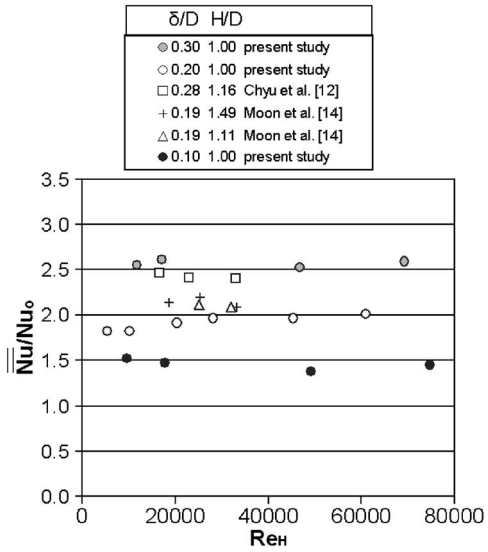

Fig. 12 Globally averaged dimpled channel Nusselt number ratios as dependent on Reynolds number Re_H for $\delta/D=0.1$ and $H/D=1$ from the present study. Results from the present study are compared to results from Burgess et al. [2], Mahmood et al. [1], Chyu et al. [12], and Moon et al. [14] for different values of δ/D, the ratio of dimple depth to dimple print diameter.

present for $\delta/D=0.3$ and $\delta/D=0.2$.

As X/D increases and one moves along the dimple surface, the $\delta/D=0.2$ Nusselt number ratio data from Mahmood et al. [1] first decrease in the first 25% of the dimple and then increase continuously over the last 75% of the dimple. The highest local Nu/Nu_o value is then present just inside of the downstream edge of the dimple. The local Nusselt number ratio data for $\delta/D=0.1$ from the present study show a decrease and then an increase in the upstream part of each dimple. Local Nusselt number ratios for $\delta/D=0.3$ from Burgess et al. [2] in Fig. 10 also show a decrease with X/D in the first 25% of the dimple. In the last 75%, Nu/Nu_o values increase until a double local peak is present at a location that is positioned about 85% through the dimple. Values then decrease to give a local minima near the downstream edge of the dimple. This is just downstream of the location where the Nu/Nu_o maximum is present for $\delta/D=0.2$. The $\delta/D=0.3$ data in Fig. 10 then increase as X/D increases further to give a maximum Nu/Nu_o value of ~ 3.7 near $X/D=22.3$, which is on the flat surface just downstream of the dimple.

These differences for different δ/D are due to shedding of vortex pairs with different strengths and to different shear layer formation, development, and reattachment. The shear layer which forms near the tops of the dimples is stronger, with more pronounced shear layer reattachment for the deeper dimples. When $\delta/D=0.3$, the reattachment location of this shear layer is slightly farther upstream then for the shallow dimples with $\delta/D=0.2$. The location of this reattachment zone changes with time in a periodic fashion for all three δ/D values, in phase with the sequence of vortex pair shedding and flow inrush to the dimples (which occur periodically and continuously). These alternating phenomena result partially from continuity considerations, which probably cause larger volumes of fluid to periodically move into and out of the deeper dimples (compared to the shallow dimples). Because of this, the ejection and local jetting of flow from the deeper dimples is stronger, which results in vortex pairs with stronger and more pronounced secondary flows. The net result is increased Nu/Nu_o values on the flat surfaces just downstream of the deeper dimples as δ/D increases in Fig. 10.

Figure 11 presents Nusselt number ratios, which are spanwise averaged over one period of dimple surface geometry, as dependent on X/D. These data are given for (i) $\delta/D=0.1$, $H/D=1$, and $Re_H=17,800$ from the present study; (ii) $\delta/D=0.2$, $H/D=1$, and $Re_H=20,000$ from Mahmood et al. [1]; and (iii) $\delta/D=0.3$, $H/D=1$, and $Re_H=17,000$ from Burgess et al. [2]. The streamwise locations of the dimples in the 27th and 29th rows are included in Fig. 11. Here, spanwise-averaged values from Mahmood et al. [1] for $\delta/D=0.2$ are significantly lower than values from Burgess et al. [2] for $\delta/D=0.3$. In addition, spanwise-averaged values from the present study for $\delta/D=0.1$ are significantly lower than values from Mahmood et al. [1] for $\delta/D=0.2$.

Also note that spanwise-averaged Nusselt number ratios from the present study for $\delta/D=0.1$ in Fig. 11 show almost no variation with X/D. Different behavior is evident when $\delta/D=0.2$ and $\delta/D=0.3$. In these cases, the lowest $\overline{Nu}/Nu_o$ values are positioned at the same locations as the upstream portions of dimples in the 27th row. The highest $\overline{Nu}/Nu_o$ values are then located at positions that correspond to the downstream parts of dimples in the 27th row, as well as on flat regions located just downstream. Of particular interest is the double peak in the $\overline{Nu}/Nu_o$ distribution for $\delta/D=0.3$, which is located at $X/D=21.8$ to $X/D=22.5$. The $\delta/D=0.2$ distribution shows only a single peak in the $\overline{Nu}/Nu_o$ variation at about the same X/D locations. Note that spanwise-averaged Nusselt number ratios for $\delta/D=0.3$, measured near the 29th row of dimples, are different from data measured farther upstream because the proximity of these data to the downstream end of the test section.

Effects of Dimple Depth and Reynolds Number on Globally-Averaged Nusselt Number Ratios, Friction Factor Ratios, and Thermal Performance Parameters. Globally-averaged Nusselt numbers are determined by averaging local data over one complete period of dimple geometry. These averages are thus conducted in both the spanwise and streamwise directions over a rectangular area from the center to center of adjacent dimples in the 27th and 29th rows. The baseline Nusselt numbers Nu_o (used for normalization) are obtained at the same Reynolds numbers as the Nusselt numbers measured on the dimpled surface.

Note that the present globally-averaged Nusselt number ratios for $\delta/D=0.1$ are about constant as Re_H increases in Fig. 12. This is consistent with Nusselt number ratios from Mahmood et al. [1] for $\delta/D=0.2$, which increase slightly or are about constant as Re_H changes. The present data in Fig. 12 are obtained with no augmentation of turbulence intensity levels (i.e., $Tu=0.033$) and are also compared to results from Chyu et al. [12] for $\delta/D=0.28$ and $H/D=1.155$ and to results from Moon et al. [14] for $\delta/D=0.19$ and two values of H/D of 1.11 and 1.49. In all cases, heat transfer coefficients and heat flux magnitudes are based on flat projected areas. Note that Chyu et al. [12] utilize dimples on two opposite channel surfaces, whereas the present study, Mahmood et al. [1], Burgess et al. [2], and Moon et al. [14] use dimples only on one

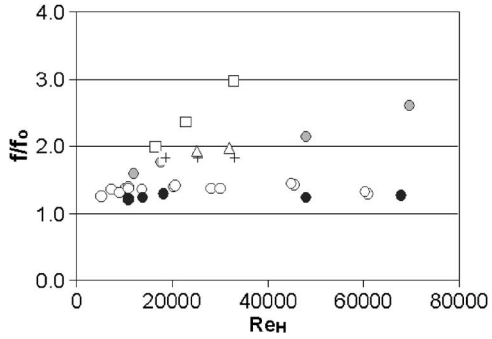

Fig. 13 Dimpled channel friction factor ratios as dependent on Reynolds number Re_H for $\delta/D=0.1$ and $H/D=1$ from the present study. Results from the present study are compared to results from Burgess et al. [2], Mahmood et al. [1], Chyu et al. [12], and Moon et al. [14] for different values of δ/D, the ratio of dimple depth to dimple print diameter. Symbols are defined in Fig. 12.

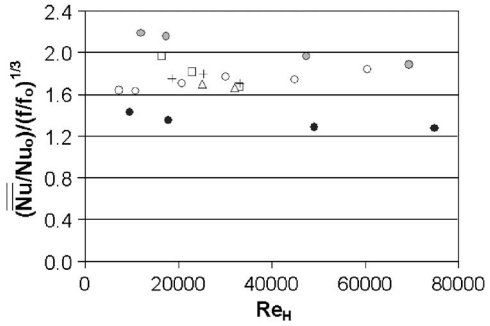

Fig. 15 Globally averaged dimpled-channel thermal performance parameters as dependent on Reynolds number Re_H for $\delta/D=0.1$ and $H/D=1$ from the present study. Results from the present study are compared to results from Burgess et al. [2], Mahmood et al. [1], Chyu et al. [12], and Moon et al. [14] for different values of δ/D, the ratio of dimple depth to dimple print diameter. Symbols are defined in Fig. 12.

channel surface.

For all Re_H examined, the data in Fig. 12 generally show increasing globally averaged Nusselt number ratios as δ/D increases from 0.10 to 0.30. This further illustrates the effects of this parameter in augmenting local and spatially averaged Nusselt numbers at different values of the Reynolds number Re_H.

Figure 13 shows that friction factor ratios for $\delta/D=0.1$ and $H/D=1$, are approximately constant as Re_H varies from 9540 to 74,800. These figures also show that the present dimpled surface friction factor ratios are less than magnitudes measured in several types of turbulated passages, where f/f_o range from 2.5 to 75 [24]. In Fig. 13, ratios from Mahmood et al. [1] ($\delta/D=2$), Burgess et al. [2] ($\delta/D=0.3$), Chyu et al. [12] ($\delta/D=0.28$), and Moon et al. [14] (for $\delta/D=0.19$) are also included for comparison. Values from all other studies are higher than ratios for $\delta/D=0.1$. This is because values generally increase as either the number of dimpled surfaces increases (i.e., from 1 to 2) or as δ/D increases.

Figures 14 and 15 show globally averaged dimpled-channel thermal performance parameters, $(\overline{\overline{Nu}}/Nu_o)/(f/f_o)$ and $(\overline{\overline{Nu}}/Nu_o)/(f/f_o)^{1/3}$, respectively, as dependent on Reynolds number Re_H for $\delta/D=0.1$ and $H/D=1$, along with results from Burgess et al. [2], Mahmood et al. [1], Chyu et al. [12], and Moon et al. [14], which are given for different values of δ/D, the ratio of dimple depth to dimple print diameter, for comparison to results from the present investigation. The first of these parameters is sometimes referred to as a Reynolds analogy thermal performance parameter. The form of the $(\overline{\overline{Nu}}/Nu_o)/(f/f_o)^{1/3}$ performance parameter provides a heat transfer augmentation quantity $(\overline{\overline{Nu}}/Nu_o)$ and a friction factor augmentation quantity $[(f/f_o)^{1/3}]$, where each is given for the same ratio of mass flux in an internal passage with augmentation devices to mass flux in an internal passage with smooth surfaces. Figure 14 shows that the highest values of the $(\overline{\overline{Nu}}/Nu_o)/(f/f_o)$ performance parameter are produced either by the $\delta/D=0.2$ dimples or the $\delta/D=0.3$ dimples, depending upon the Reynolds number. If the Chyu et al. [12] data for dimples on two channel surfaces are disregarded, then Fig. 15 shows that the $(\overline{\overline{Nu}}/Nu_o)/(f/f_o)^{1/3}$ performance parameter increases as dimple depth and δ/D increase, provided dimples are present only on one channel surface.

Correlation Equations. To account for the effects of dimple depth on globally-averaged Nusselt number ratios in a channel with dimples on one surface, the following correlation equation is recommended

$$\overline{\overline{Nu}}/Nu_o = 1.0 + 6.183(\delta/D)^{1.162} \quad (2)$$

This equation is valid for $Re_H=5000-80{,}000$, $H/D=1.0$, $\delta/D=0.1-0.3$, $Tu=0.03-0.12$, and a ratio of inlet stagnation temperature to local surface temperature equal to 0.92–1.00. Equation (2) shows good agreement with experimental data in Fig. 16. Note

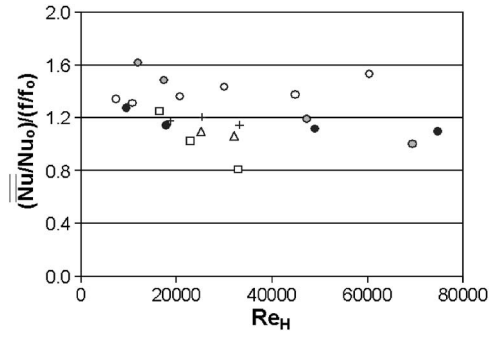

Fig. 14 Globally averaged dimpled-channel thermal performance parameters as dependent on Reynolds number Re_H for $\delta/D=0.1$ and $H/D=1$ from the present study. Results from the present study are compared to results from Burgess et al. [2], Mahmood et al. [1], Chyu et al. [12], and Moon et al. [14] for different values of δ/D, the ratio of dimple depth to dimple print diameter. Symbols are defined in Fig. 12.

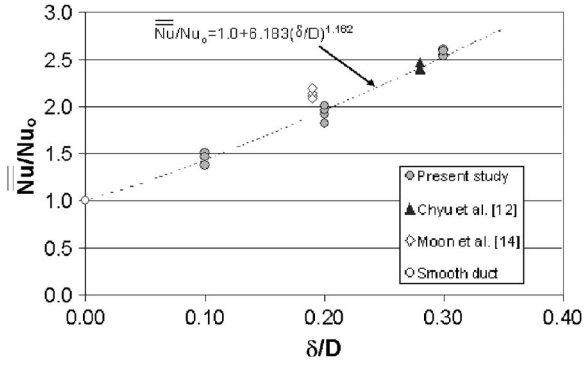

Fig. 16 Globally averaged dimpled-channel Nusselt number ratios as dependent on the ratio of dimple depth to dimple print diameter δ/D, including comparisons to a correlation equation, for $\delta/D=0.1$ and $H/D=1$ from the present study for $\delta/D=0.2$ from Mahmood et al. [1], and for $\delta/D=0.3$ from Burgess et al. [2]. Results from Chyu et al. [12] and Moon et al. [14] are included for comparison.

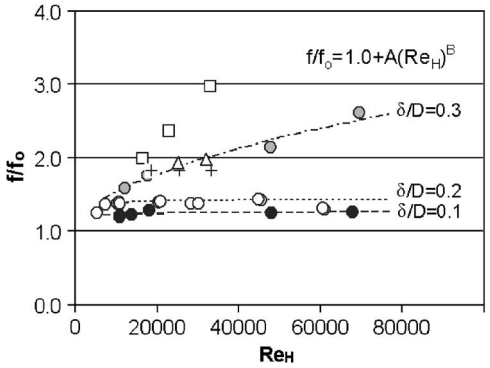

Fig. 17 Dimpled channel friction factor ratios as dependent on Reynolds number Re_H, including comparisons to correlation equations for $\delta/D=0.1$ and $H/D=1$ from the present study, for $\delta/D=0.2$ from Mahmood et al. [1], and for $\delta/D=0.3$ from Burgess et al. [2]. Results from Chyu et al. [12] and Moon et al. [14] are included for comparison. Symbols are defined in Fig. 12.

that the equation shows no dependence on Reynolds number Re_H, inlet turbulence intensity level Tu, or ratio of channel height H/D. This is because no H/D effects are considered in the present study (although the dependence of $\overline{\overline{Nu}}/Nu_o$ on H/D is very weak) and because $\overline{\overline{Nu}}/Nu_o$ is nearly constant (within its experimental uncertainty) as either Re_H or Tu is varied. This is partially illustrated by the results shown in Fig. 12.

To account for the effects of dimple depth and Reynolds number on friction factor ratios in a channel with dimples on one surface, the following correlation equation is recommended:

$$f/f_o = 1.0 + A(Re_H)^B \tag{3}$$

where $A=0.131$, $B=0.0585$ for $\delta/D=0.1$; $A=0.220$, $B=0.0585$ for $\delta/D=0.2$; and $A=0.0038$, $B=0.537$ for $\delta/D=0.3$. This equation is valid for $Re_H=5000-80{,}000$, $H/D=1.0$, $\delta/D=0.1-0.3$, $Tu=0.033$, and a ratio of inlet stagnation temperature to local surface temperature equal to 0.92–1.00. Note that Eq. (3) shows no dependence on the ratio of channel height H/D. This is because no H/D effects are considered in the present study (although the dependence of f/f_o on H/D is generally very weak). This agreement between Eq. (3) and the present experimental data is shown in Fig. 17.

Summary and Conclusions

Experimental results measured on dimpled test surfaces placed on one of the widest walls of different channels (each with an aspect ratio of 8) are given for Reynolds numbers from 9540 to 74,800, an inlet turbulence intensity level of 0.033, and a ratio of air inlet stagnation temperature to surface temperature of ~0.94. These include friction factors, local Nusselt numbers, spatially-averaged Nusselt numbers, and globally-averaged Nusselt numbers. The ratio of channel height to dimple print diameter is 1.00, and the ratios of dimple depth to dimple print diameter δ/D are 0.1, 0.2, and 0.3 to provide information on the influences of dimple depth. The data for all three δ/D values are all obtained in channels with the same dimple print diameter, same dimple spacing, same channel aspect ratio, same H/D ratio, and same type of thermal boundary condition.

At all Reynolds numbers considered, local and spatially-resolved Nusselt number augmentations increase as the ratio of dimple depth to dimple print diameter δ/D increases from 0.1 to 0.3 (and all other experimental and geometric parameters are held constant). This is because the deeper dimples produce (i) increases in the strengths and intensity of vortices and associated secondary flows ejected from the dimples, as well as (ii) increases in the magnitudes of three-dimensional turbulence production and turbulence transport. The effects of these phenomena are especially apparent in local Nusselt number ratio distributions measured just inside of the dimples and just downstream of the downstream edges of the dimples. Here, two local maxima are evident in local Nusselt number ratios when $\delta/D=0.3$, compared to a single maximum value when $\delta/D=0.2$ and when $\delta/D=0.1$.

Nusselt number ratios and friction factor ratios are also presented to illustrate the effects of Reynolds number and streamwise development for $\delta/D=0.1$ dimples. Significant local Nusselt number ratio variations are observed at different streamwise locations, whereas variations with the Reynolds number are mostly apparent on flat surfaces just downstream of individual dimples.

Acknowledgments

The work presented in this paper was conducted under the sponsorship of Pratt & Whitney-Canada Corp., Agreement 013800, PO 4500314218. Mr. Tim Blaskovich and Dr. Toufik Djeridane were project monitors. Mr. Qiang Zhang is acknowledged for his efforts in measuring inlet turbulence intensity levels.

Nomenclature

D = dimple print diameter
D_h = channel hydraulic diameter
f = channel friction factor
f_o = baseline friction factor measured in a channel with smooth surfaces and no dimples
H = channel height
h = heat transfer coefficient based on flat projected surface area, $\dot{q}_{o''}/(Tw-Tmx)$
k = thermal conductivity
Nu = local Nusselt number, hD_h/k
Nu_o = baseline Nusselt number in a channel with smooth surfaces and no dimples
p = streamwise spacing of adjacent dimple rows
Pr = molecular Prandtl number
$\dot{q}_o''$ = surface heat flux based on flat projected surface area
Re_H = Reynolds number based on channel height, $H\overline{V}/\nu$
Re_{Dh} = Reynolds number based on channel hydraulic diameter, $D_h\overline{V}/\nu$
s = streamwise spacing of every other dimple row
T = temperature
Tu = longitudinal turbulence intensity at inlet of channel test section
$\overline{V}$ = streamwise bulk velocity averaged over the channel cross section
X = streamwise coordinate measured from test section inlet
Y = normal coordinate measured from test surface dimple horizon
Z = spanwise coordinate measured from test section centerline

Greek Symbols

ν = kinematic viscosity
δ = dimple depth
ρ_a = static density

Subscripts

mx = time-averaged, local mixed-mean value
w = local wall value

Superscripts

$-$ = spatially averaged value or time-averaged value
$=$ = globally averaged value

References

[1] Mahmood, G. I., Hill, M. L., Nelson, D. L., Ligrani, P. M., Moon, H.-K., and Glezer, B., 2001, "Local Heat Transfer and Flow Structure on and Above a Dimpled Surface in a Channel," ASME J. Turbomach., **123**(1), pp. 115–123.

[2] Burgess, N. K., Oliveira, M. M., and Ligrani, P. M., 2003, "Nusselt Number Behavior on Deep Dimpled Surfaces Within a Channel," ASME J. Heat Transfer, **125**(1), pp. 11–18.

[3] Mahmood, G. I., and Ligrani, P. M., 2002, "Heat Transfer in a Dimpled Channel: Combined Influences of Aspect Ratio, Temperature Ratio, Reynolds Number, and Flow Structure," Int. J. Heat Mass Transfer, **45**(10), pp. 2011–2020.

[4] Mahmood, G. I., Sabbagh, M. Z., and Ligrani, P. M., 2001, "Heat Transfer in a Channel With Dimples and Protrusions on Opposite Walls," J. Thermophys. Heat Transfer, **15**(3), pp. 275–283.

[5] Ligrani, P. M., Mahmood, G. I., Harrison, J. L., Clayton, C. M., and Nelson, D. L., 2001, "Flow Structure and Local Nusselt Number Variations in a Channel With Dimples and Protrusions on Opposite Walls," Int. J. Heat Mass Transfer, **44**(23), pp. 4413–4425.

[6] Afanasyev, V. N., Chudnovsky, Y. P., Leontiev, A. I., and Roganov, P. S., 1993, "Turbulent Flow Friction and Heat Transfer Characteristics for Spherical Cavities on a Flat Plate," Exp. Therm. Fluid Sci., **7**, pp. 1–8.

[7] Belen'kiy, M. Y., Gotovskiy, M. A., Lekakh, B. M., Fokin, B. S., and Dolgushin, K. S., 1994, "Heat Transfer Augmentation Using Surfaces Formed by a System of Spherical Cavities," Heat Transfer Res., **25**(2), pp. 196–203.

[8] Kesarev, V. S., and Kozlov, A. P., 1994, "Convective Heat Transfer in Turbulized Flow Past a Hemispherical Cavity," Heat Transfer Res., **25**(2), pp. 156–160.

[9] Terekhov, V. I., Kalinina, S. V., and Mshvidobadze, Y. M., 1995, "Flow Structure and Heat Transfer on a Surface With a Unit Hole Depression," Russ. J. Eng. Thermophys., **5**, pp. 11–33.

[10] Schukin, A. V., Koslov, A. P., and Agachev, R. S., 1995, "Study and Application of Hemispherical Cavities For Surface Heat Transfer Augmentation," *ASME 40th Int. Gas Turbine and Aeroengine Congress and Exposition*, Houston, ASME, New York, ASME Paper No. 95-GT-59.

[11] Gortyshov, Y. F., Popov, I. A., Amirkhanov, R. D., and Gulitsky, K. E., 1998, "Studies of Hydrodynamics and Heat Exchange in Channels With Various Types of Intensifiers," Proc. of 11th Int. Heat Transfer Congress, Vol. 6, pp. 83–88.

[12] Chyu, M. K., Yu, Y., Ding, H., Downs, J. P., and Soechting, F. O., 1997, "Concavity Enhanced Heat Transfer in an Internal Cooling Passage," *ASME 42nd International Gas Turbine and Aeroengine Congress and Exposition*, Orlando, ASME, New York, ASME Paper No. 97-GT-437.

[13] Lin, Y.-L., Shih, T. I.-P., and Chyu, M. K., 1999, "Computations of Flow and Heat Transfer in a Channel With Rows of Hemispherical Cavities," *ASME 44th International Gas Turbine and Aeroengine Congress and Exposition*, Indianapolis, ASME, New York, ASME Paper No. 99-GT-263.

[14] Moon, H.-K., O'Connell, T., and Glezer, B., 1999, "Channel Height Effect on Heat Transfer and Friction in a Dimpled Passage," *ASME 44th International Gas Turbine and Aeroengine Congress and Exposition*, Indianapolis, ASME, New York, ASME Paper No. 99-GT-163.

[15] Terekhov, V. I., and Kalinina, S. V., 2002, "Flow and Heat Transfer in a Single Spherical Cavity: State of the Problem and Unanswered Questions (Review)," Thermophys. Aeromech., **9**(4), pp. 475–496.

[16] Isaev, S. A., Leontiev, A. I., Kudryavtsev, N. A., and Pushnyi, I. A., 2003, "The Effect of Rearrangement of the Vortex Structure on Heat Transfer Under Conditions of Increasing Depth of a Spherical Dimple in the Wall of a Narrow Channel," Teplofiz. Vys. Temp., **41**(2), pp. 268–272.

[17] Ligrani, P. M., Harrison, J. L., Mahmood, G. I., and Hill, M. L., 2001, "Flow Structure Due to Dimple Depressions on a Channel Surface," Phys. Fluids, **13**(11), pp. 3442–3451.

[18] Ligrani, P. M., Singer, B. A., and Baun, L. R., 1989, "Miniature Five-Hole Pressure Probe for Measurement of Three Mean Velocity Components in Low Speed Flow," J. Phys. E, **22**(10), pp. 868–876.

[19] Ligrani, P. M., Singer, B. A., and Baun, L. R., 1989, "Spatial Resolution and Downwash Velocity Corrections for Multiple-Hole Pressure Probes in Complex Flows," Exp. Fluids, **7**(6), pp. 424–426.

[20] Ligrani, P. M., 2000, "Flow Visualization and Flow Tracking as Applied to Turbine Components in Gas Turbine Engines," Meas. Sci. Technol., **11**(7), pp. 992–1006.

[21] Kline, S. J., and McClintock, F. A., 1953, "Describing Uncertainties in Single Sample Experiments," Mech. Eng. (Am. Soc. Mech. Eng.), **75**, pp. 3–8.

[22] Moffat, R. J., 1988, "Describing the Uncertainties in Experimental Results," Exp. Therm. Fluid Sci., **1**(1), pp. 3–17.

[23] Lienhard, J. H., 1987, *A Heat Transfer Textbook*, 2nd ed., Prentice-Hall, Englewood Cliffs, NJ, pp. 338–343.

[24] Ligrani, P. M., Oliveira, M. M., and Blaskovich, T., 2003, "Comparison of Heat Transfer Augmentation Techniques," AIAA J., **41**(3), pp. 337–362.

Influences of Sign of Surface Tension Coefficient on Turbulent Weld Pool Convection in a Gas Tungsten Arc Welding (GTAW) Process: A Comparative Study

Nilanjan Chakraborty
e-mail: nc246@eng.cam.ac.uk
CFD Laboratory, Engineering Department,
Cambridge University, Trumpington Street,
Cambridge, CB2 1PZ, United Kingdom

Suman Chakraborty[1]
Member, ASME
e-mail: suman@mech.iitkgp.ernet.in
Department of Mechanical Engineering, Indian
Institute of Technology, Kharagpur 721302, India

The effects of positive and negative surface tension coefficients ($\partial\sigma_{sur}/\partial T$) *on both laminar and turbulent weld pool convection are numerically studied for a typical gas tungsten arc welding (GTAW) process. Three-dimensional turbulent weld pool convection in a pool is simulated using a suitably modified high Reynolds number k-ε model in order to account for the morphology of an evolving solid-liquid interface. Key effects of the sign of surface tension coefficient* ($\partial\sigma_{sur}/\partial T$) *on the turbulent transport in a GTAW process are highlighted by comparing the turbulent simulation results with the corresponding ones from a laminar model, keeping all other process parameters unaltered. A scaling analysis is also performed in order to obtain order-of-magnitude estimates of weld pool penetration for both positive and negative surface tension coefficients. The scaling analysis predictions are in good agreement with the numerical results, in an order-of-magnitude sense.* [DOI: 10.1115/1.1928913]

Keywords: Surface Tension Coefficient, Gas Tungsten Arc Welding (GTAW), Turbulent Convection, Molten Pool, Marangoni Convection

1 Introduction

Arc welding is one of the most popular joining techniques, in which the workpieces are locally melted by an intense heat source. The microstructural constitution of the subsequent arc-welded joint is strongly dependent on the thermal history. However, in practical cases, experimental studies regarding flow visualization inside the weld pools are virtually ruled out due to the small size of the weld pool, opacity of the molten metal, and light radiation from electric arc. Therefore, it is extremely important to develop appropriate mathematical models for weld pool convection, in order to understand fundamental physics of weld pool transport, both qualitatively and quantitatively.

A vast body of literature is available on weld pool transport containing several mathematical models of relevance [1–5]. Joshi et al. [6], for the first time, reported surface oscillations under high power welding applications, which could eventually lead to turbulence. Such observations were consistent with earlier findings of Athey [7]. Mundra et al. [8] addressed the effects of variable viscosity on laser welding, however, viscosity variation due to turbulence was predetermined and was not a part of the solution procedure. Chao and Szekely [9] and Hong et al. [10] have modeled stationary turbulent GTAW weld pools using *k-ε* models. However, to date, the treatment of dynamic evolution of solid-liquid interface by proper wall conditions with the simultaneous solution of primitive variables has rarely been addressed, in the context of turbulent transport in a GTAW process. Chakraborty et al. [11] have proposed for the first time a two-dimensional mathematical model in order to address the turbulent transport in a GTAW process simulation, in which the dynamic evolution of irregular morphology of the solid-liquid interface has been addressed by employing modified wall conditions for solid-liquid phase boundaries in the framework of a standard *k-ε* model. Recently, Chakraborty et al. [12] have extended the above model successfully to analzse three-dimensional turbulent transport in GTAW applications.

The aim of the present work is to study the effects of surface tension coefficient ($\partial\sigma_{sur}/\partial T$) sign in isolation on both laminar and turbulent weld pool transport, and on the associated weld pool morphology for similar welding parameters for a GTAW process. The effects of surface tension coefficient sign on weld pool transport cannot be isolated in realistic experimental situations and therefore provide no scope for experimental validation. The present study can be treated as a set of methodically conducted numerical experiments, directed towards understanding the effects of sign of the surface tension coefficient on the overall weld pool dynamics, under turbulent flow conditions. Practical implications of this investigation lie in the fact that if surface-active elements like sulphur and manganese are present in steel, then the surface tension increases with an increase in temperature, indicating a positive surface tension coefficient ($\partial\sigma_{sur}/\partial T$). In the absence of surface-active elements, the surface tension coefficient for steel is negative. In arc welding processes, the large temperature variation on the top surface of the molten pool results in a considerable surface tension differential, which, in turn, initiates the convection process in the molten pool. Since this convection governs the temperature distribution and weld pool morphology, including weld pool shape and the penetration, it is extremely important to investigate the effects of sign of surface tension coefficient on weld pool transport.

In the present study, a modified enthalpy porosity technique [13] is used to account for the solid-liquid phase change aspects of the problem. Effects of the sign of $\partial\sigma_{sur}/\partial T$ on the turbulent transport are highlighted by comparing the turbulent simulation results with the corresponding ones from a laminar model, keeping all other process parameters unaltered. A scaling analysis is also per-

[1]Corresponding author.

Contributed by the Heat Transfer Division for publication in the JOURNAL OF HEAT TRANSFER. Manuscript received August 3, 2004; Final manuscript received March 3, 2005. Review conducted by: Ranga Pitchumani.

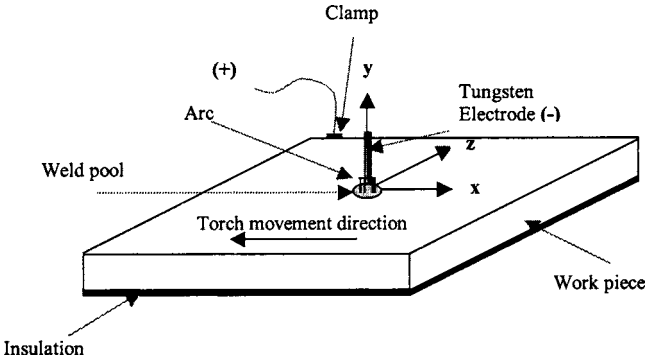

Fig. 1 Schematic diagram of a GTAW process

formed to obtain order-of-magnitude estimates of weld pool penetration, for both positive and negative surface tension coefficients.

2 Mathematical Formulation

In the GTAW welding process, the heat source in the form of an electric arc is created between a nonconsumable tungsten electrode and the workpiece in an inert gas atmosphere. A schematic diagram of the process is shown in Fig. 1. The electrode is moving with a constant speed (U_{scan}) in the negative x direction, as shown in the figure. The arc power received by the workpiece is specified by arc efficiency η, following Dutta et al. [14]. The available heat to the workpiece is related to the arc power input as $q=\eta Q = \eta VI$, where V and I are arc voltage and arc current, respectively. As the workpiece melts, the surface tension differential at the top surface initiates the fluid flow, which is responsible for the thermo-solutal transport of the inside the molten pool. A generalized form of governing transport equations, for each primitive variable ϕ, in a stationary coordinate system (x^*,y), can be written as

$$\frac{\partial(\rho\overline{\phi})}{\partial t}+\frac{\partial(\rho\overline{u^*}\,\overline{\phi})}{\partial x^*}+\frac{\partial(\rho\overline{v}\,\overline{\phi})}{\partial y}+\frac{\partial(\rho\overline{w}\,\overline{\phi})}{\partial z}=\frac{\partial}{\partial x^*}\left(\Gamma\frac{\partial\overline{\phi}}{\partial x^*}\right)+\frac{\partial}{\partial y}\left(\Gamma\frac{\partial\overline{\phi}}{\partial y}\right)+\frac{\partial}{\partial z}\left(\Gamma\frac{\partial\overline{\phi}}{\partial z}\right)+S \tag{1}$$

where Γ is a generalized diffusion coefficient and S is a source term. However, the transport phenomena occurring inside the weld pool can be conveniently studied with respect to a coordinate system that translates with the arc heat source. Accordingly, the following coordinate transformation is introduced:

$$x = x^* - (-U_{scan})t \tag{2}$$

where U_{scan} is the magnitude of welding torch scanning speed and x, y, z are coordinates in a frame moving with the torch. The negative sign in front of U_{scan} in Eq. (2) indicates that the scanning is performed in the negative x^* direction. Henceforth, we will follow the following tensorial notation for the description of conservation equation:

$$x_1 = x; \quad x_2 = y \text{ and } x_3 = z \tag{3}$$

Carrying out the transformation described in Eq. (3) we obtain

$$\partial(\rho\overline{\phi})/\partial t + \partial(\rho\overline{u_j}\,\overline{\phi})/\partial x_j = \partial[\Gamma(\partial\overline{\phi}/\partial x_j)]/\partial x_j + S - \partial(\rho U_{scan}\overline{\phi})/\partial x_1 \tag{4}$$

where $\overline{\phi}$ represents the mean component of a primitive variable ϕ in the context of Reynolds averaging. The fluctuating component of a primitive variable ϕ is represented by ϕ'. For different ϕ's, the governing equations in the moving coordinate system assume the following forms:

2.1 Conservation of Mass. In the present formulation the working fluid is assumed to be incompressible whose density ρ is a priori prescribed. Under this condition the mass conservation equation takes the following form:

$$\partial\overline{u_i}/\partial x_i = 0; \quad \partial u_i'/\partial x_i = 0 \tag{5}$$

2.2 Conservation of Linear Momentum. The equivalent single-phase Navier-Stokes equations are given by

$$\frac{\partial(\rho\overline{u_i})}{\partial t}+\rho\overline{u_j}\frac{\partial\overline{u_i}}{\partial x_j}=-\frac{\partial\overline{p}}{\partial x_i}+(\vec{J}\times\vec{B})_i+\frac{\partial}{\partial x_j}\left(\mu\frac{\partial\overline{u_i}}{\partial x_j}\right)-\frac{\partial(\rho\overline{u_i'u_i'})}{\partial x_j}-\rho U_{\text{scan}}\frac{\partial\overline{u_i}}{\partial x_1}+\rho g\,\delta_{i2}\beta(\overline{T}-T_{ref})+\overline{S_i} \tag{6a}$$

where g is the acceleration due to gravity and T_{ref} is the reference temperature which is taken to be equal to the melting temperature, T_m. The source term $\overline{S_i}$ in Eq. (6*a*) originates from the phase changing part between completely solid and liquid phase, which offers resistance towards fluid flow in that region. In a single-domain fixed-grid enthalpy-porosity formulation, this resistance can be conveniently formulated using Darcy's model for porous media in conjunction with the Cozeny-Karman relationship as done by Brent et al. [13]. In Eq. (6*a*), $\overline{S_i}$ is given as

$$\overline{S_i} = -C(1-f_l^2)\overline{u_i}/(1+f_l^3) \tag{6b}$$

where the liquid fraction $f_l=\Delta H/L$ in a given control volume is taken to be the effective porosity, with ΔH representing the latent enthalpy of a control volume and L denoting the latent heat of fusion. In Eq. (6*b*), C is a large number ($\sim 10^8$) and b is a small number ($\sim 10^{-30}$) to avoid division by zero. This formulation ensures that the velocity undergoes a smooth transition from a zero value in completely solid phase to a finite value in the fully liquid phase. The details of formulation of the above term can be found in Brent et al. [13]. The term $-\partial(\rho\overline{u_i'u_j'})/\partial x_j$ is the Reynolds stress contribution, which is modeled in accordance with the classical k-ε model. The Lorentz force term, $\vec{J}\times\vec{B}$, is evaluated by solving Maxwell's equations, following the procedure outlined by Dutta et al. [4].

2.3 Conservation of Energy. The single-phase energy transport equation for turbulent flow is given by

$$\frac{\partial(\rho\overline{T})}{\partial t}+\frac{\partial(\rho\overline{u_i}\,\overline{T})}{\partial x_i}=\frac{\partial}{\partial x_i}\left(\frac{K}{c}\frac{\partial\overline{T}}{\partial x_i}\right)-\frac{1}{c}\frac{\partial(\rho\Delta H)}{\partial t}-\frac{\partial}{\partial x_i}\left(\frac{\rho}{c}\overline{u_i}\Delta H\right)-\frac{\partial(\rho\overline{u_i'T'})}{\partial x_i}-\rho U_{scan}\frac{\partial\overline{T}}{\partial x_1} \tag{7}$$

where c is the specific heat, K is the thermal conductivity of the material, and ΔH is the latent enthalpy of the computational cell under consideration. The latent heat content of a control volume ΔH is given by

$$\Delta H = L \text{ for } \overline{T} > T_l, \quad \Delta H = f_l L \text{ for } T_l > \overline{T} \geqslant T_s, \quad \text{and } \Delta H = 0 \text{ for } \overline{T} < T_s \tag{8}$$

where T_l and T_s are the liquidus and solidus temperatures of phase change, respectively. In the present study, for simplicity, phase change is assumed to be isothermal ($T_s=T_l$), following previous studies [4–6,11,12,14] reported in the literature, pertinent to the present application.

2.4 Modeling of Reynolds Stress Terms ($-\overline{\rho u_i' u_j'}$). In the present analysis, the Reynolds stress terms appearing in Eq. (6*a*) are modeled using eddy viscosity:

$$-\rho\overline{u_i' u_j'} = \mu_t(\partial\overline{u_i}/\partial x_j + \partial\overline{u_j}/\partial x_i) - (2/3)\delta_{ij}\rho k \text{ where } \mu_t = \sqrt{f_l} C_\mu \rho k^2/\varepsilon \tag{9}$$

In Eq. (9), $C_\mu = 0.09$. In the present study the factor $\sqrt{f_l}$ is retained in the μ_t expression following Shyy et al. [15], so that the eddy viscosity undergoes a smooth transition from completely solid phase to a fully molten (liquid) phase.

2.5 Modeling of Turbulent Heat Fluxes ($-\overline{u_j' T'}$). Following the same closure technique used for the Reynolds stresses, the turbulent heat fluxes (Reynolds heat fluxes) appearing in Eq. (7) can be written as

$$-\overline{u_j' T'} = \alpha_t \partial\overline{T}/\partial x_j; \quad \alpha_t = \mu_t/\rho\sigma_t \tag{10}$$

where σ_t is the turbulent Prandtl number given by $\sigma_t = 0.9$.

2.6 Governing Equations for k and ε. The governing equations for k and ε in the present context can be written as

$$\rho\frac{\partial k}{\partial t} + \rho\overline{u_j}\frac{\partial k}{\partial x_j} = \frac{\partial}{\partial x_j}\left[\left(\mu + \frac{\mu_t}{\sigma_k}\right)\frac{\partial k}{\partial x_j}\right] + \mu_t\left(\frac{\partial\overline{u_i}}{\partial x_j} + \frac{\partial\overline{u_j}}{\partial x_i}\right)\frac{\partial\overline{u_i}}{\partial x_j} - \frac{\mu_t}{\sigma_t} g\beta\frac{\partial\overline{T}}{\partial x_2} - \rho\varepsilon - \rho U_{scan}\frac{\partial k}{\partial x_1} \tag{11}$$

$$\rho\frac{\partial \varepsilon}{\partial t} + \rho\overline{u_j}\frac{\partial \varepsilon}{\partial x_j} = \frac{\partial}{\partial x_j}\left[\left(\mu + \frac{\mu_t}{\sigma_\varepsilon}\right)\frac{\partial \varepsilon}{\partial x_j}\right] - C_{\varepsilon 2}\rho\frac{\varepsilon^2}{k} - \rho U_{scan}\frac{\partial \varepsilon}{\partial x_1} + C_{\varepsilon 1}\mu_t\left(\frac{\partial\overline{u_i}}{\partial x_j} + \frac{\partial\overline{u_j}}{\partial x_i}\right)\frac{\partial\overline{u_i}}{\partial x_j}\frac{\varepsilon}{k} - C_{\varepsilon 1}\frac{\mu_t}{\sigma_k} g\beta\frac{\partial\overline{T}}{\partial x_2}\frac{\varepsilon}{k} \tag{12}$$

where $C_{\varepsilon 1} = 1.44$, $C_{\varepsilon 2} = 1.92$, $\sigma_k = 1.0$, and $\sigma_\varepsilon = 1.3$.

2.7 Boundary Conditions. In the present case, a rectangular box-shaped workpiece is taken to be the computational domain. The boundary conditions on the faces of the workpiece are described below:

2.7.1 Top Surface. At the top surface, the incident heat flux is assumed to follow a Gaussian distribution, along with convective and radiative heat losses from the workpiece [4]:

$$-K\partial\overline{T}/\partial y = -q''(r) + h(\overline{T} - T_\infty) + \varepsilon_r\sigma_{rad}(\overline{T}^4 - T_\infty^4) \tag{13}$$

In Eq. (13) $q''(r)$ is the net arc heat flux distributed in a Gaussian manner with a radius of heat input distribution r_q as $q''(r) = (\eta Q/\pi r_q^2)\exp(-r^2/r_q^2)$. Considering a flat top pool surface following previous studies [4–6,11,12,14], the free surface shear balance between viscous force and surface tension gives rise to

$$\mu(\partial\overline{u}/\partial y) = (\partial\sigma_{sur}/\partial T)(\partial\overline{T}/\partial x); \quad \mu(\partial\overline{w}/\partial y) = (\partial\sigma_{sur}/\partial T)(\partial\overline{T}/\partial z) \tag{14}$$

where σ_{sur} is the surface tension. Further, for a flat free top surface after Dutta et al. [4], we have

$$\overline{v} = 0 \tag{15a}$$

The boundary conditions for k and ε, for the free surface, are given by [16]

$$\partial k/\partial y = 0; \quad \partial\varepsilon/\partial y = 0 \tag{15b}$$

It can be noted here that in the present study the clamp and electrode are considered to be anode and cathode, respectively. It is also assumed that all surfaces other than the top surface are electrically insulated, except for the location of clamp. Under this condition, incident current density J_n profile takes the following form on the top surface [4]:

Table 1 Table of physical properties and welding parameters.

Physical property / parameter	VALUE
Volumetric expansion coefficient (β)	0.00001 K^{-1}
Melting temperature (T_m)	1500^0C
Latent heat of fusion (L)	247196 J/kg
Density (ρ)	7800 kg/m^3
Thermal conductivity (K)	35 W/m.K
Specific heat (c)	753 J/kg
Molecular viscosity (μ)	0.006 Pa.s
Arc Voltage (V)	18.0 V
Arc Current (I)	200 Amp
Arc Efficiency (η)	90%
Scanning speed (U_{scan})	8.89 mm/s
Radius of heat flux distribution (r_q)	0.0035m
Arc radius (radius current outflow) (r_j)	0.0032m

$$J_n = (I/\pi r_j^2)\exp(-r^2/r_j^2) \tag{15c}$$

where n is the normal direction on the top surface and r_j is the electric arc radius. The condition at the clamp is such that the total current inflow at the clamp is equal to the total current outflow at the top surface [4].

2.7.2 Side and Bottom Faces. The bottom face is considered to be insulated, while the four side faces are subjected to convective heat transfer boundary condition [4]:

$$-K\partial\overline{T}/\partial n|_{wall} = h(\overline{T}|_{wall} - T_\infty) \tag{16}$$

where n is the outward normal direction of the surface concerned.

2.7.3 Solid/Liquid Interface. According to the enthalpy-porosity formulation, it is not needed to track the interface explicitly, since the interface comes out as a natural outcome of the solution procedure itself. However, the evolving interface locations are important for solution of k and ε equations, since proper values of k and ε need to be specified at the near wall points. This is done with the help of standard wall functions [17] used for the high Reynolds number k-ε model. The dissipation rate of turbulent kinetic energy at the grid point in the liquid phase next to solid-liquid interface is specified as $\varepsilon = (C_\mu^{3/4}k^{3/2}/\kappa\Delta n)$ where κ is von Karman's constant ($\kappa = 0.4$) and Δn is the normal distance of the concerned grid point from the wall. Furthermore, the conditions $k = 0$ and $\partial\varepsilon/\partial n = 0$ are used to specify k and ε at the solid/liquid interface. Eddy diffusivities at the near wall points are prescribed using well-known log-law as indicated by Durbin and Petterson Reif [17].

3 Numerical Implementation

The governing equations for the electromagnetic force field are first solved numerically in order to calculate the Lorentz force field after Dutta et al. [4]. The calculated Lorentz force field is subsequently used as a body force distribution in the Navier-Stokes equations (Eq. (6*a*)). The governing equations are solved simultaneously using a pressure-based finite volume technique according to the SIMPLER algorithm [18]. The latent heat of each control volume is updated using the temperature field predicted from the energy equation, following Brent et al. [13]. For the purpose of the present investigation, numerical simulations are performed for the case of a typical GTAW situation with steel as the base material, the thermo-physical properties and processing parameters for which are listed in Table 1. For the case of a

positive value of surface tension coefficient, $\partial\sigma_{sur}/\partial T$ is taken to be $\partial\sigma_{sur}/\partial T = 5\times10^{-4}$ N/mK. For the negative surface tension coefficient case the value of $\partial\sigma_{sur}/\partial T$ is taken to be -5×10^{-4} N/mK.

3.1 Choice of Grid Size. The choice of grid size is determined by two criteria, as follows:

3.1.1 Criterion 1. In order to obtain an estimate of viscous boundary layer thickness (δ_v) at the top surface, an appropriate scaling analysis is performed with respect to the stationary molten pool for the laminar case. Following Dutta et al. [4] the boundary layer thickness δ_v can be estimated as

$$\mu U_s/\delta_v \sim |\partial\sigma_{sur}/\partial T|\Delta T/R \tag{17}$$

where U_s is the characteristic surface velocity and ΔT is the characteristic temperature difference between the locations corresponding to the bottom of the electrode and phase changing interface which can be roughly scaled as $\Delta T \sim L/c$. In expression (17), R is the radius of molten pool, which can be taken as $R \sim r_q$. Using the process parameters selected for this study, the velocity boundary layer thickness is estimated to be of the order of 6×10^{-5} m. Accordingly, in order to resolve the flow within the surface tension driven boundary layer, typically five grid points are accommodated inside it.

3.1.2 Criterion 2. In order to specify the correct eddy diffusivity values near the wall, it is necessary to have a grid distribution such that the grid adjacent to the solid/liquid interface always falls within the logarithmic layer. This condition is mathematically given as

$$11.6 < x^+ = \rho C_\mu^{1/4} k^{1/2} x/\mu \leqslant 50 \tag{18}$$

The value of k is typically low as one approaches the wall, and the appropriate grid size, which meets the above requirement, is found by trial and error method using limiting values of k.

From the above two requirements, it is evident that the grid spacing in the y direction is principally governed by criterion 1, and that in the x and z directions is principally determined by criterion 2. Accordingly, the topmost grid spacing is chosen to be 2.7×10^{-7} m, which is followed by a grid spacing of 1.35×10^{-6} m up to a depth 6×10^{-5} m, followed by a spacing of 3.5×10^{-5} m. Thereafter a uniform grid spacing of 1×10^{-4} m is employed for most of the remaining part of the pool. Outside the molten pool, a nonuniform coarser grid is chosen. In the x direction, an optimized grid size near the wall is found to be 5×10^{-4} m. Away from the wall, the grid size increases gradually. A grid independence study confirms that a finer grid system does not alter the results appreciably. Based on the above findings, a $50\times33\times29$ grid system is used to discretize the working domain $50\times15\times40$ mm^3. It is assumed that the electrode is located at $x=25$ mm and $z=20$ mm, with respect to the moving reference frame. This location will henceforth be referred to as the center of the pool.

3.2 Choice of Time Step. Before melting, the heat transfer is within a conduction-dominated regime, for which a large time step (of about 0.05 s) is chosen so that melting temperature is reached within about five time steps. It is observed that a time step of 0.002 s leads towards monotonic convergence during this period of initial transience. Typically after about 1.5 s the effects of transience become small enough to allow a slightly bigger time step (about 0.005 s) to save the overall computational time. After 2.0 s, when the pool is sufficiently developed, time steps as high as 0.01 s could be implemented without any numerical oscillation. Finally, the computation is carried out up to 3.0 s to ensure that quasi-steady state has actually been attained.

3.3 Convergence Criteria. For a given time step, all the primitive variable ($\overline{u}, \overline{v}, \overline{w}, \overline{T}, k, \varepsilon$) values are checked after each iteration. Convergence is declared upon satisfying the following condition at each grid point:

$$|(\phi - \phi_{old})/\phi_{\max}| \leqslant 10^{-4} \tag{19}$$

where ϕ is the value of any primitive variable at a particular grid point at current iteration level, ϕ_{old} is the value of the same variable at the same grid point at the previous iteration level, and $\phi_{\max}$ is the maximum absolute value of the same over the entire domain.

4 Results and Discussion

A critical Reynolds number for onset of turbulence in the welding applications has not been reported in the existing literature. In absence of any well-established criterion, the present study makes use of a guideline presented by Bejan [19]. According to Bejan [19], a critical Reynolds number based on transverse direction length scale is of the order of 10^2. Accordingly, it is possible to define a Reynolds number as $\mathrm{Re}=\rho u_{\max} w/\mu$, where $u_{\max}$ is the maximum velocity in the direction perpendicular to the weld axis and w is the width of the weld pool. Using the scaling analysis outlined in Chakraborty et al. [5], $u_{\max}$ and w can be estimated from the given thermophysical properties and process parameters. For the present case, the critical Reynolds number is found to be in the order of 2000, which indicates that the molten metal flow within the pool is highly turbulent in nature. In the present study, simulations are carried out for both positive and negative surface tension coefficients, with turbulent transport (turbulent simulation) and without activating turbulence module (laminar simulation), for the same set of welding parameters. Effects of surface tension coefficient sign on overall weld pool morphology will be discussed first, based on laminar simulation results. This will be followed by the presentation of the corresponding turbulent simulation results, which reveals contrasting features of laminar and turbulent transport in a GTAW process. Finally, a scaling analysis will be presented in order to predict the weld pool penetration, for both positive and negative surface tension coefficient flows, in an order-of-magnitude sense.

4.1 Effect of Surface Tension Coefficient on Laminar Weld Pool Morphology. Temperature contours corresponding to the top view, and longitudinal and the cross-sectional mid-planes are presented in Figs. 2(*a*)–2(*c*), respectively, corresponding to a laminar simulation, taking a positive value of $\partial\sigma_{sur}/\partial T$. The velocity vector plots corresponding to the above-mentioned isotherms are presented in Figs. 3(*a*)–3(*c*), respectively. Since the surface tension increases with temperature in this case, velocity vectors on the surface are radially convergent [Fig. 3(*a*)]. As one approaches the center of the pool, the surface velocity increases as a result of high temperature gradients near the center of the pool. The longitudinal view of the velocity vector plot [Fig. 3(*b*)] indicates that molten metal streams from the leading edge and the trailing edge approach the maximum temperature location. Eventually, they turn in the downward direction and in the process heat is transported through advection, along with the thermal diffusion in the downward direction. From Fig. 2(*a*), it is evident that at the top surface the isotherms are elongated in the positive x direction as a result of electrode scanning. The fluid coming from the melting front in the scanning direction (negative x direction) is subjected to a higher acceleration than that experienced by the fluid approaching the trailing edge of the pool, since the scanning direction is subjected to higher temperature gradient, $\partial T/\partial x$. On the other hand, the horizontal component of the Lorentz force is radially converging [4,11], which opposes the molten metal flow from all the phase changing interfaces, once the pool center is crossed. A combined influence of all these factors determines the point at which the two hot fluid streams turn in downward direction, and finally results in a shift of maximum penetration location from the center

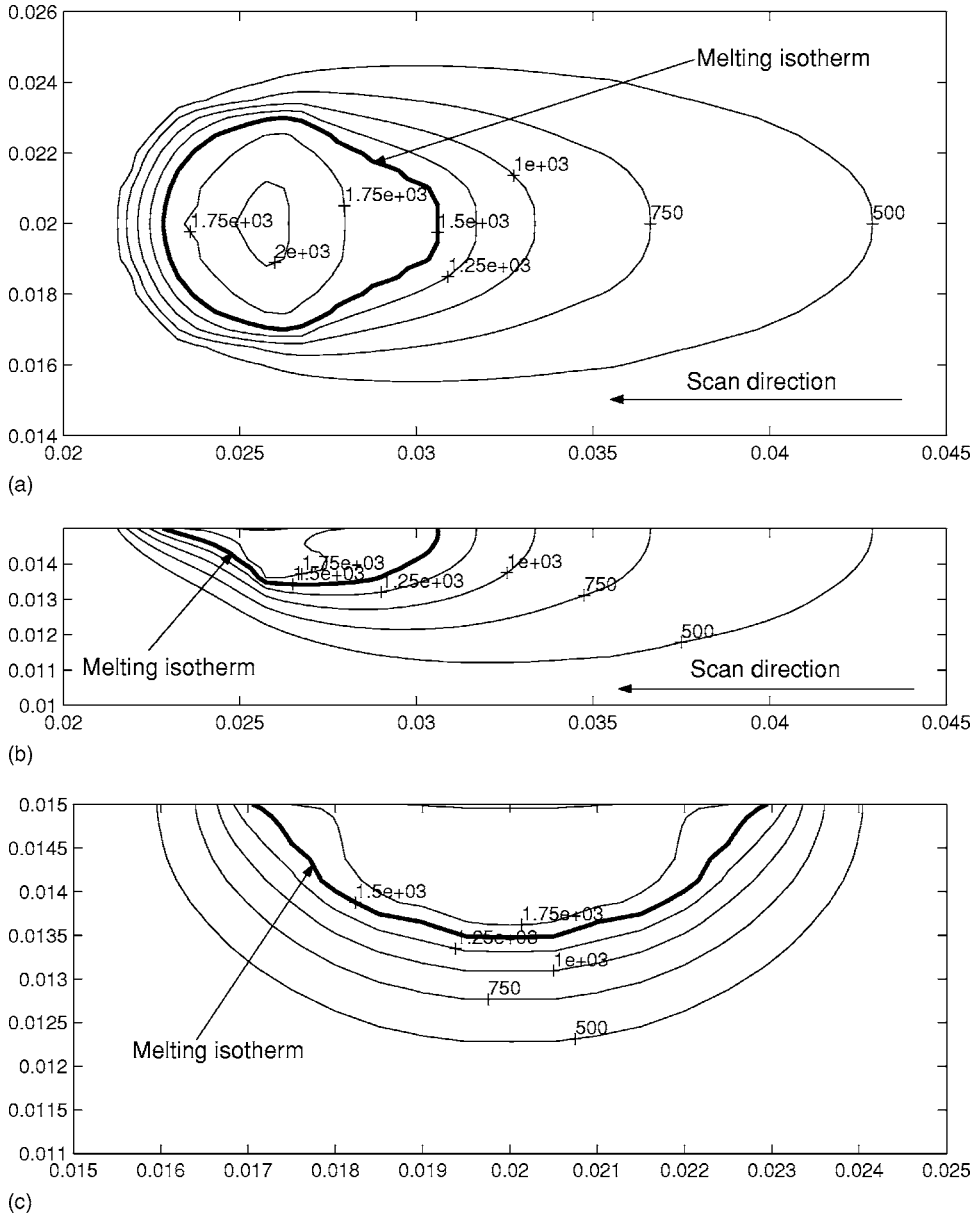

Fig. 2 Temperature distribution for the laminar case with U_{scan}=8.89 mm/s, power=3.6 kW, η=0.9, and $\partial\sigma_{sur}/\partial T$=0.0005 N/mK. (*a*) Top view, (*b*) longitudinal mid plane, and (*c*) cross-sectional mid plane. All dimensions are in meters; temperature labels are in degrees Celsius. The contour label 1500°C represents the melting temperature of the base metal.

of the pool as well as an asymmetry in the pool shape in the longitudinal direction. The cross-sectional view of the velocity vector plot [Fig. 3(*c*)] indicates that the centrally inward flow is symmetrical, and the fluid streams coming from the melting front turn in the downward direction at the center of the pool. This makes the cross-sectional view of the weld pool symmetrical, as apparent from Fig. 2(*c*).

A simulation, for the same set of welding parameters and thermophysical properties, but for a negative value of $\partial\sigma_{sur}/\partial T$, is subsequently carried out. Isotherms at the top surface, and at the longitudinal and the cross-sectional mid-planes for this case, are presented in Figs. 4(*a*)–4(*c*), respectively. It can be seen from Fig. 4(*a*) that the pool penetration does not vary appreciably in the longitudinal direction. The pool in this case is longer compared to the pool in the case of positive $\partial\sigma_{sur}/\partial T$ (see Figs. 2(*b*) and 4(*b*)). The maximum penetration in this case is attained towards the trailing edge side of the pool. The cross-sectional view at the mid-plane [Fig. 4(*c*)] suggests the pool is shallower in this case compared that in the case of a positive surface tension coefficient (see Fig. 2(*c*)). In this case isotherms are also stretched in the positive x direction because of electrode scanning. The velocity vector plots corresponding to Figs. 4(*a*)–4(*c*) are presented in Figs. 5(*a*)–5(*c*), respectively. It is evident from Fig. 5(*a*) that the surface velocities are radially divergent as the surface tension decreases with the increase in temperature. Due to radially divergent fluid flow from the hottest part of the molten pool, heat is transported primarily by the advection, in addition to the thermal diffusion process. Figures 5(*b*) and 5(*c*) suggest that the hot fluid stream from the center of the pool accelerates as it approaches the solid/liquid interface. The maximum velocity is attained towards the solid/liquid interface opposite to the direction of scanning, which is evident from Fig. 5(*b*).

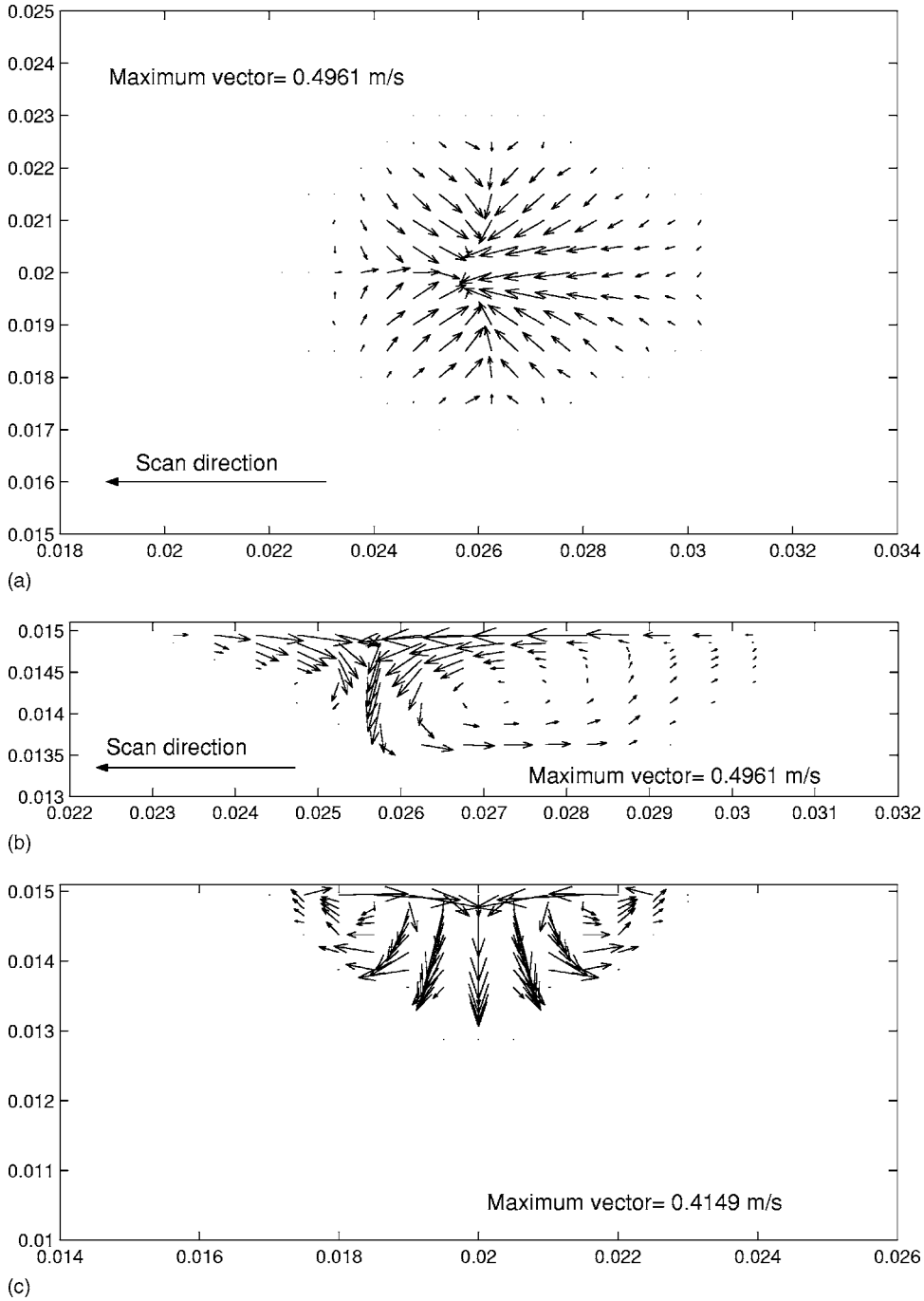

Fig. 3 Velocity distribution for the laminar case with U_{scan}=8.89 mm/s, power=3.6 kW, η=0.9, and $\partial\sigma_{sur}/\partial T$=0.0005 N/mK. (*a*) Top view, (*b*) longitudinal sectional mid plane, and (*c*) cross-sectional mid plane. All dimensions are in meters.

The contrasting behavior of laminar weld pool transport for the cases of opposite surface tension coefficient signs can be summarized as follows:

(a) The pool penetration is greater in the case of positive $\partial\sigma_{sur}/\partial T$ compared to that in the case of negative $\partial\sigma_{sur}/\partial T$. Downward convection of heat from the hot top surface in addition to the thermal diffusion transport gives rise to the greater pool penetration in the case of positive surface tension coefficient flows.
(b) In the case of negative surface tension coefficient flows, thermal diffusion is the principal mechanism determining the weld pool penetration. In this case, radially outward fluid flow aids the heat transport in the longitudinal and spanwise directions of the molten pool, which increases the length and width of the molten pool in comparison to the positive surface tension coefficient case.

4.2 Effects of Surface Tension Coefficient on Turbulent Weld Pool Morphology. Based on the fundamental understanding of the effects of surface tension coefficient ($\partial\sigma_{sur}/\partial T$) sign on laminar weld pool transport, the corresponding results from turbulent simulations will now be presented, which will reveal the

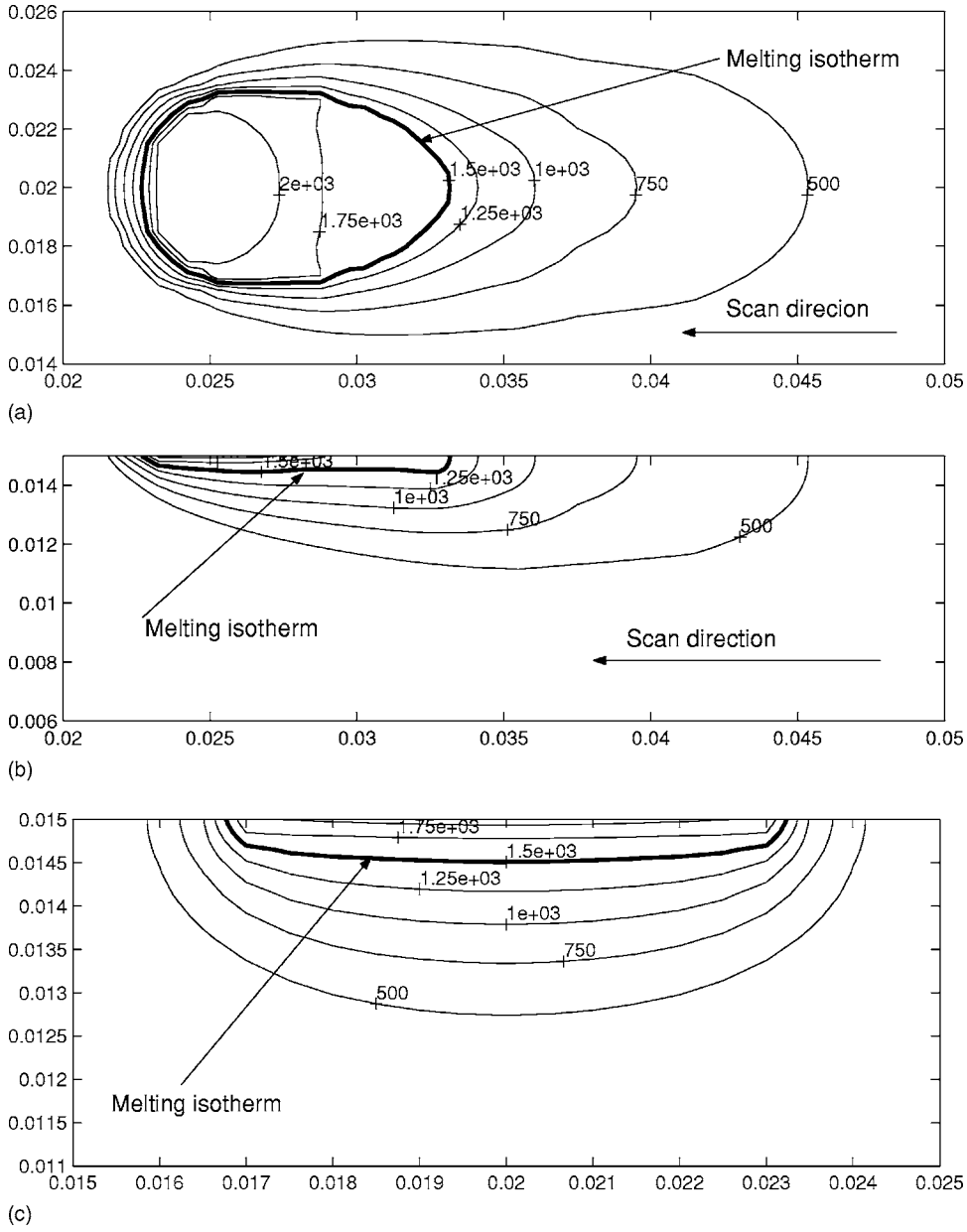

Fig. 4 Temperature distribution for the laminar case with U_{scan}=8.89 mm/s, power=3.6 kW, η=0.9, and $\partial\sigma_{sur}/\partial T$=−0.0005 N/mK. (*a*) Top view, (*b*) longitudinal mid plane, and (*c*) cross-sectional mid plane. All dimensions are in meters; temperature labels are in degrees Celsius. The contour label 1500°C represents the melting temperature of the base metal.

effects of turbulence on the weld pool convection. The isotherms for the turbulent simulation, for positive $\partial\sigma_{sur}/\partial T$, are presented in Figs. 6(*a*)–6(*c*), and the corresponding velocity vectors are presented in Figs. 7(*a*)–7(*c*). Comparing these with the results obtained from that corresponding to laminar simulation for the positive $\partial\sigma_{sur}/\partial T$ case, the following observations can be made:

1. The maximum pool penetration takes place further away from the pool center, as compared to the laminar case (see Figs. 2(*a*) and 6(*a*)). The maximum pool penetration in the case of a turbulent weld pool is found to be smaller than that corresponding to a laminar weld pool, which is evident from Figs. 2(*c*) and 6(*c*).
2. From the isotherms at the top surface it is evident that the isotherms in the turbulent case are more circular in nature as compared to those in the laminar case. This can be attributed to the fact that in the case of turbulent flow, the effect of diffusion is much more significant than that in the case of laminar convection. Since diffusion is isotropic in nature, the effect of directional asymmetry due to electrode scanning (caused by the term $-U_{scan}\partial\overline{T}/\partial x_1$) is partially nullified by the enhanced thermal diffusion in the turbulent weld pool. As a result of this, the directional effect of electrode scanning is significantly less in the turbulent pool [Fig. 6(*a*)] in comparison to that in the case of the corresponding laminar weld pool [Fig. 2(*a*)], which is also consistent with the previous studies [9,12].
3. In the case of turbulent flow, the maximum mean temperature obtained is smaller than the maximum temperature attained in the laminar simulation, due to an enhanced thermal diffusion in the pool. Because of the lower mean tempera-

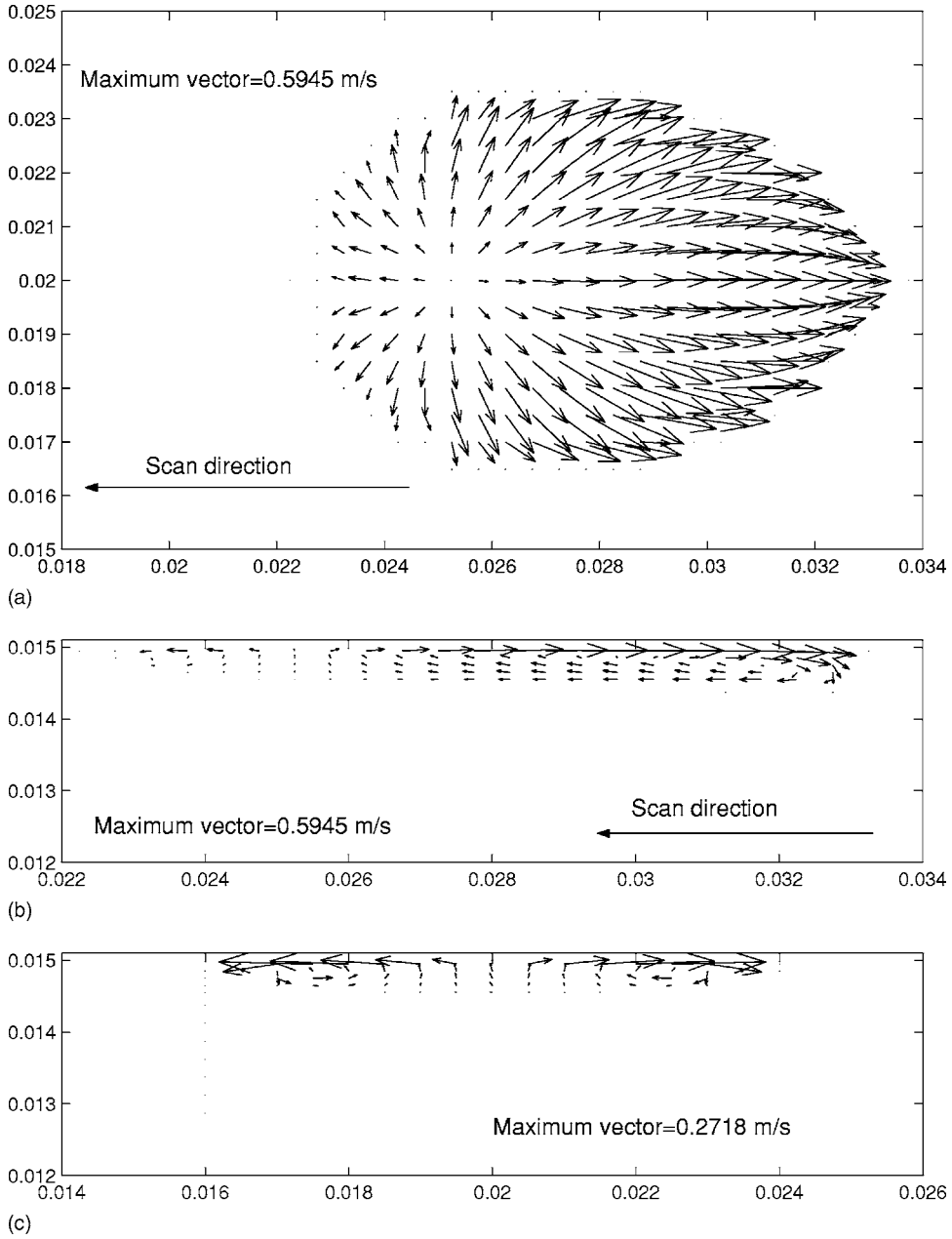

Fig. 5 Velocity distribution for the laminar case with U_{scan}=8.89 mm/s, power=3.6 kW, η=0.9, and $\partial\sigma_{sur}/\partial T$=−0.0005 N/mK. (*a*) Top view, (*b*) longitudinal sectional mid plane, and (*c*) cross-sectional mid plane. All dimensions are in meters.

ture gradients, the Marangoni convection from the trailing edge of the pool is weaker in the turbulent weld pool than that in the case of laminar convection. Consequently, the weak stream coming from the trailing edge of the pool in the turbulent case does not have enough momentum to counter the dynamic pressure imposed by the flow from the leading edge. In addition to this effect, the horizontal component of Lorentz force opposes the flow, once the center of the workpiece is crossed [4,11]. Consequently, the stream coming from trailing edge in the case of turbulent transport loses its inertia earlier and turns in the downward direction. Therefore, the toroidal circulation observed in the turbulent weld pool, extending up to the trailing edge, is smaller in size as compared to that in the corresponding laminar weld pool.

4. It is evident from Figs. 3 and 6 that magnitudes of mean velocities are smaller in the case of turbulent transport than that in laminar transport because of the enhanced momentum diffusion in turbulent pools.
5. In the case of a positive surface tension coefficient, the two streams (one coming from the melting front and another from the trailing edge) turn downwards near the center of the pool, thereby carrying the heat from the hottest part to the colder regions towards the bottom. The descending fluid, in the case of turbulent transport, has a lower momentum than that in the case of laminar transport. This tends to reduce the weld pool penetration. On the other hand, the enhanced thermal diffusion due to turbulent transport tries to increase the pool depth. The relative strength of these two effects determines the resultant pool depth. It is important to note here that in the case of molten metals, the Prandtl number ($\mathrm{Pr}=\mu c/K$) is rather small (here $\mathrm{Pr}\approx 0.13$), which im-

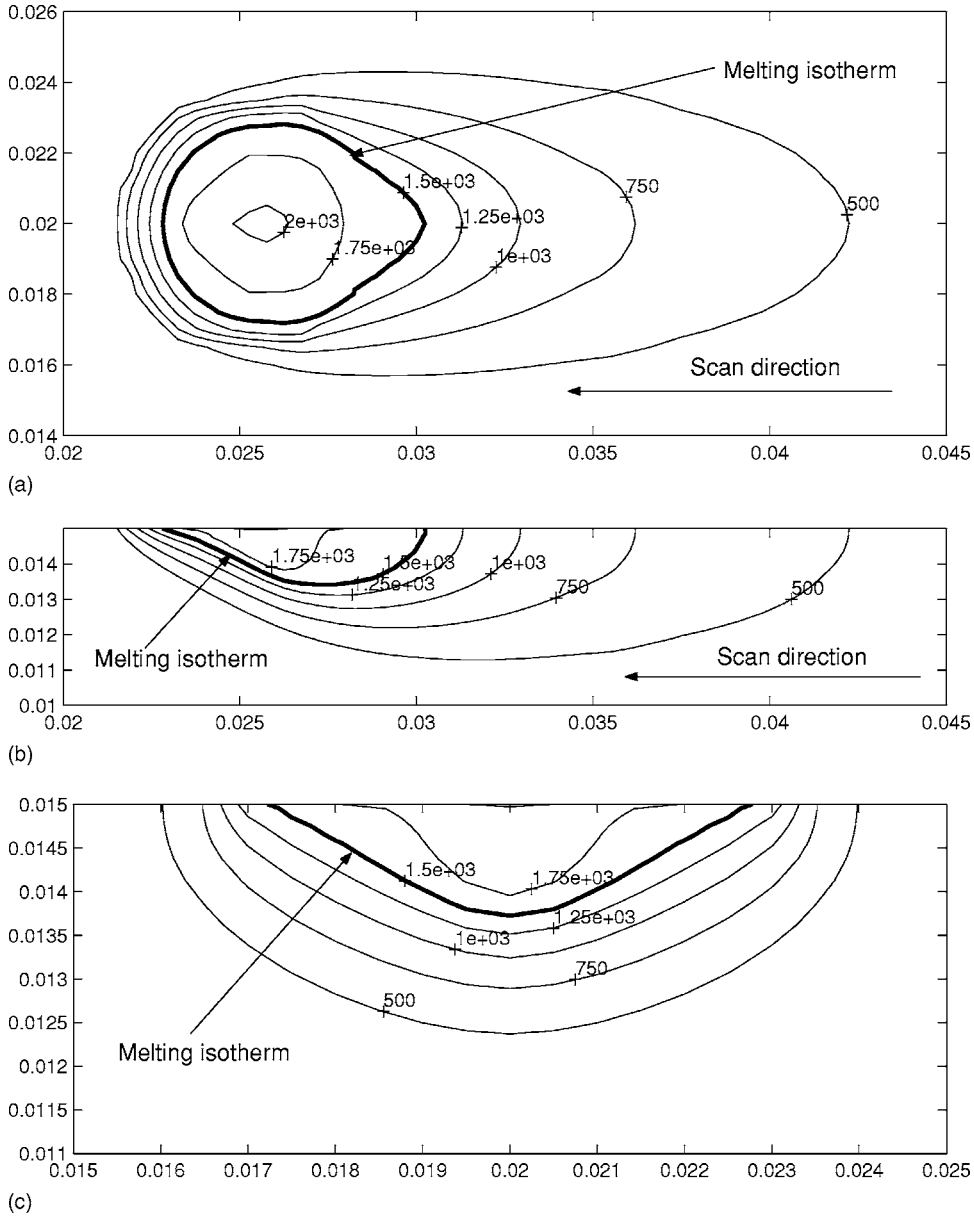

Fig. 6 Temperature distribution for the turbulent case with U_{scan}=8.89 mm/s, power=3.6 kW, η=0.9, and $\partial\sigma_{sur}/\partial T$=0.0005 N/mK. (*a*) Top view, (*b*) longitudinal mid plane, and (*c*) cross-sectional mid plane. All dimensions are in meters; temperature labels are in degrees Celsius. The contour label 1500°C represents the melting temperature of the base metal.

plies that the effect of turbulence is more pronounced on momentum transport, as compared to that on the thermal energy transport. As a result, the effects of reduced mean advective strength in the downward direction may overcome the enhancement of the thermal diffusion strength in a turbulent pool. This results in a smaller penetration in the case of turbulent transport considered here, as evident from Figs. 2(*b*) and 6(*b*).

The isotherms obtained from turbulent simulations with negative surface tension coefficient are presented in Figs. 8(*a*)–8(*c*), with corresponding velocity vectors shown in Figs. 9(*a*)–9(*c*). The contrasting features, with respect to the corresponding laminar transport, can be summarized as follows:

1. It is apparent from the comparison of Figs. 4(*c*) and 8(*c*) that maximum penetration is higher in turbulent transport than in laminar transport. It has been mentioned earlier that the pool penetration in the case of a negative surface tension coefficient is primarily governed by thermal diffusion. Therefore, in the case of the turbulent convection with a negative surface tension coefficient, an enhanced diffusive effect of turbulence causes a deeper weld pool penetration.
2. Comparing Fig. 5 with Fig. 9, it is evident that magnitudes of the mean velocity in the case of turbulent transport are smaller than the velocities in the case of laminar simulations. This is also a consequence of a greater degree of momentum diffusion in turbulent weld pools.
3. In the case of negative $\partial\sigma_{sur}/\partial T$, the molten metal from the hottest spot on the top surface carries the heat towards the colder regions near the edges of the pool. Further, in the case of the turbulent transport, due to the reduced mean thermal gradient resulting from turbulent diffusion, the Marangoni

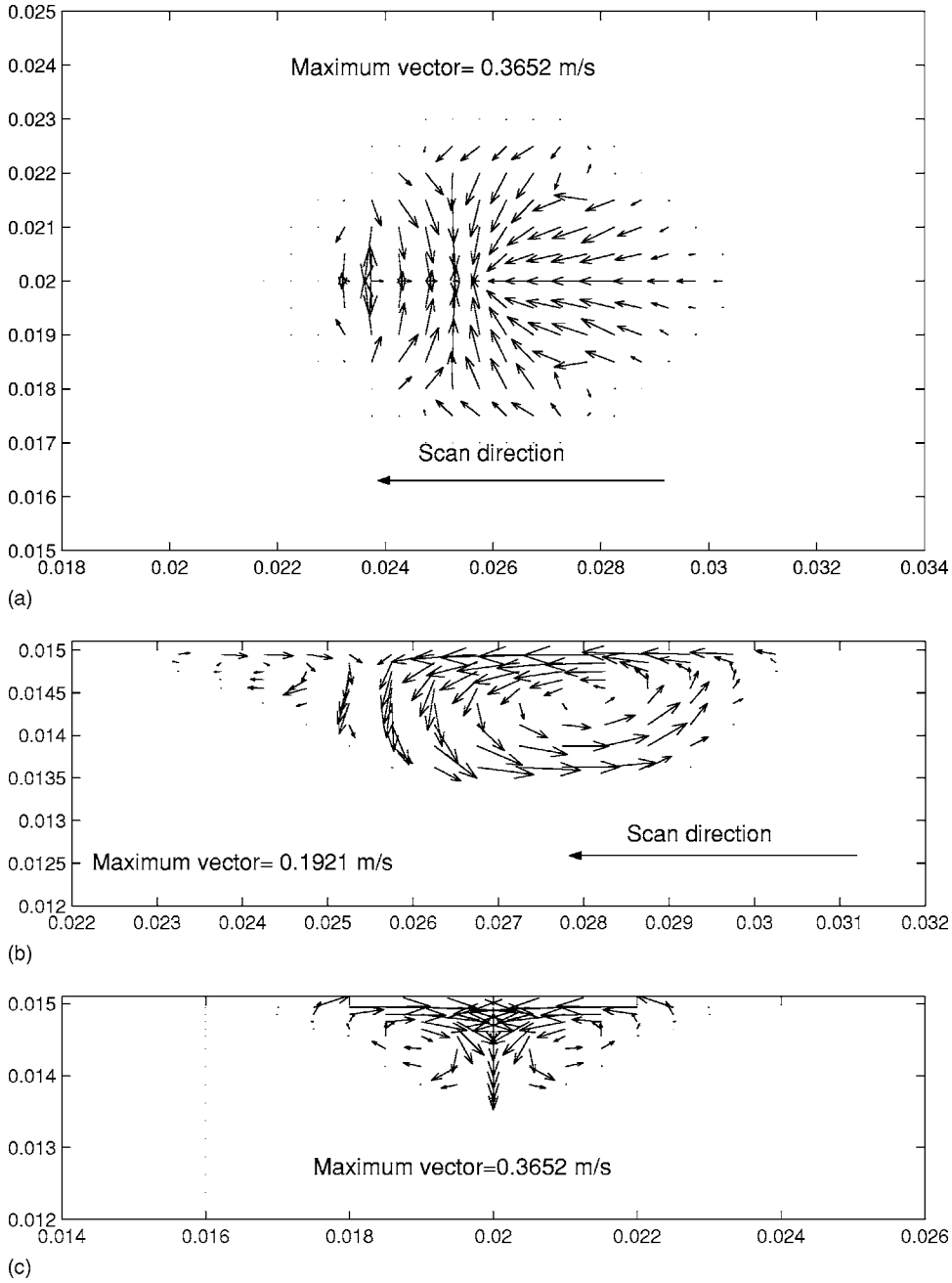

Fig. 7 Velocity distribution for the turbulent case with U_{scan}=8.89 mm/s, power=3.6 kW, η=0.9, and $\partial\sigma_{sur}/\partial T$=0.0005 N/mK. (*a*) Top view, (*b*) longitudinal sectional mid plane, and (*c*) cross-sectional mid plane. All dimensions are in meters.

convection is weaker than that in laminar transport. Consequently, the molten metal emanating from the hottest portion of the pool takes a downward turn much earlier than that in the case of laminar transport. This results in a shorter pool length (see Figs. 4(*b*) and 8(*b*)) and a shorter pool width (see Figs. 4(*c*) and 8(*c*)), in comparison to those in the case of laminar transport.

4.3 Effect of Surface Tension Coefficient on the Transport of k and ε in the Weld Pool. The turbulent kinetic energy k variations on the top surface and on the longitudinal and cross-sectional mid-planes are presented in Figs. 10(*a*)–10(*c*), respectively, for the case of positive $\partial\sigma_{sur}/\partial T$. The corresponding contours of ε are presented in Figs. 11(*a*)–11(*c*). Pertinent plots for the case of a negative surface tension coefficient are presented in Figs. 12(*a*)–12(*c*) and 13(*a*)–13(*c*). The contrasting features are summarized below:

It can be seen from the longitudinal views [Figs. 10(*b*) and 11(*b*)] that the maximum k and ε values are attained near the melting front side of the weld pool center, for positive $\partial\sigma_{sur}/\partial T$. On this side, the prevailing temperature gradients are much higher, as compared to the other parts of the pool. As a result, the effect of Marangoni convection is extremely strong, which, in turn, leads to higher values of velocity gradient. This leads to higher turbulent kinetic energy generation, and also to the dissipation of turbulent kinetic energy. On the other hand, for negative $\partial\sigma_{sur}/\partial T$, the turbulent kinetic energy and the dissipation rates attain the highest values near the interface in the spanwise direc-

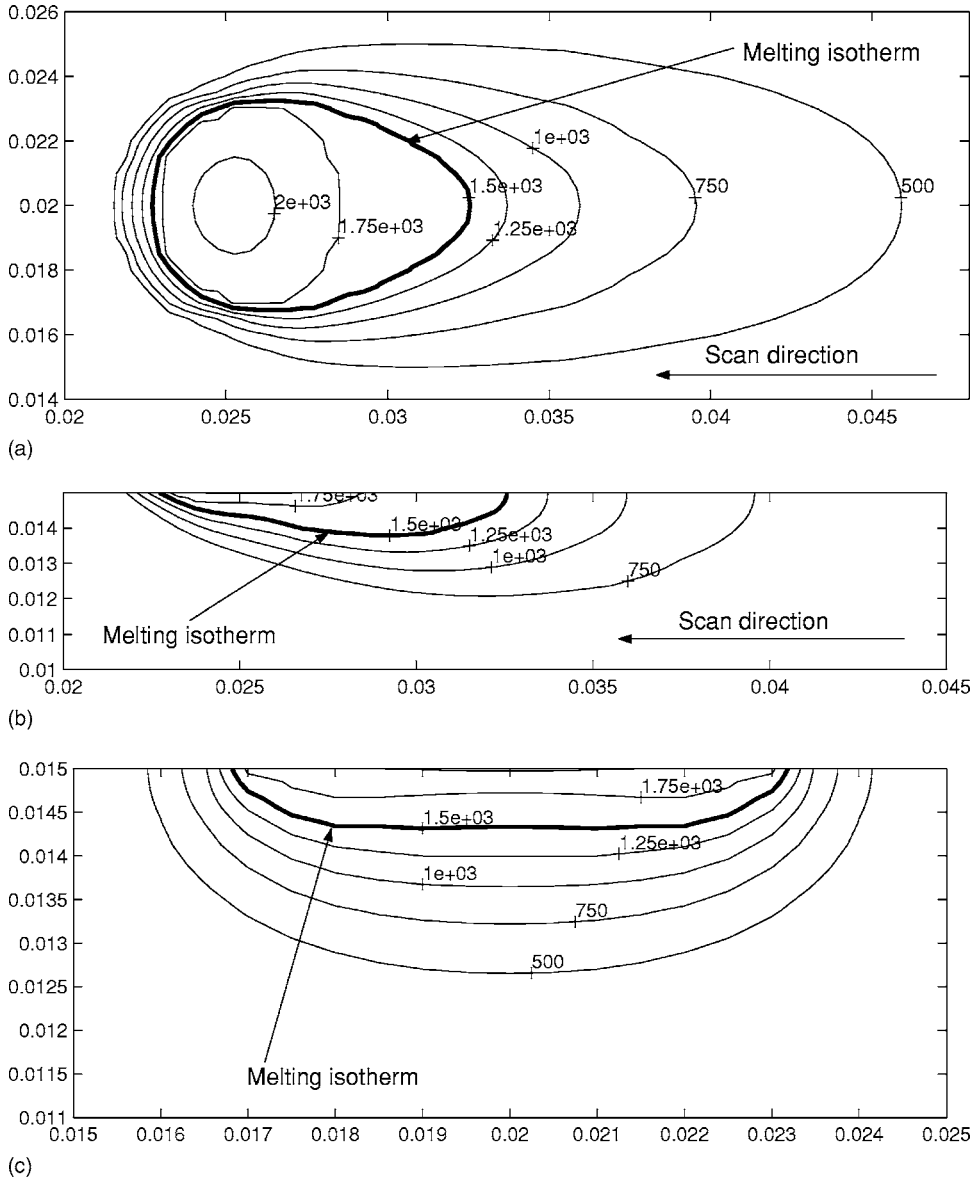

Fig. 8 Temperature distribution for the turbulent case with U_{scan}=8.89 mm/s, power=3.6 kW, η=0.9, and $\partial\sigma_{sur}/\partial T$=−0.0005 N/mK. (*a*) Top view, (*b*) longitudinal mid plane, and (*c*) cross-sectional mid plane. All dimensions are in meters; temperature labels are in degrees Celsius. The contour label 1500°C represents the melting temperature of the base metal.

tion where the temperature gradient magnitudes are high (see Figs. 12 and 13). In Marangoni convection the high velocity magnitude locations are associated with high temperature gradient locations. As turbulent kinetic energy generation is proportional to the square of strain rate, the high velocity gradient ultimately leads to the maximum turbulent kinetic energy generation as well as dissipation of the same at the locations of high temperature gradient in the spanwise direction under the local equilibrium.

4.4 Weld Pool Penetration: A Scaling Analysis. It has been demonstrated earlier that the effects of turbulent transport on positive and negative surface tension coefficient-driven flows may turn out to be markedly different, as far as the resultant convection and associated weld pool morphology are concerned. This is further elucidated in the following scaling analysis.

4.4.1 Positive Surface Tension Coefficient Flow. From the top surface boundary condition one gets

$$\mu U_s/\delta_v \sim |\partial\sigma_{sur}/\partial T|\Delta T/r_q; \quad K\Delta T/d \sim \eta Q/\pi r_q^2 \tag{20}$$

where ΔT, U_s and d are the characteristic temperature difference, surface velocity scale, and weld pool penetration, respectively. Further, the continuity equation can be scaled as

$$U_s/r_q \sim \vartheta/\delta_v \tag{21a}$$

where ϑ is a characteristic velocity scale in the vertical direction. Combining expressions (20) with expression (21*a*), one gets

$$\vartheta \sim \frac{\mu K U_s^2}{(\eta Q/\pi r_q^2)(\partial\sigma_{sur}/\partial T)d} \tag{21b}$$

Now, equating time scales for convective transport in vertical, longitudinal, and spanwise directions, one may write:

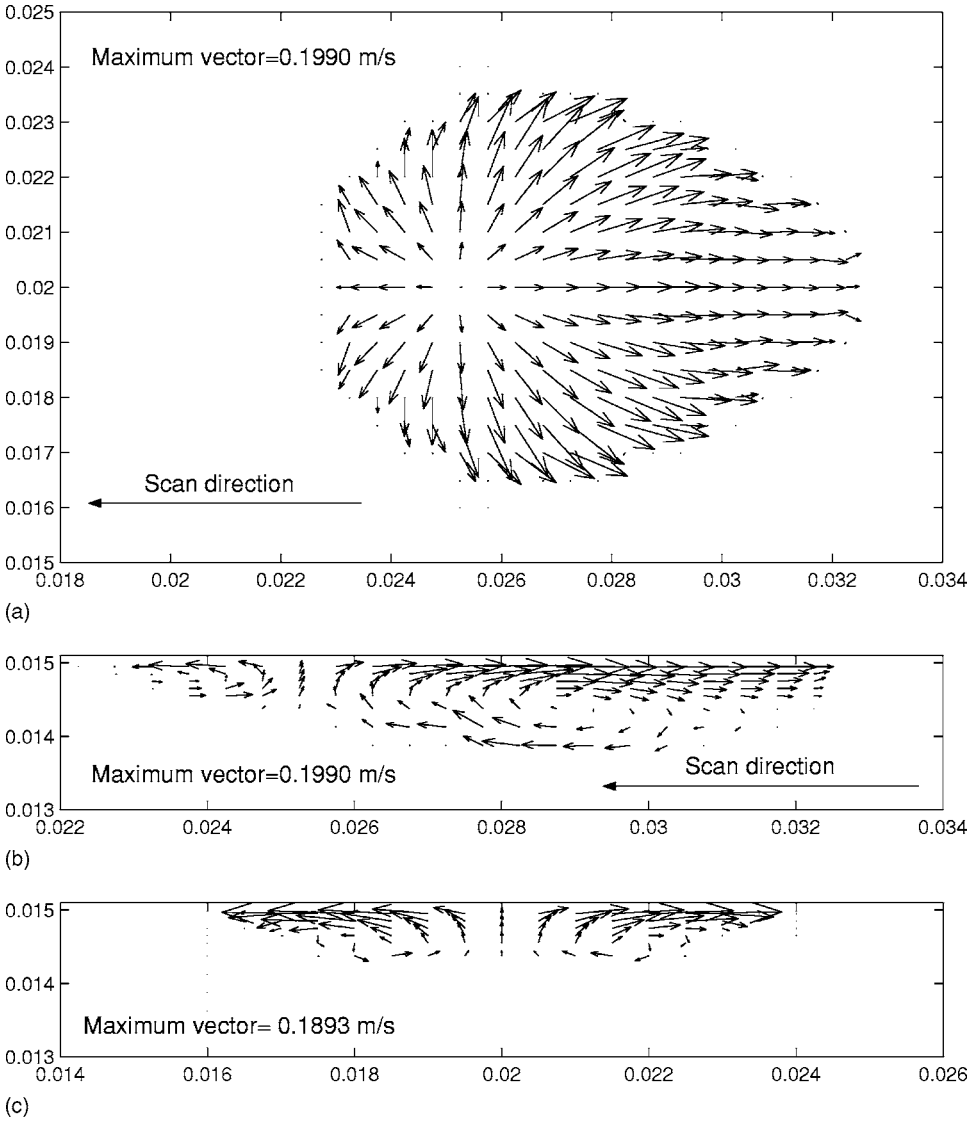

Fig. 9 Velocity distribution for the turbulent case with U_{scan}=8.89 mm/s, power=3.6 kW, η=0.9, and $\partial\sigma_{sur}/\partial T$=0.0005 N/mK. (*a*) Top view, (*b*) longitudinal sectional mid plane, and (*c*) cross-sectional mid plane. All dimensions are in meters.

$$\frac{r_q}{U_{scan}+(K/\rho c r_q)} \sim \frac{d}{\vartheta+(K/\rho c d)} \sim \frac{d}{\mu K U_s^2/(\eta Q/\pi r_q^2 \times |\partial\sigma_{sur}/\partial T| \times d)+(K/\rho c d)} \tag{22}$$

Expressions (21*a*) and (22) can be combined together, leading to the following estimation for weld pool penetration:

$$d \sim \sqrt{\frac{[\mu K U_s^2/(\eta Q/\pi r_q^2) \times (\partial\sigma_{sur}/\partial T)] r_q + (K/\rho c) r_q}{U_{scan}+(K/\rho c r_q)}} \tag{23}$$

4.4.2 Negative Surface Tension Coefficient Flow. In the case of negative surface tension coefficient-driven flow, if it is assumed that the energy transport from the center of the pool to the interface in the longitudinal and sidewise directions is governed by a velocity scale U_t, then it possible to equate time scale in either the x or z direction with that in the y direction as

$$L_d/U_t \sim \rho c d^2/K \tag{24}$$

where L_d is an appropriate length scale in the x and z directions and U_t is an appropriate velocity scale. The characteristic length scale in the x and z directions can be assumed in the order of $r_q (L_d \sim r_q)$. It can be noted here that in the case of a negative surface tension coefficient flow, the heat is transported to the phase changing interface in the longitudinal and spanwise direction by radially outward velocity from the hottest region of the pool. Accordingly, U_t is given by

$$U_t \sim U_s + U_{scan} + (K/\rho c r_q) \tag{25}$$

where U_s is the pertinent free surface velocity scale for the case of negative surface tension coefficient flow. Further, Marangoni convection dominates over thermal diffusion effects in practical arc welding situations under high thermal gradients. Accordingly, $U_s \gg (K/\rho c r_q)$, which implies that $U_t \approx U_s + U_{scan}$. Hence, expressions (24) and (25) can be combined to obtain

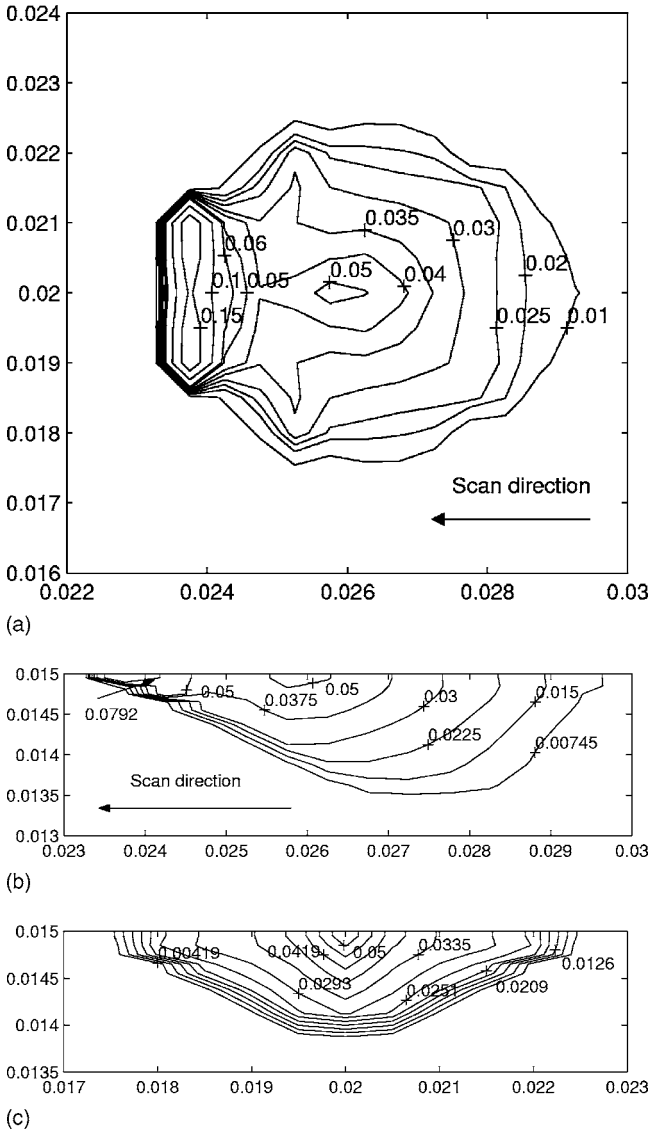

Fig. 10 Distribution of turbulent kinetic energy with U_{scan} =8.89 mm/s, power=3.6 kW, η=0.9, and $\partial\sigma_{sur}/\partial T$ =0.0005 N/mK. (*a*) Top view, (*b*) longitudinal mid plane, and (*c*) cross-sectional mid plane. All dimensions are in meters, and turbulent kinetic energy labels are in m^2/s^2.

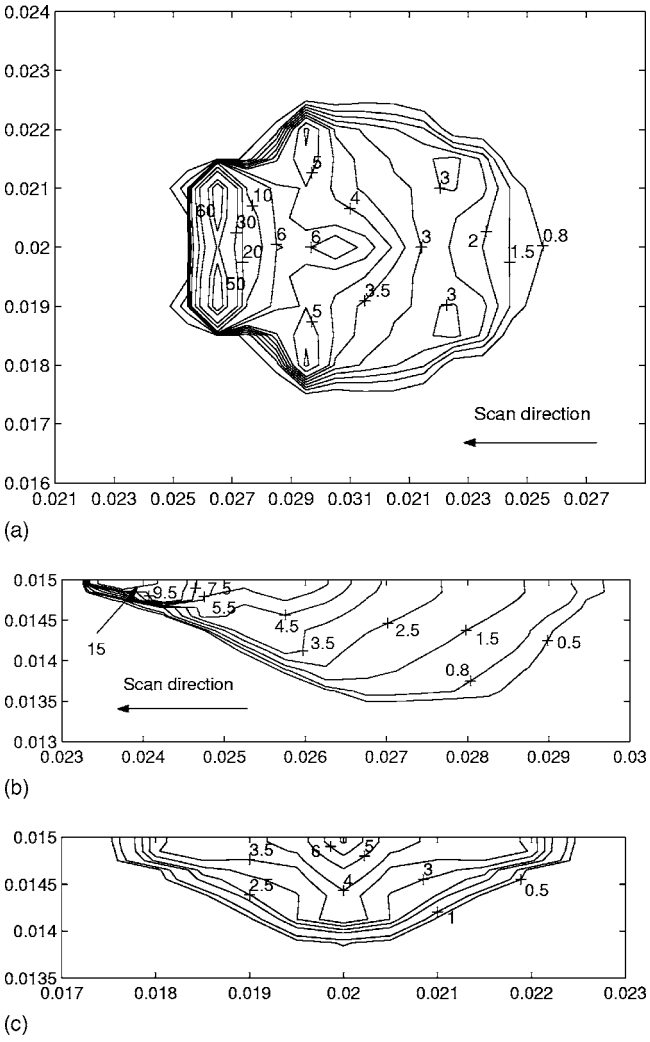

Fig. 11 Distribution of dissipation rate of turbulent kinetic energy with U_{scan}=8.89 mm/s, power=3.6 kW, η=0.9, and $\partial\sigma_{sur}/\partial T$=0.0005 N/mK. (*a*) Top view, (*b*) longitudinal mid plane, and (*c*) cross-sectional mid plane. All dimensions are in meters, and turbulent kinetic energy labels are in m^2/s^3.

$$d \sim \sqrt{Kr_q/[\rho c(U_s + U_{scan})]} \tag{26}$$

In order to proceed further towards scaling estimation of the weld pool penetration depth, one needs order-of-magnitude estimates for the velocity scale U_s, to be substituted in either of the two expressions (23) and (26). In the case of laminar flow, this can be estimated as [14]

$$U_s \sim \left(\left| \frac{\partial \sigma_{sur}}{\partial T} \right| \frac{\eta Q}{\pi r_q^2 \mu \rho c} \right)^{1/2} \tag{27}$$

For turbulent weld pool convection, the effective diffusivity of momentum transport is significantly enhanced by turbulence. However, the thermal transport is principally governed by the molecular thermal diffusivity because of low Prandtl number in this case. Under this assumption from the scaling of energy transport equation (7) it is possible to write

$$\rho c U_s(\Delta T/r_q) \sim (\eta Q/\pi r_q^2 d) \tag{28a}$$

where ΔT is the characteristic temperature increase in the molten pool which can be estimated as

$$K(\Delta T/d) \sim (\eta Q/\pi r_q^2) \tag{28b}$$

Using (28*a*) and (28*b*) the characteristic weld pool penetration d and ΔT can be estimated as

$$d \sim \sqrt{(Kr_q/\rho c U_s)} \quad \text{and} \quad \Delta T \sim [\eta Q/(K\pi q^2)]\sqrt{Kr_q/(\rho c U_s)} \tag{28c}$$

It is possible to equate Reynolds stress with the top surface shear stress in the logarithmic layer of momentum boundary layer as

$$\tau_{top} \sim \mu_t \frac{U_s}{\delta_v} \sim \left| \frac{\partial \sigma_{sur}}{\partial T} \right| \frac{\Delta T}{r_q} \quad \text{or} \quad \tau_{top} \sim \rho C_\mu \frac{k^2}{\varepsilon} \frac{U_s}{\delta_v} \sim \left| \frac{\partial \sigma_{sur}}{\partial T} \right| \frac{\Delta T}{r_q} \tag{28d}$$

where τ_{top} is top surface shear stress and δ_v is the suitable scale describing velocity boundary layer thickness. Chakraborty et al. [20], based on a scaling analysis, showed that

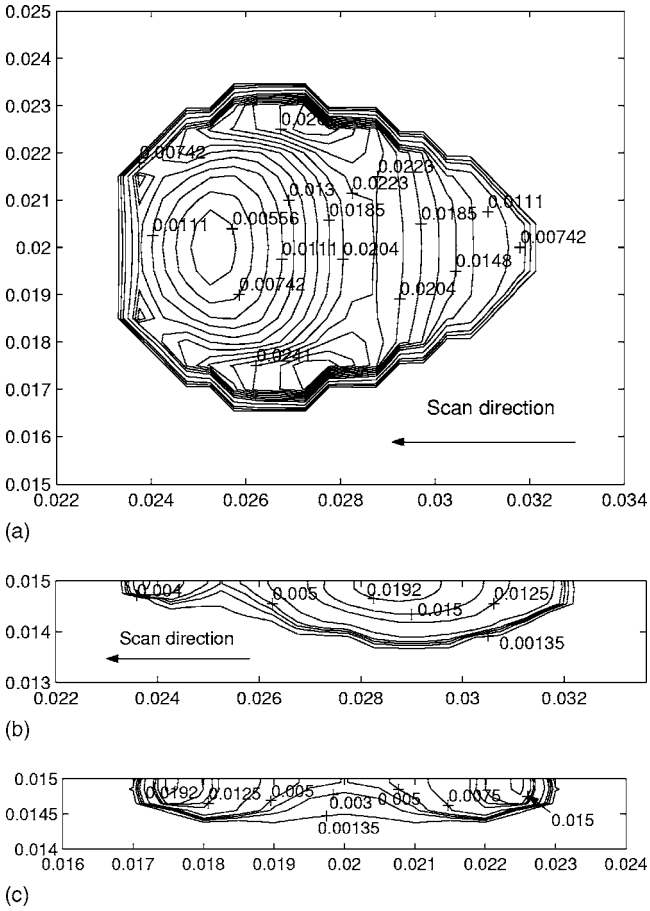

Fig. 12 Distribution of turbulent kinetic energy with U_{scan} =8.89 mm/s, power=3.6 kW, η=0.9, and $\partial\sigma_{sur}/\partial T$ =−0.0005 N/mK. (*a*) Top view, (*b*) longitudinal mid plane, and (*c*) cross-sectional mid plane. All dimensions are in meters, and turbulent kinetic energy labels are in m^2/s^2.

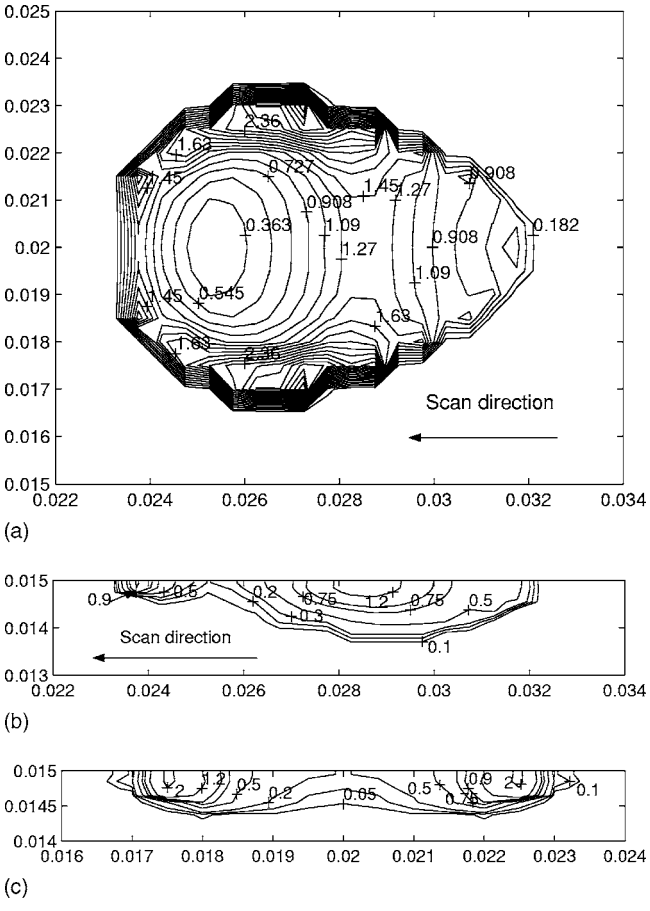

Fig. 13 Distribution of dissipation rate of turbulent kinetic energy with U_{scan}=8.89 mm/s, power=3.6 kW, η=0.9, and $\partial\sigma_{sur}/\partial T$=−0.0005 N/mK. (*a*) Top view, (*b*) longitudinal mid plane, and (*c*) cross-sectional mid plane. All dimensions are in meters, and turbulent kinetic energy labels are in m^2/s^3.

$$k = (3/2) \times u_t'^2 \quad \text{and} \quad \varepsilon \sim 0.3056 \times u_t'^3/l_t \tag{28e}$$

where u_t' is turbulent fluctuating velocity scale and l_t is the turbulent length scale. The above authors further concluded from the consideration of equilibrium of turbulent kinetic energy production and dissipation that u_t' scales with U_s as

$$u_t' \sim 0.5889 U_s \tag{28f}$$

A combination of expressions (28*d*), (28*e*), and (28*f*) yields an order of magnitude estimation for U_s, as

$$U_s \sim \left(\left| \frac{\partial \sigma_{sur}}{\partial T} \right| \frac{\eta Q}{\pi r_q^2} \sqrt{\frac{Kr_q}{\rho c}} \frac{1}{\rho C_\mu Kr_q} \right)^{2/5} \tag{28g}$$

For the process parameters listed in Table 1, it can be observed that U_s obtained from expression (28*g*) is smaller than that predicted by expression (27), which is consistent with the simulation results presented earlier. A smaller U_s corresponding to turbulent convection, in turn, indicates a deeper weld pool penetration, according to expression (26), for the case of a negative surface tension coefficient flow. This is supported by the numerical predictions as well, as evident from Figs. 4 and 8. On the other hand, in the case of positive surface tension coefficient flow, the pool depth decreases with a decrease in convection strength (i.e., decrease in U_s), as predicted by scaling estimates (21*a*) and (22). This is also in accordance with numerical simulation results, as apparent from Figs. 2 and 6. Further, for the present set of process parameters, the weld pool penetration in the case of a positive surface tension coefficient flow turns out to be in the order of 1.0 mm (as per expression (23)), which is in agreement with Figs. 2 and 6. The weld pool penetration in the case of negative surface tension coefficient flow, as predicted by expression (26), is in the order of 0.1 mm, which is also in accordance with computational results (see Figs. 4 and 8), in an order-of-magnitude sense.

5 Conclusions

A three-dimensional numerical model is employed to study the effects of sign of surface tension coefficient ($\partial\sigma_{sur}/\partial T$) on Marangoni convection in a typical GTAW pool. The weld pool penetration in the case of positive $\partial\sigma_{sur}/\partial T$ is found to be a combined effect of the thermal diffusion and convective transport mechanisms, whereas the weld pool penetration in the case of negative $\partial\sigma_{sur}/\partial T$ is predominantly determined by the thermal diffusion. In a turbulent pool, due to enhanced mixing, the mean convective effect becomes weaker in comparison to that in the corresponding laminar pool, which tends to reduce the pool penetration in the case of a positive surface tension coefficient flow. On the other hand, an effective enhancement in diffusion tends to increase the pool depth. These two counteracting mechanisms compete in deciding the resultant pool depth in the case of positive $\partial\sigma_{sur}/\partial T$. In the case of negative $\partial\sigma_{sur}/\partial T$, the weaker mean convection in a turbulent pool results in a pool of smaller length and width, as compared to that in laminar flow. However, an enhanced diffusion results in a higher weld pool penetration in a turbulent pool, as compared to that in the case of a laminar pool. Such observations are of significant consequence in relation to morphological fea-

tures of the welded joint formed, and, accordingly, the corresponding thermomechanical properties exhibited by the welded joint under actual working conditions.

Nomenclature

$\vec{B}$ = magnetic flux density
b = a small number
c = specific heat
C = morphological constant
C_μ = proportionality constant in the formula of eddy viscosity
$C_{\varepsilon 1}$ = modeling constant for production term in ε equation
$C_{\varepsilon 2}$ = modeling constant for destruction term in ε equation
d = characteristic weld pool penetration
f_l = liquid fraction
g = acceleration due to gravity
ΔH = latent heat content of a control volume
h = convective heat transfer coefficient
I = welding current
$\vec{J}$ = current density
J_n = current density in the normal direction at the top surface
k = turbulent kinetic energy
K = molecular thermal conductivity
l_t = turbulent length scale
L = latent heat of fusion
L_d = characteristic length scale in x and z directions
n = normal direction
p = pressure
Q = arc power
q = heat flux
R = pool radius
Re = Reynolds number
r_j = radius of electrical arc
r_q = radius of the heat source
S = source term
t = time
$\overline{T}$ = mean temperature
T' = temperature fluctuation
T_l = liquidus temperature
T_m = melting point temperature
T_{ref} = reference temperature
T_s = solidus temperature
ΔT = characteristic temperature difference in the molten pool
U_s = surface velocity scale
U_t = velocity in molten pool
U_{scan} = electrode scanning speed
u_i' = velocity fluctuation in ith direction
u_t' = characteristic turbulent velocity fluctuation
$\overline{u_i}$ = mean velocity in ith direction
w = width of the pool
u', v', w' = velocity fluctuation in x, y, and z directions, respectively
V = welding voltage
ϑ = characteristic velocity in vertical direction
x^+ = reduced distance normal to the wall
x_i = cartesian coordinate in ith direction
x^*, y, z = coordinate directions in a stationary reference frame
x, y, z = coordinate directions in a moving reference frame

Greek symbols

α = thermal diffusivity
α_t = eddy thermal diffusivity
β = coefficient of volume expansion
δ_v = viscous boundary layer thickness
Δn = normal distance of the near wall point from the interface
η = arc efficiency
ε = dissipation rate of turbulent kinetic energy
ε_r = emissivity
ϕ = general dependent variable
κ = Von Karman's constant
μ = coefficient of dynamic viscosity
μ_t = turbulent viscosity
σ = Prandtl number
σ_k = turbulent kinetic energy Prandtl number
σ_t = turbulent Prandtl number
σ_ε = turbulent dissipation rate of turbulent kinetic energy Prandtl number
σ_{sur} = surface tension
σ_{rad} = Stefan-Boltzmann constant
ρ = density
Γ = generalized diffusion coefficient

References

[1] Oreper, G. M., and Szekely, J., 1984, "Heat and Fluid-Flow Phenomena in Weld Pools," J. Fluid Mech., **147**, pp. 53–79.
[2] Correa, S. M., and Sundell, R. E., 1986, "A Computational and Experimental Study of Fluid Flow in Weld Pools," in Kou, S., and Mehrabian, R. (eds.), *Modelling and Control of Casting and Welding processes*, pp. 211–227, Metallurgical Society, Warrendale, PA.
[3] Kanouff, M., and Greif, R., 1992, "The Unsteady Development of a GTA Weld Pool," Int. J. Heat Mass Transfer, **35**, pp. 967–979.
[4] Dutta, P., Joshi, Y., and Janaswami, R., 1995, "Thermal Modelling of GTAW process with Non axisymmetric Boundary Conditions," Numer. Heat Transfer, Part A, **27**, pp. 499–518.
[5] Chakraborty, S., Sarkar, S., and Dutta, P., 2002, "A Scaling Analysis of Momentum and Heat Transport in Gas Tungsten Arc Welding," Sci. Technol. Weld. Joining, **7**, pp. 88–94.
[6] Joshi, Y., Dutta, P., Espinosa, P., and Schupp, P., 1997, "Non-axisymmetric Convection in Stationary Gas Tungsten Arc Weld Pools," Trans. ASME, Ser. C: J. Heat Transfer, **119**, pp. 164–171.
[7] Atthey, D. R., 1980, "A Mathematical Model for Fluid Flow in a Weld pool at high Currents," J. Fluid Mech., **98**, pp. 787–801.
[8] Mundra, K., Debroy, T., Zacharia, T., and David, S., 1992, "Role of Thermophysical Properties in Weld Pool Modeling," Weld. J. (Miami, FL, U. S.), **71**, pp. 313–320.
[9] Chao, R. T. C., and Szekely, J., 1994, "The Possible Role of Turbulence in GTA Weld Pool Behaviour," Weld. J. (Miami, FL, U. S.), **73**, pp. 25–31.
[10] Hong, K., Wakeman, D. C., and Strong, A. B., 1995, "The Predicted Influence of Turbulence in Stationary Gas Tungsten Arc welds," Trends in Welding Research, Proceedings of 4th International Conference, Gatinberg, TN, pp. 399–404.
[11] Chakraborty, N., Chakraborty, S., and Dutta, P., 2003, "Modelling of Turbulent Transport in Arc Welding Pools," Int. J. Numer. Methods Heat Fluid Flow, **13**, pp. 7–30.
[12] Chakraborty, N., Chakraborty, S., and Dutta, P., 2004, "Three-Dimensional Modelling of Turbulent Welding Pool Convection in GTAW Processes," Numer. Heat Transfer, Part A, **45**, pp. 391–413.
[13] Brent, A. D., Voller, V. R., and Reid, K. J., 1988, "Enthalpy-Porosity Technique for Modelling Convection-Diffusion Phase Change: Application to the Melting of a Pure Metal," Numer. Heat Transfer, **13**, pp. 297–318.
[14] Dutta, P., Joshi, Y., and Frenche, C., 1994, "Determination of Gas Tungsten Arc Welding Efficiencies," Exp. Therm. Fluid Sci., **9**, pp. 80–89.
[15] Shyy, W., Pang, Y., Hunter, G. B., Wei, D. Y., and Chen, M. H., 1992, "Modelling of Turbulent Transport and Solidification during Continuous Ingot Casting," Int. J. Heat Mass Transfer, **15**, pp. 1229–1245.
[16] Aboutalebi, M. R., Hassan, M., and Guthrie, R. I. L., 1995, "Numerical Study of Coupled Turbulent Flow and Solidification for Steel Slab Clusters," Numer. Heat Transfer, Part A, **28**, pp. 279–299.
[17] Durbin, P., and Petterson Reif, B. A., 2001, *Statistical Theory and Modelling for Turbulent Flows*, 1st ed., John Wiley & Sons Ltd., New York.
[18] Patankar, S. V., 1980, *Numerical Heat Transfer and Fluid Flow*, Hemisphere, Washington, DC.
[19] Bejan, A., 1995, *Convection Heat Transfer*, 2nd ed., John Wiley and Sons, New York.
[20] Chakraborty, N., Chatterjee, D., and Chakraborty, S., 2004, "A Scaling Analysis of Turbulent Transport in Laser Surface Alloying Process," J. Appl. Phys., **96**(8), pp. 4569–4577.

Numerical and Experimental Investigation of a Multiple Air Jet Cooling System for Application in a Solar Thermal Receiver

M. Röger

R. Buck

H. Müller-Steinhagen

Institute of Technical Thermodynamics,
German Aerospace Centre (DLR),
Pfaffenwaldring 38-40,
D-70569 Stuttgart, Germany

*The transparent quartz glass window of a high temperature solar receiver (*1000°C *air outlet temperature,* 15 bars*) has to be protected from overheating. The window is an axially symmetric part that can be approximated by a hemisphere with a cylindrical extension (diameter* 0.31 m*, height* 0.42 m*). The cooling is accomplished by impinging several air jets onto the concave window surface. Due to concentrated solar radiation, the air supply nozzles can only be installed at the circumference of the cylindrical extension. Symmetric configurations with six or nine nozzles, equally distributed around the window circumference, are examined. A second configuration generates a swirl in the window cavity by inclining the nozzles. In a third, asymmetric configuration, only nozzles on one side are simultaneously charged with mass flow, while a spatial homogenization of heat transfer is reached by periodically modulating the air flows with time. Computational fluid dynamics (CFD) calculations and laboratory measurements of the heat transfer have been carried out. In the performed 3-D simulations, the realizable k-ε model, the k-ω model, and the SST-k-ω model are compared. For measuring the heat transfer coefficient, a periodic-transient measurement technique with high spatial resolution is used. For the application of cooling of the solar receiver window, the jet cooling system with periodically modulated air flows is identified as the best solution.*
[DOI: 10.1115/1.1928910]

Keywords: Solar Thermal Electricity, Solar Receiver, External Window Cooling, Air Jet Cooling of a Concave Surface, Modulated Air Jets, CFD, Numerical Simulation, Heat Transfer

1 Introduction

One path to convert solar radiation into electricity is to supply solar heat to a thermodynamic cycle. This is done by concentrating solar radiation onto a receiver, which absorbs the radiant energy and heats a heat transfer medium. This medium either directly or indirectly drives a conventional thermal power block. More details about solar power plants can be found in [1].

In central receiver technology, the sunlight is concentrated into a focal spot by several two-axis tracking heliostats. Solar concentration factors between 200 and 1000 and temperatures up to 1500°C can be reached. To efficiently convert the collected heat into electricity, the use of a combined cycle is preferable. In the concept shown in Fig. 1, the solar energy is directly fed into the topping Brayton cycle of a combined cycle, ensuring a high efficiency. The compressor discharge air flows through a pressurized volumetric receiver cluster, where it is heated up to 1000°C. In the receiver cluster, individual receiver modules are connected in parallel and in series. In a series connection, the air is sequentially heated in low, middle, and high temperature receiver modules. Optionally, a further temperature rise in the combustion chamber can be achieved by burning natural gas. A conventional Rankine cycle uses the waste heat of the gas turbine. By connecting receiver modules in parallel, a wide range of power levels (1 to 100 MWe) can be covered. For smaller power levels, efficient recuperated gas turbine cycles are used instead of a combined cycle.

In [2,3] an economic analysis for a 30 MW solar-fossil combined cycle is presented. For receiver temperatures between 1000°C and 1200°C, annual thermal solar shares between 40% and 65% are expected, with levelized electricity costs in the range of 7 to 9 UScent/kWh.

Solar heating of the compressed air is realized in a pressurized volumetric receiver, shown in Fig. 2. The receiver module consists of an insulated pressure vessel, closed by a domed quartz glass window. The window is an axially symmetric part that can be approximated by a hemisphere with a cylindrical extension (diameter 0.31 m, height 0.42 m). Inside the vessel (outer diameter 1.1 m, length 1.1 m), there is a metallic or ceramic volumetric absorber structure and the flow ducts for air inlet and exit. The front side of the receiver module is protected from solar radiation by a secondary concentrator (length 1 m, optical concentration factor 4.9). The collected sunlight from the heliostat field passes through the mirrored secondary concentrator and transmits through the quartz glass window. The radiation is then absorbed in the volumetric absorber, which is locally heated up to maximal 1200°C. The "cold," compressed air of the gas turbine compressor is heated while flowing through the hot volumetric structure of the absorber. The heated air either flows to a further receiver module for additional solar heating or to the combustion chamber of the gas turbine for fossil heating. The hot, compressed air then drives the turbine section of the gas turbine.

In 1996, the REFOS[1] project was initiated to demonstrate the technical feasibility of the described receiver technology [3,4].

Contributed by the Heat Transfer Division for publication in the JOURNAL OF HEAT TRANSFER. Manuscript received: March 4, 2004; final manuscript received: March 4, 2005. Review conducted by: Chang Oh.

[1]Work supported by the German Ministry of Education and Research, Contract No. 0329695 and the German Ministry of Economy and Technology, Contract No. 0329695A/4.

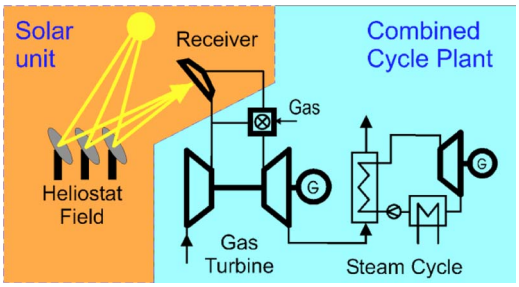

Fig. 1 Solar air heating system of combined cycle

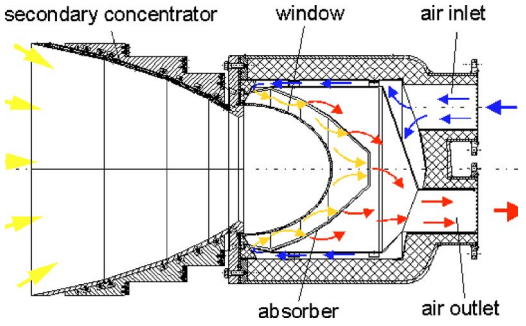

Fig. 2 Pressurized volumetric receiver (REFOS type)

The receiver was successfully tested. An air outlet temperature of 800°C was reached at an operating pressure of 15 bars. The absorbed thermal power was 400 kW_{th}. In the EC funded SOLGATE[2] project, a small solar-hybrid test system was designed, built, and tested [5]. The system includes a cost-effective, low temperature module, middle temperature module, a new high temperature module, and a modified gas turbine.

2 The Receiver Window

One major obstacle for building a high temperature module with air outlet temperatures of 1000°C and above is the excessive heating of the quartz glass window.

Particularly at high temperatures, there exists the danger of recrystallization of quartz glass. Due to structural changes of the recrystallized phase at temperature changes, chipping and cracking of the quartz glass can occur, which will lead to a degradation of the receiver window with time. Hence, an overheating of the window above 800°C has to be avoided.

To tackle this problem, different approaches are followed. On the one hand, there are passive measures, which reduce the thermal load on the window. One measure would be the application of a selective, high temperature resistant coating on the window surface that faces the absorber. This thin film should be highly transparent in the solar spectrum and reflective for wavelengths greater than approximately 2.5 μm, while proving a low absorptance. Thus, solar radiation would be transmitted, while thermal radiation, emitted by the absorber, would be reflected back onto the absorber instead of being absorbed in the window or transmitted to the ambient. Another approach is to use a quartz glass type with higher transmittance in the solar spectrum. Research and development in this direction is being done at the moment.

On the other hand, there are active measures for cooling the window from the internal or external side of the receiver. Both the external and the internal cooling option are being investigated. This paper describes the work done for the external window cooling option.

3 Window Cooling Schemes

To secure proper functioning of window and receiver, there are some requirements for the window cooling. Besides keeping the maximum quartz glass temperature below 800°C, a more or less homogeneous temperature distribution to minimize thermal stresses is required. An active cooling system should not reduce the transmission of solar radiation into the receiver and should consume little additional energy. Furthermore, it should be reliable and have low investment, operation, and maintenance costs. To comply with these requirements, forced convection air cooling of the external window surface at ambient pressure was investigated.

[2]Work supported by the European Commission under the 5th Framework Program, Contract No. ENK5-CT-2000-00333.

3.1 Examined Configurations.

The heat transfer distributions of the configurations shown in Fig. 3 are examined both numerically and experimentally. In all cases, the nozzles are distributed equally over the circumference of the window support area.

First, the symmetric configurations, in which all nozzles are continuously charged with the same mass flow, are investigated for six and nine nozzles. In order to homogenize and enhance the heat transfer distribution, symmetric configurations with different swirled flows are studied. The swirl is generated by inclining the nozzles as shown in the middle of Fig. 3.

Finally, asymmetric cases with mass flow modulation are investigated. In these configurations 18 nozzles are arranged over the circumference of the window. Only some nozzles on one side are charged with air flow, while the others at the opposite side were switched off. The situation for a specific point of time for five simultaneously operating nozzles is shown in the right illustration of Fig. 3. By sequentially switching nozzles on and off, the well-cooled region moves around the circumference of the window, achieving—averaged over time—a suitable heat transfer distribution on the window surface. The asymmetric, modulated option is studied for configurations with three to six simultaneously operating nozzles.

All cooling schemes are investigated for different nozzle outlet velocities and diameters. Also, the influence of the nozzle type is analyzed: Flow and heat transfer calculations are performed for both round and slot nozzle outlet shapes.

3.2 Dimensional Analysis and Definitions.

3.2.1 Dimensional Analysis. Flow field and heat transfer of the examined configurations depend on a large number of variables. The flow field near the nozzle exit is determined by nozzle type and dimensions (hydraulic diameter d_h), mean nozzle exit velocity w_m, turbulence intensity I, density ρ and viscosity η of the fluid. The far flow field depends additionally on the total number n and position ϕ_i of the charged nozzles $i=1,\ldots,n$ as well as on their orientation. The orientation of a nozzle can be described by an azimuth angle φ_i and a polar angle ϑ_i, which are shown in Fig. 4. For free convection, the gravitational constant g and the coefficient of thermal expansion β are relevant. Additionally, the window geometry, which can be described by the window diameter D_w and the maximum curve length L_{max}, play a role. L_{max} is the length along the window surface from the support area to the top of the window. Obviously, the heat transfer coefficient at a point P is also a function of the location on the window surface, which can be expressed by the two coordinates L_P and ϕ_P. For the temperature field, the heat transfer coefficient h (which also depends on a characteristic temperature difference ΔT), the specific heat capacity c_p, and the thermal conductivity λ are of importance. In a turbulent boundary layer, the wall roughness k has an effect on wall shear stress and heat transfer.

In total, there are 20 independent variables, whose units can be represented by the four fundamental dimensions mass (kg), length

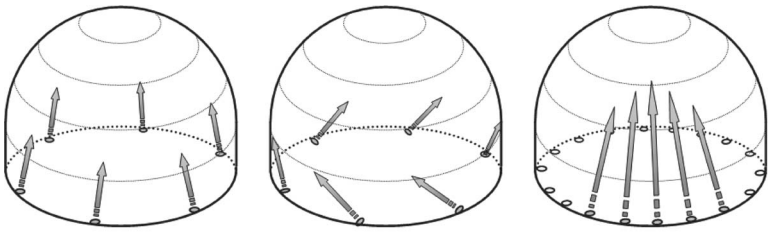

Fig. 3 Examined cooling schemes

(m), time (s), and temperature (K). Buckingham's theorem [6] states that there exist 16 dimensionless variables. A possible set of variables is given in Table 1.

The influence of non-constant properties can be expressed by an additional dimensionless number: T_w/T_f. The product of Galilei number and density quotient yields the Grashof-number Gr $=\mathrm{Ga}\Delta\rho/\rho$. In general, the Nusselt number at a point P at the window surface is a function of the following dimensionless variables:

$$\mathrm{Nu_P} = \mathrm{f}(\mathrm{Re},\mathrm{Pr},\mathrm{Ec},\mathrm{Gr},I,L_p/d_h,\phi_P,D_w/d_h,L_{max}/d_h,k/d_h,$$
$$T_w/T_f,n,\phi_i,\varphi_i,\vartheta_i) + \text{nozzle type} \quad (1)$$

For velocities smaller than the speed of sound, the Ec number can be neglected. Since the ratio $\mathrm{Gr}/\mathrm{Re}^2$ is much smaller than one for the considered configurations, forced convection dominates and free convection can be neglected. The window geometry and the surface roughness are constant, hence the numbers D_w/d_h, L_{max}/d_h and k/d_h need not be considered as variables. With these assumptions, the correlation for the Nu number at point P reduces to:

$$\mathrm{Nu_P} = \mathrm{f}(\mathrm{Re},\mathrm{Pr},I,L_p/d_h,\phi_p,T_w/T_f,\phi_i,n,\varphi_i,\vartheta_i) + \text{nozzle type} \quad (2)$$

The influence of turbulence intensity I on the mean Nusselt number over the total window surface is negligible. Hence, the mean Nusselt number depends on the following variables:

$$\mathrm{Nu_m} = \mathrm{f}(\mathrm{Re},\mathrm{Pr},T_w/T_f,n,\phi_i,\varphi_i,\vartheta_i) + \text{nozzle type} \quad (3)$$

Keeping this functional dependence in mind, different configurations are examined numerically and experimentally in the next sections.

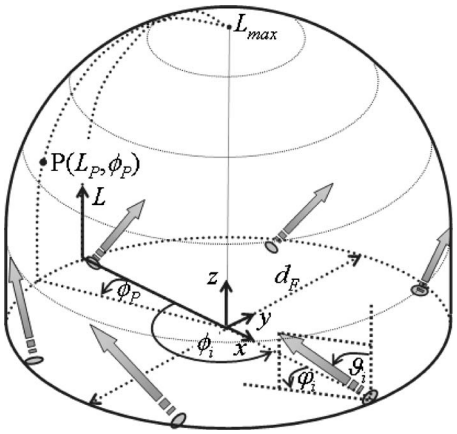

Fig. 4 Coordinate system for window surface, nozzle orientation, and dimensionless variables

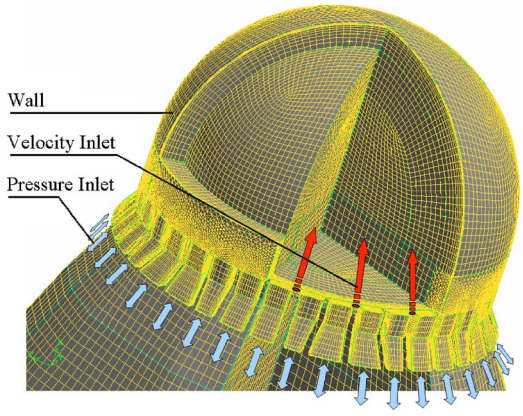

Fig. 5 Mesh and boundary conditions

Table 1 Set of dimensionless variables

1	2	3	4
$\mathrm{Nu}=\frac{h\cdot L_{max}}{\lambda}$	$\mathrm{Re}=\frac{w_m\rho d_h}{\eta}$	$\mathrm{Pr}=\frac{\eta c_p}{\lambda}$	$\mathrm{Ec}=\frac{w^2}{c_p\Delta T}$
5	**6**	**7**	**8**
$\mathrm{Ga}=\frac{gL_{max}^3\rho^2}{\eta^2}$	I	$\frac{\Delta\rho}{\rho}$	$\frac{L_P}{d_h}$
9	**10**	**11**	**12**
ϕ_P	$\frac{D_w}{d_h}$	$\frac{L_{max}}{d_h}$	$\frac{k}{d_h}$
13	**14**	**15**	**16**
n	ϕ_i	φ_i	ϑ_i

Table 2 Mesh quality statistics

		Hexa-hedra	Tetra-hedra	Prisms/ Pyramids	Sum
Total		75 %	13 %	12 %	100 %
EquiAngle Skew					
0.00-0.25	Excellent	59 %	2 %	11 %	72 %
0.25-0.50	Good	16 %	8 %	0.5 %	25 %
0.50-0.75	Fair	< 3 cells	3 %	0.1 %	3 %
0.75-0.90	Poor	-	0.1 %	-	-
0.90-1.00	Very Poor	-	-	-	-
Aspect Ratio					
<2	Good	48 %	13 %	0.6 %	61 %
2-3	Fair	9 %	0.4 %	0.14 %	10 %
>3	Ok, in BL	19 %	0.04 %	11 %	29 %

3.2.2 Definitions. The heat transfer coefficient is defined as follows:

$$h = \dot{q}_{conv}/(T_w - T_f) \tag{4}$$

The fluid temperature changes along the streamlines. For definition of the heat transfer coefficient, a mean fluid reference temperature is chosen. It can be calculated with the nozzle outlet temperature $T_{f,noz}$, the transferred heat flow rate $\dot{Q}$, the total nozzle mass flow rate $\dot{M}_0$, the specific heat capacity c_p and the entrainment ratio R:

$$T_f = T_{f,m} = T_{f,noz} + \frac{1}{2}\frac{\dot{Q}}{R \cdot \dot{M}_0 \cdot c_p} \tag{5}$$

The entrainment ratio R is defined as the ratio of the total jet mass flow (nozzles and entrainment) to the mass flow of all active nozzles $\dot{M}_0$.

The hydraulic diameter is defined with the cross section A of the nozzle outlet as:

$$d_h = 2 \cdot \sqrt{A/\pi} \tag{6}$$

The Reynolds number is defined with the hydraulic diameter d_h, while the Nu number is defined with the maximum curve length of the window $L_{max} = 0.599$ m. For the dimensionless numbers Nu, Re and Pr, air properties are used at the nozzle outlet temperature. Definitions see Table 1.

For practical reasons, the fluid temperature in the temperature ratio T_w/T_f can be represented by the nozzle outlet temperature $T_{f,noz}$. Temperatures have to be inserted in Kelvin.

4 Numerical Investigation

4.1 Computational Domain and Meshing. The computational domain comprises both the window cavity and the air volume of the secondary concentrator. A reduction of the number of cells by totally or partly neglecting the air volume of the secondary concentrator is not possible, because less confinement of the window cavity would enhance air exchange with the ambient, which would produce a higher cooling rate on the window surface. This fact has been confirmed by a numerical study with different approaches for modeling the secondary concentrator.

The most convenient way to mesh a complex 3-D computational domain is to use a tetrahedral mesh. However, to minimize diffusive effects, a large number of cells are required. Better quality meshes are structured, hexahedral meshes, but these are usually less adaptable to complex geometries and to special flow conditions. A good compromise regarding flexibility, accuracy, and number of cells is a hybrid meshing approach. For the mesh, tetrahedrons are only used, where it is unavoidable, else the use of hexahedrons is preferred. The computational domain is divided into several blocks to control mesh quality and density.

As shown in Fig. 5 most of the volume is meshed by a high-quality hexahedral mesh. The domain is divided into six 60 deg slices, because the secondary concentrator has a hexagonal inlet aperture, which transforms into an 18-cornered outlet aperture. This 60 deg slice consists of 19 blocks, from which only one is meshed by tetrahedrons. Adjacent to the window surface, one can see the boundary layer, which continuously grows to the size of the cells in the window cavity. The strong gradients in the boundary layer are efficiently resolved by cells with large aspect ratio. The near-wall mesh complies with the requirement of $y^+ \approx 1$ for the two-layer zonal model.

Table 2 gives a short summary of the mesh quality. Seventy-five percent of the meshed domain consists of hexahedra, 13% of tetrahedrons, and 12% of prisms or pyramids. A normalized measure of skewness is the so-called EquiAngleSkew. For a 3-D high quality mesh, the average EquiAngleSkew is 0.4 [7]. Ninety-seven percent of the cells are excellent or good in terms of the EquiAngleSkew, only 3% of the cells are fair. The aspect ratio of 61% of the cells is good. Only 10% of the cells have a fair aspect ratio. Cells with worse aspect ratio are only used in the boundary layer.

The total number of computational cells of the basic meshes for the asymmetric cases is about 900,000 to 1,000,000. In the symmetric cases, where a periodic boundary condition can be applied, the mesh is a little bit finer, thus resulting in 390,000 or 310,000 for the configurations with six or nine nozzles, respectively. These basic grids are successively refined to obtain a grid converged solution. For details see Sec. 4.4.

Table 3 Plenum boundary conditions

	Pressure Inlet (Gaps)	Pressure Outlet (Sec. aperture)
Gauge Total Pressure [Pa]	0	0
Total Temperature [K]	298	298
Turbulence Intensity I [%]	4.7	4.0
Turbulence length scale l [m]	0.00175	0.0896

4.2 Boundary Conditions. The window surface (see "Wall" in Fig. 5) is set to a homogeneous temperature of 1000 K. This value approximates an overall mean value during operation of the solar receiver. As the window represents a nongray radiation body, whose implementation into the CFD model would be an unreasonable high computational effort, no radiation heat transfer has been modeled in the present flow calculations. In the CFD model, only the convective heat transfer is of interest. The assumption of a homogeneous window temperature distribution for calculating the convective heat transfer coefficient is rather good, because the temperature effect on the convective heat transfer for the medium air is only small [8]. For window temperature variations of 100 K, the convective heat transfer variation is estimated to be below 0.5%. The final temperature distribution is calculated by using the convective heat transfer coefficients of the CFD calculations in a separate nongray radiation model.

As heat flows and temperatures of the secondary concentrator are not of particular interest for the window cooling, an adiabatic wall condition is applied to the secondary concentrator structure.

At the air nozzles, a velocity inlet boundary condition with profiles of velocity, turbulent kinetic energy, and dissipation rate of a developed turbulent pipe flow is applied. The inlet air temperature is 298 K. Three nozzle inlets are marked in Fig. 5 with dark arrows. For inactive nozzles, the inlet velocity boundary condition is replaced by a wall boundary condition.

Between window flange and secondary concentrator, there are small gaps, where an air exchange with the surrounding occurs. In Fig. 5, these gaps are marked with small double arrows. At this location, a pressure inlet boundary condition is applied. For the secondary aperture, where the sunlight enters, a pressure outlet boundary condition is chosen. The values are given in Table 3.

For symmetric cases, only slices of one-sixth or one-ninth of the domain are calculated by applying rotational periodic boundary conditions at the faces of the cuts.

4.3 Used Models and Solver.

4.3.1 Preselection of Turbulence Model. The choice of the turbulence model and the near wall treatment is a crucial decision for a flow calculation with heat transfer. The correct calculation of the spreading of the jets together with the quantitative determination of heat transfer, and this with reasonable computational effort, is a challenging task for turbulence modeling. The standard k-ε model calculates the spreading of a round jet 25% to 40% higher than measured [9]. The RNG k-ε model even overestimates the round jet spreading by a factor of 2 [9]. The realizable k-ε model, as proposed by Shih [10], is more consistent with the flow physics, as it does not violate certain mathematical constraints as the stan-

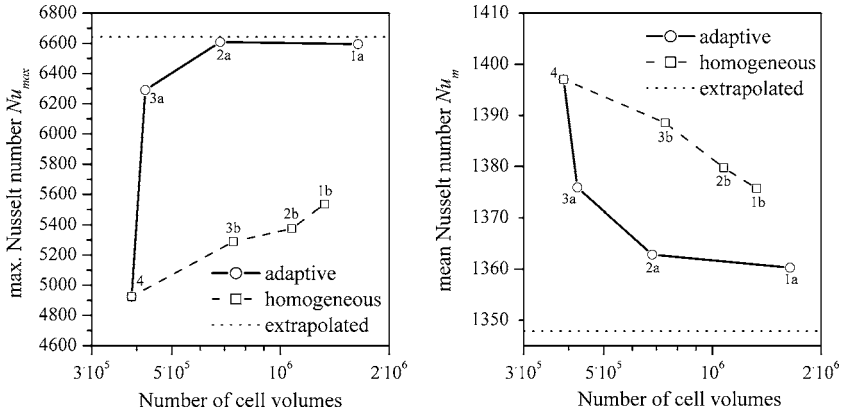

Fig. 6 Maximum (left) and mean (right) Nusselt number of the window surface versus number of grid cells

dard or RNG k-ε models do. It more accurately predicts the spreading of both planar and round jets [11]. For these reasons, the realizable k-ε model is chosen from the k-ε family.

The k-ω model, based on Wilcox [9], offers a good performance regarding the spreading of the jet. Simulated values differ from measured values in the range from 3% to 9%. Also, the k-ω model has an attractive near wall performance.

The SST-k-ω model, developed by Menter [12], combines the accurate formulation of the k-ω model in the near wall region with the k-ε model, by blending the two models.

In many cases, models based on the Boussinesq hypothesis perform very well. The additional computational expense of a Reynolds stress model (RSM) is justified if there are situations with high anisotropy of turbulence [11]. However, this is not the case in the window cooling application. Additionally, convergence problems were observed using the RSM with the steady solver. It is assumed that this is due to the strong coupling between the Reynolds stresses and the mean flow in the RSM combined with the highly transient turbulent structures of the cooling flow.

Hence, in this paper simulation results calculated with the realizable k-ε model, the k-ω model, and the SST-k-ω model are presented.

4.3.2 Near Wall Treatment. The k-ω models can also be used near walls, activating a low Reynolds number variant. In contrast, the k-ε model is primarily valid for turbulent core flows. Frequently, a wall function is used for the near wall treatment. However, this approach is not appropriate for impinging flows and developing boundary layers. For that reason, the two-layer zonal model is chosen, which activates the one-equation model of Wolfstein [13] in regions near the wall. For all simulations, the boundary layer mesh complies with the requirement of $y^+ \lesssim 1$.

4.3.3 Physical Properties. As the velocities in the flow field are much smaller than the speed of sound, the flow can be regarded as incompressible [11,14]. The medium air is implemented partly by means of user defined functions with temperature-dependent properties. Free convection is neglected, because forced convection dominates the heat transfer on the window surface. This assumption has been confirmed by calculations including gravitational forces, which did not show significant changes in heat transfer. The pressure is set to 1013 mbar.

4.3.4 Discretization and Solver. For the simulations, the commercial CFD package Fluent, versions 5.5 and 6.0, is used. Fluent is based on a finite volume discretization. The equations are solved with the three-dimensional segregated, implicit, double precision, steady solver. As pressure velocity coupling, the SIMPLE scheme is used.

4.4 Grid Refinement Study and Error Estimation.

4.4.1 Iteration/Round-Off Errors. To ensure iterative convergence, the simulations were continued, until there were no changes in residuals. The residuals were reduced at least by three orders of magnitude, i.e., the iteration error would fall below 0.1% (see also [15]). In addition to the residuals, the mean heat transfer over the window surface was observed. In a converged solution, there were no changes in the first four to five significant digits, ensuring an iteration error in mean heat transfer below 0.01%. As the calculations were performed with double precision, the influence of round-off errors on the result can be neglected. It was also checked that mass and energy balances of the flow domain were correct. Compared to discretization or modeling errors the observed iteration error of 0.1% to 0.01% is small enough to be neglected.

4.4.2 Discretization Error. All equations are discretized with a second-order upwind discretization scheme. For reducing and estimating the discretization error, a successive grid refinement on the basic grid (grid 4) was performed. Two approaches are used: adaptive refinement in zones of higher velocities (grid 3a to grid 1a) and homogeneous refinement including the whole computational domain (grid 3b to grid 1b). The refinement study was performed with the realizable k-ε model using the two-layer zonal model on a symmetric case without swirl (see Sec. 7.1).

In Fig. 6, the left diagram shows maximal, the right diagram mean Nusselt numbers on the window surface, plotted versus the number of cell volumes in the domain. The solid lines represent an adaptive grid refinement study, the dashed lines a homogeneous grid refinement study. For the homogeneous study, a Richardson extrapolation [16,17] was performed, resulting in the dotted lines.

In Table 4, the heat transfer of the adaptive grid refinement and the actual fractional error A are listed. N represents the number of cell volumes. In the calculation of the actual fractional error A, it is assumed that the correct value is represented by the extrapolated value of the Richardson extrapolation. With this assumption

Table 4 Adaptive grid refinement

Grid	N	Nu_m	$A(Nu_m)$	Nu_{max}	$A(Nu_{max})$
4	387,203	1397	3.6 %	4925	-25.9 %
3a	422,650	1376	2.1 %	6290	-5.3 %
2a	681,385	1363	1.1 %	6609	-0.5 %
1a	1,639,646	1360	**0.9 %**	6595	**-0.7 %**

Table 5 Homogenous grid refinement

Grid	N	Nu_m	$A(Nu_m)$	Nu_{max}	$A(Nu_{max})$
4	387,203	1397	**3.6 %**	4925	**-25.9 %**
3b	740,024	1389	3.0 %	5289	-20.4 %
2b	1,075,231	1380	2.4 %	5375	-19.1 %
1b	1,325,133	1376	**2.1 %**	5536	**-16.7 %**
Extrap.	∞	1348	0.0 %	6643	0.0 %

the mean Nusselt number is calculated on the finest grid of the adaptive refinement study (grid 1a) with an error of 0.9%. The maximum Nusselt number is calculated with an error of −0.7%.

In a homogenous grid refinement also regions with small gradients, where a refinement would not have been necessary, were refined. Thus, the gain in accuracy with total number of cell volumes is smaller compared to an adaptive approach. This fact can easily be observed in Fig. 6. The details of the homogenous grid refinement are listed in Table 5. On the finest grid of the homogenous refinement study (grid 1b), the actual error of the mean Nusselt number is still approximately 2.1%, the actual error of the maximum Nusselt number is even −16.7%. The refinement study was stopped when the computer resources were at the limit.

For error estimation on fine or coarse grids, Roache [18,19] suggests a grid convergence index (GCI). The GCI bases on the theory of Richardson extrapolation, which is only valid for grids in the asymptotic range. Concerning the mean Nusselt number, the grids 3b, 2b, and 1b lie in the asymptotic range, resulting in an order p of the method of $p=1.95$. For the maximum Nusselt number, it is assumed that the grids 2b and 1b lie in the asymptotic range. Table 6 shows different error bands of the discretization error. In contrast to the relative difference ε, the estimated fractional error E and the grid convergence index GCI account for the effective grid refinement ratio r_{eff} and the order p and therefore are meaningful error estimates [18,19].

It is concluded that the mean Nusselt number can be calculated with a discretization error of approximately 3.5% on the coarser grids. Maximum Nusselt numbers have a high discretization error, also on the fine grid of the homogenous discretization (~25%). However, the discretization error of the maximum Nusselt number can be reduced to ~1% by performing an adaptive grid refinement. The presented Nusselt number distributions on the window surface are all results of an adaptive grid refinement.

In addition to the presented grid refinement studies, the grid was adapted only in the near wall regions. Hence, the influence of the near wall mesh on heat transfer could be evaluated. In Fig. 7, the mean Nusselt number over the window surface is plotted versus the maximum dimensionless wall distance y^+_{max} in the domain. It is shown that the influence of the near wall mesh for values of $y^+_{max}<1.5$ is negligible.

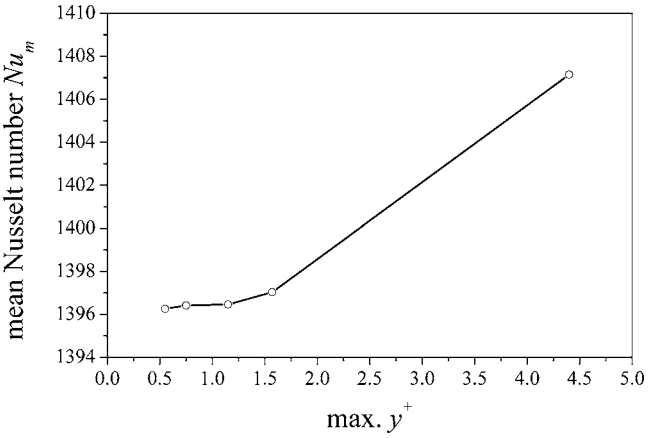

Fig. 7 Mean Nusselt number over the window surface versus maximum dimensionless wall distance

4.4.3 Modeling Errors. After having quantified iteration and discretization errors, the modeling error (turbulence model, physical property data, geometry, boundary conditions, etc.) can be estimated. This is done by means of comparison with measurement data in Sec. 7.1.

5 Experimental Investigation

For validation of the CFD results, an experimental setup was built in the heat transfer laboratory, using a periodic-transient measuring technique. The experiment was built in a scale of 1:1. The periodic-transient measuring technique was extended to a high-resolution method for measuring convective heat transfer coefficients on two-dimensionally curved surfaces. The measurement principle is shown in Fig. 8.

The window is heated from the convex side ($r=r_2$) with 41 light bulbs, whose power is modulated sinusoidally. On the concave side ($r=r_1$), the window is cooled by the air jets. The time-dependent temperature is determined by an infrared imaging system (Avio TVS 2000) on the cooled side. For each pixel, the incoming heat flux on the heated side is determined according to a special procedure, which takes into consideration the emitted power of the light bulbs, the thermal inertia of the heating system, and the thermal losses of the heated side of the window.

Table 6 Estimated error bands for different grids

Grid: i (fine) → j (coarse)	1b → 2b	2b → 3b	1b → 4
Effective grid refinement ratio $r_{ij,eff}$	1.07	1.13	1.51
Mean Nusselt number Nu_m			
Relative difference ε_{ij}	0.3 %	0.6 %	1.6 %
Estimated fractional error $E_{ij,fine\ grid}$	2.0 %	2.3 %	1.3 %
$GCI_{ij,fine\ grid}$ (F_s=1,25)	**2.5 %**	2.9 %	1.6 %
$GCI_{ij,coarse\ grid}$ (F_s=1,25)	2.9 %	3.7 %	**3.5 %**
Maximum Nusselt number Nu_{max}			
Relative difference ε_{ij}	-2.9 %	-1.6 %	-11.0 %
Estimated fractional error $E_{ij,fine\ grid}$	-20.0 %	-5.8 %	-9.0 %
$GCI_{ij,fine\ grid}$ (F_s=1,25)	**25.0 %**	7.3 %	11.3 %
$GCI_{ij,coarse\ grid}$ (F_s=1,25)	28.6 %	9.3 %	**25.1 %**

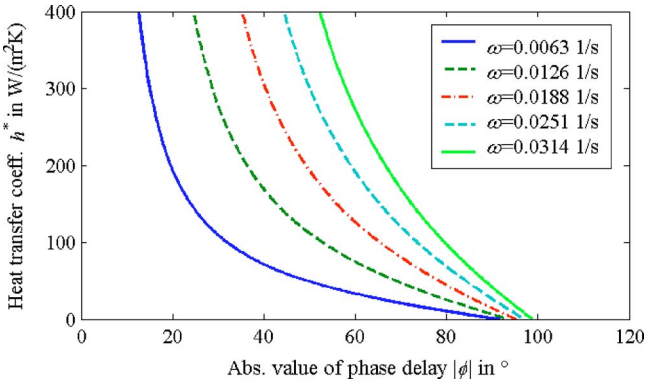

Fig. 9 Characteristic curves for different modulation frequencies

The system with its boundary conditions represents a linear system with distributed parameters. The solution of the partial equation of conduction via Laplace transformation yields a transfer function. The amplitude response and phase response of the system both depend on the heat transfer coefficient. For evaluation of the measurements, the phase response φ is used (phase delay between the incoming heat flux and the temperature fluctuation of the cooled side).

Equations (7)–(11) are valid for a hollow sphere with radii r_1 and r_2:

$$Bi = \frac{(2c^2 r_1^+ r_2^+ + 1)\cdot\sinh c\cdot\cos c + (2c^2 r_1^+ r_2^+ - 1)\cdot\cosh c\cdot\sin c + 2c\cdot\sinh c\cdot\sin c - \tan|\varphi|\cdot[(2c^2 r_1^+ r_2^+ - 1)\cdot\sinh c\cdot\cos c - (2c^2 r_1^+ r_2^+ + 1)\cdot\cosh c\cdot\sin c + 2c\cdot\cosh c\cdot\cos c]}{r_1^+\cdot[-2cr_2^+\sinh c\cdot\sin c - \sinh c\cdot\cos c + \cosh c\cdot\sin c + \tan|\varphi|\cdot(-\sinh c\cdot\cos c - \cosh c\cdot\sin c + 2cr_2^+\cosh c\cdot\cos c)]} \tag{7}$$

$$\Rightarrow h^* = \frac{\lambda}{\Delta r} Bi \tag{8}$$

with

$$c = \Delta r\cdot\sqrt{\frac{\omega}{2a}} \tag{9}$$

$$\Delta r = r_2 - r_1 \tag{10}$$

$$r_1^+ = r_i/\Delta r \tag{11}$$

Measuring the phase response φ, the Biot number and hence the heat transfer coefficient h^* can be calculated. As h^* contains both convective and radiative heat transfer, the unknown convective heat transfer coefficient h is obtained by a radiation correction: $h=h^*-h_{rad}$. Figure 9 visualizes the characteristic curves of Eqs. (7)–(11) for different angular frequencies ω. The measurements were performed at $\omega=0.0063$ 1/s ($f=1$ mHz).

The substantial advantage of this measurement principle lies in the fact that neither exact temperature measurement nor exact knowledge of the incoming heat flux are necessary, thus facilitating measurements on two-dimensionally curved surfaces.

The error for the local convective heat transfer coefficients (radiation corrected) is estimated to between −2.4% and +14.1% in the range of heat transfer coefficients from 10 to 200 W/(m^{2}K). For mean values of the convective heat transfer coefficient, the error reduces to +0.7% to +9.8% in the aforementioned heat transfer range. Due to a systematic error component (small variation of fluid temperature with time), the error band is not symmetric to the value of zero. A correction of this systematic error was not possible because of the existing uncertainties.

More details about measurement principles, experimental layout, and measurement procedures can be found in a companion paper, which will be published soon.

6 Remarks for Comparing Experiments and Simulations

Both measurement and simulation results have an uncertainty. The values are presented in the upper two parts of Table 7. However, differences between measurements and simulations also frequently originate from differing conditions in experiment and simulation. The third part of Table 7 tries to quantify the influence of these differences on heat transfer.

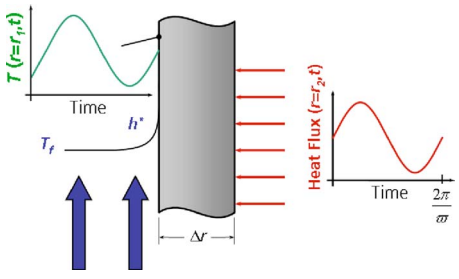

Fig. 8 Periodic-transient measurement principle

Due to the neglect of heating of the air along the streamlines and the use of a mean fluid reference temperature in the simulations, measured and simulated heat transfer coefficients at the beginning or the end of a streamline may differ in the range of ±4.7%.

The wall temperature in the simulations is 1000 K, whereas in the experiments the maximum wall temperature is 317 K. Fortunately, the influence of variable air properties with temperature on heat transfer is only small [8]. However, this small difference is accounted for by the method of temperature ratio [20]. The Nusselt number Nu (variable properties) is connected with the Nusselt number $Nu_{c.p.}$ (constant properties) by the following equation:

$$Nu/Nu_{c.p.} = (T_w/T_f)^p \tag{12}$$

In a simulation study, the exponent p was determined to $p=-0.06$ for a "constant temperature" boundary condition and p

Table 7 Overview over uncertainties in experiments and simulation and uncertainties in comparability

Description of uncertainty	Max. Nu number $Nu_{c.p.,max}$	Mean Nu number $Nu_{c.p.,m}$
1. Uncertainties of measurements		
Relative Uncertainty	-2.4 %...+14.1 % [1] -2.3 %...+9.7 % [2]	+2.0...+9.8% [1] +0.7...+6.7% [2]
2. Uncertainties of simulations (without modeling error)		
Discretization error (incl. iteration / round-off error)	±1.0 % [3]	±3.5 % [4]
3. Uncertainties in comparability		
Fluid reference temperature	±4.7 %	±0.0 %
Variable physical properties	±0.0 % [5]	±0.0 % [5]
Free convection	±0.0 %	±0.0 %
Turbulence intensity	±14.0 %	±0.7 %
Wall boundary condition	±0.0 % [6]	±0.0 % [6]
Reynolds number	±3.9 % [7]	±3.7 % [7]
Other (geometry, pressure boundary cond., etc.)	unknown	unknown
Total (Comparability)	> ±15.3 %	> ±3.8 %

[1] for h=10 W/m^{2}K → Nu=230
[2] for h=200 W/m^{2}K → Nu=4597
[3] on fine grid of adaptive grid refinement
[4] on coarse grid
[5] made comparable by applying method of temperature ratio (→$Nu_{c.p.}$)
[6] influence is already considered in line "Fluid reference temperature"
[7] uncertainty in Nusselt number due to uncertainty in Reynolds number

Table 8 Experimental conditions

SYMMETRIC CASE	
Nozzles Distribution	n=6, equally distributed
Nozzle Orientation	φ_i=0°, ϑ_i=0°
Nozzle Type	round, d=0.012 m
Mean Nozzle Outlet Velocity	w=81 m/s (Re=62100, $\dot{V}$ =194 m³/h)

=−0.03 for a "constant heat flux" boundary condition. $Nu_{c.p.}$ values of experiments and simulations can directly be compared.

As the ratio Gr/Re^2 is much smaller than one, free convection can both be neglected in experiments and simulations and the differing conditions in temperature do not have any influence.

A sensitivity analysis with simulations of different turbulence intensity levels I at the nozzle outlet showed that the turbulence intensity affects the maximum heat transfer values on the window surface (±14.0%). However, the influence on the mean value is comparable small (±0.7%). As the turbulence intensity in the experiments was not measured, this fact contributes to the uncertainty in comparability between measurement and simulations.

The wall boundary condition in the experiments is of type "constant heat flux," whereas in the simulations, it is of type "constant temperature." Due to different heating in the boundary layer in the two types, there are differences in the heat transfer coefficient; if not the adiabatic fluid temperature is chosen as fluid reference temperature [21]. However, these differences are already considered in the value of 4.7% of the fluid reference temperature.

In the experiments, the Reynolds number could only be determined with an uncertainty of ±5%. This causes an uncertainty of 3.9% or 3.7% in the maximum or mean Nusselt number, respectively.

Additionally, there are other, differing boundary conditions in experiment and simulation, such as minor deviations in geometry or pressure boundaries. Unfortunately, the effects of these differences on heat transfer cannot be quantified.

The known uncertainties in comparability between experiments and simulations are approximately ±15.3% for the maximum and ±3.8% for the mean Nusselt number. Differences between experiments and simulations that are larger than the sum of the uncertainties are due to modeling errors in the simulations.

7 Results

7.1 Symmetric, Nonswirled Case. First, the results of a symmetric, nonswirled case with six nozzles, each charged with the same mass flow, are presented. The Reynolds number is 62,100 (more details are given in Table 8).

7.1.1 Flow Field. In Fig. 10 simulated profiles of the velocity distribution in the axial direction are plotted. On plane 1, the almost unchanged turbulent velocity profile of the nozzle outlet is visible. Further downstream on plane 2, the boundary layer starts developing on the window side. On the opposite side of the jet, the free shear layer develops. From plane 3 downstream, the wall jet is fully developed. However, due to the special cavity of the concave window, the jet degenerates gradually, until the axial velocity component is zero. At the top of the window, there is a stagnation point. The mass flow of a round jet in an unconfined space normally rises linearly with distance from the nozzle outlet. This is due to mass entrainment of the surrounding fluid. In the confined space of the window cavity this entrainment is limited by walls or adjacent jets. Hence, the greatest amount of entrained air does not originate from the direct surrounding of the jet, but comes from regions below the nozzle: 70% of the window cooling air mass flow is entrainment from the secondary concentrator, 16% is entrainment of air through the gaps (see Fig. 5 "pressure inlet"), and 14% of the air originates from the nozzle flow. The

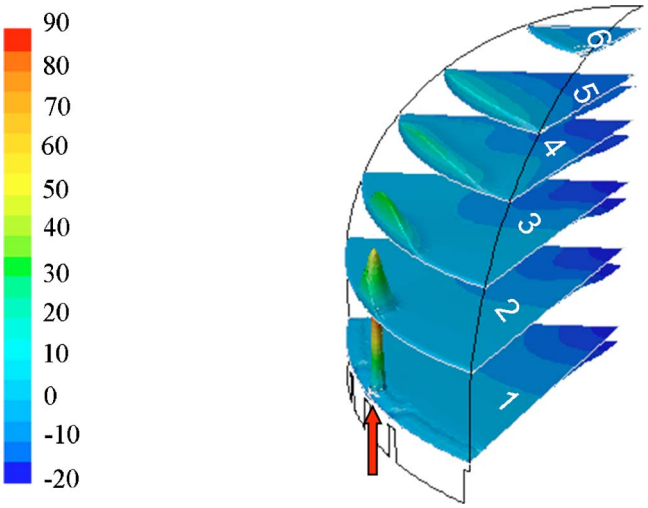

Fig. 10 Simulated contours of *z* velocity in m/s

total mass flow of the jets through each plane in Fig. 10 is listed in Table 9. Due to the confined space and the stagnation point at the top of the window, the air mass flow of the jets only increases little with distance from the nozzle, until from plane 2 downstream, the jet mass flow decreases again. R_i is defined as the ratio of the jet mass flow of plane i to the mass flow at nozzle outlet. A maximum ratio of 7.7 is reached in plane 2. The decreasing mass flow of the jet can also be observed in Fig. 10 when comparing the different integrals of the velocity profiles of different planes.

Another flow characteristic of the dome-shaped window is the second shear layer which is caused by incoming air of the jets and exiting air, which flows axially out of the cavity.

7.1.2 Heat Transfer. Figure 11 shows measured contours of the convective heat transfer. The lower edge of the window is assigned the value zero because there no measurement has been

Table 9 Mass entrainment of the six jets (symmetric)

Plane i (see Error! Reference source not found.)	Distance z_i in m	Total Jet Flow $\dot{M}_{tot,i}$ in kg/s	Ratio $R_i = \dot{M}_{tot,i} / \dot{M}_0$
1	0.050	0.47	7.4
2	0.150	0.49	7.7
3	0.230	0.48	7.5
4	0.300	0.43	6.7
5	0.350	0.32	5,0
6	0.400	0.02	0.3

Simulation with realizable k-ε Model; $\dot{M}_0$=0.064 kg/s

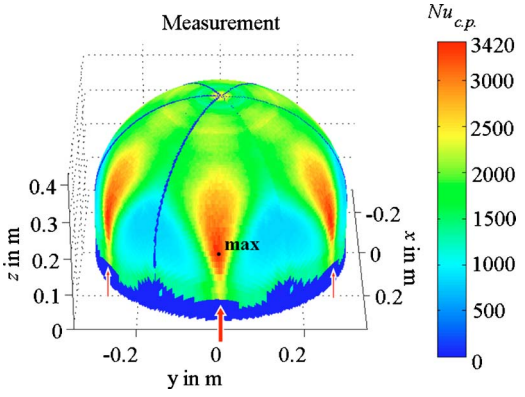

Fig. 11 Contours of measured Nusselt numbers

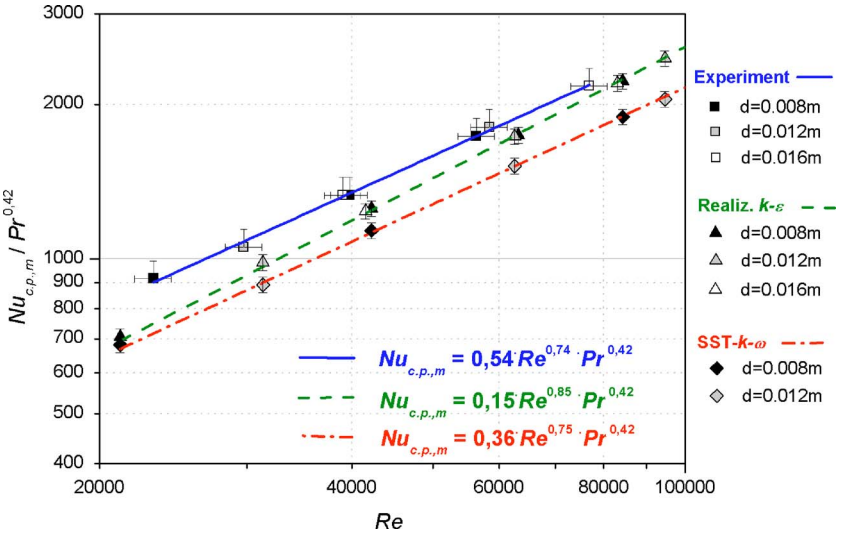

Fig. 12 Mean heat transfer on window surface, symmetric case with six nozzles

possible. As the field of vision of the camera is limited and the measurements showed periodicity, the plot in Fig. 11 is composed of identical 60 deg slices.

At the top of the window, the low Nusselt number, resulting from the stagnation point, can be seen. Also, there are high differences and high gradients in heat transfer on the window surface. This distribution causes high local temperatures and thermal stresses and is not favorable for window cooling. Configurations with nine simultaneously operating nozzles show an analogous distribution.

As expected, simulations and measurements indicate that only the flow field and heat transfer near the nozzles are influenced by the nozzle diameter. As long as the Reynolds number is kept constant, flow field and heat transfer some diameters away from the nozzle exit do not change with varying nozzle diameter. This can be seen in Fig. 12, where the mean heat transfer of six nozzles on the window surface is plotted as a function of the Reynolds number: Measurements or simulations with the same Reynolds number produce the same mean heat transfer, regardless of nozzle dimension. This finding allows us to fit the nozzle geometry to the limited available space at the receiver module, while maintaining the required heat transfer by simply adjusting the mass flow.

For measurements and simulations, the following functional dependence is found (Parameters, see Table 10):

$$\mathrm{Nu_m} = a \cdot \mathrm{Re}^m \cdot \mathrm{Pr}^n \cdot (T_w/T_f)^p \qquad (13)$$

The exponent of the Pr number has not been measured. For impinging flows, usually the exponent 0.42 is used [22,23]. The exponent p of the temperature ratio depends on the thermal boundary condition. It was determined in a simulation study. The entrainment ratio R, necessary for calculating the mean fluid temperature $T_{f,m}$ (Eq. (5)), depends on the size of the gap between the window flange and secondary concentrator. The bigger the nozzle diameter, the smaller is the gap and hence the smaller is the entrainment ratio R. For a symmetric configuration with six round nozzles and a nozzle diameter $d=0.008$ m ($d=0.012$ m, $d=0.016$ m), the entrainment ratio is $R=10$ ($R=7$, $R=5$).

Table 10 Parameters for Eq. (13), symmetric case with six nozzles

	a	*m*	*n*	*p*
Experiment	0,54 ±0,08	0,74 ±0,01	0,42	-0,06 [1] / -0,03 [2]
Realiz. *k-ε* Model	0,15 ±0,006	0,85 ±0,004	0,42	-0,06 [1] / -0,03 [2]
SST-*k-ω* Model	0,36 ±0,03	0,75 ±0,008	0,42	-0,06 [1] / -0,03 [2]

[1] "constant temperature" boundary condition
[2] "constant heat flux" boundary condition

7.1.3 Comparison Between Experiment and Simulation. Figure 14 shows measured and simulated heat transfer distributions for the above-described case. For comparison of different turbulence models, the simulations were performed with the realizable *k-ε* model, SST-*k-ω* model, and *k-ω* model. The spreading of the jet is similar in measurement and all performed simulations. Also, the low heat transfer in the stagnation point at the top of the window is observed in measurement and simulations.

However, the maximum heat transfer values of the simulations of all turbulence models are much higher than the measured ones. This is clarified in Fig. 13, in which the maximal Nusselt number of the experiments was corrected for lateral conduction in the measurements. The error bars of the experiment both contain the uncertainty of the measurement (first part in Table 7), as the uncertainty in comparability (third part in Table 7). Comparing maximum Nusselt numbers, it strikes that the difference between calculated and measured values is higher than the error bars. This implies a modeling error. It is assumed that in the simulations, even though the spreading is predicted correctly, the models do not correctly describe turbulence structure and heat transfer near the impingement point. In a comparison study, Craft et al. [24] also observed a too high heat transfer at the impingement point of a jet using a *k-ε* model. It is assumed that an excessive production of turbulent kinetic energy at the impingement point is responsible for the high heat transfer (see also [25]). The SST-*k-ω* model and the *k-ω* model also overestimate the impingement heat transfer. Under certain conditions, this observation was also made by Hofmann [26].

In Fig. 13, also the mean heat transfer over the window surface is shown. Here, the deviation between simulations and experiment is clearly smaller. The best value for the mean heat transfer is calculated with the realizable *k-ε* model. The performance of realizable *k-ε* model and SST-*k-ω* model for different Reynolds numbers is shown in Fig. 12. The mean heat transfer, calculated with the realizable *k-ε* model, is in the Reynolds number range from 20,000 to 80,000 between 5% and 18% smaller than the measured heat transfer. Considering the uncertainties in Reynolds and Nusselt numbers, this represents a good agreement. The SST-*k-ω* model shows in respect to mean values a poorer agreement. The SST-*k-ω* model predicts over the whole Reynolds number range a mean heat transfer coefficient that is about 19% smaller than the measured value.

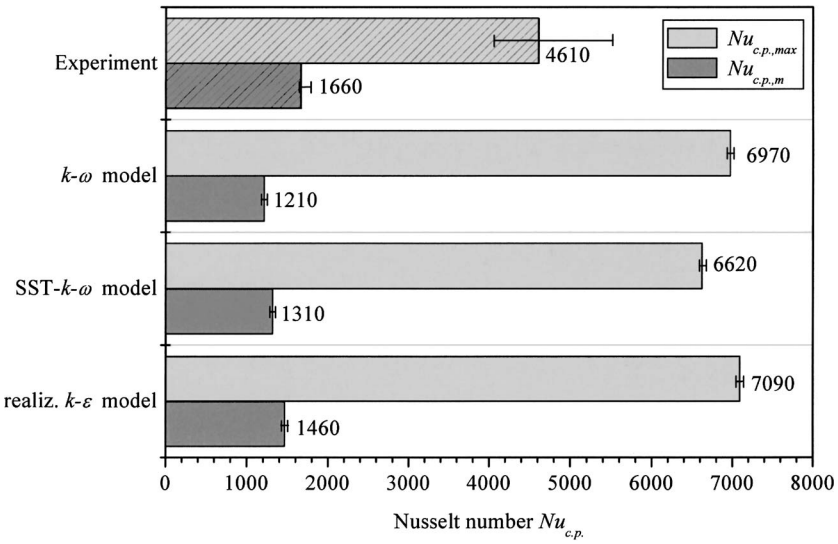

Fig. 13 Maximum and mean Nusselt numbers, symmetric case with six nozzles

It can be summarized that in the simulations, the flow field is predicted properly. Gradients in heat transfer are calculated with all examined turbulence models too high. While the maximum heat transfer at the jet impingement is predicted in all examined models too high, the mean values over the window surface in simulations with the realizable k-ε model are in good agreement.

7.2 Symmetric, Swirled Case. One idea for enhancing the heat transfer and homogenizing the temperature distribution over the window surface is to generate a swirled flow in the window cavity. This is achieved by inclining the nozzles. The setup for the investigated configuration is described in Table 11. The Reynolds number and nozzle dimension are practically the same as in the nonswirled, symmetric case.

A measured heat transfer distribution is shown in Fig. 15. In comparison with the nonswirled case in Fig. 11, it can be observed that the peaks with maximum heat transfer are lowered significantly by the inclination of the nozzles. However, in the top part of the window, a vortex is generated with low velocities in the axis of symmetry, resulting in low heat transfer coefficients. The simulations show an identical behavior. Between measurement and simulation there are analogous differences as described in Sec 7.1. Orientation azimuth angles φ between 10 deg and 80 deg have been simulated with a polar angle ϑ of 10 deg, but none of the configurations produced a better result. Hence, as a good cool-

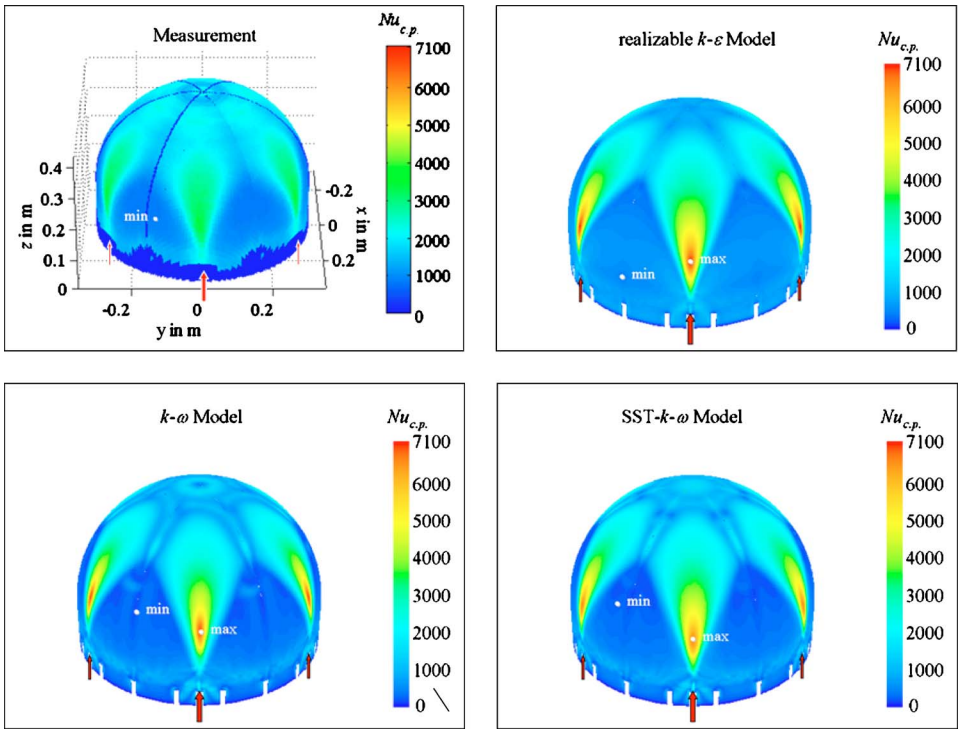

Fig. 14 Measured and simulated contours of Nusselt numbers, symmetric case with six nozzles

Table 11 Experimental conditions

SYMMETRIC CASE, SWIRLED	
Nozzles Distribution	n=6, equally distributed
Nozzle Orientation	φ_i=30°, ϑ_i=10°
Nozzle Type	round, d=0.012 m
Mean Nozzle Outlet Velocity	w=81 m/s (Re=62300, $\dot{V}$ =194 m³/h)

ing of the top of the window is essential, it can be concluded that swirled cooling schemes are not suitable for the window cooling.

7.3 Asymmetric, Modulated Case. As both the swirled and nonswirled symmetric configurations do not produce a homogeneous distribution of heat transfer on the window surface, an asymmetric configuration with flow modulation is considered. Five nozzles are simultaneously charged with air. Here, the nozzle type is rectangular, to fit into the limited available space at the solar receiver. The nozzle Reynolds number is 65,800 and the flow is not swirled. More details about this case can be found in Table 12.

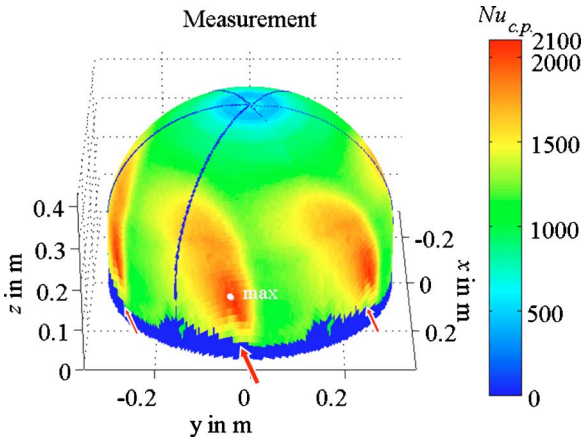

Fig. 15 Contours of measured Nusselt numbers, swirled case with six nozzles

Table 12 Experimental conditions

ASYMMETRIC CASE, MODULATED	
Nozzles Distribution	n=18, equally distributed simultaneously charged: n=5
Nozzle Orientation	φ_i=0°, ϑ_i=0°
Nozzle Type	rectangular 0.033m x 0.060m, → d_h=0.016 m
Mean Nozzle Outlet Velocity	w=64 m/s (Re=65800, $\dot{V}$ =233 m³/h)

Definition of the hydraulic diameter: $d_h = 2\sqrt{\frac{A}{\pi}}$

Table 13 Mass entrainment of the five jets (asymmetric)

Plane i	Distance z_i in m	Total Jet Flow $\dot{M}_{tot,i}$ in kg/s	Ratio $R_i = \dot{M}_{tot,i} / \dot{M}_0$
1	0.050	0.45	5.8
2	0.150	0.47	6.2
3	0.230	0.43	5.6
4	0.300	0.35	4.6
5	0.350	0.24	3.2
6	0.400	0.05	0.7

$\dot{M}_0$ =0.077 kg/s

7.3.1 Flow Field. A significant advantage of the asymmetric air injection is the absence of a stagnation point at the top of the window, i.e., the provision of sufficient heat transfer. This can be seen in Table 13, where the development of the mass entrainment over six planes is listed. At plane 6, the ratio R_6 between jet mass flow and nozzle mass flow still is 0.7, whereas in the symmetric case it is only 0.3.

In the considered asymmetric configuration, only 6% of the window cooling mass flow is drawn in from the gaps, compared to 16% in the symmetric case. In the asymmetric case, 76% of the air originates from the secondary concentrator; 18% of the window cooling air is nozzle discharge air, compared to 14% in the symmetric case.

7.3.2 Heat Transfer. Since transient analyses would have been too time consuming, this case has been simulated as steady state. This approximates a case in which the period of circulation of the charged nozzles around the window circumference is very high ($T \rightarrow \infty$ s). In actual measurements both stationary as well as transient cases have been investigated. Nevertheless, the simulation of the steady state reveals useful information about the efficiency of the cooling compared with the symmetric cases.

Figure 16 shows measured and simulated distributions of heat transfer for the considered asymmetric configuration without periodic mass flow modulation ($T \rightarrow \infty$ s). As the field of vision of the IR camera is limited, the left plot in Fig. 16 is composed of three separate measurements. The lower edge of the window and the point at the top could not be measured with satisfactory accuracy. The right plot shows a simulation performed with the realizable k-ε model.

In simulation and measurement, high Nusselt numbers at the impingement points are observed, as well as a sufficient heat transfer at the top of the window. At both sides of the region with active nozzles, the heat transfer is only poor. The maximum heat

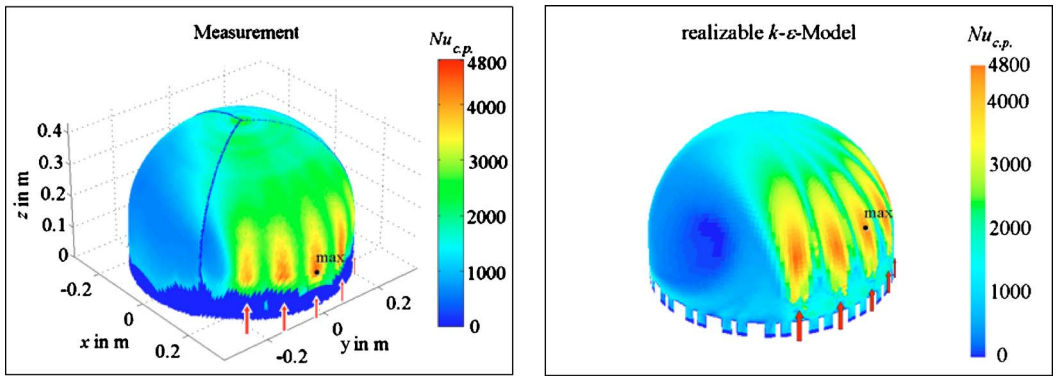

Fig. 16 Measured and simulated contours of Nusselt numbers, asymmetric case with five jets ($T \rightarrow \infty$ s)

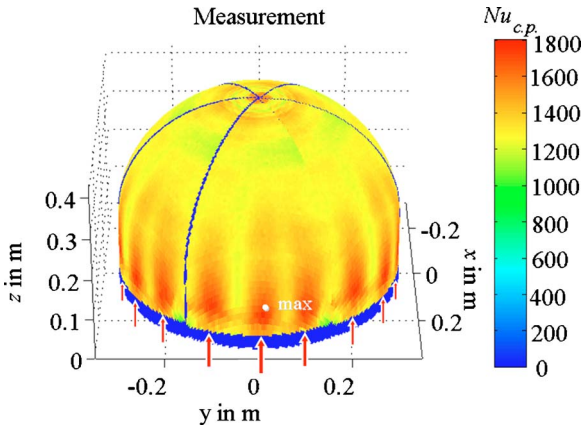

Fig. 17 Contours of measured Nusselt numbers, asymmetric case with five jets, modulated (T=22 s)

transfer values of the simulation are not much higher than in the measurements as this was the case in the symmetric configurations. This is simply due to the fact that the mesh in the asymmetric configuration was still too coarse to accurately predict maximal values. Due to limited computer resources in the asymmetric case, a further grid refinement was not possible.

The homogenization of the heat transfer distribution is achieved by a periodic mass flow modulation ($T<\infty$s). The measured heat transfer distribution for a circulation rate of the pulsating jets of T=22 s is shown in Fig. 17.

As the measurements showed periodicity, the plot in Fig. 17 is composed of identical 60° slices. As expected from the simulated flow fields and heat transfer without mass modulation, the top region is now cooled effectively.

In addition, the homogeneity of the heat transfer distribution has improved substantially in comparison to the symmetric cases. The difference in measured heat transfer coefficient between maximum and minimum is, in the asymmetric case, about 50% of the mean value, whereas for the nonswirled symmetric case this values lies in the range of 150%. Hence, the asymmetric configuration with flow modulation is a viable option for cooling the receiver window.

In Fig. 18, the mean heat transfer coefficient on the receiver window for five simultaneously operating nozzles is plotted over

Table 14 Parameters for Eq. (13), asymmetric case with five nozzles

	a	m	n	p
Experiment	0,10 ±0,04	0,87 ±0,04	0,42	-0,06 [1] / -0,03 [2]
Realiz. k-ε Model	0,10 ±0,02	0,87 ±0,02	0,42	-0,06 [1] / -0,03 [2]

[1] "constant temperature" boundary condition
[2] "constant heat flux" boundary condition

the Reynolds number. The circulation rate of the rotating flow field for one presented set of measurements was 22 s. For the other set of measurements and the simulation, it was infinite (no rotation).

The Reynolds number dependence of the measured mean heat transfer for the considered asymmetric configuration can again be expressed with Eq. (13) The parameters for the asymmetric case with five nozzles can be found in Table 14.

The entrainment ratio R, necessary for calculating the mean fluid temperature $T_{f,m}$ (Eq. (5)) for the used slot nozzles, is R=6. If round nozzles with diameter d=0.012 m are used, the entrainment ratio is R=7.

The Reynolds number dependence of the heat transfer is slightly higher than in the symmetric cases. However, in the considered Reynolds number range the mean heat transfer for the asymmetric case remains smaller than for the symmetric case.

In Fig. 18, the small difference of mean heat transfer between measurement and simulation with the realizable k-ε model is visible. The simulations predict the mean heat transfer ~11% too small.

There is no significant difference between the mean value of heat transfer between measurements with different rates of circulation. This is due to two opposing effects on the heat transfer. On the one side, if the rotational frequency is too high, the different flows in the domain create more dissipation and the heat transfer should get worse. On the other side, the heat transfer for a transient case should be higher than for a steady case, because pulsating jets generate continuously the development of new boundary layers, which enhances the heat transfer. It seems that the two effects almost compensate each other for the investigated time scale.

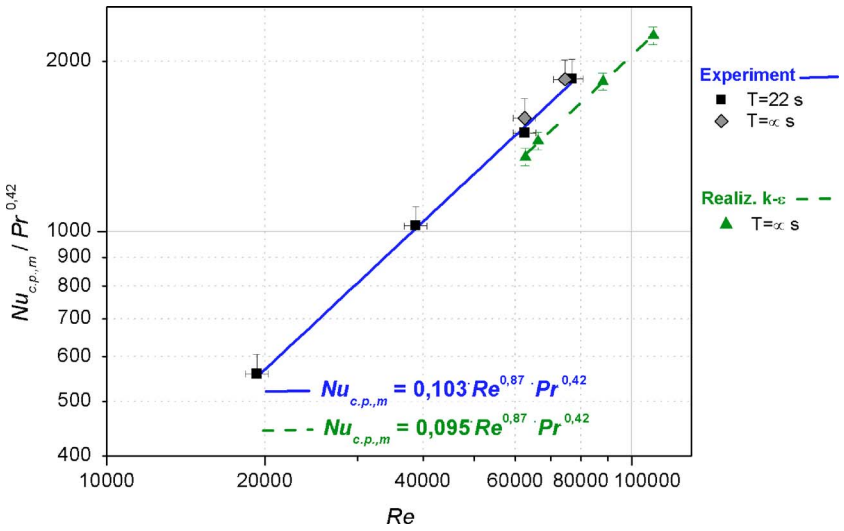

Fig. 18 Mean heat transfer on window surface, asymmetric case with five jets, modulated

8 Application

In the SOLGATE project, the asymmetric, modulated window cooling scheme was integrated in a high temperature solar receiver module. It was successfully tested under real solar test conditions on the Plataforma Solar de Almería (Spain) in summer 2003 and 2004. Operating the module with air exit temperatures of over 1000°C, the window temperature was kept below 700°C. Assuming that a receiver cluster, consisting of low, middle, and high temperature module, has a thermal output of 800 kW with a thermal to electric efficiency of 40%, the parasitic electric power consumption of the active window cooling system is only in the range of 0.2% of the produced electricity.

9 Conclusion

The comparison between experimental and numerical investigation indicates that the flow field is predicted correctly by the simulations. However, in the present case of the jet cooling system, local values of heat transfer are not always calculated accurately. The maximum heat transfer at the jet impingement is overestimated in all examined turbulence models (realizable k-ε model, SST-k-ω model, and k-ω model), resulting in higher gradients in heat transfer. However, in terms of mean heat transfer, the agreement between simulation and experiment is better. The mean heat transfer calculated with the realizable k-ε model shows a good agreement with measurements. In the investigation of the presented jet cooling system, CFD analysis with state-of-the-art turbulence models is a viable tool to compare different cooling schemes and to obtain values of mean heat transfer. However, experimental investigations are still necessary to get accurate information about local heat transfer coefficients.

It was shown that swirled and nonswirled nozzle configurations of the air jet cooling system do not provide a homogeneous heat transfer distribution. Also, the cooling of the top part of the window in the symmetric cases is insufficient. By means of the asymmetric, modulated air jet cooling scheme, it is possible to homogenize the heat transfer distribution and to generate the necessary heat fluxes at the top of the window, hence reducing high temperatures and temperature gradients. It was also shown that the nozzle geometry can be adapted to the spatial requirements of the solar receiver. With the air jet cooling, the necessary cooling flux can be adjusted to the actual operating conditions of the receiver by simply adapting the nozzle mass flow.

With the investigated air jet cooling, it is possible to maintain the receiver window at acceptable temperatures. The parasitic energy consumption of the cooling system is low compared to the produced electric energy. Investment and maintenance costs for the installations are acceptable. At times when no active cooling is needed, the installation does not block incoming solar radiation. The modulated window cooling is a reliable and low-cost way to actively cool the receiver window to meet the requirements for solar operation.

Acknowledgments

The support from the German Ministry of Economy and Technology, the German Ministry of Education and Research, and the European Commission is gratefully acknowledged. Thanks to all students and my colleagues, who supported this work.

Nomenclature

a = thermal diffusivity, constant in Eq. (13)
A = nozzle cross section, actual fractional error
Bi = Biot number
c = variable in Eqs. (7) and (9)
c_p = specific heat capacity
d_h = hydraulic diameter
D_w = window diameter
E = estimated fractional error
Ec = Eckert number
f = frequency
g = gravitational constant
Ga = Galilei number
Gr = Grashof number
GCI = grid convergence index
h = (convective) heat transfer coefficient
I = turbulence intensity
k = wall roughness, turbulent kinetic energy
L_P = curve length coordinate of point P
L_{max} = maximum curve length (=0.599 m)
l = turbulence length scale
m = exponent in Eq. (13)
$\dot{M}_0$ = nozzle mass flow rate of all active nozzles
$\dot{M}_{tot,i}$ = total jet mass flow rate through plane i
N = number of cells
n = total number of nozzles, exponent in Eq. (13)
Nu = Nusselt number ($\mathrm{Nu}=hL_{max}/\lambda$)
p = exponent in Eq. (13)
Pr = Prandtl number
$\dot{Q}$ = heat flow rate
$\dot{q}$ = heat flux rate
r = radius
$r_{eff,ij}$ = effective grid refinement ratio
R = ratio of total jet mass flow to nozzle mass flow
Re = Reynolds number ($\mathrm{Re}=\rho w_m d_h/\eta$)
T = temperature, period of circulation
$\dot{V}$ = nozzle volumetric flow rate
w = nozzle exit velocity
y^+ = dimensionless wall distance
z_i = axial coordinate of plane i

Greek symbols

β = coefficient of thermal expansion
Δ = difference
ε_{ij} = relative difference grid $i \rightarrow j$
η = viscosity
ϕ_i = position azimuth angle of nozzle i
ϕ_P = azimuth angle of point P
φ = phase response
φ_i = orientation azimuth angle of nozzle i
λ = thermal conductivity
ϑ_i = orientation polar angle of nozzle i
ρ = density
ω = angular frequency

Subscripts and Superscripts

conv = convective
c.p. = constant properties
f = fluid
i = index fine grid
j = index coarse grid
m = mean
max = max
noz = nozzle
rad = radiative
w = wall
$+$ = dimensionless
* = convective and radiative

References

[1] Winter, C. J., Sizmann, R. L., and Vant-Hull, L. L. (Eds.), 1999, *Solar Power Plants*, Springer Verlag, Berlin, Heidelberg.
[2] Schwarzbözl, P., Pitz-Paal, R., Meinecke, W., and Buck, R., 2000, "Cost Op-

timized Solar Gas Turbine Cycles using Volumetric Air Receiver Technology," Proc. 10th SolarPACES Int. Symposium "Solar Thermal 2000", March 8–10, Sydney, Australia.
[3] Buck, R., Bräuning, T., Denk, T., Pfänder, M., Schwarzbözl, P., and Tellez, F., 2002, "Solar-Hybrid Gas Turbine-based Power Tower Systems (REFOS)," ASME J. Sol. Energy Eng., **124**, pp. 2–9.
[4] Buck, R., Lüpfert, E., and Téllez, F., 2000, "Receiver for Solar-Hybrid Gas Turbine and CC Systems (REFOS)," Proc. 10th SolarPACES Int. Symposium "Solar Thermal 2000", Sydney, Australia.
[5] Sugarmen, C., Ring, A., Buck, R., Uhlig, R., Beuter, M., Marcos, M. J., and Fernandez, V., 2002, "Solar-Hybrid Gas Turbine Power System," Proc. of 11th Solar-PACES Int. Symposium on Concentrated Solar Power and Chemical Energy Technologies, September 4–6, Zurich, Switzerland.
[6] Buckingham, E., 1914, "On Physically Similar Systems," Phys. Rev., **4**(4), p. 345.
[7] Gambit 2, 2001, *User's Guide*, Fluent, Inc., Lebanon, NH.
[8] Schlichting, H., and Gersten, K., 1997, *Grenzschicht-Theorie*, 9. Auflage, Springer Verlag, Berlin.
[9] Wilcox, D. C., 1998, *Turbulence Modeling for CFD*, 2nd ed., DCW Industries, Inc., La Cañada, CA.
[10] Shih, T.-H., Liou, W. W., Shabbir, A., Yang, Z., and Zhu, J., 1995, "A New k-ε Eddy-Viscosity Model for High Reynolds Number Turbulent Flows—Model Development and Validation," Comput. Fluids, **24**(3), pp. 227–238.
[11] Fluent 6.1, 2003, *User's Guide*, Fluent, Inc., Lebanon, NH.
[12] Menter, F. R., 1994, "Two-Equation Eddy-Viscosity Turbulence Models for Engineering Applications," AIAA J., **32**(8), pp. 1598–1605.
[13] Wolfstein, M., 1969, "The Velocity and Temperature Distribution of One-Dimensional Flow with Turbulence Augmentation and Pressure Gradient," Int. J. Heat Mass Transfer, **12**, pp. 301–318.
[14] Rist, D., 1995, *Dynamik Realer Gase*, Springer Verlag, Berlin.
[15] Ferziger, J. H., and Perić, M., 1999, *Computational Methods for Fluid Dynamics*, 2nd ed., Springer-Verlag, Berlin.
[16] Richardson, L. F., 1911, "The Approximate Arithmetical Solution by Finite Differences of Physical Problems Involving Differential Equations, with an Application to the Stresses in a Masonry Dam," Philos. Trans. R. Soc. London, Ser. A, **210**, pp. 307–357.
[17] Richardson, L. F., and Gaunt, J. A., 1927, "The Deferred Approach to the Limit. Part I. Single Lattice. Part II. Interpenetrating Lattices," Philos. Trans. R. Soc. London, Ser. A, **226**, pp. 299–361.
[18] Roache, P. J., 1998, *Verification and Validation in Computational Science and Engineering*, Hermosa Publishers, Albuquerque, NM.
[19] Roache, P. J., 1993, "A Method for Uniform Reporting of Grid Refinement Studies, Quantification of Uncertainty in Computational Fluid Dynamics," FED (Am. Soc. Mech. Eng.), **158**, pp. 109–120.
[20] Herwig, H., 1985, *Asymptotische Theorie zur Erfassung des Einflusses variabler Stoffwerte auf Impuls-und Wärmeübertragung*, Fortschr.-Ber. VDI, Reihe 7, Nr. 93, VDI-Verlag, Düsseldorf.
[21] Moffat, R. J., 1990, "Experimental Heat Transfer," in Hestroni, G., (Ed.): *Heat Transfer 1990*, Vol. 1, Hemisphere, Washington, DC, pp. 187–205.
[22] Hausen, H., 1959, "Neue Gleichungen für die Wärmeübertragung bei freier oder erzwungener Strömung," Allg. Wärmetechnik, **9**(4/5), pp. 75–79.
[23] Martin, H., 1977, "Heat and Mass Transfer between Impinging Gas Jets and Solid Surfaces," Adv. Heat Transfer, **13**(1), pp. 1–60.
[24] Craft, T. J., Graham, L. J. W., and Launder, B. E., 1993, "Impingement Jet Studies for Turbulence Model Assessment-II. An Examination of the Performance of Four Turbulence Models," Int. J. Heat Mass Transfer, **36**(10), pp. 2685–2697.
[25] Behnia, M., Parneix, S., Shabany, Y., and Durbin, P. A., 1999, "Numerical Study of Turbulent Heat Transfer in Confined and Unconfined Impinging Jets," Int. J. Heat Fluid Flow, **20**, pp. 1–9.
[26] Hofmann, H., 2005, *Wärmeübergang beim pulsierenden Prallstrahl*, dissertation, Universität Karlsruhe (TH).

Self-Preserving Mixing Properties of Steady Round Nonbuoyant Turbulent Jets in Uniform Crossflows

F. J. Diez
Department of Mechanical and Aerospace Engineering,
Rutgers, The State University of New Jersey,
Piscataway, NJ 08854-8058
e-mail: diez@jove.rutgers.edu

L. P. Bernal

G. M. Faeth

Department of Aerospace Engineering, The University of Michigan Ann Arbor, Michigan 48109-2140

The self-preserving mixing properties of steady round nonbuoyant turbulent jets in uniform crossflows were investigated experimentally. The experiments involved steady round nonbuoyant fresh water jet sources injected into uniform and steady fresh water crossflows within the windowed test section of a water channel facility. Mean and fluctuating concentrations of source fluid were measured over cross sections of the flow using planar-laser-induced-fluorescence (PLIF). The self-preserving penetration properties of the flow were correlated successfully similar to Diez et al. [ASME J. Heat Transfer, ***125****, pp. 1046–1057 (2003)] whereas the self-preserving structure properties of the flow were correlated successfully based on scaling analysis due to Fischer et al. [Academic Press, New York, pp. 315–389 (1979)]; both approaches involve assumptions of no-slip convection in the cross stream direction (parallel to the crossflow) and a self-preserving nonbuoyant line puff having a conserved momentum force per unit length that moves in the streamwise direction (parallel to the initial source flow). The self-preserving flow structure consisted of two counter-rotating vortices, with their axes nearly aligned with the crossflow (horizontal) direction, that move away from the source in the streamwise direction due to the action of source momentum. Present measurements extended up to 260 and 440 source diameters from the source in the streamwise and cross stream directions, respectively, and yielded the following results: jet motion in the cross stream direction satisfied the no-slip convection approximation; geometrical features, such as the penetration of flow boundaries and the trajectories of the axes of the counter-rotating vortices, reached self-preserving behavior at streamwise distances greater than 40–50 source diameters from the source; and parameters associated with the structure of the flow, e.g., contours and profiles of mean and fluctuating concentrations of source fluid, reached self-preserving behavior at streamwise (vertical) distances from the source greater than 80 source diameters from the source. The counter-rotating vortex structure of the self-preserving flow was responsible for substantial increases in the rate of mixing of the source fluid with the ambient fluid compared to corresponding axisymmetric flows in still environments, e.g., transverse dimensions in the presence of the self-preserving counter-rotating vortex structure were 2–3 times larger than transverse dimensions in self-preserving axisymmetric flows at comparable conditions.* [DOI: 10.1115/1.1991868]

Keywords: Heat Transfer, Jets, Scaling, Dispersion, Turbulence

Introduction

Recent studies of the temporal and steady penetration properties of round turbulent puffs, thermals, starting and steady jets, and starting and steady plumes in both still fluids and uniform crossflows [1–4], were extended to consider the mixing properties of steady round nonbuoyant turbulent jets in uniform crossflows. The study of this flow is motivated by practical applications to the dispersion of potentially harmful releases of heat and substances in atmospheric crosswinds. The present study emphasized flow properties far from the source, where effects of source disturbances are lost, where the flows are largely controlled by their conserved properties, where flow properties approximate self-preserving turbulent flow behavior, and where appropriately scaled flow properties become independent of the distance from the source. The particular advantages of self-preserving turbulent flows are that their properties considerably simplify the presentation of measurements because source disturbances do not affect flow properties and flow properties can be summarized in a relatively compact manner. The present description of the research is brief; additional details about experimental and scaling considerations, and a more complete report of the results, can be found in Diez et al. [5].

It will be shown that streamwise velocities of jets in crossflow progressively decrease with increasing streamwise distance so that the streamwise velocity eventually becomes small and the trajectory of the jet in crossflow becomes nearly horizontal far from the source where self-preserving behavior is approached. When this condition is approached, the streamwise penetration of the flow approximates a two-dimensional horizontal line puff in a still fluid. Then, the streamwise motion of the line puff, retarded along its sides in the streamwise direction by the ambient uniform crossflow, naturally leads to the flow becoming two nearly horizontal counter-rotating vortices whose axes are aligned along the axis of the jet as a whole and are thus nearly horizontal as well. Evidence of the structure of the counter-rotating vortices has been observed by Smith and Mungal [6] and Lee and Chu [7].

Most practical exhaust jet releases are exposed to crossflow;

Contributed by the Heat Transfer Division for publication in the JOURNAL OF HEAT TRANSFER. Manuscript received by the Heat Transfer Division May 15, 2004; revision received March 1, 2005. Review Conducted by: J. H. Lienhard V.

therefore, there have been many attempts to extend the results just discussed for jets in still fluids to corresponding round nonbuoyant turbulent jets in uniform crossflows, e.g., see Diez et al. [4], Keffer and Baines [8], Kamotani and Greber [9], Chassaing et al. [10], Andreopoulos and Rodi [11], Broadwell and Breidenthal [12], Askari et al. [13], Kelso et al. [14], Smith and Mungal [6], Lee and Chu [7], and references cited therein. These studies generally have indicated that motion in the crossflow direction (normal to the axis of the source jet) satisfies the no-slip convection approximation and that deflection of the jet toward the crossflow direction results in the development of a counter-rotating vortex system over the cross section of the flow. Measurements of the mixing structure of these flows generally have been limited to the region near the source where the flow undergoes most of its deflection toward the cross stream direction. Detail concentration measurements in the counter-rotating vortex cross section have been performed by Smith and Mungal [6] for jets with source/crossflow velocity ratio $u_o/v_\infty=5$, 10, 15, 20, 25 (sets of 400 images) and vertical penetrations as far as 75 source diameters for their $u_o/v_\infty=25$ case. The present study complements these measurements by providing data of the concentration over the cross section of the flow in a region $14<u_o/v_\infty<139$ (sets of 4000 images) and vertical penetration as far as 260 diameters from the source. Studies of the potential self-preserving behavior of this flow show that the decay of streamwise velocities with increasing streamwise distance from the source is relatively rapid so that the flow eventually becomes nearly aligned to the horizontal direction for all initial streamwise/crossflow velocity ratios u_o/v_∞. Thus, self-preserving behavior for these flows eventually involves no-slip convection in the crossflow (horizontal) direction combined with the motion of a line puff in the streamwise (vertical) direction, see Diez et al. [4], Fischer et al. [15], and List [16]. Relationships for the self-preserving transient and steady penetration properties of these flows have been confirmed by measurements, obtaining results similar to the corresponding flows in still environments. In particular, the flows become turbulent within five source diameters from the source in the streamwise direction and their penetration properties become self-preserving at streamwise distances greater than 40–50 source diameters from the source [4]. On the other hand, the rates of mixing and structure properties of these flows at self-preserving conditions have not yet received any attention.

Motivated by the previous discussion, the objectives of the present investigation were to extend past work concerning the self-preserving penetration properties of round nonbuoyant turbulent jets in uniform crossflows, in order to develop an improved understanding of their structure, as follows:

1. Measure the mixing structure of these flows, including the trajectories of the axes of the counter-rotating vortices, and the mean and rms fluctuating source fluid concentrations within the vortex system, for steady flow conditions and various source conditions typical of practical applications.
2. Exploit the new measurements of these flows in order to evaluate the effectiveness of their self-preserving scaling relationships, given by Diez et al. [4] for penetration properties and by Fischer et al. [15] and List [16] for flow structure properties, and to determine the empirical parameters associated with the various scaling relationships.

The present description of the research begins with a discussion of experimental methods. This is followed by a discussion of the self-preserving scaling properties of the flows. Experimental scaling results are then described, considering flow penetration properties and flow structure properties, respectively.

Experimental Methods

Test Apparatus. The present experiments adopted methods of water modeling of turbulent flows as suggested by Steckler et al. [17]. Thus, the experiments involved fresh water sources injected into an unstratified and uniform fresh water crossflow produced by a water channel facility shown in Fig. 1. The test section of the water channel had cross-section dimensions of 610×610 mm and a length of 2440 mm. The side and bottom of the test section were constructed of 20 mm thick acrylic panels to provide optical access. Fresh water crossflow in the channel was driven by a propeller pump to yield test section velocities of 40–300 mm/s. The flow properties of the water channel were characterized using a hot-film anemometer to calibrate the crossflow velocity as a function of propeller speed and to measure the uniformity and the turbulence levels of the crossflow. The contraction ratio of ten to one (a fifth-order polynomial with zero slope and curvature at the entrance and exit), flow straighteners, screens, etc., of the water channel combine to yield a flow nonuniformity better than 1.5%, and turbulence intensity levels less than 1%, in the test section.

The source flows were injected vertically downward into the fresh water channel flow for measurements of steady round nonbuoyant turbulent jets in uniform crossflows and along the axis of the water channel in the direction of water flow when the water channel is circulating for measurements of steady round nonturbulent jets in a still environment. The source flow passes through smooth round tubes having inside diameters of 1.6, 3.2, and 6.4 mm. The injector passages had length/diameter ratios of 200, 100, and 50, respectively, to help insure fully developed turbulent pipe flow at the source exit for sufficiently large injector Reynolds numbers, as discussed by Wu et al. [18]. The injector tubes were mounted vertically and discharged roughly 25 mm below the liquid surface. The source tubes passed through a flat horizontal plexiglas plate (508×914 mm in plan dimensions $\times12$ mm thick) with a tight fit. The source tube exits were mounted flush with the lower surface of the plexiglas plate in order to provide well-defined entrainment conditions near the source exit. The source liquid was supplied to the tubes using either syringe pumps (Harvard Apparatus, PHD2000, Model 70-2000, with four 150 cc syringes having volumetric accuracies of ±1% mounted in parallel) for small flow rates, and a peristaltic pump (Masterflux L/S Digi-Staltic Dispersion, Model 72310-0) for large flow rates. The pumps were calibrated by collecting liquid for timed intervals [1].

Instrumentation. Observations of illuminated dye-containing source liquids were obtained using charge-coupled device (CCD) digital video cameras during earlier studies of the penetration properties of starting and steady round turbulent jets in still and crossflowing environments [1–4]. A portion of these results for steady round nonbuoyant turbulent jets in crossflowing environments will be considered here for completeness; experimental methods for these measurements are described in Refs. [1–4] which should be considered for these details. Present measurements of both penetration and structure properties, however, involved use of the planar-laser-induced-fluorescence (PLIF) technique which will be discussed in the following.

The PLIF arrangement was based on past applications of this technique reported by Ferrier et al. [19], Karasso and Mungal [20], Law and Wang [21], Cowen et al. [22], Crimaldi and Koseff [23], Webster et al. [24], and Tian and Roberts [25]. The arrangement consisted of a laser, optics for scanning the laser beam across the image area, and a digital camera for recording the image. The fluorescent dye used was Rhodamine 6G at a concentration of $3.0–5.0\times10^{-6}$ mol/l in the source liquid with a Schmidt number $Sc=1250$ (Crimaldi and Kosseff [23]). At this Schmidt number, the scalar diffuses much slower than the vorticity allowing for clear observation of the vortex core. Rhodamine 6G dye was selected because it has attractive properties concerning linearity, decay, blooming, and photobleaching. This dye has a central absorption peak at 530 nm and a central emission (fluorescence) peak at 560 nm with bandwidths of roughly 40 nm for each of these peaks [19]. Thus, an argon-ion laser (Coherent Innova 90-4)

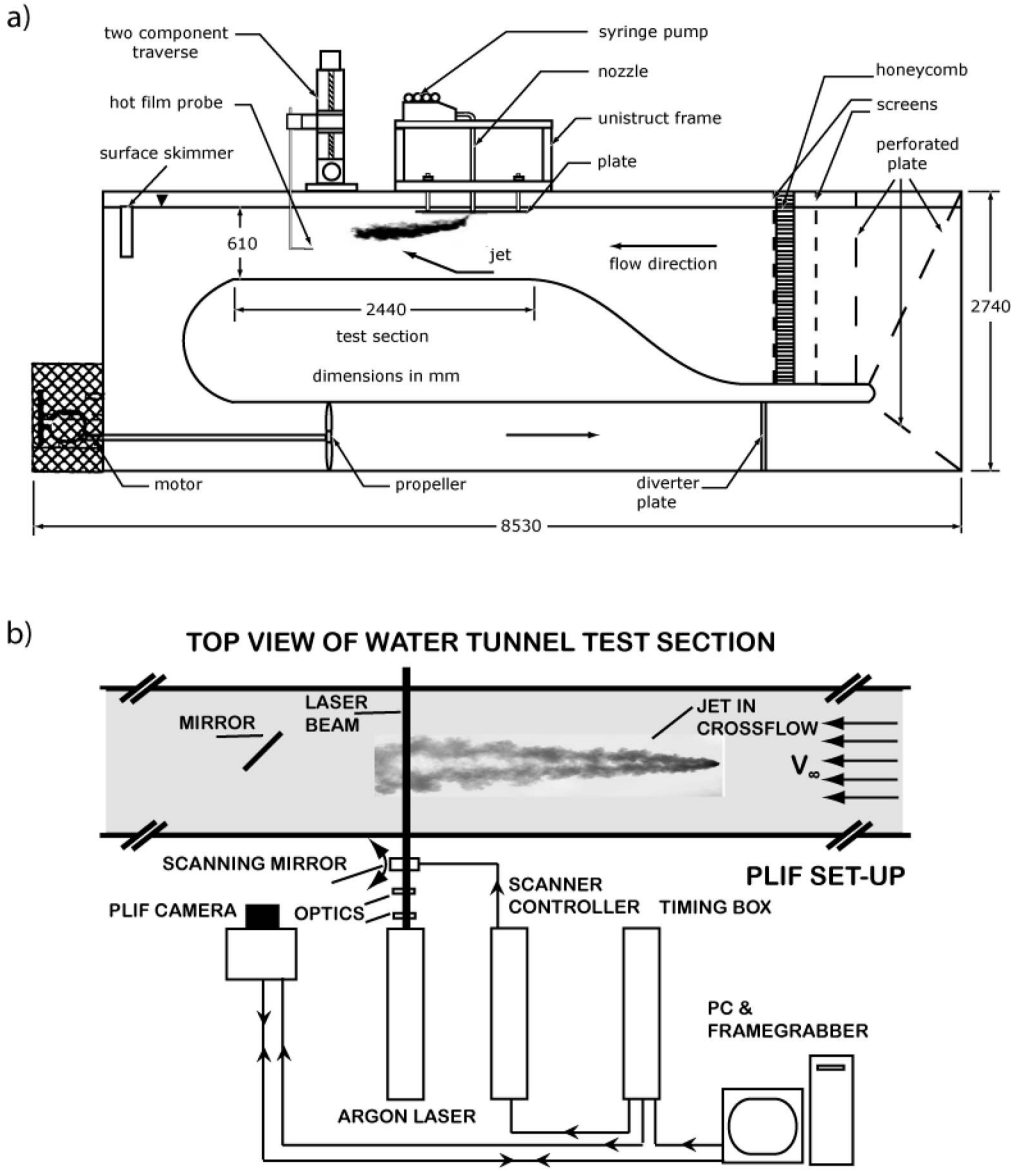

Fig. 1 Water channel facility (*a*), and experimental setup (*b*)

operated in the single-line mode at 514.5 nm with an optical power of 3500 mW and a beam diameter of 1.5 mm (at the e^{-2} intensity locations) provided effective excitation of the dye [23].

The optical arrangement was qualitatively similar to the imaging apparatus discussed by Crimaldi and Koseff [23]. The beam was swept across the measuring plane without focusing, yielding an illumination thickness of 1.5 mm (at the e^{-2} intensity locations). The beam was scanned using a General Scanning Inc. (MA, USA) Model 6120DT scanner in conjunction with a Model CX-660 controller. The scanned area had plan dimensions of 302×302 mm in the cross section which was crossed with a sweep time of 14 ms at a temporal frequency of 20 Hz.

A mirror located roughly 1000 mm downstream of the imaged cross section of the flow allowed the camera to view the image. The camera was a Redlake Inc. (CA, USA) Model Mega Plus ES 1020. This camera has a 1004×1004 pixel array with a 7.4×7.4 μm pixels to yield a 7.4×7.4 mm active sensor area. The intensity resolution of the pixels was 10-bit which provided 1024 gray levels. A PC-CamLink frame grabber from Coreco Imaging (MA, USA) transferred the camera images to a computer for processing and storage. The images were corrected for vignetting, sweep-geometry, attenuation, and background effects as discussed in earlier reports of PLIF technology [19–25]. The mean and rms fluctuating concentrations of source fluid were obtained over the cross section of the flow by averaging 4000 images.

Test Conditions. Test conditions for the present experiments considering steady round nonbuoyant turbulent jets in crossflowing fluids are summarized in Table 1. The experiments involved round fresh water source jets flowing into crossflowing fresh water environments. Other overall test conditions were as follows: source diameters of 1.6, 3.2, and 6.4 mm; corresponding source passage length/diameter ratios of 200, 100, and 50, either ambient velocities of zero or source/ambient velocity ratios 7–139, source Reynolds numbers of 3000–16,000, streamwise (vertical) penetration distances of 25–400 source diameters, and cross stream (horizontal) penetration distances of 0–440 source diameters.

Scaling Considerations

Conditions for Self-Preservation. The present discussion of scaling for round nonbuoyant turbulent jets in crossflowing envi-

Table 1 Summary of test conditions for steady round nonbuoyant turbulent jets in uniform crossflowing environments[a]

Environment	Crossflow
Source and ambient fluid	water
Fluid density (kg/cu-m)	998
Fluid kinematic viscosity (sq-mm/s)	1.0
Source diameter, d (mm)	1.6, 3.2, 6.4
Source passage length, L/d	200, 100, 50
Source flow rate (cc/s)	7-40
Source Reynolds number, $u_o d/\nu_o$	3,000-16,000
Source/ambient velocity ratio, u_o/v_∞	7-139
Streamwise (vertical) penetration distance, $(x\text{-}x_{os})/d$	25-260
Cross stream (horizontal) penetration distances, $(y\text{-}y_o)/d$	0-440
Characteristic flow times, $(t\text{-}t_o)u_o/d$	0-12,000

[a]Fresh water jets injected vertically downward from round tubes into fresh water in a 610×610 mm channel at an ambient pressure and temperature of 99.0 ± 0.5 kPa and 297.0 ± 0.5 K.

ronments addresses three aspects of scaling, in turn: (1) conditions required for self-preservation, (2) self-preserving penetration properties, and (3) self-preserving structure properties. The discussion is limited to the behavior of steady round nonbuoyant turbulent jets, see Diez et al. [2,4] for consideration of the penetration properties of starting jets.

A parameter frequently used to estimate when steady round turbulent unconfined flows satisfy self-preserving behavior is the distance from the effective (virtual) origin of the flow normalized by the source diameter, $(x\text{-}x_{os})/d$, taken to be in the streamwise (vertical) direction (parallel to the source flow) for present conditions, where the subscript os is used to denote conditions at the virtual origin of steady turbulent jets. This parameter is a measure of conditions where distributions of flow properties appropriate for the often confined conditions of a source have adjusted to reach distributions appropriate for an unconfined flow. The value of $(x\text{-}x_{os})/d$ needed for self-preserving behavior depends on the nature of the flow, the properties of the source, and the property for which self-preserving behavior is sought. For example, results for steady round turbulent nonbuoyant jets in still fluids suggests that values of $(x\text{-}x_{os})/d$ greater than roughly 40 and 100 are required to obtain self-preserving behavior for distributions of mean and rms fluctuating (turbulent) properties, respectively [26]. Measurements of the development of steady round turbulent nonbuoyant jets in still fluids also indicate that the L/d of the jet passage as well as the Reynolds number of the flow through the passage can have a profound effect on transition to turbulence and accordingly on the conditions required for self-preserving behavior to be observed [18]. In addition, similar results for steady round buoyant turbulent plumes in still fluids suggest that values of $(x\text{-}x_{os})/d$ greater than 90 are required to obtain self-preserving behavior for distributions of both mean and rms fluctuating (turbulent) concentration properties [27,28]. Finally, the crossflow was found to have a strong effect on the conditions required for the onset of self-preserving behavior during the present investigation; this effect, and the corresponding flow regime map that identifies conditions required for self-preserving flow, will be discussed subsequently.

Penetration Properties. The development of scaling relationships for the penetration properties of starting and steady round nonbuoyant turbulent jets in uniform crossflow is discussed by Diez et al. [4]; these scaling results were also evaluated successfully based on measurements of the penetration of dye-containing source liquids [4]. The present study extends these results to consider the penetration properties of the axes of the vortices in the counter-rotating vortex system observed for steady round turbulent nonbuoyant jets in uniform crossflow, based on flow structure properties measured using PLIF. Thus, the scaling relationships for the penetration properties of these flows are briefly reviewed in the following, emphasizing the steady round nonbuoyant turbulent jets of interest during the present investigation.

The development of scaling relationships for the penetration (geometrical) properties of steady round nonbuoyant turbulent jets in uniform crossflow is discussed by Diez et al. [4]. The configuration of the present steady round nonbuoyant turbulent jets in uniform crossflows considered in the following is sketched in Fig. 2. The source flow enters from a passage having a diameter d with a velocity u_o and flows into an environment having a uniform crossflow velocity v_∞, whereas the density of both the source and ambient fluid is the same, e.g., ρ_o. As discussed by Diez et al. [4], the streamwise velocity decays rapidly with increasing streamwise distance for this flow (the streamwise velocity is proportional to $(t\text{-}t_{os})^{-2/3}$ when the crossflow velocity is large compared to the streamwise velocity and the steady jet is nearly horizontal as the self-preserving region is approached far from the source [4]). In addition, the flow approximates no-slip convection in the cross stream direction. This behavior implies that the jet eventually is deflected so that its axis is nearly aligned with the cross stream direction. At this condition, the initial streamwise momentum continues to be conserved so that the flow approximates the behavior of a line puff. Then the streamwise momentum causes a counter-rotating pair of vortices to form, leading to a somewhat flattened shape of the flow cross section. The geometrical properties of interest for this flow include the trajectory of the axis of the vortex system $(x_c\text{-}x_{os})/d$ as a function of $(y\text{-}y_{os})/d$, after allowing for virtual origins to extend the self-preserving region as near to the source as possible, as well as the separation between the axis of the two counter-rotating vortices w_c. In addition, the steady penetration properties of the flow are of interest, including the farthest streamwise penetration distance $x_{ps}\text{-}x_{os}$ and the transverse penetration width of the flow w_{ps}, both as functions of the cross stream distance $y\text{-}y_{os}$.

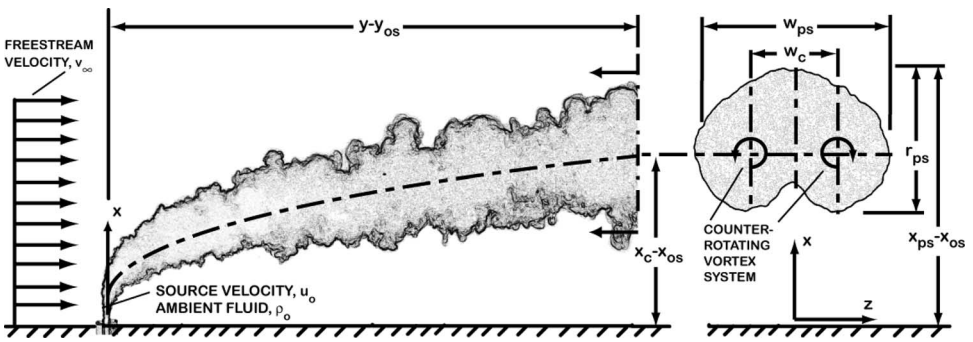

Fig. 2 Sketches of a steady round nonbuoyant turbulent jet in a uniform crossflow showing the definition of penetration properties measured in this investigation

Major assumptions used to find scaling relationships for the geometrical features of the flow, e.g., the trajectories of the vortex system axis and the counter-rotating axes, as well as the various penetration properties of the flow, are as follows: physical property variations are small, i.e., the physical properties of the source and ambient fluids are nearly the same; the flows are self-preserving so that effects of source disturbances have been lost; the streamwise source momentum is conserved; and the properties of the flow from both the source and the crossflow are independent of time, i.e., both are steady. As mentioned earlier, the detailed measurements of Diez et al. [4] show that motion in the cross stream direction satisfies the no-slip convection approximation, as follows:

$$(y_p\text{-}y_{os})/d = C_{ys}[v_\infty(t\text{-}t_{os})/d] \tag{1}$$

where t_{os} is a virtual temporal origin to be selected, whereas $C_{ys}=1$. Finally, the flow in the streamwise direction, after deflection has proceeded for a time and the axis of the counter-rotating vortex system is nearly aligned with the crossflow direction, approximates a line puff having a conserved source specific momentum force per unit length that can be expressed as follows:

$$M'_o = \dot{Q}_o u_o / v_\infty \tag{2}$$

Under these assumptions, the streamwise momentum of the flow in the deflected jet vortex system in the streamwise direction is conserved and the penetration of the flow in the streamwise direction is given as follows, see Turner [29]:

$$(x_{ps}\text{-}x_{os})/d = C_{xs}[(t\text{-}t_{os})/t^*]^n \tag{3}$$

where t^* is a characteristic time that involves the conserved specific momentum force per unit length, as follows:

$$t^* = d^3/M'_o \tag{4}$$

and $n=1/3$. Far from the source in the self-preserving region of the flow, the source diameter is no longer relevant and can be eliminated from Eqs. (1), (2), and (4) to yield

$$(x_{ps}\text{-}x_{os})/x_s^* = C_{xs} \tag{5}$$

where

$$x_s^* = [M'_o(y\text{-}y_{os})/v_\infty]^{1/3} \tag{6}$$

The steady penetration properties of jets in crossflow are given as simple ratios with respect to the streamwise distance, as follows:

$$r_{ps}/(x_{ps}\text{-}x_{os}) = C_{rs} \tag{7}$$

and

$$w_{ps}/(x_{ps}\text{-}x_{os}) = C_{ws} \tag{8}$$

where r_{ps} is the vertical size and w_{ps} is the width of the dye containing region.

In addition, the properties of the axis of the vortex system as a whole, and the spacing between the axes of the two counter-rotating vortices, as defined in Fig. 2, are given by expressions similar to Eqs. (5) and (7), as follows:

$$(x_c\text{-}x_{os})/x_s^* = C_{xcs} \tag{9}$$

and

$$w_c/(x_c\text{-}x_{os}) = C_{wcs} \tag{10}$$

Structure Properties. Analysis to find the self-preserving behavior of mean and rms fluctuating concentration distributions in self-preserving steady round nonbuoyant turbulent jets in uniform crossflows is described by Fischer et al. [15] and List [16]. The results of these analyses in terms of the present notation are as follows:

$$\overline{c}u_o(x_c\text{-}x_{os})^2/(c_oM'_o) = F[(x\text{-}x_c)/(x_c\text{-}x_{os}), z/(x_c\text{-}x_{os})]; \quad \text{crossflows} \tag{11}$$

and

$$\overline{c'}u_o(x_c\text{-}x_{os})^2/(c_oM'_o) = F'[(x\text{-}x_c)/(x_c\text{-}x_{os}), z/(x_c\text{-}x_{cs})]; \quad \text{crossflows} \tag{12}$$

where $\overline{c'}$ is the root-mean-square value of the concentration fluctuation.

The form of Eq. (12) for $\overline{c'}$ is used because it provides a compact notation that avoids defining an additional empirical parameter for the maximum concentration $\overline{c_m}$.

Results and Discussion

Flow Regime Map for Self Preservation. The conditions required to observe self-preserving behavior are influenced by the type of flow being considered, the properties of the source, and the property for which self-preserving behavior is being sought. For the present steady turbulent jets in crossflows, having relatively long source passages ($L/d \geqslant 50$) and relatively large source Reynolds numbers ($\mathrm{Re}_o \geqslant 2500$), the most conservative property for the onset of self-preserving behavior was the concentration structure of the flow. Thus, consideration of the range of conditions required for the flow to exhibit self-preserving behavior will be based on the concentration structure of the flow.

In addition to the properties just mentioned, observations during the present investigation indicated that the source/crossflow velocity ratio u_o/v_∞ substantially influenced conditions at the onset of self-preserving behavior for the concentration structure of steady turbulent jets in crossflows. This behavior follows because self-preservation was only observed when the axes of the counter-rotating vortex system were nearly aligned with the crossflow direction. At this condition, the jet was nearly horizontal so that the full effect of the streamwise source specific momentum force per unit length of a line puff could act upon the deflected jet in order to develop the full strength of the counter-rotating vortex system. In turn, conditions when the axes of the counter-rotating vortex system were nearly horizontal were a strong function of u_o/v_∞. In particular, nearly horizontal alignment of the axes of the counter-rotating vortex system was delayed when u_o/v_∞ was large because a large streamwise distance was required before u_o decayed to a value that was small compared to v_∞ so that the jet could be deflected into the nearly horizontal direction.

Present experimental observations of the onset of self-preserving behavior for the concentration structure of steady turbulent jets in crossflows were based on mean concentration distributions plotted according to the self-preserving scaling of the flows due to Fisher et al. [26], as shown in Eq. (11). The axis of the vortices are defined here as the locations of maximum concentration. The actual approach involved plotting the mean values of the concentrations according to Eq. (11) for several paths over the cross section of the jets (along a horizontal line passing through the axes of the two counter-rotating vortices, along the two vertical lines passing through the axis of each vortex, and along a third vertical line in the plane of symmetry of the counter-rotating vortex system). Given these results for a particular value of u_o/v_∞, the condition was assumed to be self-preserving when the distributions along all these paths did not depart from the average distributions for all the paths over the self-preserving region by more than 5%.

The resulting self-preserving flow regime map for steady turbulent jets in crossflows is illustrated in Fig. 3. This map was constructed based on tests specifically conducted to determine the onset of self-preservation, with conditions prior to and within the self-preserving region denoted by appropriate symbols. The flow regime map of Fig. 3 shows the developing flow and self-preserving regions of steady turbulent jets in crossflows in terms of the streamwise distance from the source, $(x_c\text{-}x_{os})/d$, for u_o/v_∞

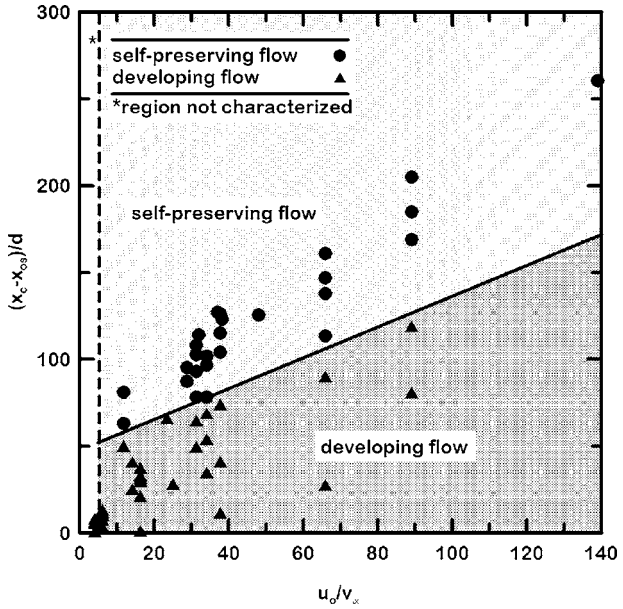

Fig. 3 Flow regime map for of the developing flow and self-preserving regions for steady turbulent plumes in crossflows

in the range 4–140. Note that values of u_o/v_∞ smaller than 4 were not considered because the plume deflects immediately upon leaving the source tube so that its properties are affected by the walls of the water channel. The tendency for increased values of u_o/v_∞ to delay the onset of self-preserving flow is evident with the onset reached at $(x_c\text{-}x_{os})/d$ of 50–60 for u_o/v_∞ of 4 (the smallest value of u_o/v_∞ considered) to 20 but increasing to 160–170 for u_o/v_∞ of 140 (the largest value of u_o/v_∞ considered).

Penetration Properties. The penetration properties of starting and steady round turbulent nonbuoyant jets in uniform crossflows are considered by Diez et al. [4]. All these results are limited to the boundaries of the source fluid flow. Thus, the present measurements of penetration properties extends these results to consideration of the trajectories of the axes of the vortices of the counter-rotating vortex system for steady round turbulent nonbuoyant jets in uniform crossflows.

The test conditions for present measurements of the properties of steady round turbulent nonbuoyant jets in uniform crossflows are summarized in Table 1. The locations of the axes of the vortices of the counter-rotating vortex system were found by averaging 4000 PLIF images at each streamwise location. The fine details of the mixing pattern of the source and ambient fluids can be seen from the typical PLIF images illustrated in Fig. 4. In order to achieve adequate spatial resolution for this PLIF image, the diameter of the laser beam sweeping the cross section of the flow was reduced to 0.5 mm. At the Reynolds number of this jet, the scanning laser beam was then thin and fast enough so that it could resolve most of the smallest scales of turbulent transport. The finest scalar fluctuations can be obtained following the analysis by Smith and Mungal [6] and Dimotakis [30] for the scalar-diffusion scale $\lambda_D \simeq 50\delta\,\mathrm{Re}_\delta^{-3/4}\,\mathrm{Sc}^{-1/2}$, where δ is the local jet width, 50 is a constant estimated from Dimotakis [30], Re_δ is the Reynolds number based on the local jet velocity and width, and Sc is the Schmidt number. For the present experiments in the cross section of a jet in a crossflow the scalar-diffusion scale can be conservatively estimated to be $1.50 < \lambda_D < 4.1$ pixels (1 pixel=301 μm). Therefore we can resolve the finest scalar fluctuations. The image series appearing in Fig. 4 shows the largely distorted presence of the instantaneous images of the two counter-rotating vortices separated along the plane of symmetry by the deeply penetrating ambient fluid of the flow. Also the presence of ambient fluid being transported deep into the vortex system of the flow along its plane of symmetry is seen to be an important effect of the flow structure, as mentioned earlier in connection with the discussion of the flow visualization of Fig. 1. Finally, by averaging 4000 images similar to Fig. 4 at each cross stream test condition that was considered, it was possible to locate the axes of the vortices with an accuracy (95% confidence) less than 5% of the transverse distance between the vortex axes w_c.

Present measurements of the penetration properties of aspects of the concentration structure of steady jets in crossflow involved

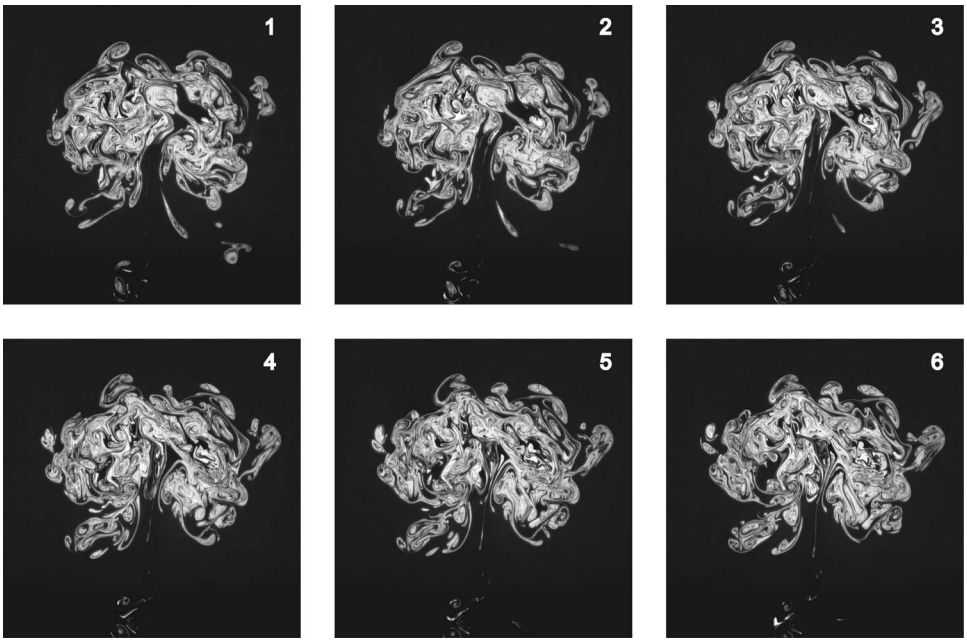

Fig. 4 Instantaneous PLIF image of the cross section of a steady round nonbuoyant turbulent jet in a uniform crossflow (d=3.2 mm, Re_o=5300, u_o/v_∞=26, $(x_c\text{-}x_{os})/d$=101 and y/d=315 and Δt=50 ms between frames)

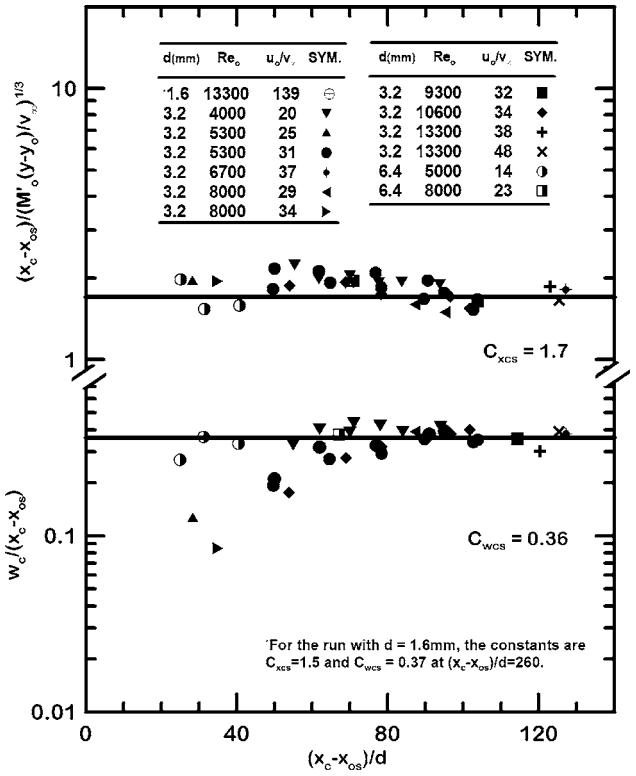

Fig. 5 Trajectory of the axes of the vortex system and transverse spacing between the vortex axes, in terms of the self-preserving variables for round nonbuoyant turbulent jets in uniform crossflows

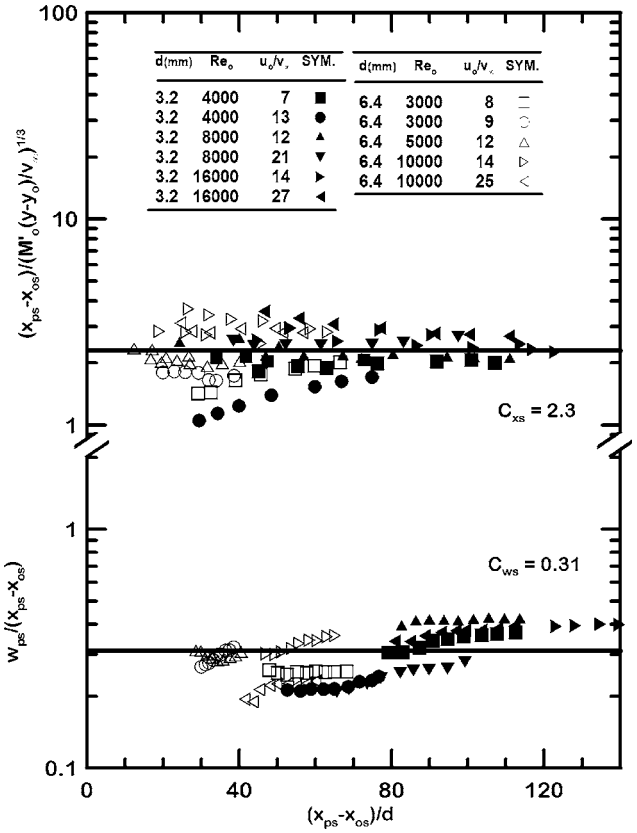

Fig. 6 Streamwise and transverse penetration distances in terms of the self-preserving variables for the penetration properties of round nonbuoyant turbulent jets in uniform crossflows

the trajectories of the counter-rotating vortex system and the normalized spacing between the axes of the counter-rotating vortices, as given by Eqs. (9) and (10). These properties are plotted as a function of the normalized streamwise vortex core penetration distance $(x_c\text{-}x_{os})/d$, in the two plots of Fig. 5. These parameters are rather scattered in the developing flow region at small streamwise distances from the source but eventually approach constant values $C_{xcs}=1.7$ and $C_{wcs}=0.36$, for self-preserving flow at large streamwise distances from the source. Notably, these measurements in the developing flow region of Fig. 5 generally involve $u_o/v_\infty < 40$ and were obtained for $(x_c\text{-}x_{os})/d < 70$ which generally agrees with the developing flow region of the flow regime map of Fig. 3.

Measurements of the penetration properties of the boundaries of the source fluid of steady jets in crossflow from Diez et al. [4] involved the farthest normalized streamwise penetration distance and the normalized lateral penetration width as given by Eqs. (5) and (8). These properties are plotted as a function of the normalized streamwise penetration distance, in the two plots of Fig. 6. These parameters are rather scattered in the developing flow region at small streamwise distances from the source but eventually approach constant values $C_{xs}=2.3$ and $C_{ws}=0.31$, for self-preserving flow at large streamwise distances from the source. Notably, these measurements in the developing flow region of Fig. 6 generally involve $u_o/v_\infty < 25$ and were obtained for $(x_c\text{-}x_{os})/d < 50$ which generally agrees with the developing flow region of the flow regime map of Fig. 3. In general, C_{xs} is greater than C_{xcs} for jets in crossflow because the farthest streamwise penetration of a jet in crossflow will always be greater than the penetration of the axis of its counter-rotating vortex pair. Also, C_{ws} is smaller than C_{wcs} because they are both measuring different properties of the flow as follows: C_{ws} is the average of the measurements made of the lateral penetration width on instantaneous video images; on the other hand, C_{wcs} is based on measurements made on images that are the average of 4000 instantaneous PLIF images which takes into account transverse deflection of the flow as a whole. Thus, in general, it is expected that the transverse dispersion of measurements made on an average field will be larger than similar measurements made on instantaneous fields.

Finally, for convenient reference, the measured parameters associated with the penetration properties of steady round nonbuoyant turbulent jets in uniform crossflows are summarized in Table 2. Experimental uncertainties for flow penetration properties (95% confidence) are as follows: less than 4% for C_{xs}, less than 3% for C_{rs}, less than 4% for C_{ws}, and less than 45% for x_{os}/d. The corresponding uncertainties (95% confidence) for the vortex axes penetration properties are as follows: less than 5% for both C_{xcs}

Table 2 Summary of empirical parameters for self-preserving flow and vortex axes penetration properties of steady round nonbuoyant turbulent jets in uniform crossflowing fluids[a]

Parameter	Value	Parameter	Value
Results for flow penetration properties from Diez et al. [4]:			
C_{xs}	2.3(0.08)	C_{ws}	0.31(0.011)
C_{rs}	0.23(0.005)	x_{os}/d	6.1(2.7)
Results for vortex axes penetration properties, from the present study:			
C_{xcs}	1.7(0.08)	x_{os}/d	0.0
C_{wcs}	0.36(0.017)		

[a]Experimental uncertainties (95% confidence) in parenthesis; also $C_{ys}=1$ and $y_{os}=0.0$.

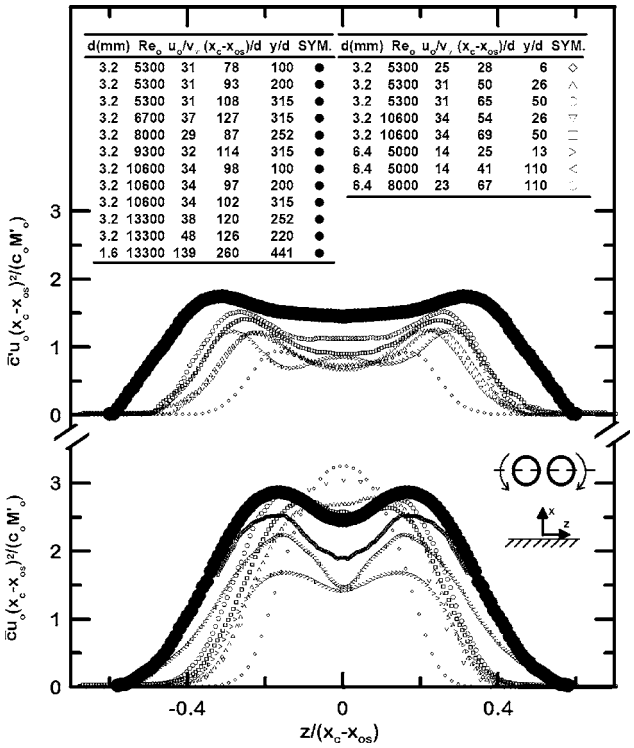

Fig. 7 Plots of the development of mean and rms concentration of source fluid in terms of self-preserving variables for transverse paths through the vortex axes for steady round nonbuoyant turbulent jets in uniform crossflows

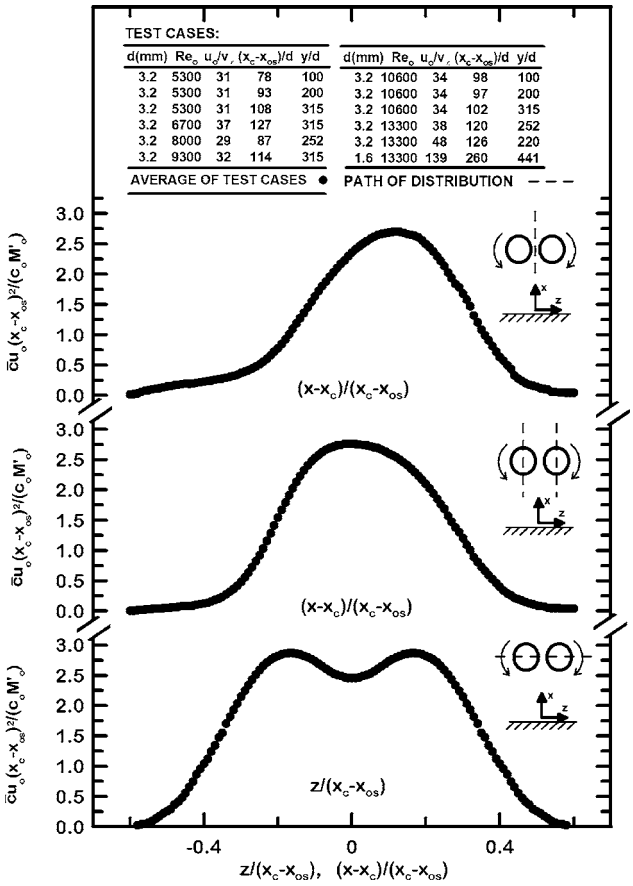

Fig. 8 Plots of mean concentrations of source fluid in terms of the self-preserving variables for various vertical and horizontal paths for steady round nonbuoyant turbulent jets in uniform crossflows within the self-preserving region

and C_{wcs}.

The counter-rotating vortex system that develops for steady round nonbuoyant turbulent jets in crossflow is seen to promote the mixing properties of the flow as a function of streamwise penetration distance compared to nonbuoyant turbulent jets in still fluids where the axis of the flow is aligned with the direction of penetration of the flow. In particular, the penetration of the flow normal to the axis is much greater for round nonbuoyant turbulent flows in crossflow than corresponding flows in still fluids, e.g., $r_{ps}/(x_{ps}\text{-}x_{os})$ and $w_{ps}/(x_{ps}\text{-}x_{os})$ are 0.23 and 0.31 for present jets in crossflow whereas $r_p/(x_p\text{-}x_o)$ is 0.15 for the measurements of Diez et al. [3] for jets in still fluids. Thus, penetration of the flow normal to its axis is 50–100% larger for jets in crossflow than for jets in still fluids for similar streamwise distances and initial source conditions. This suggests much more effective mixing between the source and ambient flows when the axes of the source flow are perpendicular to the streamwise direction of penetration which is the case for jets in crossflow than when the axis of the source flow is aligned with the direction of penetration which is the case for jets in still fluids. This behavior is very similar to numerous other fluid transport configurations where relative motion in crossflow to the axis of the source is much more effective for promoting transport between two streams than when the direction of relative motion is aligned with the flow axes.

Structure Properties: Crossflows. The development of the distributions of mean concentrations of source fluid within cross-sectional planes of steady round nonturbulent jets in uniform crossflows is illustrated in Fig. 7. This plot involves mean and fluctuating concentrations of source fluid plotted according to the self-preserving structure variables of Eqs. (13) and (14) along a horizontal line crossing the flow that intersects the axes of the two counter-rotating vortices for various test conditions including different values of $(x_c\text{-}x_{os})/d$. The distributions of mean and fluctuating concentrations of source fluid vary considerably in the region near the source [open symbols for $(x_c\text{-}x_{os})/d \leqslant 69$]. Subsequently, these distributions become relatively independent of distance from the source [shown as dark symbols taken as an average of results measured over the range $78 \leqslant (x_o\text{-}x_{os})/d \leqslant 260$], which is indicative of behavior in the self-preserving region of the flow. The path of the measurements in Fig. 7 passes through the axes of the counter-rotating vortices with mean concentrations reaching maximum values at the vortex axes. In contrast, the maximum values of rms concentration fluctuations along these paths reach maximum values at somewhat larger radial distances than the axes of the counter-rotating vortices. Finally, the region between the counter-rotating vortices involves a broad minimum in rms concentration fluctuations, which is caused by the relatively wide region dominated by entrainment of ambient fluid between the axes of the vortices seen on the PLIF images of Fig. 4.

Figures 8 and 9 are illustrations of mean and rms fluctuating concentrations of source fluid plotted according to the self-preserving structure variables of Eqs. (13) and (14). These results are for various paths over the flow cross section (horizontally through the axes of the two counter-rotating vortices, vertically through the axes of the two counter-rotating vortices, and vertically along the plane of symmetry of the counter-rotating vortex system) with averages obtained for the streamwise range of self-preserving behavior for present observations, e.g., $78 \leqslant (x_c\text{-}x_{os})/d \leqslant 260$. It was observed that variations of appropriately scaled mean and rms fluctuations of the concentrations of source fluid for these conditions were well within experimental uncertainties for the present test conditions, i.e., less than 11% (95% confidence) for $|z|/(x_c\text{-}x_{os}) < 0.4$ and $|x\text{-}x_c|/(x_c\text{-}x_{os}) < 0.3$.

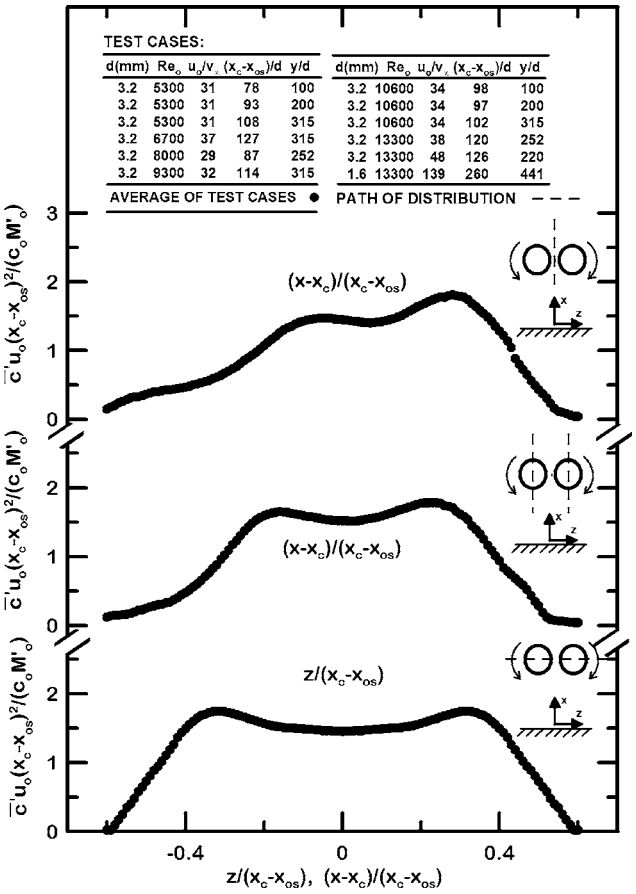

Fig. 9 Plots of rms concentration of source fluid in terms of self-preserving variables for various vertical and horizontal paths for steady round nonbuoyant turbulent jets in uniform crossflows within the self-preserving region

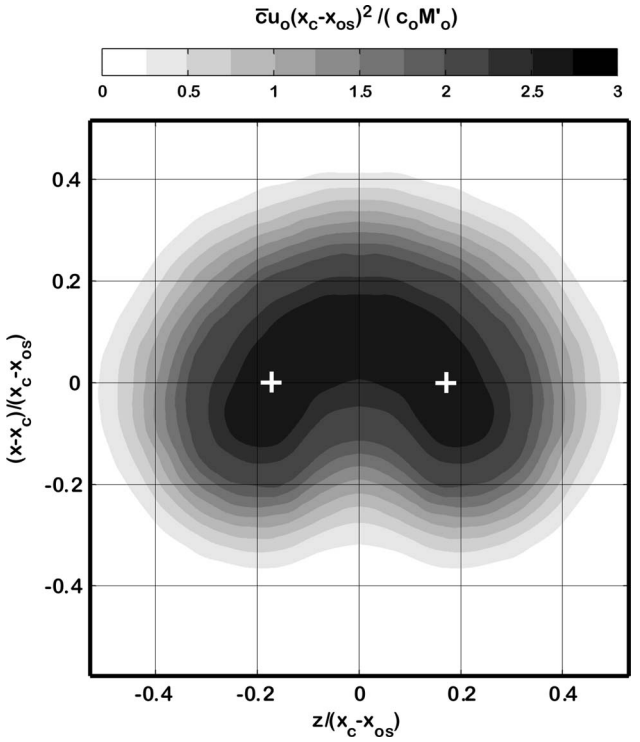

Fig. 10 Contour plot of mean concentration of source fluid in terms of self-preserving variables over the flow cross-section for steady round nonbuoyant turbulent jets in uniform cross-flows within the self-preserving region

Thus, for round nonbuoyant turbulent jets in still fluids, Diez et al. [2,3] find that penetration properties approach self-preserving behavior at 20–30 source diameters from the source which is comparable to observations that the structure properties of this flow approach self-preserving behavior at roughly 30 source diameters from the source based on the results illustrated in Figs. 5 and 6; in contrast, for round nonbuoyant turbulent jets in uniform cross-flows, penetration properties approach self-preserving behavior at 40–50 source diameters from the source based on the results illustrated in Figs. 5 and 6 whereas structure properties in this flow only approach self-preserving behavior at 80 source diameters from the source based on the results illustrated in Figs. 7–9. The reasons for these differences are not understood except that it is not surprising that the significant qualitative differences between the flow structure at the source and in the self-preserving region for jets in crossflow compared to jets in still fluids tends to defer the onset of self-preserving behavior. This behavior is similar to the properties of self-preserving steady round buoyant turbulent plumes in still environments, where self-preserving penetration properties are observed at roughly 50 streamwise diameters from the source, whereas self-preserving structure properties are not observed until roughly 80 source diameters from the source [1–4,26,27], because buoyant motion takes some time to develop which tends to delay the development of self-preserving behavior.

The distributions of mean and rms fluctuating concentrations over the cross section of steady round nonbuoyant turbulent jets in uniform crossflows in the self-preserving region are quite complex and cannot be reduced to a simple Gaussian expression similar to Eqs. (15) and (16). Instead, present measurements of mean and rms fluctuating concentrations over cross sections in the self-preserving region were reduced in terms of self-preserving variables and plotted as a function of location in the cross section according to self-preserving streamwise and transverse variables, e.g., $(x\text{-}x_c)/(x_c\text{-}x_{os})$ and $(z/x_c\text{-}x_{os})$, respectively. Results of this nature are illustrated in Figs. 10 and 11 for the present measurements. The mean locations of the two axes of the counter-rotating vortex system are shown as white crosses on these plots, for reference purposes. On both plots, the self-preserving scaled values of mean and rms fluctuating concentrations are divided into 12 gray scales, for the ranges of mean and rms fluctuating source fluid concentration values in terms of self-preserving variables of 0–3 and 0–2, respectively. The counter-rotating vortex system is seen to contribute to the two-lobed structure of the flow with the entrainment of ambient fluid along the plane of symmetry from the side of the flow opposite to the jet source tending to displace maximum mean concentrations along this plane in the streamwise (upward) direction (i.e., in the direction of penetration of the counter-rotating vortex system). A particularly surprising feature of this flow is its unusually large streamwise and transverse penetration distances of $(x\text{-}x_c)/(x_c\text{-}x_{os})$ of approximately ±0.4 and $z/(x_c\text{-}x_{os})$ of approximately ±0.5. These values are roughly two to three times larger than corresponding radial dimensions of steady round nonbuoyant turbulent jets in still fluids, seen in terms of self-preserving variables in Figs. 5 and 6 [e.g., $r/(x\text{-}x_o)$ of 0.2]. This highlights the remarkable capabilities of turbulent vortex structures to promote mixing between source and ambient fluids.

Conclusions

Scaling relationships for the penetration (geometrical) and structure properties of steady round turbulent nonbuoyant jets were evaluated based on experiments emphasizing self-preserving behavior in unstratified crossflows having uniform velocities. The test conditions consisted of dye-containing fresh water sources injected vertically downward into crossflowing fresh water within a water channel with source exit diameters of 1.6, 3.2, and 6.4

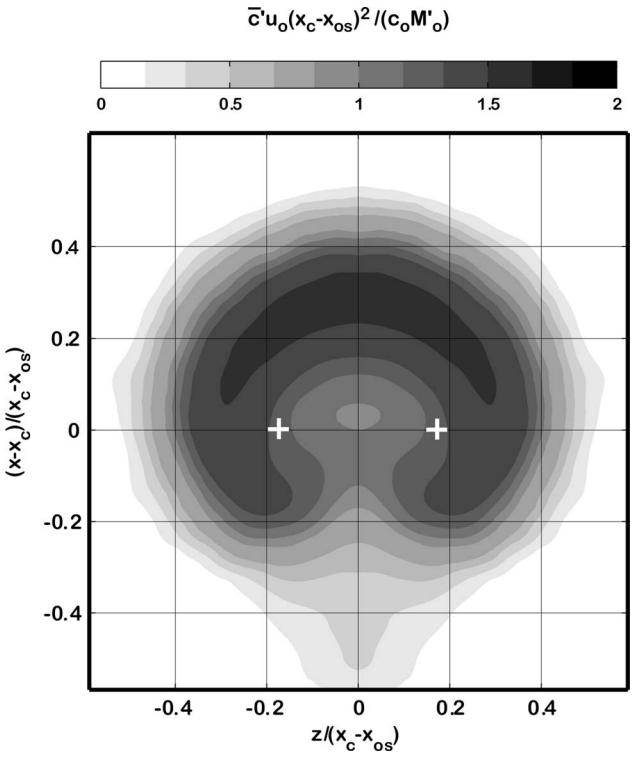

Fig. 11 Contour plots of rms concentration fluctuations of source fluid in terms of self-preserving variables over the flow cross section for steady round nonbuoyant turbulent jets in uniform crossflows within the self-preserving region

mm, source passage lengths in excess of 50 source exit diameters, source Reynolds numbers of 3000–16,000, source/ambient velocity ratios of 7–139, vertical penetration distances of 0–260 source diameters, and horizontal penetration distances of 0–440 source diameters. Major conclusions of the study are as follows:

(1) The flows became turbulent near the source exit, at streamwise distances of 0–5 source diameters from the source similar to earlier observations of these flows by Diez et al. [4]. The onset of self-preserving behavior required that axes of the counter-rotating vortex system be nearly aligned with the crossflow direction whereas this condition was strongly affected by the source/crossflow velocity ratio u_o/v_∞. As a result, self-preserving behavior was observed at streamwise distances greater than 50–60 source diameters from the source for $4<u_o/v_\infty<20$ increasing to streamwise distances greater than 160–170 source diameters from the source for $u_o/v_\infty=140$. The detailed flow regime map of the developing flow and self-preserving regions for steady turbulent jets in uniform crossflows of Fig. 3, however, should be consulted for details of the variation of $(x_c\text{-}x_{os})/d$ at the onset of self-preserving behavior as a function of u_o/v_∞.

(2) Combining the no-slip convection approximation in the cross stream direction with self-preserving scaling in the streamwise direction yielded good predictions of the steady penetration trajectories within the self-preserving region of the flows of nonbuoyant jets in uniform crossflows. Furthermore, the self-preserving streamwise motion of a jet in a crossflow scaled according to a horizontal line puff in a still fluid.

(3) Self-preserving behavior for the structure properties of steady round nonbuoyant turbulent jets in crossflows was reached for various horizontal and vertical paths through cross sections of the flow when $(x_c\text{-}x_{os})d>80$. This indicates that the jet reaches self-preserving behavior for penetration properties at much shorter streamwise distances from the source than for structure properties, which is similar to the behavior of steady round buoyant turbulent plumes in still environments.

(4) The self-preserving structure of a steady round nonbuoyant turbulent jets in a uniform crossflow involves a counter-rotating vortex system whose axes are nearly aligned with the crossflow and thus are nearly horizontal. The nearly crossflow orientation of the axes of the counter-rotating vortex system promotes unusually rapid mixing due to nearly crossflow motion in the streamwise direction compared to jets in still fluids where the flow axis is aligned with the streamwise direction, for example: $\overline{c_m}\sim(x\text{-}x_{os})^{-2}$ for jets in crossflow compared to $\overline{c_m}\sim(x\text{-}x_{os})^{-1}$ for jets in still fluids; and $(r_{ps}$ and $w_{ps})/(x_{ps}\text{-}x_{os})=0.23$ and 0.31 for jets in crossflow compared to $r_p/(x_p\text{-}x_o)=0.15$ for jets in still fluids.

The observations of conclusion (4) highlight the enhanced mixing and transport that occur when the geometry involves crossflow rather than parallel flow; this behavior is familiar in many areas of fluid mechanics, e.g., the response of hot wires mainly to crossflow rather than coflow and highly effective atomization of nonturbulent fluid jets subjected to crossflow rather than coflow, among others.

Acknowledgments

This research was supported by the United States Department of Commerce, National Institute of Standards and Technology, Grant No. 60NANB1D0006, with H. R. Baum of the Laboratory for Building and Fire Research serving as Scientific Officer. The assistance of R. Jolly, D. Ma, and D. Zoch, all students in the Undergraduate Research Opportunity Program (UROP) of the University of Michigan, in carrying out the experiments is gratefully acknowledged.

Nomenclature

c = concentration of source fluid
C_{rs} = radial penetration coefficient for steady jets, Eq. (7)
C_{wcs} = vortex core spacing coefficient for steady jets, Eq. (10)
C_{ws} = transverse penetration coefficient for steady jets, Eq. (8)
C_{xcs} = streamwise penetration coefficient of the axis of the vortex system for steady jets, Eq. (9)
C_{xs} = streamwise penetration coefficient for steady jets, Eq. (5)
C_{ys} = crosstream penetration coefficient for steady jets, Eq. (1)
d = source diameter
k_c = characteristic jet width coefficient, Eq. (16)
L = source passage length
ℓ_c = characteristic jet radius, Eq. (16)
M'_o = source specific momentum force per unit length for a line puff, Eq. (2)
n = time exponent, Eq. (3)
$\dot{Q}_o$ = volumetric rate of injection of source fluid
r = streamwise penetration normal to flow axis in a vertical plane
Re_o = source Reynolds number, $u_o d/\nu_o$
t = time
t^* = self-preserving time scale, Eq. (4)
u = streamwise (vertical) velocity parallel to the source flow

v = cross stream (horizontal) velocity in the direction of jet deflection
w_c = transverse separation of the vortex axes normal to the flow axis in a jet cross-sectional plane, Fig. 2
w_{ps} = transverse penetration normal to flow axis in a jet cross-sectional plane for steady jets
x = streamwise (vertical) distance relative to the source, Fig. 2
x_c = streamwise (vertical) distance from the jet source to the horizontal axis of the vortex system, Fig. 2
x_s^* = streamwise characteristic distance for a steady flow, Eq. (6)
y = cross-stream (horizontal) distance relative to source in the direction of jet deflection, Fig. 2
z = transverse distance relative to the source in a jet cross-sectional plane, Fig. 2
ν = kinematic viscosity
ρ = density

Subscripts

c = vortex axis
m = maximum concentration
p = maximum penetration location
s = steady-state flow property
o = source value or virtual origin location
∞ = ambient value

Superscripts

$\overline{(\,)}$ = time-averaged mean value
$\overline{(\,)}'$ = rms fluctuating value

References

[1] Sangras, R., Kwon, O. C., and Faeth, G. M., 2002, "Self-Preserving Properties of Unsteady Round Nonbuoyant Turbulent Starting Jets and Puffs in Still Fluids," ASME J. Heat Transfer, **124**, pp. 460–469.
[2] Diez, F. J., Sangras, R., Kwon, O. C., and Faeth, G. M., 2003, "Self-Preserving Properties of Unsteady Round Nonbuoyant Turbulent Starting Jets and Puffs in Still Fluids," ASME J. Heat Transfer, **125**, pp. 204–205.
[3] Diez, F. J., Sangras, R., Faeth, G. M. and, Kwon, O. C., 2003, "Self-Preserving Properties of Unsteady Round Buoyant Turbulent Plumes and Thermals in Still Fluids," ASME J. Heat Transfer, **125**, pp. 821–830.
[4] Diez, F. J., Bernal, L. P., and Faeth, G. M., 2003, "Round Turbulent Thermals, Puffs, Starting Plumes and Starting Jets in Uniform Crossflow," ASME J. Heat Transfer, **125**, pp. 1046–1057.
[5] Diez, F. J., Bernal, L. P. and Faeth, G. M., 2004, "Self-Preserving Mixing Properties of Steady Round Nonbuoyant Turbulent Jets in Uniform Crossflows," Report No. GDL/GMF-04-02, Department of Aerospace Engineering, The University of Michigan, Ann Arbor, Michigan.
[6] Smith, S. H., and Mungal, M. G., 1998, "Mixing, Structure and Scaling of the Jet in Crossflow," J. Fluid Mech., **357**, pp. 83–122.
[7] Lee J. H. W., and Chu V. H., 2003, *Turbulent Jets and Plumes a Lagrangian Approach*, Kluwer Academic, Dordrecht, The Netherlands, pp. 211–247.
[8] Keffer, J. F., and Baines, W. D., 1963, "The Round Turbulent Jet in a Cross Wind," J. Fluid Mech., **15**, pp. 481–496.
[9] Kamotami, Y., and Greber, I., 1972, "Experiments on a Turbulent Jet in Crossflow," AIAA J., **11**, pp. 1425–1429.
[10] Chassaing, P., George, J., Claria, A., and Sananes, F., 1974, "Physical Characteristics of Subsonic Jets in a Cross-Stream," J. Fluid Mech., **64**, pp. 41–64.
[11] Andreopoulos, J., and Rodi, W., 1984, "Experimental Investigation of Jets in Crossflow," J. Fluid Mech., **138**, pp. 93–127.
[12] Broadwell, J. E., and Breidenthal, R. E., 1984, "Structure and Mixing of a Transverse Jet in an Incompressible Flow," J. Fluid Mech., **148**, pp. 405–412.
[13] Askari, A., Bullman, S. J., Fairwether, M., and Swaffield, F., 1990, "The Concentration Field of a Turbulent Jet in a Cross-Wind," Combust. Sci. Technol., **73**, pp. 463–478.
[14] Kelso, R. M., Lim, T. T., and Perry, A. E., 1996, "An Experimental Study of Round Jets in Crossflow," J. Fluid Mech., **306**, pp. 111–144.
[15] Fischer, H. B., List, E. J., Koh, R. C., Imberger, J., and Brooks, N. H., 1979, *Mixing in Inland and Coastal Waters*, Academic Press, New York, pp. 315–389.
[16] List, E. J., 1982, "Turbulent Jets and Plumes," Annu. Rev. Fluid Mech., **14**, pp. 189–212.
[17] Steckler, K. D., Baum, H. R., and Quintiere, J. G., 1986, "Salt Water Modeling of Fire Induced Flows in Multicompartment Enclosures," Proc. Combust. Inst., **21**, pp. 143–149.
[18] Wu, P.-K., Miranda, R. F., and Faeth, G. M., 1995, "Effects of Initial Flow Conditions on Primary Breakup of Nonturbulent and Turbulent Round Liquid Jets." Atomization Sprays, **5**, pp. 175–196.
[19] Ferrier, A. J., Funk, D. R., and Roberts, P. J. W., 1993, "Application of Optical Techniques to the Study of Plumes in Stratified Fluids," Dyn. Atmos. Oceans, **20**, pp. 155–183.
[20] Karasso, P. S., and Mungal, M. G., 1997, "PLIF Measurements in Aqueous Flows Using the Nd:YAG Laser," Exp. Fluids, **23**, pp. 382–387.
[21] Law, A. W.-K. and Wang, H., 2000, "Measurement of Mixing Processes With Combined Digital Particle Image Velocimetry and Planar Laser Induced Fluorescence," Exp. Therm. Fluid Sci., **22**, pp. 213–229.
[22] Cowen, E. A., Chang, K.-H., and Liao, Q., 2001, "A Single-Camera Coupled PTV-LIF Technique," Exp. Fluids, **31**, pp. 63–73.
[23] Crimaldi, J. P., and Koseff, J. R., 2001, "High-Resolution Measurements of the Spatial and Temporal Structure of a Turbulent Plume," Exp. Fluids, **31**, pp. 90–102.
[24] Webster, D. R., Roberts, P. J. W. and Ra'ad, L., 2001, "Simultaneous DPTV/PLIF Measurements of a Turbulent Jet," Exp. Fluids, **30**, pp. 65–72.
[25] Tian, W. and Roberts, P. J. W., 2003, "A 3D LIF System for Turbulent Buoyant Jet Flows," Exp. Fluids, **35**, pp. 636–647.
[26] Tennekes, H., and Lumley, J. L., 1972, *A First Course in Turbulence*, MIT Press, Cambridge, Massachusetts, pp. 113–124.
[27] Dai, Z., Tseng, L.-K., and Faeth, G. M., 1994, "Structure of Round, Fully-Developed, Buoyant Turbulent Plumes," ASME J. Heat Transfer, **116**, pp. 409–417.
[28] Dai, Z., Tseng, L.-K., and Faeth, G. M., 1995, "Velocity Statistics of Round, Fully-Developed Buoyant Turbulent Plumes," ASME J. Heat Transfer, **117**, pp. 138–145.
[29] Turner, J. S., 1969, "Buoyant Plumes and Thermals." Annu. Rev. Fluid Mech., **1**, pp. 29–44.
[30] Dimotakis, P. E., 2000, "The Mixing Transition in Turbulent Flows," J. Fluid Mech., **409**, pp. 69–98.

Experimental Investigation of Natural Convection in an Asymmetrically Heated Vertical Channel with an Asymmetric Chimney

Oronzio Manca
DIAM-Dipartimento di Ingegneria Aerospaziale e Meccanica, Seconda Università degli Studi di Napoli, Real Casa dell'Annunziata, Via Roma, 29, 81031 Aversa (CE), Italy

Marilena Musto

Vincenzo Naso

DETEC-Dipartimento di Energetica, Termofluidodinamica applicata e Condizionamenti ambientali, Università degli Studi di Napoli Federico II, Piazzale Tecchio, 80, 80125, Napoli, Italy

An experimental investigation on air natural convection, in a vertical channel asymmetrically heated at uniform heat flux, with downstream unheated parallel extensions, is carried out. One extension is coplanar to the unheated channel wall and the distance between the extensions is equal to or greater than the channel gap (geometrically asymmetric chimney). Experiments are performed with different values of the wall heat flux, aspect ratio (L_h/b)*, extension ratio* (L/L_h) *and expansion ratio* (B/b)*. For the largest value of the aspect ratio* $(L_h/b=10)$*, the adiabatic extensions improve the thermal performance in terms of lower maximum wall temperature of the channel. Optimal configurations of the system with asymmetrical chimney are detected. Flow visualization shows a cold inflow in the channel-chimney system that penetrates down below the channel exit section. Maximum wall temperatures and channel Nusselt numbers are correlated to the channel Rayleigh number,* Ra^**, and to the geometrical parameters, in the ranges* $3.0\times10^2\leqslant \mathrm{Ra}^*B/b\leqslant 1.010^5$*,* $1.0\leqslant B/b\leqslant 3.0$ *and* $1.0\leqslant L/L_h\leqslant 4.0$ *with* $L_h/b=5.0$ *and 10.0.* [DOI: 10.1115/1.1928909]

Keywords: Experimental Study, Natural Convection, Vertical Asymmetrically Heated Channel, Downstream Unheated Extension

Introduction

Trends in electronics cooling by natural convection aim at obtaining new configurations and improving the thermal and geometrical parameters in order to enhance heat transfer [1]. Vertical parallel plates and channels have been widely investigated [2,3] because of their occurrence in industrial processes. Mass flow rates and heat transfer coefficients can be increased by adding an unheated extension to a channel or to a heat sink, either symmetrically or asymmetrically heated, as shown in [4–18]. A short review of these papers, focusing the analysis on experimental works, follows.

One of the first investigations on the "*chimney effect*" was carried out numerically in [4]. In this study, natural convection in a vertical channel with a point source or a distributed heat source placed at its inlet section was analyzed. Different systems with downstream adiabatic or unheated extensions, such as heat sinks [9,10,13,14] or vertical channels [5–8,11,12,15–18], were then investigated.

The first experimental investigation on chimney system was reported in [7], where a channel-chimney system was studied in air. The channel walls were at uniform temperature and experiments were performed using a Mach-Zehnder interferometer. Measurements gave the validation of numerical results for both local and global heat transfer coefficients. Results showed that heat transfer rates varied from 2.5 times for low Reynolds numbers and 1.5 times for high Reynolds numbers of a simple channel. A composite correlation for average Nusselt number in terms of channel Rayleigh number, expansion ratio and extension ratio was proposed.

A vertical parallel-plate isothermal heat sink with a chimney was studied experimentally in [13]. Results, obtained for air, were 11 percent, in line with the theoretical predictions of overall heat transfer rates and location of optimum given in [9]. Flow-field measurements validated momentum transfer and a cold inflow at the chimney exit was detected. The cold inflow along the unheated side of the chimney was episodic and nearly periodic; it reduced the overall heat transfer by approximately 4 percent. Experimental results for thermal systems consisting of pin-fin heat sinks placed below the chimneys were presented in [14]. Generally, results were in good agreement with previous theoretical predictions [10]. Velocity measurements at the chimney exit and the effects of cold inflow were discussed.

The effect of adding adiabatic extensions, downstream of a vertical isoflux, symmetrically heated channel, was investigated experimentally in [15]. Optimal configurations were identified through the measured wall temperature profiles, with reference to the extension and expansion ratios of the insulated extensions. Large extensions, about 3.0 times the height of the channel, had to be added to enhance the heat transfer rate, while the optimal expansion ratio was nearly 2.0 for all the configurations. Air natural convection in an isoflux vertical channel with an adiabatic extension, for symmetric and asymmetric heating, was investigated experimentally in [16]. The strong effect of the heating mode on the interaction among the hot plume rising from the channel, the cold inflow, and the vortex region in the chimney corner was presented.

Local air and wall temperature measurements of symmetrically heated vertical channel-chimney systems were presented in [17]. Temperature profiles showed the effect of the geometric parameters on the buoyancy driven flow in the system and different regions of fluid motions were detected inside the chimney. Local Nusselt number profiles were slightly affected by the geometric parameters. Correlations between the local Nusselt number, the

Contributed by the Heat Transfer Division for publication in the JOURNAL OF HEAT TRANSFER. Manuscript received: March 2, 2004. Final manuscript received: March 15, 2005. Review conducted by: Karen Thole.

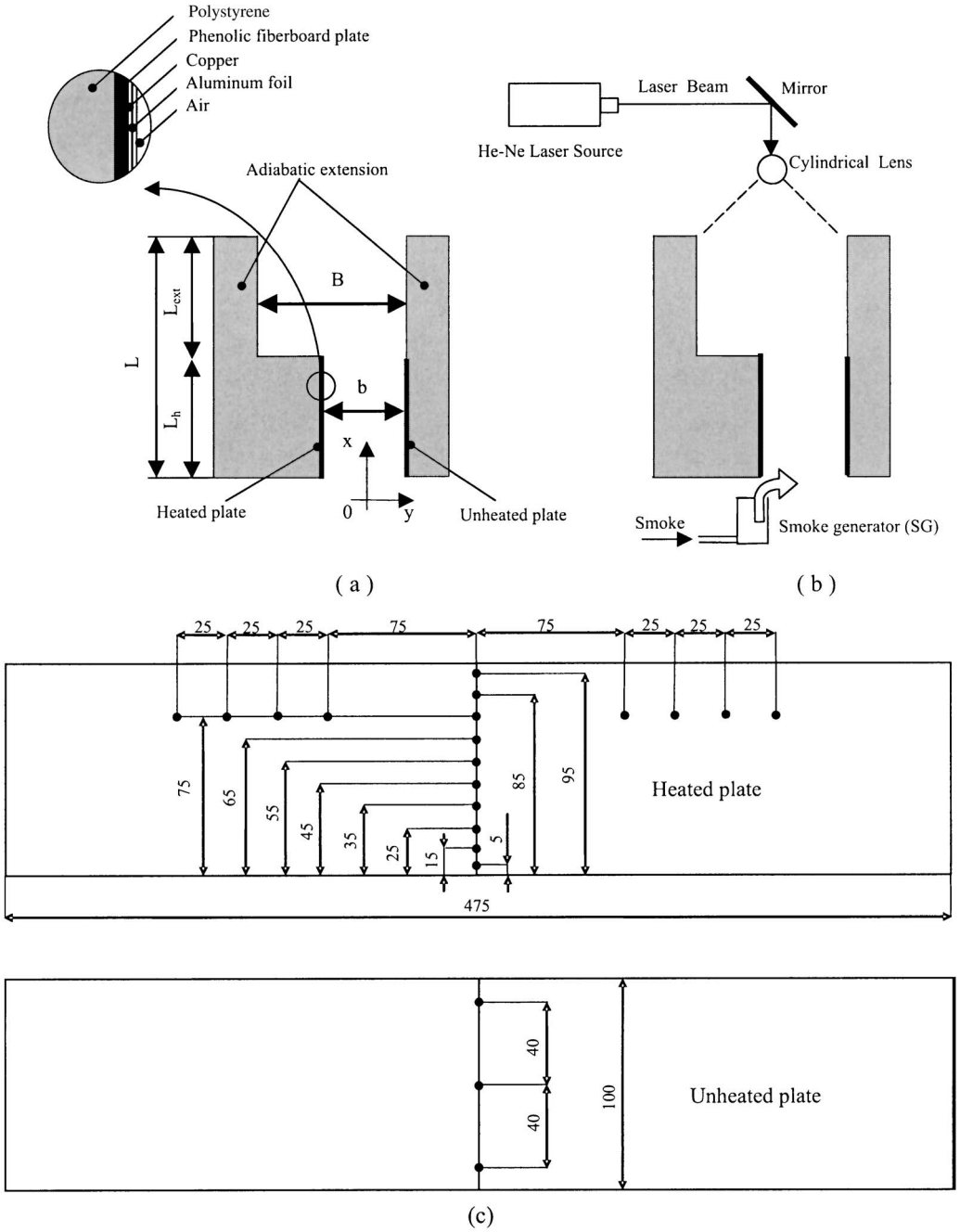

Fig. 1 Sketch of the experimental apparatus: (*a*) test section and heated wall; (*b*) visualization arrangement; and (*c*) position of thermocouples on the channel walls (all dimensions are in mm)

channel Rayleigh number, the expansion ratio, and the extension ratio were proposed. An experimental investigation on air natural convection, in asymmetrically heated vertical channel-chimney systems, was carried out in [18]. Results showed that the larger the chimney, the better the thermal performance of the system both in a large channel ($L_h/b=5.0$) and in a channel-chimney system with a large ratio of the extension length to the channel length. With a long extension ($L/L_h=4.0$) the lower the aspect ratio, the better the thermal performance of the system. For all values of the extension ratio, single correlations for both dimensionless maximum wall temperature and channel Nusselt number in terms of channel Rayleigh number multiplied by the expansion ratio were presented.

To the authors knowledge the thermal analysis of air natural convection in a channel, asymmetrically heated at uniform wall heat flux with a geometrically asymmetric downstream chimney, as sketched in Fig. 1, has not yet been carried out. Natural convection in asymmetrically heated channels with uniform wall heat flux occurs in many applications, such as thermal control of electronic systems and of nuclear plants, passive solar systems, and smoke control. As to the boundary condition of uniform heat flux at the wall, it is a good approximation of electronic systems and solar collectors. Results of an experimental investigation on the aforementioned system are presented in this paper. Wall temperature profiles along the heated plate, maximum wall temperatures and heat transfer coefficients are presented, for different values of the geometrical and thermal parameters. Optimal configurations in terms of the minimum values of maximum wall temperatures

were obtained. Some comparisons with geometrically symmetric channel-chimney systems in terms of wall temperature profiles and flow visualization are obtained. Both the dimensionless wall temperature and the channel Nusselt number are correlated to the channel Rayleigh number, Ra^*, to the expansion ratio, B/b, and to the extension ratio, in the $3.0\times10^2<Ra^*<1.0\times10^5$, $1.0<B/b<3.0$, $1.0<L/L_h<4.0$ ranges, with $L_h/b=5.0$ and 10.0.

Experimental Apparatus

The investigated test section is shown in Fig. 1(*a*), where *x* and *y* are the coordinates along the length and the gap of the channel, respectively. The transversal *z* axis, orthogonal to the picture plane, is not shown in the figure. The configuration was made up by a heated region (channel), whose length was $L_h=100$ mm, and a downstream unheated region (chimney), whose length, L_{ext}, varied in the 50–300 mm range. The investigated configuration is a good simulation for both electronic cooling systems and passive solar systems. The total length of the system is $L=L_h+L_{ext}$. The channel spacing, *b*, was 10 and 20 mm; with these dimensions the channel aspect ratio, L_h/b, was in the range 5.0–10, the expansion ratio, B/b, could range between 1.0 and 3.0, and the extension ratio, L/L_h, between 1.0 and 4.0. The test section was 475 mm wide. The cross section of the isoflux heated plate of the channel is sketched in Fig. 1(*a*). The heated wall and the shroud were made with a 3.2 mm thick and 530 mm wide phenolic fiberboard plate, with a typical thermal conductivity of 0.17 $W\,m^{-1}\,K^{-1}$. The surface of the heated wall facing the channel was coated with a 16 μm thick copper layer, which was the heater. It was obtained by cutting the copper in a 4.6 mm wide and 9.0 m long serpentine track. Its expected electric resistance was about 0.5 Ω.

A thick copper bar, bolted to the electric supply wire, was soldered to the ends of each heater. No electric resistance between the heater and the bars was measured during preliminary tests. A direct electrical current was passed through the copper and the dissipated heat flux was evaluated with an accuracy of ±2% by measuring the voltage drop and the current through the electric resistance. A maximum variation of ±10% in the electrical resistivity of the copper was evaluated in the most severe conditions, when the maximum difference in the wall temperatures was 30 K. Therefore, a uniform wall heat flux was assumed with a ±5% maximum deviation from its average value. Heat losses from the back of the heated wall were reduced by sticking a 150 mm polystyrene block on its rear surface. The principal chimney walls were two polystyrene blocks 30 mm thick and 530 mm wide. The total normal emissivity of the heated and unheated walls was 0.1 and was obtained by sticking a self-adhesive 25 μm thick aluminum foil on their surface facing the channel and the chimney. The emissivity was evaluated by means of radiometric direct measurements. The electric insulation between the copper surface of the heated wall and the aluminium foil was ensured by uniformly spraying an electrically insulating varnish onto it before coating. The typical time interval to attain steady-state conditions, after modifying the electric power supply or a geometrical configuration, was nearly 3 hours.

The side walls of the channel and the chimney were plexiglass rectangular rods, placed between the walls at their lateral edges. The rods were machined within an accuracy of ±0.03 mm. The distance between the principal walls of the channel and of the chimney was measured with an accuracy of ±0.25 and ±0.50 mm, respectively, by means of a dial-gauge caliper. The walls were fastened together by a steel frame, which had been designed in such a way as not to obstruct the fluid flow in the proximity of the channel inlet. The test section was aligned vertically, with horizontal leading edges, by means of a plumb line and a level. It was open to the ambient along the top and the bottom edges. The clearance of the bottom edge of the channel above the floor was 1.20 m and the minimum distance between the exit section of the chimney and the ceiling was 1.80 m. The entire apparatus was placed in an enclosed room, accurately sealed in order to eliminate extraneous air currents. Air drafts were further reduced by vertical screens, 2.5 m high. A large fraction of the lower part of the screens was made up by a 0.20 m high mesh.

Table 1 Values of geometrical and thermal parameters

Channel length (L_h), mm	100
Extension length (L_{ext}), mm	50, 100, 200, 300
Total length ($L = L_h + L_{ext}$), mm	150, 200, 300, 400
Channel spacing (b), mm	10, 20
Extension spacing (B), mm	10, 15, 20, 25, 30, 40, 50, 60
Aspect ratio (L_h/b)	5.0, 10
Extension ratio (L/L_h)	1.0 (base case), 1.5, 2.0, 3.0, 4.0
Expansion ratio (B/b)	1.0, 1.5, 2.0, 2.5, 3.0
Wall heat flux (q_Ω), $W\,m^{-2}$	100, 300, 450
Channel Rayleigh number (Ra*)	$3.0\times10^2 - 10^5$

The range of ambient temperature varied from 294 to 295 K during the experiments; the measured differences in the air ambient temperature in the proximity of the inlet and the exit sections of the apparatus were less than 0.8 K. Wall temperature measurements were carried out by 0.50 mm OD copper-constantan (type T) thermocouples, embedded in the fiberboard in the very proximity of the back side of the copper layer and sealed with a 3 M epoxy glue. They were run horizontally parallel to the surface, thereby lying along isotherms in order to minimize conduction heat losses in the leads. Ten equally spaced thermocouples were placed in the centerline of the heated plate: the first was placed 5.0 mm downstream of the inlet section, the distance between two successive thermocouples being 10 mm (Fig. 1(*c*)). At 75 mm from the leading edge, eight additional thermocouples were located horizontally outward from the centerline at $y=\pm75.0$, ±100.0, ±125.0, and ±150.0 mm (Fig. 1(*c*)), in order to provide indications of the horizontal variation of the wall temperature. Three thermocouples were embedded in the shroud, at different height (Fig. 1(*c*)).

The ambient air temperature was measured by the same type of thermocouples located in the proximity of the leading edge of the channel. In order to evaluate the conductive heat losses, three thermocouples were affixed to the rear surface of both the shroud and the heated wall in their centerline, 10, 50, and 90 mm downstream of the inlet section. At the same heights three thermocouples were embedded in the polystyrene block 10 mm from the rear surface of the shroud, whereas six thermocouples were embedded in the polystyrene block 10 mm from the rear surface of the heated wall 10, 25, 40, 60, 75, and 90 mm downstream of the inlet section. Thermocouple voltages were recorded to 1 μV. Each thermocouple was calibrated in a 0.01 K thermostatic bath by means of a reference standard thermometer (Pt 100). The calibration of the temperature measuring system showed an estimated precision of the thermocouple-readout system of ±0.2 K. A National Instruments SCXI module data acquisition system and a personal computer were used for the data collection and reduction. The data acquisition was performed through the LabView™ software. Wall temperature was assumed to be independent of the *z* coordinate within ±100 mm, since its maximum deviation from the centerline temperature was found to be no greater than 1.0 K when the latter was 343.2 K. The values of the geometric and thermal parameters considered in this study are reported in Table 1.

Smoke for visualization was generated by burning incense sticks in a steel tube, connected to a compressor (Fig. 1(*b*)). The smoke was passed into a plenum and its temperature was measured by means of a thermocouple located at the exit of the ple-

num. This value was close to that of the incoming air ambient to the channel. The visualization was made using a laser sheet, generated by a 5.0 mW continuous He-Ne laser source (Fig. 1(*b*)). The laser sheet was produced by placing a mirror near the end of the test section at an angle of 45° to the direction of the main flow, after which a cylindrical lens was placed to enlarge the beam as needed. The pictures were taken with a still digital camera Nikon D-100. In order to allow a thorough investigation of the flow patterns in the system, the smoke was injected in different locations of the section test.

Data Reduction

The dimensionless coordinate along the length is

$$X = \frac{x}{L_h} \tag{1}$$

The Rayleigh number and the channel Rayleigh number, which take the aspect ratio into direct account [7,15,19,20], are defined as

$$\mathrm{Ra} = \mathrm{GrPr}; \quad \mathrm{Ra}^* = \mathrm{Gr}\frac{b}{L_h}\mathrm{Pr} = \frac{g\beta q_c b^5}{\nu^2 k L_h}\mathrm{Pr}, \tag{2}$$

where q_c is the mean value of the spatially averaged convective heat flux

$$q_c = \frac{1}{L_h}\int_0^{L_h} q_c(x)dx \tag{3}$$

The channel Nusselt number is based on the difference between the wall and the inlet fluid temperatures, rather than on that between the wall and the bulk fluid temperatures, since the last one cannot be easily measured in practical applications

$$\mathrm{Nu} = \frac{q_c}{(T_w - T_o)}\frac{b}{k} \tag{4}$$

with the average wall temperature defined as

$$T_w = \frac{1}{L_h}\int_0^{L_h} T_w(x)dx \tag{5}$$

The dimensionless wall temperature is

$$T_w^* = \frac{(T_w - T_o)}{q_c b/k} \tag{6}$$

The properties of the air are evaluated at the reference temperature $(T_w + T_o)/2$.

Local convective heat flux, $q_c(x)$, is not uniform because of radiation and conduction. Experimental data are reduced first by introducing the local convective heat flux, in the equations presented above,

$$q_c(x) = q_\Omega(x) - q_k(x) - q_r(x) \tag{7}$$

In Eq. (7) the overall heat rate divided by the area of the heated wall surface is the local heat flux due to Ohmic dissipation, $q_\Omega(x)$, which was assumed to be uniform along the heated plate; $q_k(x)$ denotes the local conduction heat losses and $q_r(x)$ is the local radiative heat flux from the heated plate. For each run, the terms $q_k(x)$ were calculated by a finite difference numerical procedure, a two-dimensional distribution of the temperature being assumed in the polystyrene. Before starting the tests, several significant configurations of the system were selected, for which the temperature distribution in the polystyrene was predicted on the basis of the measured temperatures of the wall and of the ambient air. The predicted temperatures were then compared to those measured by the thermocouples embedded in the polystyrene insulation and the relationship was very good, the maximum deviation being 4%. The $q_r(x)$ terms were calculated for each temperature distribution in the walls, ambient temperature, and channel spacing, dividing each wall into ten equal length strips along the channel, according to the procedure described in [20]. Reference was made to a two-dimensional enclosure which was created by the heated and unheated plates of the channel, the inlet and the outlet sections. The solid walls were assumed to be gray surfaces and the inlet and outlet sections were assumed to be black surfaces at ambient temperature. For all the investigated configurations, the conductive heat losses were no larger than 9% of the Ohmic wall heat flux, whereas the radiative ones ranged between about 3% and 5%.

Table 2 Maximum percent uncertainties

Variable	ΔT_{max}	b	q_Ω	q_r	q_k	q_c
Uncertainty	1.1%	1.2%	2%	5%	4%	3%

Uncertainty Analysis

The uncertainty in the calculated quantities was determined according to the standard single sample analysis recommended by Kline and McClintock [21] and Moffat [22]. Accordingly, the uncertainty of a dependent variable R as a function of the uncertainties in the independent variables X_i is given by the relation

$$\delta R = \left[\left(\frac{\partial R}{\partial X_1}\delta X_1\right)^2 + \left(\frac{\partial R}{\partial X_2}\delta X_2\right)^2 + \cdots + \left(\frac{\partial R}{\partial X_n}\delta X_n\right)^2\right]^{1/2} \tag{8}$$

The uncertainty in the values of the air thermophysical properties can be assumed to be negligible. On the basis of Eqs. (2), (4), (6), and (7) and of the maximum percent uncertainties in the values of the independent variables, which are reported in Table 2, the maximum uncertainty in Ra^* ranged from 5% to 8% whereas the maximum uncertainty in Nu and in $T^*_{w,\max}$ turned out to be 4%–7%.

Results and Discussion

With reference to Fig. 1(*a*), results for extension ratios $L/L_h = 1.0, 1.5, 2.0, 3.0, 4.0$, for aspect ratios $L_h/b = 5.0, 10.0$, and for expansion ratios $B/b = 1.0, 1.5, 2.0, 2.5, 3.0$, $q_\Omega = 100, 300, 450$ W m^{-2} are presented. The configuration with $L/L_h = 1.0$ is the channel without adiabatic extensions, which in the following will be referred to as *base case*.

Temperature rises of the heated wall above the ambient temperature as a function of the dimensionless axial coordinate for different values of the above mentioned process parameters are presented in Figs. 2 and 3. Both figures show that the wall temperature attains its maximum value at nearly $x = 0.65\ L_h$ and then gradually decreases in the upper end region of the channel. The wall temperature in the exit section of the channel is nearly 90% of the maximum wall temperature. This is due to the radiative end effects to the ambient and to the conduction heat losses to the polystyrene, as shown in [23].

For $L/L_h = 1.5$ at any B/b Fig. 2(*a*), temperature profiles are similar to those in the channel without extension (base case) and no reduction in wall temperature occurs. The effect of B/b is very weak for $L/L_h = 1.5$ but it becomes stronger when the channel is provided with a longer chimney (Figs. 2(*b*)–2(*d*)). As a matter of fact, when $L/L_h = 3.0$ and 4.0 nearly all configurations exhibit lower maximum wall temperatures than in the channel without extensions, probably due to a larger flow rate determined by the chimney effect. However, in the channel inlet region the channel-chimney system exhibits a maximum percentage decrease in temperature, with respect to the simple channel, equal to 12% for $L/L_h = 4.0$ and $B/b = 2.0$. Larger and lower wall temperatures are observed at the channel outlet in contrast to the simple channel. The maximum percentage increase, for $L/L_h = 1.5$ and $B/b = 1.0$ and for $L/L_h = 2.0$ and $B/b = 2.5$, is 6%, and the maximum percentage decrease is also 6% for $L/L_h = 4.0$ and $B/b = 1.0$.

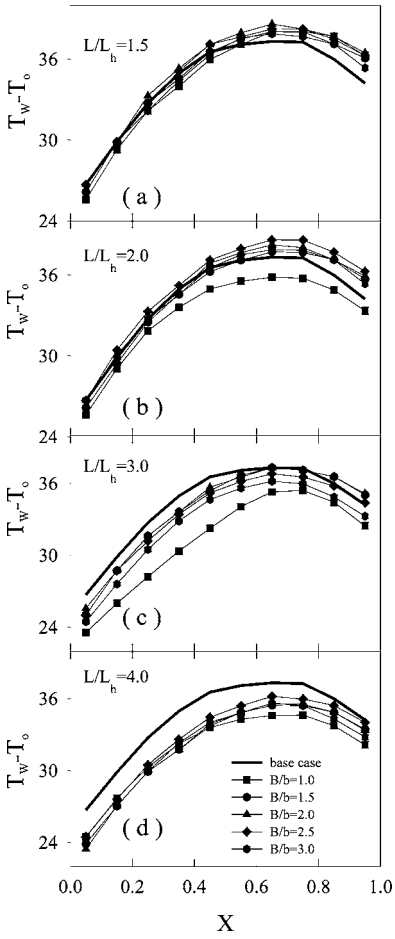

Fig. 2 Wall temperature rise versus the axial coordinate, for $L_h/b=5.0$ and $q_\Omega=300\ \mathrm{W\,m^{-2}}$ and various B/b values: (*a*) $L/L_h=1.5$; (*b*) $L/L_h=2.0$; (*c*) $L/L_h=3.0$; and (*d*) $L/L_h=4.0$

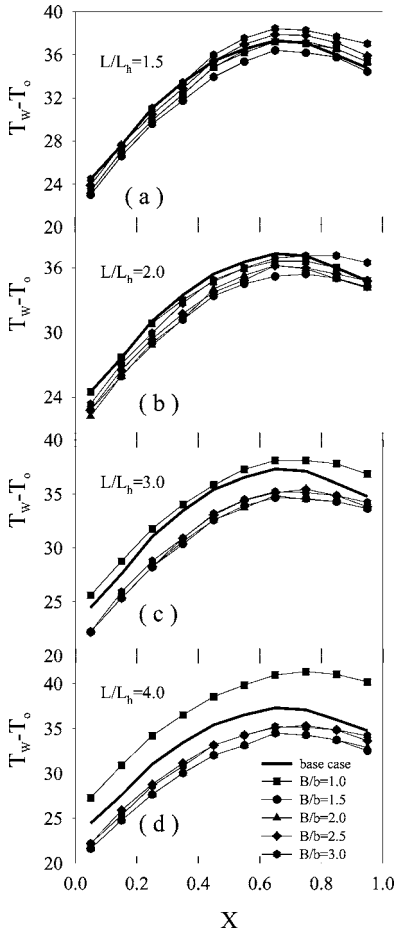

Fig. 3 Wall temperature rise versus the axial coordinate, for $L_h/b=10.0$ and $q_\Omega=300\ \mathrm{W\,m^{-2}}$ and various B/b values: (*a*) $L/L_h=1.5$; (*b*) $L/L_h=2.0$; (*c*) $L/L_h=3.0$; and (*d*) $L/L_h=4.0$

Halving the channel gap, without varying the other parameters, affects its thermal performance as can be remarked by comparing Fig. 3 to Fig. 2. First of all, Fig. 3 shows that, apart from $B/b=1.0$, whatever the expansion ratio in a narrower system, the addition of an adiabatic extension reduces the temperature of the heated wall. On the other hand, comparing the temperature profiles at $L_h/b=5.0$ and at $L_h/b=10.0$ shows that for the latter aspect ratio, adding an adiabatic extension to the channel, whatever the extension ratio, improves the thermal performance of the channel. This is due to the chimney effect that increases the flow rate of the air entrained in the channel. For this aspect ratio ($L_h/b=10.0$) the exit wall temperature is about 93% of the maximum wall temperature. The maximum temperature percentage increases and decreases between the simple channel and channel-chimney system, at the channel inlet, are about 13%, for $L/L_h=4.0$ and $B/b=1.0$, and 12%, for $L/L_h=4.0$ and $B/b=1.5$ and 2.0. At the channel outlet the percentage increase is nearly 15% for $L/L_h=4.0$ and $B/b=1.0$ and the percentage decrease is about 7% for $L/L_h=4.0$ and $B/b=1.5$.

The main effects of the geometrical and thermal parameters are highlighted in Figs. 4 and 5. The ratio of the maximum wall temperature rise above the ambient air in a channel with the adiabatic extension to the maximum wall temperature rise above the ambient air in a channel without the adiabatic extension as a function of the expansion ratio is reported in both figures. Different values of the heat flux and of the extension ratio at aspect ratios equal to 5.0 and 10.0 are presented in Figs. 4 and 5, respectively. Both figures show that the differences in the maximum wall temperatures in channels with or without the adiabatic extension are generally no larger than ±10%. For the smaller aspect ratio ($L_h/b=5.0$, Fig. 4), that is for the larger channel gap and for the larger Grashof numbers, in several cases the adiabatic extension determines higher maximum wall temperatures than in the simple channel. This occurs at any B/b in the configuration with the lowest heat flux, except $L/L_h=4.0$ (Fig. 4(*a*)), while things go slightly and gradually better at the larger heat flux values (Figs. 4(*b*) and 4(*c*)). Figure 5 points out that by increasing the aspect ratio of the system maximum wall temperatures decrease in almost all configurations, except that with $B(b=1.0$, whatever the heat flux and the length of the adiabatic extension. We can also remark that at all heat flux values, when the extension ratio, L/L_h, is larger than 1.5, the maximum wall temperature in a channel with the adiabatic extension is less than the maximum wall temperature in a channel without the adiabatic extension. On the basis of these results, one can conclude that the smaller the channel gap and the Grashof number, the larger the decrease in the temperature of the heated wall determined by the adiabatic extension, provided L is longer than 1.5 L_h and shorter than 4.0 L_h. One can argue that in a very short chimney the air inflow chokes the thermal plume arising from the channel whereas in a very long chimney the increase in buoyancy forces, due to the chimney effect, does not counterbalance the increase in pressure drop.

It is important to note that information given in the figures presented above allows an easy determination of the best performing configuration. For instance, Fig. 5 shows that the minimum value of the maximum wall temperature for $L_h/b=10.0$ is attained with $L/L_h=4.0$ and $B/b=1.5$ at all investigated q_Ω. We can also

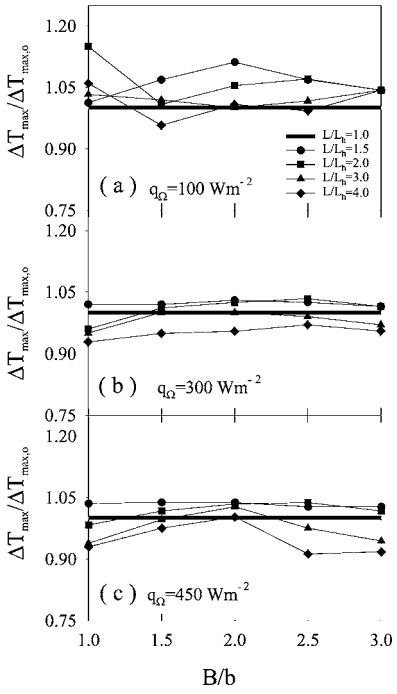

Fig. 4 Ratio of the maximum wall temperature rise above the ambient air in a channel without the adiabatic expansion ratio, for L_h/b=5.0 and different L/L_h: (*a*) q_Ω=100 W m^{-2}; (*b*) q_Ω =300 W m^{-2}; and (*c*) q_Ω=450 W m^{-2}

notice that in a shorter channel-chimney system (L/L_h=2.0) with the same expansion ratio the maximum wall temperature is only slightly higher than in the best performing configuration.

The effect of the chimney on the thermal performance of the heated channel was further investigated by comparing wall temperatures in this system with those in channels with a geometrically symmetric adiabatic extension presented in [18]. Wall temperature rise above the ambient in symmetric and asymmetric configurations as a function of the dimensionless axial coordinate for q_Ω=300 W m^{-2}, L/L_h=2.0,3.0,4.0, B/b=2.0,3.0, and L_h/b =10.0 is presented in Fig. 6. The configuration of the chimney under investigation is sketched in Fig. 6(*c*). Figure 6 shows that, in terms of maximum wall temperature, the thermal performance of the system with a symmetric chimney is very similar to that of the system with an asymmetric chimney. However, also bearing in mind results exhibited in Fig. 5, we can observe that an asymmetric chimney with B/b=1.5 yields only a slightly lower maximum wall temperature than that attained in a 33% larger symmetric chimney with B/b=2.0.

Flow visualization for L_h/b=5.0, L/L_h=1.5, and q_Ω =300 W m^{-2} is presented in Fig. 7 for B/b=2.5 and a geometrically asymmetric chimney configuration and in Fig. 8 for B/b =2.0 and 4.0 and a geometrically symmetric chimney configuration. The smoke is injected at the channel inlet from the heated

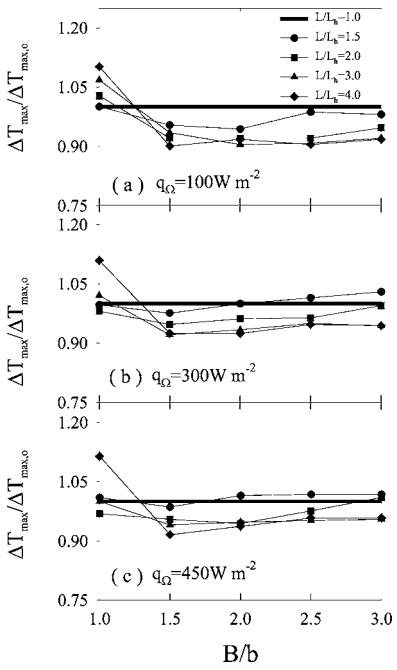

Fig. 5 Ratio of the maximum wall temperature rise above the ambient air in a channel without the adiabatic expansion ratio, for L_h/b=10.0 and different L/L_h: (*a*) q_Ω=100 W m^{-2}; (*b*) q_Ω =300 W m^{-2}; and (*c*) q_Ω=450 W m^{-2}

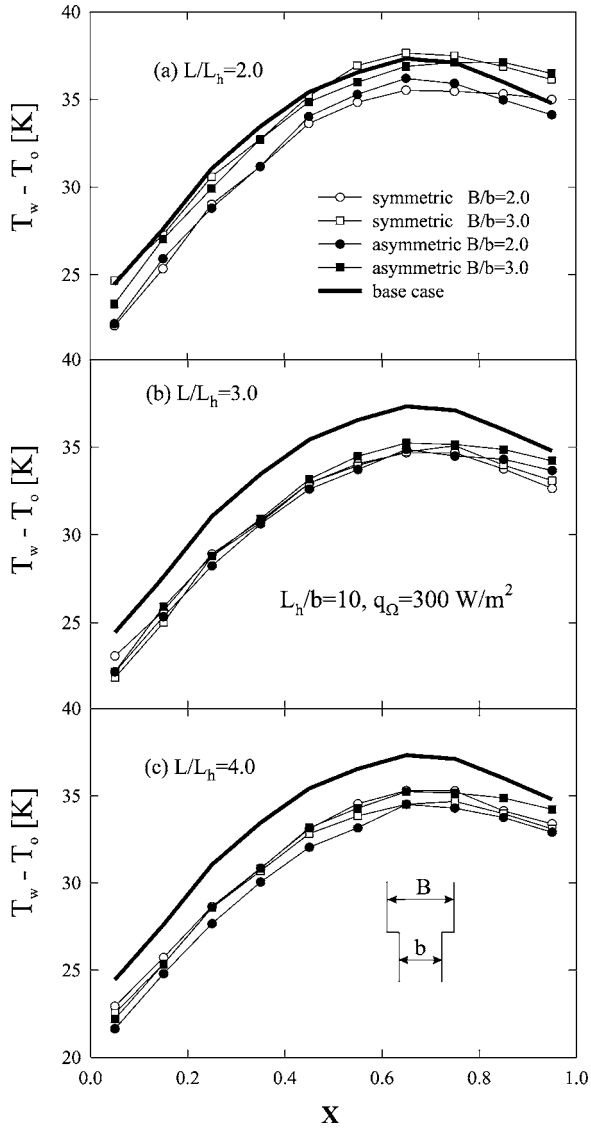

Fig. 6 Comparison between wall temperature rise profiles along axial coordinate in a channel with a geometrically symmetric extension from [18] and geometrically asymmetric extension from present data, for q_Ω=300 W m^{-2}, L_h/b=10, and various B/b values: (*a*) L/L_h=2.0; (*b*) L/L_h=3.0; and (*c*) L/L_h =4.0

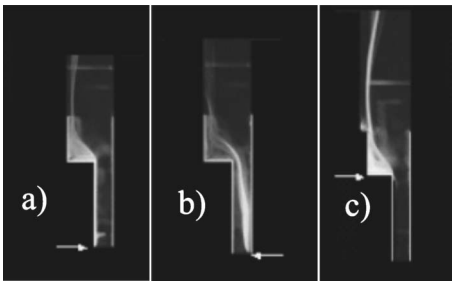

Fig. 7 Flow visualization in a system with an asymmetric chimney, q_Ω=300 W m^{-2}, L_h/b=5.0, B/b=2.5, and L/L_h=1.5. Smoke inflow: (*a*) at the channel inlet of the heated side; (*b*) at the channel inlet of the unheated side; and (*c*) at the channel outlet on the heated side.

side (Fig. 7(*a*)), from the unheated side (Figs. 7(*b*) and 8) and at the lower section of the chimney (Fig. 7(*c*)). In both configurations, the channel is asymmetrically heated.

At the inlet region of the channel, Fig. 7(*a*), the fluid flows along the heated plate of the channel and the motion is laminar. At the channel outlet, the hot plume is driven toward the unheated plate of the chimney and it flows along the wall up to the chimney upper edge, Figs. 7(*a*) and 7(*c*). A steady vortex structure is noticed in the lower corner of the chimney. On the unheated side in the channel, the fluid runs along the wall (up to about $x=3/4L_h$), then it goes toward the heated channel side. This motion determines a depression in the channel-chimney and the colder ambient fluid enters the chimney upper edge and penetrates the channel, lapping the wall. This is a fluid downflow or cold inflow in the considered system. In Fig. 7(*b*) the cold inflow exhibits a deeper penetration than in the previous case.

In Fig. 8 the smoke input is injected at the channel inlet section on the unheated plate side. The downflow penetrates the upper part of the channel. This is due to the depression zone close to the unheated plate that, in this case, is up to half the channel height. At the channel exit, i.e., chimney inlet section, the flow slightly expands and reattaches to the chimney wall on the heated side of the channel plate. In Fig. 8(*b*), for a larger expansion ratio (B/b =4.0), the vortex zone is larger and one can observe that in the left lower corner of the chimney, the vortex is quite large and covers the whole horizontal side. Figures 7 and 8 show a deeper penetration of the downflow in the geometrically symmetric chimney than in the geometrically asymmetric chimney.

Dimensionless maximum wall temperature has first been correlated to the product of channel Rayleigh number and the expansion ratio and to the extension ratio for $3\times10^2\leqslant \mathrm{Ra}^* B/b\leqslant 1.0\times10^5$, $1.0\leqslant B/b\leqslant 3.0$, $L/L_h=1.0,1.5,2.0,3.0,4.0$, and $L_h/b=5.0$ and 10.0, in the following form:

$$T^*_{w,\max}=0.125\left(\mathrm{Ra}^*\frac{B}{b}\right)^{-0.180}\left(\frac{L}{L_h}\right)^{-0.0016} \tag{9}$$

with $r^2=0.963$.

Since 0.001 6 is much smaller than 0.125 and 0.180, data have been correlated for each value of $L/L_h=1.5,2.0,3.0$, and 4.0, by means of the equation

$$T^*_{w,\max}=m'+n'\exp\left(-\frac{\mathrm{Ra}^* B/b}{o'}\right) \tag{10}$$

whose coefficients are reported in Table 3, in the $3.0\times10^2<\mathrm{Ra}^*<10^5$, $1.0<B/b<3.0$, $1.0<L/L_h<4.0$, and $L_h/b=5.0$ and 10.0 ranges.

One can observe that the coefficient m' is the asymptotic value assumed by the dimensionless temperature, as observed in Figs.

Table 3 Coefficients in Eq. (10)

L/L_h	m'	n'	o'	r^2
1.5	0.200	0.250	3851	0.980
2.0	0.200	0.240	6040	0.971
3.0	0.190	0.270	4361	0.982
4.0	0.180	0.270	5046	0.984

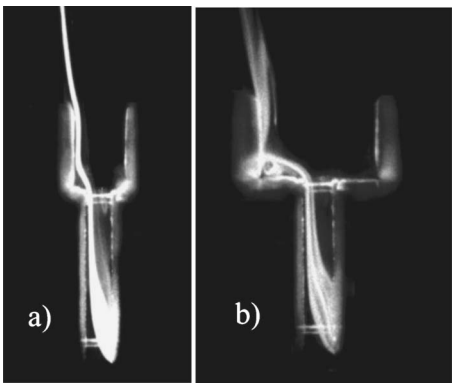

Fig. 8 Flow visualization in a system with a symmetric chimney, q_Ω=300 W m^{-2}, L_h/b=5, and L/L_h=1.5: (*a*) B/b=2.0; and (*b*) B/b=4.0

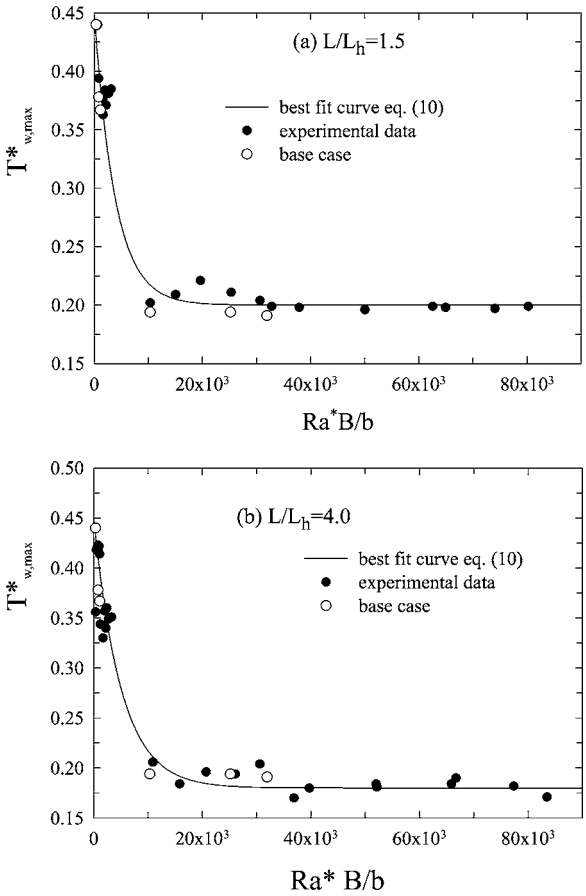

Fig. 9 Dimensionless wall temperature versus the channel Rayleigh number multiplied by the expansion ratio for L_h/b =5.0 and 10: (*a*) L/L_h=1.5 and (*b*) L/L_h=4.0

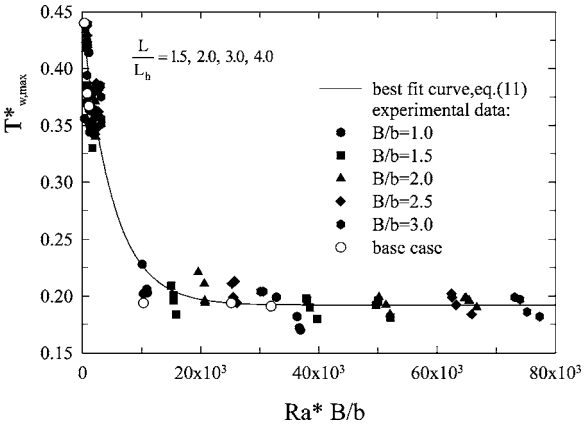

Fig. 10 Dimensionless wall temperature versus the channel Rayleigh number multiplied by the expansion ratio for $L_h/b=5.0$ and 10

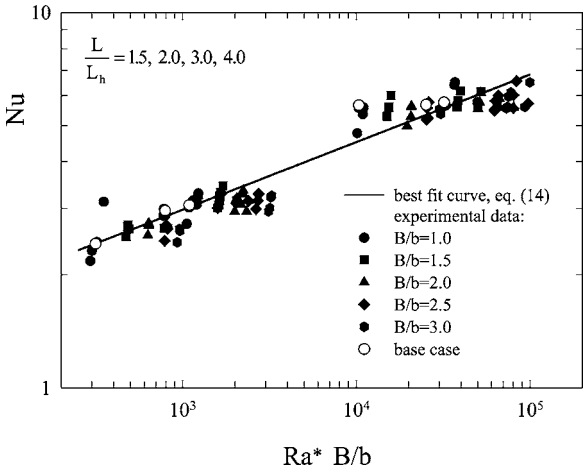

Fig. 11 Channel Nusselt number versus the channel Rayleigh number multiplied by the expansion ratio for $L_h/b=5.0$ and 10

9(*a*) and 9(*b*), where the measured values of the dimensionless wall temperature have been plotted as a function of the Rayleigh number multiplied by the expansion ratio, at $L/L_h=1.5$ and $L/L_h=4.0$, respectively. Therefore, one can conclude that beyond a certain value of the product Ra^*B/b, increasing it does not enhance the thermal performance of the channel because of the very small decrease in maximum wall temperature. As a matter of fact, the difference between the asymptotic value of the maximum wall temperature and that attained at $\mathrm{Ra}^*B/b=2.0\times10^4$ is only about 2.7%. A comparison between Figs. 9(*a*) and 9(*b*) reveals that the configurations with $L/L_h=4.0$ are more efficient than those with $L/L_h=1.5$. For instance, the asymptotic value of $T^*_{w,\max}$ is 1.80 for $L/L_h=4.0$ and 2.00 for $L/L_h=1.5$ (see also Table 3).

Finally, the same form of equation was used to correlate data for all the investigated L/L_h values:

$$T^*_{w,\max}=0.192+0.250\exp\left(-\frac{\mathrm{Ra}^*B/b}{5130}\right) \tag{11}$$

with $r^2=0.973$. Experimental data and the curve from Eq. (11) are presented in Fig. 10 for $3.0\times10^2<\mathrm{Ra}^*<1.0\times10^5$, $1.0<B/b<3.0$, $1.0<L/L_h<4.0$, and $L_h/b=5.0$ and 10.0.

Channel Nusselt numbers were first correlated to the same process parameters, for all the values of the extension ratio, by the equation

$$\mathrm{Nu}=0.860\left(\mathrm{Ra}^*\frac{B}{b}\right)^{0.170}\left(\frac{L}{L_h}\right)^{0.0230} \tag{12}$$

with $r^2=0.960$ for $3.0\times10^2<\mathrm{Ra}^*<1.0\times10^5$, $1.0<B/b<3.0$, $1.0<L/L_h<4.0$, and $L_h/b=5.0$ and 10.0.

Also in this case, since 0.0230 is smaller than 0.860 and 0.170, data have been correlated for each value of $L/L_h=1.5, 2.0, 3.0$, and 4.0, using the equation

$$\mathrm{Nu}=m''\left(\mathrm{Ra}^*\frac{B}{b}\right)^{n''} \tag{13}$$

whose coefficients are reported in Table 4, for $3.0\times10^2<\mathrm{Ra}^*<1.0\times10^5$, $1.0<B/b<3.0$, $1.0<L/L_h<4.0$, and $L_h/b=5.0$ and 10.0.

Table 4 Coefficients in Eq. (13)

L/L_h	m''	n''	r^2
1.5	0.700	0.140	0.970
2.0	1.000	0.160	0.960
3.0	0.900	0.170	0.975
4.0	0.800	0.185	0.970

Since the values of the coefficients in Eq. (13) are only fairly dependent on L/L_h, a unique correlation for all values of the extension ratio has been derived:

$$\mathrm{Nu}=0.860\left(\mathrm{Ra}^*\frac{B}{b}\right)^{0.180} \tag{14}$$

with $r^2=0.960$. Experimental data and the curve from Eq. (14) are reported in Fig. 11, for $3.0\times10^2<\mathrm{Ra}^*<10^5$, $1.0<B/b<3.0$, $1.0<L/L_h<4.0$, and $L_h/b=5.0$ and 10.0.

Conclusions

An experimental analysis of air natural convection, on a uniform heat flux vertical plate, with a downstream unheated extension and a facing parallel shroud, has been carried out. Results were obtained for different values of wall heat flux and geometrical parameters. The fundamental geometrical parameters were the distance between the plate and the shroud, b, the spacing between the adiabatic extension and the shroud, B, the height of the plate, L_h, and the total height of the system, L. The dimensionless parameters were the expansion ratio, B/b, the extension ratio, L/L_h, the aspect ratio, L_h/b, and the channel Rayleigh number, Ra^*.

Plate temperature profiles allowed the following remarks: for the lowest values of the aspect ratio and of the heat flux, the thermal performance of the system is worse than that of the channel without adiabatic extensions, except that in the configurations with the larger L/L_h values; for $L/L_h=3.0$ and 4.0, the larger the channel spacing the lower the wall temperature also at the lowest B/b; at the aspect ratio $L_h/b=10$, the channel with the adiabatic extension performed better than that without the extension, at any configurations, apart from almost all cases with $B/b=1.0$ and some L/L_h values.

The ratio of the maximum temperature in the channel with the extension to the maximum temperature in the channel without it was less than the unity for nearly all configurations with $L_h/b=10$ and $B/b>1.0$.

The adiabatic extensions improve the thermal performance, in terms of a reduction in the maximum temperature of the heated wall of the channel for an aspect ratio equal to 10. As far as the reduction in both the volume of the chimney and the maximum wall temperature is concerned, optimal configurations turned out to be those with $B/b=1.5$ and $L/L_h=2.0$ and 3.0.

Flow visualization pointed out a cold inflow in the channel-chimney system, which penetrated down below the channel exit section. The comparison of a system with an asymmetric chimney

to a system with a symmetric chimney, for the same values of other geometrical and thermal parameters and for $L_h/b=10$, exhibited a similar thermal performance in terms of wall temperature profiles, though the first system has a smaller volume than the latter one.

Both the dimensionless wall temperature and the channel Nusselt number have been correlated to the channel Rayleigh number, Ra^*, to the expansion ratio, B/b, and to the extension ratio, in the $3.0\times10^2<Ra^*<10^5$, $1.0<B/b<3.0$, and $1.0<L/L_h<4.0$ ranges. In both cases a slight dependence on L/L_h was noticed and, therefore, each of the earlier mentioned process parameters was correlated to Ra^* (B/b) by a unique correlation. Remarking that Ra^* (B/b) was an asymptote for the maximum wall temperature indicates that employing systems with Ra^* $(B/b)>2.0\ 10^4$ is unnecessary.

We can conclude that the smaller the channel gap and the Grashof number the larger the decrease in the temperature of the heated wall determined by the adiabatic extension, provided the length of the chimney is larger than 1.5 times and smaller than 4.0 times that of the heated wall. The thermal performance of the system in many applications, such as thermal control in electronic and TLC cabinets, can be predicted by means of the proposed correlations among dimensionless process parameters.

Acknowledgments

This research was supported by Ministero dell'Istruzione, dell'Università e della Ricerca (MIUR) under 2003 grant research programs. The authors are grateful to the reviewers of the paper for their useful suggestions and recommendations.

Nomenclature

b = channel spacing, m
B = extension spacing, m
g = acceleration of gravity, $m\ s^{-2}$
Gr = channel Grashof number, Eq. (2)
k = thermal conductivity, $W\ m^{-1}\ K^{-1}$
L = total length, L_h+L_{ext}, m
L_h = channel length, m
L_{ext} = extension length, m
m',n',o' = coefficients in Eq. (10)
m'',n'' = coefficients in Eq. (13)
Nu = channel Nusselt number, Eq. (4)
Pr = Prandtl number
q = heat flux, $W\ m^{-2}$
r = regression coefficient
Ra = Rayleigh number, Eq. (2)
Ra^* = channel Rayleigh number, Eq. (2)
T = temperature, K
x, y = coordinates, m
X = dimensionless coordinate

Greek symbols

β = volumetric coefficient of expansion, K^{-1}
ν = kinematic viscosity, $m^2\ s^{-1}$

Subscripts

c = convective
k = conductive
min = minimum
max = maximum
max, o = maximum, refers to *base case*
o = ambient air
r = radiative
w = wall
Ω = Ohmic dissipation

References

[1] Kim, S. J., and Lee, S. W., 1996, *Air Cooling Technology for Electronic Equipment*, CRC Press, Boca Raton, FL.
[2] Manca, O., Morrone, B., Nardini, S., and Naso, V., 2000, "Natural Convection in Open Channels," in *Computational Analysis of Convection Heat Transfer*, WIT Press, Southampton, pp. 235–278.
[3] Bianco, N., Morrone, B., Nardini, S., and Naso, V., 2000, "Air Natural Convection between Inclined Parallel Plates with Uniform Heat Flux at the Walls," Int. J. Heat Technol., **18**(2), pp. 27–36.
[4] Haaland, S. E., and Sparrow, E. M., 1983, "Solutions for the Channel Plume and the Parallel-Walled Chimney," Numer. Heat Transfer, **6**, pp. 155–172.
[5] Oosthuizen, P. H., 1984, "A Numerical Study of Laminar Free Convective Flow through a Vertical Open Partially Heated Plane Duct," ASME HTD, **32**, pp. 41–48.
[6] Asako, Y., Nakamura, H., and Faghri, M., 1990, "Natural Convection in a Vertical Heated Tube Attached to Thermally Insulated Chimney of a Different Diameter," ASME J. Heat Transfer, **112**, pp. 790–793.
[7] Straatman, A. G., Tarasuk, J. D., and Floryan, J. M., 1993, "Heat Transfer Enhancement from a Vertical, Isothermal Channel Generated by the Chimney Effect," ASME J. Heat Transfer, **115**, pp. 395–402.
[8] Lee, K. T., 1994, "Natural Convection in Vertical Parallel Plates with an Unheated Entry or Unheated Exit," Numer. Heat Transfer, Part A, **25**, pp. 477–493.
[9] Fisher, T. S., Torrance, K. E., and Sikka, K. K., 1997, "Analysis and Optimization of a Natural Draft Heat Sink System," IEEE Trans. Compon., Packag. Manuf. Technol., Part A, **20**, pp. 111–119.
[10] Fisher, T. S., and Torrance, K. E., 1998, "Free Convection Limits for Pin-Fin Cooling," ASME J. Heat Transfer, **120**, pp. 633–640.
[11] Campo., A., Manca, O., and Morrone, B., 1999, "Numerical Analysis of Partially Heated Vertical Parallel Plates in Natural Convective Cooling," Numer. Heat Transfer, Part A, **36**, pp. 129–151.
[12] Shahin, G. A., and Floryan, J. M., 1999, "Heat Transfer Enhancement Generated by the Chimney Effect in Systems of Vertical Channel," ASME J. Heat Transfer, **121**, pp. 230–232.
[13] Fisher, T. S., and Torrance, K. E., 1999, "Experiments on Chimney-Enhanced Free Convection," ASME J. Heat Transfer, **121**, pp. 607–608.
[14] Trasher, W. W., Fisher, T. S., and Torrance, K. E., 2000, "Experiments on Chimney-Enhanced Free Convection from Pin-Fin Heat Sinks," ASME J. Heat Transfer, **122**, pp. 350–357.
[15] Auletta, A., Manca, O., Morrone, B., and Naso, V., 2001, "Heat Transfer Enhancement by the Chimney Effect in a Vertical Isoflux Channel," Int. J. Heat Mass Transfer, **44**, pp. 4345–4357.
[16] Manca, O., Musto, M., and Naso, V., 2001, "Experimental Analysis of Chimney Effect in a Vertical Isoflux Channel," Proceedings of 5th World Conference on Experimental Heat Transfer, Fluid Dynamics and Thermodynamics, Thessaloniki, Greece.
[17] Auletta, A., and Manca, O., 2002, "Heat and Fluid Flow Resulting from the Chimney Effect in a Symmetrically Heated Vertical Channel with Adiabatic Extensions," Int. J. Therm. Sci., **41**, pp. 1101–1111.
[18] Manca, O., Musto, M., and Naso, V., 2003, "Experimental Analysis of Asymmetrical Isoflux Channel-Chimney Systems," Int. J. Therm. Sci., **42**, pp. 837–846.
[19] Aung, W., Fletcher, L. S., and Sernas, V., 1972, "Developing Laminar Free Convection between Vertical Flat Plates with Asymmetric Heating," Int. J. Heat Mass Transfer, **15**, pp. 2293–2308.
[20] Webb, B. W., and Hill, D. P., 1989, "High Rayleigh Number Laminar Natural Convection in an Asymmetrical Heated Vertical Channel," ASME J. Heat Transfer, **111**, pp. 649–656.
[21] Kline, S. J., and McClintock, F. A, 1953, "Describing Uncertainty in Single Sample Experiments," Mech. Eng. (Am. Soc. Mech. Eng.), **75**, pp. 3–12.
[22] Moffat, R. J., 1988, "Describing the Uncertainties in Experimental Results," Exp. Therm. Fluid Sci., **1**, pp. 3–17.
[23] Manca., O., and Naso, V., 1990, "Experimental Analysis of Natural Convection and Thermal Radiation in Vertical Channels," ASME HTD, **145**, pp. 13–21.

Effect of Buoyancy on Heat Transfer in Supercritical Water Flow in a Horizontal Round Tube

Majid Bazargan
University of Tehran, Iran

Daniel Fraser
e-mail: fraserdw@cc.umanitoba.ca

Vijay Chatoorgan
e-mail: chatoorg@cc.umanitoba.ca

Department of Mechanical and Manufacturing Engineering, University of Manitoba

Heat transfer to supercritical water and buoyancy/natural convection effects are becoming increasingly important areas of research due to current trends in nuclear reactor design and supercritical water oxidation facilities. A pilot-scale supercritical water oxidation loop was constructed at the University of British Columbia. For this work, the facility was used to study the relative importance of buoyancy effects on supercritical water flowing in a horizontal pipe. Local heat transfer coefficients at the top and bottom surfaces of the horizontal test section were systematically measured over a wide range of conditions at supercritical pressures between 23 to 27 MPa, uniform heat fluxes were up to 310 kW/m^2*, and the mass flux ranged from 330 to* 1230 $kg/m^2 s$*. It was found that neglecting buoyancy effects could cause large discrepancies between the predictions of available empirical correlations and the experimental data. The data was used to assess available criteria for the buoyancy-free region during horizontal supercritical fluid flows. The criterion of Petukhov and Polyakov, which, for the range of parameters in this study, was found to be accurate in predicting the onset of buoyancy effects. The experimental investigation is confined to supercritical flows with heat addition only. Hence, no heat loss conditions at supercritical temperatures were investigated.*
[DOI: 10.1115/1.1929787]

Keywords: Channel Flow, Energy Conversion, Forced Convection, Heat Transfer, Mixed Convection

Introduction

The thermodynamic critical point of water is 22.1 MPa and 374 °C. For any given supercritical pressure, there is a temperature at which the thermal expansion coefficient has a maximum, and variations in other thermophysical properties of water with respect to temperature are highest. This temperature is called the pseudocritical temperature. The term supercritical water is usually reserved for water at supercritical pressures, while the temperature may vary from below the critical temperature to above. Due to dramatic variations of water properties near the pseudocritical temperature (shown in Fig. 1), heat transfer characteristics are substantially different from those at subcritical pressures. The large enhancement of heat transfer possible has made supercritical water an attractive heat transfer medium for decades. Some examples of engineering applications are supercritical boilers, rocket propulsion systems, and, more recently, water oxidation systems. Also, many nuclear energy companies are investigating the potential benefits of operating under supercritical conditions. Such benefits include higher thermal efficiencies and the potential for supercritical water reactions to produce hydrogen, as are currently being investigated by General Atomics (GAT).

Many empirical correlations are available for predicting convective heat transfer coefficients in order to compute the rate of heat transfer from/to supercritical water. Correlations developed for subcritical conditions are usually inadequate for supercritical fluid flows. More than 20 correlations have been proposed that apply to internal flows through round tubes. A review of these correlations was reported by Bazargan and Fraser [1]. Disagreements between experiments, as well as disagreements between empirical correlations and experiments, were found. An example is shown in Fig. 2, in which the predictions of Miropolski and Shitsman [2], Petukhov et al. [3], Swenson et al. [4], Jackson and Fewster [5], and Razumovskiy et al. [6], along with data obtained from this study, are presented. Ghajar and Asadi [7] proposed that the large variation in fluid properties near the pseudocritical point was the main reason for discrepancies. The effect of buoyancy, however, was omitted in their assessment.

The effect of buoyancy was not properly addressed in some earlier studies. Thus, many experimental results reporting forced-convection heat transfer were really forced-convection heat transfer with tangible buoyancy effects. Our studies have shown that it is important to distinguish truly forced-convection cases with no buoyancy effects and forced-convection cases where buoyancy has a significant effect.

The vast majority of analytical and experimental studies reported in the past were for vertical flows. Very little theoretical criteria have been proposed for detecting the buoyancy-free region of a horizontal supercritical flow. Those reported were not tested extensively, due to a paucity of experimental data. In the current study, testing was done against carefully taken measurements in supercritical flows that have relatively large, moderate, and small buoyancy effects.

Experimental Apparatus

A supercritical water oxidation (SCWO) test loop was constructed at the University of British Columbia in partnership with NORAM, a Vancouver-based company. The facility was used to study convection heat transfer of pure water at supercritical pressures. A schematic of the apparatus is shown in Fig. 3. The test section was comprised of two horizontal 1.5 m long Inconel tubes connected in series, giving an overall test section length of 3 m. The inner diameter of each tube was 6.3 mm and the outer diameter was 9.4 mm. The test section was proceeded by a 0.3 m long unheated length to allow for fully developed flow. Both 1.5 m segments were electrically heated with AC current to provide a uniform heat flux across the entire test section. The maximum heat

Contributed by the Heat Transfer Division for publication in the JOURNAL OF HEAT TRANSFER. Manuscript received by the Heat Transfer Division October 2, 2003; revision received March 22, 2005. Review conducted by: J. H. Lienhard V.

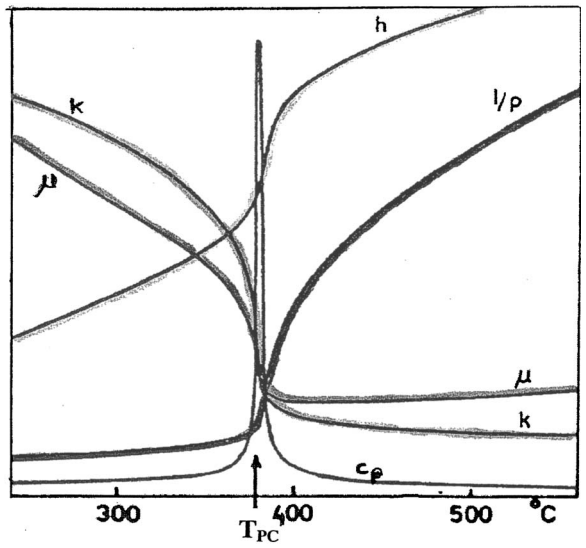

Fig. 1 Variations of properties of supercritical water with temperature at $P=235$ MPa

flux attainable was about 310 kW/m^2. The heat added to the flow was determined by the following two means: doing an energy balance on the flow between the inlet and outlet, and from the applied electrical power derived from the product of voltage and current.

The loop pressure was controlled by means of a backpressure regulator. A pressure transducer, calibrated using a digital calibrator and a deadweight tester, was used to measure the test section pressure. The uncertainty in pressure measurement [1] was 0.5% or 0.12 MPa at 24 MPa. Before the water entered the test section, it was heated to the required temperature by means of two preheaters. The fluid temperatures at the entrance, middle, and exit of the test section were measured by miniature thermocouples inserted through high-pressure fittings. The uncertainty in wall and bulk temperature measurements [1] was 0.4%, i.e., 1.5 K at 380 °C. Thirty intrinsic thermocouples were welded to the tube surface to measure wall temperatures at different locations along the test section. The two thermocouple leads were welded a small distance circumferentially apart at the same axial location to prevent error due to the voltage drop over the axial distance. The thermocouples were calibrated using ice point reference cells ($\pm$ 0.1 K) and, at higher T, using the melting point of pure alloys, such as zinc. Single-phase forced-convection studies were performed, and standard heat transfer correlations were accurate at predicting the heat transfer coefficients, thus proving the temperature measurement accuracy. Inner tube temperatures were determined from steady-state heat conduction through the tube wall. Intrinsic thermocouples allow for true surface temperature measurements, since they have no thermal mass. The thermocouples were evenly distributed along the top and bottom surfaces of the tube to allow for measuring peripheral variations of surface temperature. Bulk temperature measurements were measured using microthermocouples inserted into the centerline of the flow at each axial location as the surface thermocouples. Thus, the calculated wall inner temperature and the local bulk temperature were used when required, such as for the heat transfer calculations. The mass flux, ranging from 330 to 1200 kg/m^2 s, was obtained using an AC pump controlled by a variable frequency drive. Loop flow rates were measured using a rotameter type flow meter and checked via direct measurement. The uncertainty in the mass flow rate measurements was less than 1% [1]. The controlled variables of each test were pressure, mass flow rate, test section inlet temperature, and heat flux. The heat flux can be assumed uniform since it was via resistance heating. Any discrepancy would be due to a variation in the cross-sectional tube area along an axial location. The tubes were manufactured at a very high tolerance, though. Surface thermocouples were mounted far enough from the flow inlet so as to be unaffected by entrance region effects. Throughout this study, the thermodynamic and transport properties of water as functions of temperature and pressure were taken from the latest releases of the International Association of Properties of Water and Steam (IAPWS, formerly called IAPS).

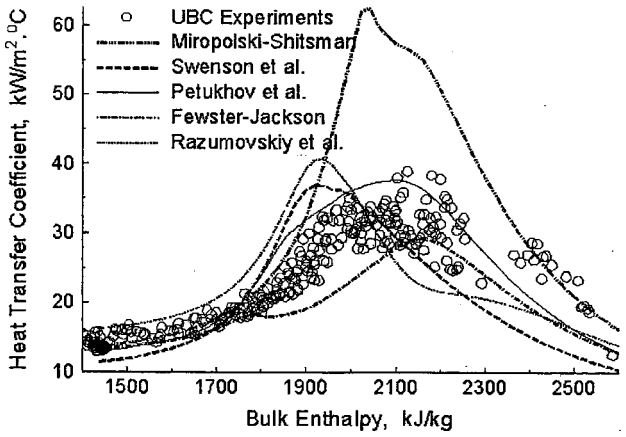

Fig. 2 Comparison of predictions of empirical correlations with UBC experiment $P=25.2$ MPa, $G=964$ kg/m^2 s, $D=6.3$ mm, $q''=307$ kW/m^2

Results and Discussion

As the mass flow rate decreases, the influence of buoyancy increases. To maximize the buoyancy effect, the highest possible heat flux permitted by the experimental apparatus ($\approx$300 kW/m^2), along with a low mass flux ($\approx$340 kg/m^2 s), was investigated. These conditions are denoted as case study A for later reference. The wall temperature distribution versus the water bulk enthalpy (evaluated at the bulk temperature) is shown in Fig. 4. The difference between the top and bottom surface temperature is about 30 K, as the bulk temperature exceeds 150 °C. The difference between the top and bottom surface wall temperature further increases up to about 70 K in the critical region where property variations and buoyancy effects are greatest.

The difference between the wall and the bulk temperatures reduces as a result of the increased heat transfer around the pseudocritical temperature [1]. However, the difference in fluid density at the wall and bulk temperatures is substantial and, hence, buoyancy becomes important. When temperatures were raised well above the critical temperature, the difference in the top and bottom surface temperatures decreased. This is shown in Fig. 5. At high temperatures up to 670 °C, the top and bottom temperatures approach each other. There is a decreasing density variation moving away from the pseudocritical temperature. Hence, the bulk density approaches the value of the density at the wall and buoyancy effects diminish.

It is worth noting the large influence that the temperature difference at the top and bottom surfaces can have on the local heat transfer coefficient. Variations of local heat transfer coefficients with bulk enthalpy, corresponding to Figs. 4 and 5, are shown in Fig. 6. Around the pseudocritical temperature, local heat transfer coefficients at the bottom surface are up to 2.5 times larger than at the top surface. No significant enhancement of heat transfer occurs at the top surface of the test section. This is sometimes referred to as deteriorated heat transfer. It is broad and covers the top surface of the test section. At the bottom surface, however, heat transfer is enhanced. This was also observed in other horizontal test section studies (e.g., [8–10]).

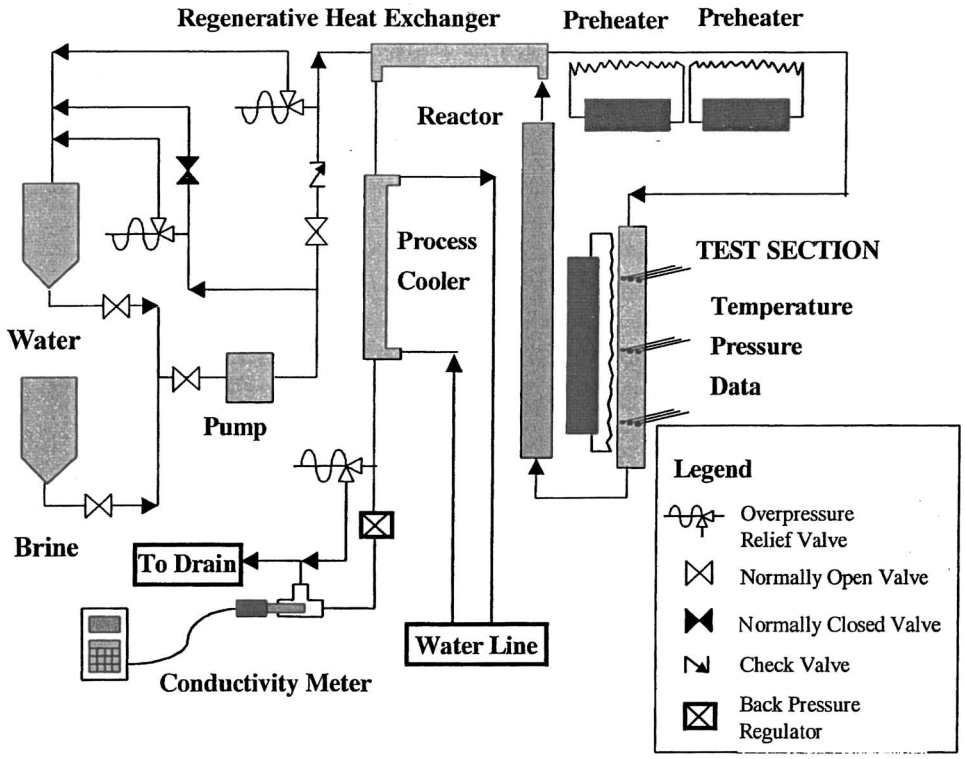

Fig. 3 Schematic of UBC test facility

The data obtained in the current study show that the effect of buoyancy is greater at subcritical bulk fluid temperatures. It is obvious from Fig. 6 that at high temperatures ($T_b \approx 550$ °C or $T_w \approx 700$ °C), the difference between the top and bottom surface temperatures vanishes. This occurs while the temperature difference between wall and bulk may be as high as 140 K. This large temperature difference at subcritical bulk temperatures would generate a significant density gradient. The reason for this is obvious from Fig. 7, where the variations of water density with temperature at $P=24.4$ MPa are shown. The pseudocritical temperature is 383 °C where, at constant pressure, the slope of $\partial\rho/\partial T|_P$ is largest. It is evident that $\partial\rho/\partial T|_P$ is greater at the precritical temperatures than at postcritical temperatures. Larger values of $\partial\rho/\partial T|_P$ imply greater values of Grashof number. The density variations, and hence the Grashof number, approach zero before the bulk temperature reaches 560 °C or even less. The same is true for the effect of buoyancy, which is proportional to the Grashof number. Similar trends exist for other water properties (except specific heat capacity). Therefore, the effect of property variations at precritical temperatures, though not as dramatic as around the pseudocritical point, is important.

In the next two sets of experiments, the mass flux was first increased to 430 kg/m^{2}s and then to 645 kg/m^{2}s, to minimize buoyancy effects. Those results are shown in Table 1 as cases B and C. The heat flux was within 2% of case A. It was found that in both of these cases (B and C), the effect of buoyancy was still considerable.

In general, for increased mass flow, heat transfer improves both at the top and bottom surfaces. Since the importance of buoyancy decreases with increasing flow rate, the ratio of top-to-bottom surface heat transfer coefficients decreased accordingly. The difference between the top and bottom surface temperatures near the

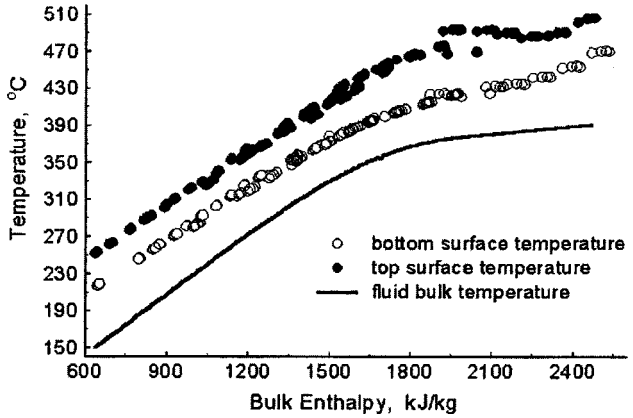

Fig. 4 Wall and bulk temperature variations with bulk enthalpy (precritical and critical regions), $P=24.4$ MPa, $G=340$ kg/m^2 s, $q''=297$ kW/m^2, case A

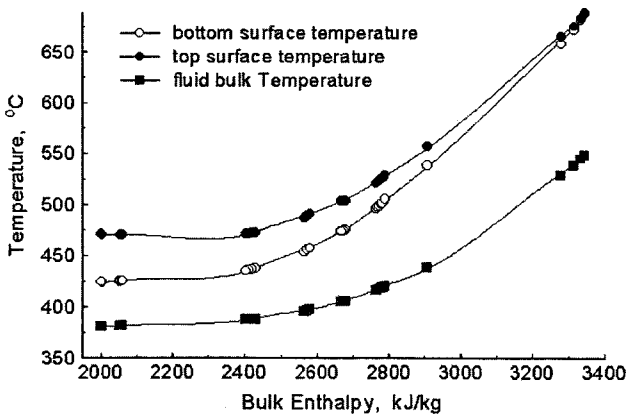

Fig. 5 Wall and bulk temperature variations with bulk enthalpy (critical and postcritical regions), $P=24.4$ MPa, $G=340$ kg/m^2 s, $q''=300$ kW/m^2, case A

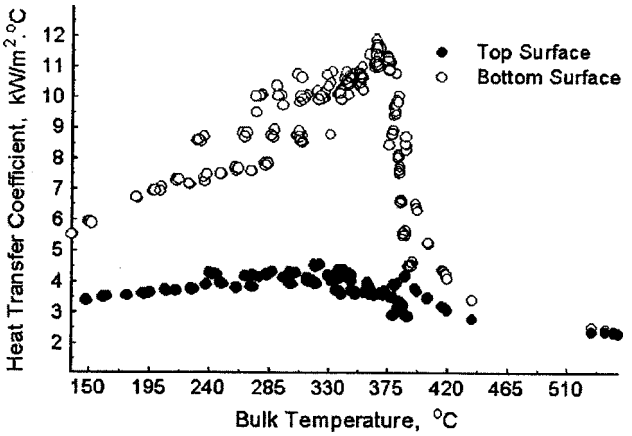

Fig. 6 Differences of heat transfer coefficients at top and bottom surfaces P=24.4 MPa, G=340 kg/m² s, q''=300 kW/m², case A

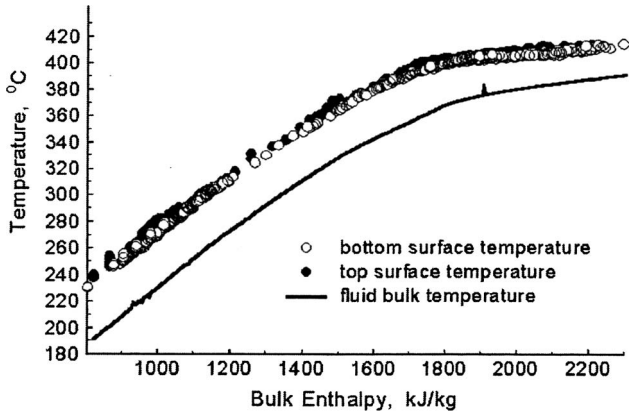

Fig. 8 Wall and bulk temperature variations along the test section P=25.2 MPa, G=964 kg/m² s, q''=307 kW/m², case D

pseudocritical temperature reached about 35 and 12 °C for cases B and C, respectively. The postcritical wall temperature, corresponding to zero temperature difference between the top and bottom surfaces, was reduced from 670 °C in case A to about 570 °C in case B, and to 460 °C in case C. In case C, once the outside wall temperature reached 460 °C, the inside wall and the bulk temperature were 445 and 400 °C, respectively. The density gradient associated with a temperature difference of about 45 K (445–400) from the wall to the center is negligible (Fig. 7).

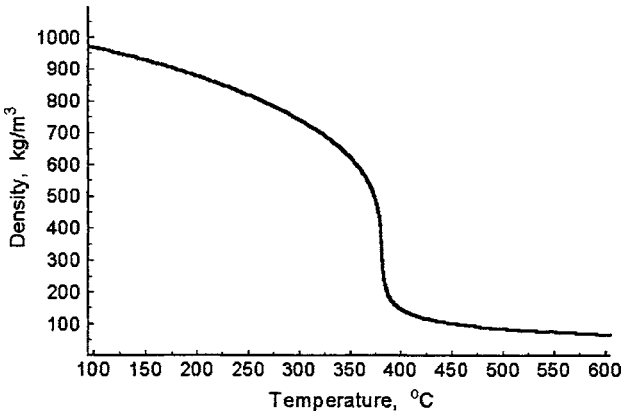

Fig. 7 Variation of water density with temperature at P =24.4 MPa (IAPWS)

Another experiment (case D) was performed where the effect of buoyancy finally vanished. The needed mass flow was around 965 kg/m²s, while the heat flux remained constant. The temperature distribution is given in Fig. 8. As shown, the temperature difference between the top and bottom surfaces is negligible.

For engineering design purposes, it is desirable to know when the effect of buoyancy is negligible and when it is not. The Grashof number represents the ratio of buoyancy forces to viscosity forces. It adequately measures the extent of the effect of buoyancy in a normal flow where property variations are not as severe. For pipe flow, it is defined as

$$\mathrm{Gr} = \frac{g\beta(T_w - T_b)d^3}{\nu^2} \tag{1}$$

where β and ν are the bulk thermal expansion and kinematic viscosity of water, respectively. T_w and T_b are wall and bulk temperatures, g is the acceleration due to gravity, and d is the tube diameter. Properties required to calculate the Grashof number can be found in various ways. For example, viscosity may be esti-

Table 1 Summary results for mixed convection flows. L=3 m, 6.3 mm 1D, and 9.4 mm OD

	mass flux, G kg/m².s	maximum value of $(T_w)_{top}$-$(T_w)_{bot}$, °C	wall T(°C) where Buoyancy diminishes	peak value of heat transfer coefficients at bottom surface, kW/m².°C	bottom surface to top surface ratio of peak values of heat transfer coefficients
CASE A	340	70	670	12	2.75
CASE B	432	35	570	15	2.15
CASE C	646	12	460	24	1.5
CASE D	965	4	405	37	1.2

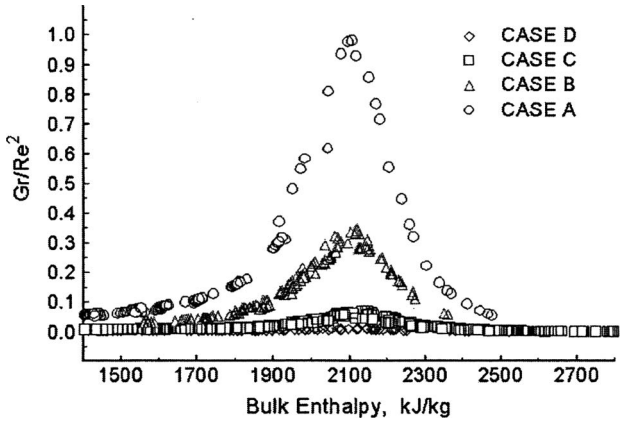

Fig. 9 Variations of Gr/Re^2 along the test section for various mass flows ($q'' \approx 300$ kW/m^2)

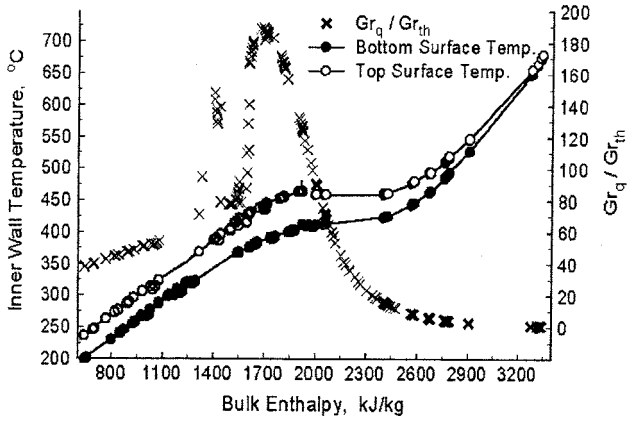

Fig. 10 Variations of Gr_q/Gr_{th} and wall temperature with bulk enthalpy for case A

mated at the bulk, wall, film, or any other temperature reference. This does not make a large difference in a near-constant property flow. Near the critical region, however, it is important to clarify at what temperature properties are determined. The choice of the top or bottom surface for T_w adds another variation.

The term Gr/Re^2 represents the ratio of buoyancy to inertia forces. Hence, as this term increases, buoyancy forces become more dominant. The term is derived from a dimensional analysis of mixed-convection heat transfer. It is usually used to distinguish the buoyancy-free region from conditions where buoyancy is significant. For near-constant property flows, once Gr/Re^2 is the order of unity or higher, buoyancy effects cannot be neglected. Figure 9, however, shows that such a criterion is inadequate for supercritical fluids. The peak value of Gr/Re^2 for case A approaches unity and thus can be considered as a criterion for buoyancy effects. However, for case C, the value is an order of magnitude less ($Gr/Re^2 = 0.1$), yet there still is a noticeable buoyancy effect. Viscosity was evaluated at the bulk temperature. The top surface temperature was used for the wall temperature.

Jackson et al. [11] recommended the use of the quantity $Gr/Re^{2.7}$ instead of Gr/Re^2 to account for the effect of buoyancy near the critical region. They showed that in vertical flows, the difference between upward and downward flows appears once $Gr/Re^{2.7} > 10^{-4}$. When this was tested against the data of the current study, it appeared to be too conservative. Even for case D (negligible buoyancy), the values of $Gr/Re^{2.7}$ were much greater than the proposed limit of 10^{-4}. Hence, the criterion recommended by Jackson et al. for vertical flows may not be applicable to horizontal flows.

Petukhov et al. [12] studied horizontal flows and derived a threshold value for Grashof number, Gr_{th}, below which the buoyancy effect can be neglected. Gr_{th} was defined to be

$$Gr_{th} = 3 \times 10^{-5} Re_b^{2.75} \overline{Pr}^{0.5} [1 + 2.4 Re_b^{-1/8} (\overline{Pr}^{2/3} - 1)] \quad (2)$$

in which

$$\overline{Pr} = \frac{i_w - i_b}{T_w - T_b} \frac{\mu_b}{\kappa_b} \quad (3)$$

Where i and T are the enthalpy and temperature. The subscripts correspond to the bulk (b) and inner tube wall (w) locations. The dynamic viscosity is given by μ_b, and K_b is the thermal conductivity of the fluid. Considering that $q'' \approx \kappa(\partial T/\partial x)$, they used a heat-flux-related definition of Grashof number as

$$Gr_q = \frac{g\overline{\beta} q'' d^4}{\nu_b^2 \kappa_b} \quad (4)$$

where q'' is the heat flux, and at constant pressure we have

$$\overline{\beta} = \frac{1}{\rho_{film}} \frac{\rho_b - \rho_w}{T_w - T_b} \quad (5)$$

The density ρ is evaluated at the bulk, wall, and film temperatures. Thus, in order to have a flow dominated by forced convection, it requires that $Gr_q < Gr_{th}$.

The criterion of Petukhov et al., given by Eq. (2), was experimentally examined by Adebiyi and Hall [10]. In their experiments with horizontal flow of supercritical carbon dioxide, the effect of natural convection was large. The value of Gr_q was much greater than Gr_{th} for all cases. Thus, Petukhov's criterion was not violated. However, it could not be considered an accurate test of the criterion, since Grashof numbers in all cases were well above the threshold value.

Petukhov and Polyakov [13] considered a larger number of experiments performed by different investigators and reported variations of Gr_q/Gr_{th} along the test section for each case. The larger the temperature difference between top and bottom surfaces, the greater was the order of magnitude of Gr_q/Gr_{th}. For example, for a 200 K temperature difference between top and bottom surfaces of the tube, Gr_q/Gr_{th} increased up to 1300. The criterion they suggested, compared to others, is a significant improvement.

The present-study data spans various flow cases, from flows with significant buoyancy effects (Case A) to flows with negligible buoyancy effects (Case D). It provides a unique opportunity to test the criterion of Petukhov et al. The value of Gr_q/Gr_{th} and wall temperature versus bulk enthalpy is shown in Fig. 10 for Case A. As expected, the peak values of Gr_q/Gr_{th} (as large as 200) occur in the pseudocritical region, where the influence of buoyancy is largest. The difference in buoyancy behavior at pre- and post-pseudo-critical regions, as discussed earlier, is also reflected by the values of Gr_q/Gr_{th}. Once the effect of buoyancy vanishes, Gr_q/Gr_{th} drops to unity, which agrees well with the criterion of Petukhov et al. [12].

In Fig. 10, Gr_q/Gr_{th} varies between 1 and 200. In order to obtain a better assessment of the criterion, a closer look at values near unity would be required. This can be met by considering the cases with lesser buoyancy effects. The results for cases C and D are shown in Fig. 11. For Case D, it was shown earlier in Fig. 8 that the effect of buoyancy was minor along most of the test section. There was a maximum of 4 K difference between top and bottom surfaces of the tube around the pseudocritical point. It was noted that even such a small effect is detected by the criterion of Petukhov et al. That corresponds to a peak of $Gr_q/Gr_{th} \approx 5$ in Fig. 11. Accordingly, for the bulk enthalpies greater than 2200 kJ/kg, where no temperature difference between top and bottom surfaces was detected, Gr_q/Gr_{th} approached unity. For case C, which had mild buoyancy effects, the criteria predicted it well. Hence, the

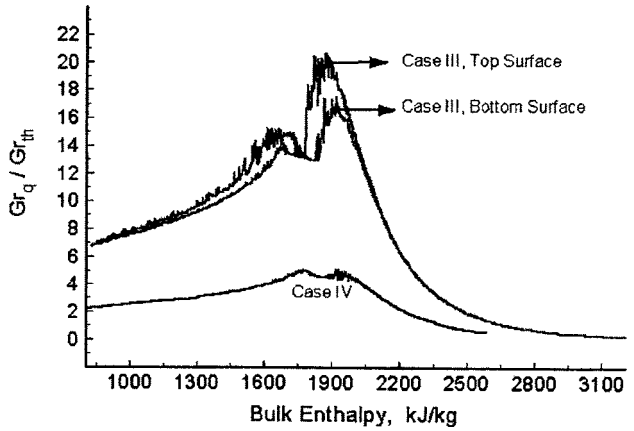

Fig. 11 Variations of Gr_q/Gr_{th} with bulk enthalpy for cases C and D

results of this study verify the Petukhov criterion with very good accuracy. Such an assessment was not done before, due to a lack of data on horizontal flows.

To estimate Gr_q and Gr_{th}, one needs to use a chosen wall temperature, such as the top or bottom. When buoyancy is negligible, the top and bottom wall temperatures are the same. Figure 11 shows the result of evaluating the criterion using both top and bottom surface temperatures for case C. The choice of top or bottom surface temperature does not substantially affect the results. In fact, the magnitude of Gr_q and Gr_{th} is considerably affected by variations of T_w, but the ratio Gr_q/Gr_{th} remains almost the same.

When buoyancy effects are appreciable, the temperature difference between the top and bottom surfaces of a horizontal test section should be evaluated by the method proposed by Petukhov and Polyakov [13]. They employed a particular pair of coordinates that correlate the temperature difference between the top and bottom surfaces with other flow parameters. Their technique was used to examine the data obtained in the current study. It was found [1], however, that their predictions, only for cases with large buoyancy effects (e.g., case A), do not agree well with our data. It is, however, the best method available for lesser buoyancy effects.

Conclusions

One of the main factors that increase the complexity of heat transfer to supercritical fluids is the large effect of buoyancy, especially near the critical region. Considerable disagreement has been shown between the predictions offered by available empirical correlations. Neglecting buoyancy is a primary reason for such discrepancies. It is crucial to know when buoyancy becomes important. The following observations were made:

- Buoyancy effects are particularly important in horizontal flows, where flow asymmetry leads to a nonuniform local temperature distribution around the tube periphery.
- The criterion developed for buoyancy-free regions in a near-constant property flow (e.g., water at low pressure) is not adequate for predicting supercritical fluid flows.
- Criteria previously developed for predicting buoyancy affected/free regions during vertical flows do not apply to horizontal flows.
- The relationship suggested by Petukhov et al. [12] was found to be very accurate in distinguishing between buoyancy-affected and buoyancy-free flows. Their criterion was not critically tested before this study.

References

[1] Bazargan, M., and Fraser, D. W., 2000, "Forced Convection Heat Transfer to Turbulent Flow of Water at Supercritical Pressure," *2000 National Heat Transfer Conf.*, Pittsburgh, Aug. 20-22.

[2] Miropolski, Z. L., and Shitsman, M. E., 1957, "Heat Transfer to Water and Steam at Variable Specific Heat (In Near-Critical Region)," Sov. Phys. Tech. Phys., **27**(10) pp. 2359–2372 English translation 2196-2208.

[3] Petukhov, B. S., Kransnoshchekov, E. A., and Protopopov, V. S. 1962, "An Investigation of Heat Transfer to Fluids Flowing in Pipes Under Supercritical Conditions", *Proc. of 1961-62 Heat Transfer Conf. on Int. Development in Heat Transfer*, Aug. 28–Sept. 1, 1961, University of Colorado, Boulder, Jan. 8–12.

[4] Swenson, H. S., Carver, J. R., and Kakarla, C. R., 1965, "Heat Transfer to Supercritical Water in Smooth-Bore Tubes," ASME J. Heat Transfer pp. 477–484.

[5] Jackson, J. D., and Fewster, J., 1975, AERE-R8158, Harwell.

[6] Razumovskiy, V. G., Ornatskiy, A. P., and Mayevskiy, Y. M., 1990, "Local Heat Transfer and Hydraulic Behavior in Turbulent Channel Flow of Water at Supercritical Pressure," Heat Transfer-Sov. Res. **22**(1) pp. 91–102.

[7] Ghajar, A. J., and Asadi, A., 1986, "Improved Forced Convective Heat Transfer Correlations for Liquids in the Near-Critical Region," AIAA J. **24**(12), pp. 2030–2037.

[8] Belyakov, I. I., Krasyakova, L. Y., Zhukovskii, A. V., and Fefelova, N. D., 1971, "Heat Transfer In Vertical Risers and Horizontal Tubes at Supercritical Pressure," Teploenergetika (Thermal Engineering) **18**(11) pp. 39–43 (55–59).

[9] Yamagata, K., Nishikawa, K., Hasegawa, S., Fujii, T., and Yoshida, S., 1972, "Forced Convective Heat Transfer to Supercritical Water Flowing in Tubes", Int. J. Heat Mass Transfer **15**, pp. 2575–2593.

[10] Adebiyi, G. A., and Hall, W. B., 1976, "Experimental Investigation of Heat Transfer to Supercritical Pressure Carbon Dioxide in a Horizontal Pipe," Int. J. Heat Mass Transfer **19**, pp. 715–720.

[11] Jackson, J. D., Hall, W. B., Fewster, J., Watson, A., and Watts, M. J., 1975, "Heat Transfer to Supercritical Pressure Fluids", UKAEA, AERER 8158, Design Report 34.

[12] Petukhov, B. S., Polyakof, A. F., Kuleshov, V. A., and Sheckter, Y. L., 1974, "Turbulent Flow and Heat Transfer in Horizontal Tubes With Substantial Influence of Thermo-gravitational Forces," *Proc. of Fifth Int. Heat Transfer Conference*, Tokyo, Sep. 3–7.

[13] Petukhov, B. S., and Polyakov, A. F., 1986, "Heat Transfer in Turbulent Mixed Convection," Translated by R. Hainsworth and G. Rybchinskaya, edited by Launder, B. E., Hemisphere Publishing Corporation 1988, orginally published as Teploobmen pri smeshannoy turbulentnoy konvektsii, by Nauka, Moscow.

Modification of Planck Blackbody Emissive Power and Intensity in Particulate Media Due to Multiple and Dependent Scattering

Ravi Prasher[1]
Sr. Thermal Engineer
e-mail: ravi.s.prasher@intel.com
Ch5-157, Intel Corporation, 5000 W. Chandler Blvd., Chandler, Arizona 85226

The dispersion relation for an electromagnetic wave is obtained in particulate media using effective field approximation (EFA) and quasi-crystalline approximation (QCA). Due to multiple and dependent scattering the density of states, phase velocity and group velocity of photons are modified. Modification of these parameters modifies the Planck blackbody equilibrium radiation intensity and emissive power. Results show that EFA can accurately capture the dependence of density of states, phase velocity, and the group velocity on volume fraction of scatterers whereas QCA can capture the dependence of effective attenuation as well as density of states, phase velocity, and the group velocity. Comparisons of the temperature, heat flux, and effective attenuation are made between EFA, QCA, and work done by C. L. Tien and co-workers. Results show that heat flux and temperature predictions made by models in the literature for multiple and dependent scattering are not correct as these models do not take the modification of the equilibrium intensity into account. Finally we introduce a new model called dependent effective field approximation (DEFA) which accurately captures the effect of volume fraction on the equilibrium intensity and effective attenuation. [DOI: 10.1115/1.1928912]

Introduction

Thermal radiation is the dominant mode of energy transfer in many modern engineering technologies. Many systems where radiation is the dominant source of energy transport contain particulates that actively participate in the radiative transfer process. Some examples that involve highly concentrated small particles are fluidized and packed beds combustors, packed bed catalytic reactors, microsphere insulation, combustors with deposited soot on the walls, and furnaces laden with agglomerated particles. In these systems the scattering and absorption of thermal radiation by particles play an important role in overall energy transfer, and its understanding is critical to the prediction and evaluation of system performance.

The equation of radiative transport (ERT) is used [1] to predict the temperature and heat flux in particulate media. For a one-dimensional system ERT is given as

$$\mu\frac{\partial I_\omega}{\partial z} = K_a(I^0_\omega - I_\omega) - K_p I_\omega + \frac{K_p}{4\pi}\int_{4\pi}\Phi(\Omega_i \rightarrow \Omega) I_\omega(\Omega_i) d\Omega_i \tag{1}$$

where μ is the direction cosine, I is the intensity, I^0 is the equilibrium intensity, ω is the frequency, K_a and K_p are the absorption and scattering coefficients, and Φ is the phase function for the scattered wave from solid angle Ω_i to Ω. ω in the subscript indicates that I is a function of ω. Multiple scattering of photon takes place in particulate media. Effect of multiple scattering of photons is included in the ERT via the in-scattering term. Dependent scattering and absorption might become important if the volume fraction of the particles is high. Dependent scattering becomes important if the distance between the scatterers is of the order of the wavelength [2–7]. Various researchers have worked on the effect of dependent scattering on the scattering cross section, transport cross section, and phase function [2–7]. For radiative heat transfer in the dependent scattering regime pioneering research was done by Tien and co-workers [2–5]. All the work done by Tien and co-workers ignored one important aspect for dense particulate media, i.e., the effect of multiple scattering on the phase and group velocity and the density states of photons. Multiple scattering changes the dispersion relation (relation between the wave vector and the frequency) in particulate media. Wave literature is full of work done on the effect of multiple scattering on the effective dispersion relation in particulate media [8–14]. It is to be remembered that dependent scattering is important only when the distance between the particles is of the order of wavelength, i.e., it depends on the closeness of the particles whereas multiple scattering is present just because there are multiple number of particles. The reason for not including the effect of multiple scattering on the dispersion relation is because most of the experimental works done for dense particulate system for thermal radiation purposes have only dealt with the attenuation of optical radiation not of thermal radiation [2–4,7,15–20]. For optical radiation the ERT modifies to

$$\mu\frac{\partial I_\omega}{\partial z} = -K_a I_\omega - K_p I_\omega + \frac{K_p}{4\pi}\int_{4\pi}\Phi(\Omega_i \rightarrow \Omega) I_\omega(\Omega_i) d\Omega_i \tag{2}$$

There is no blackbody intensity term in the ERT for optical radiation whereas for thermal radiation the ERT contains the Planck blackbody intensity term I^0_ω which decides the temperature and heat flux. I^0_ω depends on the density of states and the group velocity of photons. I^0_ω is given as [20]

$$I^0(T,\omega) = \frac{1}{4\pi}\sum_2 v_g \frac{1}{\exp(\hbar\omega/k_b T) - 1}\hbar\omega D(\omega) \tag{3}$$

where v_g is the group velocity of photons, $\hbar$ = Planck constant/2π, k_b is the Boltzmann constant, T is the temperature, and $D(\omega)$ is the

[1]Adjunct Professor, Department of Mechanical and Aerospace Engineering, Arizona State University

Contributed by the Heat Transfer Division for publication in the JOURNAL OF HEAT TRANSFER. Manuscript received: July 6, 2004; final manuscript received: March 1, 2005. Review conducted by: Karen Thole.

density of states. A2 in the summation indicates two polarizations of the EM wave.

Due to multiple scattering v_g, $D(\omega)$ gets modified, which will affect I^0. Since for optical radiation the velocity and the $D(\omega)$ do not enter into the picture, the modification of the dispersion relation due to multiple scattering is not important and one only needs to modify the scattering cross section due to dependent scattering effects.

In this paper the dispersion relation for photons will be systematically derived based on Foldy's [9] effective field approximation (EFA). Comparison is made between EFA and quasi-crystalline approximation (QCA) due to Lax [9] in the Rayleigh scattering regime. It is shown that EFA is good at capturing the effect of multiple scattering on v_g, phase velocity (v_p), and $D(\omega)$, but cannot account for the effect of dependent scattering on the scattering cross section. QCA is good at capturing the effect of multiple scattering on v_g, v_p, and $D(\omega)$ and the effect of dependent scattering on the scattering cross section, however QCA is very complicated except for the case of Rayleigh scattering. Temperature and heat flux predictions using EFA, QCA, and the approach of Tien and co-workers are made. Finally a new model which combines the simple EFA for the effect of multiple scattering on v_g, v_p, and $D(\omega)$ and Tien's approach on the effect of dependent scattering on scattering cross section is proposed. This model is called dependent EFA (DEFA).

All the formulations have been developed assuming that both the particles and the host medium are non-absorbing; however, for thermal emission to occur either the particle or the host medium have to have some absorption. In this paper, the assumption that has been made is that the refractive index of the particle has an imaginary component, but the imaginary component is very small. This basically means that the particle refractive index (m_p) is given as $m_p = m_2 + im_2'$ where m_2 is the real part of the refractive index and m_2' is the imaginary part of the refractive index; however, for the calculation of the scattering cross section, velocity, and the density of states of the photons it is assumed that $m_2' \rightarrow 0$. With this assumption the scattering cross sections, velocity, and the density of states are calculated as if m_p is real. In the calculation of the optical thickness again since it is assumed that $m_2' \rightarrow 0$, the absorption cross section is much smaller compared to the scattering cross section. While this assumption simplifies the analysis a great deal and lets us focus on the physics of the problem, it ensures that emission is present in the system because m_2' is tending to zero (it is not absolutely zero). The case with significant absorption will be considered in a future report. The physics and equations discussed in this paper provide the path for the inclusion of significant absorption in dense radiating systems.

1 Effective Field Approximation

The effective wave vector in particulate media is given as [8]

$$k^2 = k_1^2 + 4\pi n f(0) \tag{4}$$

where k is the effective wave vector of the particulate media, k_1 is the wave vector of the medium in which scatterers are present, $f(0)$ is the forward scattering amplitude of the scattered electromagnetic (EM) wave, and n is the number of scatterers per unit volume. Note that the medium is denoted as 1 and the scatterers are denoted as 2 in the rest of the paper. This relation is obtained by adding and averaging the contributions of the scatterered wave from all the scatterers on the effective field in the particulate system. For details readers are advised to read the review paper by Lax [9]. The components of the scattered wave (electric field) for spherical particles are given by [21]

$$E_{S\theta} = \frac{e^{ik_1 r}}{-ik_1 r}\cos(\phi) S_2(\theta) \tag{5}$$

$$E_{S\phi} = -\frac{e^{ik_1 r}}{-ik_1 r}\sin(\phi) S_1(\theta) \tag{6}$$

where S denotes the scattered radiation, r is the distance from the scatterer, and θ and ϕ are the polar and azimuthal scattering angles, respectively. S_1 and S_2 are the scattering functions given in Ref. [21]. The following relations can be obtained from Eqs. (5) and (6)

$$E_{S\theta}(\theta = 0, \phi = 0) = \frac{e^{ik_1 r}}{-ik_1 r} S_2(0) \tag{7}$$

$$E_{S\phi}(\theta = 0, \phi = 0) = 0 \tag{8}$$

$$f(0) = \frac{S_2(0)}{-ik_1} = \frac{i}{k_1} S_2(0) \tag{9}$$

where [21]

$$S_2(0) = \frac{1}{2}\sum_{n=1}^{\infty}(2n+1)(a_n + b_n) \tag{10}$$

where a_n and b_n are the Mie coefficients. Substitution of Eq. (9) in Eq. (4) leads to

$$\frac{k^2}{k_1^2} = 1 + \frac{2\pi n i}{k_1^3}\sum_{n=1}^{\infty}(2n+1)(a_n + b_n) \tag{11}$$

a_n and b_n are complex numbers. *Note n is used for number of scatterers per unit volume as well as the index in the Mie scattering coefficients and summations*. They can be separated into real and imaginary parts by writing

$$a_n + b_n = w_n + iy_n \tag{12}$$

Optical theorem [21] gives

$$C_{ext} = \frac{4\pi}{k_1^2}\,\mathrm{Re}\{S(0)\} = \frac{2\pi}{k_1^2}\sum_n (2n+1) w_n \tag{13}$$

where C_{ext} is the extinctions cross section. Therefore Eq. (11) can be written as

$$\frac{k^2}{k_1^2} = 1 - \frac{2\pi n}{k_1^3}\sum_{n=1}^{\infty}(2n+1) y_n + \frac{in}{k_1} C_{ext} \tag{14}$$

So far we have not assumed anything regarding absorption in the particle or the medium, i.e., all the derivations so far are equally applicable for an absorbing system. However, in the rest of the paper we will invoke the assumption that the imaginary part of the refractive index of the particle (m_2') tends to zero, i.e., $m_2' \rightarrow 0$ as mentioned before. But it is to be noted that absorption can also become dependent [5,6] and this can also affect the dispersion relation. Since we are assuming that $m_2' \rightarrow 0$, $C_{ext} \approx C_{sca}$, where C_{sca} is the scattering cross section. This leads to

$$\frac{k^2}{k_1^2} = 1 - \frac{2\pi n}{k_1^3}\sum_{n=1}^{\infty}(2n+1) y_n + \frac{in}{k_1} C_{sca} \tag{15}$$

k can be separated into real and imaginary parts as

$$k = k_R + ik_I \tag{16}$$

The imaginary part of k is related to the effective attenuation in the system whereas the real part of k is related to the modification of v_g, v_p, and $D(\omega)$ [10–14]. The effective attenuation (α) due to scattering is given as [13,14,22]

$$\alpha = 2k_I \tag{17}$$

From Eq. (15) it can be shown that in the independent scattering regime $\alpha = nC_{sca}$.

For very small n, by making a binomial expansion Eq. (15) can be written as

$$\frac{k}{k_1} = \left(1 - \frac{2\pi n}{k_1^3}\sum_{n=1}^{\infty}(2n+1)y_n + \frac{in}{k_1}C_{sca}\right)^{1/2}$$

$$= 1 - \frac{\pi n}{k_1^3}\sum_{n=1}^{\infty}(2n+1)y_n + \frac{in}{2k_1}C_{sca} \tag{18}$$

Since $\alpha = 2k_I = nC_{sca}$ we get the independent scattering result. However, this also leads to

$$\frac{k_R}{k_1} = 1 - \frac{\pi n}{k_1^3}\sum_{n=1}^{\infty}(2n+1)y_n \tag{19}$$

i.e., the real part of the effective wave vector also gets modified even in the independent scattering regime. This is solely the effect of the multiple scattering. This leads to the following dispersion relation

$$\omega = v_p(\omega)k \tag{20}$$

where v_p is a function of the frequency. Equation (19) gives

$$v_p = \frac{v_1}{1 - (3\phi/4x_1^3)\sum_n (2n+1)y_n} \tag{21}$$

where v_1 is the speed of the EM wave in medium 1. $n = 3\phi/4\pi a^3$ has been used in Eq. (21) where ϕ is the volume fraction of the scatterer, a is the radius of the scatterer, and $x_1 = k_1 a$ is the size parameter. This also modifies the effective refractive index (m_{eff}) of the medium which is given as

$$\frac{m_{eff}}{m_1} = \frac{v_1}{v_p} = 1 - \frac{3\phi}{4x_1^3}\sum_n (2n+1)y_n \tag{22}$$

and v_g is given as

$$v_g = \frac{v_p}{1 - (\omega/v_p)(dv_p/d\omega)} \tag{23}$$

For the general case Eq. (15) can written as

$$\frac{k_R + ik_I}{k_1} = \sqrt{A + iB} \tag{24}$$

where

$$A = 1 - \frac{3}{2}\frac{\phi}{x_1^3}\sum_{n=1}^{\infty}(2n+1)y_n \tag{25}$$

and

$$B = \frac{n}{k_1}C_{sca} \tag{26}$$

It can be easily shown [23] that

$$k_R = k_1\sqrt{1/2(R+A)} \tag{27}$$

$$k_I = k_1\sqrt{1/2(R-A)} \tag{28}$$

where

$$R = \sqrt{A^2 + B^2} \tag{29}$$

Therefore

$$\frac{k_I}{k_R} = \sqrt{\frac{R-A}{R+A}} \tag{30}$$

We now make the assumption that $k_R \gg k_I$, which will simplify the algebra a lot. It will be shown later that this is a very good assumption. With this assumption Eq. (15) reduces to

$$\frac{k_R^2 + 2ik_Rk_I}{k_1^2} = 1 - \frac{2\pi n}{k_1^3}\sum_{n=1}^{\infty}(2n+1)y_n + \frac{in}{k_1}C_{sca} \tag{31}$$

This leads to

$$k_R = k_1\sqrt{1 - \frac{2\pi n}{k_1^3}\sum_{n=1}^{\infty}(2n+1)y_n} \tag{32}$$

or

$$v_p = \frac{v_1}{\sqrt{1 - (2\pi n/k_1^3)\sum_{n=1}^{\infty}(2n+1)y_n}}$$

$$= \frac{v_1}{\sqrt{1 - \frac{3}{2}(\phi/x_1^3)\sum_{n=1}^{\infty}(2n+1)y_n}} \tag{33}$$

and

$$\frac{m_{eff}}{m_1} = \sqrt{1 - \frac{3}{2}\frac{\phi}{x_1^3}\sum_{n=1}^{\infty}(2n+1)y_n} \tag{34}$$

α is given as

$$\alpha = 2k_I = \frac{nC_{sca}}{\sqrt{1 - (2\pi n/k_1^3)\sum_{n=1}^{\infty}(2n+1)y_n}}$$

$$= \frac{nC_{sca}}{\sqrt{1 - \frac{3}{2}(\phi/x_1^3)\sum_{n=1}^{\infty}(2n+1)y_n}} \tag{35}$$

So far we have assumed nothing regarding the size of scatterer and the results are completely general. The Rayleigh scattering regime is now explored in detail as dependent and multiple scattering effects are very important in the Rayleigh regime.

1.1 EFA in Rayleigh Scattering Limit. In the Rayleigh limit the imaginary part of the Mie coefficient can be shown [21] to be

$$y_1 = -\frac{2x_1^3}{3}u \tag{36}$$

where only the terms of the order of x_1^3 have been retained and

$$u = \frac{m^2 - 1}{m^2 + 2} \tag{37}$$

where $m = m_2/m_1$. C_{csa} is given as

$$C_{sca} = \frac{8\pi a^2}{3}x_1^4u^2 \tag{38}$$

In the independent scattering case α is given as

$$\alpha = nC_{sca} = \frac{2u^2x_1^4}{a}\phi \tag{39}$$

For computations and comparisons between different approximations a nondimensional attenuation coefficient (β) is defined in this paper which is given as

$$\beta = \frac{\alpha}{(2u^2x_1^4/a)} \tag{40}$$

Therefore for the independent scattering

$$\beta = \phi \tag{41}$$

Substitution of y_1 and C_{sca} in Eqs. (25) and (26) gives

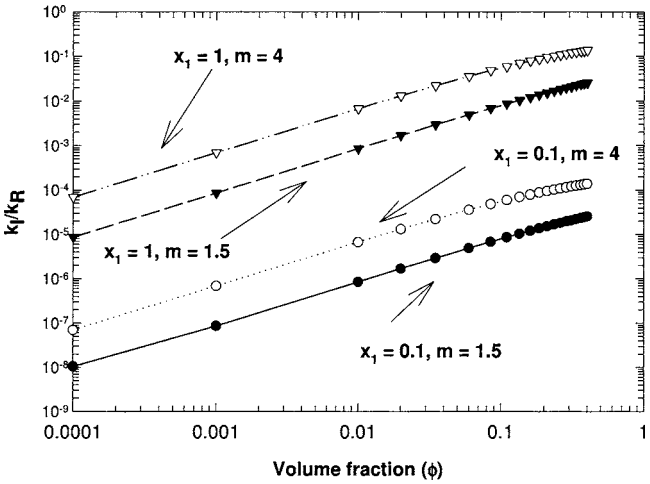

Fig. 1 Ratio of the imaginary and the real part of the effective wave vector in the particulate media

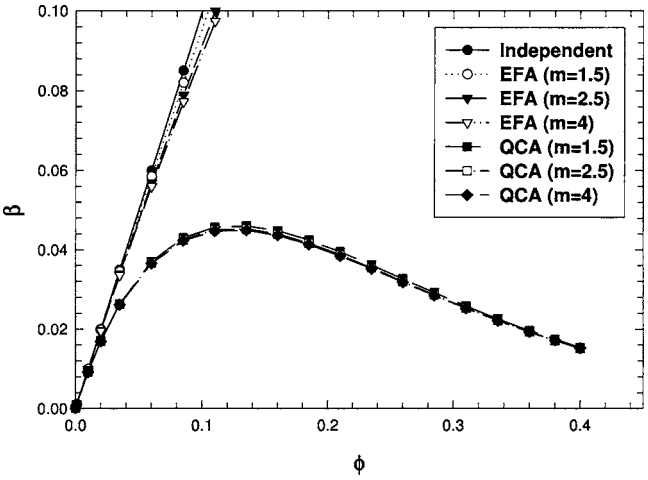

Fig. 2 Comparison of the dimensionless effective attenuation

$$A = 1 + 3\phi u \tag{42}$$

$$B = 2u^2 x_1^3 \phi \tag{43}$$

Figure 1 shows the ratio of k_I and k_R calculated from Eq. (30) for extreme cases of scattering. Figure 1 shows that even assuming x_1 as large as 1 for the Rayleigh regime, k_I is very small compared to k_R. Therefore assuming $k_R \gg k_I$ is a very good assumption. Substitution of y_1 and C_{sca} in Eqs. (33)–(35) for the EFA give

$$v_p = \frac{v_1}{\sqrt{1 + 3\phi u}} \tag{44}$$

$$\frac{m_{eff}}{m_1} = \sqrt{1 + 3\phi u} \tag{45}$$

$$\beta = \frac{\phi}{\sqrt{1 + 3\phi u}} \tag{46}$$

Therefore in the Rayleigh case v_p is independent of ω and hence v_g is the same as v_p.

2 Quasi-Crystalline Approximation (QCA)

Lax [8] modified Foldy's equation (Eq. (4)) to account for dependent scattering, leading to

$$k^2 = k_1^2 + 4\pi n c f(0) \tag{47}$$

where the correction factor c is defined by c=effective field/coherent field.

This relation is called quasi-crystalline approximation as it takes the effect of dependent scattering at high volume fraction of scatterer [8,9]. QCA has been used extensively in literature [9–14]. In applying QCA the pair distribution function of particle positions must be specified [13,14]. Use of a pair distribution function to describe the effect of dependent scattering on the scattering cross section is very standard and will not be discussed. Various authors including Tien and coauthors [1–7,13–19] have discussed various pair distribution functions. The most common and most successful pair distribution function for capturing the effects-dependent scattering is the Percus-Yevick (P-Y) equation [1–7,10–19]. Tsang and Kong [13,14] have derived the dispersion relation for EM waves using P-Y equation. The dispersion relation using the P-Y equation and QCA is very complex and will not be presented in this paper; however, for the Rayleigh scattering case Tsang and Kong [13,14] showed that the dispersion relation can be simplified a great deal and is given as

$$\frac{k^2}{k_1^2} = 1 + \frac{3\phi u}{1 - \phi y} + i\frac{3\phi u}{1 - \phi u}\frac{2k_1^3 a^3 u}{3(1 - \phi u)}\frac{(1 - \phi)^4}{(1 + 2\phi)^2} \tag{48}$$

Assuming $k_R \gg k_I$, Eq. (48) gives

$$v_p = \frac{v_1}{\sqrt{1 + 3\phi u/(1 - \phi u)}} \tag{49}$$

$$\frac{m_{eff}}{m_1} = \sqrt{1 + \frac{3\phi u}{1 - \phi u}} \tag{50}$$

$$\beta = \phi\frac{(1 - \phi)^4}{(1 + 2\phi)^2} \times \frac{1}{(1 - \phi u)\sqrt{1 + 3\phi u/(1 - \phi u)}} \tag{51}$$

The P-Y distribution should ideally be used only up to a volume fraction of 0.4 [13,14], however it is interesting to note that the P-Y distribution function leads to correct values in the limiting cases of ϕ=0 and ϕ=1 although ϕ=1 is not possible for spherical particles. Putting ϕ=1 in Eqs. (50) and (51) lead to m_{eff}=m_2 and β=0, i.e., if the medium is completely replaced by the scatterer, then attenuation goes to zero and the effective refractive index is the same as the refractive index of medium 2. However, in this paper a maximum value of ϕ=0.4 is taken as per the recommendation from Tsang and Kong [13,14].

Figure 2 shows the comparison of β calculated from various approximations. It shows that EFA clearly fails in capturing the right trend of β and EFA is very close to an independent scattering approximation. Figure 2 show that the EFA matches QCA only at very low volume fraction.

Note that Tien and co-workers [2–4] have used the P-Y distribution function to capture the effect of dependent scattering. Tien and co-workers' work will be referred simply as Tien's work in this paper. Tien's formulations lead to the following results

$$\frac{m_{eff}}{m_1} = 1 \tag{52}$$

$$\beta = \phi\frac{(1 - \phi)^4}{(1 + 2\phi)^2} \tag{53}$$

m_{eff}/m_1=1 in Tien's work because Tien did not consider the effects of multiple and dependent scattering on the dispersion relation of the EM wave. It also to be noted that β_{Tien} is different than β_{QCA} although both use the P-Y distribution function. The ratio of β_{Tien} and β_{QCA} is given as

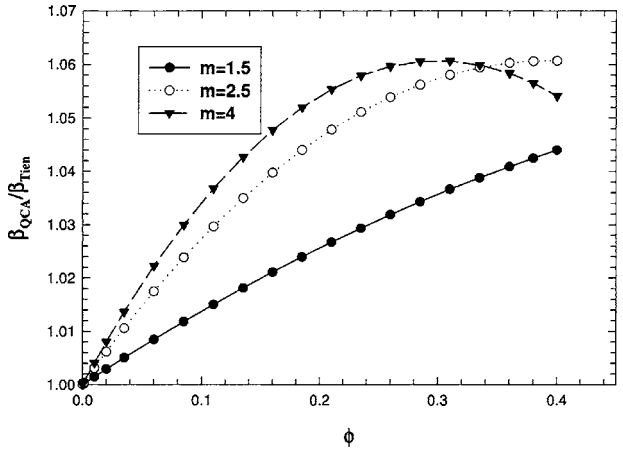

Fig. 3 Comparison of the dimensionless effective attenuation obtained from Tien's approach and QCA

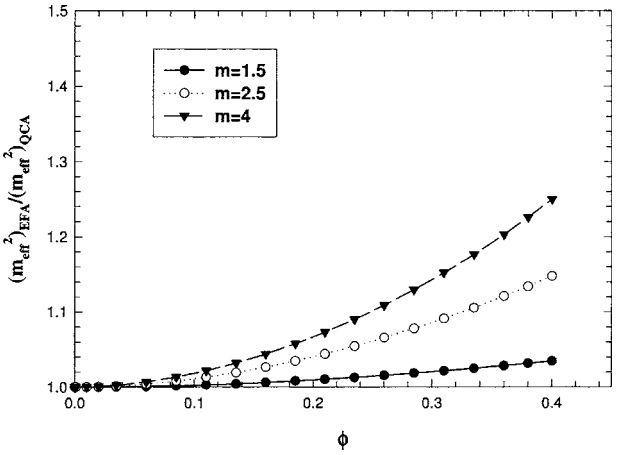

Fig. 4 Comparison between the square of effective refractive index obtained from QCA and EFA

$$\frac{\beta_{Tien}}{\beta_{QCA}} = (1-\phi u)\sqrt{1+\frac{3\phi u}{1-\phi u}} \tag{54}$$

The reason for this discrepancy is that Tien used the results of Twersky [24] and Twersky made the assumption that $m_2/m_1 \approx 1$. This assumption gives $u \approx 0$ from Eq. (37). In this limit Eq. (54) shows that $\beta_{Tien} = \beta_{QCA}$. Figure 3 shows the comparison between β_{QCA} and β_{Tien}. Figure 3 shows that $\beta_{Tien}/\beta_{QCA} \approx 1$ for different values of m. Therefore Tien's method is as good as detailed QCA for calculating β.

3 Modification of Planck Blackbody Intensity and Emissive Power

Previous sections have shown that v_p, v_g, and $D(\omega)$ get modified due to multiple and dependent scattering. In this section Planck blackbody intensity is derived for EFA and QCA in the Rayleigh scattering regime. $D(\omega)$ is given by [25]

$$D(\omega) = \frac{k^2}{2\pi^2}\frac{dk}{d\omega} = \frac{k^2}{2\pi^2 v_g} \tag{55}$$

Substituting $D(\omega)$ for the particulate media in Eq. (3) leads to

$$I^0(T,\omega) = \frac{\hbar\omega k_R^2}{4\pi^3}\frac{1}{\exp(\hbar\omega/k_bT)-1} \tag{56}$$

where k has been replaced by k_R. For EFA using Eq. (32)

$$I^0(T,\omega) = \frac{\hbar\omega k_1^2\left(1-(2\pi n/k_1^3)\sum_{n=1}^{\infty}(2n+1)y_n\right)}{4\pi^3}\frac{1}{\exp(\hbar\omega/k_bT)-1} \tag{57}$$

$$I_b(T) = \int_0^{\infty}\frac{\hbar\omega^3\left(1-(2\pi n/k_1^3)\sum_{n=1}^{\infty}(2n+1)y_n\right)}{4\pi^3 v_1^2}\frac{1}{\exp(\hbar\omega/k_bT)-1}d\omega \tag{58}$$

For the Rayleigh scattering case, since v_p and v_g are the same and are independent of frequency, it can be easily shown that

$$I^0(T) = m_{eff}^2\frac{\sigma T^4}{\pi} \tag{59}$$

where σ=Stefan-Boltzmann constant. Assuming $m_1=1$, for the EFA

$$I^0(T) = (1+3\phi u)\frac{\sigma T^4}{\pi} \tag{60}$$

and for QCA

$$I^0(T) = \left(1+\frac{3\phi u}{1-\phi u}\right)\frac{\sigma T^4}{\pi} \tag{61}$$

The emissive power (Eb) is given by $E_b = \pi I^0(T)$. For Tien's model for $m_1=1$

$$I^0(T) = \frac{\sigma T^4}{\pi} \tag{62}$$

The results on the modification of Planck blackbody intensity are not surprising. Li [25] and Cornelius and Dowling [26] have demonstrated the modification of Planck blackbody energy density for periodic photonic crystals. In their work the photonic crystal was a periodic composite and they calculated the energy density of radiation rather than the intensity. Therefore they only considered the effect of the modification of $D(\omega)$ and not the modification of v_g and v_p. In this paper we have calculated the intensity for a random composite (particulate media) and the results can also be used for the calculation of the radiative energy density of random composites. From Eqs. (60) and (61) it can be seen that both EFA and QCA reduce to $I_b(T) = \sigma T^4/\pi$ for $\phi \to 0$.Figure 4 compares the $(m_{\text{eff}})^2$ calculated from EFA and QCA for different values of $m = m_2$ (assuming $m_1 = 1$) for the Rayleigh case. Comparisons are made between $(m_{\text{eff}})^2$ because $I^0(T)$ depends on $(m_{\text{eff}})^2$. Figure 4 shows that EFA and QCA are very close to each other and the difference between EFA and QCA decreases with decreasing value of m. However, for effective attenuation β the difference between EFA and QCA is very large (Fig. 2). The reason for the difference in the behavior of m_{eff} and β is that m_{eff} mainly gets modified due to multiple scattering whereas β gets modified due to dependent scattering. Since Tien considered only dependent scattering effects, therefore Tien's results for β are in close agreement with QCA. These different models can be summarized as

EFA: independent multiple scattering model,

Tien: dependent single scattering model,

QCA: dependent multiple scattering model.

Multiple scattering effects are always present due to multiple numbers of particles whereas dependent scattering becomes important only if the wavelength becomes comparable to the interparticle distance. QCA captures the effect of both multiple and dependent scattering but is extremely complicated except for the Rayleigh case. However, it is to be remembered that the Rayleigh case is the worst case for dependent scattering as the wavelength

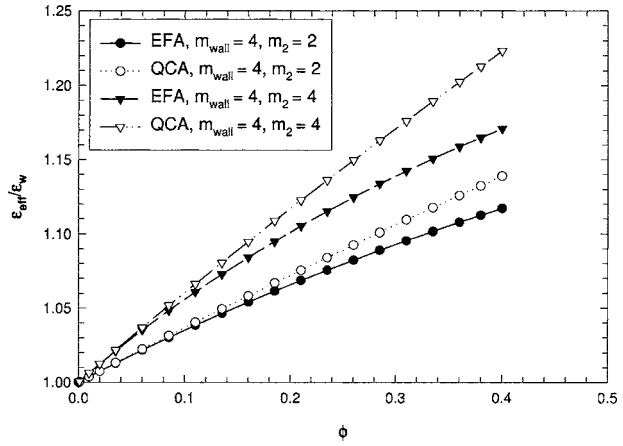

Fig. 5 Effect of multiple scattering on the effective emissivity

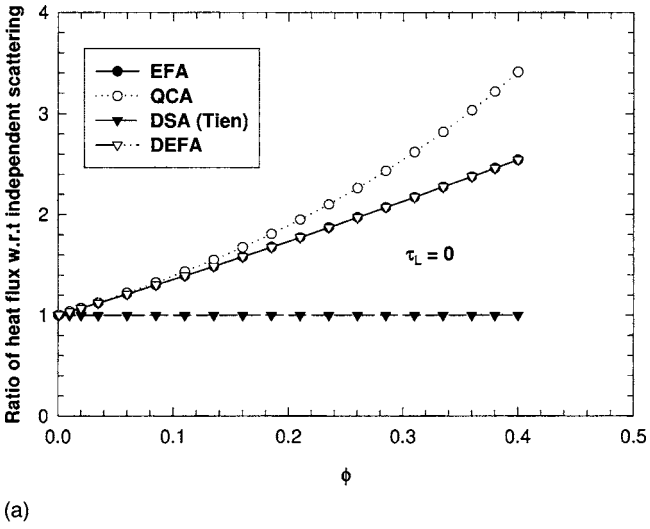

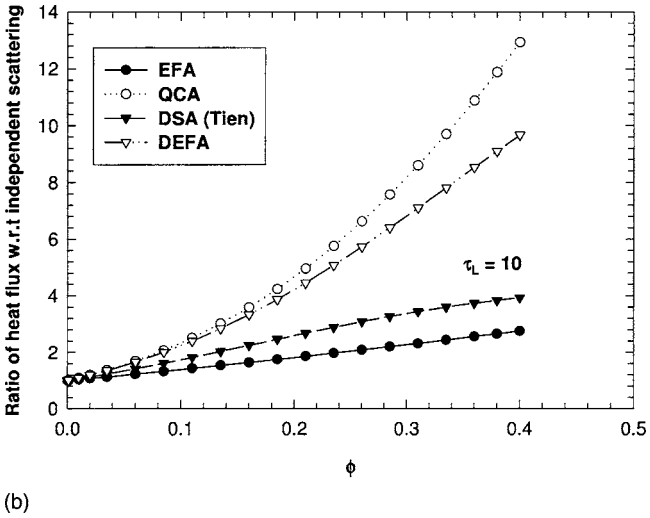

Fig. 6 (*a*) Comparison between the heat flux prediction from different models for $\tau_L=0$. (*b*) Comparison between the heat flux prediction from different models for $\tau_L=10$.

is very long. Drolen and Tien [2] have proposed that for $\delta/\lambda > 0.5$ dependent scattering effects are negligible where δ is the interparticle distance and λ is the wavelength. Since δ increases with increasing particle size, therefore if the particle size is large, then independent scattering will persist for larger volume fractions. However, the effect of multiple scattering will keep on increasing with increasing volume fractions. Since EFA is much simpler than QCA and v_p, v_g, and $D(\omega)$ are mainly affected by multiple scattering, v_p, v_g, and $D(\omega)$ can be obtained using EFA, whereas, for β, QCA needs to be used. This approach was taken by Meulen et al. [10,11] where they used EFA for effective speed and QCA for β for the scattering of acoustic waves. They compared their result for different values of size parameter x_1 and volume fraction with experimental results. Their results showed that v_p, v_g, and $D(\omega)$ can be modeled using EFA whereas β can be modeled only by using QCA.

QCA is very complicated for the non-Rayleigh case as mentioned earlier. A new model is proposed that accurately captures the multiple and dependent scattering effects. This model is a combination of EFA and Tien's approach and is called dependent effective field approximation (DEFA). Since Tien's model matches with QCA for effective attenuation and EFA is very close to QCA for v_p, v_g, and $D(\omega)$, it is proposed that effective attenuation can be calculated using Tein's approach and v_p, v_g, and $D(\omega)$ can be calculated using EFA. It is emphasized again that for the non-Rayleigh case the difference between EFA and QCA for v_p, v_g, and $D(\omega)$ will become even smaller for larger values of x_1 at the same volume fraction as the effect of dependent scattering diminishes with larger value of x_1 [2]. Therefore DEFA can be summarized as follows:

$$v_p = \frac{v_1}{\sqrt{1 - \frac{3}{2}(\phi/x_1^3)\sum_{n=1}^{\infty}(2n+1)y_n}} \tag{63}$$

$$\frac{\alpha_{Dep}}{\alpha_{ind}} = \frac{1}{4\pi}\int_{4\pi} F(\theta)\Phi(\theta)d\Omega \tag{64}$$

where α_{Dep} is the dependent attenuation, α_{ind} is the independent attenuation, $F(\theta)$ is the form factor [2], and Ω is the solid angle. Similarly the transport attenuation or transport cross section can be written as [7]

$$\frac{\alpha_{TDep}}{\alpha_{ind}} = \frac{1}{4\pi}\int_{4\pi} F(\theta)(1-\cos(\theta))\Phi(\theta)d\Omega \tag{65}$$

where α_{TDep} is the dependent transport attenuation.

4 Calculation of Heat Flux and Temperature for a One-Dimensional Parallel Slab

In this section the effect of multiple and dependent scattering on the heat flux and temperature is calculated for a 1D parallel slab geometry using QCA, EFA, Tein's approach, and DEFA for Rayleigh scattering. Tien's approach is called dependent scattering approximation (DSA). Most of the work done in the area of dependent scattering dealt only with optical radiation and no attempt was made to predict the temperature [2–4]. However, Kumar and Tien [5] made temperature and heat flux predictions for the case of dependent absorption and scattering but they assumed $I^0(T) = \sigma T^4/\pi$.

Diffusion approximation with the Deissler jump boundary condition [1] is used to calculate the heat flux and temperature. Since the effective refractive index of the particulate media gets modified, the emissivity of the wall therefore will also get modified. In all the calculations $m_1=1$ is assumed. Emissivity for the wall can be calculated using the formula given in standard text books [1] if the wall refractive index (m_{wall}) is known. Figure 5 shows the ratio of ε_{eff} and ε_w where ε_{eff} is the emissivity of the wall with respect to the effective particulate media and ε_w is the emissivity of the wall with respect to $m_1=1$. Figure 5 shows that ε_{eff} can change substantially depending on m_{wall} and m_2. Figure 5 also

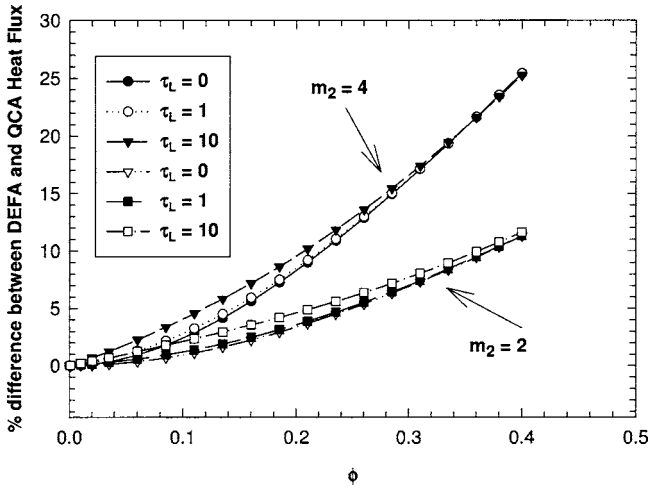

Fig. 7 Difference between the heat flux predictions of DEFA and QCA

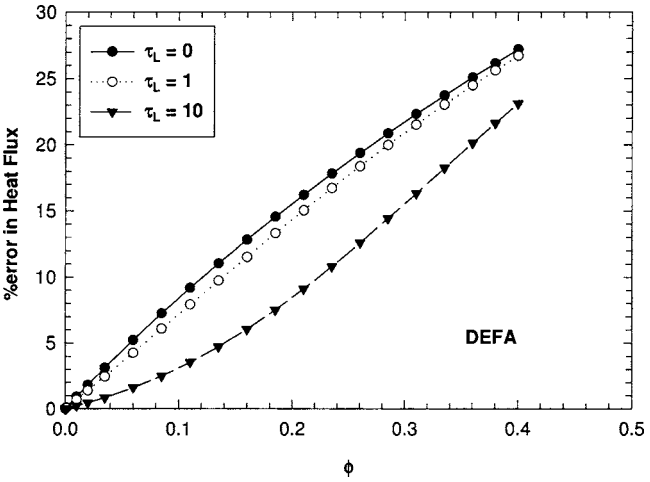

Fig. 8 Percent error in heat flux if the wall emissivity is not modified due to change in the effective refractive index of the medium for DEFA

shows that the difference between ε_{eff} prediction based on QCA and EFA decreases with decreasing m_2, i.e., with decreasing refractive index contrast between the medium and the particles. Modification of reflective properties due to multiple and dependent scattering using Tsang and Kong's [13,14] approach was considered by Stoyanov et al. [27].

The dimensionless heat flux (Ψ) can be written as [1]

$$\psi = \frac{q}{\sigma(T_{w1}^4 - T_{w2}^4)} = \frac{m_{eff}^2}{\frac{3}{4}t_L + (2/\varepsilon_{eff}) - 1} \tag{66}$$

where t_L is the optical thickness and T_{w1} and T_{w2} are the wall temperatures. The dimensionless temperature (Θ) can be written as [1]

$$\Theta = \frac{T^4(z) - T_{w2}^4}{T_{w1}^4 - T_{w2}^4} = \frac{\frac{3}{4}t_L - \frac{3}{4}(z/L)t_L + (2 - \varepsilon_{eff})/\varepsilon_{eff}}{\frac{3}{4}t_L + (2/\varepsilon_{eff}) - 1} \tag{67}$$

where z is the distance along the length of the medium and L is the physical thickness of the medium. For calculations, extreme cases (m_2=4 and m_{wall}=4) are considered to highlight the difference between different models. Figures 6(*a*) and 6(*b*) shows the ratio of heat flux based on different models and that based on independent scattering for different values of ϕ and τ_L. τ_L shown in the figures in all the calculations in this paper are the independent scattering τ_L. However, τ_L is modified for different models presented in this paper for the calculation of Ψ and Θ. Figure 6(*a*) shows that for τ_L=0 DSA (Tien's approach) results are the same as independent scattering results. This result is not surprising as DSA only modifies τ_L and since τ_L is zero in Fig. 6(*a*), DSA is the same as independent scattering whereas EFA and DEFA match because for τ_l=0 DEFA reduces to EFA. For τ_l=0, Ψ is only dependent on the m_{eff} and ε_{eff}. For increasing values of τ_L Fig. 6(*b*) shows that DEFA is closer to QCA than any other models. These figures highlight the fact that if the effective refractive index of the medium due to multiple scattering is not modified, there will be a huge error in the heat flux predictions. Figure 7 compares the heat flux results of DEFA and QCA for different values of m_2. Figure 7 shows that the difference between DEFA and QCA decreases with decreasing refractive index contrast between the medium and the particle. Figure 8 shows the error in the heat flux predictions for DEFA if the wall emissivity is not modified due to multiple scattering. The error is large for smaller values of τ_L because emissivity of the walls plays a bigger role at smaller τ_L as seen from Eq. (66). This figure shows that modification of wall emissivity should be taken into account particularly for optically thin medium. It is also to be remembered that depen-

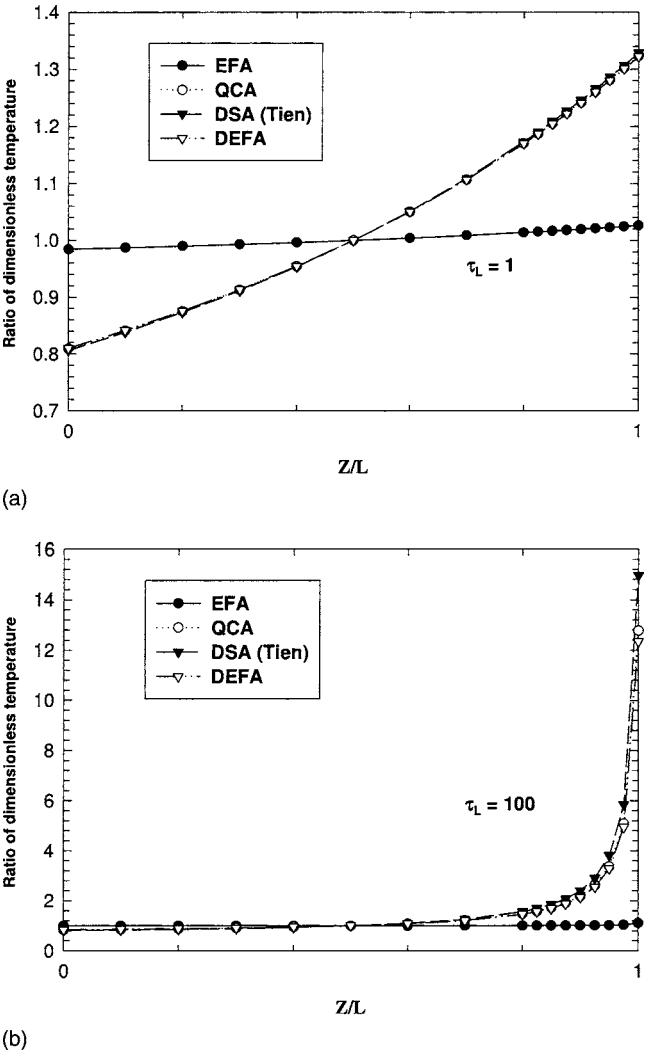

Fig. 9 (*a*) Ratio of dimensionless temperature w.r.t. independent scattering for τ_L=1. (*b*) Ratio of dimensionless temperature w.r.t. independent scattering for τ_L=100.

dent scattering leads to a decrease in the optical thickness as compared to independent scattering because the effective attenuation for dependent scattering is less than independent scattering.

Figures 9(*a*) and 9(*b*) show the results for the ratio of dimensionless temperature calculated from various models and that calculated assuming independent scattering. Figures 9(*a*) and 9(*b*) show that QCA, DEFA, and DSA match very well for the temperature prediction whereas EFA gives almost the same results as independent scattering. These trends are very obvious by looking at Eq. (67). Equation (67) shows that Θ does not depend on m_{eff} and therefore EFA results are very close to independent scattering results whereas Θ is strong function of τ_L, which gets modified due to dependent scattering. Θ is also not a very strong function of ε_{wall}, which makes DSA results close to DEFA and QCA although ε_{wall} gets modified by DEFA and QCA. Figures 9(*a*) and 9(*b*) show that temperature prediction using Tien's approach is a good approximation; however, for heat flux calculations the effect of multiple scattering has to be taken into account.

5 Conclusions

The effect of multiple and dependent scattering on Planck blackbody radiation intensity was calculated using different approximations and models. The main conclusions are the following.

(a) Planck blackbody intensity mainly gets modified due to multiple scattering.
(b) The scattering cross section mainly gets modified due to dependent scattering.
(c) The DEFA model introduced in the paper captures both the above mentioned effects.
(d) Heat flux is a strong function of both multiple and dependent scattering.
(e) Temperature prediction is not a strong function of multiple scattering but is a strong function of dependent scattering.
(f) Relations derived in this paper can also be used for the calculation of the radiative energy density and optical properties of a random composites.

References

[1] Siegel, R., and Howell, J. R., 1992, *Thermal Radiation Heat Transfer*, Hemisphere Publishing Corporation, Washington, DC.
[2] Drolen, B. L., and Tien, C. L., 1987, "Independent and Dependent Scattering in Packed Sphere Systems," J. Thermophys. Heat Transfer, **1**(1), pp. 63–68.
[3] Brewster, M. Q., and Tien, C. L., 1982, "Radiative Transfer in Packed Fluidized Beds: Dependent Versus Independent Scattering," ASME J. Heat Transfer, **1**, pp. 573–579.
[4] Tien, C. L., 1988, "Thermal Radiation in Packed and Fluidized Beds," ASME J. Heat Transfer, **110**, pp. 1230–1242.
[5] Kumar, S., and Tien, C. L., 1990, "Dependent Absorption and Extinction of Radiation by Small Particles," ASME J. Heat Transfer, **112**, pp. 178–185.
[6] Ma, Y., Varadan, V. K., and Varadan, V. V., 1990, "Enhanced Absorption Due to Dependent Scattering," ASME J. Heat Transfer, **112**, pp. 402–407.
[7] Saulnier, P. M., Zinkin, M. P., and Watson, G. H., 1990, "Scatterer Correlation Effects on Photon Transport in Dense Random Media," Phys. Rev. B, **42**, pp. 2621–2623.
[8] Lax, M., 1952, "Multiple Scattering of Waves. II, The Effective Field of Dense Systems," Phys. Rev., **85**(4), pp. 621–629.
[9] Lax, M., 1951, "Multiple Scattering of Waves. II," Rev. Mod. Phys., **23**(4), pp. 287–309.
[10] Meulen, F. V., Feuillard, G., Matar, O. B., Levassort, F., and Lethiecq, M., 2001, "Theoretical and Experimental Study of the Influence of the Particle Size Distribution on the Acoustic Wave Properties of Strongly Homogeneous Media," J. Acoust. Soc. Am., **110**(5), pp. 2301–2307.
[11] Meulen, F. V., Feuillard, G., Matar, O. B., Levassort, F., and Lethiecq, M., 1999, "Comparison Between Multiple Scattering Theories and Velocity and Attenuation Measurements in Highly Loaded Liquid Media," IEEE Ultrasonics Symposium, pp. 723–726.
[12] Kim, J.-Y., Ij, J.-G., and Lee, B.-H., 1995, "Dispersion of Elastic Waves in Random Particulate Composites," J. Acoust. Soc. Am., **97**(3), pp. 1380–1388.
[13] Tsang, L., and Kong, J. A., 1982, "Effective Propagation Constants for Coherent Electromagnetic Wave Propagation in Media Embedded with Dielectric Scattererrs," J. Appl. Phys., **53**(11), pp. 7162–7173.
[14] Tsang, L., and Kong, J. A., 1981, "Multiple Scattering of Electromagnetic Waves by Random Distributions of Discrete Scatterers With Coherent Potential and Quantum Mechanical Formulism," J. Appl. Phys., **51**(7), pp. 3465–3485.
[15] Ishimaru, A., and Kuga, Y., 1982, "Attenuation Constant of Coherent Field in a Dense Distribution of Particles," J. Opt. Soc. Am., **72**(10), pp. 1317–1320.
[16] Cartigny, J. D., Yamada, Y., and Tien, C. L., 1986, "Radiative Transfer With Dependent Scattering by Particles: Part 1-Theoretical Investigation," ASME J. Heat Transfer, **108**, pp. 608–613.
[17] West, R., Gibbs, D., Tsang, L., and Fung, A. K., 1994, "Comparison of Optical Scattering Experiments and the Quasi-Crystalline Approximation for Dense Media," J. Opt. Soc. Am. A, **11**(6), pp. 1854–1858.
[18] Garg, R., Prudhomme, R. K., Aksay, I. A., Liu, F., and Alfano, R. R., 1998, "Optical Transmission in Highly Concentrated Dispersions," J. Opt. Soc. Am. A, **15**(4), pp. 932–935.
[19] West, R., Gibbs, D., Tsang, L., and Fung, A. K., 1994, "Comparison of Optical Scattering Experiments and the Quasi-Crystalline Approximation for Dense Media," J. Opt. Soc. Am. A, **11**(6), pp. 1854–1858.
[20] Majumdar, A., 1993, "Microscale Heat Conduction in Dielectric Thin Films," ASME J. Heat Transfer, **115**, pp. 7–16.
[21] Bohren, C. F., and Huffman, D. R., 1983, *Absorption and Scattering of Light by Small Particles*, Wiley-Interscience Publications, New York.
[22] Truell, R., Elbaum, C., and Chick, B. B., 1969, *Ultrasonic Methods in Solid State Physics*, Academic Press, New York.
[23] Gaunard, G. C., and Wertman, W., 1989, "Comparison of Effective Medium Theories for Inhomogeneous Continua," J. Acoust. Soc. Am., **85**(2), pp. 541–554.
[24] Twersky, V., 1975, "Transparency of Pair-Correlated Random Distributions of Small Scatterers, with Applications to the Cornea," J. Opt. Soc. Am., **65**, pp. 524–530.
[25] Li, Z.-Y., 2002, "Modified Thermal Radiation in Three-Dimensional Photonic Crystals," Phys. Rev. B, **66**, p. 241103(R).
[26] Cornelius, C. M., and Dowling, J. P., 1999, "Modification of Planck Black Body Radiation by Photonic Band-gap Structures," Phys. Rev. A, **59**(6), pp. 4736–4746.
[27] Stoyanov, A. J., Howell, B. F., Fischer, E. C., Uberall, H., and Chouffani, K., 1999, "Effective-medium Model Dependence of the Radar Reflectivity of Conducting Particle Films," J. Appl. Phys., **86**(6), pp. 3110–3119.

Hybrid Method to Calculate Direct Exchange Areas Using the Finite Volume Method and Midpoint Intergration

Weixue Tian

Wilson K. S. Chiu
e-mail: wchiu@engr.uconn.edu

Department of Mechanical Engineering,
University of Connecticut,
Storrs, CT 06269-3139

This paper presents a hybrid method to calculate direct exchange areas for an infinitely long black-walled rectangular enclosure. The hybrid method combines the finite volume method (FVM) with the midpoint integration scheme. Direct numerical integration of direct exchange areas for adjacent and overlapping zones is difficult because of singularities in the integrand. Therefore, direct exchange areas of adjacent and overlapping zones are calculated using the FVM. Direct exchange areas of nonadjacent zones are calculated by the efficient midpoint integration scheme. Thus, direct exchange areas in an infinitely long enclosure can be obtained with both efficiency and accuracy. Volume-volume direct exchange areas of zones with various aspect ratios and optical thickness have been calculated and compared to exact solutions, and satisfactory results are found. [DOI: 10.1115/1.1929786]

1 Introduction

Direct numerical integration of direct exchange areas used in the zonal method [1,2] is computationally intensive because it generally involves evaluating multidimensional integrals, with singularities occurring when two zones are adjacent or overlapping. Considerable effort has been devoted to evaluate direct exchange areas with acceptable accuracy and efficiency. A detailed description of literature can be found elsewhere [3,4]; only those closely related to this study are presented in the following discussion. All the previously proposed methods can be divided into two categories: (i) evaluating the multidimensional integrals of direct exchange areas using a mathematical technique, for example, a reduced-order integration scheme [5,6]. However, most schemes proposed are either computationally intensive or mathematically involved. One of the most straightforward and efficient schemes to evaluate the direct exchange areas was proposed by Modest [7] and Modest and Stevens [8]. They found that, for a sufficient number of zones, all exchange areas but one may be calculated by evaluating the integrand between zone centers [9]. It was recognized that the optical thickness of each zone has to be small and the optical distance between two zones needs to be large enough to render this method sufficiently accurate, although no quantitative estimation was given. Category (ii) is evaluating the direct exchange areas based on physical interpretation, in which direct exchange areas represent the relationship between the heat flux leaving one zone and absorbed directly by another zone without reflection [9]. For example, the surface-to-surface direct exchange areas with participating media were calculated using the discrete ordinates method (DOM) [3,4]. The view factors, which are closely related to direct exchange areas with nonparticipating media, were tackled with the DOM [10] and FVM [11]. However, DOM-predicted direct exchange area accuracy deteriorates dramatically with increasing optical distance between two zones [3,4].

This paper builds a bridge between the two categories. The FVM is used for direct exchange areas of adjacent and overlapping zones, whereas the more efficient midpoint integration scheme is used for direct exchange areas of the majority of nonadjacent zones, where the integrands are smooth. Therefore, both efficiency and accuracy are achieved for evaluating direct exchange areas in the infinitely long black-walled rectangular enclosures. Based on truncation error analysis, we also provide a semiquantitative error estimation for midpoint integration in calculating direct exchange areas.

2 Analysis

The following two sections outline the proposed methodology on volume-to-volume direct exchange areas. Similar behavior can be observed for volume-to-surface and surface-to-surface direct exchange areas.

2.1 Midpoint Integration. The volume-to-volume direct exchange areas per unit length for an infinitely long (in the z direction out of page) black-walled rectangular enclosure shown in Fig. 1 can be written as the following, based on derivation by Einstein [12]:

$$\overline{g_i g_j}' = \int_{\tau_{xi}}^{\tau_{xi}+\Delta\tau_{xi}} \int_{\tau_{yi}}^{\tau_{yi}+\Delta\tau_{yi}} \int_{\tau_{xj}}^{\tau_{xj}+\Delta\tau_{xj}} \int_{\tau_{yj}}^{\tau_{yj}+\Delta\tau_{yj}} \frac{2f(\tau)}{\kappa\pi\tau} d\tau'_{yj} d\tau'_{xj} d\tau'_{yi} d\tau'_{xi} \tag{1}$$

where

$$f(\tau) = \int_0^{\pi/2} \exp(-\tau/\cos\theta) d\theta \tag{2}$$

and

$$\tau = \kappa s \tag{3}$$

Note that $\overline{g_i g_j}'$ in Eq. (1) is in units of length (m) instead of area (m^2) because it is calculated in terms of per unit length in the z direction. In two-dimensional (2D) analysis, the length in the z direction can be chosen as a unit length, therefore, direct exchange areas $\overline{g_i g_j}$ can written as $\overline{g_i g_j}'$ times unit length, and the units and numerical values are consistent. The integrand and integration limits are written as the optical length, which is the product of the absorption coefficient and length. The above integral is then approximated as the following equation for zones with uniform size [7]:

Contributed by the Heat Transfer Division for publication in the JOURNAL OF HEAT TRANSFER. Manuscript received: March 29, 2004. Final manuscript received: January 27, 2005. Review conducted by: Ashley F. Emery.

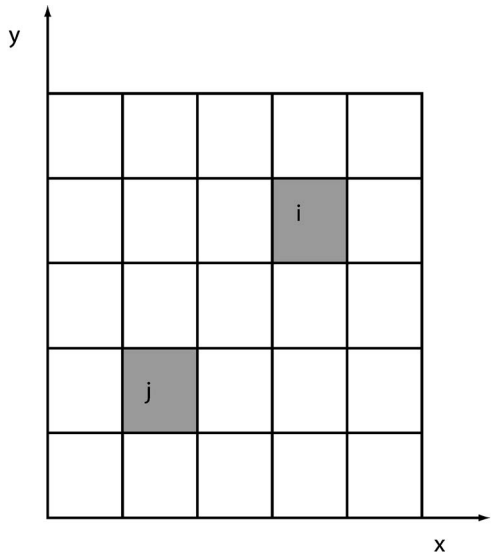

Fig. 1 Schematic of volume *i* and volume *j* zone in an infinite rectangular duct

$$\overline{g_i g_j}' = \overline{g_j g_i}' = \frac{2}{\kappa\pi}(\Delta\tau_x \Delta\tau_y)^2 \frac{f(\tau_{ji})}{\tau_{ji}} \tag{4}$$

The integrand is evaluated using the center of each zone, which is located at the "midpoint" of the integration limits in both dimensions. Mathematically, this approach is equivalent to the midpoint integration scheme [13], in which the integrand is evaluated by the midpoint of integration limits. For this approach to provide reasonable accuracy, the integrand has to be smooth within the integration limits. However, the optical distance τ is zero at the common boundary of two adjacent zones, which leads to singularities in the integrand. Thus, the midpoint integration scheme leads to a large error. It is difficult to determine the accuracy of calculating direct exchange areas using midpoint integration in a 2D domain. Thus the accuracy for a one-dimensional (1D) domain is quantitatively discussed based on truncation error analysis. One may expect similar behavior in a 2D domain. Numerical experiments are carried out to prove this assumption, as to be discussed in Sec. 3.1.

For an infinitesimal volume *i* (infinitely small in both *x* and *y* direction) to a one-dimensional volume *j* (with finite length in the *x* direction) shown in Fig. 2, the direct exchange area can be written as

$$M = \frac{\overline{g_i g_j}}{dV_i} = \int_{\tau_j}^{\tau_j+\Delta\tau} \frac{2\kappa f(\tau)}{\pi\tau} d\tau' \tag{5}$$

This integral can be evaluated using the midpoint integration scheme

$$M_n = \frac{\overline{g_i g_j}}{dV_i} = \frac{2\kappa f(\tau_{ij})}{\pi\tau_{ij}}\Delta\tau \tag{6}$$

and τ_{ij} is evaluated from *i* to the center of zone *j*. By applying the truncation error analysis for midpoint integration [13] and assuming the second derivative of the integrand is sufficiently smooth, the error of this approximation can be written as

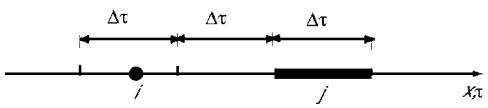

Fig. 2 Schematic of an infinitely small volume *i* to volume *j* zone

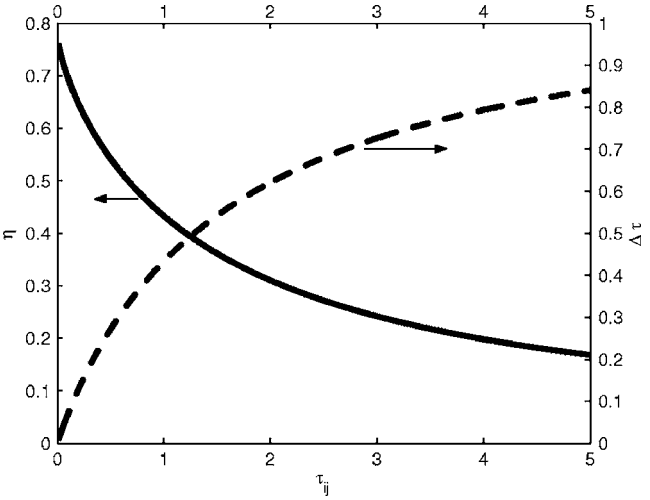

Fig. 3 Change of η and $\Delta\tau$ with τ_{ij} for 5% error

$$\epsilon = M - M_n \approx \frac{2\kappa g''(\tau_{ij})\Delta\tau^3}{24\pi} \tag{7}$$

where

$$g(\tau) = f(\tau)/\tau \tag{8}$$

The relative error can be written as

$$\epsilon_r = |M - M_n|/M_n \approx \frac{g''(\tau_{ij})}{24g(\tau_{ij})}\Delta\tau^2 \tag{9}$$

The relative error of the midpoint integration scheme is determined by the optical distance between two zones τ_{ij} and optical thickness of each zone $\Delta\tau$, as seen in Eq. (9). For an arbitrary accuracy of $\epsilon_r = 5\%$, we define a parameter η to determine the range of τ_{ij} and $\Delta\tau$ for which $\epsilon_r < 0.05$ from Eq. (9)

$$\Delta\tau < \sqrt{\frac{24g(\tau_{ij}) \times 0.05}{g''(\tau_{ij})}} \tag{10}$$

or

$$\eta = \Delta\tau/\tau_{ij} < \frac{\sqrt{\dfrac{24g(\tau_{ij}) \times 0.05}{g''(\tau_{ij})}}}{\tau_{ij}} \tag{11}$$

The right side of the inequality is then plotted in Fig. 3, where η and $\Delta\tau$ changes with τ_{ij}. The region below the $\eta - \tau_{ij}$ curve represents a truncation error of $<5\%$, as determined by Eq. (11). For uniform nonadjacent zones, $\tau_{ij} \geqslant 1.5\Delta\tau$, or $\eta \leqslant 0.67 = (\Delta\tau/1.5\Delta\tau)$, corresponding to $\tau_{ij} \approx 0.15$ on the $\eta - \tau_{ij}$ curve. Thus, one may conclude that midpoint integration for calculating direct exchange areas of nonadjacent uniform zones in a 1D domain is expected to be accurate to within 5% as long as τ_{ij} is <0.15, i.e., the optical thickness of each zone $\Delta\tau$ should be <0.1. It should be pointed out that this is a conservative estimate since $\eta = 0.67$ is the upper limit. From the $\Delta\tau - \tau_{ij}$ curve, we can see that the optical thickness of any zone $\Delta\tau$ in the domain also has a limit, depending on how far away the zones are. For example, if the optical distance between two zones is $\tau_{ij} = 5$, to achieve 5% accuracy, the optical thickness of the zone has to be less than roughly $\Delta\tau = 0.85$. Thus, one has a tool to predetermine the accuracy of calculated direct exchange areas based on the zone optical thickness. It is valid for any other accuracy requirements by simply substituting the desired accuracy for 0.05 in Eq. (11). These arguments are based on truncation error analysis for the midpoint integration scheme in a 1D domain. For a 2D domain, error analy-

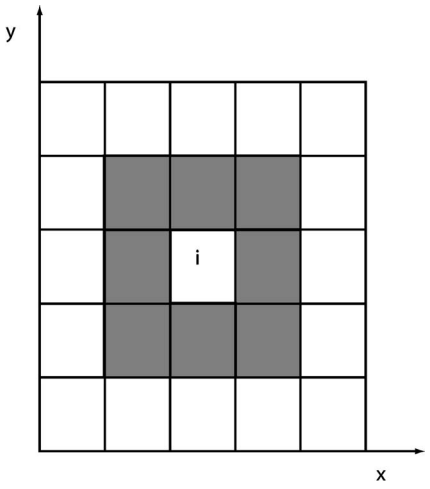

Fig. 4 Schematic of adjacent zones for direct exchange areas calculation using the FVM

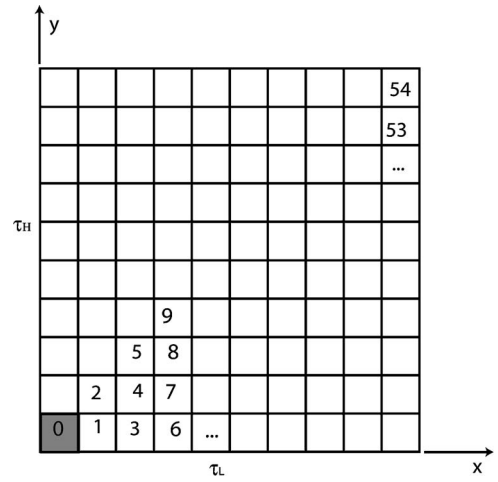

Fig. 5 Enclosure with 10×10 zones to calculate direct exchange areas to zone 0

sis involves evaluating error for a four-dimensional integral, which is quite complicated. However, numerical experiments confirm similar behavior as shown in Sec. 3.1.

2.2 Finite Volume Method. The accuracy of midpoint integration for direct exchange areas may be compromised with adjacent zones due to singularities in the integrand as discussed in Sec. 2.1. For the same reason, direct numerical integration of adjacent direct exchange areas can be difficult. Thus, the direct exchange areas of adjacent and overlapping zones are calculated using the finite volume method [14,15], shown in Fig. 4. The shaded areas are adjacent zones to zone *i*.

The FVM solves the radiative transfer equation (RTE) shown in Eq. (12) in semi-transparent media with the appropriate boundary conditions

$$\frac{dI}{ds} = -\kappa I + \kappa I_b \tag{12}$$

By assuming the intensity constant in a control volume and control angle, the final discretized equation can be written as

$$a_P^{m,l} I_P^{m,l} = \sum a_{nb} I_{nb}^{m,l} + S^{m,l} \tag{13}$$

The intensity in each control volume and control angle is obtained by solving Eq. (13). The procedure for the FVM in semi-transparent media is well documented [14,15], thus is not repeated here. The calculation of direct exchange areas with the FVM for nonscattering media is based on the physical interpretation of the direct exchange area, which represents the relationship between the energy absorbed by zone *j* and the emissive power of zone *i*, or

$$\overline{g_i g_j} = \frac{Q_{ij}}{E_{bi}} \tag{14}$$

and

$$E_{bi} = \sigma T_i^4 \tag{15}$$

$$Q_{ij} = \kappa \int_{4\pi} I_j d\Omega \Delta V_j \tag{16}$$

To calculate the direct exchange areas $\overline{g_i g_j}$, one assumes that the media in zone *i* has temperature T_i, whereas enclosure walls and media other than zone *i* are cold (i.e., temperature equals zero), so that the heat absorbed by zone *j*, Q_{ij}, solely comes from emission of zone *i*. Thus direct exchange areas can be calculated using standard FVM for radiative heat transfer. The step scheme in spatial coordinates is used to calculate the intensity field, so that no iteration is necessary for black-walled enclosures [15].

The surface-to-surface direct exchange areas and view factors have been calculated using the FVM [11] and DOM [3,4,10], but literature is lacking on calculation of volume-to-volume direct exchange areas. The finite volume method is chosen because of several reasons: conservation of radiant energy, the flexibility of choosing angular discretization, and a particular procedure capable of resolving the ray effects without substantially increasing the memory requirements developed by previous researchers [11]. However, the FVM, as well as the DOM, has some well-known shortcomings [16–18]. Ray effects, resulting from discretization of continuous intensity in the angular domain, are more prominent when two control volumes are far way. In fact, the error of DOM-calculated surface-to-surface direct exchange areas become exceedingly large as the optical distance between two zones approaches ten [3,4]. This problem can be partially resolved by using a larger number of control angles. However, this can significantly increase memory requirements as well as computational time. A procedure to alleviate memory requirements by only storing the intensity of neighboring control volumes is implemented in the current study [11]. Nevertheless, the shortcomings of FVM are less prominent in the methodology we propose because only computation of adjacent and overlapping direct exchange areas is needed, where the optical distance starts from zero.

To overcome the spatial resolution of the FVM, an adaptive procedure to refine the mesh is implemented. The initial mesh is based on the zone system. Then the mesh is refined to calculate direct exchange areas, and the procedure stops until a convergence criterion is satisfied. In the refined mesh, if zone *j* contains *N* control volumes, Q_{ij} can be calculated by the following equation:

$$Q_{ij} = \sum_{k=1}^{N} Q_{ik} \tag{17}$$

and Q_{ik} can be calculated by substituting *k* for *j* in Eq. (16).

3 Illustrative Examples and Discussion

To demonstrate the methodology we proposed, several illustrative examples are presented in this section. A rectangular enclosure shown in Fig. 5 is studied. The optical thickness of the zone system τ_L and τ_H ranges from 0.1 to 9, respectively. Studies are carried out to investigate the effects of zonal optical thickness and zone aspect ratio on the accuracy of the current method.

3.1 Illustrative Examples. A square enclosure with $\tau_L = \tau_H$ is studied in this section. The enclosure is divided into 10 by 10 zones. The direct exchange areas to zone *i*, shown as the shaded

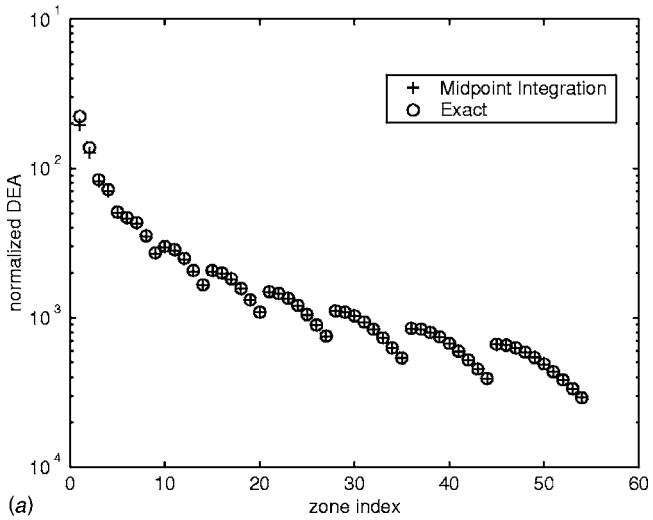

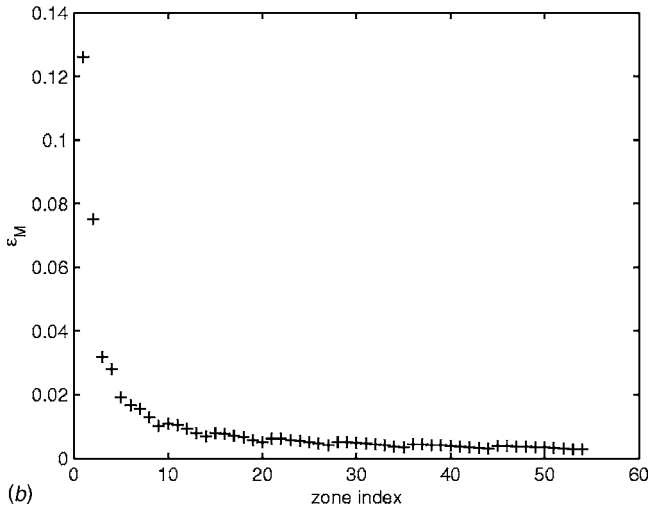

Fig. 6 Midpoint integration and its error for $\tau_L=\tau_H=1$ and $\Delta\tau=0.1$: (a) comparison of direct exchange areas by midpoint integration and exact solution; and (b) relative error by midpoint integration

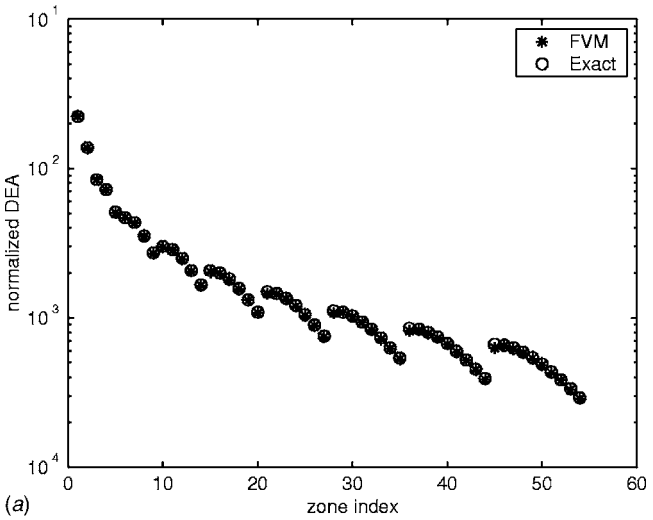

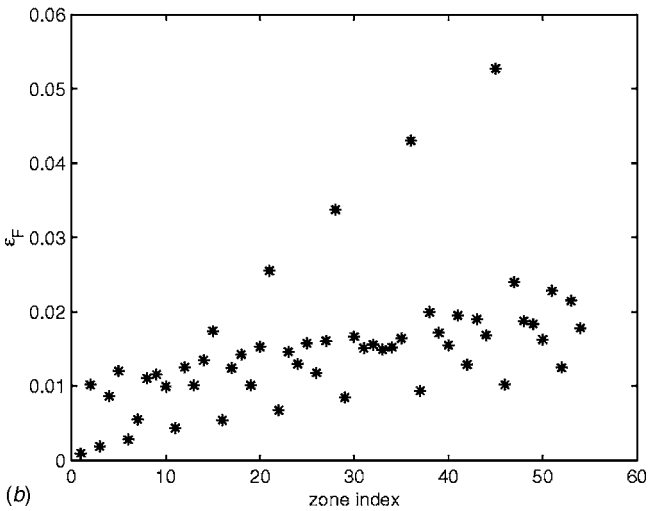

Fig. 7 Finite volume method and its error for $\tau_L=\tau_H=1$ and $\Delta\tau=0.1$: (a) comparison of direct exchange areas by FVM and exact solution; and (b) relative error by FVM

area in the Fig. 5, are evaluated using an "exact" solution—integrals in Eq. (1) are evaluated by direct numerical integration using a ten-point Gaussian quadrature. The domain in each dimension is then divided into two subdomains, and the integral is evaluated over each subdomain. The integral over the whole domain is the sum of the integrals over the two subdomains. The two evaluations of the integral are then compared. If the difference is $>0.1\%$ (convegence criterion), then each dimension is further divided into three subdomains and the integration is carried out in each subdomain using the ten-point Gaussian quadrature. Repeated steps are carried out until the convergence criterion is satisfied. A similar integration scheme was used in [6,19] to calculate direct exchange areas and view factors, where more details are given.

The midpoint integration scheme and finite volume method are used to calculate direct exchange areas in the whole enclosure to demonstrate the arguments made in the previous sections. Fifty-five direct exchange areas (between zone 0 and other zones) are unique because of symmetry. The zones with unique direct exchange areas are indexed from 0 to 54, as shown in Fig. 5 in the lower half of the enclosure. The optical distance between zone 0 and other zones generally increases with increasing zone index. A typical result using the midpoint integration scheme and the FVM is shown in Figs. 6(*a*) and 7(*a*), where the normalized direct exchange areas $\overline{g_i g_j}/4\kappa\Delta V_i$ are shown in the y axis. The direct exchange area of zone 0 to itself is not shown in the figure because the denominator is zero when midpoint integration is used. The optical thickness of the enclosure is $\tau_L=\tau_H=1$, which corresponds to $\Delta\tau=\tau_H/10=0.1$. Figures 6(*b*) and 7(*b*) are the corresponding relative errors defined by $|M_n-M|/M$. The direct exchange areas decrease significantly as the optical distance of the two zones increases as seen in Fig. 6(*a*). The accuracy of the midpoint integration scheme tends to increase with increasing optical distance, with errors well within 4% for most nonadjacent zones. For adjacent zones, the error reaches as high as 12.6%, shown as the first two data points in Fig. 6(*b*). Since only one quadrature point is used for each direct exchange area calculation, this method is extremely efficient.

The FVM calculation uses 50×40 ($\phi\times\theta$) control angles. Up to seven mesh refinement processes, with each mesh refinement doubling the number of control volumes in each direction, are performed to obtain results shown in Figs. 7(*a*) and 7(*b*). Further refinements of control angle do not significantly improve the accuracy of calculated direct exchange areas. The FVM results match the exact solution reasonably well, with a maximum error of 5.4%. This error is mainly caused by ray effects inherent in the FVM method. For direct exchange areas of adjacent zones, the errors are within 1%, as seen by the first two data points in Fig. 7(*b*) because ray effects are less prominent. For direct exchange

areas of nonadjacent zones, the error increases with increasing optical distance. The large errors shown in Fig. 7(*b*), above 2%, are associated with zones in the same row or column (e.g., 15, 21, 28, etc). It is worth pointing out that the FVM is more time consuming than midpoint integration because of the mesh refinement process and a large number of control angles used to achieve reasonable accuracy.

Thus it is rational to combine these two methods. Direct exchange areas of adjacent zones can be calculated using the FVM. Although all the direct exchange areas can be calculated by the FVM, as seen in Fig. 7(*a*), the FVM should only be used for calculating direct exchange areas for adjacent and overlapping zones for several reasons: (i) The FVM has higher accuracy for adjacent and overlapping zones than non-adjacent zones because of ray effects. (ii) By applying the FVM only to adjacent zones, computational time can be saved since the FVM can be performed in a small section of the enclosure instead of the whole enclosure, which saves computational time. (iii) Singularities in direct exchange areas of adjacent and overlapping zones render direct numerical integration difficult, which leads to the FVM as a better alternative. The majority of direct exchange areas are calculated using the midpoint integration scheme, which is efficient since only one quadrature point is used. Therefore, the overall hybrid method can be carried out efficiently.

3.2 Effect of Optical Thickness. The applicability of this proposed hybrid method may be hindered by the optical thickness of each zone, as discussed in Sec. 2.1. This section is devoted to studying the effect of optical thickness on the accuracy of the midpoint integration scheme and the FVM for a 2D case by numerical experiments.

Figure 8(*a*) shows the change of maximum error using the midpoint integration scheme for calculation of nonadjacent direct exchange areas as a function of the enclosure optical thicknesses. For all optical thicknesses, the maximum error using midpoint integration occurs at the zone next to the adjacent zones, such as zones 3, 4, or 5, in Fig. 5. The maximum error increases with optical thickness $\Delta\tau$, as seen in Eq. (9). For $\tau=1$, which corresponds to $\Delta\tau=0.1$, the error is 3.5%. This prediction agrees well with the conservative conclusion made in the 1D case for uniform zones. As long as each zone optical thickness $\Delta\tau\leqslant 0.1$, the error should be $<5\%$. Since the largest error occurs in zones next to the adjacent zones, the error of the overall direct exchange areas shall be $<5\%$. For optical thickness of zones $\Delta\tau>0.1$, the maximum error may be $>5\%$. A straightforward remedy is to divide each zone into a number of subzones so that the appropriate conditions defined by Eq. (9) are met. Only the conditions of nearest zones require checking since they pose the largest error. Then the direct exchange areas of original zones can be calculated by superposition, i.e., if each original zone is divided into K subzones, then $g_i g_j$ can be calculated as

$$\overline{g_i g_j} = \sum_{i'=1}^{K}\sum_{j'=1}^{K} \overline{g_{i'} g_{j'}} \tag{18}$$

Figure 8(*b*) shows the maximum error when the FVM is used to calculate the direct exchange areas of adjacent zones. The FVM mesh is refined, and, if calculated direct exchange areas for two subsequent refinements do not satisfy the convergence criterion (0.1% difference), up to seven mesh refinements are performed. For cases where convergence criterion is not satisfied after seven mesh refinements, results of the finest mesh are compared with the exact solutions. Even though some cases did not meet the convergence criteria after seven refinements, we stopped because FVM-predicted direct exchange areas differ less than 3.2% from direct numerical integration. As a trade-off of accuracy to computational intensity, we decided to select seven refinements as an optimum. The maximum error of FVM calculated direct exchange area decreases as τ changes from 0.1 to 0.5 and increases as τ increases

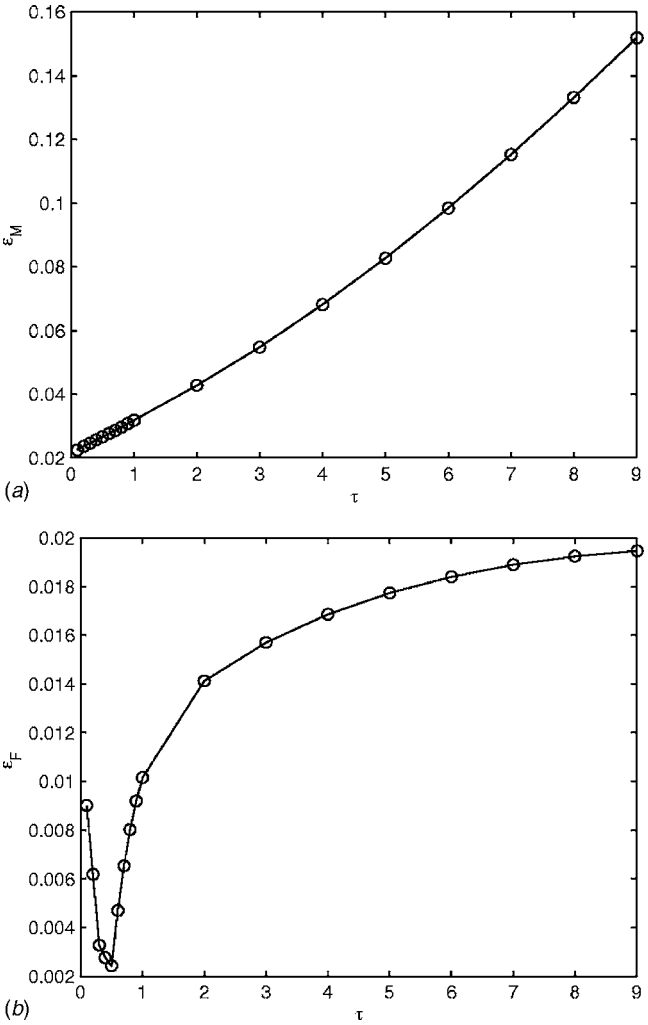

Fig. 8 Change in maximum error with optical thickness, 10 ×10 zones and $\tau_L=\tau_H$ varying from 0.1 to 9: (a) maximum relative error of nonadjacent direct exchange areas by midpoint integration; and (b) maximum relative error of adjacent direct exchange areas by FVM

from 0.5 to 9. However, for enclosure optical thickness from 0.1 to 9, corresponding to optical thickness of individual zone varying from 0.01 to 0.9, the overall maximum error of the finite volume method is $<2\%$, indicating that the FVM is capable of calculating direct exchange areas with reasonable accuracy for a range of optical thickness.

3.3 Effect of Aspect Ratio. Although the above studies are carried out using square zones, geometry and other physical constraints usually require the use of rectangular zones. Thus, the effect of zone aspect ratio is studied in this section. The changing of aspect ratio is realized by varying τ_H in an enclosure while keeping other parameters constant. A typical result for error from the midpoint integration scheme with $\tau_L=0.5$ is presented in Fig. 9(*a*). The aspect ratio of the zone changes from 1 to 5 as τ_H varies from 0.5 to 2.5. Therefore, the optical thickness of each zone in the larger dimension increases with the aspect ratio. However, the increase of optical thickness alone can not explain the magnitude of increasing error shown in Fig. 9(*a*). For example, when the aspect ratio is 5, the optical thickness of the larger dimension $\tau_H=2.5$ and the error is around 32%. This error is more than six times larger than that for $\tau_H=2.5$ when the aspect ratio is one ($\sim 5\%$), as shown in Fig. 8(*a*). Therefore, this error must be caused by both the aspect ratio and optical thickness. The error

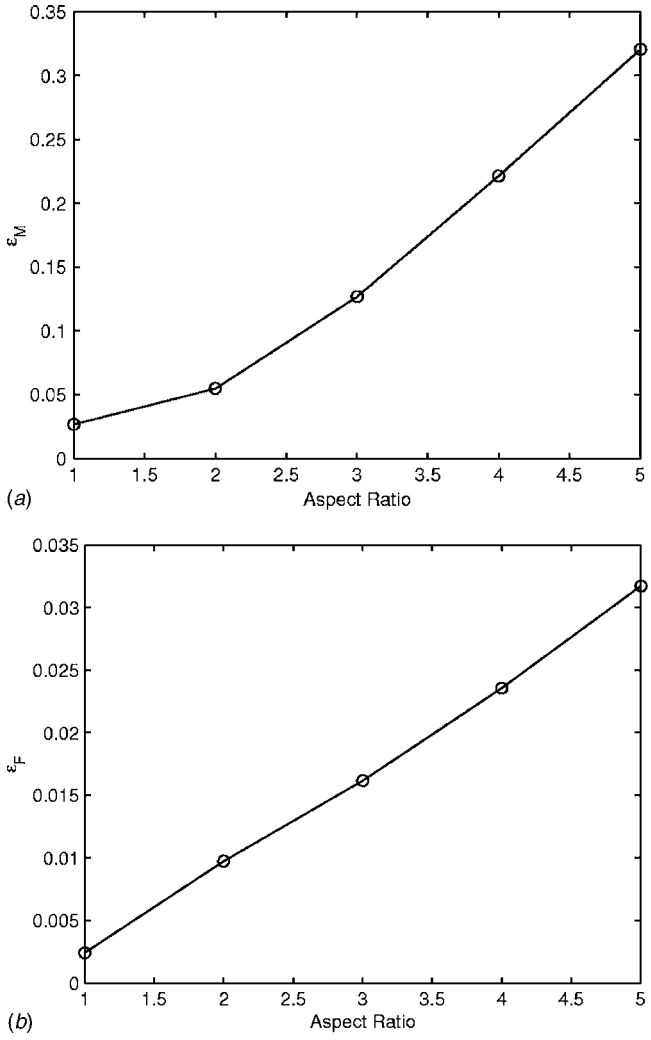

Fig. 9 Change of maximum error with varying aspect ratio, 10×10 zones, τ_L=0.5 and τ_H varying from 0.5 to 2.5: (a) maximum relative error of nonadjacent direct exchange areas by midpoint integration; and (b) maximum relative error of adjacent direct exchange areas by FVM

using midpoint integration is observed to increase with the aspect ratio. However, for aspect ratio of <2, the accuracy of the midpoint integration scheme is within 5.4% as long as the optical thickness of the larger dimension of each zone is within 0.1. Note that this is close to the 5% prediction obtained by the 1D analysis presented in Sec. 2.1.

For the FVM, the change of aspect ratio on the accuracy of the calculated direct exchange areas is less prominent. Although the error increases with increasing aspect ratio, the overall error of $<3.2\%$, as shown in Fig. 9(*b*). This result demonstrates the FVM's flexibility in handling direct exchange areas of adjacent zones with high aspect ratio.

For calculation of direct exchange areas with large aspect ratio zones using the midpoint integration scheme, a mesh refinement can be carried out in the dimension with larger length. For example, direct exchange areas of a zone with an aspect ratio of 2 can have its larger dimension divided into two in which each original zone contains two subzones, and the direct exchange areas of original zones can be obtained by superposition, as shown in Eq. (18). The maximum error using midpoint integration is $<3.5\%$ for nonadjacent zones for cases with aspect ratio of two and zone optical thickness in the larger dimension of two after the refinement is carried out, which is smaller than the 5.4% of the previous estimation without mesh refinement.

4 Conclusions

A hybrid method combining the finite volume method and the midpoint integration scheme to calculate direct exchange areas in an infinitely long black-walled rectangular enclosure is proposed in this paper. The hybrid method takes advantage of the strength of each method, while the two methods compliment each other's weakness. The direct exchange areas of adjacent zones are calculated by the finite volume method because of singularities presented in the integrand of direct exchange areas. The direct exchange areas of nonadjacent zones are calculated using the efficient midpoint integration method. A conservative estimate shows that the optical thickness should be within 0.1 for an error of $<5\%$ when midpoint integration is used. The error increases with the zone optical thickness and aspect ratio. This error can be reduced by refining the zone size with aspect ratio close to unity, i.e., square zones. When the finite volume method is used to calculate direct exchange areas of adjacent zones, ray effects are not prominent and the error is $<2\%$ for cases calculated using zones with aspect ratio of <2.

Acknowledgment

Financial support by the National Science Foundation and the Office of Naval Research is gratefully acknowledged.

Nomenclature

a = coefficient of intensity in discretized radiative transfer equation
$\overline{E}$ = emissive power, W/m^2
$\overline{g_i g_j}$ = volume-volume direct exchange area, m^2
$\overline{g_i g_j}'$ = volume-volume direct exchange area per unit length, m
I = radiation intensity, W/m^2sr
K = number of subzones of an original zone after refinement
M = integral
N = number of control volumes in an original control volume after mesh refinement
Q = heat absorption due to radiative transfer, W
S = source term in discretized radiative transfer equation
s = distance between two zones, m
T = temperature, K
V = volume of zones, m^3
x,y,z = coordinate direction

Greek Letters

ϵ = error
κ = absorption coefficient, m^{-1}
Ω = solid angle, sr
σ = Stefan-Boltzmann constant, 5.670×10^{-8} W/m^2K
τ = optical thickness
θ,ϕ = polar, azimuthal angle

Superscripts

m,l = index of discretized solid angle

Subscripts

b = blackbody
F = finite volume method
H,L = height and length, respectively, of an enclosure
i,j,k = index of zones
M = midpoint integration
n = numerical value of integral
nb = neighboring nodes
r = relative error

References

[1] Hottel, H. C., and Cohen, E. S., 1958, "Radiant Heat Exchange in a Gas-Filled Enclosure: Allowance for Nonuniformity of Gas Temperature," AIChE J., **4**, pp. 3–14.

[2] Hottel, H. C., and Sarofim, A. F., 1967, *Radiative Transfer*, McGraw-Hill, New York.

[3] Byun, K. H., and Smith, T. F., 1996, "Direct Exchange Areas for an Infinite Rectangular Duct by Discrete-Ordinate Method," *Radiative Transfer-I*, Begell House, New York, pp. 168–179.

[4] Byun, K. H., and Smith, T. F., 1998, "Direct Exchange Areas for a Rectangular Box by the Direct Discrete-Ordinates Method," *Radiative Transfer-II*, Begell House, New York, pp. 271–282.

[5] Erkku, H., 1959, Radiant Heat Exchange in Gas-Filled Slabs and Cylinders, Ph.D. thesis, Massachusetts Institute of Technology.

[6] Tian, W., and Chiu, W. K. S., 2003, "Calculation of Direct Exchange Areas for Non-Uniform Zones Using a Reduced Integration Scheme," ASME J. Heat Transfer, **125**, pp. 839–844.

[7] Modest, M. F., 1975, "Radiative Equilibrium in a Rectangular Enclosure Bounded by Gray Walls," J. Quant. Spectrosc. Radiat. Transf., **15**, pp. 445–461.

[8] Modest, M. F., and Stevens, D., 1978, "Two Dimensional Radiative Equilibrium of a Gray Medium Between Concentric Cylinders," J. Quant. Spectrosc. Radiat. Transf., **19**, pp. 353–365.

[9] Modest, M. F., 2003, *Radiative Heat Transfer*, 2nd ed., Academic Press, San Diego.

[10] Byun, K. H., and Smith, T. F., 1997, "View Factors for Rectangular Enclosures Using the Direct Discrete-Ordinates Method," J. Thermophys. Heat Transfer, **11**, pp. 593–595.

[11] Chai, J. C., Moder, J. P., and Karki, K. C., 2001, "A Procedure for View Factor Calculation Using the Finite Volume Method," Numer. Heat Transfer, Part B, **40**, pp. 23–35.

[12] Einstein, T. H., 1963, Radiant Heat Transfer to Absorbing Gases Enclosed Between Parallel Flat Plates With Flow and Conduction, Tech. Rep. R-154, NASA Lewis Research Center.

[13] Davis, P. J., and Rabinowitz, P., 1984, *Methods of Numerical Integration*, 2nd ed., Academic Press, Orlando.

[14] Raithby, G. D., and Chui, E. H., 1990, "A Finite-Volume Method for Predicting a Radiant Heat Transfer in Enclosures With Participating Media," ASME J. Heat Transfer, **112**, pp. 415–423.

[15] Chai, J. C., Lee, H. S., and Patankar, S. V., 1994, "Finite Volume Method for Radiation Heat Transfer," J. Thermophys. Heat Transfer, **8**, pp. 419–424.

[16] Chai, J. C., Lee, H. S., and Patankar, S. V., 1993, "Ray Effect and False Scattering in the Discrete Ordinates Method," Numer. Heat Transfer, Part B, **24**, pp. 373–389.

[17] Raithby, G. D., 1999, "Evaluation of Discretization Errors in Finite-Volume Radiant Heat Transfer Predictions," Numer. Heat Transfer, Part B, **36**, pp. 241–264.

[18] Coelho, P. J., 2002, "The Role of Ray Effects and False Scattering on the Accuracy of the Standard and Modified Discrete Ordinates Methods," J. Quant. Spectrosc. Radiat. Transf., **73**, pp. 231–238.

[19] Walton, G., 2002, Calculation of Obstructed View Factors by Adaptive Integration, Tech. Rep. NISTIR 6925, NIST.

Identification of Unknown Heating Elements Embedded in a Rectangular Package

Chin-Hsiang Cheng[1]
e-mail: cheng@ttu.edu.tw

Mei-Hsia Chang

Department of Mechanical Engineering,
Tatung University, 40 Chungshan N. Road,
Sec. 3, Taipei, Taiwan 10451, R.O.C.

The aim of this study is to present a novel inverse heat transfer method, which incorporates an automatic-filter scheme with the conjugate gradient method, for identifying shapes and temperatures of heating elements embedded in a rectangular package. In this report, shapes of the heating elements are visualized by using node-matrix images. A group of unknown heating elements with different shapes, positions, and temperatures are nondestructively identified simply based on the data of the upper surface temperature of the rectangular package. Effects of temperature measurement uncertainty, grid size, and number of measurement points on the top surface on the identification accuracy are evaluated. Results show that the geometric and thermal conditions of the embedded heating elements can be predicted precisely by using the present approach. The approach is found to be stable and insensitive to the temperature measurement uncertainty, and, without overwhelming mathematical manipulation, the form of objective function becomes flexible. [DOI: 10.1115/1.1929782]

Keywords: Identification, Automatic filter, Node matrix, Inverse Heat Transfer, Package

Introduction

In the past several decades, inverse analysis has been widely applied to solve engineering problems. In the heat transfer area, external inverse problems include estimation of temperature, heat flux, or heat transfer coefficient [1–6], and internal inverse problems include determination of thermophysical properties, such as thermal conductivity and heat capacity [7–10]. In addition, the inverse analysis has also been applied to the problems related to shape design [11–16] and shape identification [17–21].

For the identification of unknown boundary shape, Huang and Chao [17] solved an inverse heat conduction problem to detect the unknown irregular boundary shape with the help of the boundary element method. More recently, Cheng and Chang [18] developed an inverse approach that is particularly suitable to the shape identification for a relatively complicated boundary configuration, for example, a zigzag boundary. Park and Shin [19] dealt with a number of shape-identification problems subject to natural convection. In their report, the location of a part of the system boundary is determined from temperature measurements on other parts of the boundary. Detection of possible damage in the mechanical structures is also an important topic. dos Santos et al. [20] proposed a numerical model to identify damages in structures without knowledge of the possible damaged areas. Burczynski and Beluch [21] performed multiple-crack identification in a structure by using the boundary element method and evolutionary algorithms. The problem of estimating the internal heat sources in a body by using the inverse method has also been considered. A series of researches for identifying the location and strength of the heat sources placed in a homogeneous domain were performed by Le Niliot [22], Lefévre and Le Niliot [23], and Le Niliot and Lefévre [24].

The inverse method may be extended to identify both geometric and physical variables simultaneously. For instance, a system-identification scheme based on a minimization method of least-squared errors between measured and calculated displacements by a boundary element model was utilized by Lee et al. [25] to simultaneously determine the geometric shape and elastic material properties of an inclusion in a finite body. An experimental apparatus and a numerical method are presented in by Abou Khachfe and Jarny [26] to predict both the location and the time-varying strength of point heat sources within a body from boundary temperature measurements.

For a solid medium containing heating elements, as usually seen in electronic packaging or electrical heaters, the geometric and thermal conditions of the internal heating elements are regarded as essential information that may have profound influence on the temperature of the solid medium as well as its surroundings. Unfortunately, in general the related information of the internal heating elements is not known because the heating elements are embedded inside the solid medium and invisible. The information on the unknown internal heating elements is not easy to obtain by direct measurement; therefore, inverse methods for identification of the unknown heating elements embedded in a package may be used alternatively and, hence, are worthy of investigation. The present study presents an automatic-filter scheme, which is incorporated with the conjugate gradient method, for identifying the shape, position, temperature, and number of the unknown internal heating elements based on the inverse heat transfer concept. The inverse approach is nondestructive to the package and simply based on the data of the upper surface temperature. Its capability is evaluated for several practical test cases.

A schematic of the rectangular package is shown in Fig. 1. One may expect several flat heating elements embedded in the rectangular package; however, they are invisible and their geometrical and physical conditions are unknown. The rectangular package of length L, width W, and height H is cooled by ambient air, while the bottom surface of it is insulated. The z-direction location of the heating elements is fixed at $z=Z_e$. Heat is generated from the heating elements at temperature T_H, transferred toward the outer surface by conduction, and then dissipated to the ambient at temperature T_a by convection. The heat transfer coefficient on the outer surface is denoted by h. An array of temperature sensors is installed on the top surface to measure the surface temperature as shown in Fig. 2. In this study, the possibility of identifying shapes, positions, temperatures, and number of the heating elements simply based on these top surface temperature data is investigated. Dependence of the accuracy of identification on the temperature

[1]Corresponding author.

Contributed by the Heat Transfer Division for publication in the JOURNAL OF HEAT TRANSFER. Manuscript received by the Heat Transfer Division November 20, 2003; revision received March 15, 2005. Review conducted by: G. S. Dulikravich.

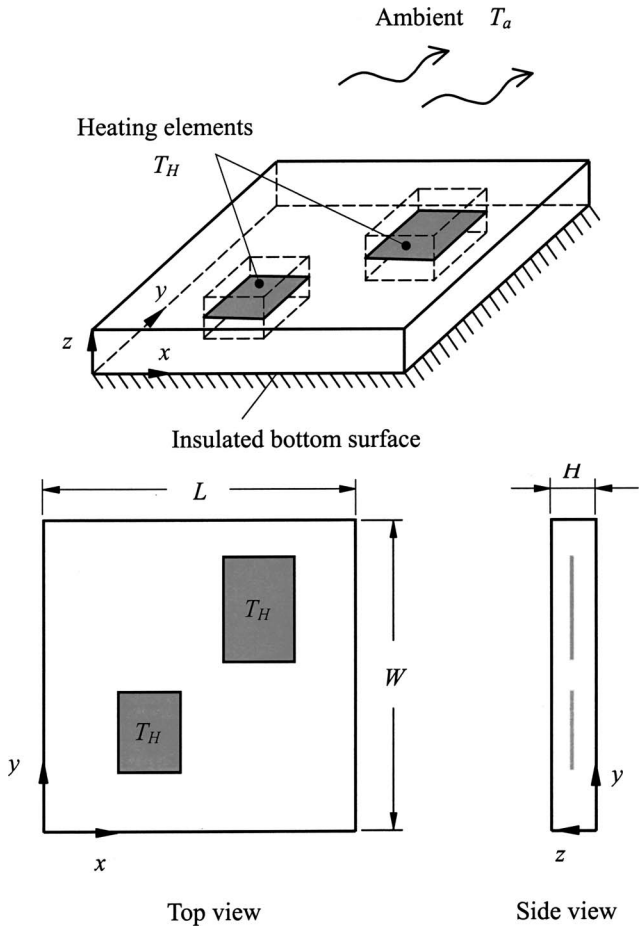

Fig. 1 Physical model for the test cases

measurement uncertainty, grid size, and number of temperature measurement points on the top surface has been evaluated.

Heat Conduction Problem Solver

Heat conduction in a homogeneous, isotropic medium is governed by the following partial differential equation:

$$\rho C\frac{\partial T}{\partial t} = k\nabla^2 T + q^* \tag{1}$$

where q^* denotes the internal heat source; ρ, C, and k are the density, heat capacity, and thermal conductivity of the solid material, respectively; and T is the temperature. The present approach is built up based on the steady thermal behavior of the package. Thus, a three-dimensional steady-state heat conduction equation without internal heat source is solved herein. That is,

$$\frac{\partial^2 T}{\partial x^2} + \frac{\partial^2 T}{\partial y^2} + \frac{\partial^2 T}{\partial z^2} = 0 \tag{2}$$

For these test cases, the boundary conditions are expressed as

$$\frac{\partial T}{\partial z} = 0 \text{ for the bottom surface (at } z = 0) \tag{3a}$$

$$\pm k\frac{\partial T}{\partial n} = h[T - T_a] \text{ for other surfaces} \tag{3b}$$

$$T = T_H \text{ at image matrix nodes visualizing heating elements} \tag{3c}$$

where n represents the coordinate normal to individual surface.

Equations (2) and (3*a*)–(3*c*) are then discretized to yield a set of simultaneous algebraic equations by the finite-difference method. With the help of the successive-overrelaxation method (SOR) [27], the numerical solution for the three-dimensional temperature distribution at $NX \times NY \times NZ$ grid points within the rectangular package can be obtained.

The number of variables ought to be limited to reduce the computational effort. Therefore, some variables are fixed for the base case in the present computation. These fixed variables are listed in Table 1. The shapes of these heating elements are approximated by the images of node matrix. It is a grid point satisfying an assessment criterion that is accepted as a node of the image matrix. The assessment of acceptance or rejection for a grid point to become an image matrix node is based on an automatic-filter scheme, which will be described in detail later. In addition, note that the temperature of the heating element T_H is another variable to identify. The heat conduction problem solver developed should be capable of predicting the change in the temperature solutions directly in response to a change in T_H or in heating element shapes.

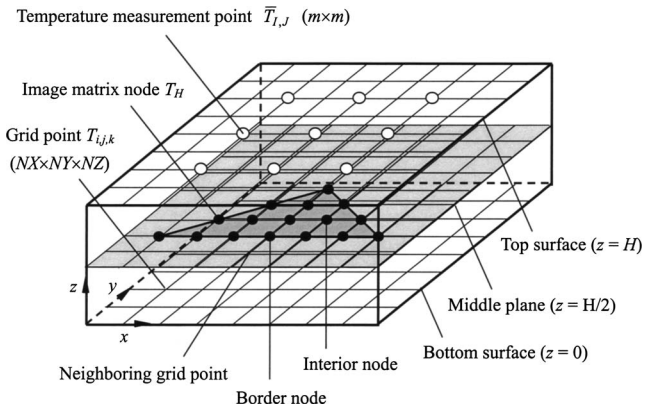

Fig. 2 Grid points, temperature measurement points, and image matrix nodes

Table 1 Fixed variables of the base case

Variable
Package
$L = 5$ cm
$W = 5$ cm
$H = 0.3$ cm
Heating element
$Z_e = H/2 = 0.15$ cm
Surface convection
$h = 10$ W/(m^2. °C)
$T_a = 25$ °C

Inverse Problem

In this study, shapes, positions, temperatures, and even the number of the heating elements in a package are regarded as unknown geometrical and physical conditions to identify. Here, inverse identification of these geometrical and physical conditions based on temperature data measured at $m \times m$ points on the top surface (at $z=H$) is attempted. The temperature data at $m \times m$ points on the top surface may be collected by using an array of distributed temperature sensors or, instead, by an infrared radiation (IR) thermal image system for a global measurement.

Let the temperature measurement data on the top surface be denoted by $\overline{T}_{I,J}$ ($I=1,\ldots,m$, and $J=1,\ldots,m$), and let $T_{i,j,k}$ denote the numerical temperature solution at the grid point (i,j,k) with $i=1,\ldots,NX$, $j=1,\ldots,NY$, and $k=1,\ldots,NZ$. Figure 2 illustrates the grid points, the temperature measurement points on the top surface, and the image matrix nodes visualizing the heating elements. The number of temperature measured points is less than or equal to the number of grid points on the top surface. An objective function of the present inverse problem is defined as

$$J = \sum_{i=1}^{NX} \sum_{j=1}^{NY} \delta_{iI}\delta_{jJ}(T_{i,j,NZ} - \overline{T}_{I,J})^2 \tag{4}$$

Note that the temperatures at the grid points on the top surface $T_{i,j,NZ}$ are provided by the heat conduction problem solver and the temperatures at the measurement points $\overline{T}_{I,J}$ are obtained by experiment. During the identification process, the geometry and temperature of the heating elements are updated iteratively toward minimization of the objective function. The minimization of the objective function makes the difference between $T_{i,j,NZ}$ and $\overline{T}_{I,J}$ to reach an extreme minimum value.

Automatic-Filter Method for Geometry Identification

Each existing image node located on the border of the shape image is reviewed individually in each iteration based on the sensitivity analysis. A grid point can be accepted as a new image node, or, on the contrary, an existing image node can be rejected and then become a grid point again. In this manner, the images of the heating elements can be adjusted until the minimization of the objective function is achieved. By means of the image node matrix method, the awkwardness of continuous numerical grid generation, which is required to fit the varying shapes in iteration (as described by Cheng and Chang [18]), is no longer needed. The criterion of acceptance or rejection for the image nodes is named the *automatic-filter method* in this study, which consists of three major steps.

Step 1. Detection of border nodes and neighboring grid points. To adjust the images of the heating elements, it is not necessary to review all the image nodes within the image areas in each iteration. To save the computation time, only the image nodes located on the borders of the images are reviewed. Therefore, the *border nodes* (BNs) must be detected in the first step. Be reminded that the image nodes are located on the middle plane at $z=Z_e$, and their temperature is T_H. If an existing image node is surrounded by four other image nodes on the middle plane, the existing image node is recognized as an *interior node* within the shape area. However, if at least one normal grid point is found in the immediate surroundings of the image node, the image node is referred to as a BN. The BNs are the ones to be reviewed to determine whether it is still accepted as an image node or rejected. When it is rejected, the BN will be changed to be a normal grid point.

On the other hand, a normal grid point that is surrounded by at least one image node is referred to as a *neighboring grid point* (NGP). Each of the NGPs is also reviewed to see if it is accepted to become a new image node or rejected. When it is rejected, the NGP will remain as a normal grid point.

Step 2. Objective function drop. Once the BNs and NGPs are recognized, the sensitivity analysis is performed to review each of them. The objective function jump ΔJ caused by a point state change from a BN to a grid point or from a NGP to an image node is calculated with

$$\Delta J_{ip}^n = J_{ip\ \text{change}}^n - J_{ip\ \text{orig}}^n, \quad n = 1 \sim \text{maximum iterations} \tag{5}$$

where ip is the common index of BNs and NGPs, and n denotes the iteration step. Only when ΔJ is negative, which implies that the point state change leads to an objective function drop, the state change of the reviewed BN or NGP is possible to be accepted. Otherwise, the point state change is denied immediately.

Step 3. Filter. The BNs or NGPs that lead to a reduction in the objective function value are forwarded to further assessment for point state changes. The assessment is based on two artificially defined rules (ADRs)

$$\text{Rule 1:} \quad |\Delta J_{ip}^n| > f^n \tag{6a}$$

$$\text{Rule 2:} \quad R_{ip} \geqslant \varepsilon_{cr} \tag{6b}$$

In application of Rule 1, the pass value f^n is decreased from an initial positive value f^o to zero at a controlled decrease rate with

$$f^n = f^{n-1} - c, \quad n = 1 \sim \text{maximum iterations} \tag{7}$$

where c is a positive coefficient that must be given properly, depending on individual cases. An optimal value of c can be determined in a trial-and-error process. In general, the value of c is chosen within the range between 1.0 and 10.0 in this study. By following Rule 1, only the BNs and NGPs that could produce a significant objective function drop greater than the pass value f are allowed to change their point states. As the iteration process progresses, the magnitudes of ΔJ_{ip}^n, for almost all the BNs and NGPs, are decreased. Therefore, the pass value f is also reduced by c per iteration with Eq. (7). In this manner, eventually ΔJ_{ip}^n approaches zero in a finite number of iterations, and the images having very small objective functions will be obtained. This is called a *subprocess* in which the value of f is decreased from $f=f^o$ to $f=0$. When the pass value f approaches zero at the end of a subprocess, the possible objective function drops caused by changes of the point states of BNs or NGPs (ΔJ_{ip}^n) also become negligibly small, and thus the objective function J reaches a local minimum $J_{\min}$ to obtain an image. Therefore, the obtained image is recorded as one of the desired candidate images.

The pass value f functions like the mesh size of a *filter*. The filter allows only the favorable changes of the node state to pass and take place. The initial pass value f^o should be properly selected to facilitate the subprocess. If f^o is lowered, the number of BNs and NGPs that pass Rule 1 will be increased. In this situation, the iterative shape will experience a severe variation or even oscillation in iteration. On the contrary, if f^o is elevated, more computer time will be consumed in a subprocess and the whole computation speed will be slowed down. It is suggested that f^o is given with the maximum objective function drop among all the BNs and NGPs in the first iteration of a new subprocess. That is,

$$f^o = \max(\Delta J_{ip}, ip = 1,2,3,\cdots) \,|\, \text{1st iteration of a subprocess} \tag{8}$$

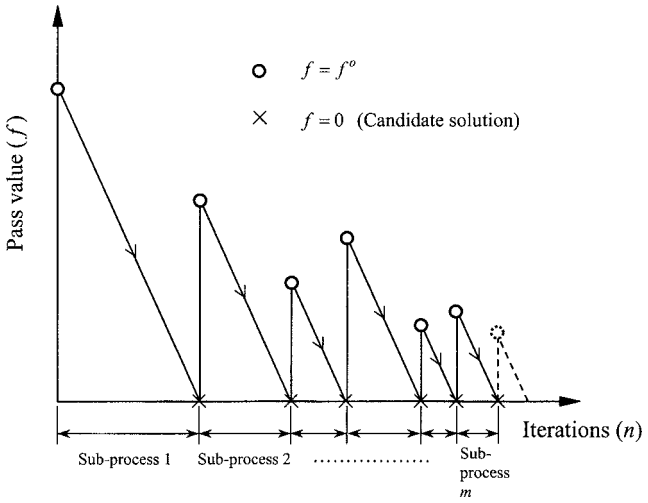

Fig. 3 Illustration for the variation of pass value f in a series of subprocesses in iteration

When a subprocess comes to an end, another initial guess of the image is generated by randomly adding (or deleting) a number of image nodes to the latest obtained image, a new initial value is assigned to the pass value f with Eq. (8), and a new subprocess is started to obtain another candidate image. The number of the added (or deleted) BNs and NGPs and their locations to form a new initial image guess at the beginning of a subprocess are determined based on Rule 2. By repeating a series of the subprocesses, a number of candidate image solutions will be collected, not only one solution. Among these candidate images, the best image with extremely minimum value of objective function can be readily chosen to represent the shape of the heating element when necessary.

In Rule 2, R_{ip} is a random number generated for each of the BNs or NGPs considered, and ε_{cr} is a critical value specified by the users. Only the BN or NGP whose R_{ip} is greater than ε_{cr} is possible to change the point state. In this study, ε_{cr} is assigned to be 0.95 for all the test cases considered.

A typical variation of the pass value f in a series of subprocesses is shown in Fig. 3. The candidate images at the ends of the subprocesses at $f=0$ are collected.

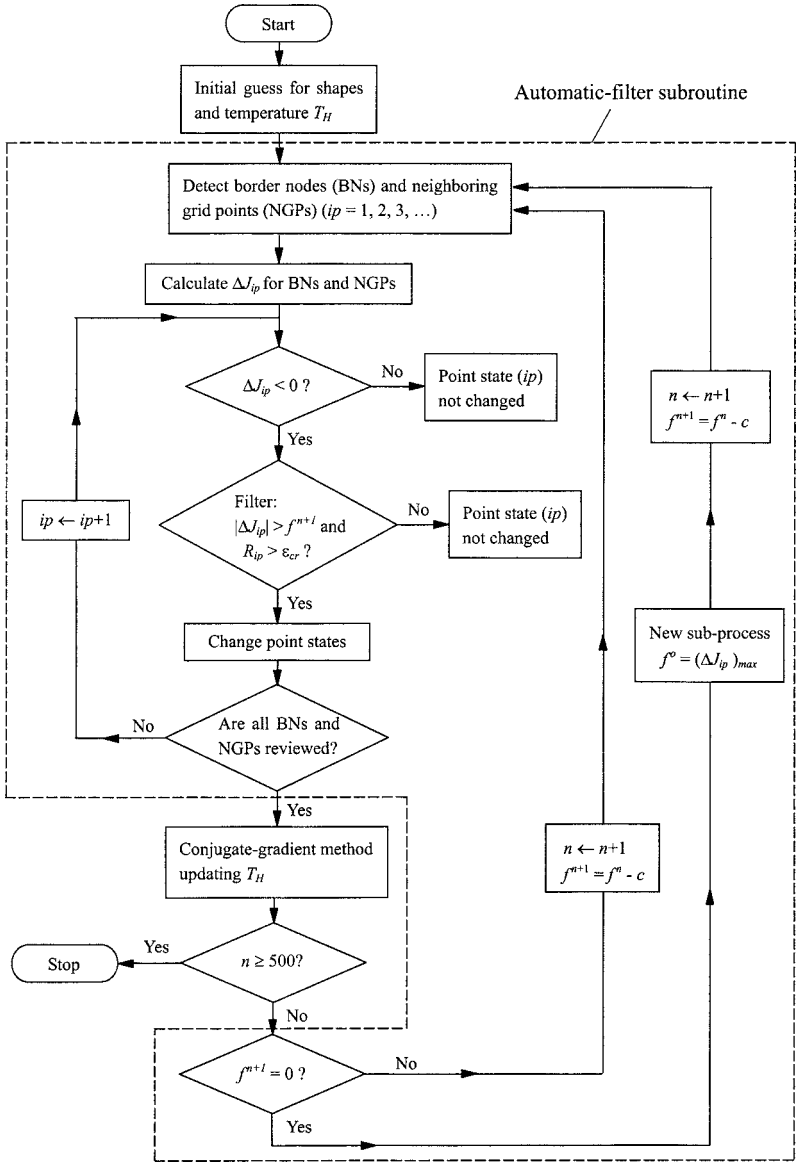

Fig. 4 Flowchart of the process for geometry and temperature identification

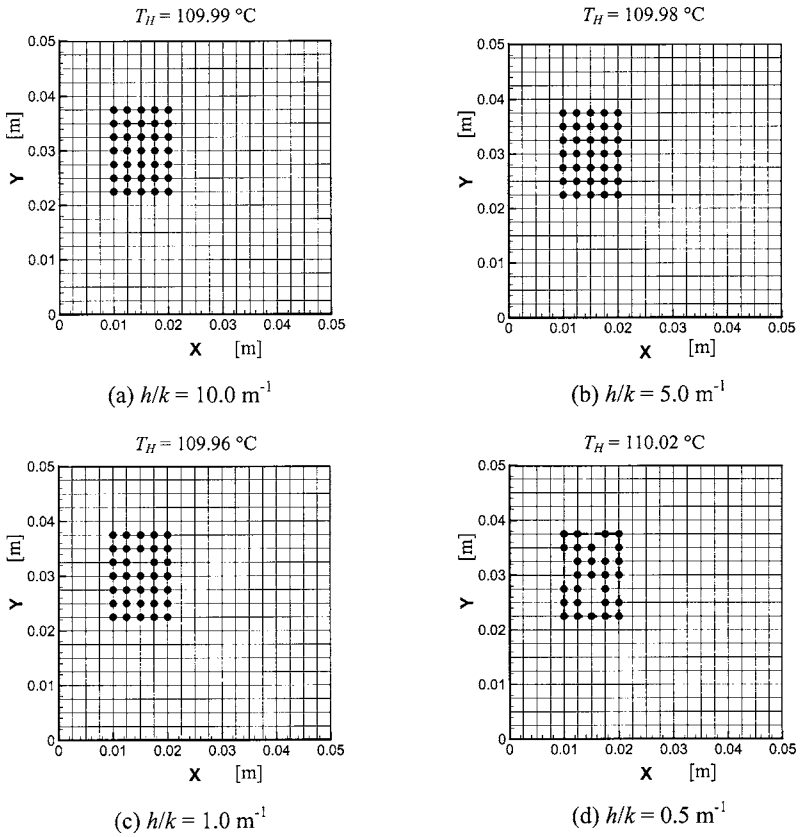

(a) $h/k = 10.0\ \mathrm{m}^{-1}$ (b) $h/k = 5.0\ \mathrm{m}^{-1}$

(c) $h/k = 1.0\ \mathrm{m}^{-1}$ (d) $h/k = 0.5\ \mathrm{m}^{-1}$

Fig. 5 Effects of h/k on the accuracy of geometry and temperature identification at $\sigma=0$ and $m\times m=21\times 21$. The exact heating element temperature $T_{H,ex}$ is fixed at 110.00 °C.

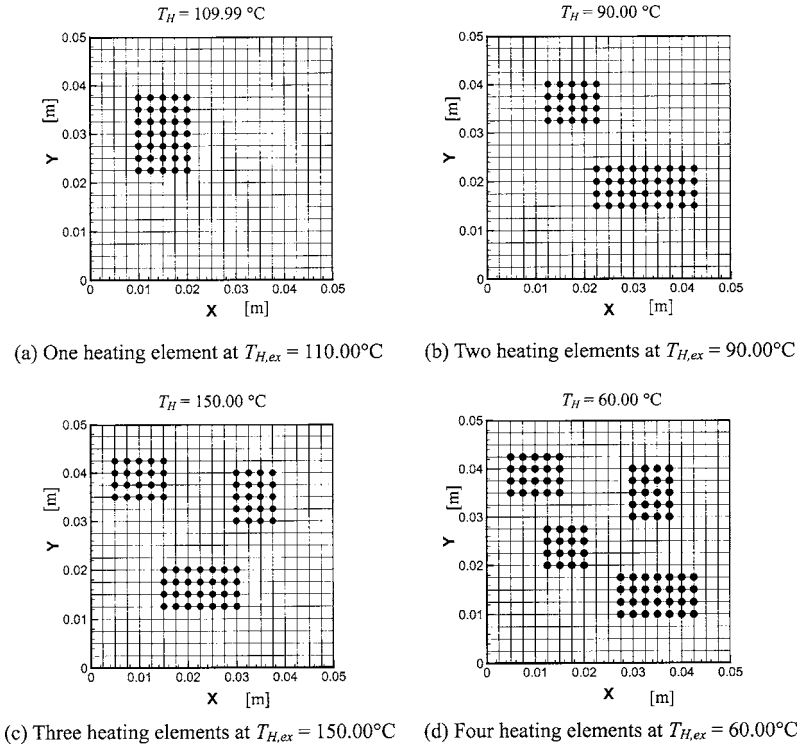

(a) One heating element at $T_{H,ex} = 110.00$°C (b) Two heating elements at $T_{H,ex} = 90.00$°C

(c) Three heating elements at $T_{H,ex} = 150.00$°C (d) Four heating elements at $T_{H,ex} = 60.00$°C

Fig. 6 Geometry and temperature identification for different numbers of heating elements. Multiples heating elements embedded in a package have equal exact temperatures. The cases at $h/k=10.0\ \mathrm{m}^{-1}$, $\sigma=0$, and $m\times m=21\times 21$. (*a*) 110.00 °C, (*b*) 90.00 °C, (*c*) 150.00 °C, and (*d*) 60.00 °C.

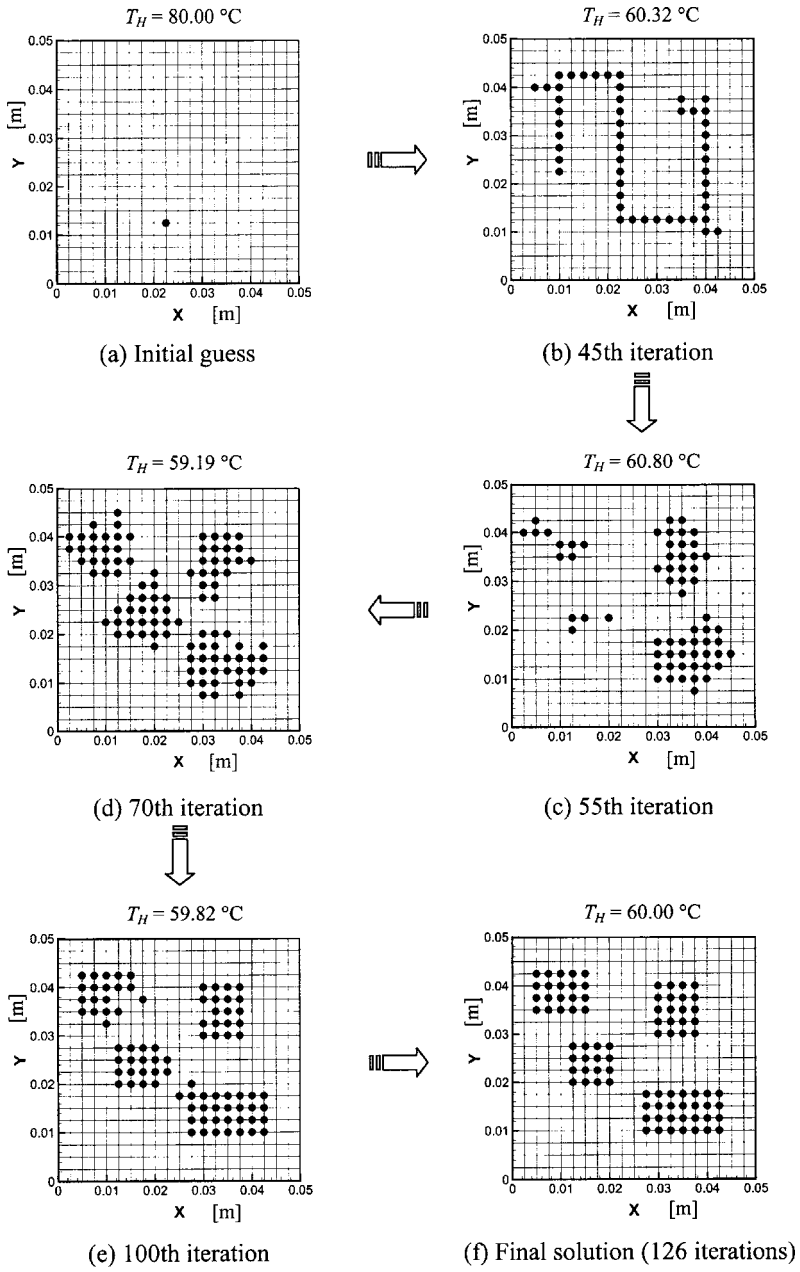

Fig. 7 Iteration process of geometry and temperature identification for the case considered in Fig. 6(*d*) ($T_{H,ex}$=60.00 °C)

By using the automatic-filter method, the geometry identification is carried out based on the ADRs, which are quite straightforward without overwhelming mathematical manipulation. In addition, the approach is not limited to the objective function defined in form of a least-squares summation as in Eq. (4). When necessary, a more flexible form may be applied.

Conjugate-Gradient Method for Temperature Identification

The conjugate gradient method is employed to predict the temperature of the heating elements along with the shape identification, in search of the minimization of the objective function. This method has been well documented in Refs. [3,7,28], and hence it is described only briefly in this report.

In the following, the sequence of the iterative temperature identification process is summarized:

1. Specify all the boundary conditions and material properties. The geometrical conditions are received from the geometry identification by the automatic-filter method.
2. Make an initial temperature guess for the temperature of the heating element T_H.
3. Use the heat conduction problem solver to obtain the temperature distribution within the package.
4. Calculate the objective function J. When n reaches the maximum iteration step number, the iteration process is terminated. When the convergence criterion of J is satisfied, proceed to the next geometry identification process. Otherwise, proceed to step 5. The convergence criterion for the temperature identification is set to be 10^{-4}.

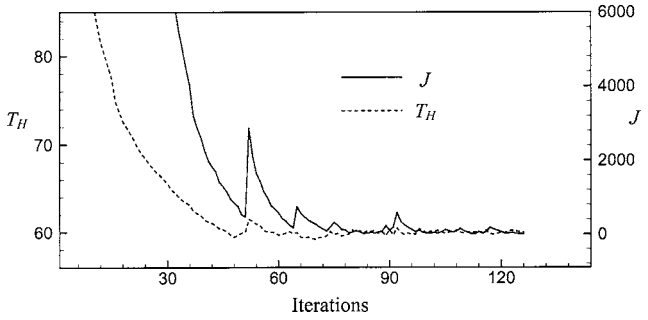

Fig. 8 Variation of objective function and temperature of heating elements for the case considered in Fig. 6(*d*)

5. Perform the sensitivity analysis to determine the gradient functions. The sensitivity equation can be derived as follows:

$$\frac{\partial^2}{\partial x^2}\left(\frac{\partial T}{\partial T_H}\right)+\frac{\partial^2}{\partial y^2}\left(\frac{\partial T}{\partial T_H}\right)+\frac{\partial^2}{\partial z^2}\left(\frac{\partial T}{\partial T_H}\right)=0 \tag{9}$$

The boundary conditions associated with the above equation are

$$\frac{\partial}{\partial z}\left(\frac{\partial T}{\partial T_H}\right)=0 \text{ for the bottom surface (at } z=0) \tag{10a}$$

$$\pm k\frac{\partial}{\partial n}\left(\frac{\partial T}{\partial T_H}\right)=h\frac{\partial T}{\partial T_H} \text{ for other surfaces} \tag{10b}$$

$$\frac{\partial T}{\partial T_H}=1 \text{ at image matrix nodes visualizing heating elements} \tag{10c}$$

The solution for sensitivity $\partial T/\partial T_H$ is obtained by solving Eqs. (9) and (10*a*)–(10*c*). A numerical method similar to that used for Eqs. (2) and (3*a*)–(3*c*) is employed. The obtained solution for $\partial T/\partial T_H$ is then introduced to calculate the gradient function $\partial J/\partial T_H$ as

$$\frac{\partial J}{\partial T_H}=\sum_{i=1}^{NX}\sum_{j=1}^{NY}2\delta_{iI}\delta_{jJ}(T_{i,j,NZ}-\overline{T}_{I,J})\frac{\partial T_{i,j,NZ}}{\partial T_H} \tag{11}$$

6. Calculate the conjugate gradient coefficients γ^n and search directions P^n with

$$\gamma^n=\left[\left(\frac{\partial J}{\partial T_H}\right)^n\Big/\left(\frac{\partial J}{\partial T_H}\right)^{n-1}\right]^2 \tag{12}$$

$$P^n=\frac{\partial J}{\partial T_H}+\gamma^n P^{n-1} \tag{13}$$

7. Calculate the step size β^n that leads to $\partial J^{n+1}/\partial\beta=0$ with

$$\beta^n=\frac{\sum_{i=1}^{NX}\sum_{j=1}^{NY}\delta_{iI}\delta_{jJ}(T_{i,j,NZ}-\overline{T}_{I,J})\left(P^n\frac{\partial T_{i,j,NZ}}{\partial T_H}\right)}{\sum_{i=1}^{NX}\sum_{j=1}^{NY}\left(P^n\frac{\partial T_{i,j,NZ}}{\partial T_H}\right)^2} \tag{14}$$

8. Update the temperature of the heating elements with

$$T_H{}^{n+1}=T_H{}^n-\beta^n P^n \tag{15}$$

and then proceed to step 3 again.

The flowchart of the combination of the geometry and the temperature identification methods is provided in Fig. 4. In each iteration, updated geometry of heating elements will be first generated by the automatic-filter method, and then the temperature of heating elements will be predicted by the conjugate gradient method. In the present study, the maximum number of iteration steps is set to be 500. Before the maximum iteration number is reached, the present approach leads to 20–30 candidate images and temperatures due to the repeating initiation of subprocesses.

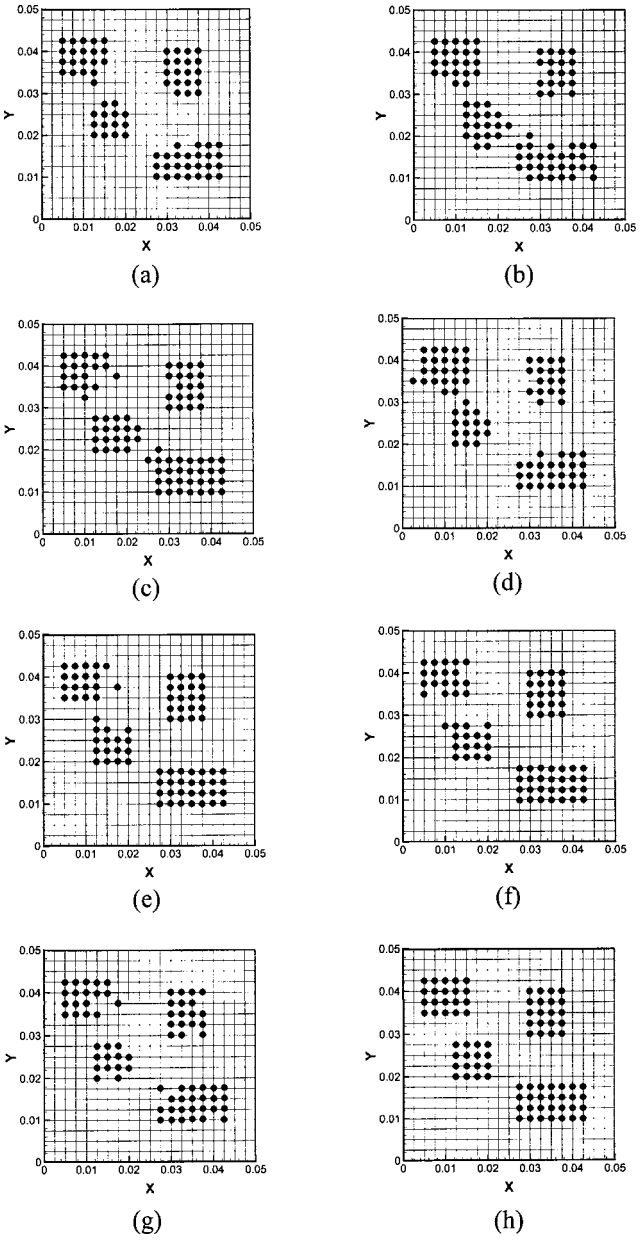

Fig. 9 Several obtained candidate images for the case considered in Fig. 6(*d*)

Simulated Experimental Data

In this study, the temperature measurement data on the top surface ($\overline{T}_{i,j,NZ}$) are simulated by adding a perturbation to the exact solution. That is,

$$\overline{T}_{i,j,NZ}=(T_{i,j,NZ})_{ex}+\sigma\boldsymbol{r}_{i,j} \tag{16}$$

where $(T_{i,j,NZ})_{ex}$ is the exact temperature solution at the grid points on the top surface for a particular case with specified geometry and temperature of interest, $\boldsymbol{r}_{i,j}$ is a random number evenly distributed between −1 and 1 and is provided by a random number

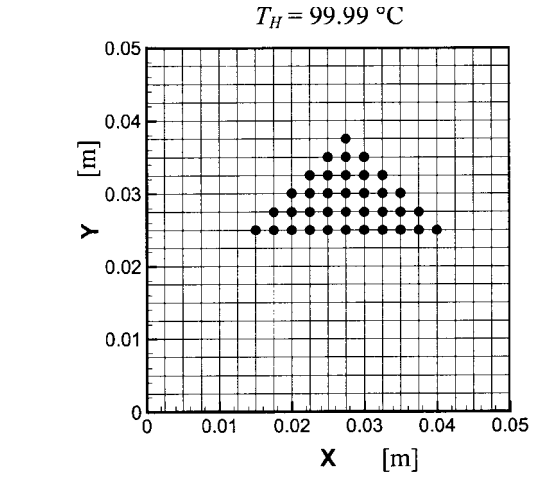

(a) Triangular heating element at $T_{H,ex}$ = 100.00°C

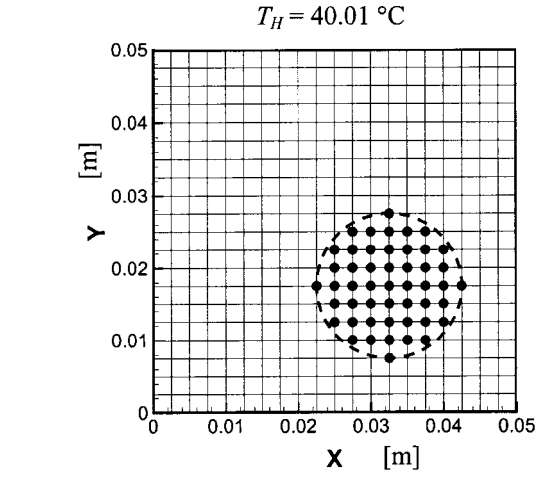

(b) Circular heating element at $T_{H,ex}$ = 40.00°C

Fig. 10 Results of geometry and temperature identification for various shapes at h/k=10.0 m^{-1}, σ=0, and $m \times m$=21×21

generator, and σ is a value given to simulate the uncertainty of experiments. Note that at $\sigma=0$, the exact top-surface temperature solution, $(T_{i,j,NZ})_{ex}$, is used directly for the inverse geometry and temperature identification.

Results and Discussion

The inverse heat transfer approach has been applied to a number of test cases to investigate its performance. A computational grid with $21\times21\times5$ nodes is adopted for most of the test cases. However, grid number effects are also evaluated by considering $41\times41\times5$ and $61\times61\times5$ grids and the results will be shown in this section. Typically, the initial guess for the image node matrix for a whole process contains only one single node located at x =0.0225 cm, y=0.0125 cm, and the initial guess for the heating element temperature is 80.00 °C.

A relative error probability of geometry identification defined by the ratio of the number of incorrectly identified image nodes M_w to the number of the grid points on the middle plane ($NX \times NY$) as

$$\xi_g = M_w/(NX \times NY) \tag{17}$$

To quantify the accuracy of the temperature identification, a relative error of temperature is defined as

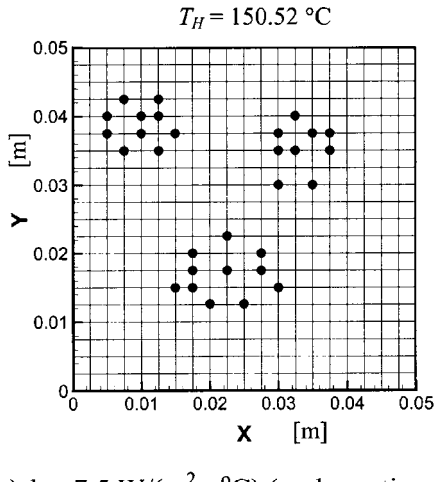

(a) h = 7.5 W/(m^2 · °C) (under-estimation)

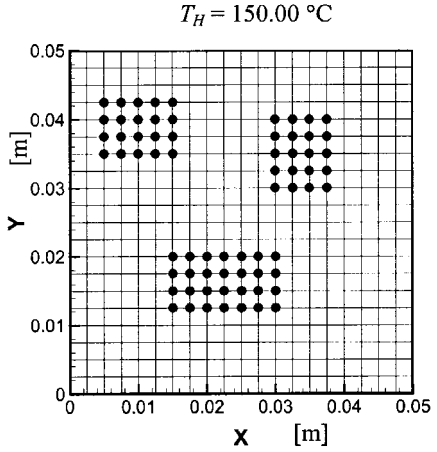

(b) Exact solution at h = 10 W/(m^2 · °C)

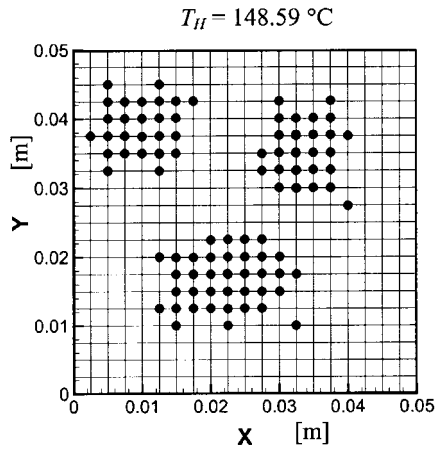

(c) h = 15 W/(m^2 · °C) (over-estimation)

Fig. 11 Effects of error in heat transfer coefficient on geometry and temperature identification for the case considered in Fig. 6(c). The exact heating element temperature $T_{H,ex}$ is fixed at 150.00 °C.

$$\xi_T = \left| \frac{T_H - T_{H,ex}}{T_{H,ex}} \right| \tag{18}$$

where $T_{H,ex}$ represents the exact heating element temperature.

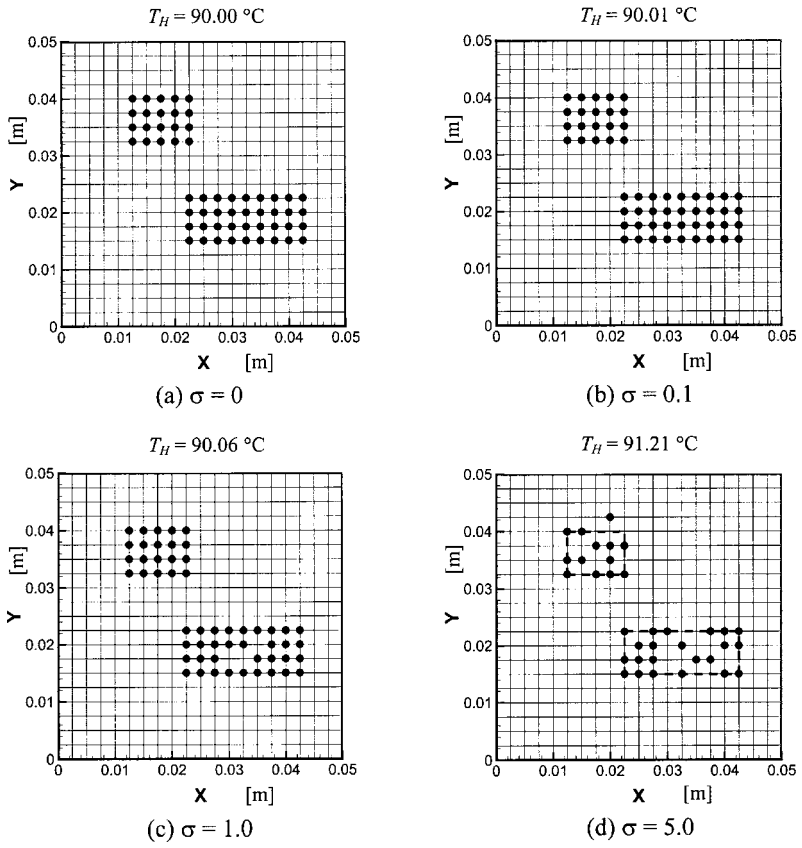

Fig. 12 Effects of temperature measurement uncertainty on geometry and temperature identification for the case considered in Fig. 6(*b*). The exact heating element temperature $T_{H,ex}$ is fixed at 90.00 °C.

Figure 5 illustrates the identification results at various ratios of heat transfer coefficient h to thermal conductivity k. The ratio h/k is assigned to be 10.0, 5.0, 1.0, and 0.5 m^{-1}. For the cases shown in this figure, the number of temperature measurement points ($m \times m$) is set to be 21×21 and the measurement uncertainty $\sigma = 0$. The exact shape of the heating element is a rectangle, which can be seen in Fig. 5, and the exact temperature $T_{H,ex}$ is assigned to be 110 °C. A lower value of h/k tends to increase the uniformity of temperature distribution within the rectangular package. Therefore, the temperature gradient along the top surface of the rectangular package becomes less appreciable such that the conditions of heating elements are more difficult to identify. The node matrix images shown in Fig. 5 reflect the expectation that the error of the geometry identification increases as the value of h/k is decreased. The relative error probability of geometry identification ξ_g is up to 1.58% at $h/k = 0.5$ m^{-1}. However, the temperature identification is rather accurate even at lower h/k. In this figure, it is observed that $\xi_T = 0.016\%$ at $h/k = 0.5$ m^{-1}.

In order to investigate the applicability for identifying multiple heating elements, the cases with one, two, three, and four rectangular heating elements are studied and the results are shown in Fig. 6. The temperature of multiple heating elements embedded in a package are equal, and their exact temperatures in Figs. 6(*a*)–6(*d*) are 110.00, 90.00, 150.00, and 60.00 °C, respectively. The cases considered are at $h/k = 10.0$ m^{-1}, $\sigma = 0$, and $m \times m = 21 \times 21$. It is observed in Fig. 6 that the identification for different numbers of heating elements at different temperatures leads to satisfaction. For the cases shown in this figure, the images of all the heating elements are clearly visualized, and the identified temperatures are 109.99, 90.00, 150.00, and 60.00 °C, which closely agree with the exact values. However, it is important to mention that the identified results are very precise because (i) the measurement data are taken on the top surface where desired temperatures are located and (ii) exact temperature data are being used. Moreover, because measured data and desired parameters are located on the same surface, the quasi-inverse problem instead of the inverse problem has been solved.

The iteration process of geometry and temperature identification for the case shown in Fig. 6(*d*) is displayed in Fig. 7. The exact geometry of this case contains four rectangular heating elements with different dimensions and positions. The exact temperature of the heating elements is 60.00 °C, and the initial temperature is set at 80.00 °C. The initial node matrix, having only one node located at $x = 0.0225$ cm, $y = 0.0125$ cm, is seen in Fig. 7(*a*), and the interesting variation of the node matrix during the iteration process is clearly observed.

Figure 8 illustrates the variations of objective function and heating element temperature for the same case considered in Fig. 6(*d*). The solid line and the dashed curves represent the variations of J and T_H, respectively. It is found that J and T_H are rapidly decreased to their respective minimum values in around 130 iterations. These local peaks of the curves indicate the onsets of the subprocesses. In this figure, approximately 12 subprocesses are observed and hence 12 candidate images are collected. Parts of the candidate images for the shapes of the heating elements for the case studied in Fig. 6(*d*) are shown in Fig. 9. It is found that all the candidate images look similar to each other. The best solution among them is shown in Fig. 9(*h*), which is perfectly identical to the exact one.

Geometry and temperature identifications for various shapes, at $h/k = 10.0$ m^{-1}, $\sigma = 0$, and $m \times m = 21 \times 21$, are shown in Fig. 10. In this figure, performance of the present approach in dealing with the triangular and circular shapes is investigated. Figures 10(*a*) and 10(*b*) show the results for a triangular heating element at

100.00 °C and a circular heating element at 40.00 °C, respectively. The dashed lines shown in Fig. 10(*b*) reveal the exact shape of the heating element. It is found that the geometry and temperature are clearly identified for both shapes.

To evaluate the effects of the uncertainty in heat transfer coefficient measurement, in Fig. 11 a deviation of ±50% in the heat transfer coefficient is introduced into the exact value and then the accuracy of geometry and temperature identification is investigated. The exact geometry and temperature are yielded at $h=10$ W/(m^2 °C). Results show that an overestimation in h leads to larger number of the image nodes and lower heating element temperature as well. For example, when h is assigned to be 15 W/(m^2 °C) incorrectly, the areas of the heating elements shown in Fig. 11(*c*) are obviously larger than the exact ones, and the temperature of the heating elements are predicted to be only 148.59 °C. On the contrary, as illustrated in Fig. 11(*a*), an underestimation in h leads to insufficient image nodes and higher heating-element temperature predictions.

The effects of temperature measurement uncertainty on geometry and temperature identification are also investigated. Figure 12 shows the identified geometries and temperatures at $\sigma=0$, 0.1, 1.0, and 5.0. For these cases, the exact temperature of heating element is 90.00 °C. It is obvious that the discrepancy between the identified and the exact geometry increases with uncertainty. However, when σ is lower than 1.0, which represents that there exist around 1% measurement error in the experiment data, the discrepancy is negligibly small. This implies that the inverse heat transfer method is rather stable and insensitive to uncertainty in temperature measurement. However, when σ is elevated to 5.0, which represents that there exist around 5% measurement error in the experiment data, the discrepancy is remarkable (which reaches approximately 5.21% in terms of the relative error probability of geometry identification ξ_g). Nevertheless, the relative error of temperature identification ξ_T is only 1.34% at $\sigma=5.0$.

The height of the package H is one of major parameters affecting the accuracy of geometry and temperature identification. Effects of package height are evaluated at $H=0.1$, 0.3, and 0.6 cm for the cases studied in Fig. 6(*b*), and the results are shown in Fig. 13. It is observed that a thicker package leads to greater error in identification. The thermal images in a thicker package are harder to identify based on the surface temperature data because the thermal diffusion length from the heating elements to the package surface is longer in the thicker package.

The cost of the experiment is reduced when the number of temperature measurement points is decreased. Now, a question arises: How many temperature measurement points are enough for identification of geometry and temperature of the heating elements? To answer this quation, the effects of number of measurement points on the top surface are evaluated and the results are presented in Fig. 14. In the right side of Fig. 14, the variations of T_H are also shown. The case considered is with one heating element at $h/k=10$ m^{-1}, $\sigma=0$, and $T_{H,ex}=110.00$ °C. The number of measurement point ($m\times m$) is assigned to be 11×11, 6×6, 4×4, and 2×2. It is observed that when the number of measurement points is $\geqslant(6\times6)$, the geometry and temperature of the heating element are identified accurately. However, for the cases whose measurement point number is $<(6\times6)$, the image node matrices may not give a clear picture for the heating elements. In addition, it is found by comparing Figs. 14(*b*) and 14(*c*) that measurement points on the edges of the top surface are essential to the accuracy of geometry identification significantly. On the other hand, based on the results for T_H shown in Fig. 14, it is obvious that the fluctuation of T_H in iteration increases when the number of measurement points is decreased. The higher temperature fluctuation corresponds to the larger error in node matrix image when the measurement point number is lowered.

The accuracy of the identification is also dependent on the number of grid points. Therefore, three grid systems, $21\times21\times5$, $41\times41\times5$, and $61\times61\times5$, are employed and part of the results are plotted in Fig. 15 for cases with a triangular heating element at $h/k=10.0$ m^{-1}, $\sigma=0$, and $T_{H,ex}=100.00$ °C. The image node matrices shown in this figure are chosen from a series of candidate images obtained. It is clearly seen that with $21\times21\times5$ grid points, all the image nodes are placed correctly in the node matrix.

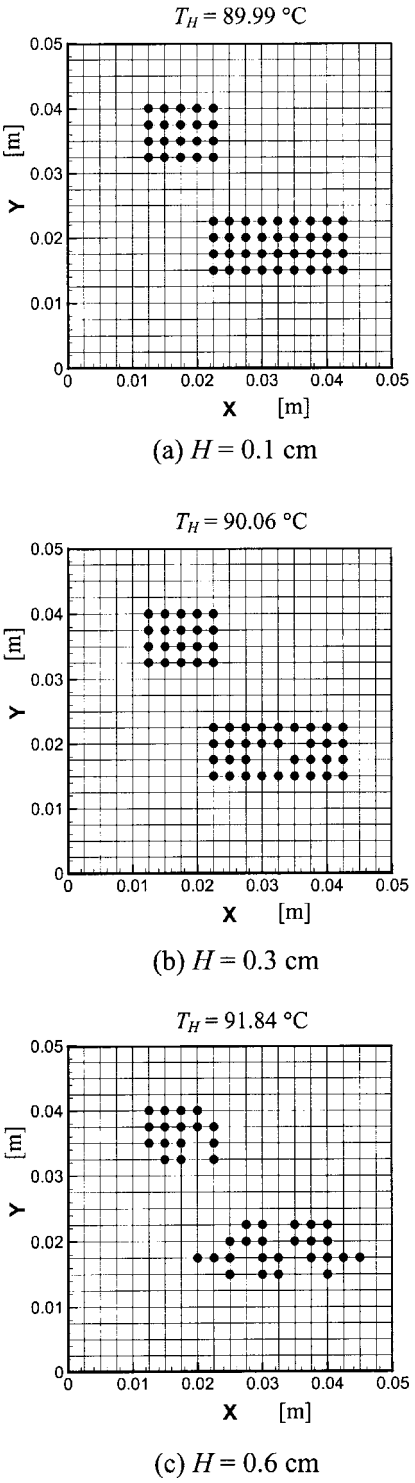

Fig. 13 Effects of height of rectangular package on geometry and temperature identification for the case considered in Fig. 6(*b*). The exact heating element temperature $T_{H,ex}$ is fixed at 90.00 °C and temperature measurement uncertainty is at $\sigma=1.0$.

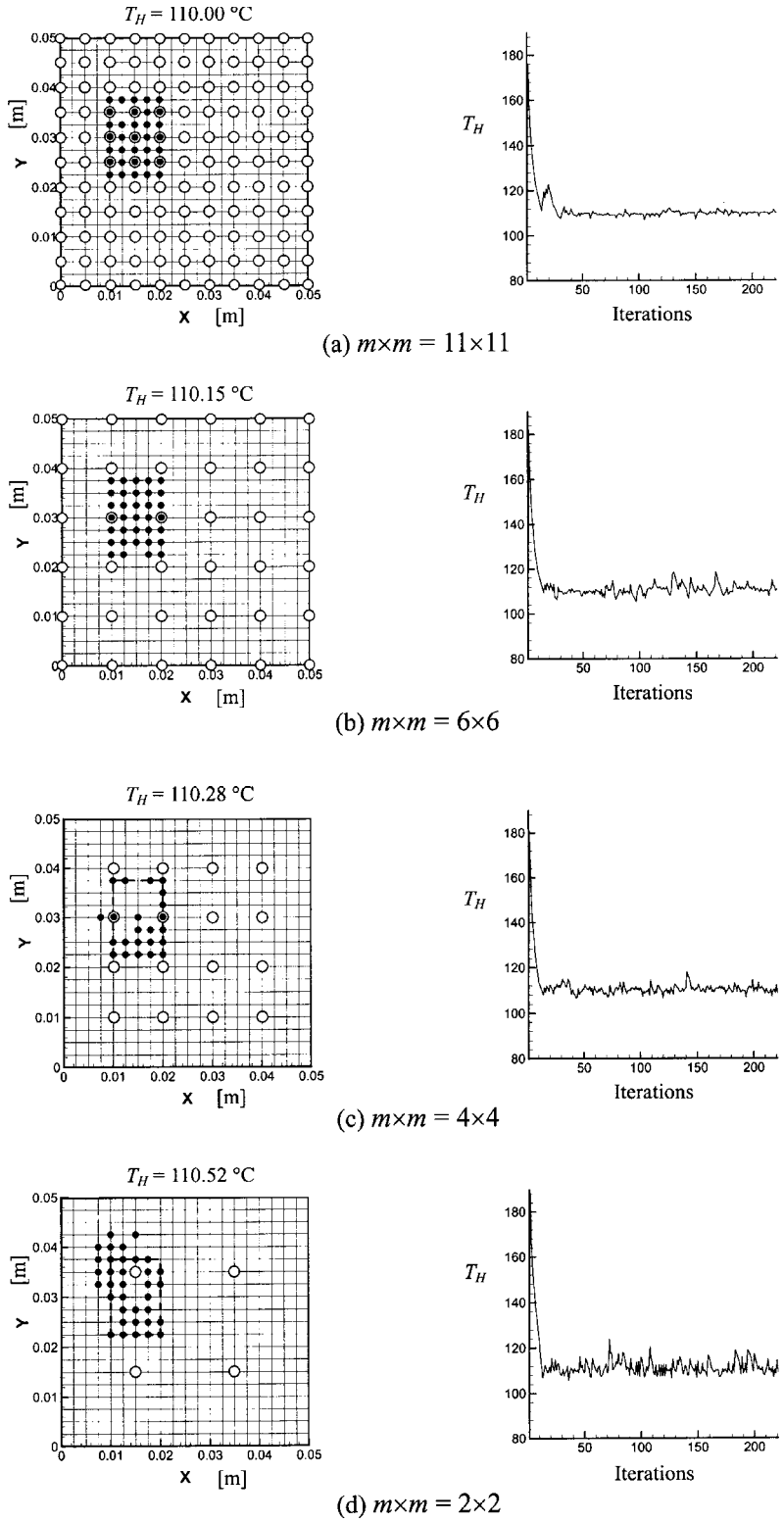

Fig. 14 Geometry and temperature identifications under various numbers of measurement points for the case with one heating element at h/k =10.0 m^{-1} and σ=0. The exact heating element temperature is fixed at 110.00 °C.

For $41 \times 41 \times 5$ and $61 \times 61 \times 5$ grids, a few image nodes move away from their correct positions and the borders of the images are slightly blurred. The relative error probability of geometry identification ξ_g is 0%, 0.595%, and 0.242% for $21 \times 21 \times 5$, $41 \times 41 \times 5$, and $61 \times 61 \times 5$ grid systems, respectively. On the other hand, the relative error in temperature identification is $<0.03\%$ for all the cases. It is obvious that resolution of the image is greatly enhanced as the grid point number is up to $61 \times 61 \times 5$. For identifying the heating elements with finer structures, the resolution of the images must be elevated to clearly visualize the

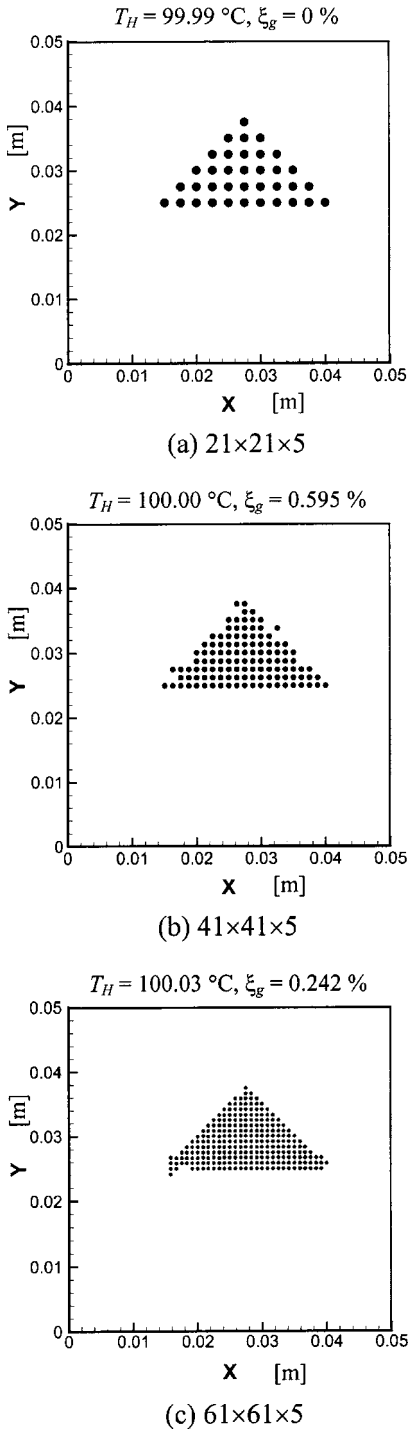

Fig. 15 Geometry and temperature identification using various grid systems for the cases with a triangular heating element at h/k=10.0 m^{-1} and σ=0. The exact temperature of heating element $T_{H,ex}$ is fixed at 100.00 °C.

structures. In these cases, a large grid number will be definitely required. However, an increase in the number of grid points leads to an increase in the number of BNs and NGPs. It is noted that the sensitivity analysis for each of the BNs and NGPs requires solving the direct problem at least one time. When the sensitivity analysis is performed to review each of the BNs and NGPs by calculating the value of the objective function drop in the iterative process, the computational effort required for the solution of the inverse problem may be greatly increased by the increasing number of BNs and NGPs. However, since the sensitivity analysis introduces only a very small perturbation by changing the state of one single node, the convergence of the numerical solution of the direct problem can be achieved rather fast. For a typical case with 21 $\times 21 \times 5$ grids, it took about 5 hr to complete one test case on a personal computer with AMD CPU (Athlon XP 2200+).

Note that the present approach is not without limitation. Either the theoretical model of the direct problem solver or the optimization scheme is needed to be improved for applications in more practical problems.

Concluding Remarks

The present study presents the automatic-filter method, which can be combined with the conjugate gradient method, to identify the geometry and the temperature of the heating elements embedded in a rectangular package. There is no need to solve any additional mathematical equations when the automatic-filter method is applied. Therefore, the overwhelming mathematical manipulation can be avoided and the form of objective function becomes more flexible. The identified geometry of heating elements is visualized by using node matrix images. In this manner, numerical grid generation usually used in numerical computation to fit the variation of the heating element shape is not required. Dependence of the accuracy of identification on major geometrical and physical variables, including the ratio of heat transfer coefficient to thermal conductivity (h/k), the number and shape of heating elements, uncertainty of temperature measurements (σ), and number of measurement points ($m \times m$), has been investigated. Meanwhile, a relative error probability (ξ_g) and a relative error to quantify the accuracy of the geometry and temperature identification are defined.

It is observed that the error of geometry and temperature identification are increased by a decrease in the ratio of h/k. When the ratio h/k is lower than 0.5 m^{-1}, the shape of the heating element may not be acceptable. When the measurement uncertainty is increased, the errors are also increased. When σ is elevated to 5.0, the discrepancy between the identified and the exact shapes becomes remarkable. However, for all cases, temperature error ξ_T is much less than geometry error probability ξ_g in order of magnitude.

In order to identify the geometry and temperature of the heating element accurately, the number of measurement points on the upper surface of the rectangular package should not be less than 6 $\times 6$ points. An insufficient number of measurement points will reduce the accuracy of geometry identification significantly. In addition, measurement points on the edges of the top surface are significantly essential to the accuracy of geometry identification. In addition, the image resolution will be enhanced by increasing the number of grid points in numerical computation.

Nomenclature

c = descent coefficient
C = heat capacity, kJ/(kg °C)
f = pass value
h = heat transfer coefficient, W/(m^2 °C)
H = height of rectangular package, cm
J = objective function
k = thermal conductivity, W/(m °C)
L = length of rectangular package, cm
m = number of temperature measurement points on top surface in x or y direction
M_w = number of incorrectly identified image nodes
P = search direction
q^* = internal heat source, W/m^3
$\boldsymbol{r}$ = random number varied between −1 and 1
R = random number varied between 0 and 1
T = temperature of rectangular package, °C

$\bar{T}$ = simulated experimental top surface temperature data, °C
T_a = ambient temperature, °C
T_H = identified temperature of heating elements, °C
W = width of rectangular package, cm
x, y, z = Cartesian coordinates, m
Z_e = z-direction location of heating element, cm

Greek Symbols

β = step size
γ = conjugate gradient coefficient
ΔJ = objective function drop
ε_{cr} = critical value for node changing
ξ_g = relative error probability of geometry identification
ξ_T = relative error of temperature identification
ρ = density, kg/m^3
σ = uncertainty of temperature measurement

Subscripts

cr = critical value
ex = exact solution
i, j, k = grid point indices
ip = border nodes and neighboring grid points
I, J = temperature measurement point indices
NX, NY, NZ = number of grid points in x,y, and z directions
max = maximum
min = minimum

Superscripts

n = iteration step
o = initial value for a subprocess

References

[1] Beck, J. V., and Arnold, K. J., 1977, *Parameter Estimation in Engineering and Science*, Willey, NY.
[2] Matsevity, Y. M, and Moultanovsky, A. V., 1984, "Statistical Identification of Local Heat Transfer Parameters," J. Eng. Phys., **45**, pp. 1298–1300.
[3] Alifanov, O. M., *Inverse Heat Transfer Problems*, 1994, Springler-Verlag, NY.
[4] Huang, C. H., and Chen, C. W., 1998, "A Boundary-Element-Based Inverse Problem of Estimating Boundary Conditions in an Irregular Domain With Statistical Analysis," Numer. Heat Transfer, Part B, **33**, pp. 251–268.
[5] Prud'homme, M., and Nguyen, T. H., 1998, "On the Iterative Regularization of Inverse Heat Conduction Problems by Conjugate Gradient Method," Int. Commun. Heat Mass Transfer, **25**, pp. 999–1008.
[6] Liu, G. R., Zhou, J. J., and Wang, J. G., 2002, "Coefficients Identification in Electronic System Cooling Simulation Through Genetic Algorithm," Comput. Struct., **80**, pp. 23–30.
[7] Alifanov, O. M., Balakovsky, S. L., and Klibanov, M. V., 1987, "The Recovery of Causal Characteristics of the Heat Conduction Process From a Solution of the Combined Inverse Problem," J. Eng. Phys., **52**, pp. 839–843.
[8] Tervola, P., 1989, "A Method to Determine the Thermal Conductivity From Measured Temperature Profiles," Int. J. Heat Mass Transfer, **32**, pp. 1425–1430.
[9] Flach, G. P., and Ozisik, M. N., 1989, "Inverse Heat Conduction Problem of Simultaneously Estimating Spatially Varying Thermal Conductivity and Heat Capacity Per Unit Volume," Numer. Heat Transfer, Part A, **16**, pp. 249–266.
[10] Moultanovsky, A. V., and Rekada, M., 2002, "Inverse Heat Conduction Problem Approach to Identify the Thermal Characteristics of Super-Hard Synthetic Materials," Inverse Probl. Eng., **10**, pp. 19–41.
[11] Kennon, S. R., and Dulikravich, G. S., 1985, "The Inverse Design of Internally Cooled Turbine Blades," ASME J. Eng. Gas Turbines Power, **107**, pp. 123–126.
[12] Dulikravich, G. S., 1992, "Inverse Design of Proper Number, Shapes, Sizes and Locations of Coolant Flow Passages," *Proc. of 10th Annual Workshop for Computational Fluid Dynamics Applications in Rocket Propulsion*, R. W. Williams, ed., NASA MSFC, Huntsville, AL, NASA CP-3163, Part 1, pp. 467–486.
[13] Fabbri, G., 1997, "A Genetic Algorithm for Fin Profile Optimization," Int. J. Heat Mass Transfer, **40**, pp. 2165–2172.
[14] Cheng, C. H., and Wu, C. Y., 2000, "An Approach Combining Body-Fitted Grid Generation and Conjugate Gradient Methods for Shape Design in Heat Conduction Problems," Numer. Heat Transfer, Part B, **37**, pp. 69–83.
[15] Cheng, C. H., and Chang, M. H., 2003, "Shape Design for a Cylinder with Uniform Temperature Distribution on the Outer Surface by Inverse Heat Transfer Method," Int. J. Heat Mass Transfer, **46**, pp. 101–111.
[16] Matsevity, Y. M., Moultanovsky, A. V., and Nemirovsky, I. A., 1991, "Optimization of Heat Engineering Processes Involving Utilization of Control and Identification Methods," J. Eng. Phys., **59**, pp. 1055–1063.
[17] Huang, C. H., and Chao, B. H., 1997, "An Inverse Geometry Problem in Identifying Irregular Boundary Configurations," Int. J. Heat Mass Transfer, **40**, pp. 2045–2053.
[18] Cheng, C. H., and Chang, M. H., 2003, "Shape Identification by Inverse Heat Transfer Method," ASME J. Heat Transfer, **125**, pp. 224–231.
[19] Park, H. M., and Shin, H. J., 2003, "Shape Identification for Natural Convection Problems Using the Adjoint Variable Method," J. Comput. Phys., **186**, pp. 198–211.
[20] dos Santos, J. V. Araújo, Soares, C. M. Mota, Soares, C. A. Mota, and Pina, H. L. G., 2000, "Development of a Numerical Model for the Damage Identification on Composite Plate Structures," Compos. Struct., **48**, pp. 59–65.
[21] Burczynski, T., and Beluch, W., 2001, "The Identification of Cracks Using Boundary Elements and Evolutionary Algorithms," Eng. Anal. Boundary Elem., **25**, pp. 313–322.
[22] Le Niliot, C., 1998, "The Boundary Element Method for the Time Varying Strength Estimation of Point Heat Sources: Application to a Two-Dimensional Diffusion System, Numer. Heat Transfer, Part B, **33**, pp. 301–321.
[23] Lefévre, F., and Le Niliot, C., 2002, "The BEM for Point Heat Source Estimation: Application to Multiple Static," Int. J. Therm. Sci., **41**, pp. 536-545.
[24] Le Niliot, C., and Lefévre, F., 2004, "A Parameter Estimation Approach to Solve the Inverse Problem of Point Heat Sources Identification," Int. J. Heat Mass Transfer, **47**, pp. 827–841.
[25] Lee, H. S., Park, C. J., and Park, H. W., 2000, "Identification of Geometric Shapes and Material Properties of Inclusions in Two-Dimensional Finite Bodies by Boundary Parameterization," Comput. Methods Appl. Mech. Eng., **181**, pp. 1–20.
[26] Abou Khachfe, R., and Jarny, Y., 2001, "Determination of Heat Sources and Heat Transfer Coefficient for Two-Dimensional Heat Flow—Numerical and Experimental Study," Int. J. Heat Mass Transfer, **44**, pp. 1309–1322.
[27] Moin, P., 2001, *Fundamentals of Engineering Numerical Analysis*, Cambridge University Press, NY.
[28] Alifanov, O. M., Artyukhin, E. A., and Rumyantsev, S. V., 1995, *Extreme Methods for Solving Ill-Posed Problems With Applications to Inverse Problems*, Begell House, Wallingfold, UK.

Performance Evaluation of Liquid Flow With PCM Particles in Microchannels

K. Q. Xing

Y.-X. Tao
e-mail: taoy@fiu.edu

Y. L. Hao[1]

Department of Mechanical and Materials Engineering,
Florida International University,
Miami, FL 33174

A two-phase, non thermal equilibrium-based model is applied to the numerical simulation of laminar flow and heat transfer characteristics of suspension with microsize phase-change material (PCM) particles in a microchannel. The model solves the conservation of mass, momentum, and thermal energy equations for liquid and particle phases separately. The study focuses on the parametric study of optimal conditions where heat transfer is enhanced with an increase in fluid power necessary for pumping the two-phase flow. The main contribution of PCM particles to the enhancement of heat transfer in a microsize tube is to increase the effective thermal capacity and utilize the latent heat effect under the laminar flow condition. An effectiveness factor ε_{eff} is defined to evaluate the heat transfer enhancement compared to the single-phase flow heat transfer and is calculated under different wall heat fluxes and different Reynolds numbers. The comparison is also made to evaluate the performance index, i.e., the ratio of total heat transfer rate to fluid flow power (pressure drop multiplied by volume flow rate) between PCM suspension flow and pure water single-phase flow. The results show that for a given Reynolds number, there exists an optimal heat flux under which the ε_{eff} value is the greatest. In general, the PCM suspension flow with phase change has a significantly higher performance index than the pure-fluid flow. The comparison of the model simulation with the limited experimental results for a MCPCM suspension flow in a 3 mm dia *tube reveals the sensitivity of wall temperature distribution to the PCM supply temperature and the importance of characterizing the phase change region for a given tube length.* [DOI: 10.1115/1.1929783]

Introduction

Since the introduction of the concept of microchannel heat sinks for electronic cooling by Tuckerman and Pease in 1981, there has been explosive growth in the field of ultracompact heat sinks and integrated cooling devices, especially for high-flux applications. It is known that the switching speed of microelectronics directly correlates to the cooling capacity of such devices. To reach an order of up to 3.8×10^{24} bits per second per cm^2 for next generation computing devices, a cooling capacity on the order of 10^5 W/cm^3 is required [1,2]. This requirement is way beyond the capability of spreader-air-cooling technique [3], and also outreached by current liquid cooling systems, including microchannel heat sinks. Therefore, active liquid cooling needs to advance to achieve the further heat enhancement capability, which is especially important for three-dimensional (3D) electronic packaging [4].

One of such enhancement techniques is to utilize phase-change material (PCM) fluids. The concept of a carrier fluid for encapsulated particles of phase-change materials was first introduced by Mechalick and Tweedie [5] in 1975. After that, a lot of research work has been conducted on the PCM suspension flow because of its many special features, such as high-energy storage density, low pumping power requirements, and high heat transfer rates between the wall and the suspension. Tao et al. [6] proposed a new design of a scalable, heat sink containing a 3D micro/nano network, utilizing liquid mixed with nanosize phase-change materials (NPCMs) and having a high surface-to-volume ratio geometry. The conceptual design is capable of reaching 10^5 W/cm^3 using encapsulated nanosize phase-change materials, which would result in an order of magnitude higher cooling capacity than typical microchannel heat sink of the same volume and same pumping power. To understand the mechanisms behind flow using PCM heat transfer fluid, Hao and Tao [7] developed a numerical model to unveil the heat transfer characteristics of PCM particles suspension in energy storage and thermal control systems. The model is based on the continuum model for the system of solid particles suspended in a Newtonian gas or liquid to the system of PCM particles suspended in a laminar flow. The preliminary results demonstrated that the model captures the essential physical phenomena, such as particle-depletion boundary effects and nonequilibrium temperature distribution between two phases. That study, however, did not address the design consideration where there might exist optimal heat enhance parameters. Motivated by this observation, this paper focuses on the performance evaluation of PCM suspension flow by applying Hao and Tao's model. In particular, the results of heat transfer enhancement are analyzed and compared to single-phase flow, in detail. In addition, we also validate the model through a comparison to the experimental results, available in the open literature, for a microencapsulated PCM (MCPCM) suspension flow in a 3 mm dia tube. The comparison is justified because the model is based on the continuum theory for which both the current and literature studies are valid.

Theoretical Model

Figure 1 shows a schematic diagram describing the problem. A laminar flow of carrier fluid with nano- or microsize encapsulated PCM particles at the temperature equal to or below the phase-change temperature of PCM enters a microtube with the heated wall. The heat transfer between the suspension and the heated wall causes PCM in the particles to absorb the thermal energy and melt while their temperature reaches the phase-change temperature. The presence of PCM particles is not only for the introduction of

[1]Present address: Department of Power Engineering, Southeast University, Nanjing 210096, Jiangsu, P. R. China

Contributed by the Heat Transfer Division for publication in the JOURNAL OF HEAT TRANSFER. Manuscript received by the Heat Transfer Division April 24, 2004; revision received March 7, 2005. Review conducted by: S. G. Kandlikar.

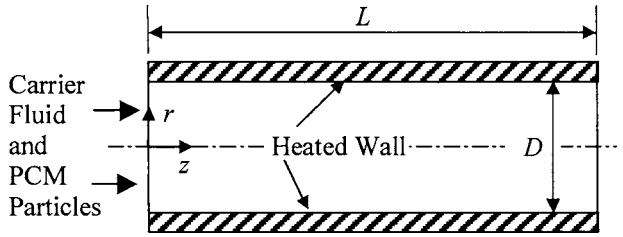

Fig. 1 Schematic diagram of fluid and PCM particle suspension flowing through a heated tube

the phase-change material into the fluid, but also results in momentum and energy interaction between particles and liquid, collisions among particles, and heat transfer between the particles and the tube wall. Those interactions will make the mechanism of hydrodynamic and heat transfer characteristics in the suspension flow very different from that in single-phase liquid flow.

In this paper we use a model of two-phase flow and heat-mass transfer with phase changes, based on the theory of interacting continua, developed by Tao and Hao [7] in a microchannel. The consideration of the continuum model for the suspension flow in a microchannel is based on the following observation: There are around 25 million molecules of air in a 1 μm cube at the standard temperature and pressure (STP). The same cube would contain around 34 billion molecules of liquid water. Therefore, liquid flow is still a continuum medium even in micrometer scale tube, whereas a gas flow through the same size tube might or might not be, depending on the gas Knudsen number. In our model, both liquid and solid phases are considered to be continuous and fully interpenetrating. Both phases are described in terms of separate conservation equations with appropriate interaction terms representing the coupling between the phases, including phase change. Fluid phase properties and the physical characteristics of the PCM particles, such as shape and size, are included in the continuum representation. For the sake of completion, we represent the model here.

The volume-averaged equations of mass and momentum conservation for the laminar flow can be expressed as follows [7]:

Continuity

$$\frac{\partial}{\partial t}(\varepsilon_l \rho_l) + \nabla \cdot (\varepsilon_l \rho_l \mathbf{v}_l) = 0 \tag{1}$$

$$\frac{\partial}{\partial t}(\varepsilon_s \rho_s) + \nabla \cdot (\varepsilon_s \rho_s \mathbf{v}_s) = 0 \tag{2}$$

Momentum

$$\frac{\partial}{\partial t}(\varepsilon_l \rho_l \mathbf{v}_l) + \nabla \cdot (\varepsilon_l \rho_l \mathbf{v}_l \mathbf{v}_l) = -\varepsilon_l \nabla p + \nabla \cdot [\varepsilon_l \mu_l (\nabla \mathbf{v}_l + \nabla \mathbf{v}_l^T)] + \varepsilon_l \rho_l \mathbf{g} - \beta(\mathbf{v}_l - \mathbf{v}_s) + (1-\varepsilon_l) \times D_v \rho_l \frac{d}{dt}(\mathbf{v}_l - \mathbf{v}_s) \tag{3}$$

$$\frac{\partial}{\partial t}(\varepsilon_s \rho_s \mathbf{v}_s) + \nabla \cdot (\varepsilon_s \rho_s \mathbf{v}_s \mathbf{v}_s) = -\varepsilon_s \nabla p - G \nabla \varepsilon_l + \nabla \cdot [\varepsilon_s \mu_s (\nabla \mathbf{v}_s + \nabla \mathbf{v}_s^T)] + \varepsilon_s \rho_s \mathbf{g} + \beta(\mathbf{v}_l - \mathbf{v}_s) - (1-\varepsilon_l) D_v \rho_l \frac{d}{dt}(\mathbf{v}_l - \mathbf{v}_s) \tag{4}$$

The enthalpy form is adopted for the energy conservation because the phase change occurs in the particle phase [7]. The properties of particle phase vary continuously with temperature, while the melting occurs in PCM. The energy equation can be solved over the entire domain. The enthalpy, density, thermal conductivity, and specific heat are all assumed to vary continuously, from their values in the solid to those in the liquid, as a function of temperature. The volume-averaged equations of energy conservation can be expressed by

$$\frac{\partial}{\partial t}(\varepsilon_l \rho_l i_l) + \nabla \cdot (\varepsilon_l \rho_l i_l \mathbf{v}_l) = -p\left[\frac{\partial \varepsilon_l}{\partial t} + \nabla \cdot (\varepsilon_l \mathbf{v}_l)\right] + \nabla \cdot (\varepsilon_l k_{\mathrm{eff},l} \nabla T_l) - h(T_l - T_s) \tag{5}$$

$$\frac{\partial}{\partial t}(\varepsilon_s \rho_s i_s) + \nabla \cdot (\varepsilon_s \rho_s i_s \mathbf{v}_s) = -p\left[\frac{\partial \varepsilon_s}{\partial t} + \nabla \cdot (\varepsilon_s \mathbf{v}_s)\right] + \nabla \cdot (\varepsilon_s k_{\mathrm{eff},s} \nabla T_s) + h(T_l - T_s) \tag{6}$$

The melting of particle phase that is in the encapsulated particles does not cause the mass transport between the particle phase and liquid phase. Therefore, the terms related to the mass transfer between two phases vanish in the above governing equations. For the liquid-particle two-phase flow, the relationship between liquid and particle volume fraction is $\varepsilon_l + \varepsilon_s = 1$. Therefore, only one of the volume fractions is independent. In the thermal energy equations, the dissipation function terms and the terms of Joule's heating and thermal radiation have been neglected. The continuum enthalpies of the liquid and particle phases can be expressed, respectively, as

$$i_l = c_{p,l} T_l + (c_{p,s,s} - c_{p,l}) T_m + h_{sl} \tag{7}$$

$$i_s = c_{p,s} T_s + f_{s,l}[(c_{p,s,s} - c_{p,s,l}) T_m + h_{sl}] \tag{8}$$

where h_{sl} is the latent heat of fusion and T_m is the melting temperature. $f_{s,l}$ is the liquid mass fraction in the particle. The density, specific heat at constant pressure, and thermal conductivity of PCM particles are given, respectively, as follows:

$$\rho_s = \xi_{s,l} \rho_{s,l} + (1 - \xi_{s,l}) \rho_{s,s} \tag{9}$$

$$c_{p,s} = f_{s,l} c_{p,s,l} + (1 - f_{s,l}) c_{p,s,s} \tag{10}$$

$$k_s = \xi_{s,l} k_{s,l} + (1 - \xi_{s,l}) k_{s,s} \tag{11}$$

In the above treatment, the mass and thermal properties of capsule shell material are neglected.

To solve the complete set of governing equations, the following are chosen as the basic variables: liquid volume fraction ε_l; pressure p; three components of liquid velocity vector u_l, v_l, w_l; three components of particle velocity vector u_s, v_s, w_s; liquid enthalpy i_l; and particle enthalpy i_s. The closure of the set of governing equations requires the specification of the constitutive equations. This implies that all other variables in the governing equations must be specified in terms of the basic variables [7].

The formulation of particle-particle interaction modulus G that Bouillard et al. [8] presented is adopted, i.e.,

$$G = -1.0 e^{100(0.45 - \varepsilon_l)} \tag{12}$$

The drag coefficient β is calculated according to two ranges of liquid phase volume fraction. If $\varepsilon_l < 0.8$, the drag coefficient β is obtained from Ergun equation as follows:

$$\beta = 150 \frac{(1-\varepsilon_l)^2 \mu_l}{\varepsilon_l d_p^2} + 1.75 \frac{(1-\varepsilon_l)\rho_l}{d_p} |\mathbf{v}_l - \mathbf{v}_s| \tag{13}$$

If $\varepsilon_l \geqslant 0.8$, the drag coefficient β becomes

$$\beta = \frac{3}{4} C_d \frac{\varepsilon_l (1-\varepsilon_l)}{d_p} \rho_l |\mathbf{v}_l - \mathbf{v}_s| \varepsilon_l^{-2.65} \tag{14}$$

In Eq. (14), $\varepsilon_l^{-2.65}$ shows the effect due to the presence of other particles in the fluid and acts as a correction to the usual Stokes law for free fall of a single particle [9]. C_d is related to the particle Reynolds number

Table 1 Thermophysical properties of octadecane PCM slurry [22]

	Density kg/m^3	Specific Heat J/(kg·K)	Thermal Conductivity W/(m·K)	Latent Heat kJ/kg	Viscosity Pa·s
Water (273K)	997.07	4179.6	0.606		8.904×10^{-4}
PCM particle (Liquid)	936	2014.0	0.144		
PCM particle (Solid)	1000	2067.0	0.310	167	

$$C_d = \begin{cases} \dfrac{24}{\mathrm{Re}_p}(1 + 0.15\,\mathrm{Re}_p^{0.687}), & \mathrm{Re}_p < 1000 \\ 0.44, & \mathrm{Re}_p \geqslant 1000 \end{cases} \tag{15}$$

where

$$\mathrm{Re}_p = \frac{\varepsilon_l \rho_l |\mathbf{v}_l - \mathbf{v}_s| d_p}{\mu_l} \tag{16}$$

In Eqs. (3) and (4), D_v is the virtual mass coefficient. For dispersed spherical particles, $D_v = 0.5$ [10].

The effective thermal conductivities are calculated using the approximate model presented by Bauer et al. [11]

$$k_{\mathrm{eff},l} = k_{b,l}/\varepsilon_l, \text{ and } k_{\mathrm{eff},s} = k_{b,s}/\varepsilon_s \tag{17}$$

where

$$k_{b,l} = (1 - \sqrt{1 - \varepsilon_l})k_l \tag{18}$$

$$k_{b,s} = \sqrt{1 - \varepsilon_l}[\eta A + (1 - \eta)\mathrm{Z}]k_l \tag{19}$$

$$\mathrm{Z} = \frac{2(B - B/A)}{(1 - B/A)^3}\ln\left(\frac{A}{B}\right) - \frac{2(B-1)}{(1 - B/A)^2} - \frac{B+1}{1 - B/A} \tag{20}$$

$$B = 1.25(1/\varepsilon_l - 1)^{10/9} \tag{21}$$

For spherical particles, $A = k_s/k_l$ and $\eta = 7.26\times10^{-3}$.

The volumetric heat transfer coefficient h is obtained from

$$h = \frac{6(1 - \varepsilon_l)}{d_p} h_p \tag{22}$$

In Eq. (22), the heat transfer coefficient h_p is estimated based on Wakao and Kaguei [12]

$$\mathrm{Nu}_p = \frac{h_p d_p}{k_l} = 2 + 1.1\mathrm{Re}_p^{0.6}\mathrm{Pr}^{1/3} \tag{23}$$

The particle phase temperature is determined as

$$T_s = \begin{cases} \dfrac{i_s}{c_{p,s,s}}; & i_s < c_{p,s,s}T_m \\ T_m; & c_{p,s,s}T_m \leqslant i_s \leqslant c_{p,s,s}T_m + h_{sl} \\ \dfrac{i_s - (c_{p,s,s} - c_{p,s,l})T_m - h_{sl}}{c_{p,s,l}}; & i_s > c_{p,s,s}T_m + h_{sl} \end{cases} \tag{24}$$

Finally, the liquid mass fraction in the melting particle can be calculated from

$$f_{s,l} = \begin{cases} 0; & T_s < T_m \\ \dfrac{i_s - c_{p,s,s}T_m}{h_{sl}}; & T_s = T_m \\ 1; & T_s > T_m \end{cases} \tag{25}$$

The liquid volume fraction in the melting particle can be calculated from

$$\xi_{s,l} = \frac{f_{s,l}\rho_{s,s}}{f_{s,l}\rho_{s,s} + (1 - f_{s,l})\rho_{s,l}} \tag{26}$$

Numerical Method

To solve the set of conservation equations in the three-dimensional Cartesian coordinate system, Hao and Tao [13] proposed a numerical method by employing the finite volume technique based on the SIMPLE algorithm. Previous work [7] was primarily on the development of the numerical code to simulate the phase change in the particle and calculate the wall–to–liquid-solid heat transfer coefficient in a cylindrical coordinate. The parametric investigation in this study focuses on optimal conditions where heat transfer is enhanced with an increase in fluid power necessary for pumping the two-phase flow.

Fluid-Particles Suspension Flow. In this paper, the fluid-particles two-phase flow consists of water as the carrier fluid and microencapsulated octadecane ($C_{18}H_{38}$, with a melting temperature of 301 K and latent heat of 223 kJ/kg) as the PCM particles, with a melamine-formaldehyde resinous wall. The thermophysical data of water and octadecane used for the computations have been summarized in Table 1. The thermophysical properties are assumed to be independent of temperature in solid and liquid. For the PCM particles, we neglect the effects of capsule shell material in this calculation. This treatment also allows the particle-fluid mixture in a form of emulsion.

The viscosity of PCM particle μ_p has to be defined since the particle is considered as a continuum in the present model. The correlation proposed by Vand [14] is extended to the study of the microencapsulated phase-change suspensions as follows:

$$\frac{\mu_b}{\mu_f} = (1 - \varepsilon_p - A\varepsilon_p^2)^{-2.5} \tag{27}$$

where μ_b and μ_f were the viscosities of the slurry and the carrier fluid, respectively. The constant A, which depends on the shape and rigidity of the particles, can be determined experimentally based on the pressure-drop measurement. The bulk viscosity μ_b is obviously not the same as the particle viscosity μ_p in a thermophysical sense. In fact, because of the lack of experimental data, the viscosity μ_p has not been available for the system of liquid-solid two-phase flow. As a first degree of approximation, the value of 0.01 Pa·s for the particle viscosity, μ_p, is used in the present study based on Ref. [7]. The further experimental measurement will give a more realistic value of μ_p, which will be used in our future work.

Geometry Description. A tube with the typical diameter of $D = 1.22\times10^{-4}$ m is used in our computation based on the design of Tao et al. [6]. The tube length of $L = 1.22\times10^{-2}$ m ($L/D = 100$) is used to ensure that the supplied slurry completed melt at the exit of the tube. The PCM particles are spherical with the diameter of $d_p = 6.3\times10^{-6}$ m and initially all in the solid phase when they enter the tube. It is assumed that the uniform suspension enters the tube at a temperature below the phase-change tem-

perature, and the surface heat flux on the sidewall is constant.

By neglecting the effect of gravity, the problem becomes steady and axisymmetrical. The radial and axial dimensions of the main hydrodynamic computational grids are, respectively, $\Delta r = 3.05 \times 10^{-6}$ m and $\Delta z = 2.44 \times 10^{-5}$ m. The total number of computational grids, including the subgrids next to the heated wall and entrance, is equal to $29 \times 509 = 14761$ [7].

All of the equations and parameters are nondimensionalized before they are solved by the numerical code on a Sun Blade 1000 workstation. The convergence criterion is that the relative changes of the variables between two successive iterations are $<10^{-6}$% [7].

Development of the field configurations through time takes place in a sequence of time steps. At each time step Δt the computation is accomplished in such a way as to utilize the results developed in the previous time step (or the initial conditions) for the calculation of new values of all field variables, and to store these in the computer in such a way that they can be processed yet again in the following cycle. Considering the balance between the computing efficiency and accuracy and/or stability, we choose the typical time steps between 0.001 and 0.01 s, where the small time step corresponds to relatively high velocity [7].

Boundary Conditions. Hydrodynamic boundary conditions: the centerline of the tube is modeled as impermeable slip boundary conditions for both phases. The tube wall is modeled as impermeable no-slip rigid surface for both phases. At the entrance, the influx of carrier fluid with a given Re based on the tube diameter is prescribed and the particles have the same inlet velocity as that of the fluid. At the exit, the continuity outflow boundary conditions are assumed for both phases.

Thermal boundary conditions: the centerline of the tube is considered to be an adiabatic surface for both phases. At the tube wall a constant heat flux is imposed. At the entrance, the inlet temperature of carrier fluid and the temperature of the PCM particles with $f_{p,l,0}=0$ are prescribed as $T_{f,0}=T_{p,0}=295$ K ($<T_{m,p}=301$ K). At the exit, the continuity energy outflow boundary conditions are assumed for both phases.

Results

Some preliminary results using this numerical model have been presented in previous papers by Hao and Tao [7,15]. As discussed in Ref. [7], for a given kind of PCM particles, there should exist an optimal relation between the channel design parameters L and D, particle volume fraction ε_p, Reynolds number Re and the wall heat flux q_w. In this paper, we will focus on the parametric study of optimal conditions where heat transfer is enhanced with an increase in fluid power necessary for pumping the two-phase flow.

Two new parameters are defined for this analysis. One is the effectiveness factor ε_{eff}

$$\varepsilon_{\text{eff}} = \frac{Q_{\text{slurry}}}{Q_{\text{pure water}}} \tag{28}$$

where

$$Q_{\text{slurry}} = q_w A = q_w \pi D L \tag{29}$$

$$Q_{\text{pure water}} = mc_p \Delta T = \rho V \frac{\pi}{4} D^2 c_p \Delta T \tag{30}$$

As shown in the above equation, ε_{eff} is defined as the ratio of the total heat transfer rate of the PCM suspension flow to the total heat transfer rate of pure water single-phase flow with the same temperature difference from the inlet to the exit. Therefore, ε_{eff} can be used to evaluate the heat transfer enhancement of the PCM suspension flow compared to the single-phase flow. The other parameter is the performance index PI

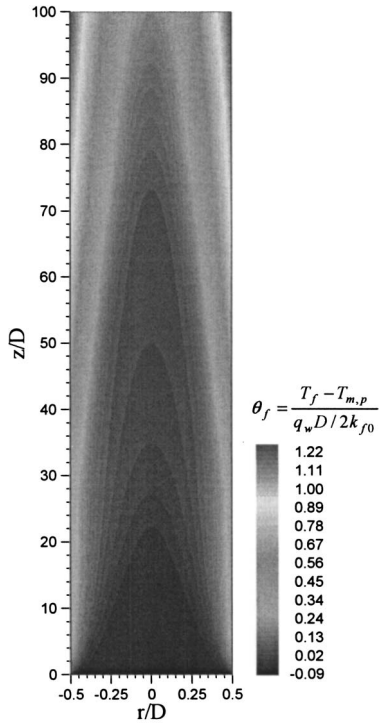

Fig. 2 Temperature of carrier fluid: $L/D=100$, Re=167, $T_{f,0}=T_{p,0}=295$ K, $\varepsilon_{p,0}=0.25$, $f_{p,l,0}=0$, $q_w=50$ W/cm^2

$$\text{PI} = \frac{(Q/P)_{\text{slurry}}}{(Q/P)_{\text{pure water}}} \tag{31}$$

where

$$P_{\text{slurry}} = \Delta p V \frac{\pi}{4} D^2 \tag{32}$$

$$P_{\text{pure water}} = f \frac{\pi^2}{8} \rho L D V^3 \tag{33}$$

$$f = \frac{64}{\text{Re}} \tag{34}$$

here the PI compares the ratio of total heat transfer rate to fluid flow power (pressure drop multiplied by volume flow rate) between the PCM suspension flow and the pure water single-phase flow.

Figures 2–4 show the distribution of fluid temperature, particle temperature, and liquid mass fraction inside of particle. The calculation is under the condition of Re=167, $T_{f,0}=T_{p,0}=295$ K ($<T_{m,p}=301$ K), $\varepsilon_p=0.25$, $f_{p,l,0}=0$, and $q_w=50$ W/cm^2. The heat transfer between the suspension and the wall occurs when it flows through the tube and the thermal boundary layers next to the sidewall. The PCM in the particles starts melting when the temperature of solid phase reaches the phase-change temperature as shown in Figs. 3 and 4.

Maximum Effectiveness Factor. Figures 5–8 show the effectiveness factor and performance index of the PCM suspension flow as a function of heat flux at different Reynolds numbers of 90, 167, 300, and 600. The calculation is under the condition of $T_{f,0}=T_{p,0}=295$ K ($<T_{m,p}=301$ K), $\varepsilon_p=0.25$, $f_{p,l,0}=0$. As shown in these figures, keeping L, D, and ε_p constant and for a given Reynolds number, there exists an optimal wall heat flux under which the ε_{eff} value is a maximum. The reason for this phenomenon is the following. For a given Reynolds number, the fluid flow rate is constant. If the PCM particles are fully melted right at the

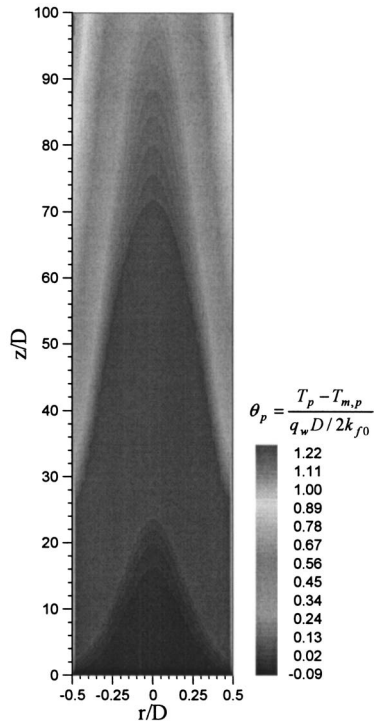

Fig. 3 Temperature of NPCM particle: $L/D=100$, Re=167, $T_{f,0}=T_{p,0}=295$ K, $\varepsilon_{p,0}=0.25$, $f_{p,l,0}=0$, $q_w=50$ W/cm^2

exit under a specified wall heat flux, the maximum heat absorbing capacity of the PCM suspension flow occurs. This means that for the given Reynolds number, when other heat fluxes apply to the wall, the PCM particles are either completely melted before reaching the exit or remain partially frozen at the exit. This indicates that there exists a unique match between a design Re number and wall heat flux in order to maximize the heat transfer enhancement of PCM suspension flow.

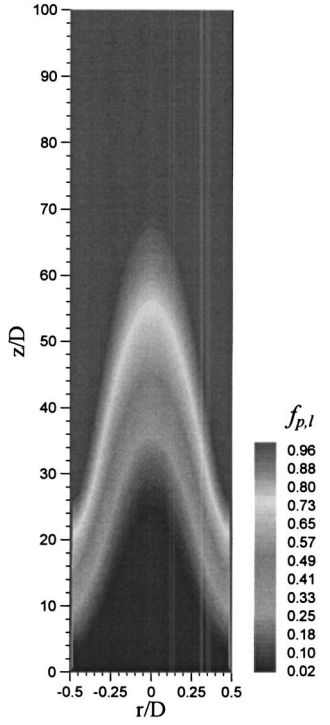

Fig. 4 Liquid mass fraction inside of NPCM particle: $L/D=100$, Re=167, $T_{f,0}=T_{p,0}=295$ K, $\varepsilon_{p,0}=0.25$, $f_{p,l,0}=0$, $q_w=50$ W/cm^2

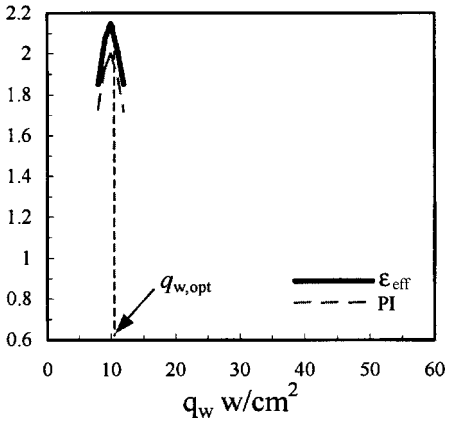

Fig. 5 Effectiveness factor and performance index of slurry at Re=90

Compared to the pure water single-phase flow, the maximum heat absorbing capacity of the PCM suspension flow is about 2.2 times higher for Re=90, i.e., the maximum effectiveness factor $\varepsilon_{eff,max}$ equals 2.2. As Re increases, $\varepsilon_{eff,max}$ decreases slightly. At Re=600, $\varepsilon_{eff,max}$ is 1.6, as shown in Fig. 9. For Re=90, $\varepsilon_{eff,max}$

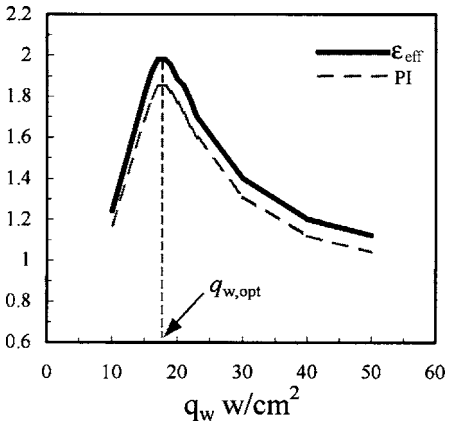

Fig. 6 Effectiveness factor and performance index of slurry at Re=167

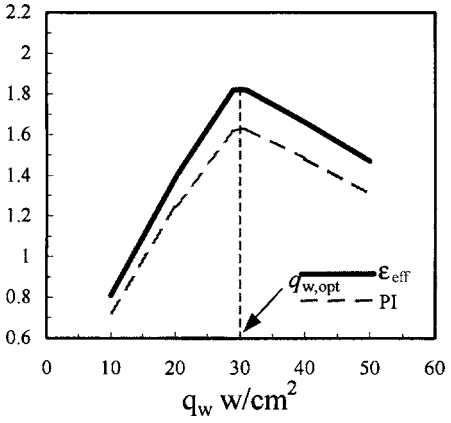

Fig. 7 Effectiveness factor and performance index of slurry at Re=300

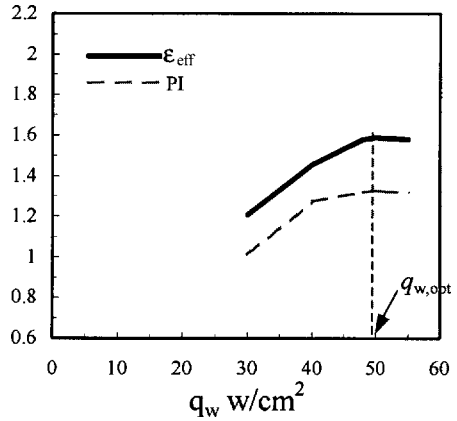

Fig. 8 Effectiveness factor and performance index of slurry at Re=600

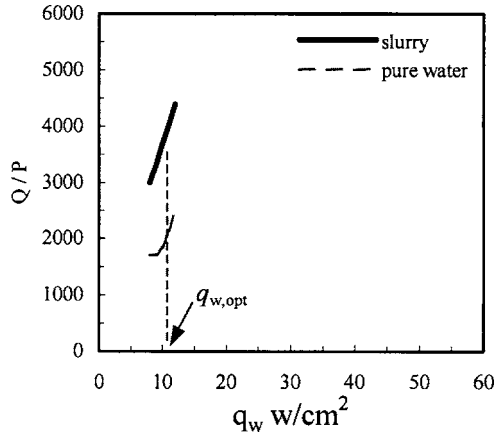

Fig. 10 *Q/P* ratio of slurry and pure water at Re=90

occurs at $q_w=10$ W/cm^2; and for Re=600, the corresponding $q_w=50$ W/cm^2. Figure 9 is very useful for designing an optimal microchannel heat exchanger.

Performance Index. One of the important factors considered in making the design decisions of a microscale active liquid cooling device is the pumping power requirement. The performance index PI introduced in this study allows the designer to quantify and compare their new designs. The results obtained in this study reveal that PI can reach as high as 2.0 and follows the same trend as the effectiveness factor with the maximum value of PI occurring at the same wall heat flux as that for $\varepsilon_{eff,max}$ (Figs. 5–8). This encouraging observation shows that the addition of PCM particles does not necessarily increase the pumping power required to move the flow. Because of the significant increases in heat transfer rate for a given pumping power, the required pumping power for a given heat transfer rate decreases ranging from 30 to 60% for the range of Re studied.

Heat Transfer Rate-to-Pumping Power Ratio. To further illustrate Figs. 10–13 show the ratio of total heat transfer rate Q to fluid flow power P of the PCM suspension flow and the pure water single-phase flow versus different wall heat flux and different Reynolds number, respectively. In general, the Q/P ratio of the PCM suspension flow with phase change is significantly higher than the pure water single-phase flow. But Fig. 12, at Re =300, when $q_w<15$ W/cm^2, the Q/P ratio of the PCM suspension flow even smaller than the pure water single-phase flow. The reason is that when $q_w<15$ W/cm^2 at Re=300, only a very small part of the PCM particles have melt at the exit of the tube, and at this situation, the existence of PCM particles will not enhance heat transfer any more, however, it even become a barrier to the fluid flow in the tube.

Local Heat Transfer Coefficient. Figures 14–17 show the local heat transfer coefficient of the PCM suspension flow with phase change along the distance from the inlet, at a given wall heat flux, and different Reynolds numbers. For comparison, the local heat transfer coefficient for the pure water single-phase flow

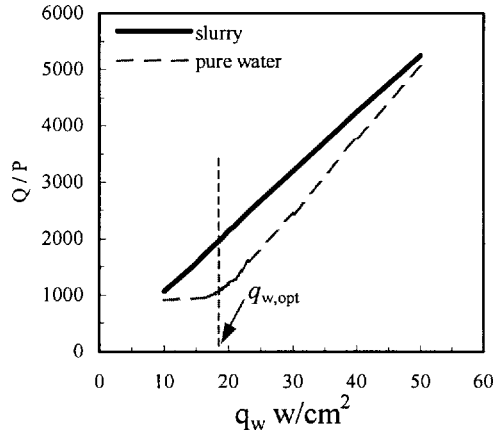

Fig. 11 *Q/P* ratio of slurry and pure water at Re=167

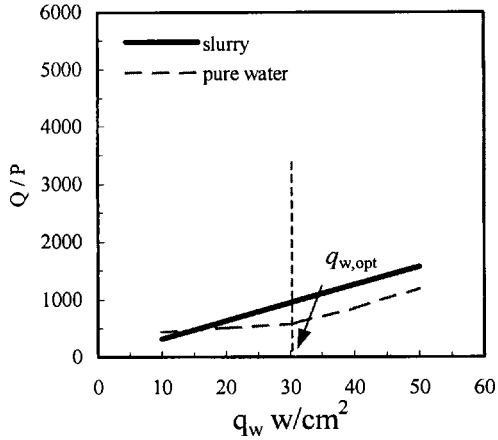

Fig. 12 *Q/P* ratio of slurry and pure water at Re=300

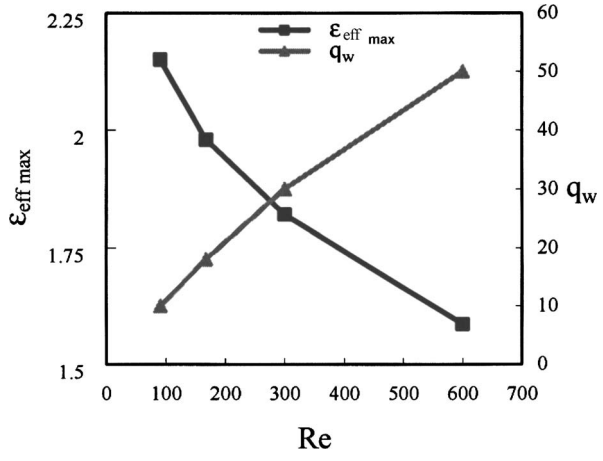

Fig. 9 Maximum ε_{eff} and corresponding q_w (W/cm^2) as a function of Reynolds number

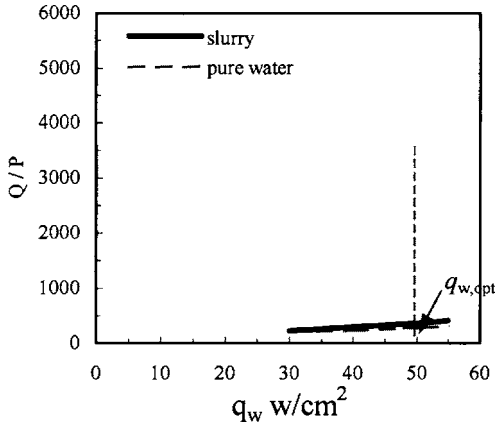

Fig. 13 Q/P ratio of slurry and pure water at Re=600

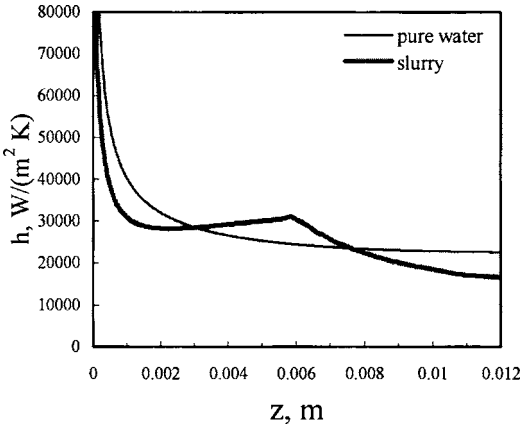

Fig. 16 Local heat transfer coefficient along the channel: Re =300, q_w=50 W/cm^2

is also shown in these figures. The local convection heat transfer coefficients are calculated from Newton's law of cooling

$$h = \frac{q_w}{T_w - T_0} \tag{35}$$

From Figs. 14–17 we can see the significant effect of PCM particles on the heat transfer characteristics between the suspension and the wall. The temperature remains at the phase-change temperature in the melting region, preventing the temperature and the thickness of thermal boundary layer from increasing. It causes the local heat transfer coefficient to increase in the melting region and reach the peak value at the location where the mean temperature of the particle reaches the phase-change temperature. The existence of a peak-value local heat transfer agrees very well with the experimental results presented in literature [16,17]. The results in Figs. 14–17 also show that the enhancement of the heat transfer mainly occurs in melting region when the suspension with PCM particles applies. In the earlier area of the *melting* region and the *melted* region, the local heat transfer coefficient is even lower than that for pure water. This prediction also agrees very well with the experiments [16,17].

Figure 18 shows the local heat transfer coefficient of the PCM suspension flow at different Reynolds numbers for a given wall heat flux. The peak value of the local heat transfer coefficient will goes toward the exit and becomes higher with the increase of the Reynolds number. The reason is that with the increase of Re, the flow rate is increased and the PCM particles needs a longer way to absorb enough heat to reach the phase-change temperature.

Particle Volume Fraction. To consider the influence of particle volume fraction ε_p on the heat transfer capacity of the PCM suspension flow, two trial cases are run by only changing the value of ε_p. The two cases are ε_p=0.25 and ε_p=0.15 for Re=300, q_w =30 W/cm^2. The change of effectiveness factor with particle volume fraction is shown in Fig. 19. From the figure, we can see that under given Reynolds number and given wall heat flux, the heat transfer enhancement of the PCM suspension flow will become higher if we increase the particle volume fraction. However the

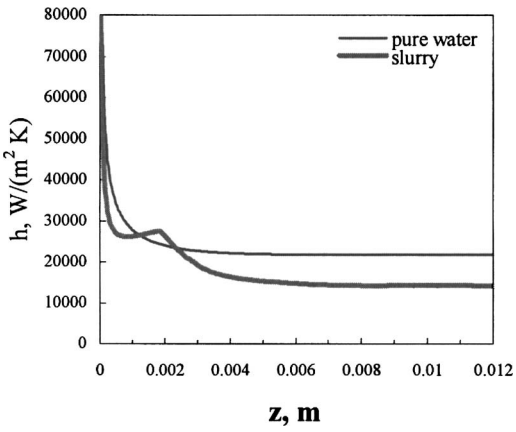

Fig. 14 Local heat transfer coefficient along the channel: Re =90, q_w=50 W/cm^2

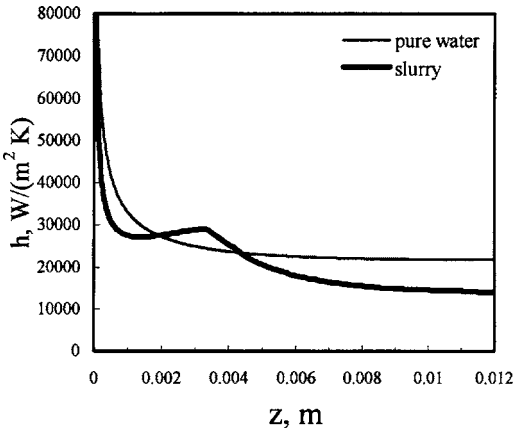

Fig. 15 Local heat transfer coefficient along the channel: Re =167, q_w=50 W/cm^2

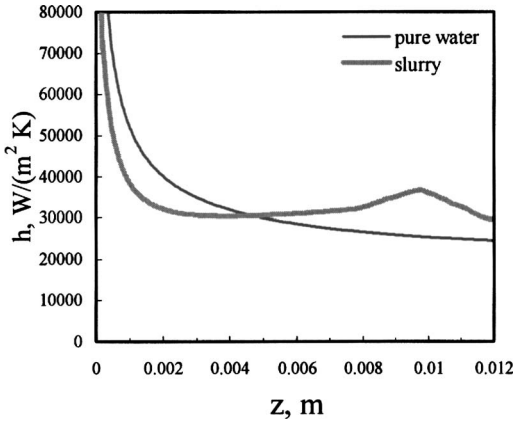

Fig. 17 Local heat transfer coefficient along the channel: Re =600, q_w=50 W/cm^2

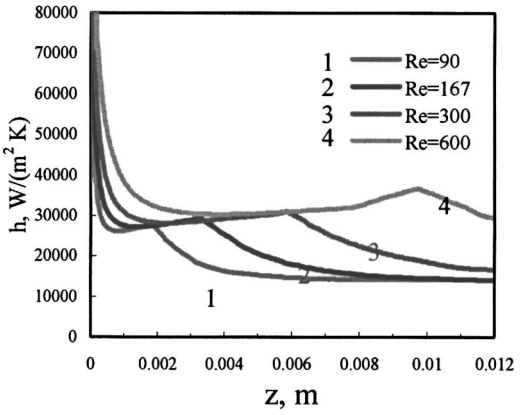

Fig. 18 Distribution of local heat transfer coefficients where $\varepsilon_{eff,max}$ and $q_{w,max}$ occur at a given Reynolds number

value of ε_{eff} will not keep going up with ε_p because too many particles will become a barrier to the fluid flow. Another parameter that needs to be considered here is the viscosity of the PCM suspension flow ε_b because by changing the particle volume fraction ε_p, the viscosity of the suspension flow is also changed. A detailed discussion of the influence of particle volume fraction will be taken in the future work.

Comparison to Experimental Results of Macroscale Slurry Flow. There has been no comparable experimental data for heat transfer involving PCM slurry flow in microchannels. To evaluate the model predictability, we conducted a simulation for a slurry flow with microencapsulated PCM suspension particles in a circular tube of 3 mm dia since our model is still within the continuum theory domain. The experimental results for this case are available from [18]. The PCM material used in the study of [18] is eicosane. The properties of eicosane are listed in Table 2. The test condition and comparison results are shown in Fig. 20, in which

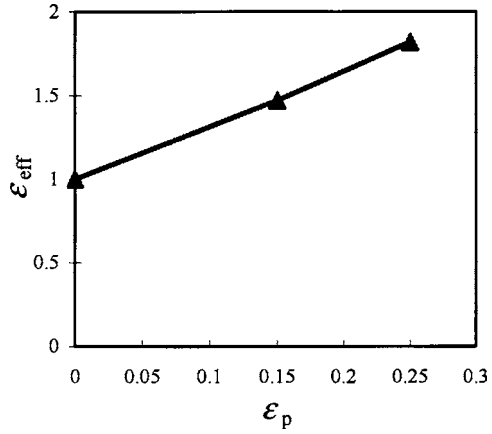

Fig. 19 Effect of solid volume fraction on ε_{eff}: Re=300, q_w =30 W/cm^2

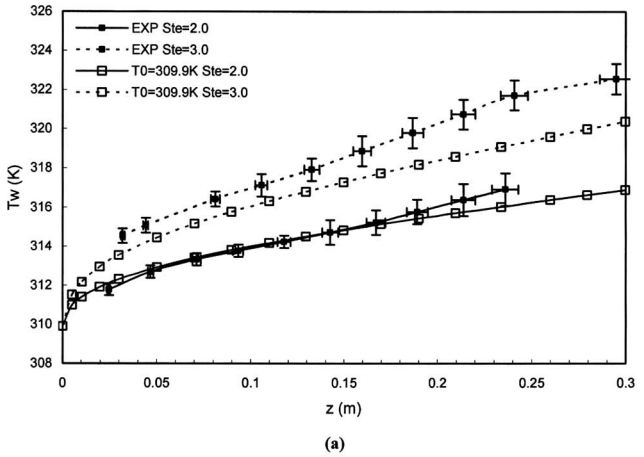

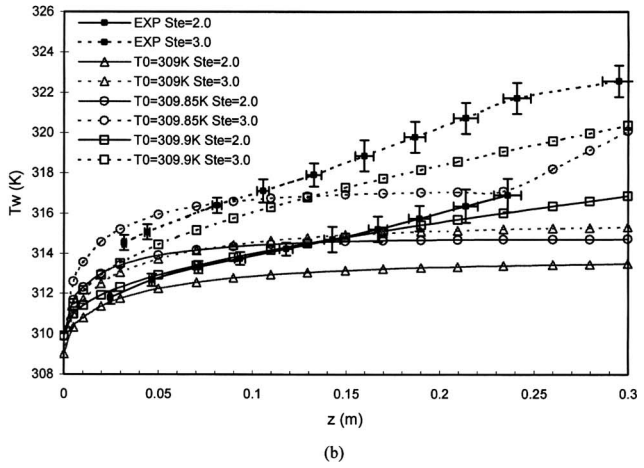

Fig. 20 (*a, b*) Comparison of simulation results with the experimental data reported in [18] under the following conditions: ε_p=0.1, Re=200, d_p=100 μm, T_0=309 K. The effect of the uncertainty in the inlet fluid temperature on the wall temperature is clearly shown.

the dimensional temperature is presented as a function of the tube distance for two different Stephan numbers (ste), which corresponds to two different wall heat fluxes. We found the wall temperature distribution is very sensitive to the inlet fluid temperature that is near the phase-change temperature of eicosane. According to [18] where the original experimental results were reported in a dimensionless form, the inlet fluid temperature was controlled at a value slightly below the phase-change temperature of eicosane, and no details on the controllability of the inlet temperature were given. We therefore present in Fig. 20 three sets of simulation results for each of two Ste numbers. They correspond to three slightly different inlet fluid temperatures T_0. It can be seen that the simulation results for T_0=309.9 K, a 0.05 K higher than the phase-change temperature (=309.85 K) under which the PCM is in liquid phase at the inlet, agrees more favorably to the experi-

Table 2 Thermophysical properties of eicosane PCM slurry [18,22]

	Density kg/m^3	Specific Heat J/(kg·K)	Thermal Conductivity W/(m·K)	Latent Heat kJ/kg	Viscosity Pa·s
Water (273K)	997.07	4179.6	0.606		8.904×10^{-4}
PCM particle (Liquid)	778	2250	0.15		
PCM particle (Solid)	856	1773	0.2583	247	

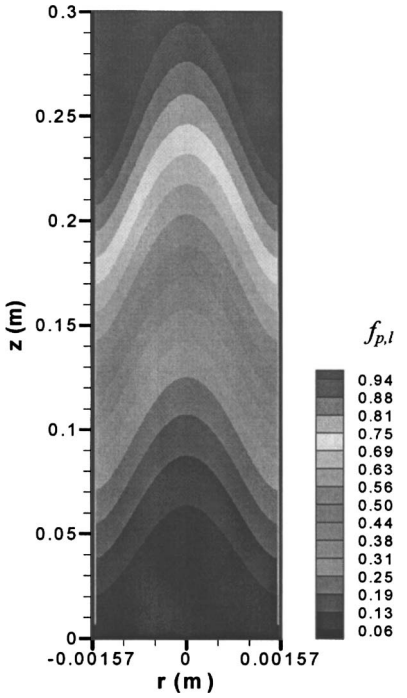

Fig. 21 Liquid mass fraction inside of PCM particle: T_0 =309.85 K, $\varepsilon_{p,0}$=0.1, Re=200, d_p=100 μm, Ste=2.0

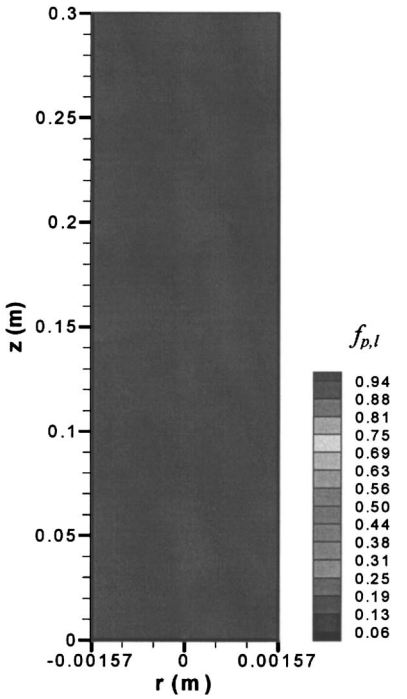

Fig. 22 Liquid mass fraction inside of PCM particle: T_0 =309.9 K, $\varepsilon_{p,0}$=0.1, Re=200, d_p=100 μm, Ste=2.0

mental results than the slightly lower inlet temperatures. The simulated wall temperature for Ste=2.0 almost coincides with the measured one within experimental error bars (Fig. 20(*a*)). For the condition that the inlet slurry is at the phase-change temperature and with the solid PCM, the simulated results clearly show the effect of phase change that yield a region where the variation of wall temperature remains flat. After the flow reaches near the exit, all the particles melt and then the wall temperature starts to increase again, a response to the fluid temperature in the melting zone. If we further reduce the inlet fluid temperature to 309 K, a 0.85 K reduction, the wall temperature shows a low rate of increase and indicates that the entire tube is under the phase-change region. As shown in Fig. 21, the liquid fraction distribution of PCM clearly indicates the gradual melting phenomena for T_0=309.85 K, while for T_0=309.9 K, PCM is all liquid throughout the tube (Fig. 22). The above observation seems to suggest that the experiments presented in [18] may not be able to control the phase-change region, which is very sensitive to the PCM slurry supply temperature. The experimentally determined wall temperature shows a trend that is similar to the postmelting region behavior that is characterized only by the liquid phase of the PCM.

It is also interesting to note from Fig. 20(*b*) that because the liquid c_p of eicosane (Table 2) is about 27% higher than that for solid; therefore, the suspension flow with initial liquid phase (309.9 K, which is 0.05 K above the melting point) results in a lower PCM-fluid temperature increase as compared to initially frozen (solid) PCM. In addition, for the same flow rate, the density difference between solid and liquid PCM could also contribute to the variation in particle velocity profiles; thus, affecting the local heat transfer coefficient. Because the wall temperature distribution follows the mean fluid temperature distribution, it is therefore shown that the wall temperature near the entrance for T_0=309.85 K is higher than that for T_0=309 K.

To further validate the model, the simulation is done for polystyrene suspension flow for which experimental data are available [19]. In this case, no phase change occurs, and only heat transfer with suspension flow is considered. A constant wall temperature condition is assumed in the simulation to be the same as the heating fluid temperature in the experiment. This would over-predict the flow exit temperature. The suspension fluid is 50 μm polystyrene spheres in 5.2% aqueous NaCl solution with the tube diameter being 0.001 m, tube length of 0.55 m and particle concentration of 0.088%. Our simulation results yield an exit mean fluid temperature of 44.12°C, versus the experimental result is 42.51°C, a 3.8% overprediction, as expected ($T_{\text{exit}}-T_{\text{inlet}}$ =42.3°C). This validation is better than, or at least the same as, that presented in [20] with their majority of discrepancies ranging from 4 to 10%.

The above comparison shows that the model presented in this study provides a more detailed, and reliable way to study the sensitivity of phase change behavior of a convective PCM slurry flow than the model that treats the slurry as a homogenous media with the modified heat capacity [20,21]. We further state that cautions should be taken in reporting the accuracy of any numerical simulation and experimental results involving PCM slurry flow where the phase-change region needs to be quantified not only by the slurry temperature but also by the liquid content (liquid mass fraction, $f_{p,l}$) of PCM. It is obvious that further studies on experimental investigations of PCM flow in microchannels are needed.

Conclusions

From the above discussion, the following conclusions may be drawn:

1. For a given Reynolds number and particle volume fraction, there exists an optimal wall heat flux that will yield a maximum effectiveness factor, $\varepsilon_{\text{eff,max}}$. At the particle volume fraction of 0.25, heat transfer can be enhanced by 60 to more than 110% with a Re between 90 and 600.
2. For a given Reynolds number and particle volume fraction, there also exists a maximum performance index PI_{max} at an optimal wall heat flux. At the particle volume fraction of 0.25, PI_{max} is between 1.3 and 2.0 for Re between 90 and 600. This indicates that at the optimal condition, PCM flow

not only significantly enhance heat transfer but also becomes more efficient, which means that less fluid pumping power is needed for a given heat transfer rate.

3. As Re increases, $\varepsilon_{\text{eff,max}}$ decreases. This indicates that to achieve the higher heat transfer rate by increasing the Reynolds number, the designer must be aware of the compromising of enhancement effects.
4. In general, the increase in the Reynolds number results in the decrease of heat transfer rate to pumping ratio Q/P. This is true for both PCM and single-phase flows in this study. Within the range of this study ($\varepsilon_p = 0.25$), Q/P is between 300 and 6000 for $\text{Re} = 90-600$ with the high Q/P corresponding to the low Re. Therefore, to best take advantage of the heat transfer enhancement for microchannel flow with PCM under laminar conditions, it is recommended that a low-Reynolds-number condition is maintained.
5. The limited comparison of the presented model to an experiment for macroscale flow shows that the model results reasonably agree with the experimental data for the condition of initial temperature at the 0.05 K above the phase change. The model results indicate for the first time the sensitivity of the simulation results to the initial flow temperature, which might explain the uncertainty in the reported experimental results in the literature. It also suggests that the evaluation on a model simulation for PCM slurry flow should consider the model ability to quantify the phase-change region characterized by both temperature and liquid-solid fractions.

The above conclusions will assist designers to make decisions that relate to the design or selection of a micropump suitable for microscale heat transfer devices.

Acknowledgment

The support from FIU Foundation and NSF (Award No. 0206028) are greatly appreciated. K.Q. Xing also acknowledges the support from FIU Presidential Ph.D. Scholarship.

Nomenclature

c_p = specific heat at constant pressure, J/(kg K)
D = tube diameter, m
D_v = virtual mass coefficient, −
d_p = particle diameter, m
f = mass fraction inside of PCM particle, −
G = particle-particle interaction modulus, Pa
$\mathbf{g}$ = gravitational acceleration vector, m/s^2
h = volumetric heat transfer coefficient, $\text{W/(m}^3\text{ K)}$
h_{ls} = latent heat for fusion, J/kg
h_p = heat transfer coefficient, $\text{W/(m}^2\text{ K)}$
i = enthalpy, J/kg
k = thermal conductivity, W/(m K)
L = tube length, m
Nu_p = Nusselt number, $h_p d_p / k_l$
p = pressure, Pa
PI = performance index, −
Pr = Prandtl number
Re_p = Reynolds number, $\varepsilon \rho_l |\mathbf{v}_l - \mathbf{v}_s| d_p / \mu_l$
Ste = bulk Stefan number, $c_{pb}(q_w D/2k_b)/(\varepsilon_s h_{ls}(\rho_p/\rho_b))$
T = temperature, K
t = time, s
u = r-direction velocity, m/s
V = inlet velocity, m/s
$\mathbf{v}$ = velocity vector, m/s
w = z-direction velocity, m/s
r, z = coordinates

Greek Symbols

β = drag coefficient, $\text{kg/(m}^3\text{ s)}$
ε = volume fraction in the suspension, −
ε_{eff} = effectiveness factor, −
μ = viscosity, Pa s
ξ = volume fraction inside of PCM particle, −
ρ = density, kg/m^3

Subscripts

0 = inlet
b = bulk
eff = effective
f = carrier fluid
l = liquid phase
m = melting
p = PCM particle
s = solid phase

References

[1] Drexler, K. Eric, 1992, *Nanosystems, Molecular Machinery, Manufacturing and Computation*, Wiley, New York.
[2] Frank, M. P., and Knight, F. T., Jr., 1998, "Ultimate Theoretical Models of Nanocomputers," Nanotechnology, **9**(3), pp. 162–176.
[3] Ortega, A., 2002, "What are the Heat Flux Limits of Air Cooling?" *2002 Int. Mechanical Congress and Exposition, Panel: Challenges in Cooling High Heat Flux Electronics Systems*, New Orleans, Nov. 17–22, ASME, New York, pp. 1–9.
[4] Gromoll, B., 1994, "Advanced Micro Air-Cooling Systems for High Density Packaging," *10th IEEE Semiconductor Thermal Measurement and Management Symposium*, Feb. 1–3, IEEE, New York, pp. 53–58.
[5] Mechalick, E. M., and Tweedie, A. T., 1975, "Two Component Thermal Energy Storage Material," Report NSF/RANN/SE/AER-74-09186, National Science Foundation, Washington, DC.
[6] Tao, Y.-X., Moreno, R., and Hao, Y. L., 2003, "Design Analysis of a 3-D, Ultra-High Performance, Scalable, Micro Convective Heat Sink With NPCM," *First Int. Conf. on Microchannels and Minichannels*, April 24–25, Rochester, NY.
[7] Hao, Y. L., and Tao, Y.-X., 2004, "A Numerical Model For Phase Change Suspension Flow In Microchannels," Numer. Heat Transfer, Part A, **46**(1), pp. 55–77.
[8] Bouillard, J. X., Lyczkowski, R. W., and Gidaspow, D., 1989, "Porosity Distributions in a Fluidized Bed With an Immersed Obstacle," AIChE J., **35**(6), pp. 908–922.
[9] Gidaspow, D., 1986, "Hydrodynamics of Fluidization and Heat Transfer: Supercomputer Modeling," Appl. Mech. Rev., **39**(1), pp. 1–23.
[10] Jackson, R., 1971, "Fluid Mechanical Theory," in: J. F. Davidson and J. Harrison eds., *Fluidization*, Academic, London, pp. 63–119.
[11] Bauer, R., and Schlunder, E. U., 1978, "Effective Radial Thermal Conductivity of Packing in Gas Flow," Int. Chem. Eng., **18**, pp. 189–204.
[12] Wakao, N., and Kaguei, S., 1982, *Heat and Mass Transfer in Packed Beds*, Gordon and Breach, New York.
[13] Hao, Y., and Tao, Y.-X., 2003, "Non-Thermal Equilibrium Melting of Granular Packed Bed In Horizontal Forced Convection, Part I: Experiment," Int. J. Heat Mass Transfer, **46**, pp. 5017–5030.
[14] Vand, V., 1945, "Theory of Viscosity of Concentrated Suspensions," Nature (London), **155**, pp. 364–365.
[15] Hao, Y., and Tao, Y.-X., 2003, "Non-Thermal Equilibrium Melting of Granular Packed Bed in Horizontal Forced Convection, Part II: Numerical Simulation," Int. J. Heat Mass Transfer, **46**(26), pp. 5031–5044.
[16] Yamagishi, Y., Takeuchi, H., Pyatenko, A. T., and Kayukawa, N., 1999, "Characteristics of Microencapsulated PCM Slurry as a Heat Transfer Fluid," AIChE J., **45**(4), pp. 696–707.
[17] Choi, E., Cho, Y. I., and Lorsch, H. G., 1994, "Forced Convection Heat Transfer With Phase-Change-Material Slurries: Turbulent Flow in a Circular Tube," Int. J. Heat Mass Transfer, **37**(2), pp. 207–215.
[18] Goel, M., Roy, S. K., and Sengupta, S., 1994, "Laminar Forced Convection Heat Transfer in Microcapsulated Phase Change Material Suspensions," Int. J. Heat Mass Transfer, **37**(4), pp. 593–604.
[19] Ahuja, A. S., 1975, "Augmentation of Heat Transfer in Laminar Flow of Polystyrene Suspensions," J. Appl. Phys., **46**, pp. 3408–3425.
[20] Charunyakorn, P., Sengupta, S., and Roy, S. K., 1991, "Forced Convection Heat Transfer in Microencapsulated Phase Change Material Slurries: Flow in Circular Ducts," Int. J. Heat Mass Transfer, **34**(3), pp. 819–833.
[21] Hu, X., and Zhang, Y., 2002, "Novel Insight and Numerical Analysis of Convective Heat Transfer Enhancement With Microencapsulated Phase Change Material Slurries: Laminar Flow in a Circular Tube with Constant Heat Flux," Int. J. Heat Mass Transfer, **45**, pp. 3163–3172.
[22] *CRC Handbook of Chemistry and Physics*, 73rd Edition, 1992–1993, CRC Press, Boca Raton.

Journal of Heat Transfer

Technical Briefs

Fully Developed Nucleate Boiling in Narrow Vertical Channels

M. S. Lakshminarasimhan

Q. Lu

Y. Chin

D. K. Hollingsworth

Larry C. Witte
e-mail: witte@uh.edu

Department of Mechanical Engineering,
University of Houston,
Houston, TX, 77204-4792

Experiments were performed to investigate nucleate flow boiling and incipience in a vertical flow channel, 20 mm wide $\times$ 357 mm long*, with one wall heated uniformly and others approximately adiabatic. Three channel spacings, 2, 1 and* 0.5 mm*, were investigated. Initially subcooled R-11 flowed upward through the channel; the mass flux varied from* 60 to 4586 kg/(m^2 s)*, and the inlet pressure ranged up to* 0.20 MPa*. Liquid crystal thermography was used to measure distributions of surface temperature from which the heat transfer coefficients on the heated surface were calculated. Fully developed saturated nucleate boiling was correlated well by a modification of Kandlikar's technique.* [DOI: 10.1115/1.1928914]

Keywords: Boiling, Narrow Channels, Convection

Introduction

Advances in high performance electronics and the miniaturization of electronic circuits require efficient heat removal techniques to accommodate high heat fluxes usually encountered in such systems. Forced convection in narrow channels has been considered for cooling of microelectronics as well as advanced nuclear reactors. Boiling in narrow channels poses some problems, however. Bubbles can quickly grow to the point where they can block a narrow channel, and potentially affect how heat is transferred to the liquid-vapor mixture typical of fully developed nucleate boiling in narrow channels. This paper concentrates on the nature of fully developed nucleate boiling. Bergles et al. [1] give an excellent review of boiling in small diameter channels that covers all work up to 2003.

Experimental Apparatus and Data Reduction

The apparatus used for these studies has been described in detail by Chin et al. [2]. A briefer description is given here.

A thermochromic liquid crystal (TLC) was chosen as the sensor for surface temperature measurement and mapping. This required a working fluid with appropriate properties to assure that the temperature range that encompasses convection, boiling incipience and fully developed nucleate boiling would fall into the active band of the TLC. R-11 was selected because its boiling point was compatible with the active band of the selected TLC.

The test section was a rectangular channel with a width of 20 mm, a length of 357 mm, with an initial height (channel spacing) of 2 mm. Modifications of the apparatus resulted in channel spacings of 1 and 0.5 mm. Figure 1 shows details of the channel. The channel was machined into one face of an aluminum bar so that the channel spacing was created by the depth of the machining operation. The test section inlet was fed by a flow loop that controlled the flow rates, temperatures and pressures of the incoming R-ll.

The heated wall of the channel was formed by a 76-μm-thick Haynes 230 alloy foil clamped to the face of the aluminum bar. The foil was heated with direct current, and the energy dissipated from the portion of the foil beneath the clamping frame was removed by chilled water flowing through passages in both the clamping frame and the edge of the aluminum bar. The sidewalls of the channel were isolated from this cooling flow by air gaps machined parallel to the channel walls into the aluminum bar.

The foil was attached so that heating began at the entrance of the test channel with no unheated starting length. The fluid temperatures in the inlet and exit plenums were measured by thermocouples and collected along with the pressures, and the foil voltage and current by a computer-controlled data acquisition system.

The visible surface of the foil was air brushed with water-soluble black paint followed by several coats of a microencapsulated TLC formulation from Hallcrest, Inc. Real-time images of the foil were recorded on videotape during experiments, and single images were digitized directly by a 3×8 bit Matrox color frame grabber. The useful active range of the selected TLC as verified by six *in situ* calibrations in the present apparatus was 44.4–59.6°C. The calibration and uncertainty computation was done in accordance with Hay and Hollingsworth [3].

The single-phase flow was characterized by a Reynolds number defined as

$$\mathrm{Re} = \frac{\rho u D_h}{\mu} \tag{1}$$

The local bulk mean temperature obtained by an enthalpy balance, $T_m(x)$, is given by

Contributed by the Heat Transfer Division for publication in the JOURNAL OF HEAT TRANSFER. Manuscript received April 12, 2004; revised manuscript received November 4, 2004. Review conducted by Ramendra P. Roy.

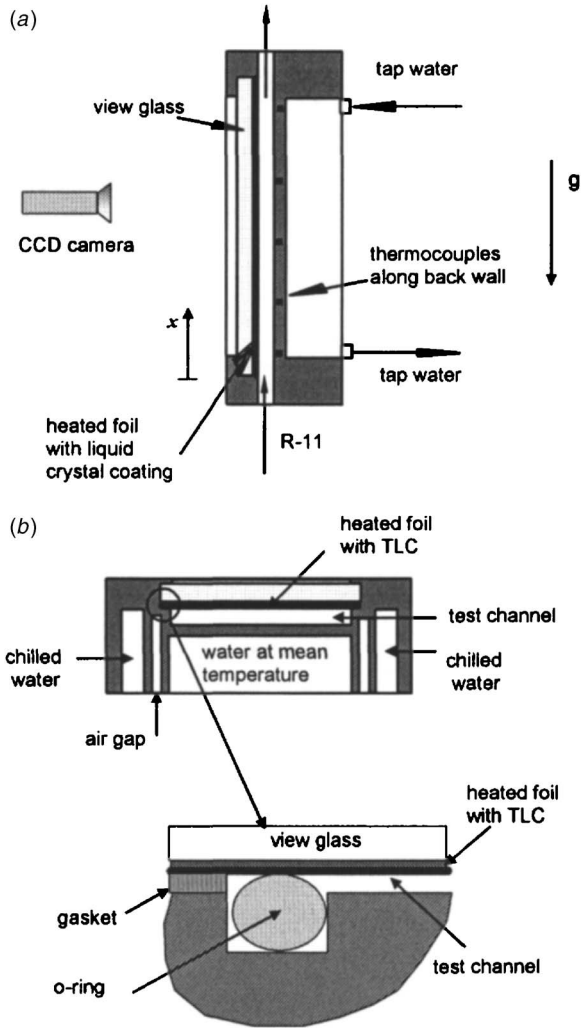

Fig. 1 Cross-section views of the channel, (a) longitudinal, (b) transverse with construction detail. For (b) the gravity vector is pointing out of the page.

$$T_m(x) = T_i + 4\frac{q_w}{\rho u C_p}\frac{x}{D_{\text{he}}} \tag{2}$$

where symbols are defined in the Nomenclature. D_{he} is the equivalent heated diameter suggested by Katto [4] for handling asymmetrical heating situations

$$D_{\text{he}} = \frac{4 \times \text{flow area}}{\text{heated perimeter}} \tag{3}$$

The heat flux from the test surface, q_w, was corrected for the heat lost through the TLC surface and view glass. For the purpose of computing $T_m(x)$, it was also corrected for the small heat loss from the fluid into the nearly adiabatic back surface of the channel. This was done numerically using a resistance circuit including the effects of conduction across the back wall and natural convection to the surrounding air. The maximum value of the backside heat loss was about 3% of the heat flux due to heat generation in the foil.

The fluid properties were evaluated at the local bulk mean temperature $T_m(x)$. The surface temperature T_w was calculated from the acquired images. The wall superheat is defined as $\Delta T_{\text{sat}} = T_w - T_{\text{sat}}$.

For a given mass flow rate, the heat flux was increased and then decreased in a series of small steps. In doing so, the heat transfer mode changes from single-phase forced convection to fully developed nucleate boiling and then back to single-phase forced convection. After steady state conditions were achieved at each step, the measurands were acquired by the data acquisition system, and a still image of the TLC surface was captured by the image processing computer.

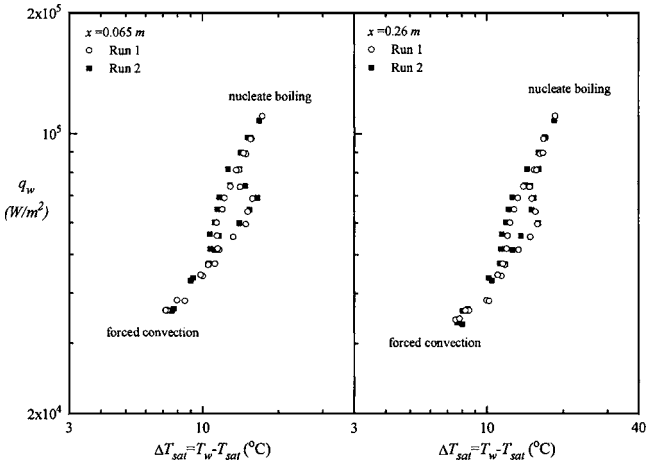

Fig. 2 The repeatability of two 2 mm channel experiments from the same heater and TLC coatings. Run 1: u=1.86 m/s, G=2647 kg/m^2 s, p_i=0.181 MPa, $\Delta T_{\text{sub},i}$=8.28°C. Run 2: u=1.86 m/s, G=2663 kg/m^2 s, p_i=0.180 MPa, $\Delta T_{\text{sub},i}$=8.23°C.

Experimental uncertainties were calculated according to Kline and McClintock [5]. The relative uncertainty in the heat flux was found to be ±2.3%, based on uncertainties of ±0.17% and ±1.1% associated with the voltage and electric current measurements. The uncertainty in wall superheat and inlet subcooling based on the TLC calibration and thermocouple uncertainties averaged ±1.93° and ±0.33°C, respectively. The uncertainties in mass velocity and Reynolds number were estimated to be less than ±5.1% and ±5.7%, respectively.

Discussion of Results

The liquid crystal images obtained from the experimental data were digitized and converted into wall temperature, $T_w(x)$, and local heat transfer coefficient, $h(x) = q_w/[T_w(x) - T_m(x)]$. Using these measurands and other channel parameters, the heat transfer processes occurring in the channel, namely, single-phase forced convection, boiling incipience, and transition to fully developed boiling, were examined. Forced convection results have been reported in [2], and boiling inception and transition boiling will be reported in a separate paper.

Transition to Fully Developed Nucleate Boiling. Chin [6] observed that in flow boiling in a 2 mm channel, the transition from single-phase flow to fully developed nucleate boiling was not a simple one-step process. She found that the transition at a given streamwise location in the channel traces out a path where fully developed boiling is approached in a gradual fashion. Figure 2 shows data from two runs each at two streamwise locations to demonstrate the repeatability of the phenomenon. The data discussed in the following section lie in the fully developed region, i.e., along the single curve that lies above the hysteresis loop in Fig. 2. The hysteresis loop is mapped by first increasing the heat flux up to the upper limit of the liquid crystal, then decreasing the flux back to the point where no boiling exists.

Fully Developed Nucleate Boiling. This regime is usually associated with uniform bubble nucleation, high void fraction, and bubbles detaching from the wall and moving into the liquid core. In narrow channels bubble sizes can grow to the size of the channel spacing rapidly if the heat flux is high enough. In this regime,

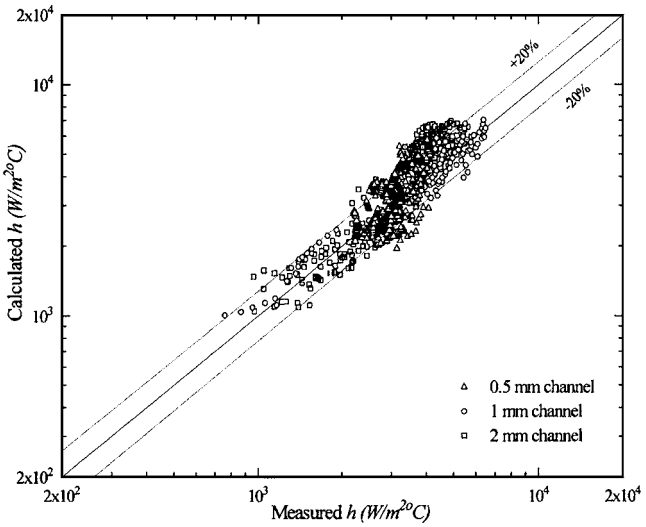

Fig. 3 Narrow channel data compared to Kandlikar's correlation

the quality of the two-phase mixture assumes special significance and has to be included as a major parameter in correlations. The equilibrium quality is defined as

$$\chi(x) = \frac{i(x) - i_{\text{sat}}(x)}{h_{\text{fg}}} \tag{4}$$

An energy balance on a segment of the duct yields

$$\chi = \frac{q_w x}{GHh_{\text{fg}}} - \frac{C_{\text{pl}}(T_{\text{sat}}(x) - T_i)}{h_{\text{fg}}} \tag{5}$$

Fully developed nucleate boiling data for all channels were compared to the correlations of Shah [7] and Liu and Winterton [8]. The details of these comparisons are omitted because we found the most suitable correlation was that of Kandlikar [9] for predicting saturated flow boiling inside tubes. He used a large database involving 24 experimental runs with ten different fluids. His model considers the total heat transfer as the sum of convective and nucleate boiling components. The basic correlation is

$$h_{\text{TP}} = C_1 Co^{C_2} h_{\text{fc}} + C_3 Bo^{C_4} h_{\text{fc}} \tag{6}$$

The convection number is defined as

$$Co = \left[\frac{1-\chi}{\chi}\right]^{0.8}\left[\frac{\rho_g}{\rho_l}\right]^{0.5} \tag{7}$$

where χ is the quality defined by Eq. (4), and *Bo* is the boiling number,

$$Bo = \frac{q_w}{Gh_{\text{fg}}} \tag{8}$$

The constants C_1 through C_4 constants depend on the dominance of the convective or the boiling region.

The final form of Kandlikar's correlation is

$$\frac{h_{\text{TP}}}{h_{\text{fc}}} = C_1 Co^{C_2} + C_3 Bo^{C_4} F \tag{9}$$

where the factor F is used to represent different fluid-surface combinations. For $Co < 0.65$, Kandlikar gives: $C_1 = 1.136$, $C_2 = -0.9$, $C_3 = 667.2$ and $C_4 = 0.7$. For $Co > 0.65$, he gives: $C_1 = 0.6683$, $C_2 = -0.2$, $C_3 = 1058.0$ and $C_4 = 0.7$.

Figure 3 shows all our data presented in terms of Kandlikar's correlation. This represents all the data for the case where $T_m \geq T_{\text{sat}}$. For R-11, Kandlikar quotes a mean deviation of ±17%. If this is taken to be one standard deviation, then ±34% would collect approximately 95% of the data. Most of our data are collected by ±20%, except at large h_{TP}, where the correlation tends to over predict somewhat. If a "thin channel" enhancement were occurring, one would expect to see the correlation under predict the data. We see no deterministic trend indicating enhancement or reduction in h_{TP} relative to large-channel expectations in the 0.5, 1 and 2 mm channels.

Warrier, Dhir and Momoda [10] proposed a correlation for fully developed, saturated boiling in narrow rectangular channels as shown below

$$\frac{h_{\text{tp}}}{h_{\text{fc}}} = 1 + 6.0 Bo^{1/16} + f(Bo)\chi^{0.65} \tag{10}$$

where

$$f(Bo) = -5.3(1 - 855Bo) \tag{11}$$

A comparison of Warrier's correlation, Eq. (10), to Kandlikar's correlation for the same heat fluxes, mass fluxes, and quality does not show good agreement, except for some cases at low quality. For example, for a quality of 0.2, wall heat flux of 75 kW/m^2, and a mass flux of 1890 kg/m^2 s, the boiling number, Bo, is 0.00022. Based on these values, the ratio of the value of h_{tp} computed by Kandlikar's correlation to the value computed by Warrier's correlation is 2.14, indicating a much higher value predicted by Kandlikar. As quality increases the ratio of the two correlations diverges. The dependence on quality causes an increase in Kandlikar's correlation while a decrease occurs when using Warrier's correlation, in the range of experimental conditions investigated. It should be noted that Warrier's correlation was based on a limited number of data, and he warned that the correlation should be limited to *Bo* numbers between 0.00027 and 0.00089, and qualities from 0.03 to 0.55.

Concluding Remarks

Kandikar's correlation provides the best fit for fully developed saturated nucleate boiling in the narrow channels used in these studies. Belhadj et al. [11] surmised that bubbles detaching from an opposite heated wall can produce heat transfer enhancement (i.e., thin channel effects) only if $H < 2D_b$. With only one wall being heated in our apparatus, thin channel effects can be expected when the bubble diameter is comparable to the channel spacing. The H/D_b ratios estimated for these experiments are between 0.75 and 1.05 for the 0.5 mm channel, 1.5 and 2.1 for the 1 mm channel, between 3.0 and 4.2 for the 2 mm channel. These estimates taken together with the noted absence of a measured heat transfer enhancement do not contradict Belhadj's estimates of an upper bound on H/D_b. However, additional experiments at a small channel height are required to directly challenge Belhadj's upper bound.

Acknowledgments

The authors appreciate the support of NSF Grant No. CTS-9701556 and TX ARP-003652118 for support of this research.

Nomenclature

Bo = boiling number, q_w/Gh_{fg}
Co = convection number
C_p = specific heat, J/(kg°C)
D_b = bubble departure diameter, m
D_h = hydraulic diameter, $D_h = 2H$, m
D_{he} = equivalent heated diameter, m
F = Kandlikar correction factor
G = mass velocity, kg/(m^2 s)
$h(x)$ = local heat transfer coefficient, W/(m^2°C)
h_{fc} = single phase heat transfer coefficient, W/(m^2°C)
h_{TP} = two phase heat transfer coefficient, W/(m^2°C)
h_{fg} = latent heat of evaporation, J/kg

H = channel spacing, m;
i = enthalpy, J/kg
q_w = wall heat flux, W/m^2
Re = Reynolds number, uD_h/ν
T_m = local bulk mean temperature of fluid, °C
T_{sat} = liquid saturation temperature, °C
T_w = local wall temperature, °C
u = velocity of fluid, m/s
x = coordinate along the heater surface in axial direction
ΔT_{sat} = wall superheat, °C

Greek

μ = dynamic viscosity, kg/(ms)
ρ = density, kg/m^3
χ = quality

Subscript

g = gas or vapor
i = inlet
ℓ = liquid
sat = saturation

References

[1] Bergles, A. E., Lienhard, V., J. L., Kendall, G. E., and Griffith, P., 2003, "Boiling and Evaporation in Small Diameter Channels," Heat Transfer Eng., **21**(1), pp. 18–40.

[2] Chin, Y., Lakshminarasimhan, M., Lu, Q., Hollingsworth, D. K., and Witte, L. C., 2002, "Convective Heat Transfer in Vertical Asymmetrically Heated Narrow Channels," ASME J. Heat Transfer, **124**(6), pp. 1019–1025.

[3] Hay, J. L., and Hollingsworth, D. K., 1996, "A Comparison of Trichromic Systems for Use in the Calibration of Polymer-Dispersed Thermochromic Liquid Crystals," Exp. Therm. Fluid Sci., **12**, pp. 1–12.

[4] Katto, Y., 1986, "A General Correlation for Saturated Two-Phase Flow Boiling Heat Transfer inside Horizontal and Vertical Tubes," *Handbook of Heat and Mass Transfer*, Gulf Publishing Co., Vol. 1, pp. 303–325.

[5] Kline, S. J., and McClintock, F. A., 1953, "Describing Uncertainties in Single Sample Experiments," Mech. Eng. (Am. Soc. Mech. Eng.), **75**, pp. 3–8.

[6] Chin, Y., 1997, "An Experimental Study on Flow Boiling in a Narrow Channel: From Convection to Nucleate Boiling," PhD Dissertation, University of Houston.

[7] Shah, M. M., 1986, "Prediction of Heat Transfer during Forced-Convection Subcooled Boiling," *Handbook of Heat and Mass Transfer*, Gulf Publishing Co., Vol. 1, pp. 385–403.

[8] Liu, Z., and Winterton, R. H. S., 1991, "A General Correlation for Saturated and Subcooled Flow Boiling in Tubes and Annuli, Based on a Nucleate Pool Boiling Equation," Int. J. Heat Mass Transfer, **34**, pp. 2759–2765.

[9] Kandlikar, S., 1990, "A General Correlation for Saturated Two-Phase Flow Boiling Transfer Inside Horizontal and Vertical Tubes," ASME J. Heat Transfer, **112**, pp. 219–228.

[10] Warrier, G., Dhir, V., and Momoda, L., 2002, "Heat Transfer and Pressure Drop in Narrow Rectangular Channels," Exp. Therm. Fluid Sci., **26**, pp. 53–64.

[11] Belhadj, M., Aldemir, T., and Christensen, R., 1991, "Determining Wall Superheat under Fully Developed Nucleate Boiling in Plate-Type Research Reactors with Low Velocity Upwards," Nucl. Technol., **95**, pp. 95–102.

Optimum Profile of Thin Fins With Volumetric Heat Generation: A Unified Approach

B. Kundu
Department of Mechanical Engineering,
Jadavpur University, Kolkata 700 032, India
e-mail: bkundu123@rediffmail.com

P. K. Das
Department of Mechanical Engineering,
Indian Institute of Technology, Kharagpur 721302, India
e-mail: pkd@iitkgp.ernet.in

In this paper, a generalized methodology for the optimum design of thin fins with uniform volumetric heat generation is described. Using variational calculus, the optimum profiles of longitudinal, annular, and pin fins are determined from the basic fin equation under the constraint of specified fin volume. From a common optimality criteria, a generalized closed form expression for the fin thickness is obtained for the above three types of fins. Closed-form expressions are also obtained for the optimum profiles of longitudinal and pin fins. As a special case, both the temperature profile and the shape of optimum fins without heat generation are determined. [DOI: 10.1115/1.1929784]

Keywords: Annular Fin, Calculus of Variation, Heat Generation, Longitudinal Fin, Optimum Profile, Pin Fin

1 Introduction

A fin is a conductive-convective protrusion attached on the primary heat transfer surface for the augmentation of heat transmission. Fins of various designs are extensively used in heat exchangers and heat sinks for electronic components. Because the addition of fins increases the cost of the equipment and the tractive power of any mobile system, continuous efforts are under way to design fins such that the maximum utilization of the fin material is achieved.

The mathematical analysis of convective fins was first provided by Gardner [1], based on the assumption of constant conductivity and a uniform coefficient of convective heat transfer along the fin surface. The heat flow due to conduction depends on the temperature gradient and the cross-sectional area at a particular location. On the other hand, the convective heat transfer depends on the local temperature excess and the surface area. The rate of heat transfer from a fin of a given volume can be maximized by a proper selection of the cross-sectional area and the surface area of the fin from its base to tip. In other words, the designer has to find the profile geometry for a given fin volume that will maximize the rate of heat transfer. This aspect of fin design was first appreciated by Schmidt [2], who proposed a heuristic reasoning to show that the heat conduction in optimum thin fins has to be one-dimensional and every section of the fin will be equally effective in dissipating the thermal energy. Duffin [3] established the proposition of Schmidt [2] on firm ground through a rigorous mathematical analysis using calculus of variation. It may be noted in these analyses [2,3] that the profile curvature is neglected for the calculation of surface area, assuming thin fins. This approximation is known as the length-of-arc idealization (LAI).

Contributed by the Heat Transfer Division for publication in the JOURNAL OF HEAT TRANSFER. Manuscript received by the Heat Transfer Division May 20, 2004; revision received January 18, 2005. Review conducted by: N. K. Anand.

Minkler and Rouleau [4] considered internal heat generation in longitudinal fins. They have made an exercise for determining the profile of minimum mass fins. Taking the lead from Schmidt [2], they have assumed that optimum longitudinal fins with internal heat generation will also have a linear temperature profile. They have not provided any mathematical justification for this assumption. Subsequently, Wilkins [5] proved that the assumption of Minkler and Rouleau [4] is not correct. Liu [6] applied the variational principle for the optimization of cooling fins with heat generation. He considered a temperature-dependent heat generation function. Natarajan and Shenoy [7] determined the optimum shape of convective pin fins with variable heat transfer coefficient, employing the calculus of variation.

The literature review shows that no effort has yet been made for a unified analysis of fins of three basic geometries. In all the previous works, specific analysis has been made for the typical fin geometry. On the contrary, in the present work, a unified approach based on the variational principle has been suggested. A single set of equations and boundary conditions have been used for finding the optimum profiles of three main types of fins, namely, longitudinal, annular, and pin fins. The formulation has been done for a generalized case of uniform volumetric heat generation. However, as a special case, a solution can be derived for fins without heat generation.

2 Statement of the Problem

The geometrical configuration of three typical fins, namely, longitudinal fin, pin fin, and annular fin are shown in Fig. 1. The present analysis is based on the idealization of Murray [8] and Gardner [1]. Additionally, it is assumed that heat sources of constant generation rate are uniformly distributed throughout the fin volume. The heat transfer through any of these fins can be expressed in a general nondimensional form as follows:

$$\frac{d}{dX}\left[Y^m(R_i+X)^n\frac{d\theta}{dX}\right]=Y^{m-1}(R_i+X)^n(m\mathrm{Bi}-N_gY)\theta \qquad (1)$$

where

$$\mathrm{Bi}=hL/k,\quad X=x/L,\quad Y=y/L,\quad R_i=r_i/L,\quad N_g=\dot{g}L^2/k \text{ and}$$

$$m=1,\quad n=0 \quad \text{for longitudinal fin}$$

$$m=2,\quad n=0 \quad \text{for pin fin}$$

$$m=1,\quad n=1 \text{ for annular fin.}$$

For all the fin geometries, Eq. (1) is subjected to the following boundary conditions:

$$\text{at } X=0,\quad \theta=1 \qquad (2)$$

$$\text{at } X=1,\quad Y^m d\theta/dX=0 \qquad (3)$$

Heat dissipation from the fin can be expressed as

$$Q=\frac{q}{(2/m)^{m+n}(T_b-T_a)\pi^{m+n-1}kL^{m+n-1}}=-\left[Y^m(R_i+X)^n\frac{d\theta}{dX}\right]_{X=0}$$

$$=\int_{X=0}^{1}Y^{m-1}(R_i+X)^n(m\mathrm{Bi}-N_gY)\theta\,dX \qquad (4)$$

The volume of the fin can be obtained from the expression given below

$$U=\frac{V}{(2/m)^{m+n}\pi^{m+n-1}L^{m+n+1}}=\int_{X=0}^{1}Y^m(R_i+X)^n\,dX \qquad (5)$$

Putting the numerical values of m, n in Eqs. (4) and (5), one gets the conventional expressions of heat transfer rate and fin volume for longitudinal, annular, and pin fins [9].

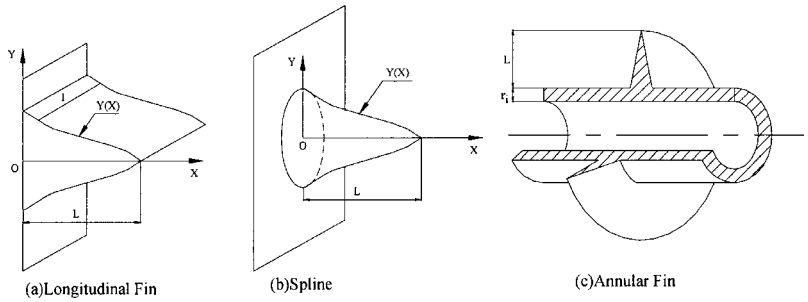

Fig. 1 Geometrical configurations of three typical fins

3 Variational Method

In the present analysis, it is intended to find the profile shape of the fin such that heat transfer rate Q is maximized for a given fin volume U. To accomplish this, a function Λ is introduced

$$\Lambda = \int_{X=0}^{1} Y^{m-1}(R_i + X)^n \left\{ \left(\frac{d\theta}{dX} \right)^2 + [m\mathrm{Bi} - N_g Y]\theta^2 \right\} dX \tag{6}$$

Furthermore, integrating by parts and utilizing $Y^m d\theta/dX = 0$ (Eq. (3)), it can be shown that

$$\int_{X=0}^{1} Y^m (R_i + X)^n \left(\frac{d\theta}{dX} \right)^2 dX = -\int_{X=0}^{1} [m\mathrm{Bi} - N_g Y][\theta(\theta - 1) \times (R_i + X)^n Y^{m-1}] dX \tag{7}$$

Substituting Eq. (7) into Eq. (6), one gets

$$\Lambda = \int_{X=0}^{1} Y^{m-1}(R_i + X)^n [m\mathrm{Bi} - N_g Y]\theta \, dX \tag{8}$$

Λ satisfies Eq. (1), along with the boundary conditions. Therefore, Q can be replaced by Λ. The present optimization problem can be solved by the calculus of variation. It may be noted that both the objective function (Eq. (4)) and the constraint (Eq. (5)) are in the integral form. Therefore, through the use of a Lagrange multiplier, a modified objective function Γ may be constructed following the methodology of Elsgolts [10]

$$\Gamma = Q - \lambda U = \Lambda - \lambda U = \int_{X=0}^{1} F \, dX = \int_{X=0}^{1} \left[Y\left(\frac{d\theta}{dX} \right)^2 + (m\mathrm{Bi} - N_g Y)\theta^2 - \lambda Y \right] Y^{m-1}(R_i + X)^n dX \tag{9}$$

The factor λ in the above equation is the Lagrange multiplier.

3.1 Condition for Optimality. The optimality conditions can be obtained by solving the Euler-Lagrange equation for the multivariable function Γ.

$$\frac{\partial F}{\partial \theta} - \frac{d}{dX}\left(\frac{\partial F}{\partial \theta'} \right) = 0 \tag{10}$$

and

$$\frac{\partial F}{\partial Y} - \frac{d}{dX}\left(\frac{\partial F}{\partial Y'} \right) = 0 \tag{11}$$

Equations (10) and (11) become

$$\frac{d}{dX}\left[Y^m (X + R_i)^n \frac{d\theta}{dX} \right] = Y^{m-1}(X + R_i)^n (m\mathrm{Bi} - N_g Y)\theta \tag{12}$$

and

$$Y\left(\frac{d\theta}{dX} \right)^2 + [\mathrm{Bi}(m-1) - N_g Y]\theta^2 - \lambda Y = 0 \tag{13}$$

When there is no constraint on the length L, it can be taken as a variable and the variation of L gives the following results:

$$\delta F = \left[Y^{m-1}(R_i + X)^n \left\{ Y\left(\frac{d\theta}{dX} \right)^2 + m(\mathrm{Bi} - N_g Y)\theta^2 - \lambda Y \right\} \delta X \right]_0^1 = 0 \tag{14}$$

at $X = 0$, the above term is zero as $\delta X = 0$

at $X = 1$, δX is not zero, therefore at the tip

$$Y\left(\frac{d\theta}{dX} \right)^2 + (m\mathrm{Bi} - N_g Y)\theta^2 - \lambda Y = 0 \tag{15}$$

Using Eq. (13), Eq. (15) becomes

$$\mathrm{Bi}\,\theta^2 = 0 \tag{16}$$

Therefore

$$\theta = 0 \text{ at } X = 1 \tag{17}$$

In order to determine the thickness at the tip, using Eqs. (3), (13), and (17), one can arrive at

$$Y = 0 \text{ at } X = 1 \tag{18}$$

Equation (1) can be written as

$$\frac{d}{dX}[Y^m (R_i + X)^n]\frac{d\theta}{dX} + Y^m (R_i + X)^n \frac{d^2\theta}{dX^2} = Y^{m-1}(R_i + X)^n (m\mathrm{Bi} - N_g Y)\theta \tag{19}$$

For the fin tip, Eq. (19) can be further simplified using Eqs. (17) and (18). Thus,

$$\frac{d}{dX}(Y^m) = 0 \tag{20}$$

4 Temperature Profile for the Optimum Fin

It may be noted that the condition for optimality given in Eq. (13) does not depend on n. Therefore, the term $(R_i + X)^n$ in Eq. (12) may be treated as a constant and can be removed from both sides of the equation. Multiplying Eq. (12) by $d\theta/dX$, one gets

$$\left(\frac{d\theta}{dX} \right)^2 \frac{d}{dX}(Y^m) + \frac{d}{dX}\left[Y^m \left(\frac{d\theta}{dX} \right)^2 \right] = Y^{m-1}(m\mathrm{Bi} - N_g Y)\frac{d}{dX}(\theta^2) \tag{21}$$

Equation (13) may be combined with Eq. (21) to give

$$\frac{d}{dX}[2\lambda Y^m - \{(m-1)\mathrm{Bi}Y^{m-1} - N_g Y^m\}\theta^2 - (m\mathrm{Bi} - N_g Y)\theta^2 Y^{m-1}] = 0 \tag{22}$$

Integrating Eq. (22) and using Eqs. (17) and (18), the following relationship is obtained:

$$\mathrm{Bi} = \frac{2Y(\lambda + N_g\theta^2)}{(2m-1)\theta^2} \tag{23}$$

Combining Eqs. (13) and (23), one gets

$$\frac{d\theta}{dX} = -\sqrt{\frac{(\lambda + N_g\theta^2)}{(2m-1)}} \tag{24}$$

Finally, the above equation may be integrated and the boundary conditions (2) and (3) may be used to determine the optimum temperature profile.

$$\theta_{\mathrm{opt}} = \frac{\sinh[\sigma(1-X)]}{\sinh(\sigma)} \tag{25}$$

where

$$\sigma = \left(\frac{N_g}{2m-1}\right)^{1/2} \tag{26}$$

5 Optimum Fin Profile

The temperature distribution given in Eq. (25) may now be substituted in Eq. (1) for finding the optimum fin profile

$$Y_{\mathrm{opt}} = \frac{(2m-1)\mathrm{Bi}}{2N_g}\left[\tanh^2\{\sigma(1-X)\} + \frac{n(X-1)}{2(R_i+X)\cosh^2\{\sigma(1-X)\}} + \frac{n\sqrt{2m-1}}{2(R_i+X)\sqrt{N_g}}\tanh\{\sigma(1-X)\}\right] \tag{27}$$

The optimum length of the fins L_{opt} can be determined from Eq. (4) using the expressions of Y_{opt} and θ_{opt} when the rate of heat dissipation and the volumetric rate of heat generation are specified. An analytical expression of L_{opt} for both the longitudinal fin and pin fin is obtained as follows:

$$L_{\mathrm{opt}} = \left[\frac{(2m-1)k}{\dot{g}}\right]^{1/2}\tanh^{-1}\left[\frac{qm^m\dot{g}^{(2m-1)/2}}{L_a}\right]^{1/(2m-1)} \tag{28}$$

where

$$L_a = (T_b - T_a)\pi^{m-1}k^{1/2}h^m(2m-1)^{(2m-1)/2} \tag{29}$$

In the case of an annular fin, the closed-form expression for L_{opt} cannot be obtained. However, L_{opt} can be determined by a suitable iterative technique for specific values of q, $\dot{g}$ and r_i.

The effects of heat generation on the optimum profile of different fins are illustrated in Fig. 2. From this figure, it can be demonstrated that for the increase of heat generation rate, the optimum profile is flatter with respect to the fin length.

6 Fin Efficiency for the Optimum Profile Fin

The actual heat transfer rate through the optimum fin above is calculated using Eqs. (4), (25), and (27), which can be expressed in dimensionless form as

$$Q = \frac{q}{(2/m)^{m+n}(T_b - T_a)\pi^{m+n-1}kL^{m+n-1}} = \frac{\mathrm{Bi}^m(2m-1)^{(2m-1)/2}}{2^{m+1}N_g^{(3m-1)/2}\sinh(\sigma)\cosh^{2m-1}(\sigma)} \times\left[4R_i^n N_g^{1/2}\sinh^2(\sigma) - 2nN_g^{1/2} + n(2m-1)^{1/2}\sinh(2\sigma)\right] \tag{30}$$

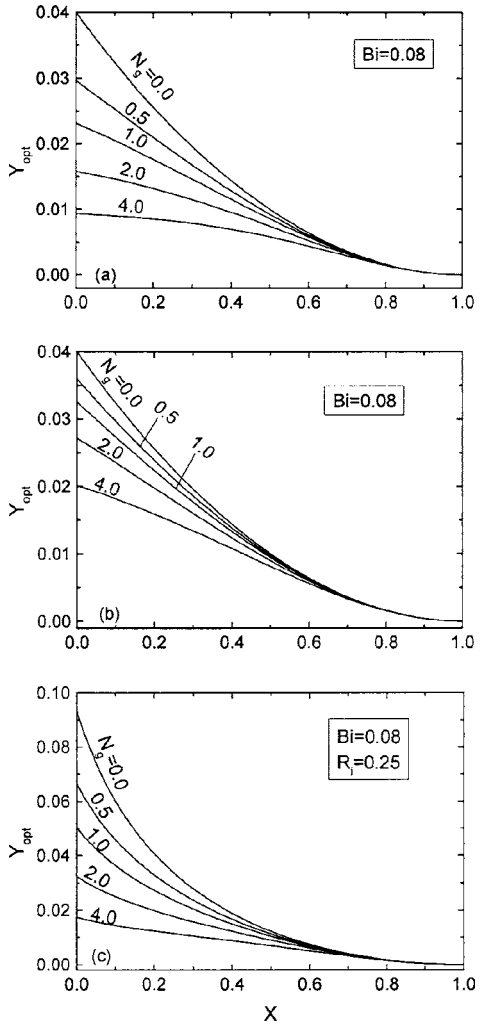

Fig. 2 Optimum profiles as a function of dimensionless heat generation rate N_g: (*a*) longitudinal fin, (*b*) pin fin, and (*c*) annular fin

The ideal heat transfer rate through the optimum fin is determined as if the entire fin surface were at its fin base temperature, which can be expressed in dimensionless form as

$$Q_i = \frac{q_i}{(2/m)^{m+n}(T_b - T_a)\pi^{m+n-1}kL^{m+n-1}} = \frac{(2m-1)\mathrm{Bi}^m}{2(m+n)N_g^{(2m+n-1)/2}}[N_g^{(n+1)/2}[1 + n(1 + 2R_i - N_g^{1/2})] + (2m + 3n - 1)^{1/2}N_g^{n/2}\tanh(\sigma)\{(3-2m)(nR_i+1) + (m-1)\tanh^2(\sigma)\} - n\ln(\cosh\sigma)] \tag{31}$$

Fin efficiency is defined as the ratio of actual heat transfer rate to the ideal heat transfer rate. Thus,

$$\eta = Q/Q_i \tag{32}$$

7 Special Case: $N_g = 0$

In the absence of volumetric heat generation inside the fin, the heat conduction equation may be written as

$$\frac{d}{dX}\left[Y^m(R_i+X)^n\frac{d\theta}{dX}\right] = mY^{m-1}(R_i+X)^n\theta \tag{33}$$

The condition for optimality is as follows [3]:

$$\frac{d\theta}{dX} = -\sqrt{\frac{\lambda}{(2m-1)}} \tag{34}$$

Integrating Eq. (34) and substituting boundary conditions given in Eqs. (2) and (3)

$$\theta_{\text{opt}} = (1 - X) \tag{35}$$

The generalized form of the fin profiles for the longitudinal fin, pin fin, and annular fin can be derived by substituting Eq. (35) in Eq. (33)

$$Y_{\text{opt}} = \frac{\text{Bi}}{(2+4n)(R_i+X)^n}[(1-X)^2 + n(3R_i + 2X - 6R_iX - 4X^2 + 3R_iX^2 + 2X^3)] \tag{36}$$

In the present case, the generalized closed-form expression for the optimum length L_{opt} can now be obtained for all three types of fins with a specified heat duty q

$$L_{\text{opt}} = (3r_i/2)^n \left[\left\{ n + \frac{(m+n)^m q k^{m-1}}{L_b} \right\}^{1/(2m-1)} - n \right] \tag{37}$$

where

$$L_b = (1+2n)(T_b - T_a) r_i^{2n} \pi^{m+n-1} h^m \tag{38}$$

Fin efficiency for the optimum three types of fins above is obtained as follows:

$$\eta = \frac{(2m+n-1)(1+3nR_i)}{(2+4n)^m(1+2nR_i)} \tag{39}$$

From Eq. (39), it may be noted that the fin efficiencies for the optimum longitudinal and pin fins are constant, whereas for the optimum annular fin, it depends on r_i and L only.

8 Conclusions

The present work gives the unified analysis for the optimum design of longitudinal, annular, and pin fins with and without volumetric heat generation. As this analysis has been developed in a compact form using a single set of equations and boundary conditions for the three different fins, it can be readily used for pedagogical instructions. Moreover, it is of use in thermal design, as the designer knows the upper bound of heat transfer for a given fin volume and can select a specific type of fin for a given primary surface. The above analysis highlights the following common characteristics of optimum fins:

1. Optimum fins, both with and without volumetric heat sources, will have zero temperature excess at the fin tip.
2. For fins with volumetric heat generation, the temperature gradient is a function of local fin temperature, while it is constant for fins without heat generation.
3. The thickness of the optimum fin reduces to zero at the tip.
4. Additionally, at the fin tip, $d(Y^m)/dX$ is also zero for optimality. The gradient of the optimum profile for both longitudinal and annular fins will be zero at the tip because $m = 1$ for both of them. On the other hand, the value of m is 2 for pin fins. So, mathematically, it does not rule out the possibility of a nonzero gradient at the fin tip.

Nomenclature

- Bi = Biot number, hL/k
- F = dimensionless function used in Eq. (9)
- $\dot{g}$ = volumetric heat generation rate, $\text{W/m}^3\,\text{K}$
- h = surface heat transfer coefficient, $\text{W/m}^2\,\text{K}$
- k = thermal conductivity of the fin material, W/m K
- L = length of the fin, m
- L_a, L_b = parameters defined in Eqs. (29) and (38), respectively
- m, n = constants, see Eq. (1)
- N_g = dimensionless heat generation rate, $\dot{g}L^2/k$
- q = actual heat transfer rate over the fin surface, W
- Q = dimensionless heat transfer rate, see Eq. (4)
- q_i = ideal heat transfer rate, W
- Q_i = dimensionless ideal heat transfer rate
- r_i = fin base radius, m
- R_i = dimensionless radius, r_i/L
- T = local fin temperature, K
- T_a = temperature of the surrounding gas medium of the fin, K
- T_b = fin base temperature, K
- U = dimensionless fin volume, see Eq. (5)
- V = fin volume, m^3
- x, y = Cartesian coordinates, m
- X, Y = dimensionless coordinates, x/L and y/L, respectively

Greek Letters

- η = fin efficiency
- λ = Lagrange multiplier
- Λ = function defined in Eq. (8)
- σ = dimensionless parameter, $[N_g/(2m-1)]^{1/2}$
- θ = dimensionless temperature, $(T-T_a)/(T_b-T_a)$
- Γ = objective function defined in Eq. (9)

Subscript

- opt = optimum

References

[1] Gardener, K. A., 1945, "Efficiency of Extended Surface," ASME J. Heat Transfer, **67**, pp. 621–631.
[2] Schmidt, E., 1926, "Die Warmenbertranung durch Rippen," Z. VDI, **70**, pp. 885–951.
[3] Duffin, R., 1959, "A Variational Problem Relating to Cooling Fins," J. Math. Mech., **8**, pp. 47–56.
[4] Minkler, W. S., and Rouleau, W. T., 1960, "The Effects of Internal Heat Generation on Heat Transfer in Thin Fins," Nucl. Sci. Eng., **7**, pp. 400–406.
[5] Wilkins, J. E., Jr., 1962, "Minimum Mass Thin Fins With Internal Heat Generation," Nucl. Sci. Eng., **14**, pp. 203–204.
[6] Liu, C. Y., 1961, "A Variational Problem With Applications to Cooling Fins With Heat Generation," J. Soc. Ind. Appl. Math., **9**, pp. 194–201.
[7] Natarajan, U., and Shenoy, U. V., 1990, "Optimum Shapes Convective Pin Fins With Variable Heat Transfer Coefficient," J. Franklin Inst., **327**, pp. 965–982.
[8] Murray, W. M., 1938, "Heat Transfer Through an Annular Disc or Fin of Uniform Thickness," ASME J. Appl. Mech., **60**, p. A-78.
[9] Kraus, A. D., 1982, *Analysis and Evaluation of Extended Surface Thermal Systems*, Hemisphere, Washington, DC.
[10] Elsgolts, L., 1977, *Differential Equation and the Calculus of Variations*, Mir Publishers, Moscow.

Local Pool Boiling Coefficients on the Outside Surface of a Horizontal Tube

Myeong-Gie Kang
Department of Mechanical Engineering Education, Andong National University 388 Songchun-dong, Andong-city, Kyungbuk 760-749, Korea

Changes in local pool boiling heat transfer coefficients on the outside surface of a 51 mm dia *horizontal tube have been investigated experimentally in water at atmospheric pressure. The local values were determined at every* 45 deg *from the very bottom to the uppermost of the tube periphery, and a representative value was suggested. The maximum and the minimum local coefficients were observed at the azimuthal angles of 45 and* 180 deg, *respectively, from the tube bottom. The coefficient at* 90 deg *can be suggested as the representative of the coefficients. The major mechanisms affecting heat transfer on the surface were liquid agitation and bubble coalescence. Moreover, it is identified that the data can be curve fitted as* $h_b = C_1 + C_2 q''$.
[DOI: 10.1115/1.1929785]

Introduction

Mechanisms of pool boiling heat transfer have been studied for a long time. Recently, it has been widely investigated in nuclear power plants for the purpose of acquiring inherent safety functions in case of no power supply [1]. Pool boiling heat transfer is very attractive from the viewpoint of enhancing the heat transfer rate in a limited space. To design more efficient passive heat exchangers, effects of several parameters on heat transfer must be studied in detail. One of the major issues is variation in local heat transfer coefficients on a horizontal tube.

Previous studies (see Table 1) on local heat transfer coefficients of the circular shape in horizontal location are about tubes [2–5] and hemispheres [6,7]. Lance and Myers [2] reports that the type of boiling liquid can change the trend of local heat transfer coefficients along the tube periphery. Lance and Myers said that because the liquid is methanol, the maximum local heat transfer coefficient was observed at the tube bottom, while the maximum was at the tube sides as the boiling liquid was *n*-hexane. Moreover, they reported that the difference among the local heat transfer coefficients decreased as the heat flux increased. Cornwell and Einarsson [3] reported that the maximum local heat transfer coefficient was observed at the tube bottom, as the boiling liquid was R113. The location of the maximum heat transfer coefficient moves toward the tube sides as the fluid flow around the tube increases. Cornwell and Houston [8] explained the reason of the difference in local heat transfer coefficients along the tube circumference with introducing effects of sliding bubbles on heat transfer.

According to Gupta et al. [4], the maximum and the minimum local heat transfer coefficients are observed at the bottom and top regions of the tube circumference, respectively, using a tube bundle and water. Kang also reported the similar results using a single tube of 19.05 mm dia and water [7]. Gupta et al. [4] studied azimuthal angles of every 45 deg along the tube periphery while Kang studied only three angles of 0, 90, and 180 deg.

Contributed by the Heat Transfer Division for publication in the JOURNAL OF HEAT TRANSFER. Manuscript received by the Heat Transfer Division March 31, 2004; revision received December 15, 2004. Review conducted by: J. N. Chung.

Results by El-Genk and Gao [5] and Cheung et al. [6] for a hemisphere also said that local heat transfer coefficients were changing along the circumference. Much difference between two local values at the bottom and sides were observed. The local heat transfer coefficients were increased as the liquid changed from subcooled to saturated conditions.

Summarizing the published results, some parts are still remaining to be investigated in detail. The present study is aimed to improve Kang's previous result [7] and to add some pool boiling data, which can be used for more accurate design of passive heat exchangers.

Experiments

A schematic view of the present experimental apparatus and test sections is shown in Fig. 1. The water storage tank (Fig. 1(*a*)) is made of stainless steel and has a rectangular cross section (950×1300 mm) and a height of 1400 mm. This tank has a glass view port (1000×1000 mm), which permits viewing of the tubes and photographing. The tank has a double container system. The sizes of the inner tank are $800 \times 1000 \times 1100$ mm (depth $\times$ width $\times$ height). The inside tank has several flow holes (28 mm dia) to allow fluid inflow from the outer tank. Four auxiliary heaters (5 kW/heater) were installed at the space between the inside and outside tank bottoms to boil the water and maintain the saturated condition. To reduce heat loss to the environment, the left, right, and rear sides of the tank were insulated by glass wool of 50 mm thickness.

The heat exchanger tubes were simulated by resistance heaters (Fig. 1(*b*)) made of a very smooth stainless steel tube ($L = 300$ mm and $D = 51$ mm). Several rows of resistance wires are arrayed uniformly inside the heated tube to supply power to the tube. Moreover, insulation powder was packed into the space between the tube inside wall and the wires to prevent any possible current flow to the data acquisition system and to heat the outer stainless steel tube uniformly. The surface of the tube was finished through a buffing process to have a smooth surface. Electric power was supplied through the bottom side of the tube. To make the azimuthal angle, one side of the test section has a flange. The peripheral variation in heat transfer was determined by rotating the tube following each set of readings. The angular increment between reading positions was 45 deg. For the test, 220 V AC was used.

The tube outside was instrumented with five T-type sheathed thermocouples (diameter is 1.5 mm). The thermocouple tip ($\sim$10 mm) was bent at a 90 deg angle and the bent tip brazed on the tube wall. The locations of the thermocouples are 50, 100, 150, 200, and 250 mm from the heated tube bottom as shown in Fig. 1(*b*). The water temperatures were measured by the specially manufactured temperature measuring device (Fig. 1(*c*)) with six sheathed T-type thermocouples and placed vertically at a corner of the inside tank. All thermocouples of the heated tube and the device were calibrated at a saturation value (i.e., 100°C since all the tests are run at atmospheric pressure condition).

To fix the heated tube onto the right position, a supporter was manufactured as shown in Fig. 1(*d*). The heated tube and the supporter were assembled by the sets of a bolt and a nut. To measure and/or control the supplied voltage and current, two power supply systems (each having three channels for reading of voltage and current in digital values) were used. The capacity of each channel is 10 kW.

For the tests, the heat exchanging tube and the tube supporter were assembled and place at the bottom of the tank. After the water storage tank is filled with water until the initial water level is 750 mm from the outer tank bottom, the water is heated using four preheaters. When the water temperature reaches the saturation point, it was boiled for 30 min to remove any dissolved gases. Then, the supply of electricity to the test tube started. The temperatures on the tube surface are measured while controlling the

Table 1 Summary of the previous works about local boiling heat transfer on outside of horizontal circular heating geometries

Author	Geometry	Material	Fluid	Boiling condition
Lance and Myers (1958)	1.25 in. tube 2 in. tube	Copper	Methanol n-hexane	Saturated Pool boiling
Cornwell and Einarsson (1990)	27.1 mm tube	Thin stainless steel sleeve on a copper rod	R113	Saturated Flow boiling Pool boiling
Gupta et al. (1995)	19.05 mm tube	Stainless steel	Water	Saturated Flow boiling Pool boiling
El-Genk and Gao (1999)	15.2 mm dia hemisphere	Aluminum Stainless steel	Water	Saturated Pool boiling
Cheung et al. (1999)	0.305 m dia hemisphere	Aluminum	Water	Saturated Subcooled Pool boiling
Kang (2000)	19.05 mm tube	Stainless steel	Water	Saturated Pool boiling

heat flux. In this manner a series of experiments has been performed for various combinations of the azimuthal angle. Every experimental data were measured as the heat flux was increasing. According to Kang [9], there was no evidence of hysteresis due to the heat flux increase and decrease for the combination of water and a smooth stainless steel tube, as in the present study.

The error bound of the voltage and current meters used for the test are ±0.5% of the measured value. Therefore, the calculated power (voltage × current) has ±1.0% error bound. Since the heat flux has the same error bound as the power, the uncertainty in the heat flux is estimated to be ±1.0%.

The measured temperature has uncertainties originated from the thermocouple probe itself and instrument. To evaluate the error bound of a thermocouple probe, three thermocouples brazed on tube surface were submerged in an isothermal bath of ±0.01 K accuracy. The measured temperatures were compared to the set temperature. The deviation of the measured value from the set temperature is within ±0.1 K, inclusive of the bath accuracy. The error bound of the data acquisition system is ±0.05 K. Therefore, the total uncertainty of the measured temperatures is defined by adding the above errors, and it is ±0.15 K.

The heat flux from the electrically heated tube surface is calculated from the input power as follows:

$$q'' = \frac{q}{A} = \frac{VI}{\pi DL} = h_b(T_W - T_{\text{sat}}) = h_b \Delta T_{\text{sat}} \tag{1}$$

where V and I are the supplied voltage (in volts) and current (in amperes), and D and L are the outside diameter and the length of the heated tube, respectively. T_W and T_{sat} represent the measured temperatures of the tube surface and the saturated water, respectively. The tube temperatures used in Eq. (1) are the arithmetic average value of the measured temperatures.

Results and Discussion

Figure 2 shows variations in the heat flux and the local heat transfer coefficient as the degree of superheating changes. To obtain local coefficients exactly, heat transfer along the tube periphery has been evaluated based on the measured local temperatures at the given azimuthal angles. The largest heat transfer occurred at $q''=50$ kW/m^2. For the case, the maximum temperature difference is 1.8 K between the temperatures at $\theta=45$ and 180 deg. The one-dimensional conduction heat transfer along the tube periphery is calculated as 0.45 kW/m^2. This value is just 0.9% of the radial heat flux. Moreover, as the heat flux is more or less than 50 kW/m^2, the amount of the peripheral heat flux is decreasing. Since the amount of peripheral heat transfer is not very large, its effect on the local heat transfer coefficients has been neglected. The maximum and minimum local coefficients are observed at $\theta=45$ and 180 deg, respectively. The minimum point is same to Gupta et al. [4] and Kang [7]. The difference in the maximum point between the present results and Gupta et al. is assumed to be originated from the difference in geometry and the tube diameter (see Table 1). At $\Delta T_{\text{sat}}=6$ K the maximum local heat transfer coefficient is eight times larger than the minimum value. The local coefficient is increasing as the azimuthal angle is <45 deg and, then, it decreases, as the angle is >45 deg. The slopes of the curves are increasing suddenly as the degree of liquid superheating is increasing. The major cause of the increase in heat transfer coefficients is liquid agitation due to rising bubbles. As a bubble moves along the tube periphery, it agitates relevant liquid. Moreover, since some amount of space is generated as the bubble departs, liquid rushes to the space. At $\theta=45$ deg, the intensity of liquid agitation seems to have its largest value, since enough moving bubbles are observing and the region is relatively free from the bubble coalescence as shown in Fig. 3. As the azimuthal angle is >90 deg, bubbles that came from the lower side start to depart from the surface due to buoyancy, and the intensity of liquid agitation decreases. This generates a big bunches of bubbles on the surface as shown in Fig. 3. The region of bubble bunches is spreading toward the lower side of the tube circumference as the heat flux increases. The coalesced bubbles prevent easy access of relevant liquid to the heated surface and decrease the heat transfer rate at the upper regions of the tube. At lowermost region of the tube ($\theta=0$ deg), very small amounts of active liquid generation is

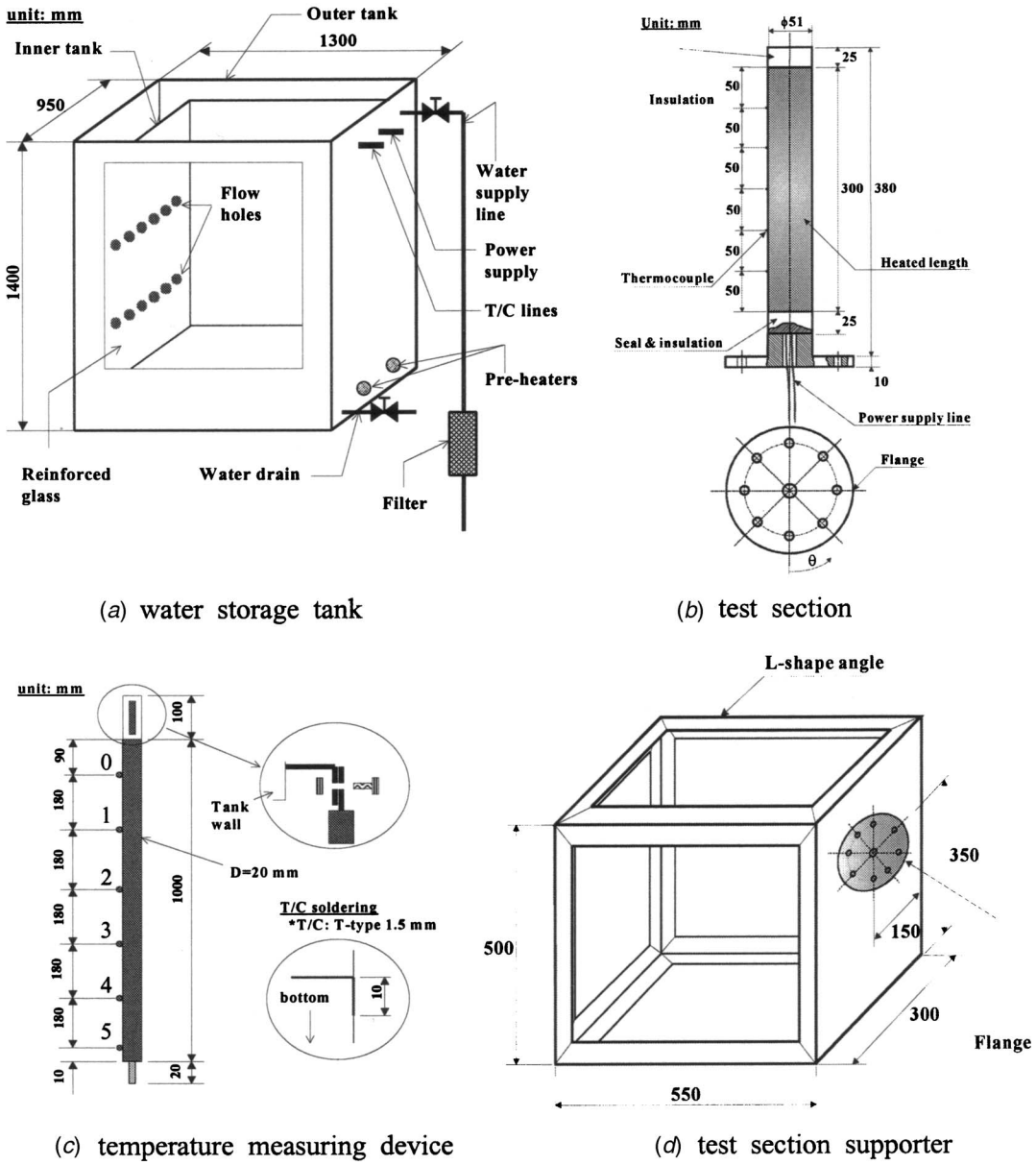

Fig. 1 Schematic of the experimental apparatus

expected at lower heat flux. Therefore, the active nucleation sites can be treated as the major heat transfer mechanism at the lower heat fluxes. As the heat flux increases, the number of sites is increased and the rate of flow circulation along the tube is also increasing. Therefore, the intensity of liquid agitation at the lowermost region gets increased and results in a somewhat sharp increase in the curve slope. The angle of the largest heat transfer coefficient was decided as the location where the effect of liquid agitation was high and the effect of bubble coalescence was low. Therefore, it can be moved to other locations since these two mechanisms depend on the heat flux for the present case. A greater supply of electric power could move the angle to the tube bottom due to the growth of the bubble coalescence region.

One of the important subjects in pool boiling heat transfer on a horizontal tube is the suggestion of a method to predict an average value along the tube periphery. One way of calculating the average coefficient is to measure and average every heat transfer coefficient along the tube periphery. However, this approach is very cumbersome and not simple. If a representative temperature on the horizontal tube circumference was not fixed, much scattering would exist in the data because of the difference in the measuring locations. Kang's previous result [7] suggests that the local heat transfer coefficient at $\theta=90$ deg is just similar to the averaged value of the local coefficients at $\theta=0$ and 180 deg in saturated pool boiling. To define the representative location the data points, measured at the several different azimuthal angles, are curve fitted using the least-squares method and the resulting equation is $h_{b,\mathrm{avg}}=0.49515+0.14171q''$ (kW/m^2 K); q'' is in kilowatts per meters squared. The calculated values have been compared to the local coefficients, and the best-fitted results are shown in Fig. 4. As shown in the figure the measured values at $\theta=90$ deg are within ±5% error bound of the calculated values. Therefore, it can be suggested that the local heat transfer coefficient at $\theta=90$ deg can be treated as the average value along the tube circumference similar to Kang's results [7].

To predict the data quantitatively, several empirical correlations have been suggested by using the least-squares method and experimental data. Results of the calculation are listed in Table 2. The empirical equation for the saturated boiling can be correlated

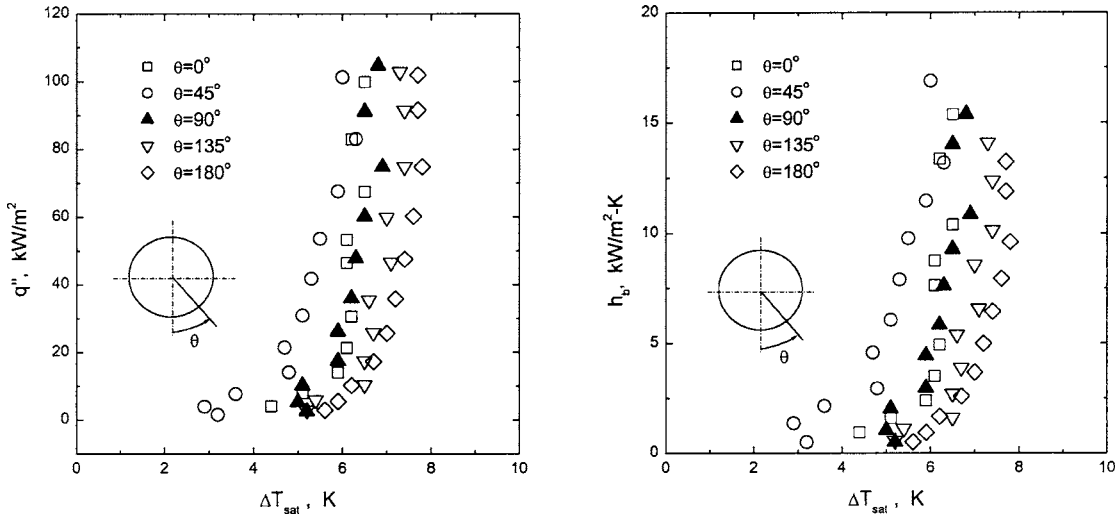

Fig. 2 Plots of q'' and h_b versus ΔT_{sat}

as a function of the heat flux and/or the tube wall superheat. Since the tube wall superheat is dependent on the heat flux, the equation is correlated as a function of the heat flux and has a first-order polynomial equation, such as $h_b = C_1 + C_2 q''$, where the units of h_b and q'' are $kW/m^2\,K$ and kW/m^2, respectively. Comparison of the calculated and measured values is shown in Fig. 5. In the figure empirical equations suggested in Table 2 are used to calculate local heat transfer coefficients. According to the results, the correlations can predict the measured experimental data within ±5% error bound. Therefore, it can be said that the suggested correlations could predict the experimental data very well.

Conclusions

Local heat transfer coefficients on a horizontal tube of 51 mm dia have been investigated experimentally in the water at atmospheric pressure. The major conclusions of the present study are as follows:

1. Much variation in local coefficients was observed along the tube periphery. The maximum and minimum values are observed at $\theta = 45$ and 180 deg, respectively. Major causes of the difference are liquid agitation and bubble coalescence.
2. The local heat transfer coefficient measured at $\theta = 90$ deg can be recommended as the representative value of the tube periphery.

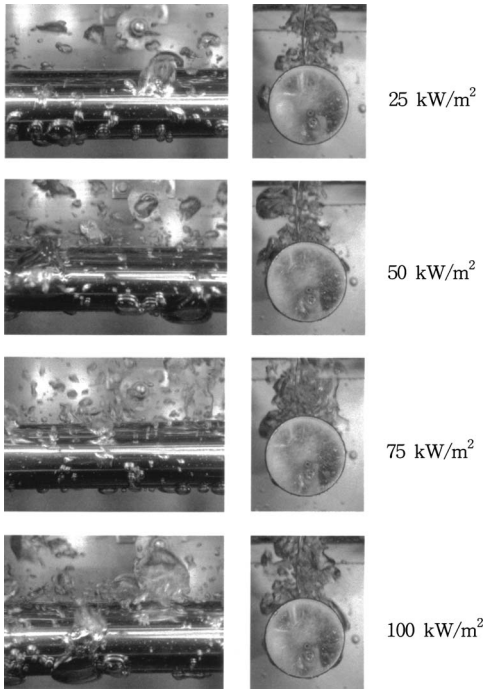

Fig. 3 Photos of pool boiling on the horizontal tube surface

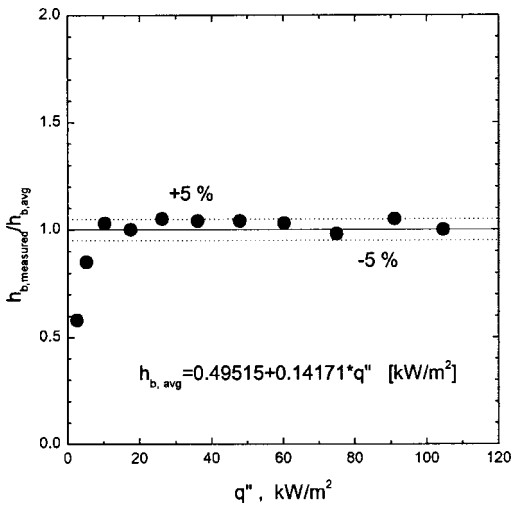

Fig. 4 Comparison of the calculated average heat transfer coefficients with the measured coefficients at $\theta = 90$ deg

Table 2 Curve fitting results for the h_b versus q'' Data ($h_b = C_1 + C_2 q''$)

Thermocouple location	Parameter value		Standard deviation
θ deg	C_1	C_2	
0	0.31685	0.15329	0.21909
45	0.86808	0.15730	0.42260
90	0.42325	0.14533	0.26334
135	0.33929	0.13326	0.17326
180	0.32045	0.12644	0.11298

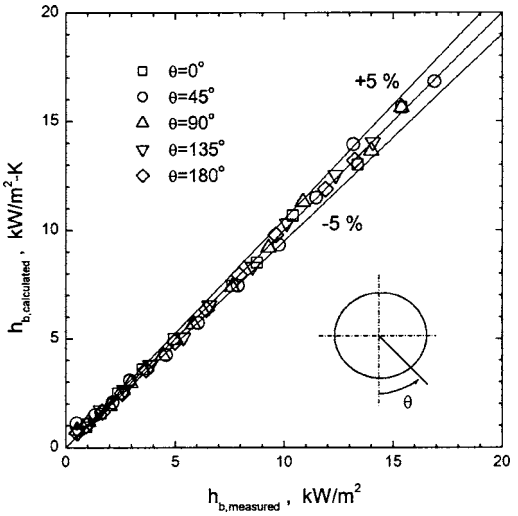

Fig. 5 Comparison of the calculated heat transfer coefficients with the measured coefficients

3. The measured heat transfer coefficients and heat fluxes can be correlated as $h_b = C_1 + C_2 q''$. The correlation predicts the experimental data within ±5% error bound.

Acknowledgment

This work was supported by Grant No. R05-2000-000-00309-0 from the Basic Research Program of the Korea Science and Engineering Foundation.

Nomenclature

A = heat transfer area
C = constant
D = heating tube diameter
h_b = boiling heat transfer coefficient
I = supplied current
L = tube length
q = input power
q'' = heat flux
T_{sat} = saturated temperature
T_W = temperature of heating surface
V = supplied voltage
ΔT_{sat} = the degree of liquid superheating ($=T_W - T_{sat}$)
θ = azimuthal angle along the tube periphery

References

[1] Chun, M. H., and Kang, M. G., 1998, "Effects of Heat Exchanger Tube Parameters on Nucleate Pool Boiling Heat Transfer," ASME J. Heat Transfer, **120**, pp. 468–476.
[2] Lance, R. P., and Myers, J. E., 1958, "Local Boiling Coefficients on a Horizontal Tube," AIChE J., **4**(1), pp. 75–80.
[3] Cornwell, K., and Einarsson, J. G., 1990, "Influence of Fluid Flow on Nucleate Boiling from a Tube," Exp. Heat Transfer, **3**, pp. 101–116.
[4] Gupta, A., Saini, J. S., and Varma, H. K., 1995, "Boiling Heat Transfer in Small Horizontal Tube Bundles at Low Cross-flow Velocities," Int. J. Heat Mass Transfer, **38**(4), pp. 599–605.
[5] El-Genk, M. S., and Gao, C., 1999, "Experiments on Pool Boiling of Water from Downward-facing Hemispheres," Nucl. Technol., **125**, pp. 52–69.
[6] Cheung, F. B., Haddad, K. H., and Liu, Y. C., 1999, "Boundary-Layer-Boiling and Critical-Heat-Flux Phenomena on a Downward-Facing Hemispherical Surface," Nucl. Technol., **126**, pp. 243–264.
[7] Kang, M. G., 2000, "Effect of Tube Inclination on Pool Boiling Heat Transfer," ASME J. Heat Transfer, **122**, pp. 188–192.
[8] Cornwell, K., and Houston, S. D., 1994, "Nucleate Pool Boiling on Horizontal Tubes: A Convection-based Correlation," Int. J. Heat Mass Transfer, **37** (Suppl. 1), pp. 303–309.
[9] Kang, M. G., 2001, "Hysteresis Effects in Pool Boiling of Water," JKSME B, **25**(8), pp. 1037–1045.